Title
Experimental and Numerical Studies of Mechanically- and Convectively-Driven Turbulence in Planetary Interiors

Author
Grannan, Alexander Michael

Publication Date
2017

Peer reviewed|Thesis/dissertation

UNIVERSITY OF CALIFORNIA

Los Angeles

Experimental and Numerical Studies of Mechanically- and Convectively-Driven Turbulence in Planetary Interiors

A dissertation submitted in partial satisfaction
of the requirements for the degree
Doctor of Philosophy in Geophysics and Space Physics

by

Alexander Michael Grannan

2017

ABSTRACT OF THE DISSERTATION

Experimental and Numerical Studies of Mechanically- and Convectively-Driven Turbulence in Planetary Interiors

by

Alexander Michael Grannan
Doctor of Philosophy in Geophysics and Space Physics
University of California, Los Angeles, 2017
Professor Jonathan M. Aurnou, Chair

The energy for driving turbulent flows in planetary fluid layers comes from a combination of thermocompositional sources and the motion of the boundary in contact with the fluid through mechanisms like precessional, tidal, and librational forcing. Characterizing the resulting turbulent fluid motions are necessary for understanding many aspects of the planet's dynamics and evolution including the generation of magnetic fields in the electrically conducting fluid layers and dissipation in the oceans. Although such flows are strongly inertial they are also strongly influenced by the Coriolis force whose source is in the rotation of the body and tends to constrain the inertial effects and provide support for fluid instabilities that might in-turn generate turbulence. Furthermore, the magnetic fields generated by the electrically conducting fluids act back on the fluid through the Lorentz force that also tends to constrain the flow. The goal of this dissertation is to investigate the characteristics of turbulent flows under the influence of mechanical, convective, rotational and magnetic forcing.

In order to investigate the response of the fluid to mechanical forcing, I have modified a unique set of laboratory experiments that allows me to quantify the generation of turbulence driven by the periodic oscillations of the fluid containing boundary through tides and libration. These laboratory experiments replicate the fundamental ingredients found in planetary environments and are necessary for the excitation of instabilities that drive the turbulent

fluid motions. For librational forcing, a rigid ellipsoidal container and ellipsoidal shell of isothermal unstratified fluid is made to rotate with a superimposed oscillation while, for tidal forcing, an elastic ellipsoidal container of isothermal unstratified fluid is made to rotate while an independently rotating perturbance also flexes the elastic container. By varying the strength and frequencies of these oscillations the characteristics of the resulting turbulence are investigated using meridional views to identify the dominate modes and spatial location of the turbulence. For the first time, measurements of the velocity in the equatorial plane are coupled with high resolution numerical simulations of the full flow field in identical geometry to characterize the instability mechanism, energy deposited into the fluid layer, and long-term evolution of the flow. The velocities determined through laboratory and numerical simulations when extrapolated to planets allow me to argue that that the dynamics of mechanical forcing in low viscosity fluids may an important role as new and potentially large source of dissipation in planetary interiors.

To study convective forcing, I have modified and performed a set of rotating and non-rotating hydrodynamic convection experiments using water as well as rotating and non-rotating magnetohydrodynamic convection in gallium. These studies are performed in a cylindrical geometry representing a model of high latitude planetary core style convection wherein the axis of rotation and gravity are aligned. For the studies using water, the steady columns that are characteristic of rotating convection and present in the dynamo models are likely to destabilize at the more extreme planetary parameters giving way to transitions to more complex styles of rotating turbulent flow. In the studies of liquid metal where the viscosity is lower, the onset of rotating convection occurs through oscillatory columnar convection well below the onset of steady columns. Such oscillatory modes are not represented at the parameters used by current dynamo models. Furthermore a suite of laboratory experiments shows that the imposition of rotational forces and magnetic forces both separately and together generate zeroeth order flow transitions that change the fundamental convective modes and heat transfer. Such regimes are more easily accessible to laboratory experiments then to numerical simulations but demonstrate the need for a new generation of dynamo simulations capable of including the fundamental properties of liquid metals as are relevant

for understanding the dynamics of planetary interiors.

The dissertation of Alexander Michael Grannan is approved.

Jeff D. Eldredge

James C. McWilliams

Gerald Schubert

Jonathan M. Aurnou, Committee Chair

University of California, Los Angeles

2017

Dedicated to my family

Table of Contents

List of Figures

List of Tables

Acknowledgments

My deepest gratitude goes to my thesis advisor, Jonathan Aurnou, whose enthusiasm, ideas, and perspective are a constant source of inspiration.

I also want to thank Michael Le Bars for his guidance both at UCLA and in France. To Benjamin Favier, whose numerical simulations and analysis were vital to this work. To the technical and facilities staff, specifically Shylo Stiteler and Ron Mears for their guidance in modifying the laboratory experiments. To my lab mates, Ashna Aggarwal, Vincent Bertin, Mickael Bosco, Jonathan Cheng, Emily Hawkins, Susanne Horn, Daphné Lemasquerier, Adolfo Ribeiro, and Jean-Baptiste Wacheul for their useful discussions and welcome distractions. Finally, I want to thank my doctoral committee, Jeff D. Eldredge, Jim McWilliams, and Gerald Schubert as well as Jon Mound for their feedback that improved this thesis.

This work is supported by the Earth Science Division Geophysics Program of the United States National Science Foundation, NASA Planetary Geology and Geophysics Program, and the Chateaubriand Fellowship Program.

Chapter 3 is a modified reprint of a first author peer-reviewed publication. Chapter 4 is a modified reprint of a peer-reviewed publication in which I was a coauthor. Chapter 5 is a modified reprint of a first author peer-reviewed publication reproduced following the terms of the Creative Commons Attribution License. Chapter 6 is modified from a manuscript submitted for review in which I am a coauthor. Chapter 8 is a modified reprint of a peer-reviewed publication in which I am a coauthor and reproduced following the terms of the Creative Commons Attribution License. Chapter 9 is modified from a manuscript submitted for review in which I am a coauthor.

Vita

2011	B.Sc. Physics and Mathematics, Indiana University - Bloomington.
2011	Minor, Geology, Indiana University - Bloomington.
2011-2017	Graduate Student Researcher, University of California, Los Angeles.
2013	Chateaubriand Fellowship
2011,‘12,‘14-‘16	Teaching Assistant, University of California, Los Angeles.
2016-2017	Dissertation Year Fellowship

Publications

T. Vogt, S. Horn, **A. M. Grannan**, J. M. Aurnou (2017), “On the interpretation of turbulent convective large scale circulation ”, *Nature*, In Prep

A. M. Grannan, T. Vogt, E. Hawkins, A. Aggarwal, S. Horn, and J. M. Aurnou (2017), “Behaviors and transitions along the path to magnetostrophic convection”, *J. Fluid Mech.*, In Prep

D. Lemasquerier, **A. M. Grannan**, B. Favier, J. Vidal, D. Cébron, M. Le Bars, and J. M. Aurnou (2017), “Libration Driven Elliptical Instability Experiments in Ellipsoidal Shells”, *J. Geophys. Rev. Planets*, Submitted

V. Bertin, **A. M. Grannan**, and J. M. Aurnou (2017), "Rotating convection in liquid gallium: Oscillations, Wall Modes, and Turbulence", *J. Fluid Mech.*, Submitted

A. M. Grannan, B. Favier, M. Le Bars, and J. M. Aurnou (2017), "Tidally-forced turbulence in planetary interiors", *Geophys. J. Int.*, 208(3):16901703

B. Favier, **A. M. Grannan**, M. Le Bars, and J. M. Aurnou (2015), "Generation and maintenance of bulk turbulence by libration-driven elliptical instability", *Phys. of Fluids*, 27, 066601

J. S. Cheng, A. Ribeiro, E. M. King, S. Stellmach, **A. Grannan**, and J. M. Aurnou (2015), "Laboratory-numerical models of rapidly rotating convection in planetary cores," *Geophys. J. Int.*, 201, 1-17

A. M. Grannan, M. Le Bars, D. Cébron, and J. M. Aurnou (2014), "Experimental study of global-scale turbulence in librating ellipsoid," *Phys. of Fluids*, 26, 126601

CHAPTER 1

Introduction

1.1 Geophysical Context

Ground and space based measurements have improved and constrained our understanding of many celestial bodies. These data allow us to infer, among various things, a body's interior structure, composition, and magnetic field. Through such observations, scientists have confirmed that differentiated celestial bodies, bodies that have separated into distinct solid and liquid layers, are ubiquitous. These include the liquid metal cores of our own Earth, Mercury, Io, and Ganymede and the subsurface oceans found on Europa, Callisto, and Enceladus [e.g., Margot et al. (2007); Anderson et al. (1996); Schubert et al. (2004); Anderson et al. (1998, 2001); Cedak et al. (2016); Thomas et al. (2016)].

With the Earth as an example for which we know the most about its structure, the interior is divided into a solid iron inner core, a liquid iron outer core, the mantle, and the outermost layers containing the crust, oceans, and atmosphere. When considering the Earth's dipolar magnetic field, we search for its origins in the liquid metal outer core. Because the interior is much hotter than the material's Curie temperature, there cannot be permanent magnetization [e.g., Stacy and Davis (2008)]. Furthermore, any ancient magnetic field originating from the planet's formation would have decayed on timescales much shorter then the evidence we have for the duration of its existence, upwards of roughly 4 billion years [e.g., Tarduno et al. (2015)]. The persistence of the dynamo as well as the presence of field variations, like polar reversals on long timescales and secular variations on shorter time scales, suggest a field of dynamic origins [e.g., Johnson et al. (2003); Finlay et al. (2012)]. It is widely believed that the field is constantly being regenerated by the turbulent motions of the electrically

conducting liquid metal in the outer core. The process by which the kinetic energy of such fluid motions is converted to electromagnetic energy is referred to as dynamo action.

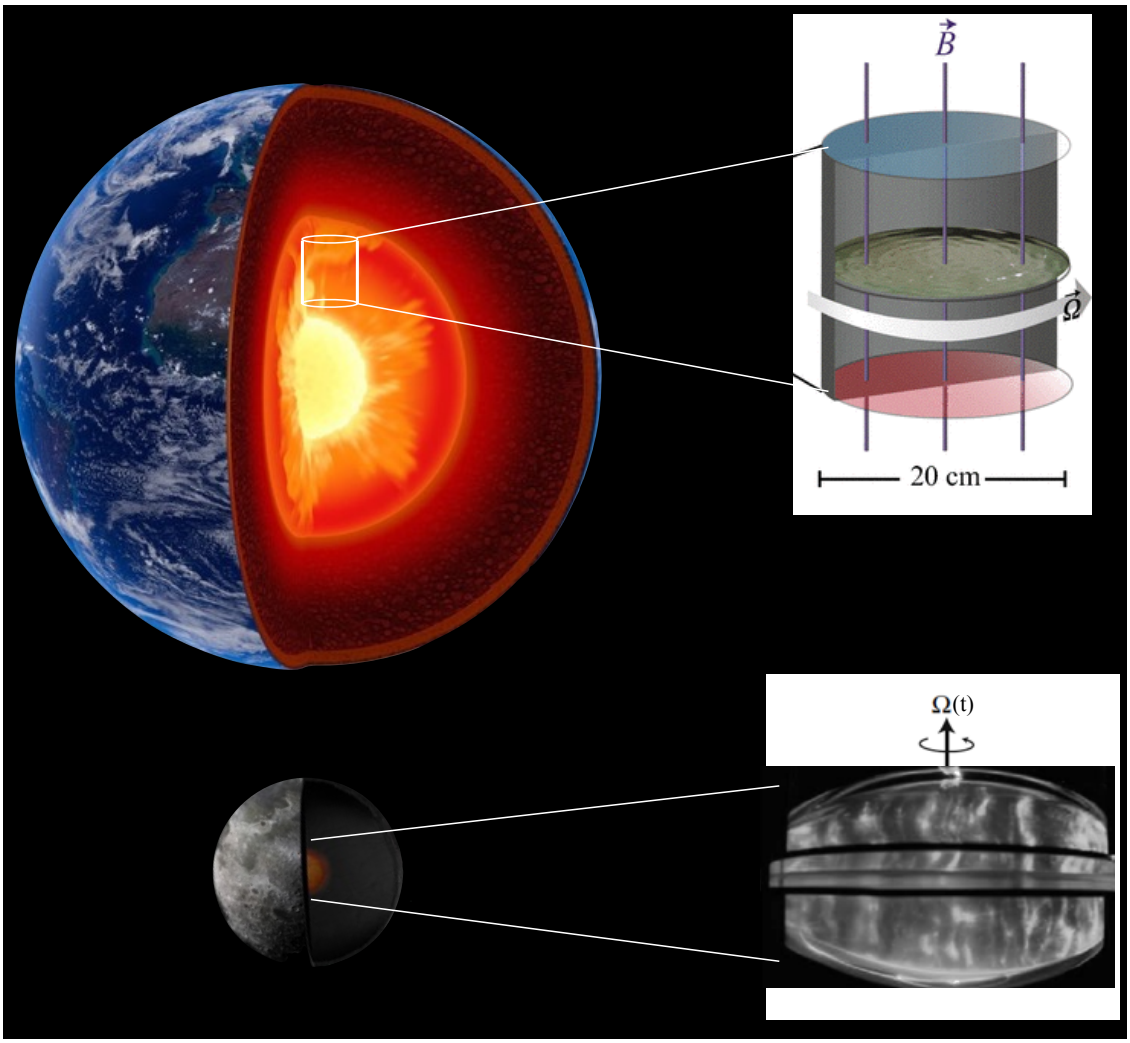

Figure 1.1: The work carried out in this thesis is relevant for the study of the rotating turbulence in the low viscosity oceans and atmosphere and in the liquid metal cores of the Earth, Moon, and other planetary bodies subjected to thermocompositional and mechanical forcing. Images modified from www.livescience.com/images, King and Aurnou (2015), and www.space.com.

This dissertation will focus on the modeling of two ways that these turbulent fluid motions are driven as shown in Figure 1.1. The most common source, and the one generally assumed for Earth, is from convective instability wherein the heat generated by planetary formation, radioactive decay, and the growth of the inner core is released into the outer core driving thermo-compositional convection [e.g., Jones (2011); Schubert and Soderlund (2011);

O'Rourke and Stevenson (2016)]. Another important source of energy is from mechanical forcing through precession and nutation, libration, tidal, and even impacts from small bodies that lead to the oscillations of the boundary in contact with the liquid metal layers. The role of mechanical forcing, while not generally considered in planetary fluid layers and not as thoroughly studied as its convective counterpart, may have important consequences for the thermal evolution, dissipation, and magnetic field generation in small bodies like the Moon in Figure 1.1.

In order to address the role of mechanical forcing, I focus on tidal and librational forcing whose schematics are shown in Figure 1.2.a and b. respectively. Many bodies are ellipsoidally deformed either naturally or by gravitational forcing and rotate at an average angular rotation rate, $\overline{\Omega}_{spin}$. In Figure 1.2.a, a planet having low rigidity is deformed by an orbiting attractor and generates tidal deformations that perturb the enclosed fluids. It is well known that in Earth's case, tidal forcing in the ocean is primarily responsible for dissipation [e.g., Egbert and Ray (2003)]. Despite its potential importance, tidal forcing processes are not generally considered in the subsurface oceans and liquid metal cores on other bodies.

In addition to tidal forcing, many satellites also experience librational forcing as shown in Figure 1.2.b. Librational forcing arises when a deformed body is in synchronous or nearly synchronous orbit in that the orbital and spin rate are commensurate. The eccentricity of the orbit leads to variations in the orbital rate following Kepler's third law and creates a phase lag between the equatorial bulge and the line connecting the centers of mass for the two bodies as shown by the dashed and solid red arrows in Figure 1.2.b, respectively. Periodic torques, shown as black arrows, are induced to restore this alignment, leading to oscillations in the rotation rate, $\Omega_{spin}(t)$, of the deformed boundary about the average spin rate $\overline{\Omega}_{spin}$. Both types of mechanical forcing have been shown to give rise to complex flows [e.g., Le Bars et al. (2007, 2010); Cébron et al. (2012b); Noir et al. (2012)]. A primary objective of this dissertation is to provide the first quantitative laboratory experimental analysis of the onset of turbulence via tidal and librational forcing and effects of such flows on planetary dynamics like dissipation and magnetic field generation.

The relationship between the turbulent flows generated by these forcing mechanisms and

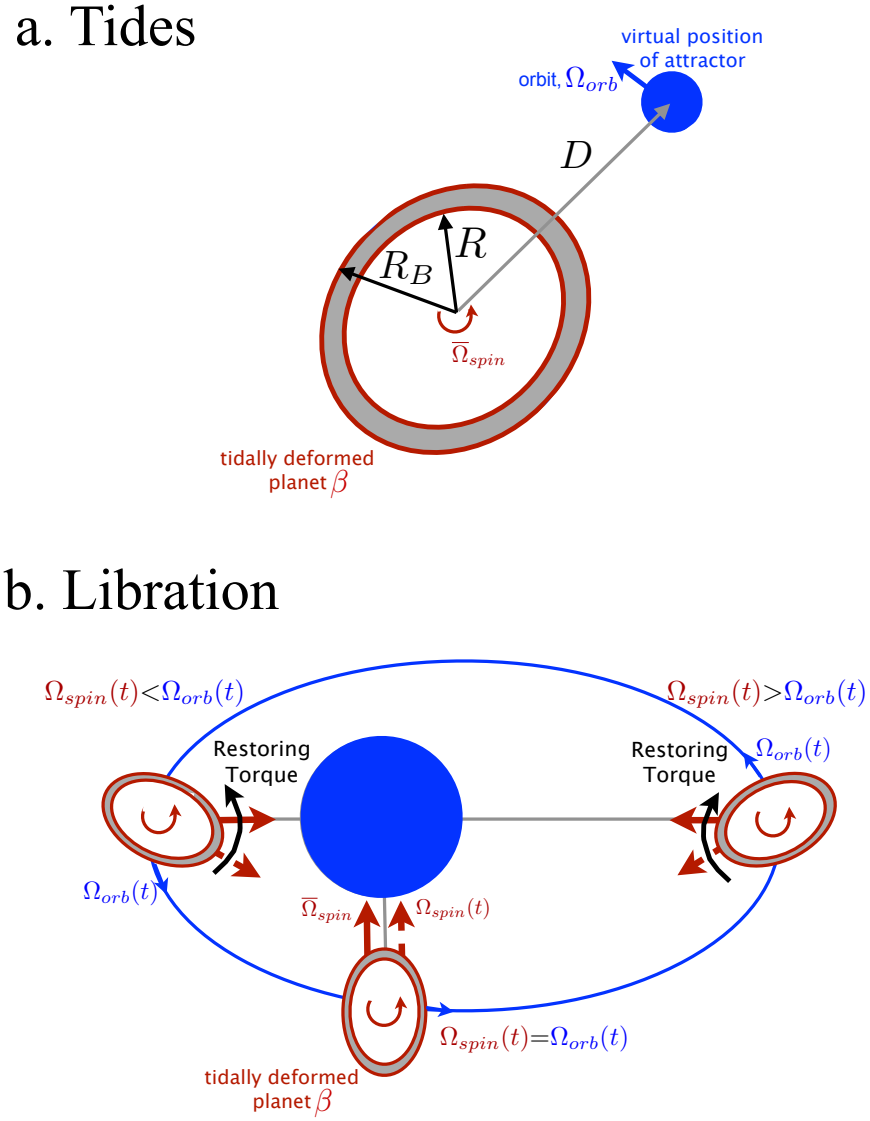

Figure 1.2: **a)** A polar-view of the model for a tidally deformed elastic body of amplitude β with a fluid interior spinning at $\overline{\Omega}_{spin}$. A virtual attractor orbits at Ω_{orbit}. The deformed body's r.m.s radius is R_B, the fluid radius is R, and the average distance between the two bodies is D. **b)** A polar-view of the model for longitudinal libration of a rigid synchronous planet with a fluid interior rotating at $\Omega_{spin}(t)$, and orbiting at $\Omega_{orbit}(t)$ where, when time-averaged, $\overline{\Omega}_{spin} = \overline{\Omega}_{orbit}$. The solid red arrow denotes the direction toward the gravitational partner. The dashed red arrow denotes the direction of the long axis of the deformed ellipsoid. The misalignment between the two red arrows leads to restoring torques (black arrow) that oscillate the deformed boundary. Schematics adapted from Le Bars et al. (2010); Noir et al. (2012) and repeated from Grannan et al. (2017) and shown in Figure 5.1.

the resulting magnetic fields produced is complex and remains an important open question in studying geophysics and astrophysics. One of the reasons for this is the material properties

associated with the fluids participating in the magnetic field generation. For galaxies and stars, the electrically conducting fluid is plasma while for terrestrial planets and asteroids the working fluid is typically a liquid metal. The inverse thermal conductivity of the fluid is characterized non-dimensionally by the Prandtl number,

$$Pr = \frac{\text{Viscous Diffusivity}}{\text{Thermal Diffusivity}} = \frac{\nu}{\kappa} \tag{1.1}$$

where ν is the viscous diffusivity and $\kappa = k/\rho C_p$ is the thermal diffusivity with k being the thermal conductivity, ρ being the density, and C_p being the specific heat of the fluid. For typical liquid metals and plasmas where the thermal conductivity is high and the viscosity is low, the Prandtl number typically ranges between 10^{-2} to 10^{-7}. Similarly, the strength of the electrical conductivity is described non-dimensionally by the magnetic Prandtl number,

$$Pm = \frac{\text{Viscous Diffusivity}}{\text{Magnetic Diffusivity}} = \frac{\nu}{\eta} \tag{1.2}$$

where $\eta = 1/\mu_o\sigma$ is the magnetic diffusivity with μ_o being the permeability of free space and σ being the electrical conductivity. The magnetic Prandtl number ranges from 10^{-5} to 10^{-9} indicating high magnetic diffusivity relative to the viscous diffusivity. The scaling of these diffusivities suggests that, for these fluids that are highly magnetically diffusive and highly thermally diffusive, the length and time scales for the magnetic field are larger than those of the thermal scales, which are larger than the viscous scales associated with the flow field.

To characterize the dynamic vigor of the underlying flow, we first look at the ratio of the inertial forces to the viscous forces that dampen the flow. This ratio is encapsulated by the Reynolds number,

$$Re = \frac{\text{Inertia}}{\text{Viscous}} = \frac{UL}{\nu}, \tag{1.3}$$

where U is a typical flow velocity. L is the typical lengthscale of the fluid layer, and ν the viscous diffusivity of the fluid. For typical flows, $Re \gtrsim 1000$ is called turbulent where the advection dominates the effects of viscosity. Taking values for Earth's outer core, the kinematic viscosity for liquid metals is $\nu \sim 10^{-7}\,\mathrm{m/s^2}$, the length scale is $L \sim 10^6\,\mathrm{m}$, and

the velocity is taken as $U \sim 10^{-4}$m/s from observations of secular variation of the magnetic field. These values give $Re \sim 10^9$ indicating strongly turbulent fluid motions [e.g., Bloxham and Jackson (1991)].

Another aspect needed to characterize flow in planetary layers is to account for the importance of rotation. Rotation manifests its influence in the form of the Coriolis force which acts to constrain the flow and align it with the axis of rotation. The ratio of the viscous force to the Coriolis force is defined as the Ekman number,

$$E = \frac{\text{Viscous}}{\text{Coriolis}} = \frac{\nu}{2\Omega L^2}. \tag{1.4}$$

The rotation rate Ω is, for Earth, $\Omega = 7 \times 10^{-5}\,\text{rad/s}$. The Ekman number is taken to be $E \ll 1$ in many geophysical flows, indicating that viscous forces are negligible compared to rotational forces. The ratio of inertial forces to the Coriolis forces is encapsulated by the Rossby number, Ro,

$$Ro = \frac{\text{Inertia}}{\text{Coriolis}} = \frac{U}{L}\frac{1}{\Omega} = 2ReE \tag{1.5}$$

In planetary settings $Ro \ll 1$ indicating that rotational forces also dominate inertial forces.

For the electrically conducting liquid metal fluid in planetary interiors where the magnetic field is generated, that magnetic field also acts back on the flow. The ratio of the Lorentz force to viscous force is defined by the Chandrasehkar number,

$$Q = \frac{\text{Lorentz}}{\text{Viscous}} = \frac{\sigma B_o^2 L^2}{\rho\nu}, \tag{1.6}$$

where B_o is the characteristic magnetic field strength, σ is the electrical conductivity of the fluid, and ρ is the fluid density. Similar to the Rossby number in (1.5), a magnetic Rossby number is defined as:

$$Ro_{\text{M}} = \frac{\text{Inertia}}{\text{Lorentz}} = \frac{U}{L}\frac{\rho}{\sigma B_o^2} = ReQ^{-1} \tag{1.7}$$

In planetary settings $Ro_{\text{M}} \ll 1$. In other texts, the magnetic Rossby number is also related to the interaction number, $N = 1/Ro_{\text{M}}$. A summary of these parameters with their definitions and values for the Earth are given in Table 1.1.

1.2 Open Questions

Thus, taking all the parameters together, it is expected that in the low viscosity fluids of the Earth and many planets, rotational forces are much stronger than both viscous ($E \ll 1$) and inertial forces ($Ro \ll 1$). In the Earth's core, it is also expected that Lorentz forces, which also tend to constrain the flow, are much stronger than both viscous ($Q \gg 1$) and inertial forces ($Ro_{\mathrm{M}} \ll 1$). Despite such constraints, the inertial force greatly exceed the viscous force rendering the fluid turbulent ($Re \gg 1$). Thus, for convectively- and mechanically-driven flows, under the constraints just described, the important open questions are as follows:

- **What is the nature of the turbulent flow constrained by strong and rotation and magnetic fields? What are the characteristic frequencies and flow structures?**
- **How do such flows evolve through time and how do they change as the strength of mechanical forcing, convective forcing, rotational forcing, and Lorentz forces ar varied?**
- **How can the findings from laboratory experiments and numerical simulations be extended to planetary settings?**

In this dissertation I will provide insights into these fundamental questions using a combination of laboratory experiments that I have performed coupled with numerical simulations.

1.3 Simulating Planetary Core Flows

1.3.1 Governing Equations

The equations that govern the complex flows present in planetary fluid layers are also quite complex. For processes investigated in this thesis, the fluid is taken to be homogeneous and incompressible with a Newtonian viscosity and spatially uniform diffusivities. Furthermore, in implementing convective forcing, the Boussinesq approximation is used such that the

Parameter	Symbol	Meaning	Definition	Earth's core
Prandtl number	Pr	$\frac{\text{Viscous Diffusion}}{\text{Thermal Diffusion}}$	$\frac{\nu}{\kappa}$	$\sim 10^{-1}$
Magnetic Prandtl number	Pm	$\frac{\text{Viscous Diffusion}}{\text{Magnetic Diffusion}}$	$\frac{\nu}{\eta}$	$\sim 10^{-6}$
Reynolds number	Re	$\frac{\text{Inertia}}{\text{Viscous}}$	$\frac{UL}{\nu}$	$\sim 10^{9}$
Magnetic Reynolds number	Rm	$\frac{\text{Magnetic Induction}}{\text{Magnetic Diffusion}}$	$\frac{UL}{\eta} = RePm$	$\sim 10^{3}$
Ekman number	E	$\frac{\text{Viscous}}{\text{Coriolis}}$	$\frac{\nu}{2\Omega L^2}$	$\sim 10^{-15}$
Rossby number	Ro	$\frac{\text{Inertia}}{\text{Coriolis}}$	$\frac{U}{\Omega L} = 2ReE$	$\sim 10^{-6}$
Chandrasekhar number	Q	$\frac{\text{Lorentz}}{\text{Viscous}}$	$\frac{\sigma B_o^2 L^2}{\rho\nu}$	$\sim 10^{15}$
Magnetic Rossby number	Ro_m	$\frac{\text{Inertia}}{\text{Lorentz}}$	$\frac{U\rho}{L\sigma B_o^2} = ReQ^{-1}$	$\sim 10^{-6}$
Elsasser number	Λ	$\frac{\text{Lorentz}}{\text{Coriolis}}$	$\frac{\sigma B_o^2}{2\rho\Omega} = QE = \frac{Ro}{2Ro_m}$	~ 1
Flux Rayleigh number	Ra_F	$\frac{\text{Buoyancy}}{\text{Diffusion}}$	$\frac{\alpha_T g L^4 q_{\text{SA}}}{k\nu\kappa}$	$\sim 10^{27} - 10^{32}$
Nusselt number	Nu	$\frac{\text{Total Heat Transfer}}{\text{Conduction}}$	$\frac{q_{\text{SA}} L}{k\Delta T_{\text{SA}}}$	$\sim 10^{2} - 10^{7}$
Rayleigh number	Ra	$\frac{\text{Buoyancy}}{\text{Diffusion}}$	$\frac{\alpha_T g \Delta T_{\text{SA}} L^3}{\nu\kappa} = \frac{Ra_F}{Nu}$	$\sim 10^{20} - 10^{30}$

Table 1.1: Non-dimensional parameters that describe the properties of liquid metals in geophysical settings. The dimensional values used are the viscous diffusivity, ν [m^2/s], thermal diffusivity, κ [m^2/s], magnetic diffusivity, η[m^2/s], the characteristic velocity scale, U [m/s], length scale of the system L [m], the average rotation rate of the fluid Ω [rad/s], the electrical conductivity, σ [S/m] or σ [$\text{kg}^{-1}\text{m}^{-3}\text{s}^3\text{A}^2$] in standard SI units, mean density, ρ [kg/m^3], average background magnetic field, B_o [T], thermal expansivity, α_T [K^{-1}], gravitational acceleration, g [m/s^2], the superadiabatic heat flux, q_{SA} [W/m^2], the thermal conductivity k [$\text{Wm}^{-1}\text{K}^{-1}$], and the superadatiabatic temperature contrast, ΔT_{SA} [K].

density variations are only relevant in the gravitational and hence the buoyancy term. The set of equations are:

$$\frac{\partial \mathbf{u}}{\partial t} + \mathbf{u}\cdot\nabla\mathbf{u} + 2\boldsymbol{\Omega}\times\mathbf{u} = -\frac{1}{\rho}\nabla P + \alpha_T T\mathbf{g} + \frac{1}{\rho}\mathbf{J}\times\mathbf{B} + \nu\nabla^2\mathbf{u} - \frac{\partial\boldsymbol{\Omega}}{\partial t}\times\mathbf{x} \tag{1.8}$$

$$\nabla\cdot\mathbf{u} = 0 \tag{1.9}$$

$$\frac{\partial T}{\partial t} + \mathbf{u}\cdot\nabla T = \kappa\nabla^2 T \tag{1.10}$$

$$\frac{\partial \mathbf{B}}{\partial t} + \mathbf{u}\cdot\nabla\mathbf{B} = \mathbf{B}\cdot\nabla\mathbf{u} + \eta\nabla^2\mathbf{B} \tag{1.11}$$

$$\nabla \cdot \mathbf{B} = 0 \tag{1.12}$$

This coupled system of equations consist of the Navier-Stokes equation governing the evolution of momentum in the rotating reference frame of a fluid, the continuity equation, the temperature or energy equation, the induction equation that governs the evolution of the magnetic field, and finally the divergence free condition of the magnetic field. The variables in this system of equations are the velocity, $\mathbf{u}$, the rotation rate, $\mathbf{\Omega}$, the density, ρ, the modified pressure, $P = p + \phi + \Omega^2 s^2/2$, containing the centrifugal acceleration and gravitational potential from the mean (hydrostatic) gravity term, the thermal expansivity, α_T, temperature anomaly, T, the gravitational acceleration $\mathbf{g}$, the magnetic field, $\mathbf{B}$, the electric current density, $\mathbf{J} = 1/\mu_o \nabla \times \mathbf{B}$, the kinematic viscosity, ν, the displacement vector, $\mathbf{x}$, the thermal diffusivity, κ, and the magnetic diffusivity, η.

The terms in (1.8) are the time rate of change of momentum, the advection term, Coriolis acceleration, the modified pressure gradient, thermal bouyancy, Lorentz term, viscous diffusion, and the change in rotation rate. In the thermal equation (1.10), the terms from left to right are the time rate of change of thermal anomaly, advection, and the thermal diffusion. For the induction equation given by (1.11), the terms from left to right are the time rate of change of the magnetic field, advection, induction, and the magnetic diffusion term.

1.3.2 The effects of strong rotation

To examine the effects of strong rotation, the rotation is assumed to be constant and the convective and Lorentz forces are not considered. In the limit that rotational forces dominate both inertia and viscous forces such that $Ro \ll 1$ and $E \ll 1$, the primary balance is between the Coriolis force and the pressure gradient terms such that,

$$2\Omega \hat{\mathbf{z}} \times \mathbf{u} \sim -\frac{1}{\rho} \nabla P, \tag{1.13}$$

where the axis of rotation is assume to be aligned with the $\hat{\mathbf{z}}$ axis. This balance is defined as geostrophy. By taking the curl of (1.13), using vector identities, and implementing the

incompressibility velocity condition, the resulting balance yields,

$$-2\Omega\hat{\mathbf{z}}\cdot\nabla\mathbf{u}\sim-\nabla\times\nabla P=0\Rightarrow\frac{\partial\mathbf{u}}{\partial z}=0. \tag{1.14}$$

This condition, where the velocity does not vary along the axial direction, is referred to as the Taylor-Proudman theorem.

We consider small departures from geostrophic balance by including the effects of time dependence on small velocity perturbations. By once again taking the curl of (1.13) with the time derivative term and using the same vector identities as used to arrive at (1.14) gives:

$$\frac{\partial}{\partial t}\nabla\times\mathbf{u}=2\Omega\hat{\mathbf{z}}\cdot\nabla\mathbf{u}. \tag{1.15}$$

By again taking the curl of (1.15) as well as a time derivative and by using the incompressibility condition on the velocity, $\nabla\cdot\mathbf{u}=0$, the term on the left side can be written as $\nabla\times(\nabla\times\mathbf{u})=-\nabla^2\mathbf{u}$. A Poincaré equation for inertial waves is then given by,

$$\frac{\partial^2}{\partial t^2}\nabla^2\mathbf{u}=-4\Omega\frac{\partial^2}{\partial z^2}\mathbf{u}. \tag{1.16}$$

The properties for inertial waves can be determined by assuming plane wave solutions of the form $\mathbf{u}=\tilde{\mathbf{u}}e^{i(\mathbf{k}\cdot\mathbf{r}+\omega t)}$. The dispersion relation for these inertial waves is found by plugging this solution into (1.16) and is given from Tilgner (2007) as:

$$\omega=\pm2\Omega(\hat{\mathbf{z}}\cdot\hat{\mathbf{k}})=\pm2\Omega\cos\theta, \tag{1.17}$$

where θ is the angle between the wave vector $\mathbf{k}$ and the axis of rotation, $\hat{\mathbf{z}}$ and the magnitude of the frequency of the inertial wave varies between 0 and two times the rotation rate. Furthermore, plugging the wave solution into the incompressibility condition on the velocity reveals $\mathbf{u}\cdot\mathbf{k}$=0 indicating that motion of the fluid is transverse to the wave direction. Figure 1.3.a shows inertial waves excited in a rotating fluid by an oscillating sphere. The solid and dashed lines designate the waves and crests inside a wavepacket with thick solid lines.

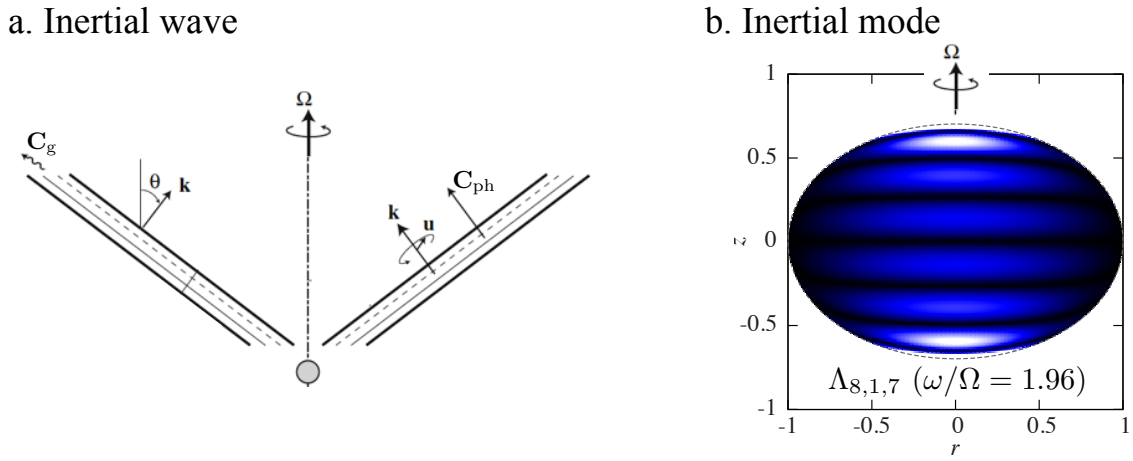

Figure 1.3: **(a)** Schematic of inertial wave packet enclosed by thick lines in an infinite rotating fluid layer generated by an oscillating sphere. The solid and dashed lines correspond to the trough and crest of the wave **(b)** Inertial mode in a finite equatorially symmetric container with frequency $\omega \sim 2\Omega$ such that the wavevector $\mathbf{k}$ and phase velocity $\mathbf{C}_{\rm ph}$ are parallel to the rotation axis. Modified from images in Messio et al. (2008) and Favier et al. (2015).

The phase velocity that describes the motion of the crests and troughs of the wave is given from Messio et al. (2008) as,

$$\mathbf{C}_{\rm ph} = \frac{\omega}{|\mathbf{k}|}\hat{\mathbf{k}} = \pm\frac{2\Omega}{|k|}\cos\theta\hat{\mathbf{k}}. \tag{1.18}$$

Because the phase speed of the inertial waves depends on both the direction and magnitude of the wave vector, inertial waves are said to be both dispersive and anisotropic. The direction of energy transport by the waves is described by the group velocity such that:

$$\mathbf{C}_{\rm g} = \nabla_k\omega = \pm\frac{2\Omega}{|k|}\,\hat{\mathbf{k}}\times(\hat{\mathbf{k}}\times\hat{\mathbf{z}}) = \pm\frac{2\Omega}{|k|}\,\left[\cos\theta\hat{\mathbf{k}} - \hat{\mathbf{z}}\right], \tag{1.19}$$

where ∇_k is the gradient in wavenumber space and the vector triple product identity given by $\mathbf{a}\times(\mathbf{b}\times\mathbf{c}) = (\mathbf{a}\cdot\mathbf{c})\mathbf{b} - (\mathbf{a}\cdot\mathbf{b})\mathbf{c}$ has been used. In the limit that the frequency of the inertial waves is very slow, $\omega \ll 2\Omega$, the angle $\theta \to \pi/2$ meaning the direction of the group velocity tends toward the axis of rotation. Thus, the principle of the Taylor-Proudman theorem has been recovered in that the slow motions of fluid in a rapidly rotating system move along the axis of rotation. Another interesting property of inertial waves is that it can be shown that

the phase velocity and group velocity are perpendicular,

$$\mathbf{C}_{\mathrm{ph}} \cdot \mathbf{C}_{\mathrm{g}} = 0, \tag{1.20}$$

meaning that the energy is focused and is not spread out in the direction of the wave packets motion.

When rotating fluids are confined to finite volumes, the inertial waves reflected at the boundaries preserve the angle, θ, between the wave vector and the rotational axis. The waves and their reflections can interfere constructively leading to inertial modes. Analytical solutions of inertial modes exist for the cylinder, cylindrical shell, spheroid, and a polynomial description also exists for the ellipsoids considered in the majority of the mechanical forcing experiments in this dissertation [e.g., Kerswell (1993); Herreman (2009); Zhang et al. (2004); Vantieghem (2014). Such analytical descriptions cannot be extended to the more geophysically relevant geometry of spherical shells due to the ill-posed nature of the well-known Poincaré equation for inertial modes with non-penetrating boundary conditions. Numerical studies, in this geometry, have shown that solutions converge to attractors [e.g., Rieutord and Valdettaro (1997); Rieutord et al. (2001)].

1.3.3 Elliptical Instability in Mechanically-Forced Flows.

To understand how mechanical forcing can drive turbulent fluid motions through a fluid instability, I will focus on librational forcing. This theoretical framework is also applicable to tidal forcing as shown in Chapter 5. In librational forcing, we consider a homogenous isothermal fluid enclosed inside an ellipsoid whose equatorial ellipticity is described by $\beta = (a^2 - b^2)/(a^2 + b^2)$ where a is the long equatorial axis, b is the short equatorial axis. The rotation of the container is implemented by applying a constant rotation with a sinusoidal oscillation such that the rate is:

$$\mathbf{\Omega}(t) = \Omega_0(1 + \epsilon \sin(\omega_{\mathrm{lib}} t))\,\hat{\mathbf{z}} \tag{1.21}$$

Here, $\epsilon = \Delta\phi f$ is the non-dimensional measure of the differential rotation of the ellipsoidal distortion with respect to the background rotation where $\Delta\phi$ [rad] is the angular amplitude of libration and $f = \omega_{\rm lib}/\Omega_0$ is the ratio of the libration frequency $\omega_{\rm lib}$ to the rotation rate of the background container, Ω_0. The momentum equation is then rewritten as a modified version of (1.8) written in the frame fixed to the ellipsoidal container and without the presence of thermal or magnetic forcing,

$$\frac{\partial \mathbf{u}}{\partial t} + \mathbf{u}\cdot\nabla\mathbf{u} + 2(1+\epsilon\sin(ft))\hat{\mathbf{z}}\times\mathbf{u} = -\nabla P + E\nabla^2\mathbf{u} - \epsilon f\cos(\omega_{lib}t)(\hat{\mathbf{z}}\times\hat{\mathbf{x}}). \tag{1.22}$$

This equation has been non-dimenisionalized using the long axis a for the length scale and Ω_0^{-1} as the time scale. In this formulation, the Ekman number is defined as $E = \nu/(\Omega_0 a^2)$. A solution of the inviscid form of (1.22) that satisfies the no penetration condition for the fluid at the boundary is the libration-driven base flow given by Kerswell and Malkus (1998); Cébron et al. (2012b) as:

$$\mathbf{U}_B = -\epsilon\sin(ft)\left[\hat{\mathbf{z}}\times\mathbf{x} - \beta\nabla(xy)\right], \tag{1.23}$$

whose streamlines are ellipsoidal (having an azimuthal wavenumber, $m_{\rm lib} = 2$) reflecting the equatorial ellipticity of the container. While this base flow oscillates back and forth, satisfaction of the no-slip boundary condition for the velocity at the boundary leads to steady zonal flows in the bulk which have been studied in detail by Wang (1970); Suess (1971); Busse (2010); Calkins et al. (2010); Noir et al. (2010); Sauret et al. (2010); Chan et al. (2011); Zhang et al. (2011)]. Of particular interest is the condition when small flow perturbations, $\mathbf{u}'$, may grow through an instability that may lead to turbulence. The first order equation governing the evolution of the perturbation is given by,

$$\frac{\partial \mathbf{u}'}{\partial t} + \mathbf{U}_B\cdot\nabla\mathbf{u}' + \mathbf{u}'\cdot\nabla\mathbf{U}_B + 2\hat{\mathbf{z}}\times\mathbf{u}' = -\nabla P' + E\nabla^2\mathbf{u}'. \tag{1.24}$$

A complete theoretical description of the onset of elliptical instability based on a normal-mode analysis is given in Section 3.2.4. For other problems like pipe flow, the onset of

instability is better explained by non-normal mode growth rates that are larger than those of normal mode growth and better explain experimental observations of the onset of turbulence [Schmid (2007); Schmid and Henningson (2012)]. The techniques of non-normal mode growth have not, to date, been applied to flows addressed in this work but may provide unique insight into aspects of the transition to turbulence. In the current work, we thus omit any non-normal mode analysis and focus on normal mode techniques that have successfully predicted the observed growth rates and flow magnitudes generated by elliptical instability [e.g., Le Bars et al. (2010); Cébron et al. (2012b); Noir et al. (2012)].

In brief, the librational forcing initiates the ellipsoidal base flow as well as noise (a sum of all inertial modes). Assuming the perturbations can be written as a series of inertial modes, an elliptical instability is possible if there exist two inertial modes that are related to the base flow by the following instability conditions for the frequency and the azimuthal wavenumber:

$$|\omega_1 - \omega_2| = \omega_{\text{lib}}, \tag{1.25}$$

and for the azimuthal wavenumbers,

$$|m_1 - m_2| = m_{\text{lib}} = 2. \tag{1.26}$$

Thus, the difference in the frequencies of the inertial modes must be equal to the frequency of the applied librational forcing and the difference of the azimuthal wavenumbers of the inertial modes must equal the azimuthal wavenumber of the base flow $m_{\text{lib}} = 2$. Crucially, this instability acts as a conveyor that transmits a portion of the large reservoir of rotational energy into the fluid layer.

The growth rate, σ is given from Cébron et al. (2012b); Grannan et al. (2014); Favier et al. (2015); Grannan et al. (2017) as:

$$\sigma \sim \epsilon\beta - K\sqrt{E}, \tag{1.27}$$

Planet	Layer	M(kg)	$R_p(km)$	T_{spin}	T_{orb}	R_o/R_p	χ	$\Delta\phi$(rad)	β	E	$\epsilon\beta/\sqrt{E}$
Earth[a]	LC	5.98e24	6378	1	27.32	0.55	0.35	-	8.44e-8	1.12e-15	2.4313
Venus[a]	LC	4.87e24	6051	-243	224.7	0.17	0.00	-	1.08e-7	3.16e-12	0.1276
Mercury[a]	LC	3.30e23	2440	58.6	87.97	0.80	0.00	2.0e-4	4.00e-7	2.11e-13	0.0001
Moon[e]	LC	7.34e22	1737	27.32	27.32	0.20	0.00	7.0e-5	1.13e-5	3.11e-12	0.0004
Ganymede[a]	LC	1.50e23	2631	7.16	7.16	0.27	0.00	5.6e-6	2.86e-4	1.95e-13	0.0037
Io[a]	LC	8.93e22	1822	1.77	1.77	0.52	0.00	1.3e-4	2.59e-3	2.71e-14	2.0424
Enceladus[b,c,d]	SO	1.08e20	252	1.37	1.37	0.91	0.83	2.1e-3	9.23e-3	3.60e-13	32.323
Europa[a]	SO	4.80e22	1561	3.55	3.55	0.99	0.94	2.0e-4	7.51e-4	2.04e-14	1.0504
Dione [f]	SO	1.09e21	561	2.74	2.74	0.82	0.86	9.3e-5	2.54e-3	1.78e-13	0.0560
Callisto[a]	SO	1.10e23	2410	16.69	16.69	0.94	0.93	4.2e-6	5.56e-5	4.47e-14	0.0011
Titan[a]	SO	1.35e23	2576	15.95	15.95	0.97	0.92	2.3e-5	5.88e-5	3.51e-14	0.0072
Ganymede[a]	SO	1.50e23	2631	7.16	7.16	0.96	0.94	5.6e-6	2.86e-4	1.54e-14	0.0130

[a] Cébron et al. (2012a) and references therein
[b] McKinnon (2015)
[c] Thomas et al. (2016)
[d] Cedak et al. (2016)
[e] Noir et al. (2009)
[f] Estimated in Beuthe et al. (2016)

Table 1.2: Physical and dimensionless parameters for tidal and librational forcing in planets. Earth and Venus are assumed to be tidally forced while all other bodies librating. The fluid layers considered are the liquid metal core (LC) and subsurface ocean (SO). The outer radius of the planet, R_p, is given in kilometers. The spin period $T_{\text{spin}} = 2\pi/\Omega_{spin}$ and orbital period $T_{\text{orb}} = 2\pi/\Omega_{orb}$ are given in days. The outer radius of the fluid layer is R_o, and the inner radius of the fluid layer is R_i so that the aspect ratio is given by $\chi = R_i/R_o$. The angle of the libration, $\Delta\phi$, is given in radians. The ellipsoidal distortion, β is given in (1.28). The Ekman number, $E = \nu/(2\Omega_{spin}R_{out}^2)$ is estimated using a kinematic viscosity $\nu = 10^{-6}\text{m}^2/\text{s}$. The stability criteria in the final column is the ratio of the strength of mechanical forcing to viscous dissipation where, for tidal forcing in planetary settings, $\epsilon = (1 - T_{spin}/T_{orb})$ and for librational forcing in planetary settings, $\epsilon = \Delta\phi T_{spin}/T_{orb}$.

where the first term, $\epsilon\beta$, is a non-dimensional measure of the strength of the ellipsoidal base flow and hence the strength of the librational forcing on the fluid. The second term, $K\sqrt{E}$, represents the retarding effects of viscous dissipation that tends to stabilize fluid motions and K is a dissipation factor with typical values $K \in [1-10]$. The criteria for the growth of the instability such that $\sigma > 0$ thus requires that $\epsilon\beta/\sqrt{E} > K$.

The characteristics of tidal and librational forcing in bodies around the solar system are compiled in Table 1.2. A first order estimate of the non-dimensional ellipsoidal distortion of an incompressible, homogeneous, and non-spinning body that omits the heterogeneously distributed densities and material rigidity for simplicity is given from Cébron et al. (2012a) as:

$$\beta = \frac{3}{2}\frac{M_2}{M}\frac{R_p^3}{D^3}, \tag{1.28}$$

where M and R_p are the mass and radius of the distorted body. The mass of the body responsible for the gravity field and the distance between it and the distorted body are M_2 and D, respectively. The final column in Table 1.2 provides an estimate for the stability of planetary fluid layers to mechanical forcing. Using these estimates, tidal forcing in the Earth's liquid metal core may be capable of generating intense flows while librational forcing in the liquid metal core of Io and the subsurface oceans of Enceladus and Europa may also generate turbulence.

1.3.4 The effects of strong magnetic fields

Under the influence of a strong magnetic field, a similar phenomenon to the aforementioned Taylor-Proudman theorem occurs in that the velocity can act to constrain the flow to horizontal directions perpendicular to that of the applied magnetic field. This setting may be relevant for understanding the sun where the effects of rotation are negligible in comparison to those of a strong magnetic field. For a steady, uniform and vertical magnetic field, $\mathbf{B} = B_o\hat{\mathbf{z}}$, the induction equation in (1.11) can be written as:

$$\mathbf{B}\cdot\nabla\mathbf{u} = B_o\frac{\partial\mathbf{u}}{\partial z} = 0 \Rightarrow \frac{\partial\mathbf{u}}{\partial z} = 0, \tag{1.29}$$

where the time and spatial derivatives of the magnetic field are zero and magnetic diffusion is neglected. The result that the flow field is invariant of the direction of the applied magnetic field is again analogous to that of the Taylor-Proudman theorem for strong rotation.

1.3.5 Magnetostrophic flows

While the effects of rotational and magnetic forces applied separately to the fluid tend to constrain the fluid and suppress convection, when the two are applied simultaneously the constraint is relaxed and the critical value at which the convection sets in is also decreased [e.g., Chandrasekhar (1961)]. Such a state is referred to as magnetostrophy ($\Lambda \sim 1$) and is thought to be the state where planetary dynamos might naturally settle [e.g., Stevenson (2003)]. This regime has been explored in laboratory experiments where maxima in the dimensionless heat transfer were found around $\Lambda \sim 2$ [e.g., King and Aurnou (2015)].

1.3.6 Heat Transfer

The primary method for investigating the convective flows in this thesis focuses on changes in heat transfer efficiency (Nu) and modes of convective flow as a function of the buoyancy, rotational, and magnetic strength ($Ra,\ E,\ Q,$) using thermal measurements. The Nusselt number is defined as

$$Nu = \frac{\text{Total Heat Transfer}}{\text{Conductive Hear Transfer}} = \frac{qL}{k\Delta T} \tag{1.30}$$

where q is the total (superadiabatic) heat flux, L is the height of the container, k is the thermal conductivity of the fluid and ΔT is the temperature difference between the top and bottom thermal horizontal fluid boundaries. Because q is the sum of the convective and conductive heat fluxes, the lowest value for the Nusselt number is $Nu = 1$ corresponding to the purely conductive state. Unlike for planets, the adiabatic thermal gradient in experiments is negligible [e.g., $dT/dz = \alpha_T T g/C_p \sim 10^{-3}$ [K/m] using the properties of the liquid metal gallium]. And, as the convective vigor increases, Nu increases.

The heat transfer behaviour changes under the influence of strong rotation and strong magnetic fields. The difference between inertially dominated flow and constrained convection

a. Rotating convection in water

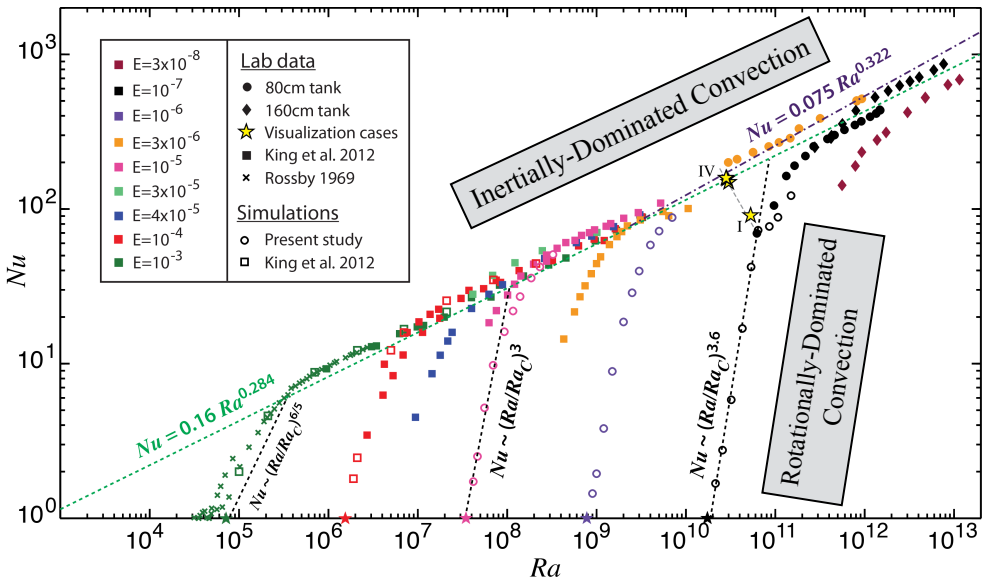

b. Magnetoconvection in gallium

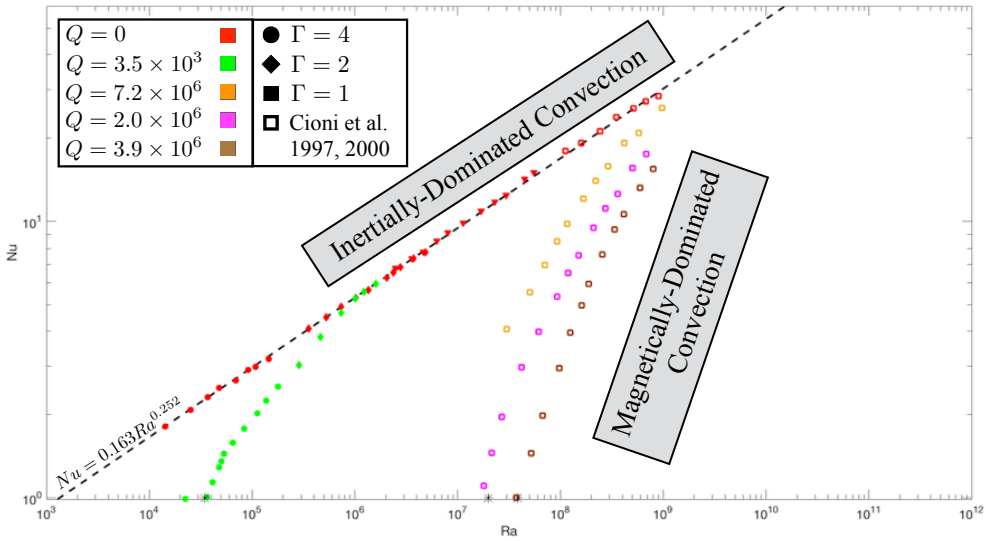

Figure 1.4: The transition in heat transfer from **(a)** rotationally constrained to inertially-dominated convection with water as the fluid working fluid $Pr \sim 6$ and **(b)** The transition from magnetically-constrained convection to inertially-dominated convection in $Pr = 0.025$ liquid metals. Image in *(a)* modified from Cheng et al. (2015) and the data used in *(b)* is from Ribeiro et al. (2015); Cioni et al. (1997, 2000)

is shown in Figure 1.4. The upper bounding regime on the heat transfer corresponds to Rayleigh-Bénard convection (RBC) where-in the flow is dominated by inertial forces and has been studied in detail.

To begin, the heat transfer efficiency is greatly affected by the boundary layers. For an idealized quasi-static boundary layer in which the heat transfer is purely conductive, the total heat transfer must pass through the boundary layers such that $q_{\text{Total}} = k\Delta T/2\lambda_\kappa$ where λ_κ is the thickness of the thermal boundary layer. The conductive heat transfer across the fluid layer is $q_{\text{cond}} = k\Delta T/L$, therefore

$$Nu \equiv \frac{q_{\text{Total}}}{q_{\text{cond}}} = \frac{L}{2\lambda_\kappa} \tag{1.31}$$

In the majority of studies, the heat transfer efficiency is found to scale with the strength of buoyancy such that $Nu \sim Ra^\alpha$. A classical prediction for the heat transfer in $Pr \sim 1$ is found where the interior is assumed to be well-mixed and the boundary layers do not communicate with one another. The heat transfer efficiency is assumed to be independent of the total fluid height such that

$$Nu \sim Ra^\alpha \Rightarrow L \sim (L^3)^\alpha, \tag{1.32}$$

and hence it is necessary that $\alpha = 1/3$ [e.g., Malkus (1954)]. This 1/3 scaling has been found in several studies [e.g., Ahlers et al. (2009); Cheng et al. (2015)].

Another classical scaling law has been put forth for liquid metals where strong forcing and low Prandtl numbers tend to generate strongly inertial flows. Such a scaling may be derived by balancing the inertia terms with the buoyancy terms in the momentum equation such that

$$\frac{U^2}{L} \sim \alpha_T g \Delta T \tag{1.33}$$

The solution of (1.33) for the velocity gives $U = \sqrt{\alpha_T g \Delta T L}$. This velocity is referred to as the free-fall velocity. From the thermal equation in (1.10), the scaling balance between thermal advection in the bulk and diffusion that dominates the thermal boundary layer is

given by

$$\frac{U\Delta T}{L} \sim \kappa \frac{\Delta T}{\lambda_\kappa^2} \tag{1.34}$$

This balance can be rewritten using the definition of the Nusselt number in (1.31) and the free-fall velocity from (1.33)

$$Nu \equiv \frac{L}{2\lambda_\kappa} = \frac{1}{2}\left(RaPr\right)^{1/4} \tag{1.35}$$

This $\alpha = 1/4$ scaling has been found in RBC studies using the liquid metals mercury and gallium as the working fluid [e.g., Rossby (1969); King and Aurnou (2013)]. Other studies have found a scaling that lies between $\alpha = 1/4 = 0.25$ and $\alpha = 1/3 = 0.33$ notably $\alpha = 2/7 = 0.29$ [e.g., Castaing et al. (1989); Glazier et al. (1999); Ahlers and Xu (2001)]. Such a scaling can be derived assuming that a large scale circulation persists that allows for communication between the boundary layers. By including a shear velocity in a theory of the flow in the thermal boundary, a scaling law of $\alpha = 2/7$ is derived [e.g., Shraiman and Siggia (1990)].

As was discussed previously, the inclusion of strong rotation or strong magnetic fields tends to suppress convective fluid motions. The convective forcing described by Ra must be sufficiently strong to overcome the suppressing effects described by critical Rayleigh numbers, Ra_c^E, that increase in proportion to the rotation rate $Ra_c^E \sim \Omega$. The onset of steady rotating convection for moderate Pr fluids in infinite plane layer analyses is determined from Chandrasekhar (1961) as:

$$Ra_{\mathrm{c,S}}^{E,\infty} = 8.7E^{-4/3}. \tag{1.36}$$

Figure 1.4.a shows with different colors how the heat transfer varies for different values of the Ekman number. As the Ekman number decreases, the critical Rayleigh number in (1.36) increases and, thus, the onset of convection requires that $Ra > Ra_{c,\mathcal{O}}^{E,\infty}$ which shifts the heat transfer scaling to the right. In low Prandtl number fluids like liquid metal where $Pr < 0.68$, the onset of convection occurs in the form of oscillatory columns and in a plane layer analysis

the critical value is given by Chandrasekhar (1961) as:

$$Ra_{c,\mathcal{O}}^{E,\infty} = 17.4\left(\frac{E}{Pr}\right)^{-4/3}. \tag{1.37}$$

While the heat transfer is well defined for RBC, the scaling for the heat transfer in the presence of strong rotation or strong magnetic fields is still being debated and is the topic of current research. One such scaling is derived from King et al. (2012) who modified the boundary layer stability arguments from Malkus (1954). They assumed that the thermal boundary layer of height, λ_κ, is marginally unstable such that $Ra_{\lambda_\kappa} \sim E_{\lambda_\kappa}^{-4/3}$ and thus:

$$\frac{\alpha g \Delta T_{\lambda_\kappa} \lambda_\kappa^3}{\nu\kappa} \sim \left(\frac{\nu}{2\Omega\lambda_\kappa^2}\right)^{-4/3} \Rightarrow Ra\left(\frac{\lambda_\kappa}{L}\right)^3 \sim E^{-4/3}\left(\frac{\lambda_\kappa}{L}\right)^{8/3}, \tag{1.38}$$

where Ra and E are the Rayleigh and Ekman numbers for the whole fluid layer and the total temperature drop is related to the temperature drop in the boundary layer by $\Delta T = 2\Delta T_{\lambda_\kappa}$. Using the definition for the Nusselt number from (1.31) then a scaling for the rotationally constrained regime is given by

$$Nu \sim \left(\frac{Ra}{E^{-4/3}}\right)^3. \tag{1.39}$$

This scaling helps to characterize the steep branch of heat transfer where rotation constrains the flow. However, the asymptotic scaling for the has not been determined.

Several characterizations have been proposed for the transition from this steep branch to the shallower RBC branch. The first is through a convective Rossby number defined as

$$Ro_c = \frac{\text{Buoyancy}}{\text{Coriolis}} = \frac{U_{ff}}{\Omega L} = \sqrt{\frac{RaE^2}{Pr}} = Re_c E, \tag{1.40}$$

where U_{ff} is the free fall velocity and $Re_c = \sqrt{Ra/Pr}$ is the convective Reynolds number. It is generally assumed that for $Ro_c < 1$ rotation dominates the flow. While this transition might be of interest for low Pr fluids, another transition is determined by assuming the Ekman boundary layer is nested within the thermal boundary layer such that $\lambda_\kappa = \lambda_E = \sqrt{E}L$. Inserting this assumption into the Nusselt number of (1.31) and then the steep scaling

in (1.39), a transition Rayleigh number can be determined such that

$$Ra_T^E \sim E^{-3/2}. \tag{1.41}$$

This transition has been confirmed in the large Pr studies of King et al. (2012) and Cheng et al. (2015).

The presence of strong magnetic fields also tends to suppress convection. Thus the critical Rayleigh number is proportional to the magnetic field such that $Ra_c^Q \sim B_o^2$. The onset of convection in the presence of strong magnetic fields is given by Chandrasekhar (1961) as:

$$Ra_c^{Q,\infty} = \pi^2 Q. \tag{1.42}$$

Similar to the studies of rotating convection, magnetically-constrained convection as shown in Figure 1.4.b also exhibits two distinct scalings. The colors indicate the different values of Q. The data sets at larger values of Q require larger values of $Ra > Ra_c^{Q,\infty}$ and thus are shifted to the right. Following the marginal boundary layer arguments used to arrive at (1.39), the critical Rayleigh number in the boundary layer $Ra_{\lambda_\kappa} \sim Q_{\lambda_\kappa}$ and thus:

$$\frac{\alpha g \Delta T_{\lambda_\kappa} \lambda_\kappa^3}{\nu\kappa} \sim \left(\frac{\sigma B_o^2 \lambda_\kappa^2}{\rho\nu}\right) \Rightarrow Ra\left(\frac{\lambda_\kappa}{L}\right)^3 \sim Q\left(\frac{\lambda_\kappa}{L}\right)^2, \tag{1.43}$$

and finally

$$Nu \sim \frac{Ra}{Q}. \tag{1.44}$$

Although this scaling was found in Cioni et al. (2000), the robustness of this scaling remains to be determined [c.f., Aurnou and Olson (2001)]. Transition arguments can be derived in the same way as done using rotational arguments. A convective magnetic Rossby number is given by $Ro_{m,c} = \sqrt{Ra/(PrQ^2)} = Re_c Q^{-1}$ and a transition Rayleigh number is given by $Ra_T^Q \sim Q^{3/2}$. To date, none of these transition arguments have been robustly verified.

1.3.7 Characteristic flow length scales in planetary interiors

The three dimensional turbulence, as is relevant for the generation of planetary magnetic fields, requires that the Taylor-Proudman theorem be broken. Such dynamics are then considered quasigeostrophic and the Taylor-Proudman theorem becomes the Taylor constraint that becomes the leading order balance in strongly rotating geophysical fluid dynamics and leads to coherent flow structures that are axially invariant.

While the extension of these structures along the axial length of the fluid layer is determined by the Taylor-Proudman constraint at zeroth order, the width of the flow structures is determined by the first order balance that now includes the effects of viscous forces, $\nu\nabla^2\mathbf{u}$. With the inclusion of the viscous force in (1.13) and after taking the curl, the resulting balance then becomes:

$$2\Omega\frac{\partial\mathbf{u}}{\partial z} \sim \nu\nabla^2\left(\nabla\times\mathbf{u}\right). \tag{1.45}$$

Note that $\nabla\times\mathbf{u}=\boldsymbol{\omega}$ is the vorticity. The perpendicular component of the axial direction in (1.45), $\partial/\partial z \sim 1/L$ and ℓ_h is the typical horizontal length scale such that $\nabla\sim 1/\ell_h$. Plugging in these scalings and focusing on the horizontal component of the velocity, $\mathbf{u}_\perp \sim U_\perp$ returns

$$2\Omega\frac{\partial\mathbf{u}_\perp}{\partial z} \sim \nu\nabla^2\left(\nabla\times\mathbf{u}\right)_\perp \rightarrow \frac{U_\perp}{L} \sim \frac{\nu}{2\Omega}\frac{U_\perp}{\ell_h^3}. \tag{1.46}$$

Thus the aspect ratio for these structures can be written as:

$$\ell_h/L \sim E^{1/3}. \tag{1.47}$$

This scaling is shown to hold in models of quasigeostrophic convection and dynamo simulations where the viscous forces are still playing an influential role in the first order dynamics. In the core, the aspect ratio for convective core structures where $E\sim 10^{-15}$ is $\ell_h/L\sim 10^{-5}$. Such thin structures that extend across the axial direction of the fluid layer are likely fragile and easily destroyed in this turbulent environment.

In mechanical forcing, the size of the typical flow structures of the perturbations can

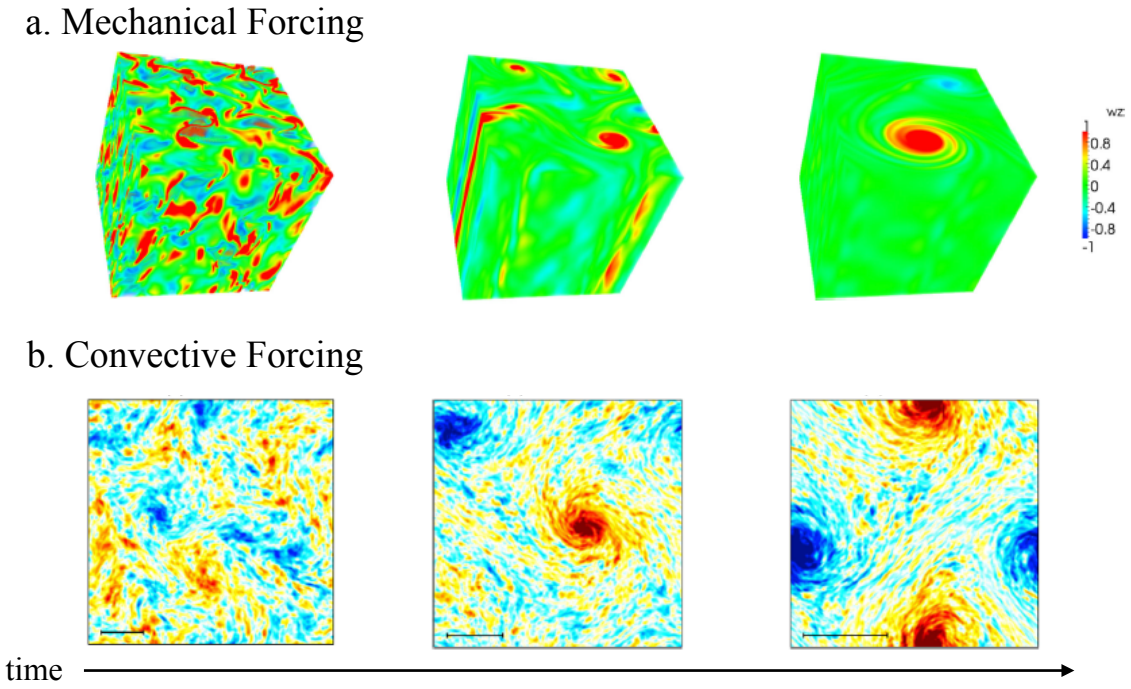

Figure 1.5: The development of system sized flow structures out of small-scale forcing in rotating turbulence. **(a)** Three snapshots of the vertical vorticity in a local simulations of tidal forcing in a Cartesian geometry. Image modified from Barker and Lithwick (2013). **(b)** Three snapshots of the vertically averaged vertical vorticity in local simulations of rotating convection. Image modified from Rubio et al. (2014).

be determined by equating the dimensional advection term from (1.24) in the bulk where the base flow can drive the growth of the perturbation with diffusion term. In the frame rotating with the fixed background rotation, Ω, the base flow may be scaled as $U_B \sim \beta\Omega L$ [e.g., Barker and Lithwick (2013) and Chapter 5]. The characteristic structure size is then,

$$\frac{U_B u'}{L} \sim \nu \frac{u'}{\ell^2} \Rightarrow \ell/L \sim (E/\beta)^{1/2}\,, \tag{1.48}$$

where, for simplicity, $E = \nu/(\Omega L^2)$. In planetary interiors, the characteristic flow structures in mechanical forcing scale as $\ell/L \sim 10^{-6}$ for typical bodies with $E \sim 10^{-15}$ and $\beta \sim 10^{-3}$ and are also quite thin.

Figure 1.5 shows the presence of such thin structures at early times generated via **(a)** mechanical forcing and **(b)** convective forcing. In these recent local studies performed in Cartesian geometries where more extreme Ekman numbers can be reached, turbulent cas-

cades transport energy from the small scales to large scale vortices (LSV) that may be crucial for energy dissipation and the generation of the large scale magnetic fields present on many bodies. Note that the existence of the LSV in Figure 1.5.a from Barker and Lithwick (2013) tends to inhibit the elliptical instability. As such the LSV break down and the process for the generation of the LSV persists in the form of cycles.

1.4 Summary of Chapters

In Chapter 2, a standard operating procedure, SOP, has been written for completeness as well as for the edification of current and future lab members. This SOP describes the major components of the librating experiment, how they are connected electrically, and the steps necessary for performing fundamental operations like assembly, and the application of rotation with superimposed sinusoidal oscillations.

By using the libration apparatus described in Chapter 2, the laboratory experimental results presented in Chapter 3 demonstrate that the librational forcing of an ellipsoidal water-filled container can produce intense motions through the mechanism of a libration driven elliptical instability (LDEI). These libration studies are conducted using an ellipsoidal acrylic container filled with water. I designed a support system for lasers in the librating frame and implemented a non-intrusive particle image velocimetry measurement technique that was used to measure flow in the equatorial frame in the fully assembled ellipsoid. In doing so, I measured the 2D velocity field in the equatorial plane over hundreds libration cycles for a fixed rotation rate. In doing so, I recover the libration induced base flow and a time averaged zonal flow. Further, we show that LDEI in non-axisymmetric container geometries is capable of driving both intermittent and saturated turbulent motions in the bulk fluid. Additionally, we measure the growth rate and amplitude of the LDEI induced excited flow in a fully ellipsoidal container at more extreme parameters than previously studied. Excitation of bulk filling turbulence by librational forcing provides a mechanism for transferring rotational energy into turbulent fluid motion and thus can play an important role in the thermal evolution, interior dynamics, and magneto-hydrodynamics of librating

bodies, as appear to be common in solar system settings.

Chapter 4 was a numerical study motivated by my laboratory experiments of libration in ellipsoidal containers. In this study, I present the results from a combination of direct numerical simulations and laboratory experiments, modeling this geophysically relevant mechanical forcing. To do so, I performed additional laboratory experiments and accompanying analysis using the methods described in Chapter 3 and created a benchmark experimental case that was compared with the numerical simulations. In doing so, we investigate the fluid motions inside a longitudinally librating ellipsoidal container filled with an incompressible fluid. The elliptical instability, which is a triadic resonance between two inertial modes and the oscillating base flow with elliptical streamlines, is observed both numerically and experimentally. The large-scale inertial modes eventually lead to small-scale turbulence, provided that the Ekman number is small enough. The transition to turbulence is characterized by additional triadic resonances develop while also investigating the properties of the turbulent flow that displays both intermittent and sustained regimes. These turbulent flows may play an important role in the thermal and magnetic evolution of bodies subject to mechanical forcing, which is not considered in standard models of convectively driven magnetic field generation.

Chapter 5 focuses on tidal forcing and was afforded by a nine month Chateaubriand Fellowship in Marsille, France. I designed and built a support for a new wireless camera used in the implementation of PIV system in the rotating frame. In this work, I model the response of an enclosed constant density fluid to tidal forcing by combining laboratory equatorial velocity measurements with selected high-resolution numerical simulations to show, for the first time, the generation of bulk filling turbulence. The transition to saturated turbulence is characterized by an elliptical instability that first excites primary inertial modes of the system, then secondary inertial modes forced by the primary inertial modes, and then bulk filling turbulence. The amplitude of this saturated turbulence scales with the bodys elliptical distortion, while a time- and radially averaged azimuthal zonal flow scales with the square of the ellipsoidal distortion.

The results of the current tidal experiments are compared with recent studies of the

libration-driven turbulent flows our previous laboratory experimental and numerical studies of libration. Tides and libration correspond to two end-member types of geophysical mechanical forcings. For satellites dominated by tidal forcing, the ellipsoidal boundary enclosing the internal fluid layers is elastically deformed while, for librational forcing, the core-mantle boundary possesses an inherently rigid, frozen-in ellipsoidal shape.We find striking similarities between tidally and librationally driven flow transitions to bulk turbulence and zonal flows. This suggests a generic fluid response independent of the style of mechanical forcing. Since the elliptical distortion is quite small $\mathcal{O}(10^{-4})$ in planetary bodies, it is often argued that mechanically driven zonal velocities will be small. In contrast, our linear scaling for mechanically driven bulk turbulence suggests geophysically significant velocities that can play a significant role in planetary processes including tidal dissipation and magnetic field generation.

In Chapter 6, I further modified the libration apparatus in Chapter 2 by designing and building an adapter that rigidly supports an inner core, and designing and building an adapter to mount a wireless camera into the librating frame. I investigate whether the LDEI mechanism persists in an ellipsoidal shell, which is more geophysically relevant to model planetary liquid layers, using both experimental and numerical approaches. I use an ellipsoidal acrylic container filled with water and add five differently sized spherical inner cores. Direct side-view visualizations of the flow were made in the librating frame using Kalliroscope particles. A Fourier analysis of the light intensity extracted from the recorded movies shows that LDEI persists for various libration frequencies, and allows an identification of the mode coupling. Particle Image Velocimetry (PIV) and Direct Numerical Simulations (DNS) are performed on selected cases to confirm the results.

The presence of the inner core does not prevent the instability mechanism from occurring and leads to spatial inhomogeneities in the fluid response at high and low latitudes that increase as the shell thickness decreases. Additionally, for a fixed forcing frequency and variable Ekman number reveals that the libration amplitude at the threshold of the instability varies as $E^{0.63-0.72}$. This particular scaling is explained by the existence of a transition regime between viscous dissipation in the bulk, which scales as $\mathcal{O}(E)$ for large Ekman numbers and

viscous dissipation in the boundary layers that follows the classical scaling $\mathcal{O}(E^{1/2})$ relevant for planetary setting where $E \sim 10^{-15}$. Furthermore, I hypothesize that for very thin subsurface oceans like that of Enceladus, inhomogeneities in the response of LDEI may help explain the first order ice thickness variations.

In order to carry out laboratory experiments of convective forcing, Chapter 7 is meant to be used as a standard operating procedure for future lab members and as a companion document to the description of the RoMag convective experiment and its capabilities as outlined in Chapter 2 of King (2009). In this chapter, I detail the procedures for performing various tasks associated with running the experiment as well as describing the modifications that I have made to improve the device.

By using the RoMag experiment described above, I present, in Chapter 8, a study of rotating and non-rotating convection experiments using a combined laboratory-numerical approach that uses right cylindrical geometries in order to represent planetary core-style convection in the high latitude of spherical shell layers. Using flow visualizations and heat transfer measurements at more extreme parameters where viscous effects are weaker, we study the axialized flows that occur near the onset of convection as well as three-dimensional flows that develops as the buoyancy forcing is strengthened.

Using the working fluid water, in the rapidly rotating convection regime where axialized, coherent columns exist, the heat transfer efficiency (Nusselt number) is found to scale more steeply with the thermal forcing (Rayleigh number) than found in previous studies. Such steep trends cannot currently be reached by the current numerical dynamo models and indicate that that axialized structures associated with rotationally constrained have a narrow range of stability. Consequently, convective motions in the core may not be related to the columnar motions found in present day global-scale models. Instead, we hypothesize that turbulent rotating convection cascades energy upwards from three dimensional motions to large-scale quasi-two dimensional flow structures that are capable of efficiently generating planetary-scale magnetic fields. We argue that the turbulent regimes of rapidly rotating convection are essential aspects of core dynamics and will be necessary components of robust, next-generation and multiscale dynamo models.

In Chapter 9, I characterize rapidly rotating thermal convection in the liquid metal gallium with a low Prandlt number, $Pr \simeq 0.025$. This is relevant for the study of liquid metals akin to those in Earth's outer core, and leads to fundamentally different flow regimes than those found using water and the fluids used in numerical studies of dynamos where $Pr \sim 1$. The Ekman number varies from $E = 5 \times 10^{-5}$ to 5×10^{-6} and the Rayleigh number, Ra varies from $Ra = 2 \times 10^5$ to 1.5×10^7. Using measurements of heat transfer efficiency, characterized by the Nusselt number Nu, as well as temperature at points within the fluid, we characterize the different styles of low Pr rotating convective flow. The convection threshold is first overcome in the form of a container scale inertial oscillatory mode. At stronger forcing, sidewall-attached modes are identified for the first time in liquid metal laboratory experiments. These wall modes coexist with the bulk oscillatory modes.

At Ra well below the values given in (1.36) where steady rotating columnar convection occurs, the bulk flow in our experiments becomes turbulent while the wall modes remain intact. Our results imply that rotating convective flows in liquid metals do not develop in the form of quasi-steady columns, as in $Pr \sim 1$ dynamo models, but in the form of oscillatory motions. Therefore, the flows that drive thermally-driven dynamo action in low Pr geophysical and astrophysical fluids can differ substantively than those occuring in current-day $Pr \sim 1$ numerical models. Since oscillatory convection is significantly easier to excite than steady convection, it may be that thermally-driven oscillatory motions will generate dynamo action in planetary settings, well before steady convective flows are even actuated. Furthermore, our experimental results suggest that relatively low wavenumber, wall-attached modes may be dynamically important in rapidly-rotating convection in liquid metals.

Lastly, in the conclusion I summarize my work and discuss the future directions that have been motivated by, and build upon, the work that I have performed in this dissertation.

CHAPTER 2

Libration Experimental Anatomy

In this chapter I describe the major components and steps necessary for performing longitudinal libration experiments at the UCLA Spinlab. In summary, this experiment supports an acrylic ellipsoid or ellipsoidal shell filled with water. This fluid volume is then rotated at constant rate provided by one motor and with a superimposed sinusoidal oscillation provided by a separate servomotor. This document is meant as a Standard Operating Procedure (SOP), for understanding and running the device. Films of the device in motion may be found on Youtube. Web addresses, below, are clickable on the electronic version.

- https://www.youtube.com/watch?v=WGe-vLsm9Ho
- https://www.youtube.com/watch?v=VYxMjd5TsVo

In Section 2.1, I first describe the major structures and the major components related to generating motion. In Section 2.2, I lay out the wiring diagram for the major components and the method for filling the experimental volume in Section 2.3. Section 2.4, describes how the major components and subsystems are controlled. The methods for making fluid visualizations and running experiments are described in Sections 2.5 and 2.6, respectively.

2.1 Support Structure and Motor Systems

The libration experiment is composed of the mechanical structure, the two motors, the control console, computer, and peripherals. The image on the left of Figure 2.1 shows a top view of the layout for the room where the primary components of the libration experiment are distributed. The image on the right in Figure 2.1 shows a side-view of the libration

apparatus and the major components in the rotating frame.

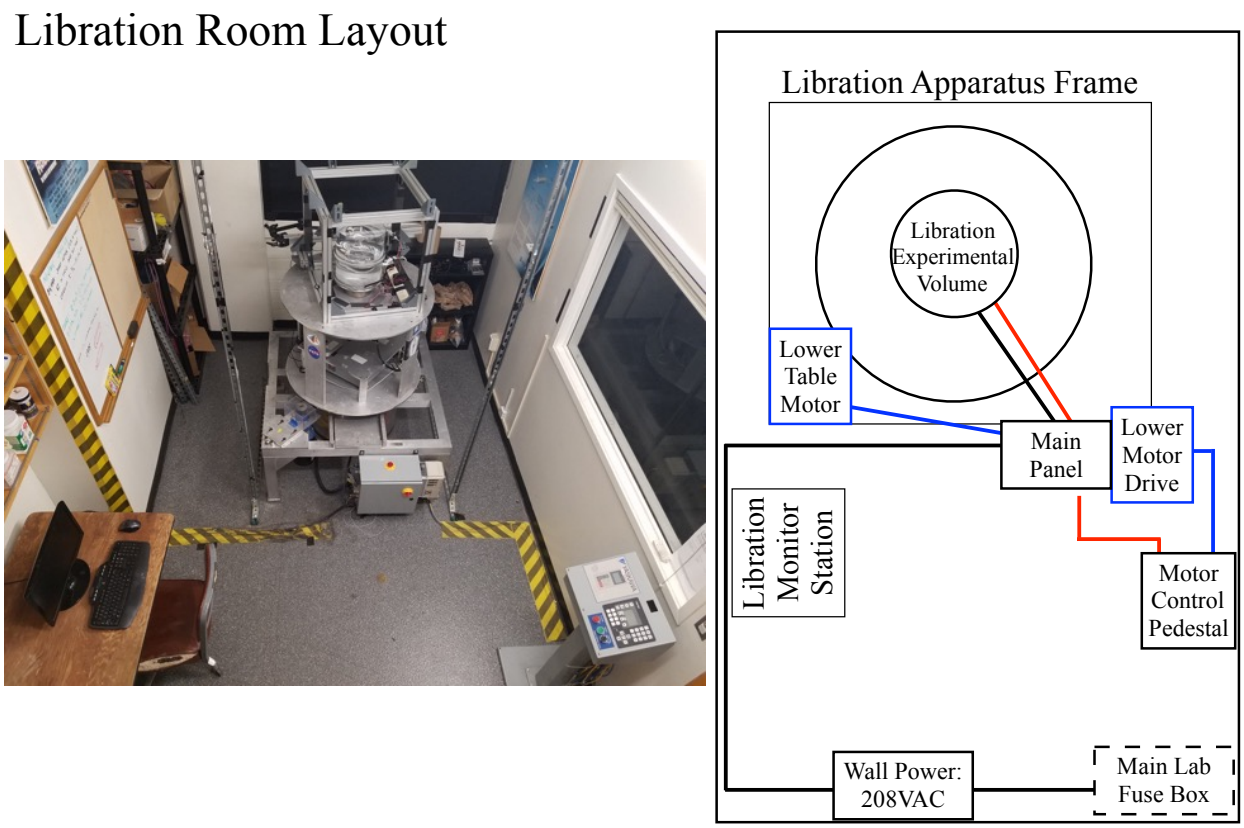

Figure 2.1: **Left** A top-view image of the libration room and **Right** an accompanying schematic view of the major components in the libration room. Note that the Main Lab Fuse Box is outside of the libration room and the major wiring components for the servomotor are shown in red while the major components and wiring for the lower motor are given in blue.

2.1.1 Motor Control Pedestal

Figure 2.1 shows the pedestal, next to the door, where the controls for the two different motors are located. The controls for the lower motor, as shown in Figure 2.8, are located on the left side of the panel while the main system power and the servomotor control are located on the right of the panel.

- Note that the panel is hinged and by removing the screws in the control panel there may be wiring diagrams, documentation, or small electronic components associated with libration controls.

2.1.2 Libration Apparatus Frame

The largest part of the system is the libration apparatus frame, shown in Figure 2.2. The lower frame is constructed from 6061-T6 Aluminum with welded joints and supports the main bearing, lower motor, and wiring junction box. The lower platform is a 50 by 50 inch square and is raised 24 inches off the ground by four legs. Mounted in the center is an extreme capacity turntable bearing with a 14,000 lb capacity which is more than enough to handle the load applied by the libration assembly. This bearing is bolted to a stainless steel pulley. This pulley has a diameter of 12" and has a bead blasted surface to which the belt connected to the lower motor drives the table.

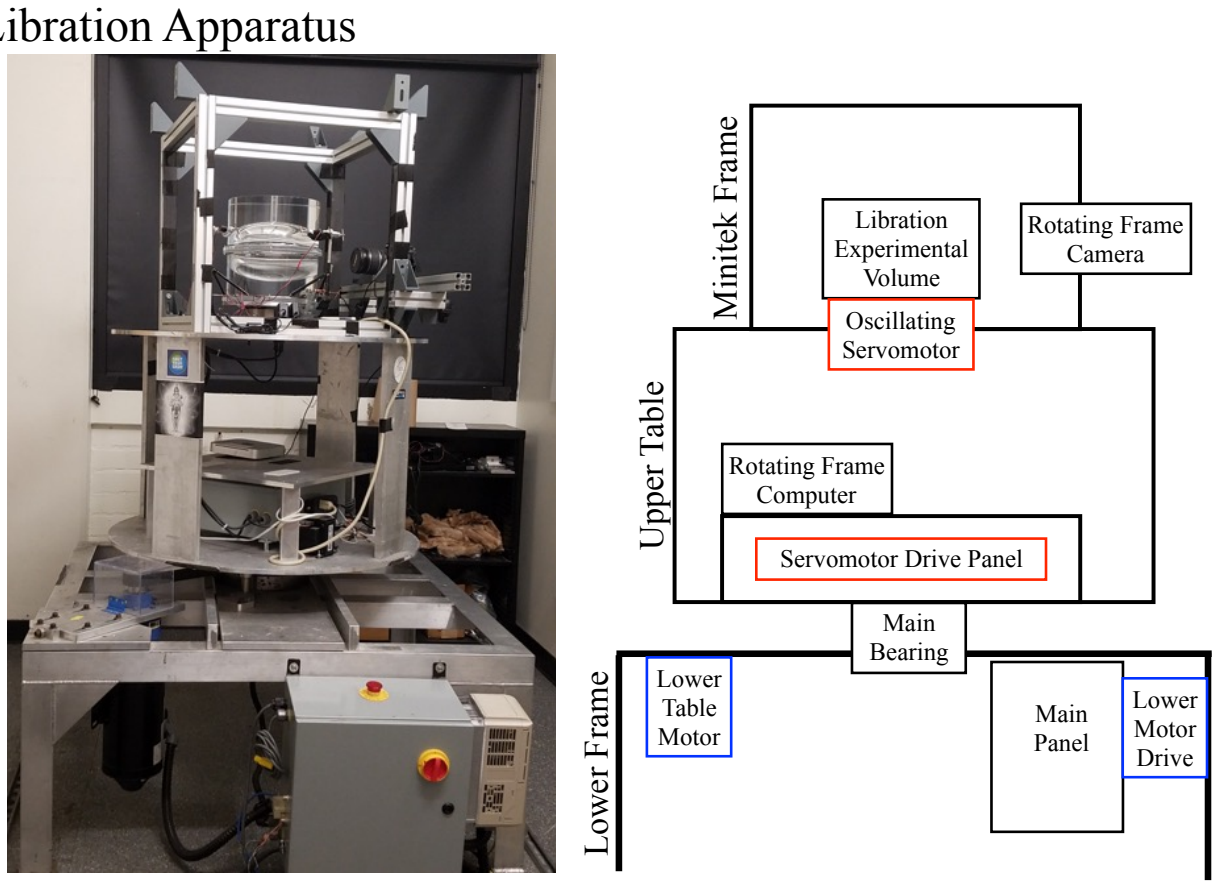

Figure 2.2: A layout of the major components on the libration apparatus. The red outlined components are associated with the servomotor system. The blue outlined components are related to the lower motor system.

The upper table is composed of the top and bottom plate assemblies. The bottom plate assembly is a circle with a 38" diameter.

- Note that at the outer edge of the bottom plate, tick marks etched with a one degree separation.

Bolted to this table is attached the servomotor drive system and platform that protects the servomotor drive system and allows for the attachment of peripherals including the rotating frame computer. There are two sets of legs that can be used to connect the bottom plate assembly with the top plate assembly. The legs typically used are in 20" long and the other shorter set is 5". The top plate assembly is also a 38" diameter plate.

Mounted onto the top plate is a frame constructed from Minitek rails. In addition to the mounting bolts used to secure this frame to the top plate, a waterproof silicone is used at the base to create a watertight seal in case of spills. Using Minitek braces and additional rails, a mounting system is constructed to support larger cameras, and lasers.

2.1.3 Lower Table Motor System

The lower table motor provides a belt-driven constant rotation rate to the entire libration assembly. A stainless steel pulley of diameter 2.95" connects the lower motor to the belt that drives the libration assembly.

2.1.3.1 Lower Table Motor and Servo Drive

The lower table motor is a Marathon Black Max Y535 one horsepower DC motor with a 6:1 gear head reducer (Sumitomo CNFJ-6085Y). Thus, the total gear reduction between the motor and the rotation of the libration table is approximately 24:1 meaning the the motor rotates 24 times for every turn of the libration table. The librating table can rotate from 1 to 60 RPM and is stable to within $\pm 0.5\%$.

The motor is driven by a Yaskawa CIMR-F7U20P71 inverter drive.

2.1.4 Oscillating Servomotor System

The oscillating servomotor is attached to top plate assembly and is connected directly to the librating experimental volume.

2.1.4.1 Servomotor

The servomotor is a 400W ring-style servomotor (Yaskawa SGMCS-10C3B11). The servomotor is capable of rotating at a constant rate or, as is it is typically used, oscillating with an angular amplitude between 2.5^o to 360^o and with frequency $f_L = \omega_L/2\pi = [0.1 - 4.5]$Hz with an error of $\pm 0.25\%$.

- Note that as the amplitude increases the range of possible frequencies decreases. For instance, at a frequency of 4.5 Hz that maximum angular amplitude is approximately 5 degrees. Oscillating at a high enough frequency for a given amplitude will generate an error and the servomotor will stop. Power cycling (turning the device off and on) will clear this error.

2.1.4.2 Servomotor Drive

The servomotor drive is a Yaskawa SGMPH enclosed in a box attached to the bottom plate assembly. A motion control card (Trio MC202) is mounted in the motor control pedestal and generates the signal for setting the sinusoidal oscillation.

2.1.5 Libration Experimental Volume

The libration experimental volume is composed of an adapter plate that connects the acrylic volume to the oscillating servomotor, the two hemispheres of the acrylic container, and a set of metal bands used to connect the two hemispheres. These parts are shown in Figure 2.3.

2.1.5.1 Support Platforms

An aluminum adapter plate annulus is used to connect the oscillating servomotor to the acrylic container. Metal rings placed on the flanges of the acrylic hemisphere are used to distribute pressure so as not to crack the acrylic. Another set of rings have been modified with vertical posts so that small cameras like GoPros and lasers can be placed in the librating frame where the acrylic is stationary. A full stainless steel ring with through holes is placed on the upper hemisphere flange while a set of two circular rings with threaded holes is placed on the underside of the lower hemisphere flange.

- Note that the modified flanges that support the laser and the GoPro can flex slightly as the container librates. It is recommended that, in the future, the aluminum adapter plate used to connect the servomotor to the acrylic container be remade with a larger diameter. Then custom mounts may be made that directly connect the lasers or cameras rigidly to the adapter plate itself and not to the metal bands.

2.1.5.2 Acrylic Volumes

There are three sets of acrylic volumes that may be used. The experimental volumes have been machined from the interior of cylindrical pieces with diameter 12" and cut in half to separate the upper and lower hemispheres. The outside of this cylinder has been machined with flanges that allow for the hemispheres to be fastened to one another and to the adapter plate attached to the servomotor. There is a 0.5" diameter hole in the center of the upper hemisphere that allows for filling the experimental volume with fluid and as a mounting point for the inner core support rods. The acrylic containers include a sphere, an intermediate ellipsoidal container, and a strongly ellipsoidal container. They are defined by a long equatorial axis of length a, a short equatorial axis of length b, and a short axial axis of length c.

For all these containers $b = c$ meaning that along the long equatorial axis, the ellipsoid is axisymmetric which can help when modeling libration using some numerical schemes. The

strength of the ellipsoidal distortion is defined non-dimensionally by,

$$\beta = \frac{a^2 - b^2}{a^2 + b^2}, \tag{2.1}$$

and hence the three experimental volumes are described by $\beta = 0.34, 0.06, 0$. A more complete list of the geometrical properties of the experimental volume are provided in Table 2.1.

Parameter	Definition	Values
a	Long equatorial length	127mm
b	Short equatorial length	89mm, 119mm, 127mm
c	Short axial length	89mm, 119mm, 127mm
r	Inner core radius	25.1mm, 38.2mm, 50.7mm, 61.2mm, 76.2mm
β	$\frac{a^2-b^2}{a^2+b^2}$	0.34, 0.06, 0
χ	$\frac{r}{c_{\beta=0.34}}$	0.28, 0.43, 0.57, 0.69, 0.86

Table 2.1: Geometry of acrylic ellipsoidal containers and inner cores. Note that the radius ratio χ has been defined using c for the strongly ellipsoidal container $c_{\beta=0.34} = 89$mm.

2.1.5.3 Inner Spheres and Supports

There are five spherical inner cores that may be used in the libration experiments. Their radii are listed in Table 2.1. All of these cores are drilled and tapped such that the threads are provided by a locking helicoil of size $5/16" - 18$. The inner cores are threaded into 3/8" diameter stainless steel support rod that is used in tandem with a custom made delrin adaptor and stainless steel clamping collar in order to support the inner core inside the experimental volume.

2.1.5.4 Assembling the Experimental Volume

The parts of the experimental volume are shown in Figure 2.3. The instructions for assembly the stack are described below.

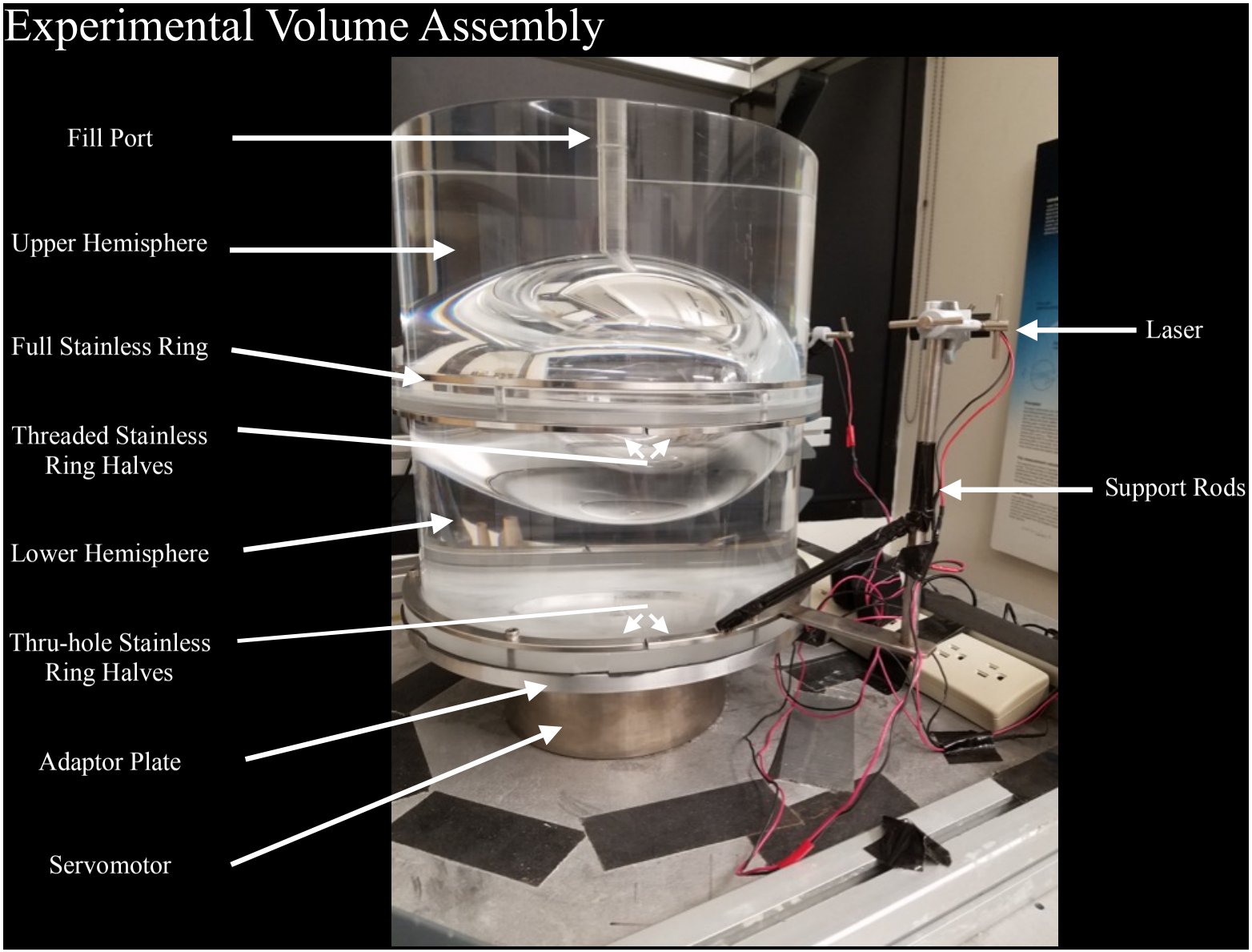

Figure 2.3: Schematic of the major components used in assembling the experimental volume and mounting lasers and other components.

1. Make sure the interiors of the container have been cleaned to remove smudges and debris that might obscure the visualizations or contaminate the water.

2. Set the lower hemisphere onto the adapter plate and place the two stainless rings with thru-holes onto the lower flange so that all holes in the ring and acrylic flange are aligned with the threaded holes in the adapter plate. These three pieces are secured together using six 10-32×1" hex head screws. Take care when tightening these six screws to make them snug but not too tight so as too avoid cracking or scratching the acrylic. The order by which the screws are tightened should follow a star pattern wherein the screws are at or nearly 180 degrees apart are screwed sequentially in order to distribute pressure as uniformly as possible.

3. Place a large oring (Dash No. 275 Mcmaster #:9464K573) in the groove of the lower hemisphere.

4. If there is an inner core then the inner core must be screwed into the support rod and the support rod must be placed through the central hole in the upper hemisphere. The delrin adapter and clamping collar, as shown in Figure 2.4, should also be assembled and used to the support rod so that the inner core isn't bouncing around during the assembly process. Take care in placing this piece onto the lower hemisphere as the entire assembly can be heavy. Additional helpers might be required with one person standing on the lower frame.

5. If there is no inner core then place the upper hemisphere on top of the lower hemisphere making sure the geometries and by extension the thru-holes in the acrylic flanges are aligned.

6. If there is no inner core then place the upper hemisphere on top of the lower hemisphere making sure the geometries and by extension the thru-holes in the acrylic flanges are aligned.

7. The two hemispheres can now be secured using the stainless ring with counter-sinked thru-holes facing up on the top of the central connecting flange and stainless steel

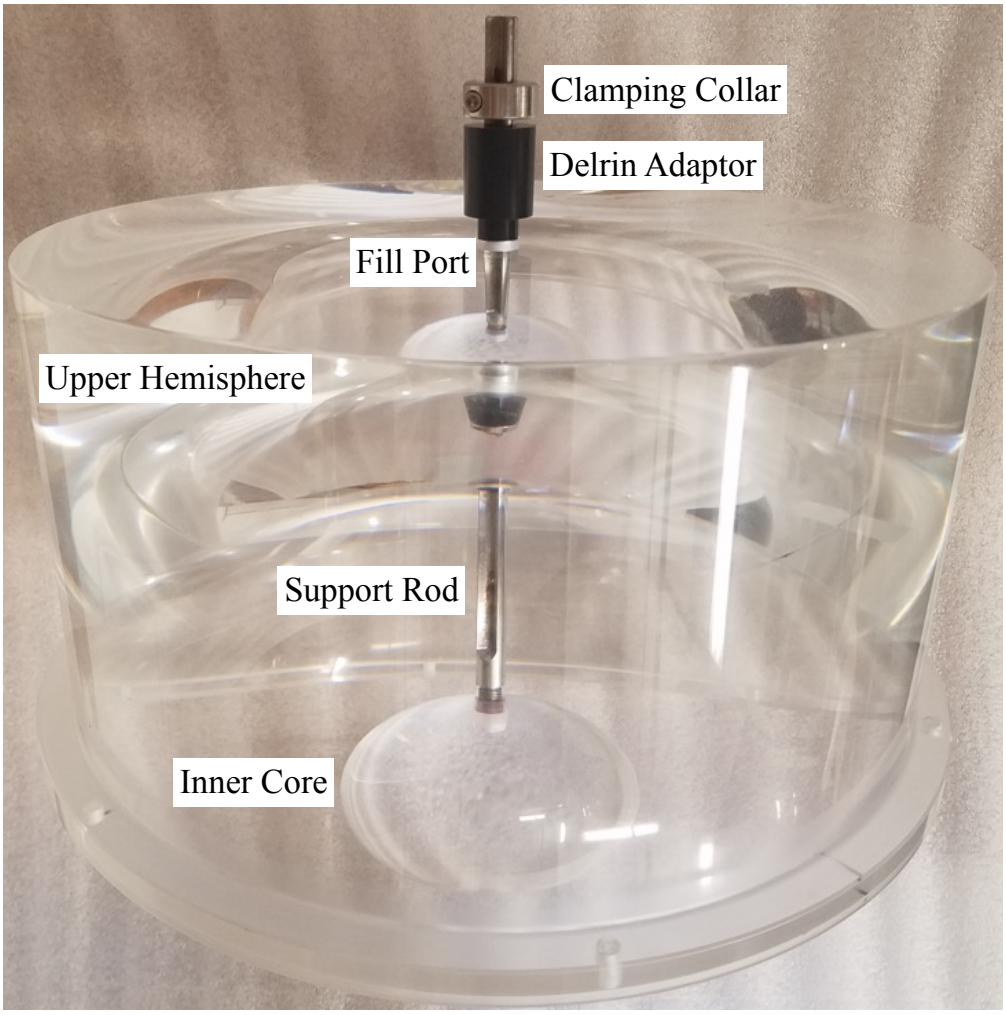

Figure 2.4: Schematic of the inner core support rod being held in the the fill port with the black Delrin adapter and clamping collar. A groove as been machined into the support rod so that the filling tube shown in Figure 2.7 can pass through the groove to fill the volume while the inner core is in position.

ring halves with threaded holes on the underside of the central flange. These parts should be screwed snugly with six flathead 10-32×1" screws. Take care to use a star pattern when tightening these six screws and make them snug but not too tight as to avoid cracking the acrylic. Some small minor cracks are already present around the thru-holes

8. Clean the outside of the container to remove any smudges or debris gathered during assembly.

2.2 Libration System Wiring

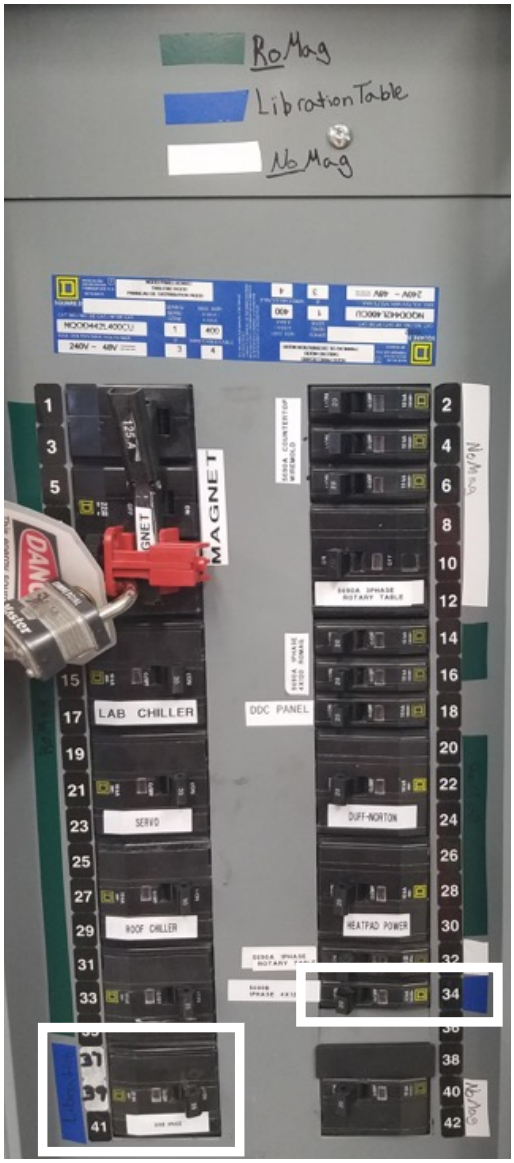

Figure 2.5: Layout of the Main Lab Fuse Box located outside of the libration room. The two circuit breakers for the libration room are indicated with the white outlined boxes in this image and blue tape on the box itself. The 120VAC 10A breaker is currenlty being unused in the libration room.

2.2.1 Laboratory Frame Wiring

The Main Lab Fuse Box provides 3 phase 208VAC power to the libration room and is shown in Figure 2.5. In the Main Lab Fuse Box, blue tape indicates that the 208VAC 3 phase circuit

breaker is located in sockets (37-39-41). The other 120VAC circuit is currently unused. The 3 phase power is transmitted via a wall outlet to the main panel box attached to the libration table frame. The main panel is the main distribution center for all power, signals, and safety controls is shown in Figure 2.6.a The main components in the main panel are:

- A red and yellow disconnect switch that should be activated once the main panel has been closed. For safety reasons when this switch is activated the panel cannot be opened.
- A red illuminated emergency stop that cuts power to the entire system when the activated.
- PS1: A power supply that generates 24 VDC that is used to power many components including the light inside the emergency switches in the main panel and in the motor control pedestal and the controllers located and sub-components located in the motor control pedestal.
- CB1: Circuit breaker also used to cut power in the main box.
- C1: Capacitors used for the lower motor servodrive.
- C2: Capacitors used for sending 220VAC to the servomotor drive in the rotating frame

The lower motor draws power from the main panel and takes in signal information from the motor control pedestal.

The signals used to drive the servomotor in the rotating frame are input through the Red Lion controller which sends signals into the rotating frame. This controller draws power from the 24VDC line coming from the main panel.

2.2.2 Slip Ring

The slip ring is the mechanism that allows for the transfer of signals and power from the laboratory frame to the rotating frame. The slip ring used in the libration experiment is a

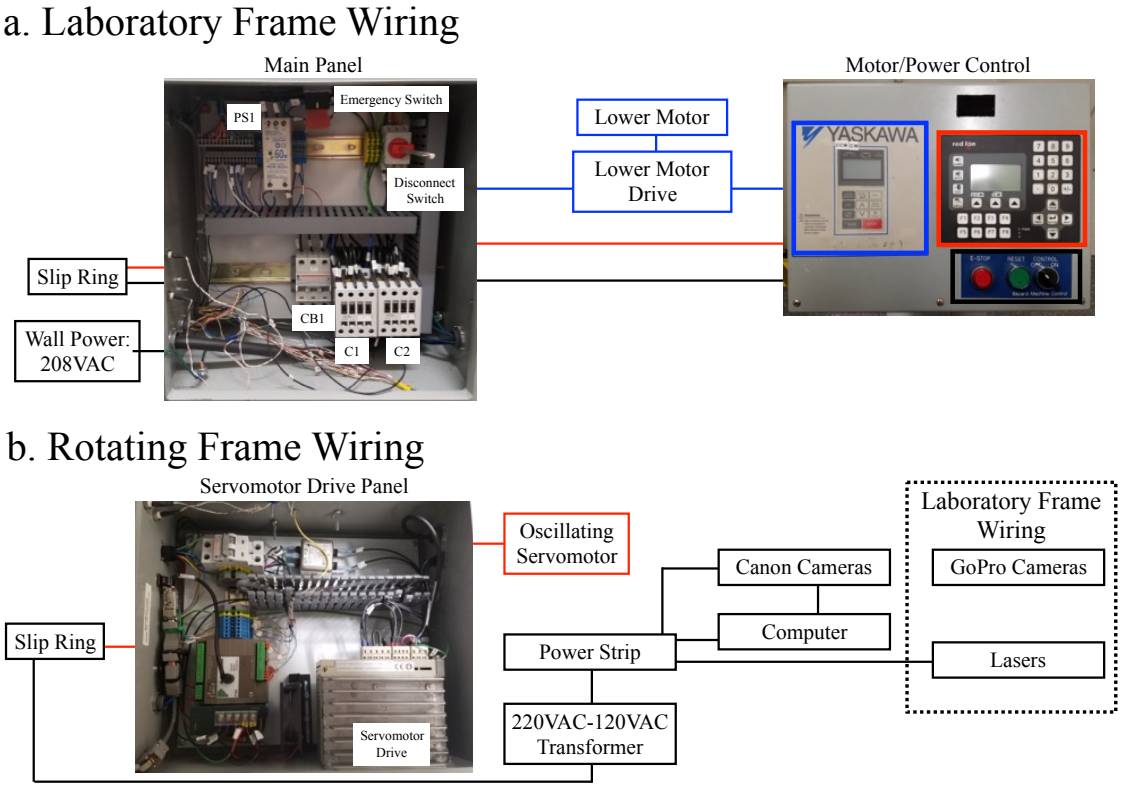

Figure 2.6: **(a)** A layout of the major components in wiring system located in the laboratory frame. **(b)** A layout of the major components in wiring system located in the rotating frame. Note that the dashed box indicates the electronics in the librating frame.

MOOG AC6355-56. It contains 56 2 amp lines and runs through the center of the table's bearing. The primary signals passed are 220VAC power lines and the signals for oscillating the servodrive.

2.2.3 Rotating Frame Wiring

As shown in Figure 2.6.b. After the signals are passed through the slip ring, the 220VAC signal is converted to 120VAC by a transformer and the signal is then sent to a power strip which is used to power cameras, lasers, computers, and other power strips placed on the top plate assembly.

The 220VAC and signals are sent from the slip ring into the servomotor drive box. The power and signals are filtered and sent to the servodrive and the servodrive then sends commands to the servomotor to rotate or oscillate.

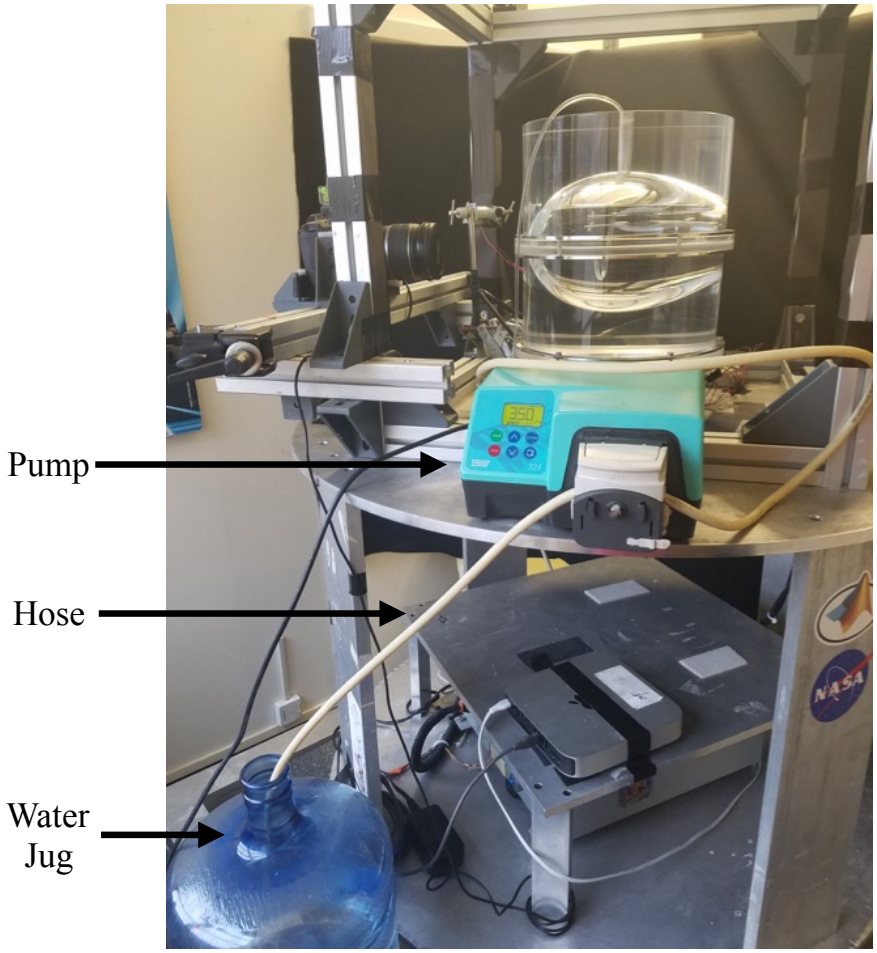

Figure 2.7: A layout of the pumping system used to move degassed water from the jug to the experimental volume using a peristaltic pump and hose.

2.2.4 Librating Frame Wiring

The librating frame wiring, shown in the dashed box in Figure 2.6.b, primarily consists of power lines used for running the laser during flow visualizations.

- Note that although a change in reference frame is occurring, there is no slip ring. Since the motion of the rotating frame is primarily oscillatory it is sufficient to make the laser power lines long enough so that lines themselves can move without being stretched or strained.

2.3 Filling the Experimental Volume

The process for filling the experimental volume, as shown in Figure 2.7, begins by filling a container or jug of distilled or tap water and letting the container sit so that the fluid is degassed for around a day. A peristaltic pump is used to transfer the water from this container to the experimental volume after one end of the hose is placed in the storage tank and the other hose is place inside the fill port in the upper hemisphere of the experimental volume. The hose should be placed below the water level to prevent splashing. If necessary, once the experimental volume is filled, it can be left to sit and degas further inside the experimental volume.

If an inner core is present then the filling hose can be inserted into a machined groove in the inner core support rod and the cavity can be filled without changing the changing the setup.

2.3.1 Removing Bubbles

The presence of bubbles can hinder visualization of the flow. During the filling process, air tends to get trapped in the thin space where the two hemispheres are attached. The air is best removed by performing a particularly vigorous librational forcing experiment. One such forcing that is referred to in the publication is the spin-over mode. The parameters for such a flow are 30RPM on the lower table motor, frequency of 1.15Hz, and an input angular amplitude of 70 degrees. Such a mode can be typically run for 5-10 minutes or until the release of air bubbles is no longer seen. After this is done, the water level will be lower and need to be refilled again.

If an inner core is also included there may be bubbles trapped in the southern hemisphere of the inner core and may be removed also by rocking the inner core before it is permanently affixed. Additionally, tiny bubbles may persist on the surface of the acrylic and degassing of the water in the fluid volume can help to remove these bubbles.

2.4 Libration System Controls

The control console for the librational apparatus is shown in Figure 2.8 and is composed of three parts: the main table and motor power switches outlined in black, the control of the oscillating servomotor is outlined in red, and the control pad of the motor that provides a constant lower rotation is outlined in green.

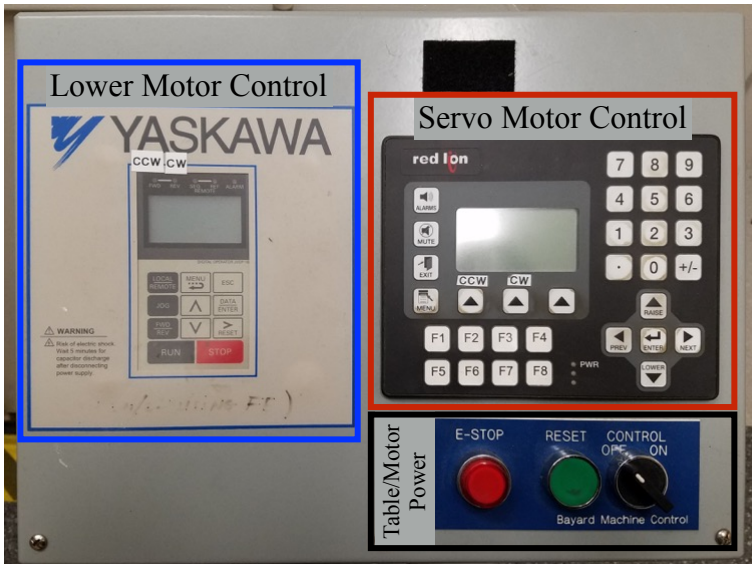

Figure 2.8: Control console for the librational forcing experiment. The green outlined region is the control pad for the lower table that provides a constant rotation rate. The red outlined area is the control pad for the oscillating servomotor. The lower controls outlined in black are the main power switches for the entire device.

2.4.1 Turning on the Power

Figure 2.9: The power controls for the libration experiment.

To turn on the power to the libration apparatus, first switch the black Control On/Off

knob and then press the green Reset button as shown in Figure 2.9. Upon doing so, make sure the emergency stop button light, servo motor control screen, emergency stop light on the main panel should be on. A high pitched noise should be emanating from the servomotor.

- Note: The main power must be on to operate the entire system. This can be inconvenient for several reasons:
  - If the user wishes to make a minor modification or adjustment, the high pitched whine from the servomotor can be unpleasant over long periods.
  - None of the wired systems are independent so by turning off the power any computer in the rotating frame will automatically lose power as well. It is tempting to circumvent this by plugging components into the laboratory frame. However, care must be taken so rotation isn't begun with these wires in place.
  - Another consequence of the dependencies in the system is that the servomotor is enabled meaning it will not freely rotate by hand which can be helpful during the assembly process.

2.4.2 Lower Table Control

The lower motor rotating the libration stucture is controlled using the console shown in Figure 2.10 while the power switch for the lower motor is found on the Servo Motor Control. First make sure the system has been turned on following the step in Section 2.4.1.

1. Press Fr 1 or F2 as it doesn't matter for this step.
2. Turn the INVERT ON/OFF by pressing on F5 on the keypad in Figure 2.10.2. An audible click should be heard from the lower motor and the lights on the Lower Motor Control panel will be on.
3. Press DATA/ENTER to edit the frequency associated with the lower table rotation.
4. To change the speed of the motor use the UP and DOWN arrow buttons to change each digit of the frequency, the right RESET arrow to move through the different digits,

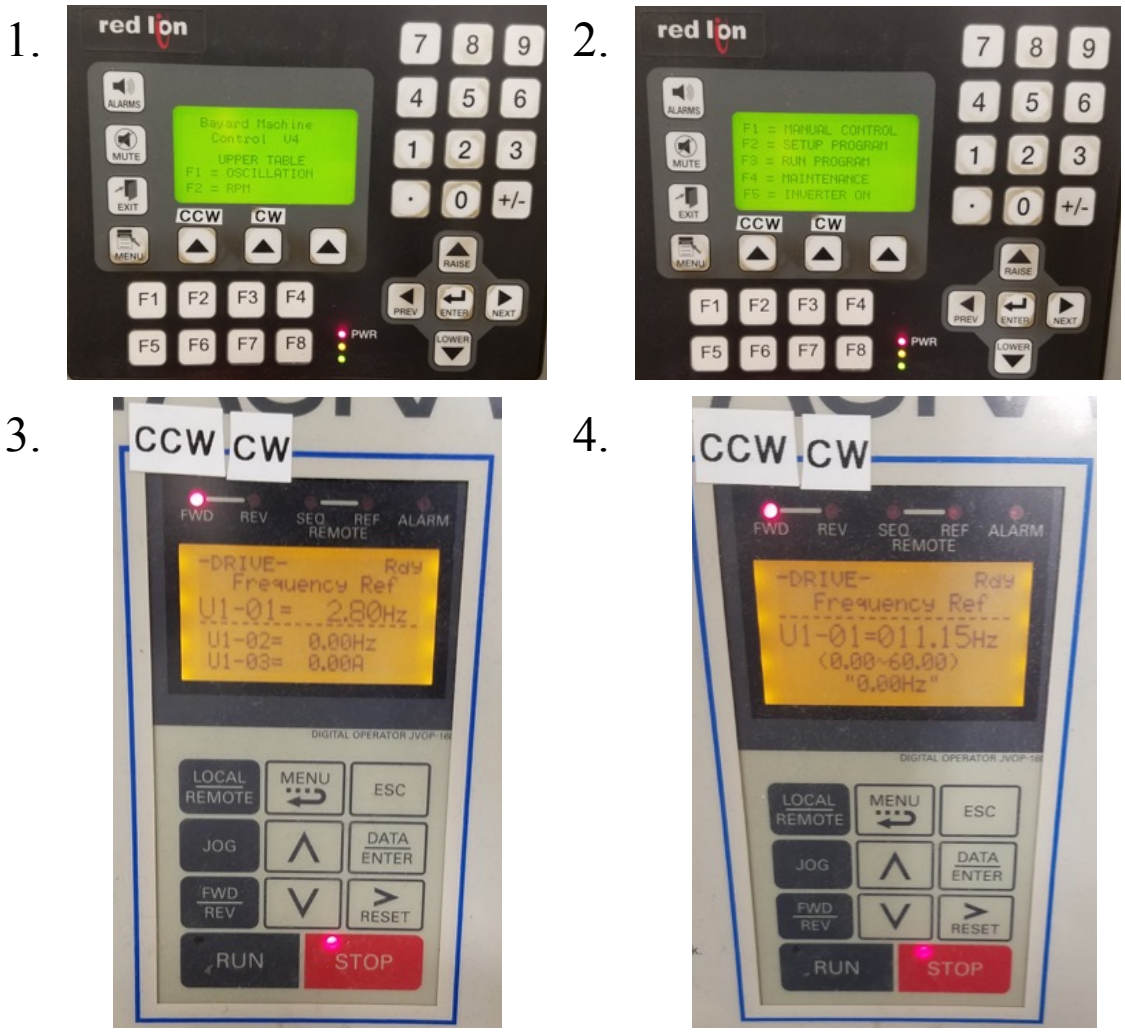

Figure 2.10: The lower table motor control steps for the libration experiment. These steps are described in Section 2.4.2.

and the DATA/ENTER button to save the new frequency.

Note that the frequency is related to the RPM by:

$$\text{Freq.(Hz)} = 0.782\text{RPM} - 0.201. \tag{2.2}$$

A table of frequencies vs. RPM are provided in a table located on the wall above the control pedestal.

- Before turning on the rotation make sure that all the wires and devices are secure, that there is nothing plugged into the laboratory frame, and that there are no loose tools

on the table.

- To turn on/off the rotation use the gray RUN button and the red STOP button.

Before changing the direction make sure the the apparatus has come to a complete stop.

- To change the direction of the rotation press the FWD/REV button and note that the light at the top of the pad will change from clockwise(CW) to counter-clockwise(CCW). For all experiments the rotation is CCW to keep the rotation axis pointing upward.

2.4.3 Servomotor Control

Once the power is turned on to the system the screen should be lit as shown in Figure 2.11.

2.4.3.1 Setting Oscillations

1. Press F1 on the keypad for oscillations. Note that pressing the MENU button will return you to this initial screen

2. Move to SETUP PROGRAM by pressing F2 on the keypad. The user should see the screen shown in Figure 2.11.2.

3. Use the UP, DOWN, RIGHT, and LEFT arrows and the keypad to specify the frequency in Hertz and the amplitude of the angle in degrees. Note that the system requires you specify the peak to peak angle. For instance, if the angle of oscillation is 40 degrees (0.7 rad) then the necessary input is 80 degrees or the peak to peak amplitude of oscillation. Once the frequency and oscillation is specified, press the arrow under RUN.

4. Use the arrows beneath the START and STOP to implement the oscillation. There are several important notes before beginning oscillations.

    - If lasers or other components affixed to the librating frame are wired in the rotating frame then a safe method for determining whether the wires allow for the

1. 2.

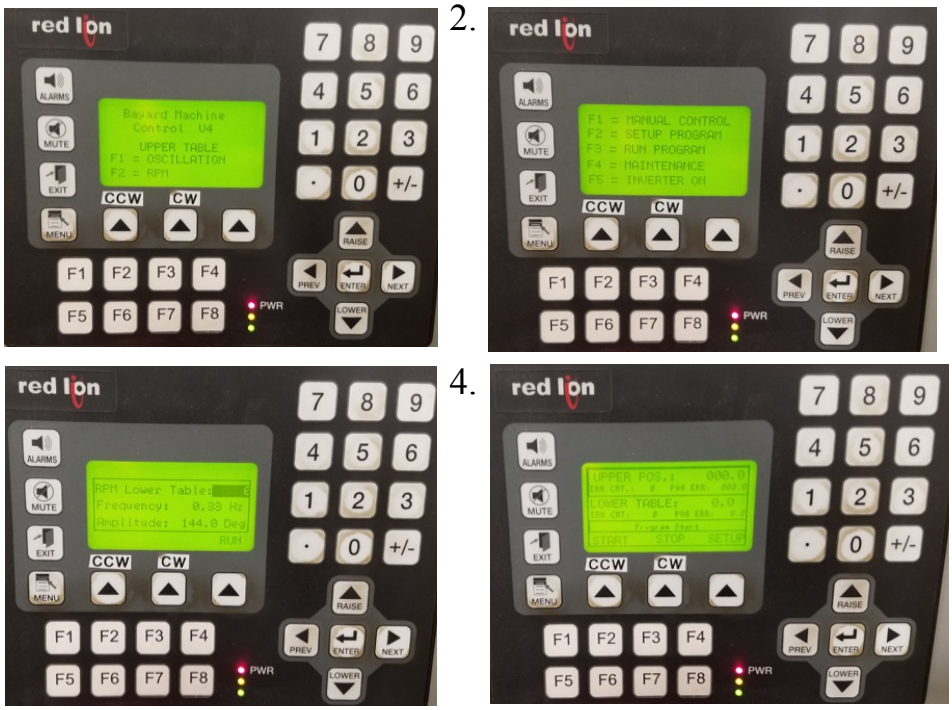

3. 4.

Figure 2.11: The controls for the servomotor on the libration experiment.

movement of libration is to set the requested angle and librate at a slow frequency first so as not to destroy the wires.

- The slower the libration frequency the slower the control program tends to respond to changes. Thus it is necessary to hold the STOP arrow longer when slow frequencies are required.
- The maximum possible frequency of libration decreases as the angle of libration increases. If the frequency is too high for a given libration angle the servo drive will return an error that requires cycling the power on and off to clear the error. This is particularly inconvenient as cycling the power may also kill the computer in the rotating frame.

5. The menu for changing the angle and frequency can be reached by pressing the arrow under SETUP.

1. 2.

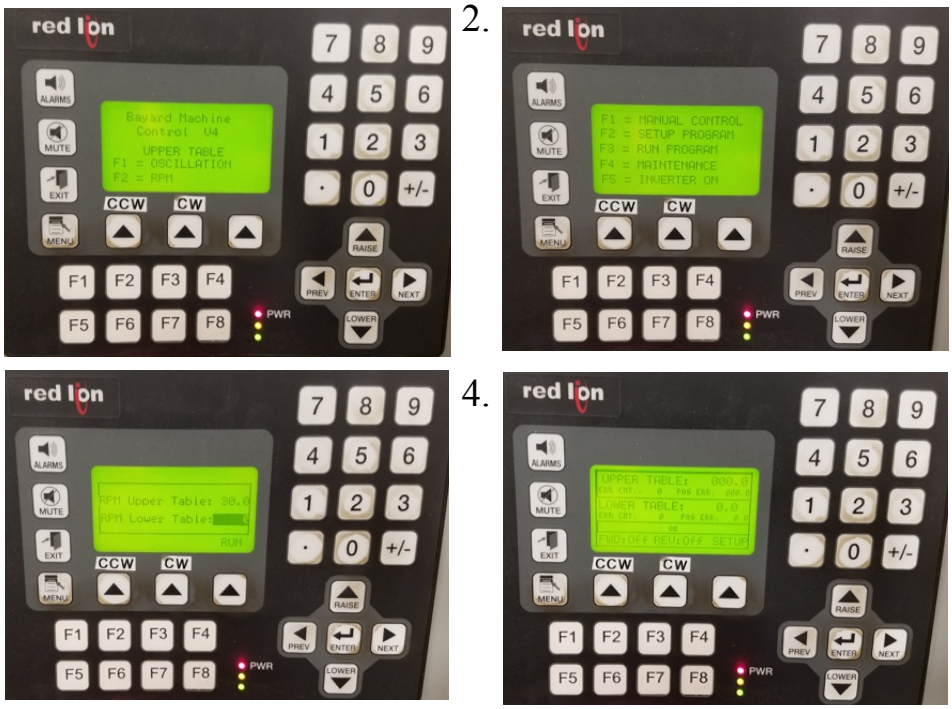

3. 4.

Figure 2.12: The controls for the servomotor on the libration experiment.

2.4.3.2 Setting Constant Rotation

1. Press F2 on the keypad for Constant Rotation. Note that pressing the MENU button will return you to this initial screen

2. Move to SETUP PROGRAM by pressing F2 on the keypad. The user should see the screen shown in Figure 2.11.2.

3. Use the UP, DOWN, RIGHT, and LEFT arrows and the keypad to specify the rotation rate in RPM Upper Table. Once the frequency and oscillation is specified press the arrow under RUN. Note that the input for RPM Lower Table has no function.

4. Use the arrows beneath the CW(REV) and CCW(FWD) to implement the rotation in the clockwise or counter-clockwise direction and press the same button to stop the rotation.

5. A separate menu for changing the rotation rate can be reached by pressing the arrow under SETUP. Note that returning to the setup screen also stops the rotation.

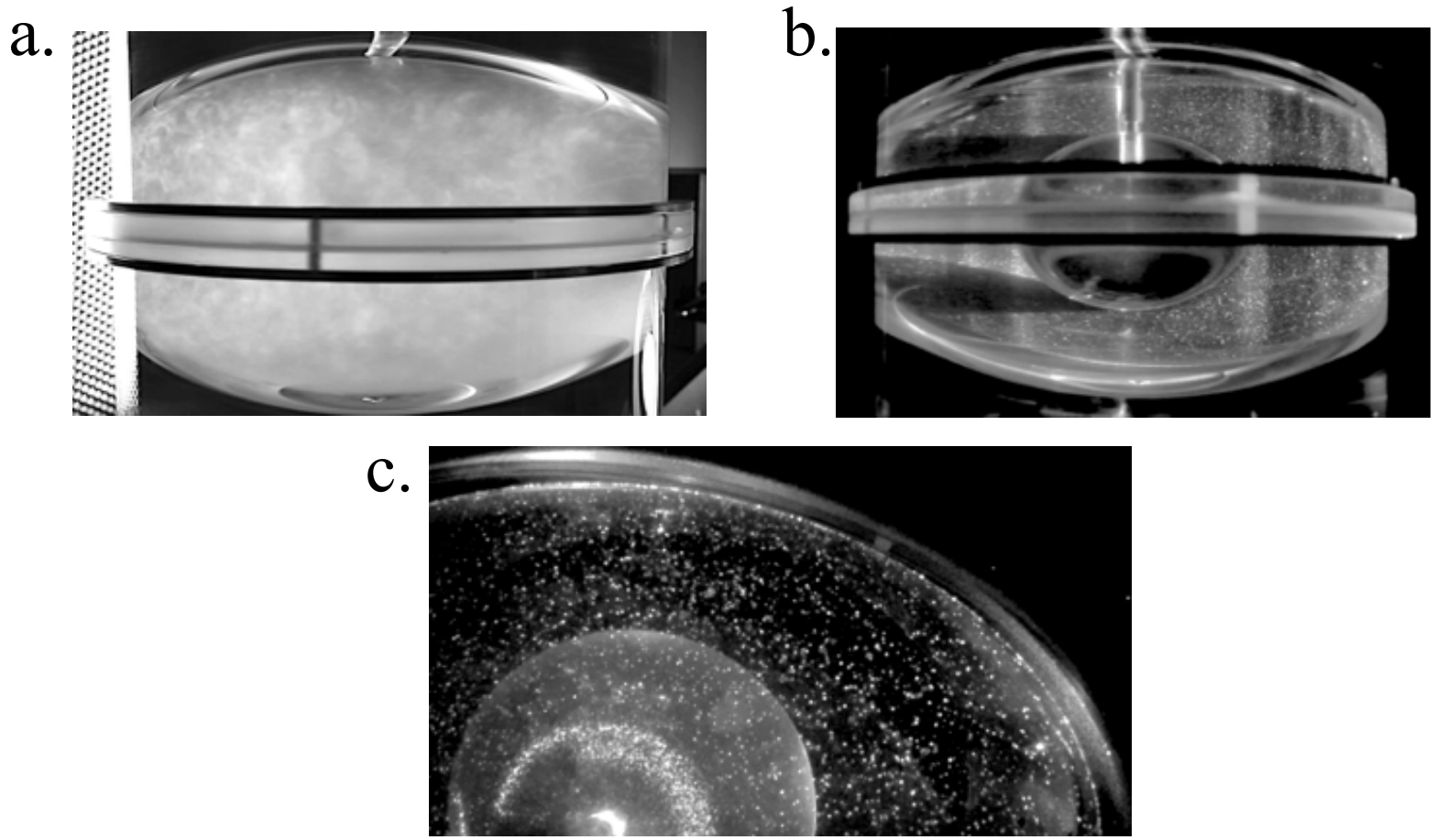

Figure 2.13: **(a)** Sideview image taken in the rotating frame with heavy Kalliroscope concentration and ambient light used to visualize flow structures near the boundary. **(b)**: Sideview image taken in the rotating frame with a light Kalliroscope concentration and laser light sheet used to visualize flow structures in the bulk interior. **(c)**: Top view image taken in librating frame with a standard PIV particle concentration.

2.4.4 Rotating Frame Computer Control

The computer in the rotating frame is controlled through a screen sharing program on a separate computer or through a wireless mouse and monitor located on the table in the libration room as indicated by the Libration Monitor Station in Figure 2.1. The cameras affixed to the rotating frame are connected to the rotating frame computer and all light intensity and filter settings are refined in-situ and recording is done remotely.

2.5 Visualizing Fluid Motions

In order to visualize fluid motions water is seeded with light reflecting particles, illuminated by lasers affixed to the librating frame, and recorded using a Canon EOS 7D camera placed in the rotating frame and/or a Gopro wireless camera placed in the librating frame.

Two types of flow visualization particles are well-mixed in the water as shown in Figure 2.13. The first, Kalliroscope solutions contains flake-like particles with a long axis such that they tend to align with shear structures in the flow. The Kalliroscope concentration can may be greatly increased such that ambient lighting can illuminate fluid flows near the boundaries (2.13.a). In contrast, the Kalliroscope solution may be low enough such that the laser illuminations can pass through the entire fluid layer (Figure 2.13.b). The second type of particles are microspheres of varying sizes (Figure 2.13.c) that follow the path of the fluid motions and are used in techniques like particle image velocimetry, PIV, to measure the velocity of the flow.

- Note that by looking at snapshots of Kalliroscope vs. PIV particles in Figures 2.13:middle and right respectively, there is not much visual difference. However, the Kalliscope is better able to visualize flow structures which are shown through differences in light intensity. In contrast, PIV particles, are better suited for following the flow and thus velocity information can be extracted using such particles.

These PIV particles and light Kalliroscope concentraitons are illuminated by lasers with cylindrical lenses such that the laser casts a plane of light or laser light sheet. These light

sheets are oriented parallel with the axis of rotation or horizontally through the equator. Because of the ellipsoidal geometry, the laser light sheets can be strongly refracted and hence their positions are limited to vertical or equatorial slices where the refraction is minimized. Such refraction is unavoidable when inner cores are placed inside the fluid volume as is shown in Figure 2.13:middle.

The visualizations are saved as movies with frequencies up to 60 frames per second. The Canon cameras used are connected to a computer in the rotating frame and accessed remotely. The settings and recording for the Canon are controlled through the Canon EOS Utility software while the GoPro camera can be controlled remotely through a GoPro application. All movies are read into MATLAB and the individual frames are analyzed or saved for additional processing including measuring light intensity variations and determining velocities through an open source PIV program called DPIVSoft2010.

2.6 Running Cases

After the experimental volume has been assembled, seeded with particles, illuminated, and the camera settings and filtering have been refined, data acquisition can commence. In order to run a case, the lower table rotation and frequency and angular amplitude of the oscillations are determined. The whole frame is set in motion at the table's rotation rate until solid body rotation has been reached. The typical spin-up time is determined by $\tau_{\text{spin}} \sim \Omega^{-1}E^{-1/2}$ where Ω is the rotation rate of the container in rad/s and $E = \nu/(2\Omega a^2)$ is the Ekman number where a is the long axis of the container found in Table 2.1 and $\nu \sim 10^{-6}$ is the kinematic viscosity of water. For solid body-rotation to occur, it is necessary for rotation to occur for approximately three to four spin-up times. If water is seeded and illuminated, the user can wait until no fluid motions are visible.

After solid body rotation is reached and before the oscillations commences, recording is begun to capture the onset of mechanically-forced motions. Typically the ambient lights in the room are flashed on and off to indicate that the oscillations are about to begin. The oscillations and the onset of instability are recorded for several spin up times, around

approximately 10 minutes. This process is repeated in order to gather a broad survey of flow information at varying parameters.

CHAPTER 3

Experimental study of global-scale turbulence in a librating ellipsoid

Reproduced from: **A. M. Grannan**, M. Le Bars, D. Cébron, and J. M. Aurnou. Phys. Fluids, 26:126601, 2014.

In this work, I modified the libration device, described in Chapter 2, by designing a support system for lasers in the librating frame and implemented a non-intrusive particle image velocimetry measurement technique that was used to measure flow in the equatorial frame in a fully assembled ellipsoid for the first time. I performed and analyzed a suite of libration experiments by fixing the rotation rate and varying the strength and frequency of libration. This work provides the first experimental verification of the characteristics of the libration-driven elliptical instability that drives turbulence in the bulk fluid. I was the primary author of the final document.

3.1 Introduction

The interactions between satellites and their primary gravitational partners distort the shapes of both bodies and give rise to periodic mechanical forcings that, in turn, drive precessional, tidal, and librational motions [e.g., Comstock and Bills (2003)]. The current work focuses specifically on the longitudinal libration in so-called synchronized systems where the secondary body's rotation rate undergoes periodic oscillations about its orbital rate. Additionally, some librating bodies are differentiated and contain liquid metal cores such as those of Mercury [e.g., Margot et al. (2007)], Io [e.g., Anderson et al. (1996)], Ganymede [e.g., Schubert et al. (2004)], as well as subsurface oceans in Europa [e.g., Anderson et al.

(1998)], Ganymede [e.g., Schubert et al. (2004)], and Enceladus [e.g., Anderson et al. (2001)]. The fluid layer response to the librational forcing through viscous [e.g., Noir et al. (2009); Calkins et al. (2010); Sauret et al. (2010)], topographic [e.g., Noir et al. (2012); Calkins et al. (2012a)], and electromagnetic coupling [e.g., Deleplace and Cardin (2006); Buffett and Christensen (2007); Roberts and Aurnou (2012)] is important for understanding the thermal, magnetic, and orbital evolution of the body. Importantly, while it is often assumed that thermo-compositional convection drives the fluid motions responsible for dynamo generation [e.g., Kagayama and Sato (1995); Glatzmeier and Roberts (1996); Schubert and Soderlund (2011)] recent studies [e.g., Tilgner (2005); Wu and Roberts (2009, 2013); Cébron and Hollerbach (2014)] have characterized how mechanical forcing can also drive dynamos by injecting a portion of the vast quantity of rotational energy from primary-satellite orbital systems into driving fluid motions.

The first studies of libration in spheres [e.g., Aldridge (1967); Aldridge and Toomre (1969)] showed, using pressure measurements, that a resonant response occurs when the forcing frequency matches an eigenfrequency of the system. While this excitation was inferred to be an eigenmode of the system, a recent analytical study in the limit of small viscosity found no resonant excitations and only anomalous pressure variations along the axis of rotation [e.g., Zhang et al. (2013)]. Librational forcing also gives rise to centrifugal instabilities that are confined to the boundary layers of cylinders and spheres [e.g., Noir et al. (2009); Calkins et al. (2010)]. Additional theoretical, numerical, and experimental work has verified the stationary zonal flow caused by non-linear interactions in the Ekman boundary layers of cylinders, spheres, and spherical shl fiells [e.g., Wang (1970); Calkins et al. (2010); Sauret et al. (2010); Noir et al. (2012); Sauret and Le Dizes (2013)].

Recent studies have focused on simulating librational effects in more realistic geometries that reflect the non-axisymmetric shape of planetary interior fluid layers. Theoretical and numerical studies of flows in non-axisymmetric containers have shown that longitudinal librational forcing cannot, through a *direct* resonance, excite eigenmodes of the system [e.g., Chan et al. (2011); Zhang et al. (2011)]. Importantly, this does not preclude the resonance of two inertial modes interacting with an elliptically-deformed base flow [e.g., Kerswell and

Malkus (1998); Cébron et al. (2012a)]. Numerical simulations using finite element methods at an Ekman number, $E = 5 \times 10^{-4}$, defined in Section 5.2, have shown that a triadic resonance between two inertial modes and a librationally induced elliptically-deformed base flow [e.g., Malkus (1989)] excites a LDEI. This instability gives rise to three-dimensional (3D) motions in the bulk fluid that act to modify the base flow thus truncating the instability. The base flow is then re-established and this cycle of growth and collapse continues [e.g., Cébron et al. (2012b)]. Experimental laser doppler velocimetry (LDV) measurements at a single point attributed a growth and decay of the zonal flow strengths in a half-ellipsoid to the existence of an LDEI [e.g., Noir et al. (2012)] The aspects of the mechanically forced flows, described above, are thoroughly reviewed in Le Bars et al. (2015).

In this experimental work, a particle image velocimetry (PIV) method is used to measure the libration induced base flow, time-averaged zonal flow, and fully turbulent libration driven flow in the equatorial plane of an ellipsoidal container at a fixed $E = 2 \times 10^{-5}$ more extreme than currently possible through numerical simulations. In Section 5.2, the mathematical framework is developed for libration driven flows as well as the resonant conditions and growth rates associated with the LDEI. The experimental method is described in Section 3.3 and the results are discussed in Section 5.5. The conclusions are presented in Section 5.6.

3.2 Mathematical Background

In this experiment, we consider a homogenous, incompressible, Newtonian fluid that is enclosed in an ellipsoidal container. The boundary of this shape is specified by the equation for an ellipsoid, $x^2/a^2 + y^2/b^2 + z^2/c^2 = 1$, set in a Cartesian coordinate system affixed to the librating container where $\hat{\mathbf{x}}$ is along the long equatorial axis of the ellipsoid with length a, $\hat{\mathbf{y}}$ is the short equatorial axis with length b, and $\hat{\mathbf{z}}$ is along the axis of rotation with length c. The equatorial ellipticity of the cavity is defined as $\beta = (a^2 - b^2)/(a^2 + b^2)$. The rotation rate $\Omega(t)$ for librational forcing is composed of a constant rotation Ω_0 plus a sinusoidal perturbation:

$$\Omega(t) = \Omega_0 + \Delta\varphi \; \omega_{lib} \sin(\omega_{lib} t), \tag{3.1}$$

where ω_{lib} [rad/s^{-1}] is the angular frequency of libration and $\Delta\varphi$ [rad] is the amplitude of libration. The equations of fluid motion and continuity, written in the librating frame and non-dimensionalized using the long axis a for the length scale and Ω_0^{-1} as the time scale, are:

$$\frac{\partial \mathbf{u}}{\partial t} + \mathbf{u}\cdot\nabla\mathbf{u} + 2\big(1+\epsilon\sin(ft)\big)\hat{\mathbf{z}}\times\mathbf{u} = -\nabla\Pi + E\nabla^2\mathbf{u} - \epsilon f\cos(ft)(\hat{\mathbf{z}}\times\mathbf{r}), \tag{3.2}$$

$$\nabla\cdot\mathbf{u} = 0. \tag{3.3}$$

In (6.4), the first two terms on the left side are the inertial terms, and the third term is the time-dependent Coriolis acceleration. The terms on the right side are the pressure gradient, the viscous dissipation, and the Poincare force due to the time dependent rotation rate respectively. The non-dimensional libration frequency is $f = \omega_{lib}/\Omega_0$, $\epsilon = f\Delta\varphi$ is the dimensionless libration forcing amplitude, and Π is the modified pressure term containing the time varying centrifugal acceleration. The Ekman number, $E = \nu/(\Omega_0 a^2)$, characterizes the ratio of viscous to Coriolis forces and $\mathbf{r} = (x, y, z)$ is the position vector in the librating frame.

3.2.1 Base Flow

Making a perturbation expansion of (6.4), the flow is decomposed into $\mathbf{u} = \mathbf{U} + \mathbf{u}'$ and $\Pi = \Pi_0 + \pi'$ where the perturbed flow $\mathbf{u}'(\pi')$ is much smaller than the base flow $\mathbf{U}(\Pi_0)$ i.e., $|\mathbf{u}'| \ll \mathbf{U}$ and $\pi' \ll \Pi_0$. Focusing first on the the base flow and taking (6.4) in the limit that $E \ll 1$, the flow is decomposed into $\mathbf{U} = \mathbf{U}_{lib} + \widetilde{\mathbf{U}}$ with an inviscid bulk component, $\mathbf{U}_{lib}$, and a flow in the viscous boundary layer of depth $\sqrt{E}$ attached to the outer boundary, $|\widetilde{\mathbf{U}}| \propto \epsilon$, that is proportional to the libration forcing. An inviscid solution of (6.4) for the bulk base flow velocity that satisfies the non-penetration condition in the librating frame of reference is given by Kerswell and Malkus (1998):

$$\mathbf{U}_{lib} = -\epsilon\sin(ft)\big[\hat{\mathbf{z}}\times\mathbf{r} - \beta\nabla(xy)\big], \tag{3.4}$$

with coordinates (x, y, z) and equatorial flow components (U_{lib}, V_{lib}). In the librating frame, fluid parcels oscillate back and forth along elliptically deformed streamlines as shown in a vector field snapshot of Figure 3.1.a. For the current analysis, this flow is transformed to the steadily rotating frame of reference reflecting the same frame where experimental measurements are performed. This base flow (U_{rot}, V_{rot}) in the steadily rotating frame is given in (3.5) with X and Y being the spatial coordinates fixed to this frame such that X is aligned with the average location of the container's long-axis. Figure 3.1.b shows a snapshot of the oscillating velocity field exhibiting a strain field with an azimuthal wavenumber $m = 2$, and an oscillating direction and amplitude:

$$
\begin{aligned}
U_{rot} &= \epsilon\beta \sin(ft)\Big[Y \cos\left(\frac{2\epsilon(1-\cos(ft))}{f}\right) - X \sin\left(\frac{2\epsilon(1-\cos(ft))}{f}\right)\Big]\hat{\mathbf{i}} \\
V_{rot} &= \epsilon\beta \sin(ft)\Big[Y \sin\left(\frac{2\epsilon(1-\cos(ft))}{f}\right) + X \cos\left(\frac{2\epsilon(1-\cos(ft))}{f}\right)\Big]\hat{\mathbf{j}}
\end{aligned}
\tag{3.5}
$$

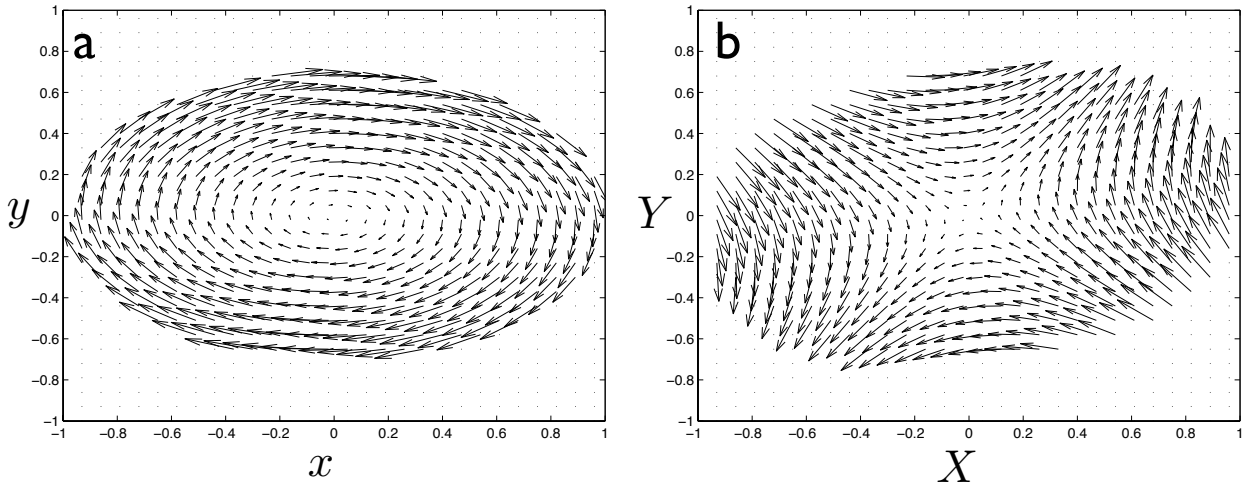

Figure 3.1: (a) Theoretical vector field snapshot (U_{lib}, V_{lib}) of the elliptically deformed base flow in the librating frame, (x, y, z). (b) The same base flow transformed into the steadily rotating reference frame, (X, Y, Z), where the current experimental measurements are performed.

3.2.2 Zonal Flow

In the librating frame, to satisfy the no-slip boundary conditions, viscous corrections in the Ekman boundary layer generate a flow, $\tilde{\mathbf{U}}$, with axisymmetric and non-axisymmetric components, $\widetilde{\mathbf{U_0}}$ and $\widetilde{\mathbf{U_2}}$ respectively, given as:

$$\widetilde{\mathbf{U}} \propto \epsilon \sin(ft)(\widetilde{\mathbf{U_0}} + \beta \widetilde{\mathbf{U_2}} \mathrm{e}^{\pm 2i\phi}), \tag{3.6}$$

where ϕ is the azimuthal angle measured with respect to $\widetilde{\mathbf{X}}$. The non-linear self-interaction of (3.6) leads to an axisymmetric stationary zonal flow in the boundary layer that, by continuity, generates a flow in the interior fluid, as confirmed in axisymmetric containers [e.g., Wang (1970); Busse (2010, 2011); Calkins et al. (2010); Noir et al. (2010); Sauret et al. (2010, 2012)]. This stationary flow scales as ϵ^2 with an azimuthal wavenumber $m = 0$ and is expected in the ellipsoidal container. Additional axisymmetric and non-axisymmetric stationary flows arise due to the ellipsoidal geometry and scale as $\epsilon^2\beta$ and $\epsilon^2\beta^2$ with azimuthal wavenumbers $m = 2$ and $m = 0, 4$ respectively [e.g., Sauret (2012)].

3.2.3 Inertial Modes

For rotating fluids in finite volumes, inertial waves reflected at boundaries conserve the angle between the wave vector and the axis of rotation θ. Thus reflections and waves may, through constructive interference, generate inertial modes of the form, $\mathbf{u'}_j \propto \mathrm{e}^{i\lambda_j t}\mathbf{\Phi}_j(\mathbf{r})$ that satisfy the linearized inviscid equations motions given by Greenspan (1969),

$$\frac{\partial \mathbf{u'}}{\partial t} + 2\hat{\mathbf{z}} \times \mathbf{u'} = -\nabla \pi'. \tag{3.7}$$

The j^{th} inertial mode is the solution of (3.7) such that

$$i\lambda_j \mathbf{\Phi}_j + 2\hat{\mathbf{z}} \times \mathbf{\Phi}_j = -\nabla \pi'_j, \tag{3.8}$$

where $\mathbf{\Phi}_j \propto \mathrm{e}^{im_j\phi}$ with m_j being the azimuthal wavenumber [e.g., Tilgner (2007)]. Additionally, the inertial modes are orthogonal such that $\int \mathbf{\Phi}_k^* \mathbf{\Phi}_j \, dV = \delta_{j,k}$ [e.g., Greenspan (1969)]. Analytical solutions of inertial modes exist for the cylinder [e.g., Kerswell (1993)], cylindrical shell [e.g., Herreman (2009)], spheroid [e.g., Zhang et al. (2004)], and a polynomial description also exists for the ellipsoids [e.g., Vantieghem (2014)] considered in our experiments. Although not considered here, such analytical descriptions can not be extended to the more geophysically relevant geometry of spherical shells due to the ill-posed nature of the well-known Poincaré equation for inertial modes with non-penetrating boundary conditions. Numerical studies, in this geometry, have shown that solutions converge to attractors [e.g., Rieutord and Valdettaro (1997); Rieutord et al. (2001)].

3.2.4 Elliptical Instability

The elliptical instability arises due to the growth of perturbations induced by the interaction between a libration induced base flow from (3.4) and two inertial modes. Despite the open questions regarding the completeness property of inertial modes whereby an arbitrary velocity field may be expanded into a series of inertial modes [e.g., Greenspan (1969)], the velocity and pressure perturbations are written as a linear combination of inertial modes and later seek to identify the participating inertial modes experimentally. Then, $(\mathbf{u}', \pi') = \sum_j a_j(t)\mathrm{e}^{i\lambda_j t}(\mathbf{\Phi}_j, \pi_j)$ where $a_j(t) \ll 1$ is a small time-dependent coefficient and the evolution for the velocity perturbation in (6.4) is given by

$$\frac{\partial \mathbf{u}'}{\partial t} + \mathbf{U}_{lib} \cdot \nabla \mathbf{u}' + \mathbf{u}' \cdot \nabla \mathbf{U}_{lib} + 2\big(1 + \epsilon \sin(ft)\big)\hat{\mathbf{z}} \times \mathbf{u}' = -\nabla \pi' + E\nabla^2 \mathbf{u}'. \tag{3.9}$$

By substituting the solutions for $(\mathbf{u}', \pi')$ into (3.9) and analyzing the resulting equations, we seek to determine the conditions that are required on the coefficients a_j such that they grow

through time.

$$\sum_j \mathrm{e}^{i\lambda_j t}\Big\{\frac{\partial a_j}{\partial t}\mathbf{\Phi}_j + a_j\big[\mathbf{U}_{lib}\cdot\nabla\mathbf{\Phi}_j + \mathbf{\Phi}_j\cdot\nabla\mathbf{U}_{lib} + 2\epsilon\sin(ft)(\hat{\mathbf{z}}\times\mathbf{\Phi_j})\big] + a_j\big(i\lambda_j\mathbf{\Phi}_j + 2\hat{\mathbf{z}}\times\mathbf{\Phi}_j = -\nabla\pi_j\big)\Big\}. \tag{3.10}$$

Here we have neglected viscous dissipation for simplicity. The last expression in parentheses of (3.10) is zero using (3.8). To isolate $\frac{\partial a_j}{\partial t}$, (3.10) is multiplied by an inertial mode $\mathbf{u}'^*_k \propto \mathrm{e}^{-i\lambda_k t}\mathbf{\Phi}^*_k$ and integrated over the entire fluid volume. Using the orthogonality of inertial modes, the evolution of the coefficient a_k is:

$$\frac{\partial a_k}{\partial t} = -\sum_j a_j \mathrm{e}^{i(\lambda_j-\lambda_k)t}\int \mathbf{\Phi}^*_k\big(\mathbf{U}_{lib}\cdot\nabla\mathbf{\Phi}_j + \mathbf{\Phi}_j\cdot\nabla\mathbf{U}_{lib} + 2\epsilon\sin(ft)(\hat{\mathbf{z}}\times\mathbf{\Phi}_j)\big)dV. \tag{3.11}$$

The libration driven non-axisymmetric base flow at frequency f with an azimuthal wavenumber $m_{lib} = 2$ may be written as $\mathbf{U}_{lib} \propto \mathrm{e}^{\pm i(m_{lib}\phi+ft)}\widetilde{\mathbf{U}_{lib}}(r,z)$ and the inertial mode as $\mathbf{\Phi}_j \propto \mathrm{e}^{im_j\phi}\widetilde{\mathbf{\Phi}_j}(r,z)$. Substituting these dependencies into (3.11) gives for a_k

$$\frac{\partial a_1}{\partial t} = a_2\mathrm{e}^{i(\lambda_2-\lambda_1\pm f_{lib})t}\int \mathrm{e}^{i(m_2-m_1\pm m_{lib})\phi}\big(\widetilde{\mathbf{U}_B}\cdot\nabla\widetilde{\mathbf{\Phi}_j} + \widetilde{\mathbf{\Phi}_j}\cdot\nabla\widetilde{\mathbf{U}_B} + 2\epsilon\sin(ft)(\hat{\mathbf{z}}\times\widetilde{\mathbf{\Phi}_j})\big)\mathrm{dV}, \tag{3.12}$$

and for the coefficient a_j

$$\frac{\partial a_2}{\partial t} = a_1\mathrm{e}^{i(\lambda_1-\lambda_2\pm f)t}\int \mathrm{e}^{i(m_1-m_2\pm m_{lib})\phi}\big(\widetilde{\mathbf{U}_B}\cdot\nabla\widetilde{\mathbf{\Phi}_j} + \widetilde{\mathbf{\Phi}_j}\cdot\nabla\widetilde{\mathbf{U}_B} + 2\epsilon\sin(ft)(\hat{\mathbf{z}}\times\widetilde{\mathbf{\Phi}_j})\big)\mathrm{dV}. \tag{3.13}$$

For the growth of a_k and a_j to occur, the periodicity in time is removed by setting $\lambda_j-\lambda_k\pm f = 0$. The integral over the fluid volume is only non-zero for $m_j - m_k \pm m_{lib} = 0$. These resonant conditions are summarized as:

$$\begin{aligned} |m_j - m_k| &= m_{lib}, \\ |\lambda_j - \lambda_k| &= f. \end{aligned} \tag{3.14}$$

Importantly, the coupled equations show that the interaction of one of the inertial modes $\mathbf{u'}_k, (\mathbf{u'}_j)$ with the base flow $\mathbf{U_{lib}}$ reinforces the other inertial mode $\mathbf{u'}_j, (\mathbf{u'}_k)$. To solve for a_k, we can take the time derivative of (3.12) and plugging in (3.13) to get a second order temporal equation for a_k that admits exponential solutions [e.g., Cébron et al. (2012a, 2014)]. An analogous equation can be made for a_j. Since inertial modes exist within a frequency from $[-2, 2]$, the resonance condition in (3.14) allows for the existence of elliptical instability in flows from $|f| = 0 - 4$.

3.2.5 Growth Rates

While these conditions on the frequency and azimuthal wavenumber form a portion of the global analysis of the LDEI, a complete analytical description of the inertial modes is still needed for the large β of our present ellipsoidal geometry. One such method characterizes the inertial modes by assuming a polynomial spatial description of space coordinates for the velocity and decomposes the flow field into a set of basis vectors that satisfy the continuity equation and boundary conditions [e.g., Gledzer and Ponomarev (1992); Vantieghem (2014); Wu and Roberts (2009)]. While this method may be extended to any polynomial degree n and thus characterize any coupling of inertial modes, the analytical expressions involved quickly become very complex (e.g. see $n_{poly} = 6$ in Wu and Roberts (2009), especially for small-scale modes.

Instead, local stability analyses are used to derive analytical expressions of the growth rate for the LDEI. The first approach, using a Wentzel-Kramers-Brillouin (WKB) [e.g., Le Dizes (2000)] method for $\epsilon, \beta \ll 1$, gives an upper bound for the growth rate by assuming that short wavelength plane wave perturbations characterized by the wave vector $\mathbf{k}$ whose norm $|k| \gg 1$ are advected along streamlines. The inviscid growth rate σ_{inv} is found by solving the inviscid equations of motion to the first order in $\epsilon\beta$:

$$\sigma_{inv} = \frac{16 + f_{res}^2}{64}\beta\epsilon \tag{3.15}$$

where f_{res} is a resonant forcing frequency [e.g., Cébron et al. (2012a)]. This method was

confirmed in numerical simulations of the LDEI in Cébron et al. (2012b).

A second local WKB method uses a multiple scale analysis [e.g., Kevorkian and Cole (1996)] of a multipolar instability for any ϵ in the limit that $\epsilon\beta \ll 1$. The inviscid growth rate solution is then given by

$$\sigma_{inv} = \frac{16 + (jf_{res})^2}{64} \left| J_{j-1}(n\Delta\varphi) + J_{j+1}(n\Delta\varphi) \right| \beta\epsilon \tag{3.16}$$

where J_j is the Bessel function of the first kind with integer j and the resonance condition is written as $|\lambda_1 - \lambda_2| = jf$ [e.g., Cébron et al. (2014)]. The degree n of multipolar deformation is taken to be $n = m_{lib} = 2$ for the ellipsoid. This method was confirmed in the multipolar stability analysis in a librating deformed cylinder and sphere in Cébron et al. (2014). A general formula of the typical growth rate for each calculation of σ_{inv} is given for f around the resonant forcing frequency [e.g., Cébron et al. (2012a)],

$$\sigma_{Theory} = \sqrt{\sigma_{inv}^2 - (f_{res} - f)^2} - K\sqrt{E} \tag{3.17}$$

The first term on the right hand side is the band of unstable frequencies about f_{res}, and the second term is the viscous dissipation in the Ekman boundary layer scaling as $E^{1/2}$ where K is a viscous dissipation factor typically between $[1 - 10]$.

The goal of our work here is to quantitatively validate all of the theoretical predictions presented above: [1] the existence of the two-dimensional libration induced base flow in (3.5), [2] the zonal flow generated by the non-linear self interaction of the base flow correction in (3.6), and [3] the three-dimensional destabilization via LDEI by making velocity measurements in the equatorial plane of a full ellipsoidal container at Ekman, $E = 2 \times 10^{-5}$. Our work complements and extends the three-dimensional numerical simulations of Cébron et al. (2012b), performed at larger $E = 5 \times 10^{-4}$, and the experimental analysis of Noir et al. (2012) that made point velocity measurements in the half-ellipsoid.

3.3 Method

3.3.1 Experimental Approach

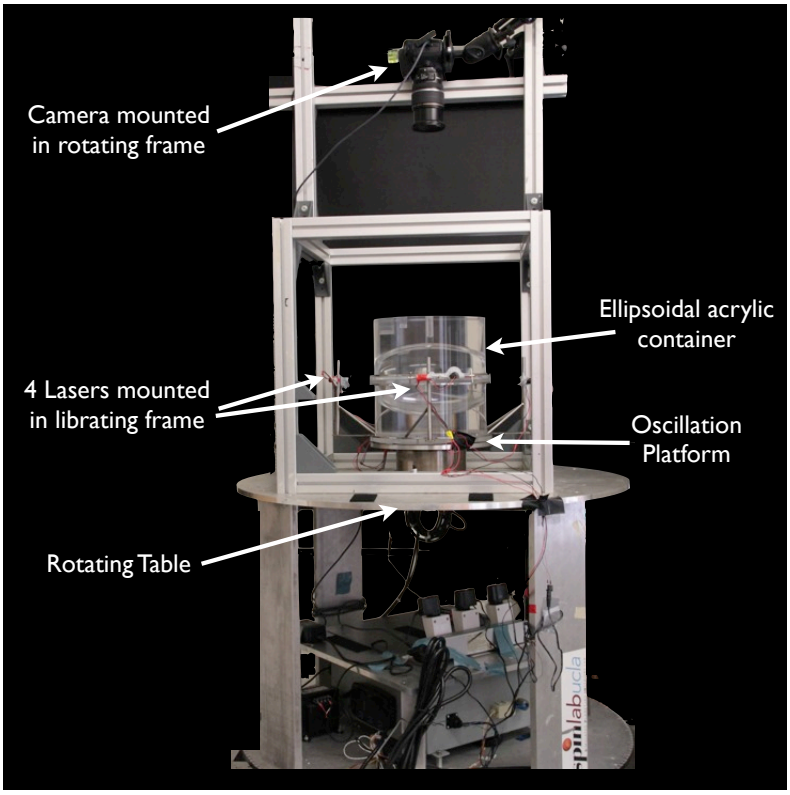

Figure 3.2: The libration experimental apparatus. The high definition camera is shown in top view position for PIV. The camera is also used in side-view for Kalliroscope visualizations of meridional flows.

The experimental setup used in the present work is adapted from the same apparatus used previously in Noir et al. (2009, 2010, 2012). Librational forcing is replicated using two motors. The first motor rotates the turntable and super-structure at a constant angular velocity of $\Omega_0 = 30$ rpm corresponding to $E = 2 \times 10^{-5}$. The second, which is directly coupled to the acrylic cavity, superimposes a sinusoidal oscillation whose parameter range is $[\Delta\phi, f] = [0.05 - 2.5, 0.5 - 9]$. The container used for this experiment is made from two non-axisymmetric hemispheres machined from solid cast acrylic cylinders and polished for optical clarity. The enclosed fluid cavity is ellipsoidal with a long axis $a = 127$mm and short axes $b = c = 89$mm. Axis c is aligned with the axis of rotation and the equatorial ellipticity is fixed in all our experiments at $\beta = 0.34$.

To characterize meridional fluid motions, direct flow visualizations are performed by using a laser light sheet, oriented along a vertical plane that passes through the container's origin, to light Kalliroscope^{TM} particles suspended in the water. A Canon EOS 7D digital camera with a resolution of 1080×720 pixels is positioned on the rotating table to the side of the container to record movies of the meridional flow field at 60 frames per second.

To make quantitative measurements, a particle image velocimetry (PIV) technique is employed in the rotating reference frame. Nearly spherical, 100 μm diameter Optimage^{TM} particles of density $(1 \pm 0.02 \mathrm{g/cm}^3)$ are added to the water. Four laser light sheets are fixed in the librating frame several millimeters above the equatorial plane due to the presence of the joining seam for the two acrylic hemispheres. The camera is fixed in the rotating frame, positioned overhead (i.e., Figure 5.2) in order to acquire 1080×720 resolution movies of the horizontal flow field. These movies are made only after solid body rotation has been reached; they are initiated at the start of oscillatory motion and the recordings are typically 12 minutes in duration. The camera is connected directly to a computer in the rotating frame, which, in turn, is controlled remotely from the lab frame.

Additionally, the camera settings were optimized and physical masks were implemented to produce well-resolved movies that could yield accurate PIV results. These movies are separated into their constituent frames and passed through an open source PIV software, DPIVSoft2010 [e.g., Meunier and Lewecke (2003)], that has been successfully employed in previous [e.g., Sauret et al. (2010); Morize et al. (2010)]. The velocity field for an entire equatorial plane is resolved into a 23x40 grid with a typical spatial resolution of 8mm. All velocity measurements presented below have been non-dimensionalized using the long axis length, a, and the steady rotational period Ω_0^{-1}.

3.4 Results

3.4.1 Base Flow

Figure 3.3.a shows an instantaneous PIV vector field of the elliptically deformed base flow in the fluid interior induced by the topographic coupling of the librating non-axisymmetric

boundary for $f = 1.46, \epsilon = 0.73$. This comparison provides a qualitative match to the bulk interior inviscid solution of the base flow [e.g., Kerswell and Malkus (1998)] in the steadily rotating reference frame shown in Figure 3.1.b. For a quantitative comparison, Figure 3.3.b shows a profile of the magnitude of the base flow velocity, $|U|$(squares), along the X-axis(dashed black line in Figure 3.3.a) compared to the theoretical base flow(solid black line) in Figure 3.3.b at the same phase of libration. The experimental results in Figure 3.3.b follow the base flow trend while the velocity magnitudes are slightly above the theoretical flow with an increase near the boundaries. This deviation is associated with the axisymmetric flow generated through viscous non-linear interactions in the boundaries driving a zonal flow.

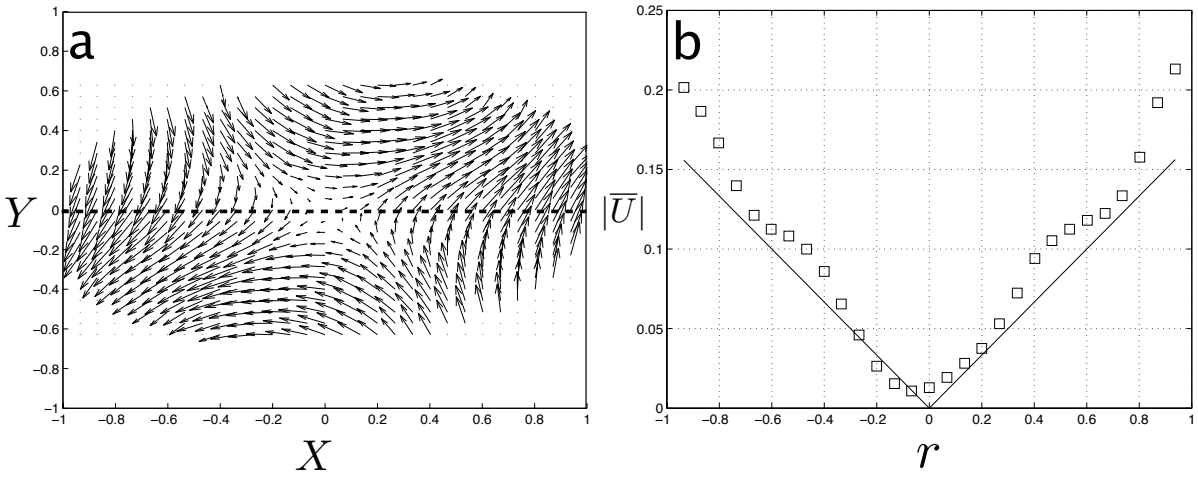

Figure 3.3: PIV data for $f = 1.46, \epsilon = 0.73$. (a) Snapshot showing the libration induced base flow and (b) the snapshot profile of the velocity magnitude $|U|$ (squares) along the X-axis (dashed black line in (a) with the theoretical base flow from (3.5) (black line).

3.4.2 Zonal Flow

An analysis of the zonal flow is performed for fixed $f = 1.46$ and $E = 2\times10^{-5}$ for six values of ϵ in the range $[0.146-1.022]$. We make use of continuous PIV measurements in the equatorial plane averaged over at least 50 libration cycles. Figure 3.4.a shows a time-averaged azimuthal velocity $\overline{U_\phi}/\epsilon^2$ contour plot. Since the system rotation is counter-clockwise, a mean zonal flow in the bulk is clockwise (retrograde) in all cases studied. Figure 3.4.b clearly shows the

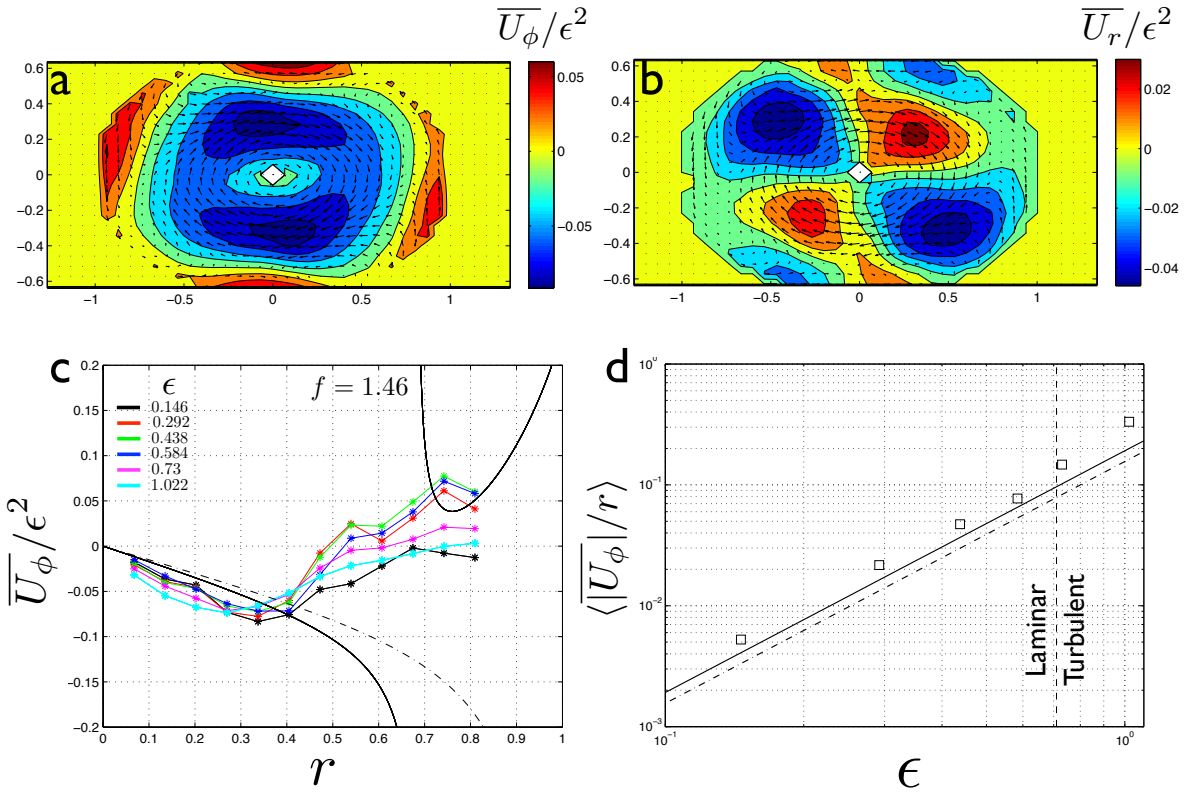

Figure 3.4: (a) Zonal flow azimuthal velocity $\overline{U_\phi}/\epsilon^2$ and (b) zonal flow radial velocity component $\overline{U_r}/\epsilon^2$ for $(f = 1.46; \epsilon = 0.73)$ normalized by ϵ^2. (c) Radial profile of the normalized azimuthal velocity profile $\overline{U_\phi}/\epsilon^2$. (d) Comparison of spatially averaged $\langle|\overline{U_\phi}|/r\rangle$ from $r \in [0.1 \sim 0.35]$ as a function of ϵ with theoretical values $\langle|\overline{U_\phi}|/r\rangle = 0.156\epsilon^2$ from Busse (2010) (dashed black line) and $\langle|\overline{U_\phi}|/r\rangle = 0.192\epsilon^2$ from Sauret and Le Dizes (2013) (solid black line). Experimental results (squares) for $E = 2 \times 10^{-5}$, $f = 1.46; \epsilon = 0.146, 0.292, 0.438, 0.584, 0.73, 1.022$.

$m = 2$ structure in the time-averaged radial velocity $\overline{U_r}/\epsilon^2$ reflecting the $m_{lib} = 2$ ellipsoidal container.

Figure 3.4.c shows a linear collapse of the radial profiles of $\overline{U_\phi}$ when normalized by ϵ^2 indicating the presence of the theoretically predicted solid body rotation between $r = [0.1 \sim 0.35]$ whose magnitude scales as ϵ^2. Theoretical zonal flow radial profiles are taken from Busse (2010) (black dot-dash line) and from Sauret and Le Dizes (2013) (solid black line). Both theoretical flows include singularities around the critical cylindrical radius [e.g., Bondi and Lyttleton (1953)], $s_c = \sqrt{1 - f^2/4}$ due to the exclusion of inertial modes for $f \leq 2$. For a spherical geometry, Busse (2010) assumes $f, \epsilon \ll 1$ with $s_c = 1$ while Sauret and Le Dizes (2013) assumes that $\epsilon \ll 1$ and $s_c = 0.68$ for $f = 1.46$. Inertial modes generate internal

shear layers whose affect on the zonal flow is still poorly understood. Thus solid body zonal flow is expected for $r \ll s_c$ where the profiles are nearly linear and may help explain the deviation of the experimental velocity profiles with the theoretical trends.

The linear collapse of the velocities for all cases studied between $r = [0.1 \sim 0.35]$ is indicative of the presence of the theoretically predicted solid body rotation whose magnitude scales as ϵ^2 such that $|\overline{U_\phi}| = \alpha\epsilon^2 r$ where α is a prefactor. Figure 3.4.d shows the average experimental values of the $\langle|\overline{U_\phi}|/r\rangle$ between $r = [0.1 \sim 0.35]$ at each ϵ. The same averaging is performed for the theoretical profiles yielding $\alpha = 0.156$ from Busse (2010) (black dot-dash line) and $\alpha = 0.192$ from Sauret and Le Dizes (2013) (solid black line). The experimental values scale with ϵ^2 in good agreement with the theoretical values attained in the spherical geometry despite the rather large ϵ and f, and the finite equatorial ellipticity of the container used in the experiment. The scaling of the minimum flow velocity with ϵ^2 is indicative of the possibility for shear instability as shown for tidal forcing experiments [e.g., Sauret et al. (2014)]. However, this instability was shown to generate local turbulence and does not explain the bulk interior turbulence observed in our experiments.

The universal quadratic scaling of the axisymmetric component of the zonal flow helps explain the lack of dependence on the geometry found from the LDV measurements in Noir et al. (2012). Those point measurements, on time-average at a fixed radius, remove any non-axisymmetric component. Importantly, this data includes a transition from laminar to turbulent flow, determined through side view-visualizations, that will be discussed in the following sections. This transition occurs around $f = 1.46; \epsilon = 0.71$ (vertical dashed line in Figure 3.4.d).

3.4.3 LDEI

3.4.3.1 Libration Regime Diagram

By varying $f \in [0 - 9]$ and maximizing the range of ϵ for each f, a regime diagram of laminar(red open squares) and turbulent flows(closed blue diamonds) in the $[f, \epsilon]$ parameter space is constructed in Figure 3.5.a. Note that we focus on the range $f \in [0 - 5]$ in Figure

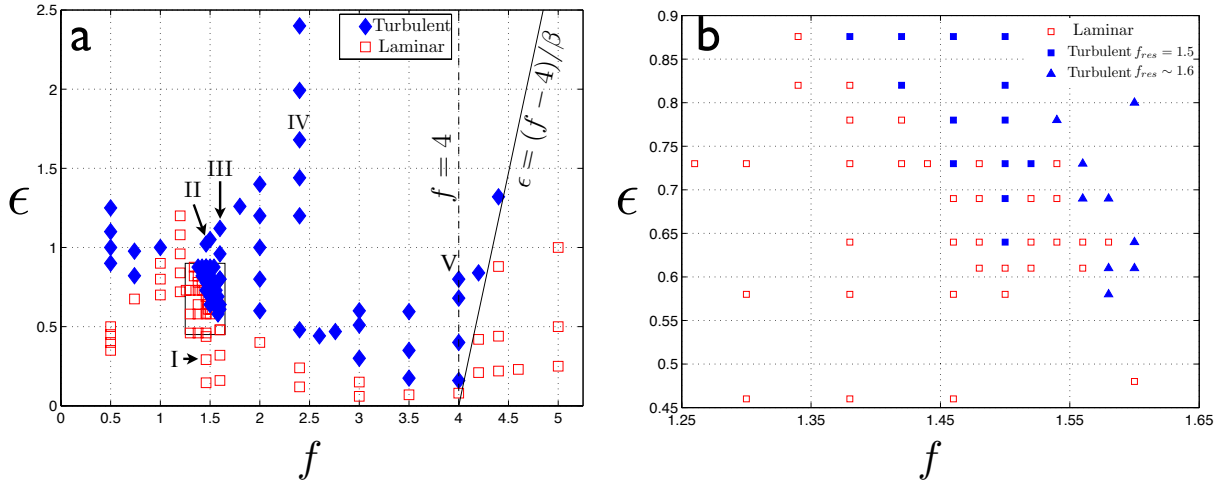

Figure 3.5: (a) Laminar(open red squares) where I shows the case $f = 1.46; \epsilon = 0.292$ is used in Figure 3.6.I. Turbulent cases(blue-filled symbols) are found from $f = 0$ to $f = 4$(dashed black line) and up to $f = 4 + \epsilon\beta$(solid black line). The non-dimensional velocity Ro_{eq} and associated Re_{eq} for cases II-V is shown in Figure 3.6.II-V while the associated flow structures, shown in Figure 3.7.II-V, are used for LDEI confirmation. (b) A fine scale diagram of the box where turbulent flows are distinguished by separate coupled modes associated with $f_{res} = 1.5$(blue squares) and $f_{res} \sim 1.6$(blue triangles).

3.5.a since no turbulent flows were found in the range $f \in [5-9]$. The rectangle in the regime diagram is magnified in Figure 3.5.b where, by fine variations in $[f, \epsilon]$ space, two separate turbulent cases are distinguished as well the threshold of stability. The verification of the LDEI is performed using cases $f = 1.46, 1.5, 1.6, 2.4, 4$ with $\epsilon = 1.022, 1.05, 1.12, 1.68, 0.8$ respectively.

As the librational forcing frequency f and strength ϵ are varied, the libration driven flows are separated by side-view direct visualization into laminar and turbulent flows. From equatorial PIV analysis, measurements of the spatially averaged magnitude of the velocity are non-dimensionalized using the long axis length a and steady rotational period Ω_0^{-1}. Thus, we define an equatorial Rossby number, $Ro_{eq} = \langle |U| \rangle$, as the ratio of inertial to Coriolis forces. Additionally, for fixed $E = 2 \times 10^{-5}$, an equatorial Reynolds number, $Re_{eq} = Ro_{eq}/E$, provides a measure of equatorial flow turbulence.

A comparison of laminar and turbulent flows are shown in Figure 3.6 with Ro_{eq} on the left axis and associated Re_{eq} on the right axis using four measurements per libration cycle filtered over a moving window average over 10 librational periods with a 90% overlap. In side-view,

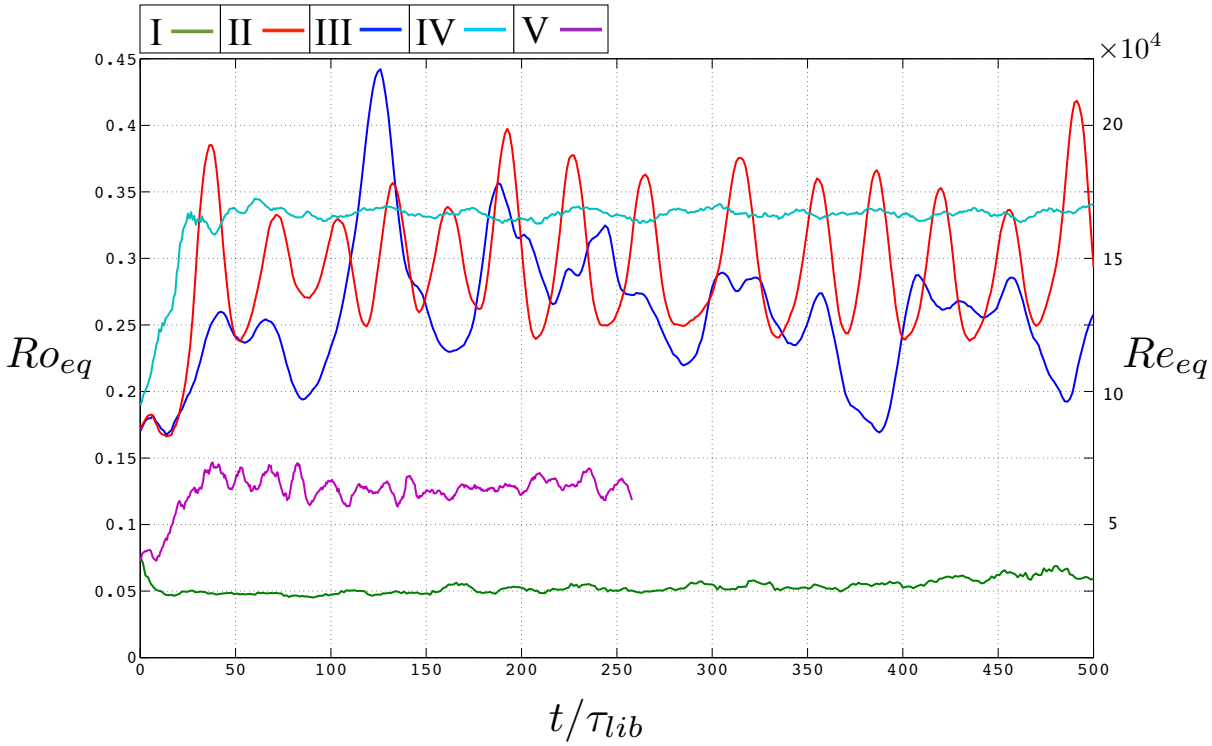

Figure 3.6: Time evolution of the non-dimensional spatially averaged velocity $Ro_{eq} = \langle |U| \rangle$ and associated $Re_{eq} = Ro_{eq}/E$ using four points per libration cycle over 500 librational periods where $\tau_{lib} = 2\pi/\omega_{lib}$. The data is filtered using a moving average window over 10 libration cycles with a 90% overlap. I. The laminar case ($f = 1.46; \epsilon = 0.292$). The intermittently turbulent flows of II. ($f = 1.46; \epsilon = 1.022$) and III. ($f = 1.6; \epsilon = 1.12$), and saturated turbulent flows of IV. ($f = 2.4; \epsilon = 1.68$) and V. ($f = 4; \epsilon = 0.8$).

laminar flows exhibit calm flow in the bulk interior and do not exhibit any vertical motions. Figure 3.6.I shows the steady flow at $f = 1.46; \epsilon = 0.292$ with no clear growth phase.

Turbulent flows exhibit three-dimensional motions with either intermittent or saturated turbulence in the bulk interior. First, intermittently turbulent flows, as seen in side-view and from studies Noir et al. (2012); Cébron et al. (2012b), are characterized by the growth of the LDEI until the flow collapses after some time, leading to relaminarization and the re-establishment of the base flow and, by extension, the LDEI itself becomes cyclic. Figure 3.6.II and 3.6.III show the intermittent turbulence in cases $f = 1.46; \epsilon = 1.022$ and $f = 1.6; \epsilon = 1.12$. After an initial growth phase, the intermittently turbulent cases show large cycles of growth and collapse. For these two cases $\overline{Ro_{eq}} = [0.249, 0.299]$ with variances $[2.3 \times 10^{-3}, 2.6 \times 10^{-3}]$. The strength of the resulting turbulence is $\overline{Re_{eq}} = [1.2 \times 10^4, 1.4 \times 10^4] \gg 1$

emphasizing the strong turbulence generated.

Figure 3.6.IV and 3.6.V show the saturated turbulence in cases $f = 2.4; \epsilon = 1.68$ and $f = 4; \epsilon = 0.8$. For these cases, after an initial growth phase, the cycles are smaller than for intermittent turbulence and side-view visualizations show that once the bulk turbulence is initiated, no clear cycles are visible. As such, the corresponding variances in these cases are an order of magnitude smaller $[3.05 \times 10^{-4}, 1.88 \times 10^{-4}]$ while the strong turbulence persists with $\overline{Re_{eq}} = [1.65 \times 10^4, 6.25 \times 10^3] \gg 1$. However, a comparison of intermittent and saturated turbulent flows in Figures 3.6.III, and 3.6.V shows the existence of qualitatively similar cycles above the base state despite the clear distinction in side-view visualization discussed. A more quantitative distinction between flows as well as the long term turbulent evolution will be the subject of future studies. Values for $\overline{Ro_{eq}}$ and the variance for each case studied are given in the appendix.

The existence of these turbulent flows span from $f = 0$ to $f = 4$ (dashed vertical line in Figure 3.5.a) in agreement with the range provided by the resonant conditions, (3.14), for the LDEI. Specifically, even if a direct resonant forcing were to exist, there can be no direct forcing mechanism causing excitations in the range $f \in [2 - 4]$. As f is increased, the growth rate increases following the WKB formulation of (3.17) and thus the stability threshold separating laminar and turbulent flows decreases to a minimum at $f = 4$. Figure 3.5.b shows a finer scan of the stability threshold around $f = 1.46$ with an intermingling of laminar and turbulent flows. By comparing the symmetry of the excited flow at $f = 1.46$, discussed further in the next section, we distinguish separate symmetry properties from the LDEI of other cases around $f_{res} \sim 1.6$ and track the excited LDEI for $f = 1.46$ to a minimum at $f = 1.5$. Since the growth rate in (3.17) attains a maximum when $f = f_{res}$, the associated stability threshold also attains a local minimum. Thus, we find that the LDEI associated with $f = 1.46$ has its source at $f_{res} = 1.5$. As a consequence of the rather large Ekman number used in our experiment, only selected resonances can occur and, as the Ekman number is reduced, more resonances may be excited leading to transition from the intermingling of laminar and turbulent states to a sharper boundary between the two as seen in studies of tidal instability in Le Bars et al. (2010).

Furthermore, excitations beyond $f = 4$ are associated with a higher order solutions in $\epsilon\beta$ at the large ellipticity β of the container and the large librational forcing ϵ [e.g., Le Dizes (2000)]. The large ϵ and β limit of instability is $f = 4 + \epsilon\beta + \mathcal{O}(\epsilon^2\beta^2)$ and the black line associated with the limit is show in Figure 3.5.a as $\epsilon = (f - 4)/\beta$ and is confirmed by the data. Additionally, the existence of many novel turbulent flows including $f = 1, \epsilon = 1$, builds upon the previous experimental work in the half-ellipsoid of Noir et al. (2012) that prevented the growth of turbulent flows via elliptical instability of equatorially antisymmetric inertial modes.

3.4.3.2 Mode Coupling

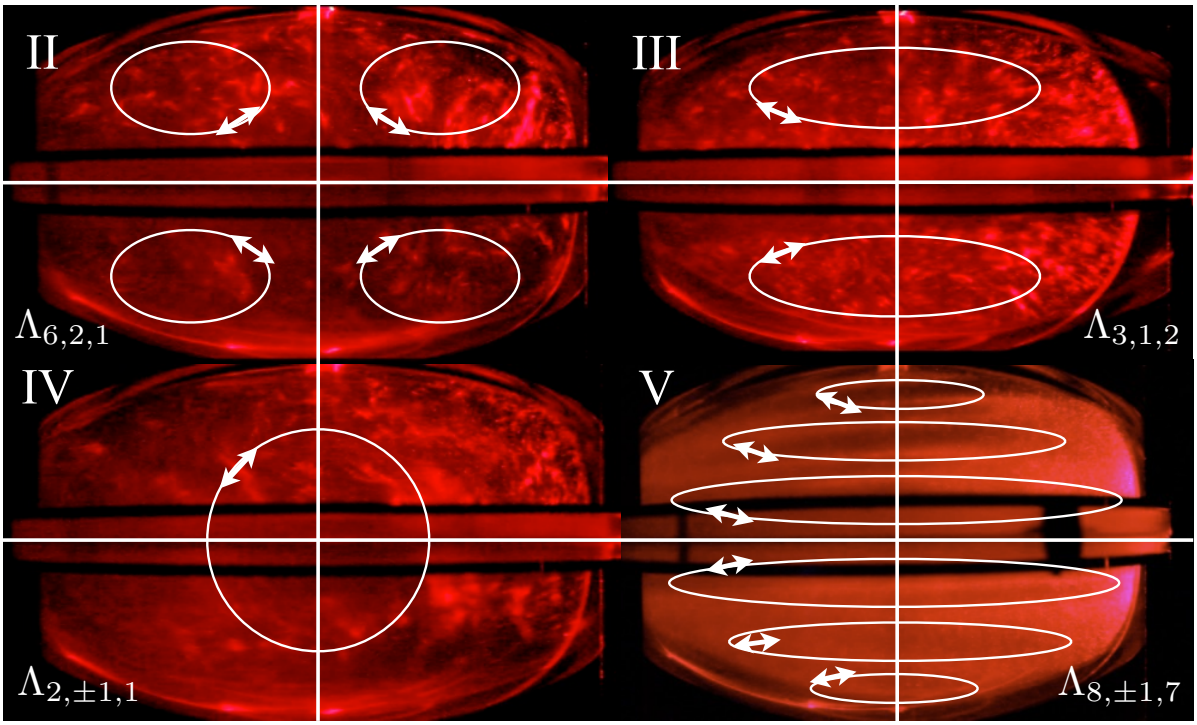

Figure 3.7: Direct side-view visualization snapshots of the turbulent flow cases indicated in Figure 3.5.a and Figure 3.6.II-V with II. ($f = 1.46, 1.5; \epsilon = 1.022, 1.05$) III. ($f = 1.6; \epsilon = 1.12$), IV. ($f = 2.4; \epsilon = 1.68$), and V. ($f = 4; \epsilon = 0.8$). Representative inertial modes, $\Lambda_{n,m,k}$ are taken from polar flattened spheroid calculations in Kerswell (1994). Movies for these individual cases are available as a supplement to this work online (multimedia view).

Here we seek to demonstrate that the presence of bulk turbulent flow in our system is due to the LDEI, i.e. to the resonance of two inertial modes with a libration induced base flow.

To do so, we combine several techniques including the identification of the inertial modes from side-view direct visualizations using Kalliroscope, and via Fourier analysis of filtered reconstructions of the velocity fields and growth rate measurements from the equatorial plane PIV data. Figure 3.7 (multimedia view) shows snapshots from side-view movies for four of the distinct modes observed during the amplitude growth of the inertial mode. [Movies for these cases are available as a supplement online] We use spheroidal inviscid modes, $\Lambda_{n,m,k}$, from Kerswell (1994) to both look for modes with similar flow structures and symmetries and find the simplest mode couplings. Here n is the degree of the associated Legendre polynomial that combines the radial and axial wavenumbers, m is the azimuthal wavenumber for the mode, and k represents the k^{th} eigenfrequency. The general schematic for the dominant modes with the largest frequency is superimposed in white on Figure 3.7.

The clearest determination of the mode and frequency coupling is provided using the $f = 4$ case at the extreme range of the instability where we expect the participating modes with eigenfrequencies $|\lambda_{1,2}| = f/2 = 2$. First, the side-view visualization in Figure 3.7.V shows a large number of structures stacked horizontally as might be expected from the inertial wave dispersion relation for $|\lambda_{1,2}| = 2$ where the wave vector is parallel to the rotation axis. Second, Figure 3.8 shows the power spectrum of the velocity magnitude for $f = 4$ where the strongest peaks are associated with the librational forcing frequency at $f = 4$, steady zonal flow around $f = 0$, and the inertial modes at $|\lambda_{1,2}| = f/2$. The filtered reconstruction at this frequency shows that the base flow in Figure 3.8.c is in good qualitative agreement with the libration driven base flow of Figure 3.1.b. A retrograde zonal flow snapshot is reconstructed around the zonal wind frequency, $f = 0$, in Figure 3.8.a. Finally, the flow in Figure 3.8.b, filtered around $f = 2$, is identified as an $|m| = 1$ inertial mode and the side view helps us identify the spherical modes $\Lambda_{8,1,7}$ and $\Lambda_{8,-1,7}$ that exhibit a similarly large vertical wavenumber and $|m| = 1$ near the equator.

For the LDEI in the $f = 1.46, 1.5, 1.6, 2.4$ cases, such a complete confirmation of the resonance conditions is more complicated for several reasons. Figure 3.9.a shows the temporal FFT for the case of $f = 1.5$ where two distinct inertial mode frequencies are found only by carefully choosing the area of the PIV field to perform the FFT. These distinct frequencies

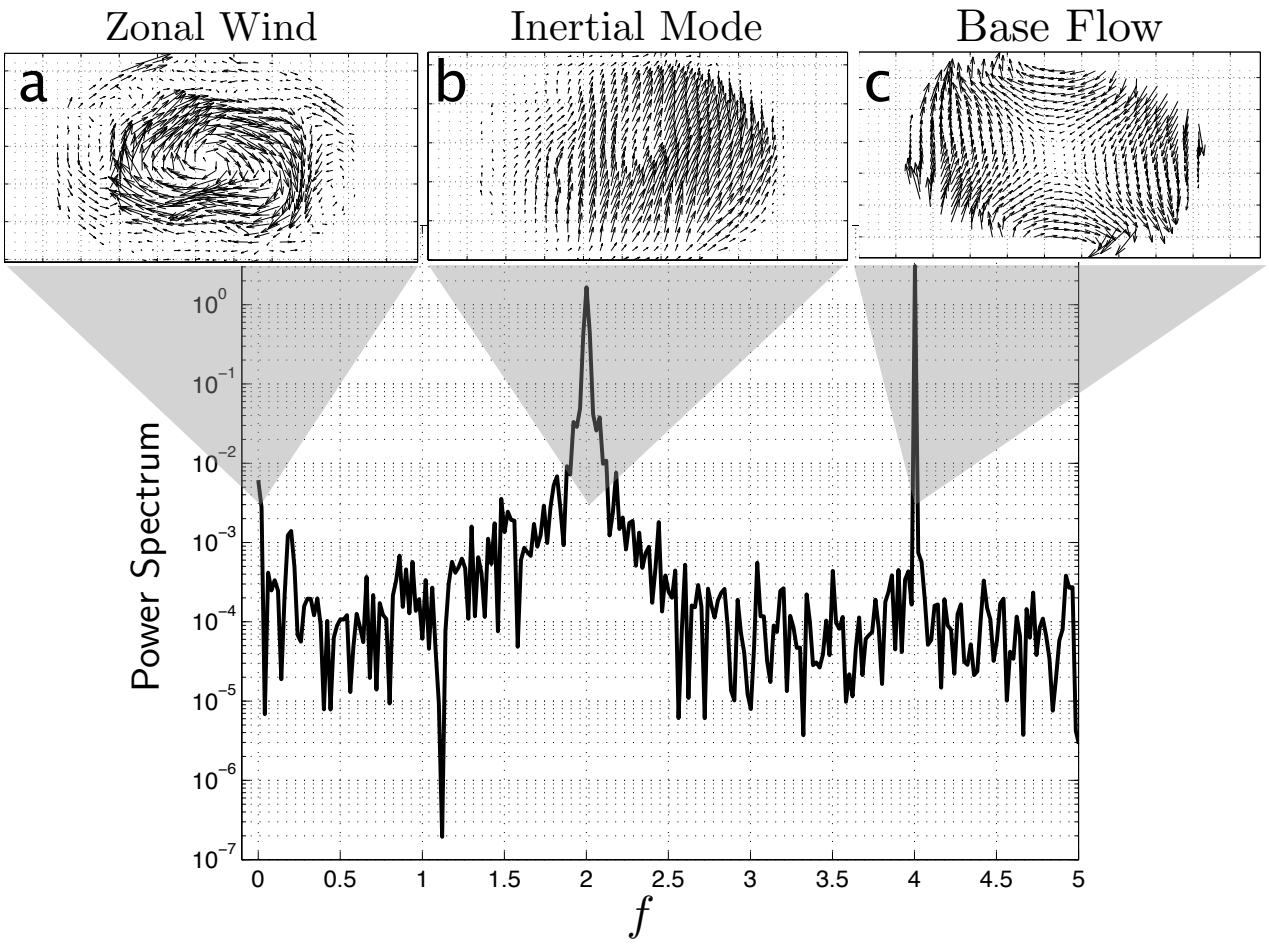

Figure 3.8: : Power spectrum of the velocity magnitude for $f = 4; \epsilon = 0.8$. (a) Steady component with snapshot of filtered steady component of flow. (b) Snapshot of the filtered $m_{1,2} = |1|$ inertial mode at half the driving frequency $\lambda_{1,2} = |f/2|$ satisfying the resonance conditions. (c) The filtered snapshot of the librational base flow at the driving frequency f.

are found around $\lambda_1 \sim 1.62$ close to the driving frequency f and the second inertial mode with frequency $\lambda_2 \sim 0.12$ close to the zonal wind frequency. Figure 3.7.II shows that the mode excited around $f = 1.46$ and $f = 1.5$ is symmetric across both the equator and the meridional axis. The dominant excited flow structures, as seen from the vertical cross-section, are qualitatively similar to the mode $\Lambda_{6,2,1}$ with the frequency closer to the driving frequency and azimuthal wavenumber $m = 2$. A second possible mode, coupled to form the LDEI, is similar to the inertial mode, $\Lambda_{8,4,2}$, with a frequency close to zero with $m = 4$. This low frequency mode is not clear in the Kalliroscope movies that only show strong shear structures. Filtered flow reconstruction around the driving frequency cannot distinguish an

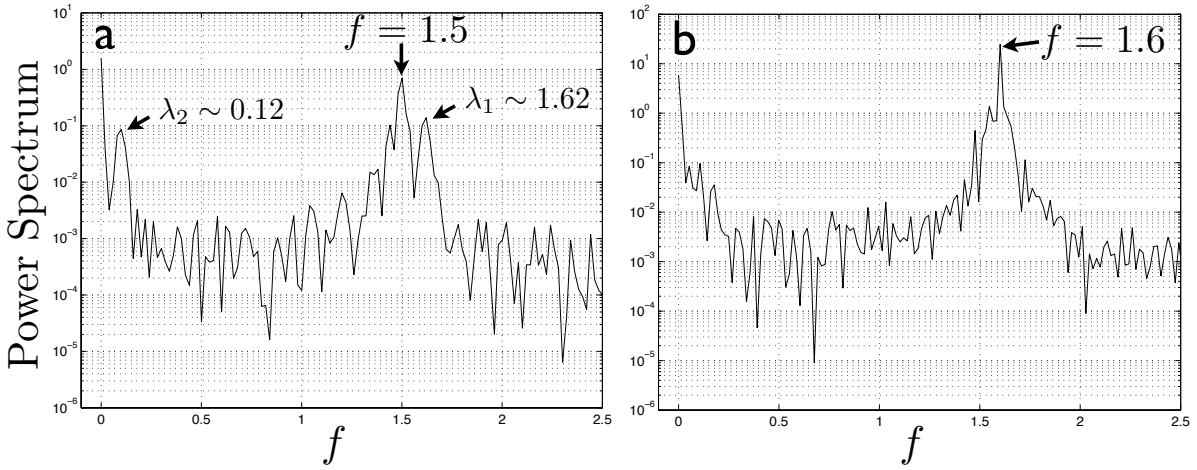

Figure 3.9: Power spectrum of the velocity magnitude for (a)$f = 1.5; \epsilon = 1.05$ and (b)$f = 1.6; \epsilon = 1.12$ showing the most prominent peaks at the forcing frequency f and for the steady component $f = 0$.

$m = 2$ or $m = 4$ mode because of its superimposition with the base flow driven by the $m = 2$ librational forcing. At the low frequency, an inertial mode cannot be clearly distinguished from the zonal flow. However, further arguments in favor of the LDEI triadic resonance in this case will be given below using the growth rate calculations.

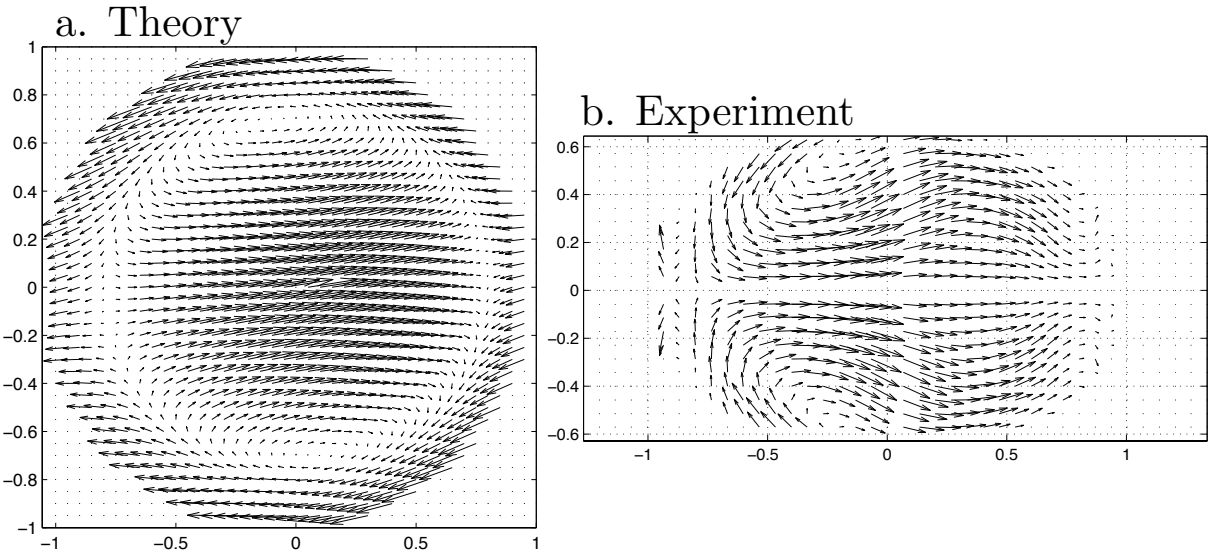

Figure 3.10: Comparison of snapshots for (a) the equatorial plane of the theoretical spherical inviscid mode $\Lambda_{3,1,2}$ and (b) the filtered reconstruction of the experimental equatorial flow around the driving frequency with the even $m = 2$ symmetry removed for $(f = 1.6, \epsilon = 1.12)$.

For the $f = 1.6$ case, analysis of the FFT spectrum in Figure 3.9.b does not yield any

additional peak aside from the zonal flow and forcing frequency. The side-view visualization in Figure 3.7.III shows that the coupled modes are symmetric across the equator and anti-symmetric across the meridian. This description is similar to $m = 1$ inviscid modes $\Lambda_{3,1,2}$ near the forcing frequency and the possible coupling of the $m = 3$ mode, $\Lambda_{5,3,1}$, closer to zero. Since the librational forcing, $m = 2$, is even and the proposed mode coupling is odd, the even symmetry is subtracted around the forcing frequency indeed revealing an m=1 mode as shown in Figure 3.10. Figure 3.10.a shows the theoretical spheroidal mode $\Lambda_{3,1,2}$ while Figure 3.10.b shows the subtraction of the even symmetry around $f = 1.6$ in the PIV data, revealing a separate odd symmetry associated with the excited inertial mode. The similarity between the two images provides a qualitative verification for $m = 1$ inertial mode near the driving frequency. No additional low frequency mode can be distinguished from the steady zonal flow.

Finally, side-view visualizations indicate that the triadic resonance at $f = 2.4$ are due to a coupling of spinover modes. Each mode is characterized by rotation about an axis perpendicular to the rotation axis as indicated in Figure 3.7.IV. Because the velocity at the equator is dominated by vertical motion, the PIV data taken of the horizontal velocity does not provide a clear insight into the excited spinover mode coupling. The spinover inviscid mode descriptions $\Lambda_{2,1,1}$ and $\Lambda_{2,-1,1}$ provide a qualitative analytical structural comparison with Figure 3.7.III, while a polynomial decomposition of the spinover mode in Vantieghem (2014) gives the inviscid inertial mode frequencies at $|\lambda_{1,2}| = 1.15$, yielding $f_{res} = 2.3$. This value is close to the observed frequency $f = 2.4$.

In general, we find that the coupling of a mode near the libration forcing frequency with a low frequency mode is always associated with the intermittent turbulence whose velocity magnitude is shown in Figure 3.6.II and 3.6.III while the coupling of inertial modes with frequencies $\pm f/2$, including the spinover mode coupling, is associated with saturated turbulence from Figure 3.6.IV and 3.6.V. Furthermore, the coupling of large scale inertial modes for $f = 1.46$ and $f = 1.6$ are promoted by the large Ekman number in our experiment. As the Ekman number is decreased toward planetary values, more resonance couplings excite smaller scale modes that are the most unstable through the WKB analysis of the growth

f	ϵ	f_{res}	ϵ_{Thresh}	$K_{Thresh}(a)$	$\frac{\sigma_{Theory}}{\sigma_{Data}}(a)$	$K_{Thresh}(b)$	$\frac{\sigma_{Theory}}{\sigma_{Data}}(b)$
1.46	0.876	1.5	0.69-0.73	12.0-13.1	0.95-1.2	7.3-9.2	0.59-1.2
1.46	1.022	1.5	0.69-0.73	12-13.1	0.65-1.3	7.1-7.8	0.83-1.1
1.5	1.05	1.5	0.61-0.64	13.2-13.9	0.95-1.2	8.3-9.9	0.74-0.96
1.6	1.12	1.6	0.48-0.61	10.9-13.5	0.71-1.0	3.4-5.1	0.55-0.78

Table 3.1: Growth rates for the LDEI in $f = 1.46, 1.5, 1.6; \epsilon = 1.022, 1.05, 1.12$ taking f_{res} and ϵ_{Thresh} from the regime diagram in Figure 3.5.b σ_{Data} is extracted from a fit of the spatially averaged magnitude of velocity $\langle |U| \rangle$ filtered through a moving window average over 10 libration cycles with an overlap of 90% (a) The comparison with the WKB stability analysis from (3.15). (b) The comparison with the asymptotic multipolar stability analysis from (3.16).

rates [e.g., Lacaze et al. (2004); Le Bars et al. (2010)]. In this sense, the small scale inertial modes with frequencies $\pm f/2$ excited by $f = 4$ case may be more relevant to planetary applications.

3.4.3.3 Growth Rates

To verify the LDEI growth rate we focus on the $f = 1.46, 1.5$ and $f = 1.6$ cases where the excited modes have non-zero horizontal velocities and the Fourier analysis is unconvincing. The regime diagram in Figure 3.5 provides upper and lower bounds for the stability threshold at each f. A fine regime diagram of the boxed-in area is shown in Figure 3.5.b. Using side-view visualizations, the laminar and the separated turbulent cases associated with $f = 1.46, 1.5$ and $f = 1.6$ can be distinguished. Finding the threshold in the fine regime diagram at $f = 1.5$ verifies that the resonant frequency associated with the $f = 1.46, 1.5$ is $f_{res} = 1.5$ around $\epsilon_{thresh} \in [0.61 - 0.64]$ and $\epsilon_{thresh} \in [0.69 - 0.73]$ for $f = 1.46$. The threshold around the resonant frequency for $f = f_{res} = 1.6$ is $\epsilon_{thresh} \in [0.48 - 0.61]$.

At the threshold of instability where $\sigma = 0$, by using $\sigma_{inv}(f_{res}, \epsilon_{thresh})$ in (3.15), we solve for the dissipation factor K to get a range for $K_{thresh} = K$. By plugging this range into (3.17), a range of values for σ_{theory} is created. Separately, σ_{Data} is calculated after filtering spatially averaged PIV velocity magnitude of four points for every libration cycle using running average over 10 libration cycles with a 90% overlap. To compare the theoretical growth rate with the data, the growth phase is fitted to an equation of the form $\langle |U| \rangle = A + B\, e^{\sigma_{Data}(t-t_0)}$ where

A and B are fitting coefficients.

Table 3.1 shows the value range $\sigma_{Theory}/\sigma_{Data}$ and its range for $f = 1.46, 1.5, 1.6$ using (a) a local WKB analysis using plane wave perturbations of (3.15) and (b) a separate multiple scale asymptotic WKB analysis using (3.16). This finds good agreement between the theoretical growth rates using the local approaches and the measured growth rates for $f = 1.46$, $f = 1.5$, and $f = 1.6$ where for perfect agreement $\sigma_{Theory}/\sigma_{Data} = 1$ despite discrepancies that result since neither $\epsilon \ll 1$ nor $\epsilon\beta \ll 1$ hold at the large experiments values used. The error associated with the growth rate ratios stems from the noise from PIV signal in measuring σ_{Data} and in the determination of ϵ_{thresh} using Figure 3.5.b that is used to deduce K_{thresh}.

3.5 Discussion and Concluding Remarks

In the present experimental study we have used a combination of direct flow visualizations and PIV measurements in the equatorial plane to prove the existence of the libration driven elliptical instability, LDEI, as the cause of intermittent and saturated space filling turbulence in the interiors of an ellipsoidal container. To do so, we have explored the flow regimes found in longitudinal libration in the (f,ϵ)-parameter space at a fixed Ekman number $E = 2 \times 10^{-5}$. Our results confirm that the librationally induced base flow is established in the bulk and is in good quantitative agreement with the theoretical base flow when transformed into the steadily rotating frame. We have been able to quantitatively distinguish between laminar flows and intermittent or saturated turbulent flows in the bulk interior. By analyzing the zonal flow induced by the non-linear interaction of the librational forcing, we recover a $|U_\phi| \sim \epsilon^2$ scaling behavior. We have found the presence of turbulent fluid motions from $f \in [0-4]$ in accordance with the theoretical limits of the resonance condition for the LDEI. By choosing the most representative examples of the turbulent flows, we have used the $f = 4$ case to verify the spatial and temporal resonance conditions and the $f = 1.46, 1.5, 1.6$ to verify the theoretical growth rate calculations.

While we have identified the essential characteristics of LDEI, several important ques-

tions remain. The first open question is the origin of the difference between the onset of intermittent and saturated turbulence. The analysis indicates that intermittently turbulent flows are the generated through an LDEI having inertial modes near driving frequency, f and at a low frequency inertial mode that may be obscured by the zonal flow. For cases where saturated turbulence persists, the participating inertial modes have frequencies at $\pm f/2$. Secondly, due to current experimental difficulties, we have only measured the velocity in the nearly equatorial plane and, thus, it is not possible to fully measure the energy associated with turbulent three-dimensional motion.

Although our experimental parameters are far from planetary values, we have confirmed the characteristics of the LDEI mechanism by compensating for large Ekman number with the exaggerated equatorial ellipticity of our experimental container. As such, we may extrapolate from our current work to planetary settings using the growth rate formula (3.17) and planetary values to provide a critical value for the equatorial ellipticity needed to generate a planetary LDEI following Cébron et al. (2012b). By requiring a positive growth rate and assuming perfect resonance $f = f_{res}$, (3.17) is rewritten as $\beta_c > 64K\sqrt{E}/(16 + f_{res}^2)\epsilon$. Using parameters for longitudinal libration where $f = 1$, $E \sim 10^{-14}$, $\epsilon \sim 10^{-4}$ and a minimum dissipation factor $K = 1$, the critical ellipticity is $\beta_c > 10^{-3}$ indicating that Io, Europa, and telluric exoplanets CoRoT-7b, GJ1214b, and 55CnCe can support turbulent interior fluid motions generated by LDEI [e.g., Cébron et al. (2012a)].

Furthermore, we find a lower bound on the amount of rotational energy injected into the fluid layer through equatorial plane measurements at $E = 2 \times 10^{-5}$. For the saturated turbulence driven in $f = 4; \epsilon = 0.8$, from Figure 3.6.V, the percentage of rotational energy injected into the fluid is $\overline{Ro_{eq}}^2/2 \sim 1\%$ generating strong turbulence where $\overline{Re_{eq}} = 6.25 \times 10^3$. For celestial bodies where $E \sim 10^{-14}$, only a small percentage of the tremendous amounts of spin-orbital rotational energy must be transmitted into the fluid layer to drive strongly turbulent motions. These turbulent flows can lead to energy dissipation [e.g., Rieutord (2003)] that effects the orbital evolution of these bodies [e.g., Le Bars et al. (2010)] and may drive dynamo processes. Convectively driven planetary magnetic field generation suffers from tight budget constraints [e.g., Verhoogen (1973); Pozzo et al. (2012)]. Such energetic limitations

become more severe in smaller bodies [e.g., Nimmo (2009)]. However, our results suggest that mechanically-forced orbital systems can harvest significant amounts of spin-orbital energy to drive turbulent processes without the need for convection. Together with recent numerical findings showing that mechanically forced instabilities can drive dynamos in precessing spheres [e.g., Tilgner (2005)], spheroids [e.g., Wu and Roberts (2009)], in longitudinally-librating systems [e.g., Wu and Roberts (2013)], and in tidal forced systems [e.g., Cébron and Hollerbach (2014)], our results support the possibility that mechanical forcing leads to dynamo generation in smaller bodies, like the early Moon [e.g., Le Bars et al. (2011)] and asteroids [e.g., Fu et al. (2012); Tarduno et al. (2012)], explaining data that do not presently fit into the standard model for convective dynamos.

3.6 Appendix A: Experimental Parameters

Table 3.2: Physical and dimensionless parameter definitions and their range of values in the experiment

Parameter	Definition	Experiment
a	long axis along $\hat{\mathbf{x}}$	127 mm
b	short axis along $\hat{\mathbf{y}}$	89 mm
c	short axis along $\hat{\mathbf{z}}$	89 mm
$\Omega_0/2\pi$	Mean rotation frequency	0.5 Hz
$\omega_{lib}/2\pi$	Libration frequency	0.25 - 5.0 Hz $\pm 0.1\%$
ν	Kinematic viscosity	10^{-6} m^{2}s^{-1}
E	Ekman number $\nu/(\Omega_0 a^2)$	2×10^{-5}
f	ω_{lib}/Ω_0	0.5 - 9.0
$\Delta\phi$	Angular displacement	0.5 - 2.5 rad
ϵ	$(\Delta\phi)f$	0.06 - 2.4
β	$\frac{a^2-b^2}{a^2+b^2}$	0.34
$\overline{c}$	$\frac{c}{\sqrt{(a^2+b^2)/2}}$	0.812

3.7 Appendix B: Experimental Data

Table 3.3: Mean velocity magnitude and variance for laminar and turbulent flows and zonal flow data from Figure 3.4.d.

f	ϵ	$\langle\lvert\overline{U_\phi}\rvert/r\rangle$	$\overline{\langle\lvert U\rvert\rangle} = \overline{Ro_{eq}}$	$\langle\lvert U\rvert\rangle_{var}$	Bulk Int. Flow
1.46	0.146	0.005	0.025	2.04×10^{-6}	Laminar
1.46	0.292	0.02	0.057	6.95×10^{-5}	Laminar
1.46	0.438	0.05	0.152	8.62×10^{-4}	Laminar
1.46	0.584	0.08	0.2459	8.86×10^{-4}	Laminar
1.46	0.73	0.15	0.1931	7.44×10^{-4}	Intermit.
1.46	0.876	—	0.1234	1.00×10^{-3}	Intermit.
1.46	1.022	0.3	0.2489	2.3×10^{-3}	Intermit.
1.5	1.05	—	0.1681	1.40×10^{-3}	Intermit.
1.6	1.12	—	0.299	2.6×10^{-3}	Intermit.
2.4	1.68	—	0.3305	3.05×10^{-4}	Saturat.
4.0	0.8	—	0.125	1.88×10^{-4}	Saturat.

Table 3.4: Experimental data from Figure 3.5 laminar and turbulent flows. Laminar, intermittent turbulence, and saturated turbulence are determined through side-view direct visualization

f	ϵ	Bulk Int. Flows	f	ϵ	Bulk Int. Flows	f	ϵ	Bulk Int. Flows
1	0.7	Laminar	1.38	0.58	Laminar	2	1.2	Intermit.
1	0.8	Laminar	1.3	0.58	Laminar	2	0.6	Intermit.
1	0.9	Laminar	1.3	0.46	Laminar	2	1	Intermit.
1.2	0.84	Laminar	1.38	0.46	Laminar	3	0.3	Saturat.
1.2	0.96	Laminar	1.46	0.46	Laminar	3.5	0.35	Saturat.
1.2	1.08	Laminar	1.46	0.64	Laminar	4	0.4	Saturat.
1.2	1.2	Laminar	1.42	0.73	Laminar	3.5	0.175	Saturat.
1.46	0.876	Laminar	1.54	0.73	Laminar	4.2	0.84	Saturat.
1.46	0.584	Laminar	1.44	0.73	Laminar	4.4	1.32	Saturat.
1.46	0.438	Laminar	1.46	0.69	Laminar	0.5	1.25	Saturat.
1.46	0.292	Laminar	1.54	0.69	Laminar	4	0.8	Saturat.
1.46	0.146	Laminar	1.54	0.64	Laminar	3	0.6	Saturat.
1.6	0.48	Laminar	1.48	0.73	Laminar	2.4	1.992	Saturat.
1.6	0.32	Laminar	1.48	0.69	Laminar	2.4	2.4	Saturat.
1.6	0.16	Laminar	1.34	0.876	Laminar	2.4	0.48	Saturat.
2	0.4	Laminar	1.34	0.82	Laminar	2.4	1.2	Saturat.
4	0.08	Laminar	1.38	0.82	Laminar	0.5	1.44	Saturat.
3.5	0.07	Laminar	1.42	0.78	Laminar	0.5	1.1	Saturat.
3	0.06	Laminar	1.6	0.48	Laminar	0.5	1	Saturat.
3	0.15	Laminar	1.52	0.69	Laminar	0.5	0.9	Saturat.
4.2	0.21	Laminar	1.52	0.64	Laminar	2	0.8	Intermit.
4.2	0.42	Laminar	1.56	0.64	Laminar	0.74	0.82	Saturat.
4.4	0.88	Laminar	1.58	0.64	Laminar	0.74	0.9768	Saturat.
4.4	0.44	Laminar	1.38	0.64	Laminar	1.5	1.05	Intermit.
4.4	0.22	Laminar	1.48	0.64	Laminar	1.46	0.73	Intermit.
4.6	0.23	Laminar	1.38	0.78	Laminar	2	1.2	Intermit.
5	0.25	Laminar	1.48	0.61	Laminar	1.5	0.73	Intermit.
5.5	0.275	Laminar	1.46	0.58	Laminar	1.38	0.876	Intermit.
6	0.3	Laminar	1.5	0.61	Laminar	1.5	0.64	Intermit.
6.6	0.33	Laminar	1.52	0.61	Laminar	1.5	0.69	Intermit.
7	0.35	Laminar	1.56	0.61	Laminar	1.46	0.876	Intermit.
8	0.4	Laminar	2.4	0.12	Laminar	1.5	0.82	Intermit.
9	0.45	Laminar	2.4	0.24	Laminar	1.42	0.876	Intermit.
5	0.5	Laminar	2.6	0.442	Saturat.	1.5	0.876	Intermit.
6	0.6	Laminar	2.76	0.4692	Saturat.	1.42	0.82	Intermit.
7	0.7	Laminar	3	0.51	Saturat.	1.46	0.78	Intermit.
5	1	Laminar	3.5	0.595	Saturat.	1.5	0.78	Intermit.
0.5	0.5	Laminar	4	0.68	Saturat.	1.52	0.73	Intermit.
0.5	0.45	Laminar	1.46	1.022	Intermit.	1.5	0.73	Intermit.
0.5	0.4	Laminar	1.6	1.12	Intermit.	1.38	0.876	Intermit.
0.5	0.35	Laminar	2	1.4	Intermit.	1.5	0.64	Intermit.
2.4	0.12	Laminar	2.4	1.68	Saturat.	1.5	0.69	Intermit.
2.4	0.24	Laminar	1.8	1.26	Intermit.	1.46	0.876	Intermit.
0.74	0.675	Laminar	1	1	Intermit.	1.5	0.82	Intermit.
1.38	0.73	Laminar	1.46	0.876	Intermit.	1.42	0.876	Intermit.
1.3	0.73	Laminar	1.6	0.96	Intermit.	1.5	0.876	Intermit.
1.26	0.73	Laminar	1.6	0.8	Intermit.	1.42	0.82	Intermit.
1.5	0.58	Laminar	1.6	0.64	Intermit.	—	—	—
2.4	0.12	Laminar	4	0.16	Intermit.	—	—	—
2.4	0.24	Laminar	1.46	0.73	Intermit.	—	—	—

CHAPTER 4

Generation and maintenance of bulk turbulence by libration-driven elliptical instability

Reproduced from: B. Favier, A. M. Grannan, M. Le Bars, and J. M. Aurnou. *Phys. Fluids*, 27(6):066601, 2015.

In this work, I performed and analyzed the laboratory experiments used to compare with high resolution numerical simulations, performed by Benjamin Favier, of LDEI in identical ellipsoidal geometries. The onset of instability is described first by a discrete frequency response of the base flow and excited inertial modes and culminates in a continuous energy spectra as the strength of the viscous force is decreased and turbulence is generated. At nearly identical values of the Ekman number, the numerical simulations verify the measured flow velocities of the turbulent flow and the steady zonal flow enhanced by the LDEI described in Chapter 3. I contributed to the writing of the experimental method in Section 4.4.

4.1 Introduction

The role of turbulence is critical in geophysical flows as it contributes to the mixing of chemical species and temperature, can enhance the viscous dissipation of energy or lead to dynamo action for example. A conventional approach to sustain turbulent motions in the internal fluid layers of planets or satellites is to consider the continuous action of unstable entropy or compositional gradients associated with secular cooling and solidification. While this scenario has been very successful in explaining planetary magnetic fields [e.g., Jones (2011)], some celestial objects might be too small for thermo-solutal convection to be the only plausible source of motion (see for example Le Bars et al. (2011) and Dwyer et al. (2011)

for the Moon). A complementary mechanism has been proposed and relies on large-scale mechanical forcings to drive intense turbulent motions in the interiors of planets or satellites Kerswell and Malkus (1998). Gravitational interactions between an orbiting body and its primary partner distort the shape of both bodies and give rise to periodic mechanical forcings such as precession, tides, and libration[e.g., Le Bars et al. (2015)]. While several studies have already demonstrated the dynamo capability of the flows resulting from these forcings [e.g., Tilgner (2005); Wu and Roberts (2013); Cébron and Hollerbach (2014)], our understanding of the basic properties of these turbulent flows is still lacking.

This paper focuses on longitudinal libration, where the body's rotation rate undergoes periodic oscillations about its orbital rate [e.g., Comstock and Bills (2003)]. Early works focused on the libration of axisymmetric containers such as cylinders or spheres, which can lead to centrifugal instabilities [e.g., Noir et al. (2009); Calkins et al. (2010); Lopez and Marques (2011)] and stationary zonal flows caused by non-linear interactions in the Ekman boundary layers [e.g., Wang (1970); Sauret et al. (2010, 2012); Noir et al. (2012); Sauret and Le Dizes (2013)]. In the case of non-axisymmetric containers, the coupling between the solid boundaries and the fluid is not only viscous, as in axisymmetric cases, but also of a topographic nature. Although librational forcing cannot directly excite eigenmodes of the system through a direct resonance in the inviscid case [e.g., Zhang et al. (2011); Chan et al. (2011)], it has been shown that three-dimensional flows can be driven by the resonance of two inertial modes with an elliptically-deformed base flow [e.g., Kerswell and Malkus (1998); Cébron et al. (2012a,b); Grannan et al. (2014)], the so-called libration-driven elliptical instability (LDEI).

More generally, the elliptical instability [e.g., Kerswell (2002)] is a resonance mechanism between a pair of normal modes of the system and the underlying strain field associated with regions of two-dimensional, elliptical streamlines. Although it has been demonstrated that the instability ultimately leads to small-scale disorder both experimentally [e.g.,Malkus (1989)] and numerically [e.g., Lundgren and Mansour (1996); Schaeffer and Le Dizes (2010), our theoretical understanding of this process is mostly limited to the initial exponential phase of the instability mechanism [e.g., Mason and Kerswell (1999)]. The eventual collapse of the

excited inertial modes and the properties of the small-scale flow resulting from it are still not well understood. This turbulent regime in closed geometries has been barely considered mainly for technical reasons: it is difficult to obtain reliable laboratory measurements of the small-scale flow and numerical simulations are rare due to the difficulty in considering a large-scale non-axisymmetric geometry and a small-scale turbulent flow at the same time.

In order to improve our understanding of the elliptical instability and its possible applications to geophysical flows, we focus on the properties of the turbulence generated by such an instability driven by the libration of an ellipsoidal container. Our paper builds upon the recent laboratory experimental work by Grannan et al. (2014), where quantitative measurements were only available for the horizontal flow in the equatorial plane. We therefore complement their experimental results with high-resolution direct numerical simulations (DNS), from which a complete three-dimensional description of the flow is available. The paper is organized as follows. The model, numerical approach and experimental setup are described in Sections 4.2, 4.3 and 4.4 respectively. Our results are discussed in Section 5.5, where we focus on the transition to turbulence and the properties of the turbulence itself.

4.2 Model and equations

We consider the flow of an incompressible fluid with constant kinematic viscosity ν inside a rigid ellipsoid whose surface is defined by the Cartesian equation

$$\frac{x^2}{a^2} + \frac{y^2}{b^2} + \frac{z^2}{c^2} = 1 \ . \tag{4.1}$$

The equatorial ellipticity of the container is defined as

$$\beta = \frac{a^2 - b^2}{a^2 + b^2} \ . \tag{4.2}$$

The ellipsoid is rotating around the vertical axis $\hat{\boldsymbol{z}}$ with a time-dependent frequency Ω given by

$$\Omega(t) = \Omega_0 + \Delta\phi \ \omega_l \sin(\omega_l t) \tag{4.3}$$

where Ω_0 is the main rotation rate, $\Delta\phi$ is the libration amplitude and ω_l is the libration frequency.

In this paper, we work in a frame of reference that is attached to the walls of the container, referred to as the librating frame in the following. The solid boundaries of the ellipsoid are fixed in that frame, which is advantageous from a numerical point of view. The equations of motion in the librating frame are

$$\frac{\partial \boldsymbol{u}}{\partial t} + \boldsymbol{u}\cdot\nabla\boldsymbol{u} + \underbrace{2\big[1+\epsilon\sin(ft)\big]\hat{\boldsymbol{z}}\times\boldsymbol{u}}_{\text{Coriolis}} = -\nabla\Pi + E\nabla^2\boldsymbol{u} \underbrace{-\epsilon f\cos(ft)\hat{\boldsymbol{z}}\times\boldsymbol{r}}_{\text{Poincaré}} \tag{4.4}$$

$$\nabla\cdot\boldsymbol{u} = 0\ , \tag{4.5}$$

where we use the semi-major axis a as a length scale and Ω_0^{-1} as a time scale. The librating frame is a non-inertial frame so that two fictitious forces appear in equation (4.4): the Coriolis force which depends on the total rotation vector $\Omega(t)\hat{\boldsymbol{z}}$ and the Poincaré force which depends on its time derivative. Π is the modified pressure taking into account the time-dependent centrifugal acceleration. The Ekman number is $E=\nu/(\Omega_0 a^2)$, $f=\omega_l/\Omega_0$ is the dimensionless libration frequency and $\epsilon=\Delta\phi\ f$ is the libration forcing parameter. We only consider the case of no-slip boundary conditions.

In this paper, we study this system using both experimental and numerical approaches. Our geometrical parameters are similar to the ones considered by Grannan et al. (2014). In particular, the ellipsoid is characterized by a fixed equatorial ellipticity of $\beta=0.34$ (see Section 4.5.6 though), which corresponds in our dimensionless units to a semi-major axis $a=1$ and $b=0.7$ and the aspect ratio c/b is equal to one. We explore Ekman numbers between $10^{-3}<E<2\times10^{-5}$ and consider the librating frequencies $f=4$ and $f=2.4$. In order to focus on the parametric excitation of inertial modes, we only consider cases where $f>2$ so that the direct excitation of inertial modes, for which the frequency of the forcing matches the frequency of an inertial mode, is not possible. The different simulations and experiments considered in this paper and the corresponding parameters are summarized in Table 4.1.

Table 4.1: Summary of the experimental (case Exp., corresponding to case V in Grannan et al. (2014)) and numerical parameters considered in this study. E is the Ekman number, $\mathcal{E}$ is the number of elements, N is the order of the Legendre polynomials, f is the normalized libration frequency, ϵ is the libration amplitude, U_{rms} is the root mean square velocity defined by equation (4.11), l_0 is the integral length scale defined by equation (4.14), Re_L and Re_l are the large-scale and small-scale Reynolds numbers respectively defined by equations (4.13) and (4.15), Ro is the small-scale Rossby number defined by equation (4.16). Case $A1$ is stable whereas all other cases are unstable.

Case	E	$\mathcal{E}$	N	f	ϵ	β	U_{rms}	l_0	Re_L	Re_l	Ro
Exp.	2×10^{-5}	–	–	4	0.8	0.34	–	–	–	–	–
$A1$	10^{-3}	1280	7	4	0.8	0.34	–	–	–	–	–
$A2$	5.5×10^{-4}	1280	11	4	0.8	0.34	0.060	0.16	110	18	0.19
$A3$	5×10^{-4}	1280	11	4	0.8	0.34	0.064	0.16	128	20	0.2
$A4$	3.5×10^{-4}	3200	7	4	0.8	0.34	0.067	0.13	191	25	0.26
$A5$	2×10^{-4}	3200	11	4	0.8	0.34	0.072	0.12	360	43	0.3
$A6$	10^{-4}	3200	15	4	0.8	0.34	0.076	0.1	760	76	0.38
$A7$	5×10^{-5}	3200	23	4	0.8	0.34	0.085	0.08	1700	136	0.53
$B1$	10^{-4}	3200	13	4	0.8	0.17	0.043	0.12	430	52	0.18
$B2$	10^{-4}	3200	13	4	0.8	0.26	0.060	0.11	600	66	0.27
$C1$	10^{-4}	3200	13	2.4	1.2	0.34	0.28	0.2	2800	560	0.7

4.3 Numerical method

We solve the fully three-dimensional equations (4.4)-(4.5) in their weak variational form [e.g., Fischer et al. (2007)] with the spectral element code Nek5000 (http://nek5000.mcs.anl.gov) developed and supported by Paul Fischer and collaborators (see Fischer et al. (2007), and references within). Since the spectral element method combines the geometric flexibility of finite element methods with the accuracy of spectral methods, it is particularly well adapted to our problem involving turbulent flows in complex non-axisymmetric geometries. Nek5000 has for example already been used in the context of tidally-forced rotating flows [e.g., Favier et al. (2014b)]. The computational domain is decomposed into $\mathcal{E}$ non-overlapping hexahedral elements, and within each element, unknown velocity and pressure are represented as the tensor-product Lagrange polynomials of the order N and $N-2$ based at the Gauss-Lobatto-Legendre and Gauss-Legendre points respectively. The convergence is algebraic with increasing number of elements $\mathcal{E}$ and exponential with increasing polynomial order N. The number of degrees of freedom for each velocity component is scaling as $N^3\mathcal{E}$. For all the simulations discussed in this paper, numerical convergence was checked by fixing the number of elements $\mathcal{E}$ and increasing the degree N of the polynomial decomposition. The temporal discretization in Nek5000 is based on a semi-implicit formulation in which the nonlinear and rotation terms are treated explicitly in time and all remaining linear terms are treated implicitly. Note that our solution is dealiased following the 3/2 rule for an exact evaluation of quadrature of inner products for non-linear terms. The code is efficiently parallelized using MPI, and we use up to 480 processors for the highest resolution considered in this paper.

The whole ellipsoid is discretized using 1280 or 3200 elements. The mesh is a combination of a Cartesian mesh close to the origin and a spherical mesh close to the external boundary, as shown in Figure 4.1. The boundary geometry is initially spherical with a unit external radius centered around the origin and with a denser element distribution close to the external boundary. This, in addition to the Gauss-Lobatto-Legendre points distribution close to the element boundaries, ensures an appropriate resolution of the Ekman boundary layers with

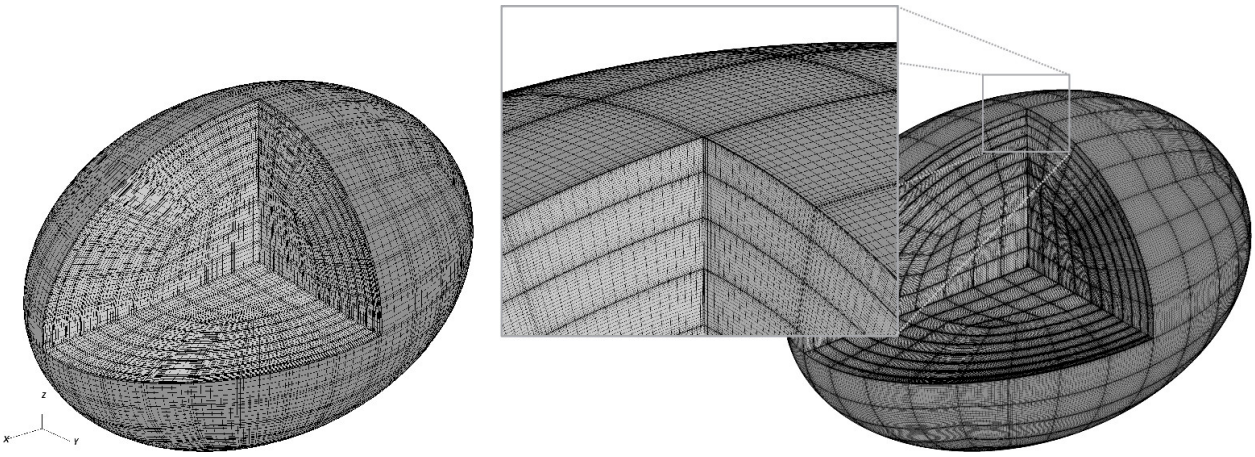

Figure 4.1: Cut through the complete three-dimensional ellipsoidal mesh with 3200 elements and a polynomial order of $N = 7$ (left) and $N = 23$ (right). The equatorial deformation is $\beta = 0.34$.

approximately ten grid points to describe them in all cases. Due to numerical limitations in terms of resolution, we can only consider flows down to $E = 5 \times 10^{-5}$. The ellipsoidal grid point positions (x_e, y_e, z_e) are obtained from the initial spherical grid points (x_s, y_s, z_s) according to $(x_e, y_e, z_e) = (ax_s, by_s, cz_s)$. Using this mapping approach, we can consider values of the ellipticity up to $\beta \approx 0.5$. Larger value of β would lead to overly stretched elements with poor convergence properties, so that another type of mesh would have to be used in that case. An example of the mesh for two different polynomial orders N is shown in Figure 4.1.

4.4 Experimental setup

The experimental setup used in the present work is adapted from the same apparatus used previously in several studies [e.g., Noir et al. (2009, 2010, 2012); Grannan et al. (2014)]. The fluid cavity, contained within a solid cast acrylic cylinder, is ellipsoidal with a long axis $a = 127$mm and short axes $b = c = 89$mm, leading to a fixed equatorial ellipticity of $\beta = 0.34$. A first motor rotates the turntable at a constant angular velocity $\Omega_0 = 30$ rpm (corresponding to an Ekman number of $E = 2 \times 10^{-5}$ for water). The second motor, situated on the turntable, is directly coupled to the acrylic container and superimposes a sinusoidal

oscillation whose parameter range is $[\Delta\phi, f] = [0.05 - 2.5, 0.5 - 9]$.

A particle image velocimetry (PIV) technique in the rotating reference frame is employed to obtain quantitative measurements in a horizontal plane close to the equator. The laser light sheet is horizontal and the camera is positioned above the system. PIV measurements are made only after solid body rotation has been reached and the librating forcing is turned on. The velocity field for an entire equatorial plane is resolved into a 23×40 grid with a typical spatial resolution of 8mm. More details about the experimental setup and results can be found in Grannan et al. (2014).

4.5 Results

In this paper, we focus mostly on the particular case where the librating frequency is $f = 4$ and the libration amplitude is $\epsilon = 0.8$ for both the laboratory experiment and the simulations. This corresponds to case V of Grannan et al. (2014). The reason why we focus on the case $f = 4$ is the following. The simplest determination of the mode and frequency coupling is provided by the $f = 4$ case at the extreme range of the instability where we expect the participating modes to have an eigenfrequency $|\omega| \approx f/2 = 2$ (Although inertial modes with $|\omega| = 2$ exactly do not exist in the inviscid limit, viscous modes with frequency close to but below 2 can be excited through imperfect resonances, as discussed into more details in section 4.5.4). Inertial modes with a dimensionless frequency $|\omega| \approx 2$ are easy to identify since their group velocity is nearly horizontal. Finally, it has been experimentally observed that the case $f = 4$ leads to a sustained quasi-steady state of turbulence [e.g., Grannan et al. (2014)], which is easier to characterize and is the main focus of this paper. Note however that the intermittent regime is briefly discussed in Section 4.5.6 whereas other frequencies are considered in Section 4.5.7.

For the numerical simulations, the Ekman number is varied from $E = 10^{-3}$ down to $E = 5 \times 10^{-5}$, whereas the experimental setup is characterized by $E = 2 \times 10^{-5}$. The simulations are initialized with a fluid at rest, but results are qualitatively the same with random velocity perturbations of small amplitude. A summary of the numerical input parameters can be

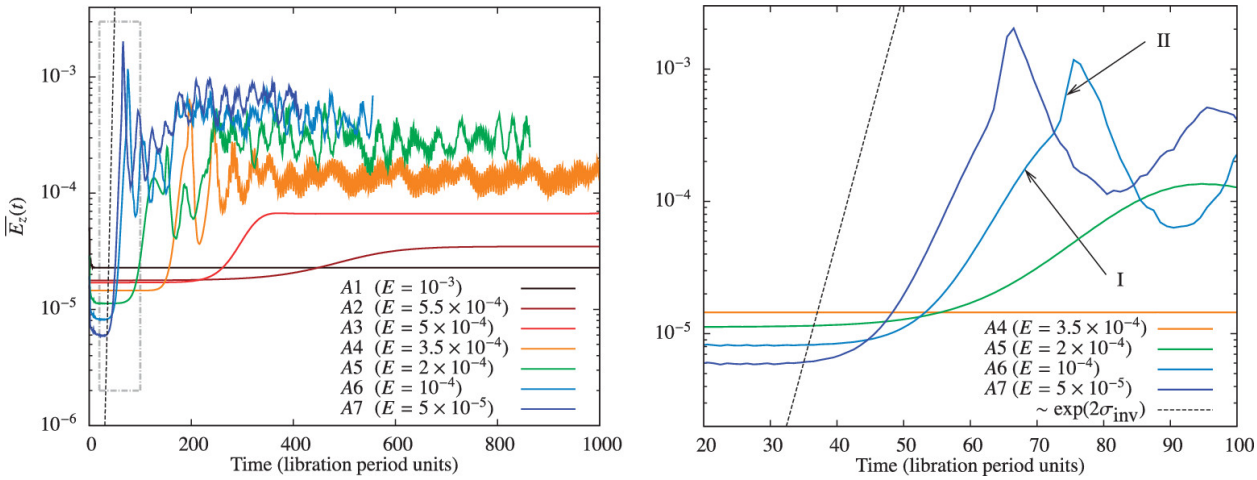

Figure 4.2: Left: time evolution of the volume-averaged squared vertical velocity given by equations (4.7)-(4.8) for cases $A1$ to $A7$. Right: zoom on the early stage of the instability shown by the dotted contour on the left panel. The inviscid theoretical growth rate $\propto \exp(2\sigma_{\mathrm{inv}}t)$ as defined by equation (4.9) is plotted as a dotted line. The arrows indicate the times at which the enstrophy is visualized in Figure 4.3. In all cases, the results are time-averaged over each libration period according to equation (4.8).

found in Table 4.1.

4.5.1 General properties

The general properties of the flows observed experimentally have already been discussed by Grannan et al. (2014), so that we focus here on the new numerical results. The base flow, driven by the Poincaré force and only accounting for the non-penetrative condition on the solid boundaries, is [e.g., Kerswell and Malkus (1998); Cébron et al. (2012b)]

$$\boldsymbol{U}_b = -\epsilon \sin(ft) \left[\hat{\boldsymbol{z}} \times \boldsymbol{r} - \beta \nabla xy \right] . \tag{4.6}$$

This flow is purely horizontal so that any departure from it, being due to viscous effects close to the boundaries or due to instabilities, will be observable in the vertical component of the velocity. We first consider the volume average of the squared vertical velocity component defined as

$$E_z(t) = \frac{1}{2V} \int_V u_z^2 \, \mathrm{d}V \tag{4.7}$$

where V is the total volume of the ellipsoid and u_z is the vertical velocity component. Note that this quantity is not accessible in the experimental apparatus since the PIV measurements are limited to the horizontal components of the flow in the equatorial plane only. In addition to the volume average defined previously, we also consider quantities averaged over one libration period according to

$$\overline{A}(t) = \frac{1}{T}\int_t^{t+T} A(\tau)\ \mathrm{d}\tau\ , \tag{4.8}$$

where $T = 2\pi/f$ is the librating period. Because the statistics discussed here evolve over hundreds of librating periods, looking at the time evolution of period-averaged quantities is much clearer since the oscillating contribution from the base flow is removed.

We show in Figure 4.2 the time evolution of the volume- and period-averaged squared vertical velocity $\overline{E_z}(t)$ for cases $A1$ to $A7$ as defined in Table 4.1. The only physical parameter that is varied between these cases is the Ekman number E. At very early times, the very low steady values (typically of order 10^{-5}) of squared vertical velocity scaling as $\sqrt{E}$ are associated with the viscous corrections to the base flow given by equation (4.6) in order to match the no-slip boundary condition. Note that for the smallest Ekman number considered here (case $A7$, $E = 5\times10^{-5}$), we do not reach a steady base state before the instability develops. For all cases apart from case $A1$ ($E = 10^{-3}$), we then observe an exponential growth rate followed by a nonlinear overshoot and a steady or quasi-steady saturation of the squared vertical velocity. Case $A1$ is stable and we do not observe any modifications of the base flow even after thousands of librating periods. It has been previously shown that this exponential growth phase is associated with the elliptical instability [e.g., Cébron et al. (2012b); Grannan et al. (2014)]. A Wentzel-Kramers-Brillouin local stability analysis, valid in the regime $\epsilon \ll 1$ and $\beta \ll 1$, leads to the following inviscid growth rate for the libration-driven elliptical instability [e.g., Le Dizes (2000); Cébron et al. (2014)

$$\sigma_{\mathrm{inv}} = \frac{16 + f_{\mathrm{res}}^2}{64}\epsilon\beta\ , \tag{4.9}$$

where f_{res} is the resonant forcing frequency at which the frequencies of the two inertial modes

involved exactly follow the relation $|\omega_1 - \omega_2| = f_{\rm res}$. In the general viscous case and away from perfect resonances (*i.e.* $f \neq f_{\rm res}$), the growth rate is reduced and given by Cébron et al. (2012a),

$$\sigma = \sqrt{\sigma_{\rm inv}^2 - (f_{\rm res} - f)^2} - K\sqrt{E}, \tag{4.10}$$

where K is a constant factor of order unity. The last term on the right-hand side of equation (4.10) is due to viscous dissipation in the Ekman boundary layers, and is the reason why we have to consider sufficiently large values of β and ϵ since we are limited to moderately low values of the Ekman number. As expected from these theoretical predictions, the growth rate of the instability observed in Figure 4.2 increases as the Ekman number decreases, and eventually tends towards the inviscid growth rate (4.9) with $f_{\rm res} = 4$. The right panel in Figure 4.2 shows this exponential phase and compares it against the inviscid growth rate given by equation (4.9) (multiplied by two since we consider the squared vertical velocity). A more detailed comparison between theoretical predictions and numerical simulations can be found in Cébron et al. (2012b).

After the exponential phase, the nature of the saturation depends on the Ekman number. For cases $A2$ and $A3$, the saturation leads to a steady-state characterized by a constant value of the volume- and period-averaged squared vertical velocity. For cases $A4$ to $A7$, a quasi-steady state is obtained but significant fluctuations are observed. We also observe a strong overshoot, followed by a phase of gradual increase in the vertical energy until a quasi-steady state is eventually reached. Apart for the large E cases $A2$ and $A3$, we also observe a low frequency modulation of the signal with a typical period of 30 librating periods. The period of these low-frequency oscillations does not depend on the Ekman number for the values considered here. Finally, note that the amplitude of saturation of the instability increases as the Ekman number decreases. This has already been discussed in Cébron et al. (2012b, 2014) and our results are consistent with their conclusions, where the amplitude A of the saturation scales as the square-root of the distance to the threshold $A \approx \sqrt{E_c/E - 1}$ where E_c is the critical Ekman number below which the elliptical instability grows.

A volume rendering of the enstrophy is shown in Figure 4.3 (multimedia view) for the

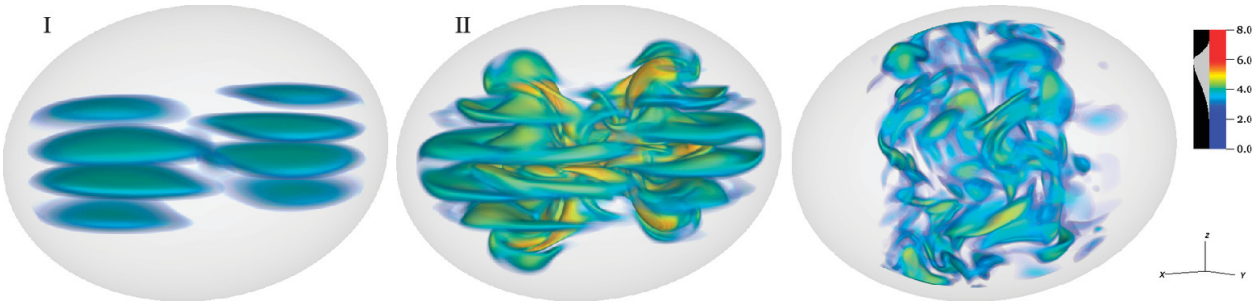

Figure 4.3: Volume rendering of the enstrophy in the bulk of the ellipsoid (the boundary layers are removed from the visualization) for case $A6$. We visualize the flow just during the exponential growth of the instability (left, $t = 68$, see I in Figure 4.2), during the first collapse (middle, $t = 75$, see II in Figure 4.2) and during the quasi-steady saturated state (right, $t = 200$). A first movie is available as a supplement (multimedia view) showing the collapse of the inertial modes from $t \approx 68$ to $t \approx 78$ in the librating frame. It can be compared with a similar movie (presented in the frame rotating at constant rate Ω_0 and not in the librating frame)corresponding to case V in Grannan et al. (2014) (`http//dx.doi.org/10.1063/1.4903003.4`). A second movie showing the quasi-steady regime ($186 < t < 196$) is also available (multimedia view).

case $A6$ with $E = 10^{-4}$. We consider three different times: an arbitrary time during the exponential phase, just before the first overshoot and, finally, during the quasi-steady state. During the exponential phase, the flow is characterized by three components: the base flow given by equation (4.6), the zonal flow (discussed in Section 4.5.3 below) and the inertial modes. The layered structures observed in the left panel of Figure 4.3 corresponds to the dominant $|\omega| \lesssim 2$, $m = 1$ inertial modes resonating with the base flow. When the instability first saturates (see Figure 4.3 II), a sudden wave breaking event occurs, leading to intense three dimensional motions. Finally, in the quasi-steady state, a sustained inhomogeneous state of bulk turbulence is observed. The initial collapse of the inertial modes and the quasi-steady saturated state are best visualized by the two movies in Figure 4.3 (multimedia view).

We now define various dimensionless numbers to describe the nature of our solutions. The typical velocity of the small-scale flow is estimated as

$$U_{\text{rms}} = \sqrt{\left\langle (\boldsymbol{u} - \boldsymbol{U}_b)^2 \right\rangle_{\text{bulk}}} \tag{4.11}$$

where $\boldsymbol{U}_b$ is the base flow defined by equation (4.6) and $\langle . \rangle_{\text{bulk}}$ denotes the volume average over the bulk of the flow. Similarly to Cébron et al. (2014), the bulk is obtained by removing the contribution from the viscous boundary layer by assuming that their thickness is of order Wang (1970)

$$\delta = \sqrt{\frac{2E}{f}} \ . \tag{4.12}$$

First, a large-scale Reynolds number, based on the semi-major axis of the ellipsoid and the root-mean-square velocity, is defined using our dimensionless units as

$$Re_L = \frac{U_{\text{rms}}}{E} \ . \tag{4.13}$$

In addition, we also quantify the small-scale Reynolds number based on the fluctuations generated by the instability. In order to measure the typical length scales associated with the fluctuations, we defined the correlation length scale of the vertical velocity in the bulk of the domain as

$$l_0 = \int_0^{r_0} \frac{\langle u_z(\boldsymbol{x}) u_z(\boldsymbol{x} + r\boldsymbol{e}_i) \rangle_{\text{bulk}}}{\langle u_z^2(\boldsymbol{x}) \rangle_{\text{bulk}}} \, \mathrm{d}r \tag{4.14}$$

where the integral of the correlation function is carried out up to the first zero-crossing only. We only consider the transverse correlations (where we average over both horizontal directions) of the vertical velocity since the horizontal components are dominated by the presence of large-scale inertial modes (see Section 4.5.4 below). The small-scale Reynolds number is then defined as

$$Re_l = \frac{U_{\text{rms}} l_0}{E} \ . \tag{4.15}$$

Finally, the Rossby number associated with the instability is given in our dimensionless units by

$$Ro = \frac{U_{\text{rms}}}{2l_0} \ . \tag{4.16}$$

The values of these dimensionless numbers, time-averaged during the quasi-steady saturated phase, are gathered in Table 4.1. In all cases, the large-scale Reynolds number is very large, but note that for all cases considered in this section, we did not observe a destabilization of

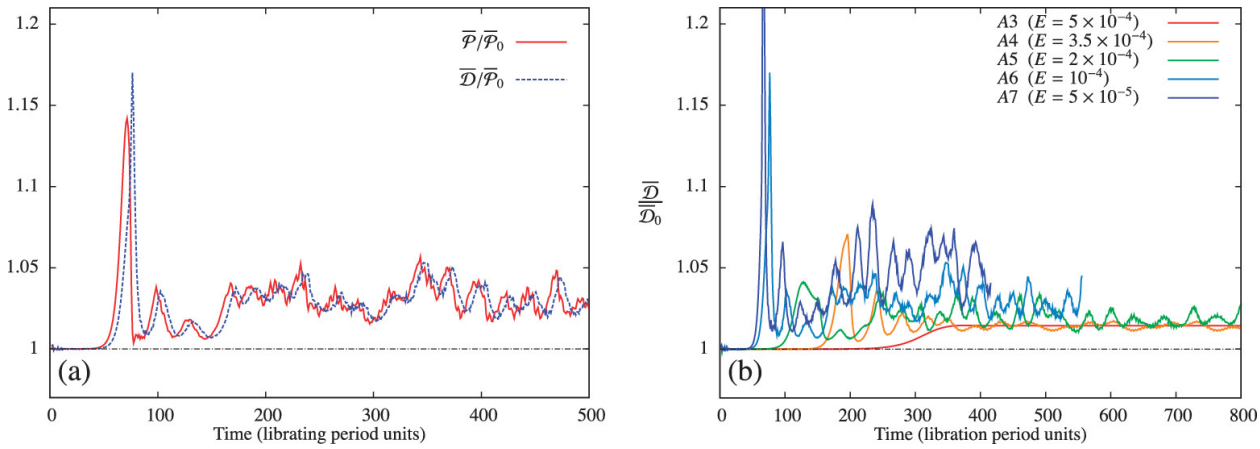

Figure 4.4: (a) Time evolution of the power injected by the Poincaré force and the viscous dissipation for case $A6$. Values are normalized by the averaged power input $\overline{\mathcal{P}}_0$ before the instability develops. (b) Viscous dissipation rate normalized by its value associated with the base flow only.

the boundary layers due to centrifugal instabilities for example. The small-scale Reynolds number is however much smaller, which explains why the unstable cases $A2$ and $A3$ remain laminar even in the presence of the instability. As the Ekman number is decreasing further, Re_l is rapidly increasing up to 136 for case $A7$ which implies that the small-scale flow is in a developed turbulent state. Finally, the Rossby number is gradually increasing as the Ekman number decreases but is always smaller than unity. This indicates that the fluctuations associated with the instability are significantly affected by rotation in all the cases considered here.

4.5.2 Energetics

Taking the dot product of the velocity with equation (4.4) divided by two leads to the equation for the total kinetic energy

$$\frac{\partial K}{\partial t} = \underbrace{-\frac{\epsilon f \cos(ft)}{2}\int_V \boldsymbol{u}\cdot(\hat{\boldsymbol{z}}\times\boldsymbol{r})\,\mathrm{d}V}_{\mathcal{P}} \underbrace{-\frac{E}{2}\int_V \boldsymbol{\omega}^2\mathrm{d}V}_{\mathcal{D}} \tag{4.17}$$

where K is the volume averaged kinetic energy, the first term on the right-hand side is the power injected by the Poincaré force and the last term is the viscous dissipation. The

advection term and the Coriolis terms do no work and the pressure contribution vanishes since the normal component of the velocity is zero at the boundary in the librating frame. In the frame rotating at constant rate Ω_0, there is no Poincaré force since the frame rotation vector is steady. The pressure term does not vanish however, since the external boundary is moving. Figure 4.4 shows an example of the time evolution of both quantities $\mathcal{P}$ and $\mathcal{D}$ for case *A6*, normalized by the averaged value of the power injected before the instability develops and temporally averaged over each libration period. As expected, the steady base flow is maintained by an exact balance between the power injected by the Poincaré force and the viscous dissipation. As the instability develops, we first observe an increase in the power injected, followed by an increase in the dissipation. The peak of viscous dissipation occurs approximately 5 libration periods after the peak in power. This lag in the dissipation remains the same as the instability saturates, and does not depend on the Ekman number for the parameters considered here.

We now describe the effect of the instability on the overall viscous dissipation. The volume-averaged viscous dissipation is first estimated before the instability develops. In this case, the dissipation is mostly concentrated in boundary layers where the base flow is forced to match the no-slip boundary condition on the ellipsoid surface. Again, we use the period average defined by equation (4.8) to obtain the average dissipation over each librating period. Figure 4.4(b) shows the time evolution of the viscous dissipation normalized by its value during the initial state where the base flow is dominating the dynamics. The instability is characterized by a significant increase in the volume-averaged viscous dissipation. This additional dissipation takes place in the bulk of the fluid domain, and is not associated with boundary layers. Again, the quasi-steady value of the viscous dissipation measured during the saturated phase increases when the Ekman number is decreasing, as discussed in Cébron et al. (2014).

4.5.3 Enhanced zonal flows

Even without the presence of the elliptical instability, librating flows are known to drive persistent zonal flows [e.g., Busse (2010); Calkins et al. (2010); Noir et al. (2012); Sauret et al. (2013)]. The amplitude of this zonal flow does not depend on the Ekman number and scales as ϵ^2. Here, we discuss the effect of the libration-driven elliptical instability on such zonal flows for the case $f = 4$.

We assume that the zonal flow is dominated by its azimuthal component in cylindrical coordinates and that it is mostly varying in the cylindrically-radial direction. We therefore define the zonal flow as

$$\langle U_\phi \rangle_c (\rho) = \frac{1}{N_\rho} \sum_z \sum_\phi \sum_{\rho - \frac{d\rho}{2} < \rho < \rho + \frac{d\rho}{2}} U_\phi(\rho, \phi, z) \ , \tag{4.18}$$

where N_ρ is the total number of grid points lying inside the cylindrical shell and $d\rho$ is the width of the cylindrical shell. Here we average the azimuthal flow over 30 different cylindrical shell from $\rho = 0$ to $\rho = 1$ and over all vertical positions z. In addition, these zonal flows are averaged over an arbitrary number of libration periods.

Figure 4.5(a) shows the radial profile of the zonal flow for different Ekman numbers. The time average is performed over two different regimes, before and after the instability kicks in. The zonal flow associated with the initial base state is shown in dotted lines, where we average the zonal profile before the exponential phase (typically for $t < 200$, see Figure 4.2). For cases $A3$ to $A5$ ($5 \times 10^{-4} < E < 2 \times 10^{-4}$) we recover the zonal flow with an amplitude independent of the Ekman number. For the cases with $E \leq 10^{-4}$ (including experimental results), the initial transient phase before the base flow is established is very long and the duration of the stable regime is too short to be able to obtain meaningful averages. As observed in previous theoretical studies, the zonal flow is prograde close to the equatorial boundary and retrograde in the bulk. The dotted-dash line corresponds to the theoretical prediction of Sauret et al. (2013) in the case of the sphere for $f = 4$ and is shown for reference. The departure between their result and our numerical simulations is attributed

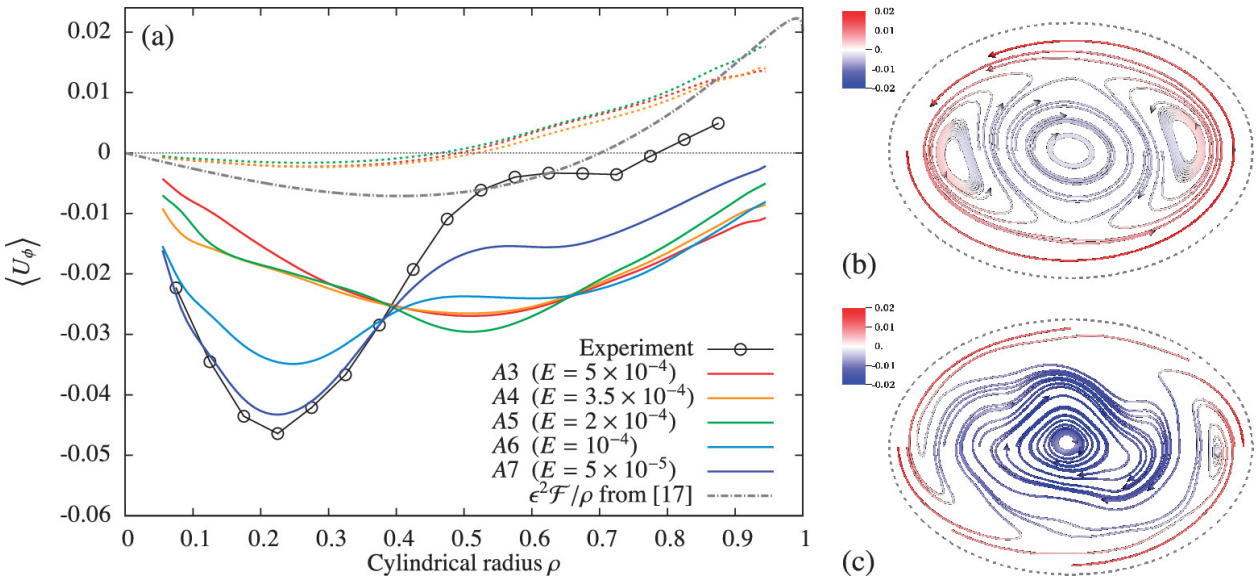

Figure 4.5: (a) Comparison between the zonal flow obtained experimentally and numerically using equation (4.18) for various Ekman numbers. The dotted lines correspond to the initial steady state before the instability grows whereas the solid lines correspond to the quasi-steady state after the instability has saturated. Experimental results at $E = 2 \times 10^{-5}$ are shown as empty symbols. The dash-dotted line correspond to theoretical results by Sauret et al. (2013) for the same parameters but in spherical geometry and without instabilities. Comparison of the equatorial zonal flows between the initial (b) and saturated (c) phases for case $A6$ ($E = 10^{-4}$). The streamlines are colored with the value of azimuthal velocity.

to geometrical effects as we consider a non-axisymmetric container here. In particular, two persistent recirculation cells are observed in the equatorial plane (see Figure 4.5(b)).

When the elliptical instability saturates, the zonal flow observed in numerical simulations increases in amplitude and is now retrograde in all the bulk of the fluid (see solid lines in Figure 4.5(a)). Very close to the threshold (*i.e.* for $E > 2 \times 10^{-4}$, cases $A3$ and $A4$), the amplitude of this enhanced retrograde zonal flow does not scale with the Ekman number, but for smaller Ekman numbers the amplitude of the zonal flow increases as the Ekman number decreases. This is observed both numerically for $E = 10^{-4}$ and $E = 5 \times 10^{-5}$ and experimentally at $E = 2 \times 10^{-5}$. Note in addition that the trend observed in the numerical results at $E = 5 \times 10^{-5}$ are consistent with the experimental results at $E = 2 \times 10^{-5}$, shown as empty symbols in Figure 4.5(a). As the Ekman number decreases, a strong anticyclonic vortex flow develops close to axis of rotation (see Figure 4.5(c)), whereas its amplitude decreases close to the boundaries and eventually becomes prograde again in the experiment. Note that we observed similar behaviors for other librating frequencies such as $f = 3$, so that it appears to be a generic result. Since the zonal flow associated with the base flow scales as ϵ^2 but does not depend on the Ekman number, the relevance of such libration-driven zonal flows in geophysical systems has been questioned [e.g., Calkins et al. (2010); Sauret et al. (2013)]. Here, we show that for the particular case $f = 4$, the saturation of the elliptical instability leads to an enhanced zonal flow with an amplitude increasing as the Ekman number decreases. This new nonlinearly driven zonal flow might be more relevant to the geophysical regime characterized by very low Ekman numbers. We do not have enough numerical or experimental data to provide a scaling for this mechanism at this stage, but all of our results point towards a strong retrograde axial vortex driven by nonlinearities in the turbulent bulk. Note that Mason and Kerswell (1999) also found a strong retrograde zonal flow driven by the saturation of the elliptical instability.

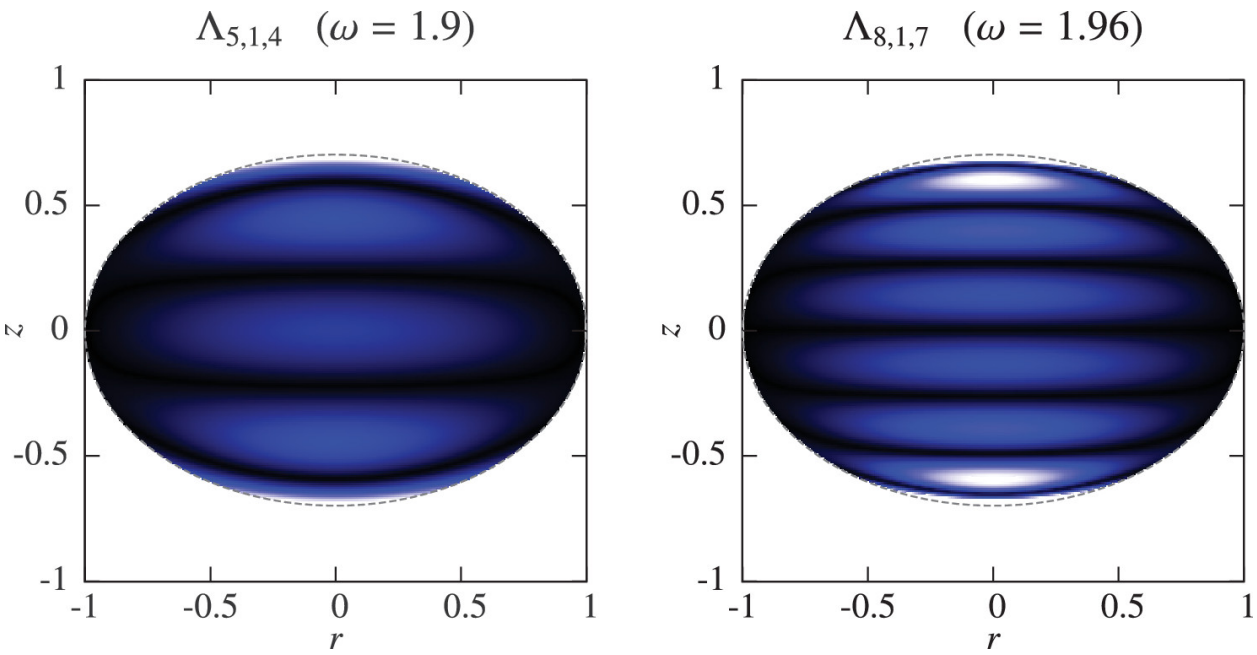

Figure 4.6: Amplitude $|\boldsymbol{Q}|$, as defined by equation (2.30) in Kerswell (1994), of an inertial mode $\Lambda_{n,m,\kappa}$ for a spheroid with $c = 0.7$. Bright and dark colors correspond to large and low amplitudes respectively. The results are shown in a meridional slice and we compare two inertial modes with an azimuthal wave number $m = 1$ and an eigenfrequency ω close to 2.

4.5.4 Mode couplings and transition to turbulence

In this section, we explore the transition between a laminar base flow driven by the Poincaré force and a bulk-filling turbulent flow initially driven by the elliptical instability as the Ekman number is decreased. In this study, we only considered an Ekman number of $E = 2 \times 10^{-5}$ in the laboratory experiment so that the transition to turbulence occurring at larger Ekman numbers is mainly discussed from a numerical point of view. A comparison between numerical and experimental data is however presented below at the end of this section.

Before discussing the transition to turbulence in our system, let us briefly describe the spatial structures and frequencies of the inertial modes that can resonate with the harmonic forcing at $f = 4$. The case of the tri-axial ellipsoid has been recently considered by Vantieghem (2014), but the libration frequency $f = 4$ primarily excites high wave number inertial modes and this paper mostly focuses on inertial modes with linear or quadratic spatial dependence. Following Grannan et al. (2014), we consider for simplicity the inviscid inertial modes in cylindrical coordinates and for a spheroidal container defined by $r^2 + z^2/c^2 = 1$ as

derived by Kerswell (1994). The inertial modes are denoted $\Lambda_{n,m,\kappa}$ where n is the order of the associated Legendre polynomials that combines the radial and axial wavenumbers, m is the azimuthal wavenumber and κ represents the κ^{th} eigenfrequency. For each couple (n, m) there are $n - |m|$ eigenfrequencies (or $n - 1$ if $m = 0$). For an elliptical deformation with azimuthal wave number $m = 2$, the resonance condition imposes $|m_2 - m_1| = 2$ where m_2 and m_1 are the azimuthal wave numbers of the inertial modes. We focus here on the case $|m| = 1$ shown to be relevant by Grannan et al. (2014). Since the frequency of the forcing is $f = 4$, we expect inertial modes with eigenfrequencies $|\omega| \lesssim 2$. As already mentioned, the frequency of the inertial modes cannot be exactly equal to 2. However, an imperfect resonance is possible provided that the frequency mismatch in order to satisfy the resonance condition $|\omega_1 - \omega_2| = f$ is less than the elliptical deformation β [e.g., Lacaze et al. (2004)]. Since we focus here on a large elliptic deformation $\beta = 0.34$, resonance bands are very broad and many imperfect resonances can occur [e.g., Le Bars et al. (2010)]. Note finally that resonances were observed experimentally [e.g., Grannan et al. (2014)] up to $f = 4+\epsilon\beta+O(\epsilon^2\beta^2)$, which is consistent with theoretical predictions in the large β and large ϵ regime [e.g., Le Dizes (2000)]. Figure 4.6 shows the amplitude of modes with moderately large n, $m = 1$ and frequency close to $\omega = 2$. As n increases, the largest eigenfrequency $\kappa = n - |m|$ tends towards $\omega = 2$ [e.g., Lacaze et al. (2004)]. In the presence of viscosity, inertial modes with large n will however be damped. Since these modes have a frequency close to $\omega = 2$, their group velocity is quasi-horizontal and they are characterized by a pancake-like structure. We recall that such modes correspond to a spheroidal geometry, but we nevertheless expect the results to be similar in the ellipsoidal case. Grannan et al. (2014) have, for example, reported a mode with spatial structure very similar to the spheroidal mode $\Lambda_{8,1,7}$ in their laboratory apparatus for the case $f = 4$.

We now come back to the numerical results discussed in the previous sections. We place 100 numerical probes homogeneously distributed inside the bulk of the ellipsoid (*i.e.* outside of the viscous boundary layers). The three components of the velocity and the pressure are saved at these locations at every time step, and we perform a spectral analysis of these signals. Since we use an adaptive time step method, the signals from the numerical simula-

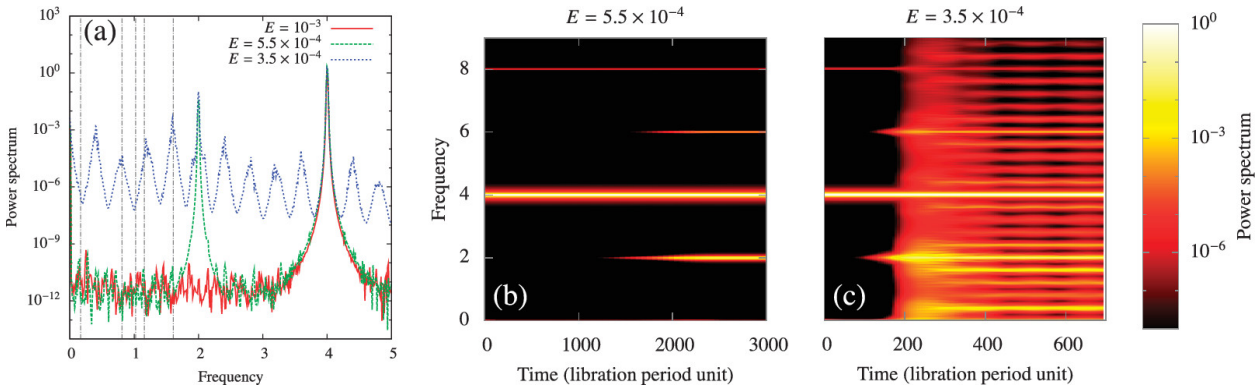

Figure 4.7: Temporal power spectrum for cases $A1$ ($E = 10^{-3}$), $A2$ ($E = 5.5 \times 10^{-4}$) and $A4$ ($E = 3.5 \times 10^{-4}$). (a) Power spectra are averaged over 500 libration periods during the saturated phase. The vertical dot-dash lines correspond to the theoretical predictions of Vantieghem (2014) for the eigenfrequencies of linear and quadratic inertial modes in the ellipsoid. Time evolution of the power spectrum with a sliding window of 50 libration periods for cases $A2$ (b) and $A4$ (c).

tions need to be evaluated on a uniform grid which is done using a sixth order Lagrangian interpolation scheme. For each of the three velocity components, we compute the discrete Fourier transform of the signal during an arbitrary time interval. Note that the input signal is not necessarily periodic so that we need to multiply it by a periodic window function to avoid spectral leakage associated with the discontinuity between the start and the end of the signal. Here, we use the Hanning window defined as

$$w(n) = \frac{1}{2}\left[1 - \cos\left(2\pi \frac{n}{N-1}\right)\right] \quad , \quad 0 \leq n \leq N-1 \tag{4.19}$$

where N is the total number of samples. We checked that using other window functions does not qualitatively change the results.

Figure 4.7(a) shows the resulting power spectra for cases $A1$, $A2$ and $A4$, where we only used the signals obtained after the instability has saturated. For case $A1$, the flow is actually stable so that we only observe two peaks, one corresponding to the base flow at $\omega = f = 4$ and one corresponding to the zonal flow at $\omega = 0$. Case $A2$ is unstable and the peaks associated with the base and zonal flows are still present and unchanged, but we now see a peak at $\omega = f/2 = 2$ and subsequent harmonics at $\omega = 6, 8, \ldots$. We argue that these peaks are associated with the two resonating inertial modes at the origin of the elliptical

instability with frequencies $|\omega| \lesssim 2$ which satisfied the resonance condition $|\omega_2 - \omega_1| \approx f$. Finally, the third spectrum corresponds to the case $A4$, where the Ekman number is reduced even further to 3.5×10^{-4}. In addition to the previous features, many additional peaks are now clearly visible. A first indication that these are also inertial modes is that their frequencies are comparable with eigenfrequencies of linear and quadratic inertial modes of the full ellipsoid [e.g., Vantieghem (2014)] as shown in Figure 4.7(a) (additional theoretical frequencies would be found by increasing the order of the polynomial expansion). These additional frequencies we observed are, in decreasing order of amplitude, $\omega \approx 1.6$, 0.4, 1.2 and 0.8. These frequencies are therefore compatible with quadratic interactions between the primary inertial modes at $\omega \approx 2$ and two of the daughter modes (*i.e.* 1.6 and 0.4 on the one hand, 1.2 and 0.8 on the other hand), as further discussed below. Note that for the particular simulations $A2$ to $A4$ considered here, the saturation of the elliptical instability does not lead to turbulence, as the Ekman number is too large. The power spectrum remains quasi-discrete since mode couplings are very limited for these viscously-dominated cases. The two right panels in Figure 4.7 show the time evolution of the power spectra for cases $A2$ and $A4$. At each time step, the Fourier analysis is performed over a window of 50 libration periods. The chronology of the various resonances becomes clear. The libration forcing sustains the base flow at $f = 4$ from the beginning of the simulation. We then observe a primary resonance involving two inertial modes with frequencies $\omega \approx \pm 2$ and the base flow at $\omega = 4$. As the amplitude of these primary inertial modes becomes larger, and if the Ekman number is low enough (*i.e.* $E \leq 4 \times 10^{-4}$ in our case), secondary quadratic interactions are allowed with two sets of daughter inertial modes whose frequencies are given by the resonance condition $|\omega_2 - \omega_1| = 2$. Note that no further resonances are observed for case $A4$.

We now compare numerical and experimental data in order to confirm the quadratic interactions observed numerically in the laminar regime. In particular, we focus on simulation $A6$, for which $E = 10^{-4}$, whereas we recall that $E = 2 \times 10^{-5}$ for the experiment. Since the Ekman numbers are different, we expect quantitative differences between the two approaches. Note that both simulation $A6$ and the experiment are in the turbulent regime, but as we show below, we can still distinguish between the dominant low-frequency interactions and the

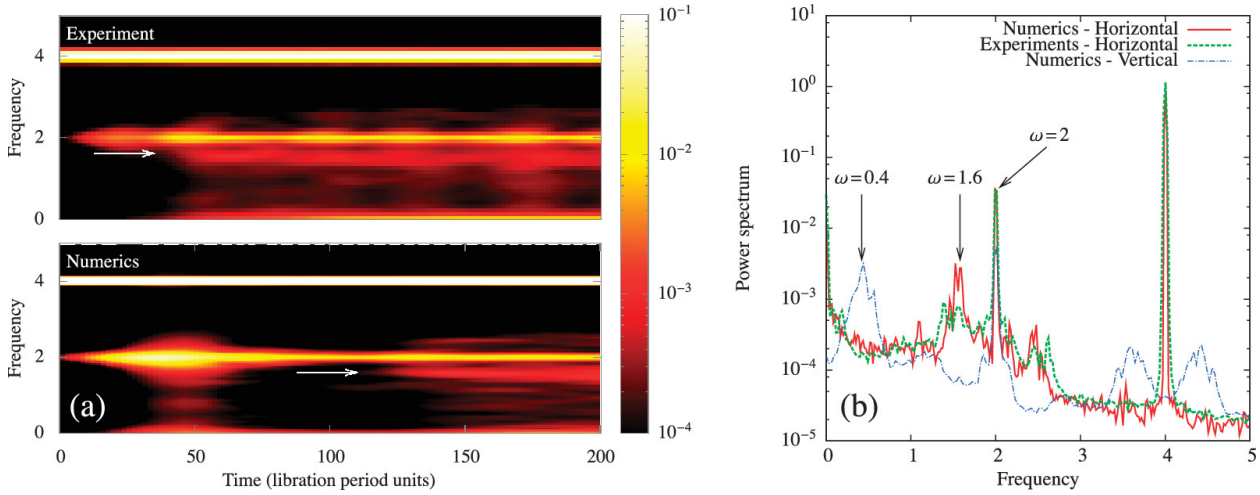

Figure 4.8: Comparison between experimental and numerical results. (a) Spectrograms computed using horizontal velocity signals in the equatorial plane only. The top panel corresponds to the experimental results at $E = 2 \times 10^{-5}$ (case V in Grannan et al. (2014)) whereas the bottom panel corresponds to the numerical case $A6$ at $E = 10^{-4}$. The white arrow indicates the appearance of the particular frequency $\omega = 1.6$ involved in the secondary quadratic interactions. (b) Power spectra time-averaged during the saturated phase. We also show the numerical power spectrum associated with the vertical component (not available experimentally).

background turbulence noise. The frame rate of the camera used for the PIV is 23.9 frames per second. In our dimensionless units, this leads to a maximum frequency of $\omega = 24$ which is not enough to compare with the high-frequency range available numerically. We note in addition that experimental time spectra tend to be flat at high-frequencies, probably due to uncertainties. For these reasons, we focus on the low frequencies $\omega \leq 4$. The behaviors of the high frequencies in the numerical simulations will be discussed below in Section 4.5.5. Numerical probes are placed at the same location as for the PIV measurements and the power spectra are computed using a sliding window of 20 libration periods. Experimental and numerical results are presented in Figure 4.8(a), where we show the spectrogram associated with the equatorial horizontal flow only. In both cases, we see the dominant contribution from the base flow at $\omega = 4$ from the beginning of the experiment. As time is evolving, the first resonance with the primordial inertial modes at $\omega = 2$ occurs as already observed in the laminar regime. Once the primary inertial modes have grown in amplitude, the secondary resonance at $\omega = 1.6$ is also visible in both cases and is indicated by a white arrow. This

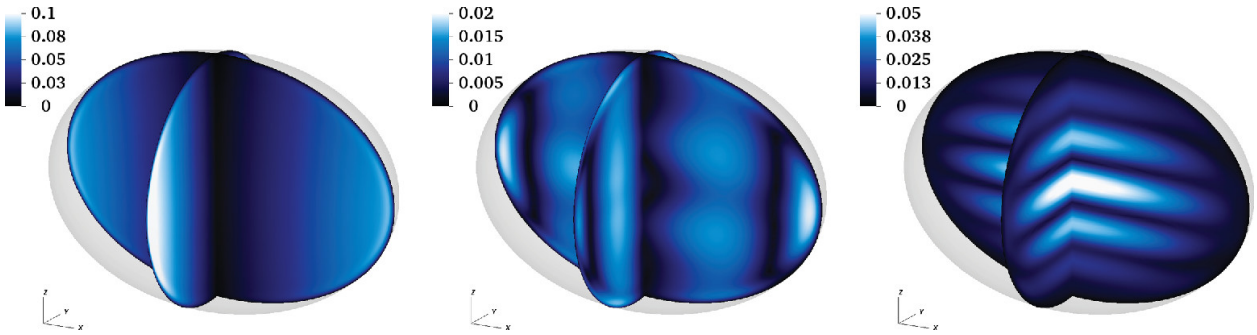

Figure 4.9: Velocity amplitude associated with filtered velocity fields at various frequencies using equation (4.20) for case $A3$ ($E = 5 \times 10^{-4}$). Left: Base flow obtained by filtering at $\omega_f = f$ over 100 libration periods. Middle: Zonal flow obtained by time averaging. Right: Inertial modes filtered at $\omega_f = f/2$.

secondary resonance occurs earlier in the experiment than in the numerical simulation due to the lower Ekman number in this case (and therefore a larger growth rate for the elliptical instability).

Interestingly, the frequency $\omega = 0.4$, already observed numerically in Figure 4.7, is not seen in the horizontal flow. However, when looking at the vertical component from the numerics in the same equatorial plane, we recover the frequency $\omega = 0.4$ required by the resonance condition. This is visible in Figure 4.8(b), where we show the power spectra averaged during the saturated phase for the numerical simulation (the vertical component of the flow is not available experimentally). We also show in Figure 4.8(b) the horizontal power spectra from both the experiment and the numerics. Note the excellent agreement between both approaches in this frequency range. No rescaling has been applied.

In order to extract the spatial structure of the different components of the flow, we follow the approach used by several authors [e.g., Hazewinkel et al. (2008); Grisouard et al. (2008); Jouve and Ogilvie (2014)] in the context of internal gravity or inertial wave attractors. The velocity field is filtered at a particular frequency ω_f according to

$$\hat{\boldsymbol{u}}(\omega_f, \boldsymbol{x}) = \frac{\omega_f}{N\pi} \int_{t_i}^{t_f} \boldsymbol{u}(\boldsymbol{x}) e^{i\omega_f (t-t_i)} \mathrm{d}t \tag{4.20}$$

where the arbitrary times t_i and t_f are separated by N periods $T = 2\pi/\omega_f$. Here, we consider the velocity fields filtered at $\omega_f = f$, $\omega_f = 0$ and $\omega_f = f/2$, which correspond respectively

to the base flow, the zonal flow and the primordial inertial modes. Figure 4.9 shows the amplitude of each of these filtered velocity fields. The base flow (4.6) is recovered in the bulk. The zonal flow is averaged over the initial phase before the instability develops. We recover the strong prograde circulation close the equatorial boundary and the weaker retrograde interior jet, as already discussed in Section 4.5.3. Finally, the inertial modes correspond to layered structures dominated by horizontal motions, and is very similar to the inertial modes for a spheroid as shown in Figure 4.6. In particular, the structure observed in the rightmost panel of Figure 4.9 corresponds to the inertial mode $\Lambda_{7,1,6}$ with an eigenfrequency of $\omega = 1.95$. The wave number n of the inertial modes observed by this filtering approach increases as we decrease the Ekman number. We indeed observe the inertial mode $\Lambda_{8,1,7}$ for cases $A6$ and $A7$, which is consistent with the experimental observation made by Grannan et al. (2014). Although removed from Figure 4.9 by the averaging process defined in equation (4.20), the inertial modes also have an azimuthal wave number $m = 1$ component, as expected due to the resonance conditions with the elliptical base flow with $m = 2$.

Although the appearance of a mode at half the frequency of the forcing is a strong indication of a parametric resonance, the power spectrum is not enough to conclude since the phase information is lost. In order to explicitly show that quadratic couplings are responsible for the growth of the $\omega \approx 2$ modes, one has to rely on higher-order spectral analysis. In particular, we choose the consider the bicoherence defined as

$$B^2(f_1, f_2) = \frac{\left|\sum_{i=1}^{N} u_i(f_1) u_i(f_2) u_i^*(f_1 + f_2)\right|^2}{\sum_{i=1}^{N} \left|u_i(f_1) u_i(f_2)\right|^2 \sum_{i=1}^{N} \left|u_i(f_1 + f_2)\right|^2} \tag{4.21}$$

where $u_i(f_1)$ is the temporal Fourier mode of the velocity component i at frequency f_1 and the star denotes the complex conjugation. Time signals are split into N individual time windows over which the Fourier components are calculated using the same approach as for the power spectrum discussed previously. As N increases, the bicoherence $B^2(f_1, f_2)$ tends to zero if the amplitude of the frequencies f_1, f_2 and $f_1 + f_2$ are zero, or if the phase of each of these frequencies are uncorrelated. Values of the bicoherence close to unity indicate quadratic phase coupling, where the signal phases ϕ_1, ϕ_2 and ϕ_3 at frequencies f_1, f_2 and $f_3 = f_1 + f_2$,

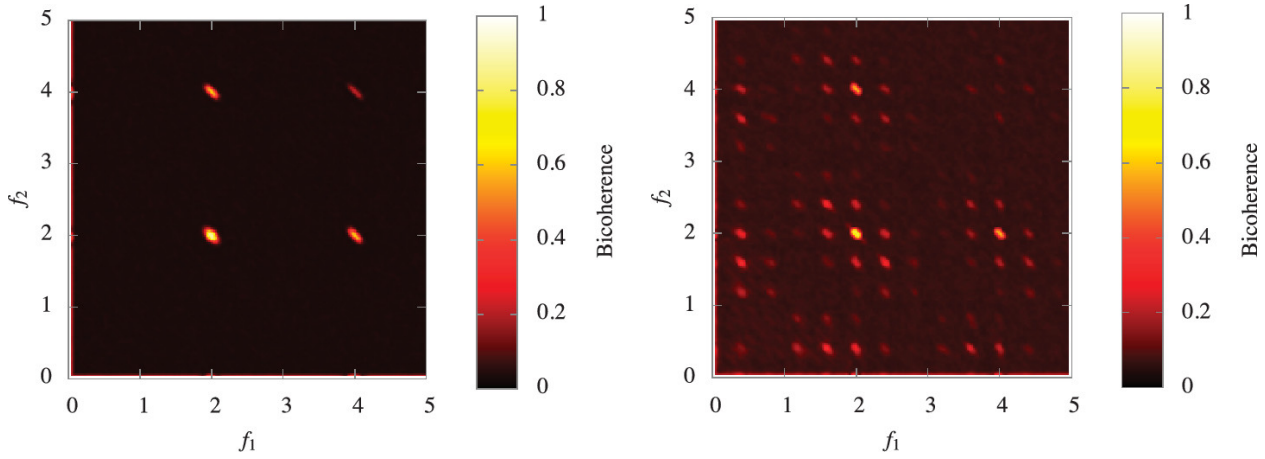

Figure 4.10: Bicoherence as defined by equation (4.21) for cases $A2$ (left) and $A4$ (right). Values close to unity indicates a near-perfect phase coherence between energetic modes at frequencies f_1, f_2 and $f_1 + f_2$.

respectively, follow the relation $\phi_3 = \phi_1 + \phi_2$. We show in Figure 4.10 the bicoherence map for cases $A2$ and $A4$. We average the results over 50 different probe signals, all three components of the velocity and splitting each time signal into 30 smaller temporal windows. For case $A2$ where only the inertial modes $\omega = 2$ are excited, a clear peak in the bicoherence is seen for $f_1 = f_2 = 2$ indicating coherent phases between modes at those frequencies. As the Ekman number decreases, the other modes already discussed in Figure 4.7 are also phase coherent, as indicated by large values of the bicoherence. This further confirms that the observed frequencies $\omega < 2$ are generated by quadratic interactions.

This small window of parameters where the primary elliptical instability saturates in a laminar state is only obtained for $6 \times 10^{-4} < E < 3 \times 10^{-4}$. This is consistent with the experimental results of Eloy et al. (2000) who observed a laminar saturation of the primary elliptical instability for $E > 2.5 \times 10^{-4}$ and with the theoretical results of Kerswell (1999) who predicted that the inertial mode should become linearly unstable to triadic interactions at $E \leq 2.5 \times 10^{-4}$. In our case, smaller values of the Ekman number do not lead to additional resonances but to small-scale disorder. Note that the detailed mechanism by which this transition to turbulence initially occurs remains to be identified. We focus in the next section on the statistical properties of the developed turbulent state.

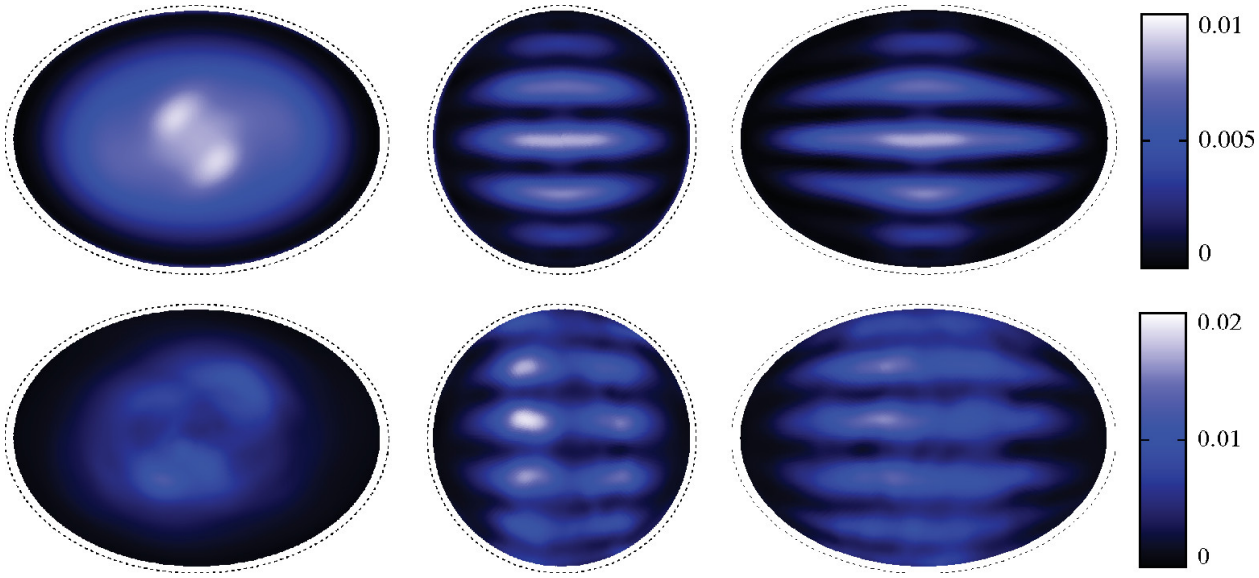

Figure 4.11: Turbulent kinetic energy $\mathcal{K}$ as defined by equation (4.22) plotted on the xy equatorial plane (left), the yz meridional plane (middle) and the xz meridional plane (right). Results at the top correspond to the laminar case $A4$ whereas results at the bottom correspond to the turbulent case $A6$. In both cases, the average required in equation (4.22) is performed over approximately 100 libration periods.

4.5.5 Fully-developed turbulent regime

We now focus our attention on simulations leading to a turbulent saturated regime: cases $A5$ to $A7$. In all turbulent cases, the flow is far from being homogeneous due to the presence of solid boundaries but also due to energy injection mechanism by the sudden breaking of inertial modes. To identify the spatial region where turbulence is preferentially driven, we compute the spatial distribution of the turbulent kinetic energy as follows

$$\mathcal{K} = \frac{1}{2} \left\langle \left(\boldsymbol{u}' - \langle \boldsymbol{u}' \rangle \right)^2 \right\rangle \tag{4.22}$$

where $\boldsymbol{u}' = \boldsymbol{u} - \boldsymbol{U}_b$ is the fluctuating velocity around the base flow given by equation (4.6). The brackets denotes here a temporal average performed over 100 libration periods during the quasi-steady phase. A similar approach has been used to characterize the turbulence driven in a precessing sphere [e.g., Goto et al. (2014)]. The spatial distribution of the turbulent kinetic energy is shown in Figure 4.11 for cases $A4$ (top row) and $A6$ (bottom row). Case $A4$ is still laminar and is shown for reference. In that case, the fluctuating flow is

dominated by the primordial inertial modes $\Lambda_{7,1,6}$, and their signature is clearly visible in the fluctuating kinetic energy (compare with Figures 4.6 and 4.9 for example). Interestingly, the overall layered structure of the inertial modes is also visible in the turbulent kinetic energy distribution associated with the fully-turbulent case $A6$. Note that the average process used in equation (4.22) converges after approximately 20 libration periods for case $A4$, whereas case $A6$ requires averaging over more than 100 libration periods. The maximum of the turbulent kinetic energy in the turbulent case occurs when the amplitude of the inertial modes is maximum. This correlation between the structure of the inertial modes and the turbulent kinetic energy indicates that the primordial inertial modes are still being excited even after the instability saturates and remain of larger amplitude than the small-scale turbulent flow. Even if turbulence is filling most of the ellipsoid, only motions generated at the maximum of the inertial modes amplitudes are long-lived and continuously fed by the instability whereas other fluctuating motions cascade to small-scales and are rapidly dissipated by viscosity.

We now repeat the same spectral analysis as in Section 4.5.4, in order to extract the temporal power spectra in the turbulent regime. The time signals are multiplied by a Hanning window over 200 libration periods and we average the results over 100 different probes located within the bulk of the ellipsoid. Figure 4.12(a) shows the corresponding spectra in log-log scale, where we also plot the results corresponding to cases $A2$ and $A4$, already discussed in Section 4.5.4. It is clear that, for $E \leq 2 \times 10^{-4}$, the spectra are now continuous with a large range of excited frequencies. The zonal flow (not visible in this logarithmic scale), the base flow and primordial inertial modes are still clearly distinguishable and dominate the spectra for all Ekman numbers considered. The secondary quadratic interactions involving $\omega = 0.4$ and $\omega = 1.6$ are also still observable whereas the frequencies $\omega = 0.8$ and $\omega = 1.2$ are now dominated by low-frequency components with a rather flat spectrum. As the Ekman number decreases, the high-frequency part of the spectrum is more and more populated, which further confirms that the flow is in a developed and sustained state of turbulence, with small spatial scales and short time scales. The dash dot line shown in Figure 4.12(a) corresponds to a slope ω^{-3} and is shown for reference. Note that from an energetic point

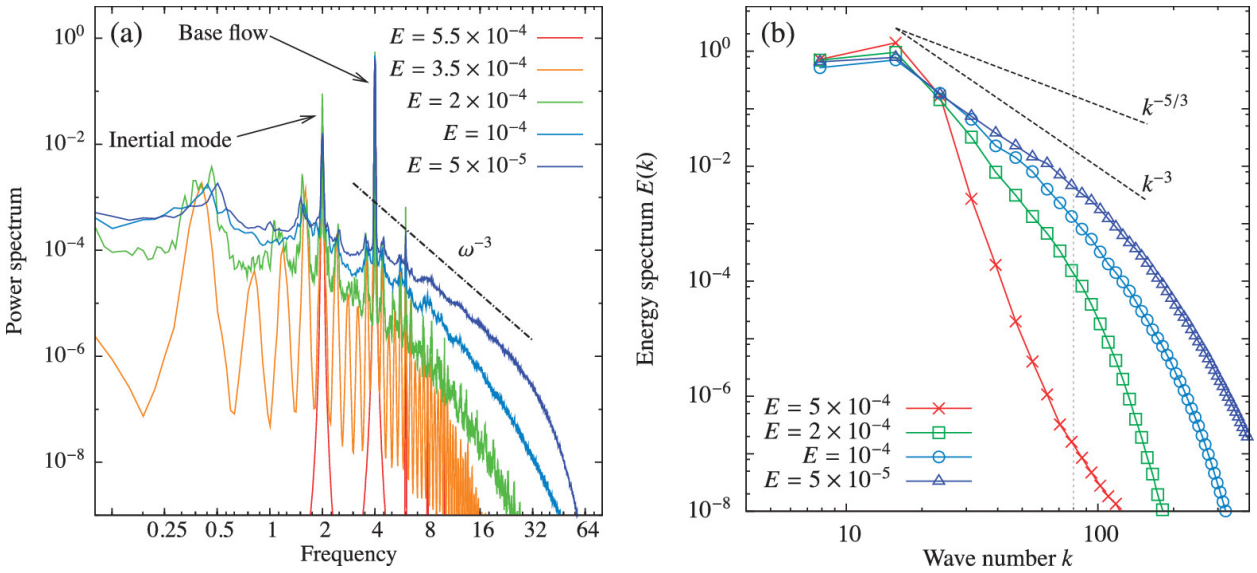

Figure 4.12: (a) Temporal power spectrum averaged over 100 probes distributed within the ellipsoid. The temporal spectral analysis is performed after the instability has saturated. The dash dot line corresponds to the power law ω^{-3} and is shown for reference. (b) Spatial power spectrum computed inside a cube centered around the origin. Velocity signals are made spatially-periodic by using the window function (4.19) in all three directions and the resulting energy spectra are time-averaged during the saturated phase. The vertical dashed line indicates the Zeman scale as defined in the main text.

of view, the sustained turbulent regime is still dominated by the base flow, followed by the primary inertial modes (which is consistent with the result presented in Figure 4.11), the secondary inertial modes and finally the small-scale turbulent flow.

Additional information can be obtained by looking at the energy distribution among the different spatial scales of the flow. As discussed above, the turbulent flow is inhomogeneous but we nevertheless use a Fourier decomposition. We focus on a cube centered around the origin and with side 0.8, fully enclosed inside the ellipsoid and outside of the boundary layers. The velocity components are interpolated with spectral accuracy on a uniform Cartesian grid and the periodicity is enforced using the window function (4.19) in all three directions. The energy spectrum is then computed as

$$E_K(k) = \sum_{k-1/2<|\boldsymbol{k}|<k+1/2} \hat{\boldsymbol{u}}(\boldsymbol{k}) \cdot \hat{\boldsymbol{u}}^*(\boldsymbol{k}) \tag{4.23}$$

where $\hat{\boldsymbol{u}}(\boldsymbol{k})$ is the three-dimensional Fourier transform of $\boldsymbol{u}(\boldsymbol{x})$ and the star denotes complex

conjugation. The resulting spatial energy spectra are shown in Figure 4.12(b), where the results are further averaged over time during the saturated phase. As the Ekman number decreases, small spatial scales appear and a tendency toward a scaling $E(k) \propto k^{-3}$ is observed. Such a scaling for the energy spectrum has also been observed in homogeneous simulations of the elliptical instability using a shearing-box approximation and a tidal forcing [e.g., Barker and Lithwick (2013)]. We recall that the small-scale Rossby number is below unity for all our simulations (see Table 4.1). The exponent observed in our temporal and spatial energy spectra could therefore be related to the effect of the background rotation on the small-scale turbulence generated by the inertial mode breaking. In the case of homogeneous rotating turbulence, a transition from the usual $-5/3$ scaling of Kolmogorov theory to the steeper -3 scaling is associated with a reduction of the forward energy cascade due to Coriolis effects [e.g., Cambon et al. (1997)]. Note however that our Rossby number is close to unity ($Ro \approx 0.5$ for case $A7$ for example). We therefore expect the Kolmogorov scaling to reappear at small scales as the effective Rossby number increases. The reisotropization of rotating turbulence is usually associated with the so-called Zeman scale [e.g., Zeman (1994); Zhou (1995)] defined as $l_\Omega = \sqrt{\epsilon_t/\Omega_0^3}$, where ϵ_t is the dissipation rate and Ω_0 the rotation rate. Using the bulk dissipation rate from case $A7$, the critical wave number associated with this Zeman scale is $k_\Omega \approx 80$, which correspond to the end of the inertial range as indicated by the vertical dashed line in Figure 4.12(b). It is therefore possible that for even lower Ekman numbers, we would observe an isotropic state of turbulence at scales smaller than l_Ω, as it has already been reported in the case of homogeneous rotating turbulence [e.g., Mininni et al. (2012); Delache et al. (2014)]. We cannot verify this claim at this stage since we are limited in the range of spatial scales we can consider, having to solve for the large-scale elliptical base flow responsible for the instability in addition to the small-scale turbulent flow.

4.5.6 Reducing the eccentricity

In order to compensate for the dissipation in the viscous boundary layers, we have to consider sufficiently large values of the deformation β for the elliptical instability to be numerically tractable (*i.e.* for the growth rate to be large enough). So far, the value we considered was

$\beta = 0.34$, which was chosen to be the same as in the laboratory experiment of Grannan et al. (2014). However, the eccentricity of celestial objects is usually much smaller [e.g., Noir et al. (2009); Cébron et al. (2012a)] so that decreasing β and studying its effect on the resulting flow is of interest.

In this section, we repeat simulation $A6$, but with a reduced equatorial deformation of $\beta = 0.17$ and $\beta = 0.26$ (cases $B1$ and $B2$ respectively in Table 4.1). For all cases, the aspect ratio $c/b = 1$ and the Ekman number $E = 10^{-4}$ are kept constant. By reducing β, we reduce the super-criticality and, thus, the growth rate σ of the instability (see the growth rate defined by equation (4.10)). This means that our simulation are getting closer and closer to the onset of the elliptical instability. One would like to keep reducing E as β is decreased in order to keep the ratio E/E_c constant, but this is unfortunately not numerically feasible with our current computing capabilities.

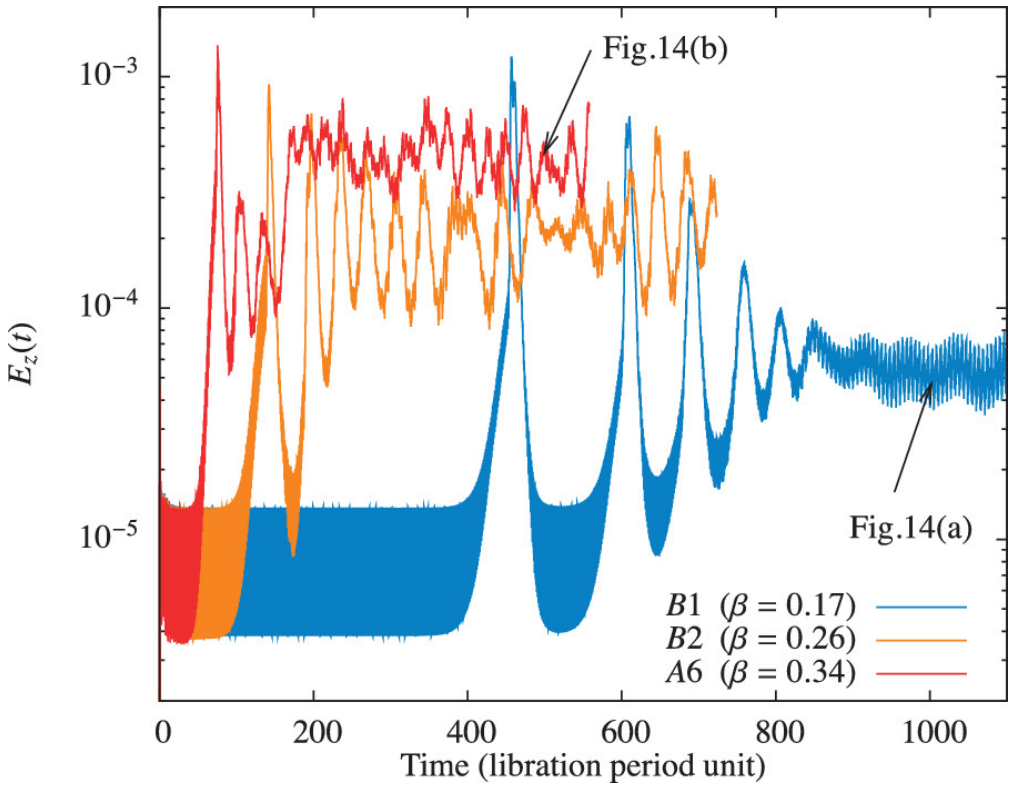

Figure 4.13: Volume averaged vertical kinetic energy for three different ellipticities of the container (cases $B1$, $B2$ and $A6$). Apart from β, the parameters are the same for all three cases. The arrows indicate the times at which the visualizations shown in Figure 4.14 are realized.

The time evolution of the volume averaged vertical kinetic energy is shown in Figure 4.13 for the three cases $\beta = 0.17$, 0.26 and 0.34. As expected, the growth rate of the instability is reduced as β is decreasing. In addition, the final amplitude at which the instability saturates is again decreasing as β decreases. The main difference between the three cases lies in the transient phase before the eventual quasi-steady saturation. As already observed in Section 4.5.1 for $\beta = 0.34$, the laminar state is never recovered after the instability grows. The first saturation does lead to a decay in the vertical kinetic energy for a short time, but another growth eventually takes place and a quasi-steady state is reached after a couple of cycles. This is at odds with the case $\beta = 0.17$, where a complete relaminarisation of the flow is observed after the first development of the instability (around $t \approx 500$ in Figure 4.13 for example). In addition, many cycles of growth and collapse are required to eventually reach a quasi-steady phase. The saturated phase is still moderately turbulent, but the small-scale Reynolds is much smaller than for $\beta = 0.34$. The case $\beta = 0.26$ is somewhere in between, with alternation between intermittent phases (for $t \approx 300$ or $t \approx 700$ for example) and sustained phases (for $t \approx 500$). Note that in all cases, we still observe the same resonance mechanism (primordial inertial modes excited by the elliptical instability followed by subsequent triadic interactions) although the frequencies of the modes involved are slightly shifted due to the change in geometry. As in Figures 4.7, 4.8 and 4.12, the inertial modes are still dominating the spectrum in the frequency range $0 < \omega < 2$. This is, however, only true for our cases in which E is fixed and β is varied. It might not be applicable to the geophysically relevant regime where both E and β are reduced simultaneously in order to remain far from the instability threshold.

This transition between a sustained level of turbulence and an intermittent regime has already been observed in shearing-box simulations of the elliptical instability in a tidal forcing context [e.g., Barker and Lithwick (2013)]. In that paper, the authors found a critical value for the eccentricity of the streamlines of $\beta \approx 0.15$ above which a sustained level of turbulence activity is observed. While our setup is different due to the presence of solid boundary conditions and the use of a librational forcing to excite the elliptical instability, the transition observed in our simulations might be of similar nature. We indeed observe

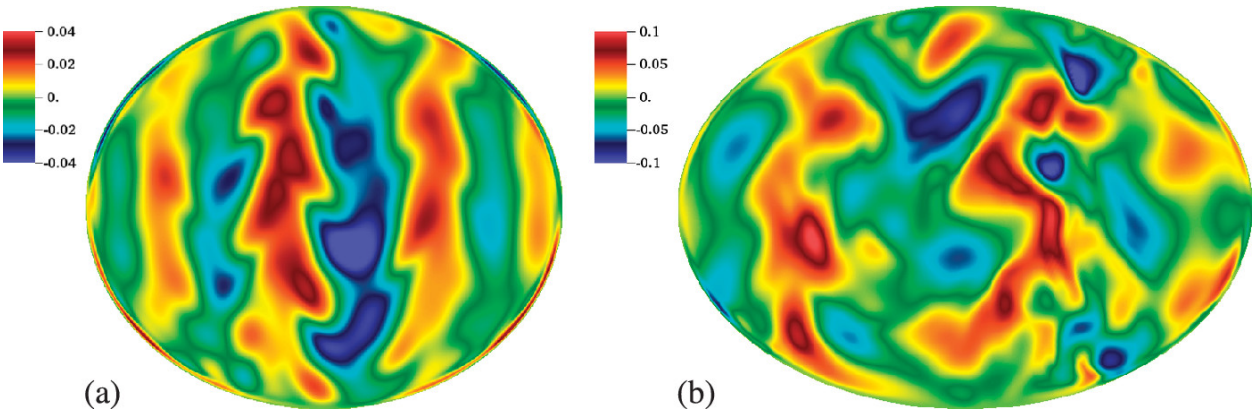

Figure 4.14: Vertical component of the velocity in the (x, z) meridional plane during the saturated phase for (a) $\beta = 0.17$ ($t \approx 1000$) and (b) $\beta = 0.34$ ($t \approx 500$), as indicated by arrows in Figure 4.13.

a very long intermittent transient when $\beta = 0.17$, so that it is possible that an even lower value of the equatorial deformation would only lead to an intermittent behavior. However, due to the stabilizing effect of viscous dissipation, it is not possible to further reduce β while keeping the growth rate sufficiently large for the instability to be numerically tractable.

Barker and Lithwick (2013) argued that the presence of large-scale vortices invariant in the vertical direction is responsible for the decay observed after the initial collapse. This columnar flow is produced by the decay of the small-scale turbulence under the influence of rotation and could damp the resonances required to sustain the small-scale turbulence. There are indeed indications that such a vertically-invariant flow does develop in our simulations as β is decreased, as can be seen in Figure 4.14, where we show the vertical velocity at an arbitrary time during the saturated phase in a meridional plane for both $\beta = 0.17$ and $\beta = 0.34$. We observe vertically-coherent structures for the case with $\beta = 0.17$ whereas the flow appears to be more isotropic when $\beta = 0.34$. In addition, reducing β is also dramatically increasing the importance of viscous effects as can be seen in Figure 4.13 where the growth rate rapidly decreases with β. A detailed analysis of the interaction between these large-scale coherent structures and the inertial modes excited by the elliptical instability is beyond the scope of this paper. It therefore remains to be seen whether the elliptical instability saturates in an intermittent or quasi-steady manner in the geophysical regime at low-β *and* low-E. This is a crucial question since the efficiency of the elliptical instability in terms of energy

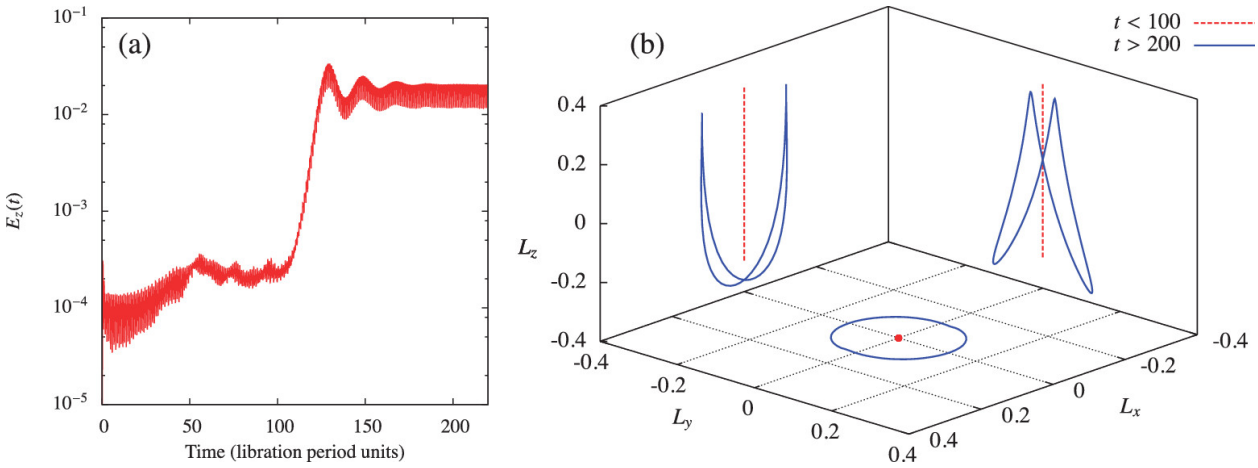

Figure 4.15: Results for case $C1$ with $f = 2.4$, $\epsilon = 1.2$ and $E = 10^{-4}$. (a) Time evolution of the vertical kinetic energy. (b) Phase diagram of the three components of the angular momentum. We show the two-dimensional projections $(L_x(t), L_y(t))$, $(L_x(t), L_z(t))$ and $(L_y(t), L_z(t))$, on each side.

dissipation and dynamo action is at play.

4.5.7 Varying the librating frequency

In this section, we briefly discuss the behavior of the system for another librating frequency $f = 2.4$. It was shown experimentally by Grannan et al. (2014) that varying the librating frequency leads to a variety of behaviors as the resonant modes change. One of the reasons why we focus on the $f = 4$ case so far is that it is very easy to obtain a turbulent regime numerically since the critical Ekman number for instability is quite large. This might be related to the peculiar spatial structure of the inertial modes with $|\omega| \lesssim 2$, as shown in Figure 4.6. As the librating frequency decreases, turbulence is only observed for more extreme values of the control parameters. At the fixed experimental Ekman number of $E = 2 \times 10^{-5}$, the critical libration amplitude ϵ to reach a turbulence regime is $\epsilon \approx 0.12$ for $f = 4$, whereas it is $\epsilon \approx 0.7$ for $f = 1.46$ (see Figure 5 in Grannan et al. (2014)). For these reasons, numerical simulations of the libration-driven elliptical instability at lower libration frequencies are only turbulent for large values of the libration amplitude. This leads to numerical complications as the boundary layers can then be unstable to centrifugal instabilities, eventually leading to turbulence before the elliptical instability develops.

As an example of other flows driven by the saturation of the elliptical instability, we consider the case $f = 2.4$, $\epsilon = 1.2$, $\beta = 0.34$ and $E = 10^{-4}$. Figure 4.15(a) shows the time evolution of the squared vertical velocity. Contrary to the case $f = 4$, the Ekman boundary layers do not remain laminar during the initial phase of the instability. Taylor-Görtler vortices are generated through a centrifugal instability in the equatorial boundary regions [e.g., Calkins et al. (2010)]. This is a direct consequence of the large value of ϵ considered here. The fluctuations associated with these vortices are visible in Figure 4.15(a) for $0 < t < 100$. The exponential growth phase is clearly visible for $100 < t < 150$ and is followed by the saturation of the instability. Note that the saturated phase corresponds to a quasi-steady evolution of the kinetic energy, contrary to the case with $f = 4$, where a strongly fluctuating regime with low frequency modulations is observed at $E = 10^{-4}$. The flow is not turbulent (as can be seen on the power spectrum or by direct visualization, not shown), but dominated by a large-scale periodic flow. The amplitude of this large-scale flow is much larger than the typical turbulent fluctuations observed for $f = 4$ (see the values of $U_{\rm rms}$ in Table 4.1 or the typical amplitude of E_z in Figures 4.15(a) and 4.2(a)).

The main difference with the case $f = 4$ is the angular momentum evolution. For $f = 4$, the angular momentum remains purely vertical during the numerical experiment, even in the saturated quasi-steady phase. This is not the case for $f = 2.4$ and the horizontal components of the angular momentum grow in amplitude when the instability starts to saturate. Figure 4.15(b) shows the phase diagram of the volume-averaged angular momentum defined as

$$\boldsymbol{L} = \int_V \boldsymbol{x} \times \boldsymbol{u} \, \mathrm{d}V \ . \tag{4.24}$$

Initially (*i.e.* for $t < 100$), the Poincaré force generates a quasi-horizontal flow with dominant vertical angular momentum. As the instability develops, the horizontal components start to grow in amplitude while the periodic variations of the vertical component remain nearly unchanged. Finally, in the quasi-steady saturated phase, the direction of the angular momentum corresponds to the combination of a quasi-circular evolution of the horizontal angular momentum and the oscillating vertical component driven by the Poincaré force. The

generation of a significant horizontal angular momentum is related to the excitation of the spin-over mode [e.g., Lacaze et al. (2004); Cébron et al. (2010a)] and is clearly visible when looking at the streamlines during the saturated phase, as shown in Figure 4.16. Note that such a large-scale flow does not remain laminar as the Ekman number decreases and it is indeed turbulent according to case IV of Grannan et al. (2014) for which $E = 2 \times 10^{-5}$, but this turbulent regime is unfortunately not within reach of our numerical simulations. The amplitude of the excited flow therefore crucially depends on the excitation of the spin-over mode, and therefore on the libration frequency. When the spin-over mode is not excited (as in the case $f = 4$), the amplitude of the fluctuations remains small when compared to the initial base flow, whereas they can become comparable when the spin-over mode is excited. More detailed studies about the excitation and saturation of the spin-over mode depending on the geometry, boundary conditions and type of mechanical forcing are therefore needed.

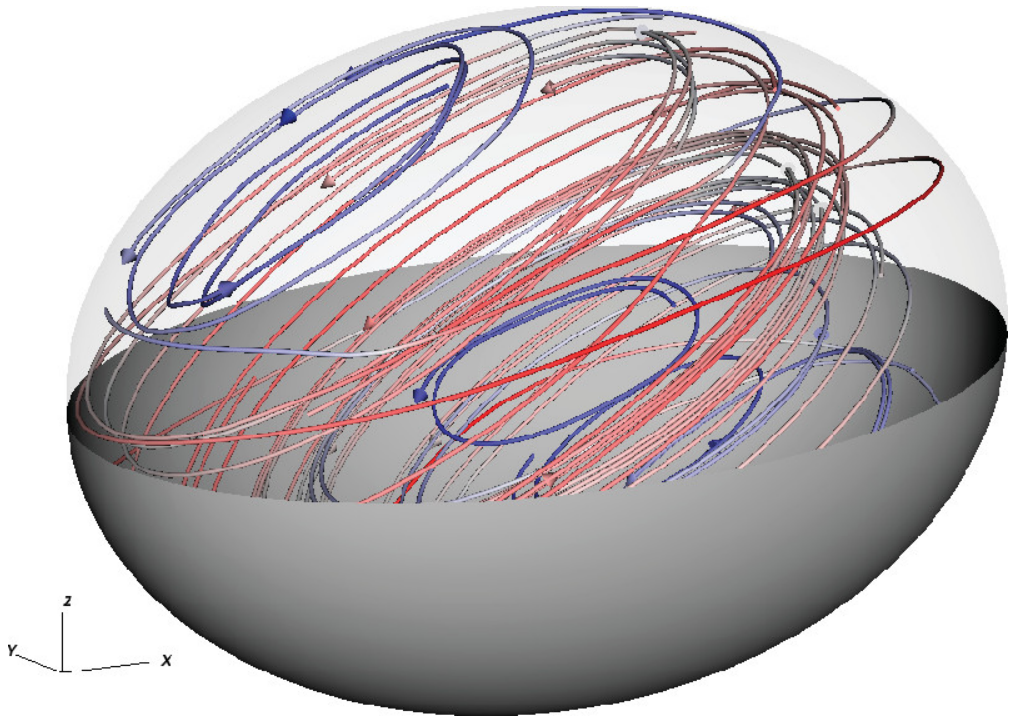

Figure 4.16: Streamlines during the saturated phase colored with the flow speed for case $C1$ in Table 4.1 with $f = 2.4$, $\epsilon = 1.2$ and $E = 10^{-4}$.

4.6 Conclusion

We have qualitatively and quantitatively compared numerical and laboratory measurements of fluid motions inside a longitudinally-librating rigid ellipsoid. In order to reduce the large number of control parameters, we have mostly focused on the interesting case $f = 4$ for a fixed geometry $\beta = 0.34$ and $c/b = 1$, and for a fixed librating amplitude $\epsilon = 0.8$. As the Ekman number is reduced, the elliptical instability is excited and we observe a transition from a laminar saturation to a fully-developed sustained turbulent state. We observed both numerically and experimentally that the saturation of the elliptical instability drives an enhanced zonal flow whose amplitude increases as the Ekman number decreases. This is at odds with the zonal flow driven by nonlinearities in the Ekman boundary layers associated with the base flow only, which does not depend on the Ekman number and is therefore not relevant from a geophysical point of view.

The transition to turbulence is characterized by a succession of resonances between the dominant inertial modes at half the frequency of the forcing and the base flow, followed by additional triadic interactions between the dominant modes and other inertial modes of the ellipsoid. For the parameters considered, the turbulent saturation is characterized by an initial collapse of the primary inertial modes eventually leading to a sustained turbulent flow provided that the Ekman number is low enough (typically $E < 3 \times 10^{-4}$). The resulting bulk turbulence is best characterized as rotating turbulence with a spatial and temporal energy spectra scaling approaching k^{-3} and ω^{-3} respectively. The turbulence is however strongly inhomogeneous and is still being dominated by the primary inertial modes. As the eccentricity is reduced, a more intermittent regime is observed, with a complete relaminarization in some cases.

The current numerical and laboratory models are limited to large elliptical deformation and moderately low Ekman numbers. We consider cases which have centrifugally stable boundary layer flows in order to focus on the generation of bulk turbulence by the elliptical instability alone, but the interplay between these two instabilities could be of interest [e.g., Sauret et al. (2013)]. We have focused our analyses on the particular case $f = 4$, for which

turbulence is more easily observed than for other librating frequencies and for which the spin-over mode is not excited. Finally, the fundamental difference between the sustained and intermittent turbulence regimes, and their respective relevance for planetary flows, needs to be addressed. Thus, further progress in understanding the generic features of the saturation of the elliptical instability and its relevance to geophysical flows will require additional work.

CHAPTER 5

Tidally-forced turbulence in planetary interiors

Reproduced from: **A. M. Grannan**, B. Favier, M. Le Bars, and J. M. Aurnou. *Geophys. J. Int.*, **208**(3): 1690-1703, 2017.

This work was performed at the IRPHE Laboratory in Marseille, France and was facilitated by a Chateaubriand Fellowship that funded me for a nine-month stay in Marseille. I designed and built a support for a new wireless camera used to perform PIV in the rotating frame. I performed and analyzed all of the laboratory experiments that were then compared to high resolution numerical simulations performed by Benjamin Favier. This work provides the first quantitative description of the tide-driven elliptical instability, TDEI. The mathematical formalism underpinning TDEI and LDEI and the resulting excited turbulence is shown to be generic despite the fact that tides and libration represent end-member types of planetary forcing. The velocity scaling when the TDEI saturates is shown to scale with the ellipsoidal distortion β. In planetary bodies where $\beta < 10^{-4}$, this scaling is significantly larger than the β^2 scaling found for zonal flows and thus may play a crucial role in planetary processes. I am the principal author of this paper.

5.1 Introduction

Observations made from Earth and from spacecraft missions suggest the presence of liquid metal cores in terrestrial bodies like Mercury [Stark et al. (2015)], Mars [Yoder et al. (2003)], Io [Anderson et al. (1996)], and Ganymede [Schubert et al. (2004), as well as subsurface oceans in Europa [Anderson et al. (1998)], Ganymede [Schubert et al. (2004)], and Enceladus [Cedak et al. (2016); Thomas et al. (2016)]. Gravitational interactions between a

variety of celestial bodies, from stars and planets to satellites and asteroids, can periodically perturb both a body's shape and the direction and magnitude of its rotation vector. Such perturbative effects can generate mechanical forcing of interior fluid motions through libration, tidal deformation, and precession/nutation [Comstock and Bills (2003); Van Hoolst et al. (2013)].

Paleomagnetic measurements of rock samples from smaller terrestrial bodies reveal the remnant signatures of self-generated dynamo fields [e.g., Garrick-Bethell et al. (2009), Tarduno et al. (2012); Fu et al. (2012); Johnson et al. (2015)]. The assumed driver for the fluid motions responsible for dynamo generation is thermo-compositional convection [e.g., Jones (2011); Schubert and Soderlund (2011); O'Rourke and Stevenson (2016)]. However, the existence of dynamos on smaller bodies is difficult to reconcile with our current understanding of the conditions necessary for magnetic field generation in terrestrial bodies through thermo-compositional convection alone [e.g., Nimmo (2009); Pozzo et al. (2012); Olson (2013); Zhang et al. (2015)]. Thus, recent numerical studies, [e.g., Tilgner (2005); Wu and Roberts (2009, 2013); Cébron and Hollerbach (2014); Wei et al. (2014)] have begun to address how mechanical forcing can also drive dynamos by injecting a portion of the vast quantity of rotational energy from the primary-satellite orbital systems into the interior fluid motions. However, even the basic properties of turbulence generated by mechanical forcing are not yet well characterized.

The current work focuses on comparing new results from purely hydrodynamic analog models of tidal forcing with previous studies of longitudinal librational forcing, referred hereafter as librational forcing. In order simulate the basic physics of such flows one important ingredient is the shape of the planetary body and, by extension, the layers that bound a fluid layer. This problem of determining the equilibrium shape of a body due to gravitational forces, rotation, density distribution, material rigidity, and even internal dynamics is generally referred to as the theory of figures [e.g., Chandrasekhar (1969); Kippenhang et al. (1990); Van Hoolst et al. (2008); Cébron et al. (2012a); Kong et al. (2012)]. At the lowest order, the rotation of the body leads to polar flattening and an equatorial bulge while gravitational forcing from an orbiting attractor tends to deform the body into an ellipsoidal figure

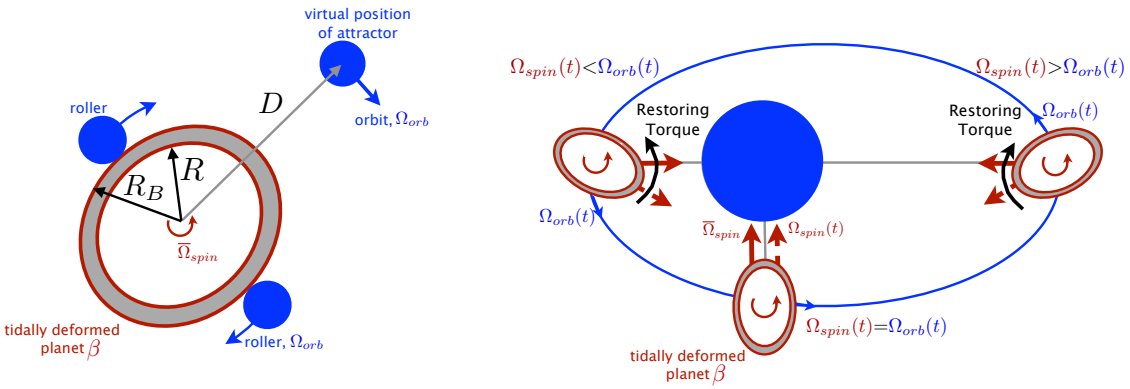

Figure 5.1: **a)** A polar-view of the model for a tidally deformed elastic body of amplitude β with a fluid interior spinning at $\overline{\Omega}_{spin}$. A virtual attractor orbiting at $\Omega_{orbit}(t)$ is simulated in experiments by using two symmetric rollers. The deformed body's r.m.s radius is R_B, the fluid radius is R, and the average distance between the two bodies is D. **b)** A polar-view of the model for longitudinal libration of a rigid synchronous planet with a fluid interior rotating at $\Omega_{spin}(t)$, and orbiting at $\Omega_{orbit}(t)$ where, when time-averaged, $\overline{\Omega}_{spin} = \overline{\Omega}_{orbit}$. The solid red arrow denotes the direction toward the gravitational partner. The dashed red arrow denotes the direction of the long axis of the deformed ellipsoid. The misalignment between the two red arrows leads to restoring torques (black arrow) that oscillate the deformed boundary. Schematics adapted from Le Bars et al. (2010); Noir et al. (2012).

[e.g., Stacy and Davis (2008)]. As such, two methods are used simulate the motion of fluid boundary in orderto investigate the flow driven by mechanical forcing. The first method is to solve the linearized Laplace Tidal Equations where the gravitational forcing potential that varies in time and space is the primary driver [e.g., Tyler (2008, 2014); Chen et al. (2014); Matsuyama (2014); Kamata et al. (2015)].

The second method, used by Malkus (1989); Le Bars et al. (2010); Morize et al. (2010); Sauret et al. (2014) and in the current work, imposes an ellipsoidally deformation and the differential motion of the boundary relative to the fluid layer in order to investigate the fully-nonlinear response to mechanical forcing. Models of tidal and librational forcing in deformed bodies are shown in polar view in Figure 5.1.a and 5.1.b, respectively. For tides and libration, the fluid enclosed by the gray-colored ellipsoidal shell is constrained by a time-averaged angular rotation rate, $\overline{\Omega}_{spin}$. In Figure 5.1.a, a planet having low rigidity and hence a high tidal potential Love number k_2, is deformed by an orbiting attractor [e.g., Suess (1969); Greff-Lefftz et al. (2005)]. As such, the planet and boundary deformation rotate at

separate rates $\overline{\Omega}_{spin}$ and Ω_{orb}, respectively.

In librational forcing of a rigid (low k_2), synchronized planet, the *time-averaged* spin and orbital rates are equal, $\overline{\Omega}_{spin} = \overline{\Omega}_{orb}$ [e.g., following the $\Re \gg 1$ limit in Goldreich and Mitchell (2010)]. The model for this librational forcing is shown schematically in Figure 5.1.b The eccentricity of the orbit leads to variations in the orbital rate following Kepler's third law and creates a phase lag between the equatorial bulge and the line connecting the centers of mass for the two bodies as shown by the dashed and solid red arrows in Figure 5.1.b, respectively. Periodic torques, shown as black arrows, are induced to restore this alignment, leading to oscillations in the rotation rate, $\Omega_{spin}(t)$, of the deformed boundary about the average spin rate $\overline{\Omega}_{spin}$.

Mechanical forcing through tides and libration is capable of generating laminar and turbulent fluid motions in the bulk of the fluid. It has been well-established that a laminar zonal flow is generated by the non-linear self interaction of the viscous flow in the boundary layer [e.g., Wang (1970); Suess (1971); Busse (2010); Calkins et al. (2010); Noir et al. (2010); Sauret et al. (2010); Chan et al. (2011); Zhang et al. (2011)]. However, at planetary settings, these laminar flows are expected to be weak and we will focus instead on the generation of turbulent flow.

The generation and characteristics of bulk turbulence driven by mechanical forcing is less well understood but crucial for understanding many planetary processes including tidal dissipation. It is well known that for the Earth, the ocean is primarily responsible for tidal dissipation [e.g., Egbert and Ray (2003)]. However, considering other planetary bodies, many previous studies have considered tidal dissipation in the solid planet and neglected any contributions from lower viscosity fluid layers [e.g., Williams and Boggs (2015)]. More recent studies have begun to consider the dynamic response of these fluid layers to directly forced resonances from surface gravity waves, planetary Rossby waves where the Coriolis forces of the rotating body provides a restoring force, and viscous drag at the fluid-solid interface [e.g., Tyler (2008, 2014); Chen et al. (2014); Matsuyama (2014); Kamata et al. (2015)]. In this work, we take a different approach by considering *indirectly* forced resonances where the Coriolis force alone provides the restoring force and can drive turbulence in the entire fluid

layer.

A necessary ingredient for such indirectly forced turbulence is the presence of flows with elliptically deformed streamlines that can then support elliptical instabilities. This instability is a parametric resonance between the elliptically deformed flow and two resonating inertial modes of the system [e.g., Kerswell (2002)]. The instability was found in elliptically deformed flows driven by tidal and librational forcing and referred to as tide- (libration-) driven elliptical instability, TDEI (LDEI) [e.g., Kerswell and Malkus (1998); Le Bars et al. (2007, 2010); Cébron et al. (2012b)]. In both TDEI and LDEI, the periodic forcing of an ellipsoidal cavity can generate a triadic resonance between the inviscid elliptically deformed base flow and two inertial modes of the system that can globally destabilize the layer leading to bulk turbulence.

Parameter	Definition	Tides	Libration
Equatorial ellipticity	β	$\frac{a^2-b^2}{a^2+b^2}$	$\frac{a^2-b^2}{a^2+b^2}$
Mean rotation rate		$\overline{\Omega}_{spin}$	$\overline{\Omega}_{spin}$
Ekman number	$E = \frac{\text{Viscous Force}}{\text{Coriolis Force}}$	$\frac{\nu}{\overline{\Omega}_{spin} R^2}$	$\frac{\nu}{\overline{\Omega}_{spin} R^2}$
Elliptical distortion rotation rate		Ω_{orb}	$\Omega_{spin}(t) = \overline{\Omega}_{spin} + \omega_{lib}\Delta\phi \sin(\frac{\omega_{lib}}{\overline{\Omega}_{spin}} t))$
Elliptical distortion frequency		$\omega_{tide} = 2(\overline{\Omega}_{spin} - \Omega_{orb})$	ω_{lib}
Forcing frequency ratio	$f_{tide,lib} = \frac{\omega_{tide,lib}}{\overline{\Omega}_{spin}}$	$2(1 - \frac{\Omega_{orb}}{\overline{\Omega}_{spin}})$	$\frac{\omega_{lib}}{\overline{\Omega}_{spin}}$
Rotation rate ratio	$\gamma_{tide,lib} = \frac{\text{Elliptical dist. rotation rate}}{\text{Mean rotation rate}}$	$\frac{\Omega_{orb}}{\overline{\Omega}_{spin}}$	$1 + f_{lib}\Delta\phi \sin(f_{lib} t)$
Forcing amplitude	$\epsilon_{tide,lib} = (1 - \gamma_{tide,lib})_{max}$	$f_{tide}/2$	$f_{lib}\Delta\phi$
Inviscid growth rate	$\sigma_{inv}^{tide,lib}$	$\frac{\epsilon_{tide}\beta}{64}(4 + f_{tide})^2$	$\frac{\epsilon_{lib}\beta}{16}(16 + f_{lib})^2$

Table 5.1: Comparison of tidal and librational forcing parameters. The definitions for equatorial ellipticity, β, mean rotation rate, $\overline{\Omega}_{spin}$, and the Ekman number, E are shared by both types. The differences arise in how the mechanical forcing is implemented at the boundary. In the current work, $f_{tide,lib} = 4$ is fixed allowing for a comparison between both mechanisms.

TDEI experiments in a deformable sphere and cylinder have shown, through side-view visualizations, that this triadic resonance between the base flow and two inertial modes can generate either intermittent or saturated turbulence [e.g., Lacaze et al. (2004, 2005); Le Bars et al. (2007, 2010)]. These works confirmed the instability regime, growth rates, and the turbulent transition associated with the TDEI. Recent LDEI studies in rigid ellipsoids have also shown both intermittent and saturated globally turbulent flows [e.g, Cébron et al. (2012b); Noir et al. (2012); Grannan et al. (2014); Favier et al. (2015)]. The aspects of, and instabilities related to, mechanically forced flows are reviewed in Le Bars et al. (2015).

We perform experiments here measuring, for the first time, the TDEI-driven flow velocities in the equatorial plane of a deformable spherical container. These results are coupled with selected direct numerical simulations (DNS). For these studies, the Ekman number, $E = \nu/(\overline{\Omega}_{spin} R^2)$, is defined as the ratio of viscous to Coriolis forces where ν is the kinematic viscosity, $\overline{\Omega}_{spin}$ is the mean rotation rate, and R is the r.m.s elliptical boundary radius. For the laboratory experimental and numerical work, the Ekman number is fixed at $E = 1.5 \times 10^{-5}$ and $E = 5 \times 10^{-5}$, respectively. Such efforts incorporate the more extreme parameters available to experiments with the full flow field available to numerical simulations.

We extend the previous experimental and numerical studies of libration in a rigid cavity with a fixed deformation at the dimensionless frequency, $f_{lib} = 4$ [e.g., Grannan et al. (2014); Favier et al. (2015)]. In our studies of TDEI, we fix the dimensionless frequency at $f_{tide} = 4$. This dimensionless frequency is outside the range for directly forced inertial resonances [e.g., Greenspan (1969)] and allows us then to focus only on the indirect forcing provided by TDEI mechanism.

By comparing the tidal forcing results from the current work with the previous studies of libration, strong similarities between tidal- and libration-driven flows are found, suggesting a generic response of the fluid layer independent of the specific forcing. In Section 5.2, the mathematical framework is developed for tide- and libration-driven flows, the experimental method is described in Section 5.3, and the numerical method is outlined in Section 5.4. The results for tide-driven flows and their comparison with libration-driven flows are provided in

Section 5.5. Finally, our conclusions are summarized in Section 5.6.

5.2 Mathematical Background

In our tidal forcing scenario, we consider a homogenous, incompressible, Newtonian fluid that is enclosed in an ellipsoidal container. The boundary of this ellipsoid is specified by, $x^2/a^2 + y^2/b^2 + z^2/c^2 = 1$, set in a Cartesian coordinate system affixed to the ellipsoid with the long axis, $\hat{\mathbf{x}}$, of length a. The short equatorial axis with length b is along $\hat{\mathbf{y}}$ while $\hat{\mathbf{z}}$ is along the axis of rotation with length c. Non-dimensionalizing the ellipsoid equation using the r.m.s. fluid layer length scale, $R = \sqrt{(a^2 + b^2)/2}$, yields:

$$\frac{x^2}{1+\beta} + \frac{y^2}{1-\beta} + \frac{z^2}{c^{*2}} = 1. \tag{5.1}$$

The equatorial ellipticity of the cavity is defined as $\beta = (a^2 - b^2)/(a^2 + b^2)$, while the axial deformation is $c^* = c/R$.

From a numerical perspective, it is advantageous to work in the reference frame fixed to the elliptical distortion, termed the orbital frame rotating at Ω_{orb}. The generalized equations of motion:

$$\frac{\partial \mathbf{u}}{\partial t} + \mathbf{u}\cdot\nabla\mathbf{u} + 2\gamma(t)\hat{\mathbf{z}}\times\mathbf{u} = -\nabla\Pi + E\nabla^2\mathbf{u} - \frac{\partial\gamma(t)}{\partial t}\hat{\mathbf{z}}\times\mathbf{x}, \tag{5.2}$$

$$\nabla\cdot\mathbf{u} = 0, \tag{5.3}$$

are non-dimensionalized using R as the length scale and the mean spin rate of the fluid, $\overline{\Omega}_{spin}^{-1}$, as the time scale. In (6.4), the first two terms on the left hand side are the inertial terms, and the third term is the Coriolis acceleration. Here,

$$\gamma_{tide} = \frac{\Omega_{orb}}{\overline{\Omega}_{spin}}, \tag{5.4}$$

is the ratio of the elliptical distortion rotation rate to the mean spin rate of the fluid. The forcing frequency felt by a fluid parcel, ω_{tide}, due to the elliptical distortion is related to the both rotation rates by $\omega_{tide} = 2(\overline{\Omega}_{spin} - \Omega_{orb})$. The dimensionless forcing frequency due

to the elliptical distortion is then $f_{tide} = \omega_{tide}/\overline{\Omega}_{spin} = 2(1-\gamma_{tide})$. On the RHS of (6.4), Π is the modified pressure term where the centrifugal acceleration, $-\gamma(t)\hat{\mathbf{z}} \times \gamma(t)\hat{\mathbf{z}} \times \mathbf{x} = \nabla\gamma^2(t)(x^2+y^2)/2$, is absorbed into the pressure gradient. The next term on the right is the viscous diffusion term where $E = \nu/(\overline{\Omega}_{spin}R^2)$ is the Ekman number defining the ratio of the viscous forces to Coriolis forces where ν is the kinematic viscosity.

The final term on the RHS is the Poincaré acceleration associated with the time-dependent elliptical distortion rotation rate. This term is zero for the current tidal forcing studies since γ_{tide} is constant. For tidal forcing, an impermeable, no-slip boundary condition is implemented with a horizontal tangential velocity given by:

$$\mathbf{u}_{b.c.} = (1-\gamma_{tide})\sqrt{\frac{a'^2+b'^2}{2}}\boldsymbol{\tau}, \tag{5.5}$$

where $\boldsymbol{\tau}$ is the normalized tangent vector and $[a', b'] = [a, b]\sqrt{1-z^2/c^2}$. More details are provided in Appendix 5.7.

In the studies of longitudinal libration, the reference frame is fixed to the elliptical distortion such that the equations of motion in (6.4) and (5.3) are still used. However, the ratio of the elliptical distortion rotation rate to the mean spin rate of the fluid now takes the form:

$$\gamma_{lib}(t) = \frac{\Omega_{spin}(t)}{\overline{\Omega}_{spin}} = (1+\epsilon_{lib}\sin(f_{lib}t))\,, \tag{5.6}$$

where $\epsilon_{lib} = f_{lib}\Delta\phi$ is the dimensionless amplitude of librational oscillation where the dimensionless frequency ratio, $f_{lib} = \omega_{lib}/\overline{\Omega}_{spin}$, is the ratio of the elliptical distortion frequency to the mean rotation rate and $\Delta\phi$ is the librational amplitude in radians [e.g., Cébron et al. (2012b); Noir et al. (2012); Sauret (2012); Favier et al. (2015)]. Because of the time-dependence in (5.6), the Poincaré term in (6.4) is now non-zero. Finally, an impermeable, no-slip condition is implemented with $\mathbf{u}_{b.c.} = 0$.

An inviscid solution of (6.4), generalized for tidal or librational forcing in the orbital

reference frame, is given in Cébron et al. (2012a) as:

$$\mathbf{U}_B = (1-\gamma_{tide,lib}) \begin{pmatrix} 0 & -(1+\beta) & 0 \\ 1-\beta & 0 & 0 \\ 0 & 0 & 0 \end{pmatrix} \mathbf{x}, \tag{5.7}$$

where $\mathbf{x} = (x, y, z)$ is a general position vector and $(1-\gamma_{tide,lib})$ is the forcing amplitude. The maximum amplitude of this forcing is defined as $\epsilon_{tide,lib} = (1-\gamma_{tide,lib})_{max}$. The purely horizontal base flow in (5.7) satisfies a non-penetration condition at the boundary and follows the ellipsoidal shape of the container characterized by an azimuthal wavenumber in cylindrical coordinates, $m_{tide,lib} = 2$, and forced at the dimensionless frequency $f_{tide,lib}$ contained in the forcing amplitude $(1-\gamma_{tide,lib})$. The total kinetic energy associated with this flow in the orbital frame is:

$$E_B = \frac{4\pi}{15} (1-\gamma_{tide,lib})^2 \left(1-\beta^2\right)^{3/2} c^* \ . \tag{5.8}$$

It is experimentally advantageous to work in the spin frame fixed at $\overline{\Omega}_{spin}$ and, as such, the base flow is transformed into the spin frame where:

$$\mathbf{U}_{B_{rot}} = (1-\gamma_{tide,lib})\beta \begin{pmatrix} -\sin(2\theta(t)) & -\cos(2\theta(t)) & 0 \\ -\cos(2\theta(t)) & \sin(2\theta(t)) & 0 \\ 0 & 0 & 0 \end{pmatrix} \mathbf{x}_{rot}. \tag{5.9}$$

Here $\mathbf{x}_{rot} = (X, Y, Z)$ is a general position vector in the spin frame and $\theta(t) = \int_0^t (1-\gamma_{tide,lib}(t'))dt'$ is the total angle between the axes of the spin frame and the orbital frame. The total kinetic energy associated with this flow in the spin frame is:

$$E_{B_{rot}} = \frac{4\pi}{15} (1-\gamma_{tide,lib})^2 \beta^2 \left(1-\beta^4\right) c^*. \tag{5.10}$$

To satisfy the no-slip boundary conditions, viscous corrections in the Ekman boundary layer generate a flow linear in β that connects the base flow with the no-slip boundary. The non-linear self-interaction of this $m_{tide,lib} = 2$ flow generates flows of azimuthal wavenumbers

$m = 4$ and $m = 0$, the latter of which is associated with an axisymmetric, steady zonal flow that scales with β^2 in the boundary layer and is independent of the Ekman number [e.g., Sauret (2012)].

Perturbations in rotating fluids can generate inertial waves whose restoring force is the Coriolis force and whose dimensionless frequency is given by the dispersion relation, $\lambda = \omega_{tide,lib}/\overline{\Omega}_{spin} = \pm 2\cos\theta$, where θ is the angle between the wave-vector and the axis of rotation. In closed cavities, reflections and constructive interference support inertial modes with the same frequency range, namely $-2 \lesssim \lambda \lesssim 2$ [e.g. Greenspan (1969); Vantieghem (2014)]. Mechanical forcing can excite these inertial modes, in addition to generating the aforementioned elliptically deformed base flow (5.7). An elliptical instability, (EI) can be generated when two inertial mode frequencies and azimuthal wavenumbers are related to those of the base flow given in Kerswell (2002) by:

$$|\lambda_1 - \lambda_2| = f_{tide,lib}, \tag{5.11}$$

$$|m_1 - m_2| = m_{tide,lib} = 2. \tag{5.12}$$

Using the inertial mode frequency range, the maximum frequency for exciting EI is $f_{tide,lib} \lesssim 4$. Uniquely for tides, since the tidal forcing frequency is given by $f_{tide} = 2(1 - \gamma_{tide})$, this unstable range can be written as $-1 \leq \gamma_{tide} \leq 3$ [e.g., Le Bars et al. (2010)]. In contrast, for libration, γ_{lib}, in (5.6) can take any value to drive elliptical instability as long as the elliptical distortion frequency ω_{lib} is no greater than four times the mean rotation rate (i.e.., $\omega_{lib}/\overline{\Omega}_{spin} = f_{lib} \lesssim 4$).

To calculate the inviscid growth rates, local stability analyses were performed based on the Wentzel-Kramers-Brillouin method in Le Dizes (2000). There it was shown, in the limit of $\epsilon_{tide,lib}, \beta \ll 1$, that the inviscid growth rates for TDEI and LDEI are given respectively as:

$$\sigma_{inv}^{tide} = \frac{\epsilon_{tide}\beta}{64}(4 + f_{tide})^2, \tag{5.13}$$

$$\sigma_{inv}^{lib} = \frac{\epsilon_{lib}\beta}{16}(16 + f_{lib})^2. \tag{5.14}$$

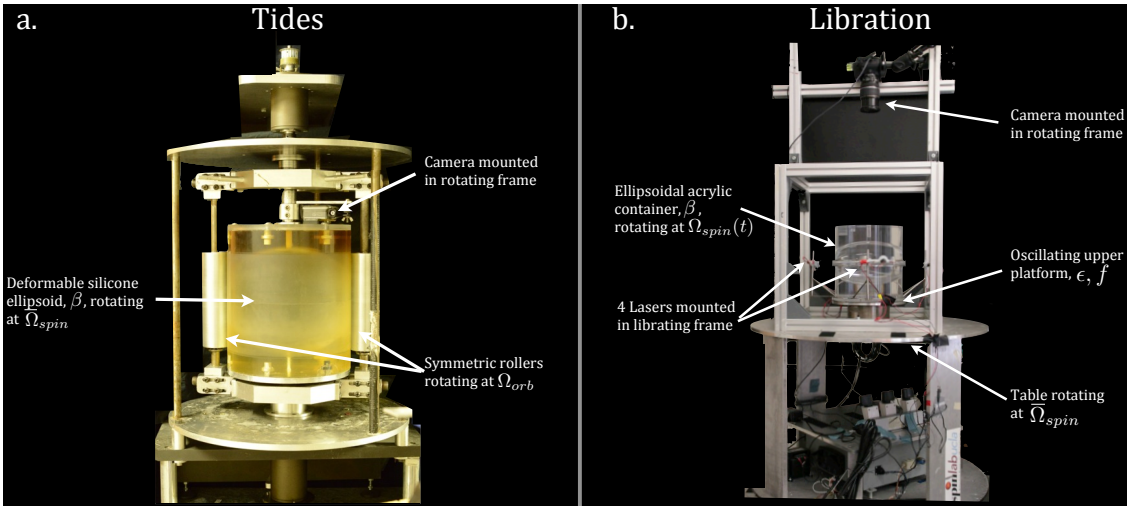

Figure 5.2: Comparison of tide and libration experimental setups. **a)** The tidal deformation experiment where the camera is fixed to a deformable container with equatorial ellipticity, β, rotating at $\overline{\Omega}_{spin}$. The two symmetric rollers rotate independently at Ω_{orb}. **b)** The libration experimental setup used in Grannan et al. (2014). A rigid ellipsoid with equatorial ellipticity, β, rotates at a constant spin rate and oscillates using two motors such that $\Omega_{spin}(t) = \overline{\Omega}_{spin}(1 + \epsilon_{lib}\sin(f_{lib}t))$. Image from *b)* adapted from Grannan et al. (2014).

The similarity of the growth rates in (5.13) and (5.14) suggest that the response of a localized fluid parcel away from the elliptical boundary is independent of the forcing mechanism. The general form of the equation including viscous effects and the proximity of the forcing frequency to some resonant frequency, f_{res}, is given from Cébron et al. (2012a) as:

$$\sigma = \sqrt{\sigma_{inv}^2 - (f_{res} - f)^2} - K\sqrt{E}. \tag{5.15}$$

The second term on the right-hand side of (5.15) is due to viscous dissipation in the Ekman boundary where K is a constant typically $[1 - 10]$. Table 5.1 provides a comparison of tidal and librational formulae.

5.3 Experimental Method

The experimental setup, shown in Figure 5.2.a is adapted from the same apparatus used previously in Le Bars et al. (2010); Morize et al. (2010); Sauret et al. (2010, 2014). A hollow sphere is enclosed in a cast cylinder of deformable semi-transparent silicone gel.

Parameter	Definition	Tides	Libration
a	Long equatorial axis(cm)	$10.05 - 10.8$ cm	12.7 cm
b	Short equatorial axis(cm)	$9.95 - 9.2$ cm	8.9 cm
c	Short rotational axis(cm)	10 cm	8.9 cm
β	$\frac{a^2-b^2}{a^2+b^2}$	$0.01 - 0.16$	0.34
R	$\sqrt{\frac{a^2+b^2}{2}}$	10 cm	10.97 cm
ν	Kinematic viscosity	$10^{-6}\ m^2/s$	$10^{-6}\ m^2/s$
$\overline{\Omega}_{spin}/2\pi$	Mean rotation rate	1.05 Hz	0.5 Hz
$\Omega_{orbit}/2\pi$	Elliptical distortion rotation rate	-1.03 Hz	$0.5(1 + 0.8\sin(4\pi t))$ Hz
$\omega_{tide,lib}/2\pi$	Elliptical distortion frequency	4.16 Hz	2.0 Hz
c^*	$\frac{c}{R}$	1	0.81
$f_{tide,lib}$	$\omega_{tide,lib}/\overline{\Omega}_{spin}$	3.96	4.0
$\gamma_{tide,lib}$	$\frac{\text{Elliptical dist. rotation rate}}{\text{Mean rotation rate}}$	-0.98	$1 + 0.8\sin(4\pi t)$
$\epsilon_{tide,lib}$	$(1 - \gamma_{tide,lib})_{max}$	1.98	0.8
E	$\frac{\nu}{\overline{\Omega}_{spin}R^2}$	1.5×10^{-5}	2.7×10^{-5}

Table 5.2: Comparison of laboratory experimental tidal and librational forcing parameters. The definitions for equatorial ellipticity, β, mean rotation rate, $\overline{\Omega}_{spin}$, and the Ekman number, E are shared by both types. The differences arise in how the mechanical forcing is implemented at the boundary. However, in the current work, $f_{tide,lib} \simeq 4$ is fixed allowing for a comparison between both mechanisms.

Tidal forcing is replicated using two motors. The first motor rotates the sphere about the $\hat{\mathbf{z}}$ axis at a constant counter-clockwise rate, $\overline{\Omega}_{spin}/2\pi = 1.05$ Hz. The second motor generates the tidal deformation by rotating two symmetric axial rollers pressed radially into the silicone at a fixed clockwise rate, $\Omega_{orb}/2\pi = 1.03$ Hz. The rotation rate ratio of the two motors is fixed at $\gamma_{tide} = \Omega_{orb}/\overline{\Omega}_{spin} \simeq -1$, indicating that the rates are nearly equal and moving in opposite directions. The amplitude of the equatorial ellipticity in the tidal forcing, the amount by which the orbiting rollers are pressed radially inward, is given by, $\beta = (a^2-b^2)/(a^2+b^2) \in [0.01-0.09]$. For completeness, the axial deformation $c^* = c/R \sim 1$, where $R = \sqrt{(a^2+b^2)/2} \sim 10$ cm for all cases. Finally, the Ekman number defining the ratio of viscous forces to the Coriolis forces is fixed at $E = 1.5 \times 10^{-5}$ using water, for which $\nu \cong 10^{-6}\mathrm{m}^2/\mathrm{s}$.

For comparison, the libration setup used in Grannan et al. (2014) is included in Figure 5.2.b. In brief, two motors generate a constant background rotation, $\overline{\Omega}_{spin}$, and superimposed sinusoidal oscillations at a fixed Ekman number, $E = \nu/(\overline{\Omega}_{spin}R^2) = 2.7 \times 10^{-5}$. Details of the experimental method are found in Grannan et al. (2014) and Table 5.2 provides a comparison of laboratory experimental tidal and librational forcing parameters.

To make quantitative measurements in the tidal forcing laboratory experiments, a particle image velocimetry (PIV) technique is employed in the $\overline{\Omega}_{spin}$ reference frame. Nearly spherical, $100\mu m$ diameter Optimage particles of density $(1 \pm 0.02\mathrm{g/cm}^3)$ are added to the water. Two oppositely faced laser light sheets are fixed in the laboratory frame several millimeters above the equatorial plane due to the presence of the joining seam of the silicone hemispheres. Mirrors are also implemented in the laboratory frame to create a more uniform laser light sheet. A GoPro Hero3+ camera is fixed in the spin frame, in order to acquire 1920×1280 resolution movies of the horizontal flow field at 60 frames per second. These movies are made only after solid body rotation has been reached; they are initiated at the start of tidal forcing and the recordings are typically 10 minutes in duration. The camera is controlled wirelessly using a GoPro smartphone application.

All movies are separated into their constituent frames and pre-processed to remove the Go-Pro's fish-eye distortion and to adjust the brightness and contrast. All adjusted images

are passed through Meunier and Lewecke (2003)'s open source PIV software, DPIVSoft2010, that has been successfully employed in previous studies [e.g., Sauret et al. (2010); Morize et al. (2010); Sauret et al. (2014); Grannan et al. (2014)]. The velocity field for an entire equatorial plane is resolved spatially into a 40x60 grid with a typical resolution of 3mm and the temporal resolution of the PIV is 59Hz. The practical dimensional and non-dimensional temporal frequency limit for our setup is $\sim$ 8Hz and $f \sim 8$, respectively. For higher frequencies above $f > 8$ where the power spectra falls below $\mathcal{O}(10^{-5})$, the noise is on the order of the signal. This frequency cutoff is shown in Figure 5.8 and is discussed in Section 5.5.3.

All velocity measurements presented below are non-dimensionalized using the radius, R, and spin period $\overline{\Omega}_{spin}^{-1}$. Thus, the dimensional velocity is found by multiplying the dimensionless velocity by $\overline{\Omega}_{spin}R$. The dimensional energy density is found by multiplying the dimensionless energy by $\rho\overline{\Omega}_{spin}^{2}R^{2}$.

5.4 Numerical Method

Numerical simulations were performed with the massively parallel spectral-element code Nek5000 (http://nek5000.mcs.anl.gov) developed by Paul Fischer and collaborators (see Fischer et al. (2007) and references within). Nek5000 solves the incompressible Navier-Stokes equations via a Legendre polynomial based spectral element method which combines the geometrical flexibility of finite element methods with the accuracy of spectral methods. It is therefore particularly well adapted to our problem involving turbulent flows in complex non-axisymmetric geometries and has been used previously in the context of tidally-forced spheres and librationally-forced elliptical flows (e.g., Favier et al. (2014a, 2015); Barker et al. (2016)).

5.5 Results

The laboratory experimental cases investigated in this work are denoted by $L-$ while the numerical cases are denoted by $N-$. The parameters for all the experimental and numerical

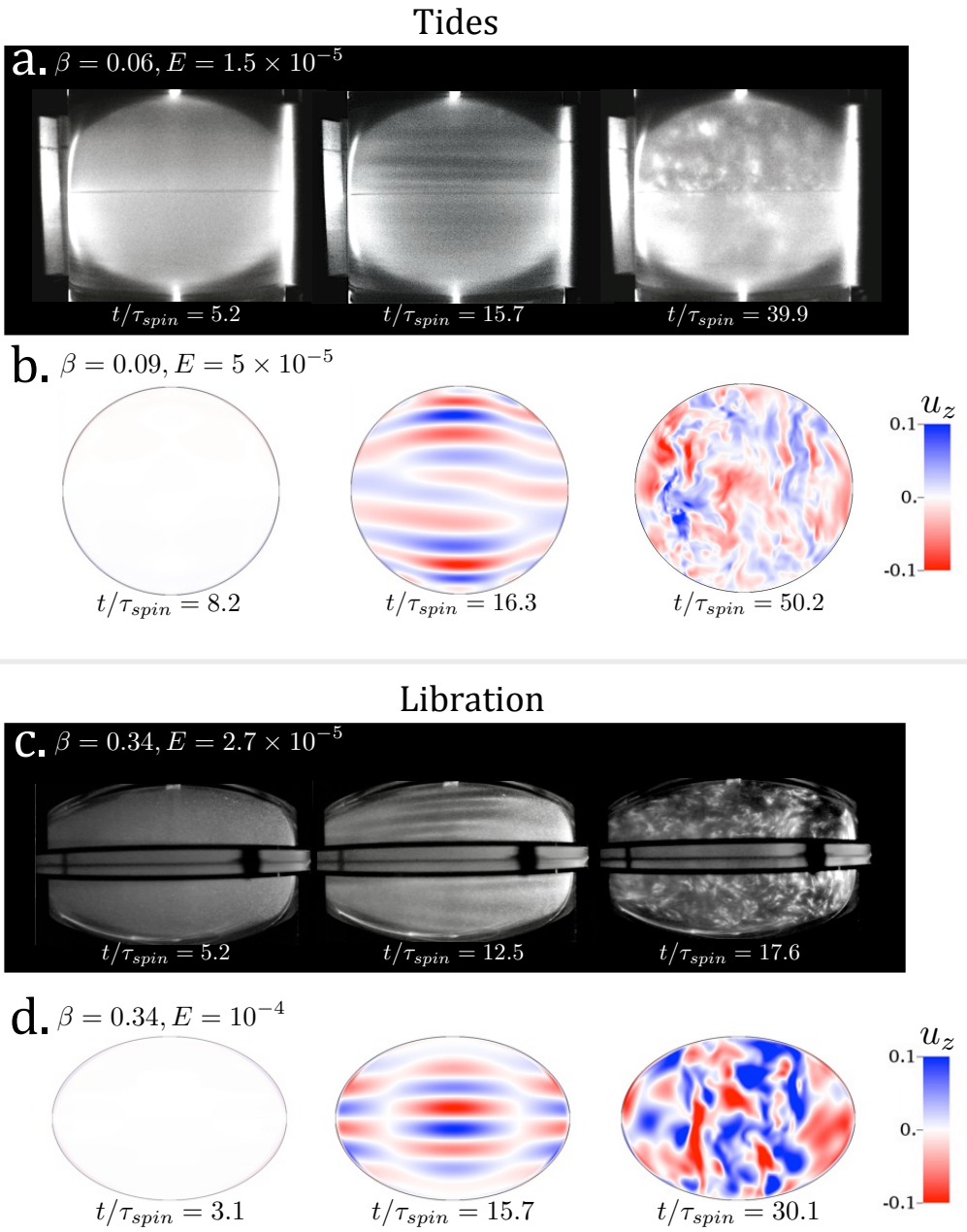

Figure 5.3: Comparison of sideview visualizations showing the onset of the EI at $f_{tide,lib} = 4$. For all cases, from left to right, first the base flow is established in the bulk and axial flow occurs in the boundary layer, followed by the stacked structures indicating the growing inertial modes, and finally the breakdown to sustained bulk turbulence. For experiments, Kalliroscope visualizations of the meridional flows illuminated by axial laser light sheets are shown while the axial velocity is shown for the numerical simulations. **a)** Tidally forced flow case $L5$ where $\beta = 0.06$ and $E = 1.5 \times 10^{-5}$ as seen in the laboratory frame. **b)** Excitation of TDEI from case $N4$ where $\beta = 0.09$ and $E = 5 \times 10^{-5}$. **c)** LDEI experimental case from V in Grannan et al. (2014) with frequency $f_{lib} = 4$, equatorial ellipticity $\beta = 0.34$, and Ekman number $E = 2.7 \times 10^{-5}$ seen in the rotating frame. **d)** Numerical simulation of case $A6$ in Favier et al. (2015) showing the excitation of the LDEI where $\beta = 0.34$ and $E = 10^{-4}$.

cases studied are listed in Tables 5.3 and 5.4 respectively of Appendix 5.8.

5.5.1 General Properties

Figure 5.3 shows, for the first time, the strong similarities found between the TDEI excited in the experiments and numerics of the current work with the LDEI found in the 0previous works of Grannan et al. (2014); Favier et al. (2015). Kalliroscope visualizations are illuminated by an axial laser light sheet in order to take high resolution movies of the experiments. The tidal forcing images in Figure 5.3.a are taken from case $L5, (\beta = 0.06, E = 1.5 \times 10^{-5})$ in the laboratory frame while librational forcing images of Figure 5.3.c from case $V, (\beta = 0.34, E = 2.7 \times 10^{-5})$ in Grannan et al. (2014) are taken in the rotating frame. Snapshots of the numerical simulations in Figure 5.3.b and 5.3.d show the axial velocities from the TDEI in case $N4, (\beta = 0.09, E = 5 \times 10^{-5})$ and the LDEI from case $A6, (\beta = 0.34, E = 10^{-4})$ of Favier et al. (2015) in the ellipsoidal frame.

Moving from left to right through the three time steps of Figure 5.3, after solid body rotation has been reached, the forcing commences with no visible flow in the bulk. Since the base flow is purely horizontal, the numerical simulations in Figure 5.3.b and 5.3.d show that axial velocity is non-zero only in the thin boundary layer. After some time, for forcing above a critical value such that the growth rate in (5.15) is positive, the excited inertial modes participating in the instability grow and become visible. Since $f_{tide,lib} = 4$ is at the limit of elliptical instability, the coupled inertial modes are necessarily $|\lambda_{1,2}| = f_{tide,lib}/2 \approx 2$ by (5.11), and the wave crests are perpendicular to the rotation axis as indicated by the layered structures. It is noted that inviscid inertial modes with $|\lambda| = 2$ exactly do not exist but may be just below 2 due to viscous effects and imperfect resonances. On the right of Figure 5.3, the growth of the inertial modes leads to a wave breaking event that transitions to sustained bulk filling small-scale turbulence that does not return to the laminar base state found at early times.

Side-view visualizations reveal that as the strength of tidal deformation is varied between $\beta \in [0.01 - 0.16]$, the transition to bulk turbulence, shown in Figure 5.3, is seen in all cases

except for $\beta = 0.01$ which remains laminar for all times. Using this critical value for tidal deformation, $f_{res} = 4$, and setting the growth rate in (5.15) equal to zero, the dissipation constant is then $K = 3$ and 5 for DNS and experiments, respectively. These Kvalues are within the typical range for $K = [1 - 10]$ also found in previous studies [e.g., Cébron et al. (2012b); Noir et al. (2012)].

The onset of turbulence is quantified using the averaged axial kinetic energy defined as:

$$E_z = \frac{1}{2V} \int_V u_z^2 \mathrm{dV}, \tag{5.16}$$

where $V = 4/3\pi abc$ is the ellipsoidal volume and u_z is the axial velocity component. This diagnostic is a natural choice since the tide-induced base flow of (5.7) and (5.9) are purely horizontal and any increase in the axial energy indicates the excitement of the TDEI.

Additionally, these flow quantities vary in time due to the oscillating base flow and may be sufficiently smoothed by averaging over one spin period defined as:

$$\overline{A}(t) = \frac{1}{\tau_{spin}} \int_t^{t+\tau_{spin}} A(t')\mathrm{d}t', \tag{5.17}$$

where $\tau_{spin} = 2\pi/\overline{\Omega}_{spin}$.

The axial kinetic energy in (5.16) is not measurable in the experimental PIV which is limited to only the horizontal energy. Since the experimental data is inherently more noisy, the horizontal flows for experiments and DNS are computed by subtracting out the base flow in (5.7) and (5.9), respectively. After the base flow is removed from the experimental data, the horizontal energy in the bulk is integrated, in the rotating frame, over an equatorial surface area with a maximum radius $0.5R$ where $R = \sqrt{a^2 + b^2}/2$:

$$E_H^S = \frac{1}{2S} \int_S \left(\mathbf{u}_{H_{rot}} - \mathbf{U}_{B_{rot}}\right)^2 \mathrm{dS}. \tag{5.18}$$

In comparison, the volume averaged horizontal energy of the DNS is computed in the ellip-

soidal frame by:

$$E_H^V = \frac{1}{2V} \int_V (\mathbf{u}_H - \mathbf{U}_B)^2 \, \mathrm{dV}. \tag{5.19}$$

Figure 5.4.a shows the transition from laminar to turbulent flow as the equatorial ellipticity, β, is increased by plotting the unaveraged horizontal energy from (5.18) in gray and the time average in color as a function of the number of spin periods τ_{spin} for the experiments. The laminar case, $\beta = 0.01$, (blue line) shows no transition after the base flow is established at early times.

For $\beta \in [0.03 - 0.16]$, after the base flow is established, the energy grows exponentially followed by an overshoot and then oscillations around a saturated phase. This is corroborated in Figure 5.4.b where an analysis of the volume averaged horizontal energy computed in the ellipsoidal frame of the DNS reveals the same transitions. Once the transition occurs we find no evidence for relaminarization wherein the flow returns to the laminar base state found at early times. For all cases, the energy of the unstable flow is quite small, $\mathcal{O}(10^{-3} - 10^{-2})$, indicating that although the instability conveys just a small portion of the available kinetic energy of the system, first order changes are generated in the flow.

To verify the characteristics of the EI mechanism, we focus on the transitions in the axially-averaged energy of the DNS in Figures 5.4.c and 5.4.d. The growth rates for different β are predicted using the theoretical growth rate given by (5.15) for fixed $f_{tide} = 4$, $E = 5 \times 10^{-5}$, and $K = 3$ plotted using solid black lines of the form, $e^{2\sigma t}$, in Figure 5.4.c. The slope of the exponential phase is well-matched with the theoretical prediction. Note that the same analysis of the exponential growth rate of the horizontal energy shown in Figure 5.4.a and 5.4.b is also in general agreement.

Because the base flow in (5.7) is purely horizontal, the non-zero axial energy for early times in Figure 5.4.c is associated with viscous corrections in the boundary proportional to β^2. Thus, normalizing the axial energy by β^2 collapses all the energy profiles to a constant value as shown in Figure 5.4.d at early times. Unexpectedly, at later times after the exponential growth of the flow energy, the amplitudes of the saturated turbulent energy also collapse to oscillations around a constant value as shown by the black horizontal line and indicate that

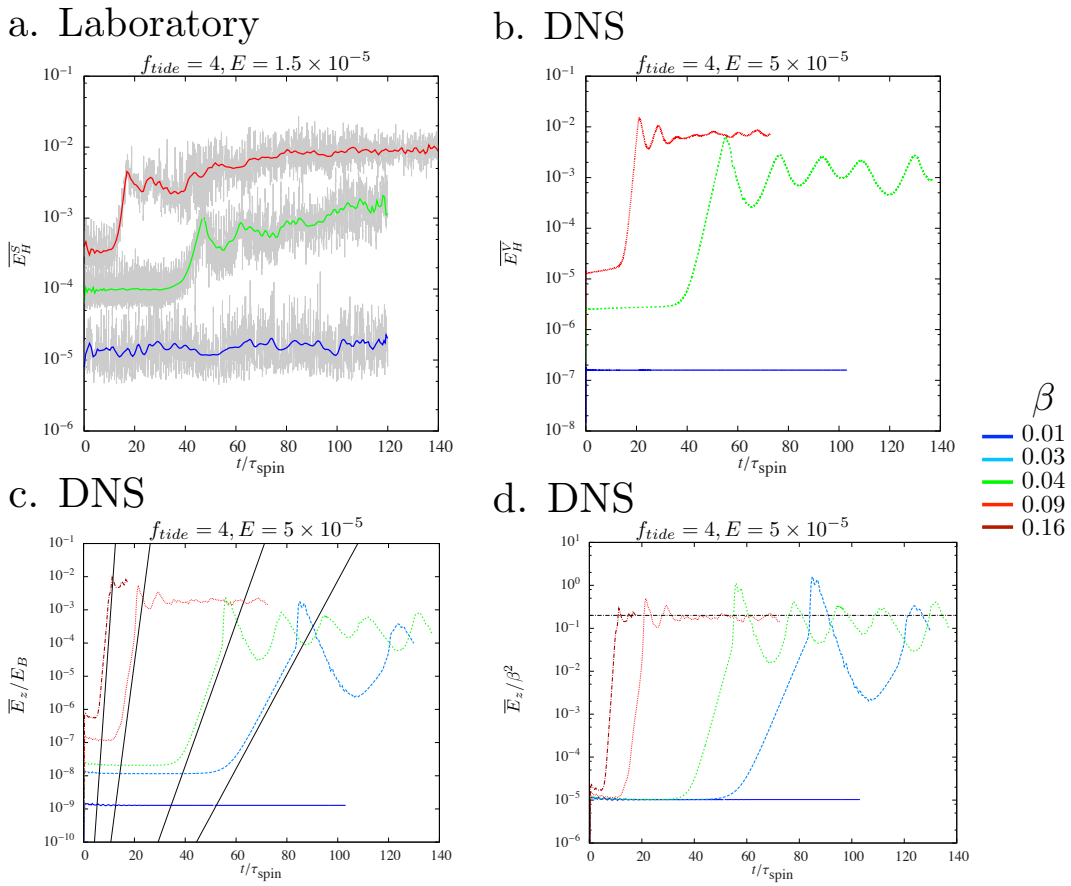

Figure 5.4: Tidally-driven laboratory experiments and numerical simulations. **a)** Laboratory measurements of the instantaneous surface averaged horizontal energy in the rotating frame with the base flow removed, E_H^S, as defined in (5.18) and shown in gray. The colored curves correspond to the averages over a spin period following (5.17). The cases shown are $L1, \beta = 0.01$, $L3, \beta = 0.04$, and $L8, \beta = 0.09$. **b)** For numerical simulations, the volume averaged horizontal energy in the ellipsoidal frame with the base flow removed, E_H^V, as defined in (5.19). The cases shown are $N1, \beta = 0.01$, $N3, \beta = 0.04$, and $N4, \beta = 0.09$. **c)** Time evolution of field-averaged axial kinetic energy $\overline{E}_z$ normalized by the kinetic energy associated with the base flow in the rotating frame, E_B, from (5.8). The solid black lines are the theoretical growth rates from (5.15) of the form $e^{2\sigma t}$ with $K = 3$. **d)** Same averaged axial kinetic energy $\overline{E}_z$ now normalized by β^2. All energies are time-averaged using (5.17). The black dashed line indicates a constant saturation value. The cases in *c)* and *d)* are $N1, \beta = 0.01$, $N2, \beta = 0.03$, $N3, \beta = 0.04$, $N4, \beta = 0.09$, and $N5, \beta = 0.16$. For all numerical simulations, $E = 5 \times 10^{-5}$.

the saturation energy also scales with β^2. By extension, the saturation amplitude for the turbulent velocity, U_{TDEI}, is then:

$$U_{TDEI} \sim \beta. \tag{5.20}$$

Note that since $\beta \ll 1$ in the current work and in planetary settings, this novel scaling for the turbulent saturation velocity is larger than the amplitude associated with laminar zonal flows that scale with β^2. Note that a collapse of the saturation in the horizontal flows in Figure 5.4.a and 5.4.b is also found, but is not shown for brevity.

In Figure 5.4 we also note a general increase in the frequency of the oscillations as β increases during the saturated flow phase. This increase is expected because as the saturation velocity scales with β, the oscillations after the exponential growth phase correspond to a typical oscillation frequency that scales as $U_{TDEI}/\ell \sim \mathcal{O}(\beta)$ for a fixed length scale ℓ. The relation between these oscillations and the participating inertial modes requires a more complete analysis of the long term evolution characteristics of the flow and is currently being performed using numerical simulations in a local cartesian geometry [i.e., Barker and Lithwick (2013)].

The response of the flow to TDEI and LDEI was also addressed in previous studies examining kinetic energy dissipation. For turbulent flow, the dissipation is expected to scale as u^3, where u is the velocity [i.e., Kolmogorov (1941)]. In the numerical studies of the current work, we also find that the dissipation in the bulk scales as $U_{TDEI}^3 \sim \mathcal{O}(\beta^3)$. A scaling for boundary layer dissipation is given by $\beta^2 E^{1/2}$ [i.e, Cébron et al. (2010b)]. For the current work and in planetary setting where $\beta \ll E^{1/2}$, the bulk dissipation is larger than the boundary layer dissipation. The scaling for the turbulent bulk dissipation is also found in numerical simulations of tidal forcing in a periodic box and in the ellipsoidal geometry with a free surface [e.g., Barker and Lithwick (2013); Barker et al. (2016)]. This result is expected since there are no boundaries and thus no viscous dissipation in the boundary. In the study of turbulence generated by LDEI in ellipsoids where both bulk and viscous boundary dissipation are present, the bulk dissipation is also found to be larger than the viscous dissipation. [e.g., Favier et al. (2015)].

5.5.2 Zonal Flows

Tide-driven forcing can generate steady zonal flows driven by non-linear self interactions of the boundary flow that satisfy the no-slip boundary condition. The amplitude of the typically retrograde zonal flows scales with β^2 and is independent of the Ekman number. However, as shown in recent numerical studies of libration by Favier et al. (2015) where the Ekman number is varied, the zonal flow amplitude is increased by the presence of elliptical instability. To look at the influence of the TDEI on the zonal flow, we assume the mean velocity is strongly azimuthal and after subtracting the base flow in (5.7) and (5.9), we decompose the flow into its mean azimuthal component in cylindrical coordinates:

$$\left\langle \overline{U_\phi} \right\rangle (r) = \frac{1}{N_r} \sum_z \sum_\phi \sum_{r-\frac{dr}{2}<r'<r+\frac{dr}{2}} \overline{U_\phi}(r', \phi, z), \tag{5.21}$$

where N_r is the number of points averaged in each radial ring. Note that z is fixed for the experiments.

By separating the azimuthal flow into approximately 30 radial rings and averaging the azimuthal velocity in each ring, radial profiles of the time-averaged azimuthal velocities are shown in Figure 5.5.a where the symbols and dotted lines indicate the experimental and DNS measurements respectively. Beginning with $\beta = 0.01$(blue), the retrograde azimuthal flow velocity is quite small.

As β is increased the amplitude of the retrograde zonal flow grows as well. For all profiles, the experimental data at $E = 1.5 \times 10^{-5}$ shows a larger magnitude and more centralized peak than numerical studies at $E = 5 \times 10^{-5}$ for the same values of β. A transition to a stronger more centralized geostrophic flow was also found in studies of LDEI enhanced zonal flow where the Ekman number was decreased and β was held constant [i.e., Favier et al. (2015)]. Thus we believe that the disparity found for zonal flow peaks and locations in the current work may also be related to differences in Ekman number. More generally, the presence of such strong zonal flows generated as the elliptical instability saturates [c.f., Favier et al. (2015)] may play a crucial role for the long term flow evolution and will be the

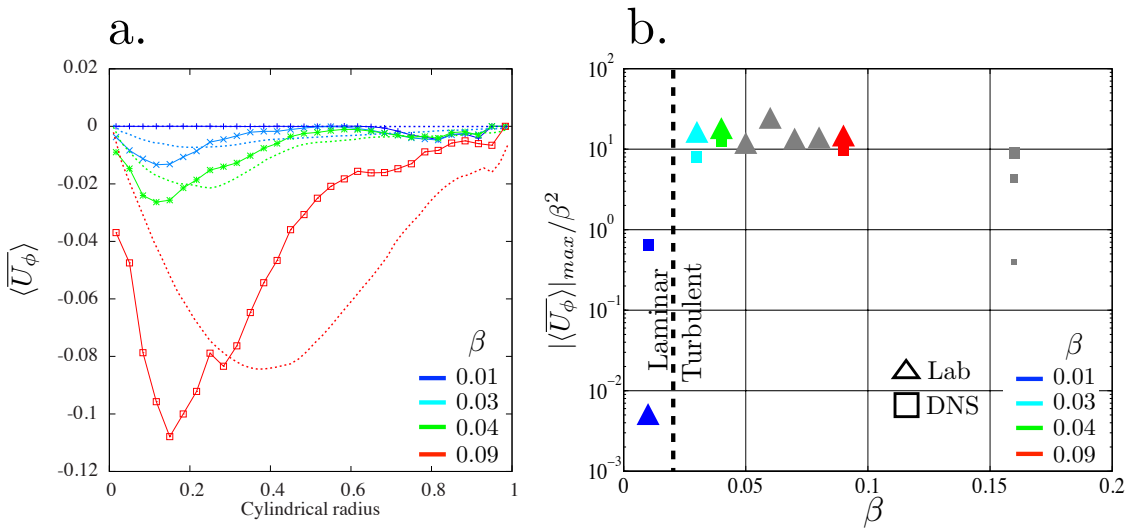

Figure 5.5: Measurements of tidally-driven zonal flows. **a)** Radial profiles of the time-averaged dimensionless azimuthal flow velocity, $\langle \overline{U_\phi} \rangle$, with normalized radius r. The experimental data at $E = 1.5 \times 10^{-5}$ from cases $L1, \beta = 0.01$, $L2, \beta = 0.03$, $L3, \beta = 0.04$, and $L8, \beta = 0.09$ are shown with symbols and the DNS cases at $E = 5 \times 10^{-5}$ with $N1, \beta = 0.01$, $N2, \beta = 0.03$, $N3, \beta = 0.04$, and $N4, \beta = 0.09$ are shown with dotted lines. **b)** The maximum velocities, $|\langle \overline{U_\phi} \rangle|_{max}$, are normalized by β^2 and plotted as a function of β where triangles, ($\triangle$), indicate laboratory experiments and boxes, ($\square$), denote DNS velocity peaks. The colored symbols for the max values in *b)* match the profiles in *a)* from which they came. The gray symbols denote additional cases whose profiles were not included in *a)*. The size of the symbols is inversely proportional to the Ekman number, E^{-1}. The vertical dashed line represents the transition from laminar to turbulent flows.

subject of future studies.

In previous studies of tidal forcing, zonal flow peak amplitudes were shown to scale with β^2 [e.g., Suess (1971); Morize et al. (2010); Sauret et al. (2014)]. As such, the maximum values of the the azimuthal velocity in the radial profiles of Figure 5.5.a are shown as colored points in Figure 5.5.b normalized by β^2 as a function of β. The additional gray symbols denote peaks from other profiles excluded in Figure 5.5.a only for clarity. Triangle and square symbols denote experiments and DNS, respectively. The size of the symbols are inversely proportional to the Ekman number, E^{-1}, varied between $E = [1.5 \times 10^{-5} - 5 \times 10^{-4}]$.

The dotted vertical line denotes the transition between laminar and TDEI induced turbulent flow around $\beta \sim 0.02$. Below this threshold, no clear trend is revealed and the experimental data at $\beta = 0.01$ and zonal flow peaks are on the order of the noise in the system. Above the threshold, the bulk of experimental and numerical data are relatively flat

around:

$$|\langle\overline{U_\phi}\rangle|_{max}/\beta^2 \sim 10, \tag{5.22}$$

indicating that β^2 normalization is well chosen. Additional numerical data at fixed $\beta = 0.16$ on the right side of Figure 5.5.b clearly reveal that the amplitude increases as the Ekman number is decreased. However, it is not clear from the present study if this trend continues or the zonal flow saturates at some critical value [c. f., Sauret et al. (2014)]. A summary of the laboratory experimental and numerical zonal flow velocities shown in Figure 5.5.b are compiled in Table 5.3 and Table 5.4 of Appendix 5.8.

5.5.3 Mode Coupling and the Transition to Turbulence

The transition to turbulence is explored by increasing the strength of the tidal deformation from $\beta \in [0.01 - 0.16]$ while keeping the tidal frequency fixed at $f_{tide} = 4$ and the Ekman numbers fixed at $E = 1.5 \times 10^{-5}, 5 \times 10^{-5}$ for experiments and DNS, respectively.

To characterize the turbulent transition, all velocity components are analyzed in the rotating frame at probe points distributed homogeneously in the bulk of the ellipsoid for DNS and in the equatorial plane for the experiments. Because an adaptive time stepping method is used in the DNS, signals must be evaluated on a uniform grid formed using a Langrangian interpolation method. For DNS and experiments, velocity signals are multiplied by a time-periodic Hanning function to ensure all signals are periodic.

A comparison of the power spectrograms from experimental cases $L1(\beta = 0.01)$, $L3(\beta = 0.04)$ and $L8(\beta = 0.09)$ and DNS cases $N1(\beta = 0.01)$, $N3(\beta = 0.04)$, and $N4(\beta = 0.09)$ are shown in Figure 5.6. Sliding window discrete Fourier transforms are performed on a moving window of 10 spin periods with a 90% overlap. The first signal is the strong peak at $f = 4$ corresponding to the $f_{tide} = 4$ of the tidal forcing that drives the ellipsoidal base flow and persists for all times. The second shared signal is the zonal flow at $f = 0$ whose characteristics are discussed in Section 5.5.2.

From side-view visualizations and from the flow energetics provided in Figure 5.4, the case $\beta = 0.01$ shown in Figure 5.6.a and 5.6.b is stable, exhibiting no signs of bulk turbulence

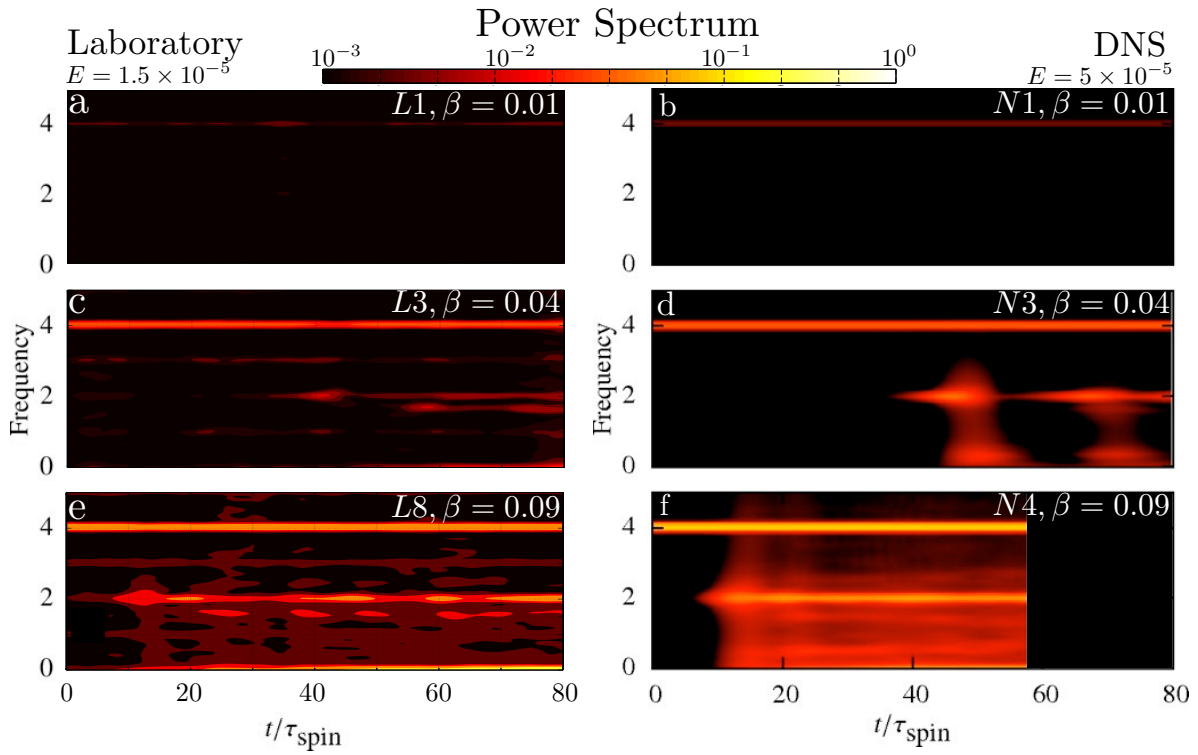

Figure 5.6: Tidal forcing power spectrograms showing the dominant flow frequencies. Shown are cases **a.)** $L1, \beta = 0.01$, **b.)** $N1, \beta = 0.01$, **c.)** $L3, \beta = 0.04$, **d.)** $N3, \beta = 0.04$, **e.)** $L8, \beta = 0.09$, and **f.)** $N4, \beta = 0.09$ where $f_{tide} = 4$ and the Ekman number is fixed at $E = 1.5 \times 10^{-5}, 5 \times 10^{-5}$ for the laboratory experiments and DNS, respectively.

for all times and one strong peak at the tidal forcing, $f_{tide} = 4$. Figure 5.6.c and 5.6.d show the spectrogram for $\beta = 0.04$. Following the onset of the tidal forcing, after a certain amount of time that depends on the strength of the tidal forcing and Ekman number, a strong persistent signal appears at $f = 2$, associated with the excitation of primary inertial modes at half of the forcing frequency.

The existence of these inertial modes at $f = 2$ satisfies the temporal resonance condition in (5.11). Spatially, the modes are identifiable by their axial pancake-like structures as shown in the middle images of Figure 5.3.a and 5.3.b. Although we have not explicitly determined the wavenumbers of these modes, nearly identical modes have also been found in laboratory experiments and numerical simulations of LDEI [i.e., Grannan et al. (2014); Favier et al. (2015)]. In those studies, the inertial modes have an eigenfrequency $|f_{tide}/2| \lesssim 2$ and their spatial structure is characterized by both an azimuthal wavenumber, $m_{1,2} = 1$, and a large

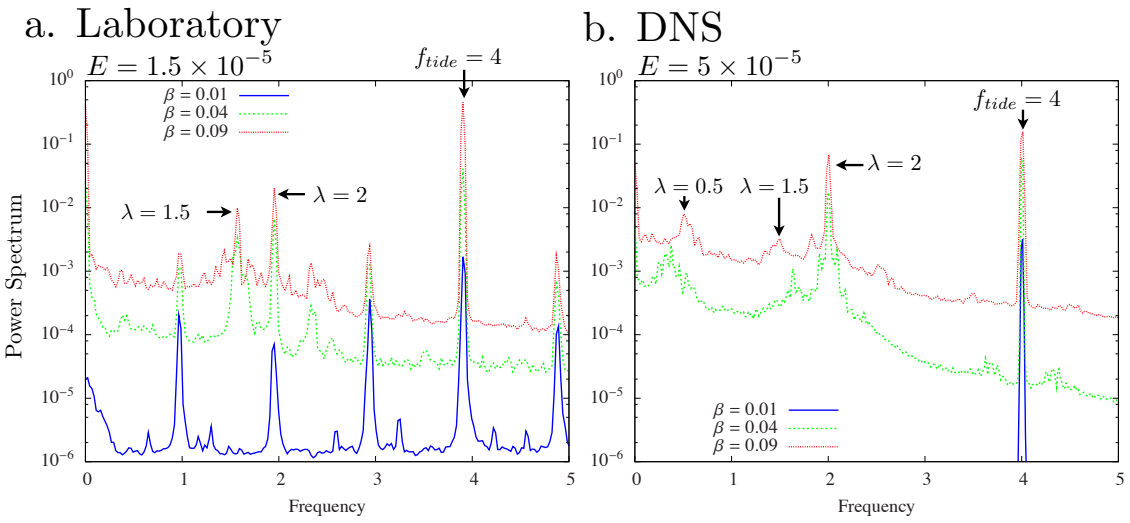

Figure 5.7: The time-averaged tidal forcing power-spectrum of the saturated turbulent flow. **a)** Laboratory experiments $L1, \beta = 0.01$, $L3, \beta = 0.04$, and $L8, \beta = 0.09$ where Ekman, $E = 1.5 \times 10^{-5}$. **b)** A similar power-spectrum from DNS cases $N1, \beta = 0.01$, $N3, \beta = 0.04$, and $N4, \beta = 0.09$ where $E = 5 \times 10^{-5}$.

number of stacked axial structures. Analytical descriptions of these ellipsoidal modes are theoretically possible using a polynomial description of the modes but difficult in practice because of the need to use high degree polynomials to resolve these high axial wavenumber modes [i.e., Vantieghem (2014)]. Instead analytical solutions from the sphere and polar flattened spheroid have been implemented and show the existence of $m_{1,2} = 1$ that satisfies the spatial resonance condition in (5.12) and have high frequencies at $\lambda \sim 1.9$ [i.e., Grannan et al. (2014); Favier et al. (2015). Thus, we contend that similar inertial modes with the same spatial description exist in the ellipsoidal geometry of the current work at an adjusted frequency, $|\lambda_{1,2}| \sim 2$.

As the tidal deformation is increased again, the growth rate given by (5.15) also increases and thus the TDEI for $\beta = 0.09$, shown in Figure 5.6.e and 5.6.f, occurs earlier in time. For both cases $\beta = 0.04, 0.09$, after the amplitude of the primary inertial modes has grown, secondary resonances can occur whose driving force is the primary inertial mode frequency $f = 2$, instead of the tidal forcing at $f = 4$.

Evidence for these secondary resonances is seen more clearly in the full time-averaged frequency spectrum shown for experiments and numerics in Figure 5.7.a and 5.7.b, respec-

tively. We first note strong spectral peaks at frequencies $f = 1, 2, 3$ are found only in the experiments, and non-existent in the DNS. For $\beta = 0.01$ in Figure 5.7.a, the signals at $f = 1, 2, 3$ may have two causes. The first may be periodic light intensity changes occurring as the camera, in the rotating frame, moves between different laser light sources and the mirrors used for reflecting the light mounted in the lab frame.

The second cause may be a misalignment of the rotating container or the rollers replicating the tidal deformation. In any case, these signals are related to the harmonics associated with the rotating frequencies $|\overline{\Omega}_{spin}, \Omega_{orb}| \sim 1$Hz and are found in all the experimental measurements. However, the good agreement with the DNS suggests that these signals do not appear to noticeably affect the results and the peaks are still quite small in comparison to the primary forcing at $f_{tide} = 4$ for cases above the stable one at $\beta = 0.01$.

Concerning the secondary modes excited by the primary inertial modes at $f = 2$, although the spatial structures for these secondary modes have not been uniquely determined, peak frequencies at $f \sim 1.5$ and $f \sim 0.5$ are still evident in Figure 5.7.b. The frequency condition (5.11) is satisfied for a secondary resonance being driven by the primary inertial mode at $f_{tide}/2 = 2$. For the horizontal spectra from the experiments in Figure 5.7.a, the only clear peak resides at $f \sim 1.5$ while Figure 5.7.b shows a second peak at $f \sim 0.5$. Similar to the method used in libration simulations from Favier et al. (2015), a decomposition of the tidal simulation spectra into axial and horizontal components (not shown) reveals that the mode at $f \sim 0.5$ is characterized by strong axial motions untraceable in the experimental data. The mode at $f \sim 1.5$ is composed of strong horizontal motions and visible by both methods.

Finally, a comparison of the full power spectra generated through TDEI and LDEI is shown in Figure 5.8.a and 5.8.b respectively. Figure 5.8.a display cases $L8(\beta = 0.09, E = 1.5 \times 10^{-5}$, blue) and $N4(\beta = 0.09, E = 5 \times 10^{-5}$, red) from the current work. Figure 5.8.b is reproduced from the experimental (blue) and DNS (red) spectra in the LDEI studies of Favier et al. (2015) where $f_{lib} = 4$, $\epsilon_{lib} = 0.8$, and $\beta = 0.34$ are fixed and $E = 2.7 \times 10^{-5}$ and $E = 10^{-4}$ for the experiments and numerics, respectively. In both images the forcing, primary inertial modes, secondary inertial modes, and high frequency tails are nearly identical. Note that the experimental data has been cut at $f \sim 8$ where the spectra is $\mathcal{O}(10^{-5})$. At greater

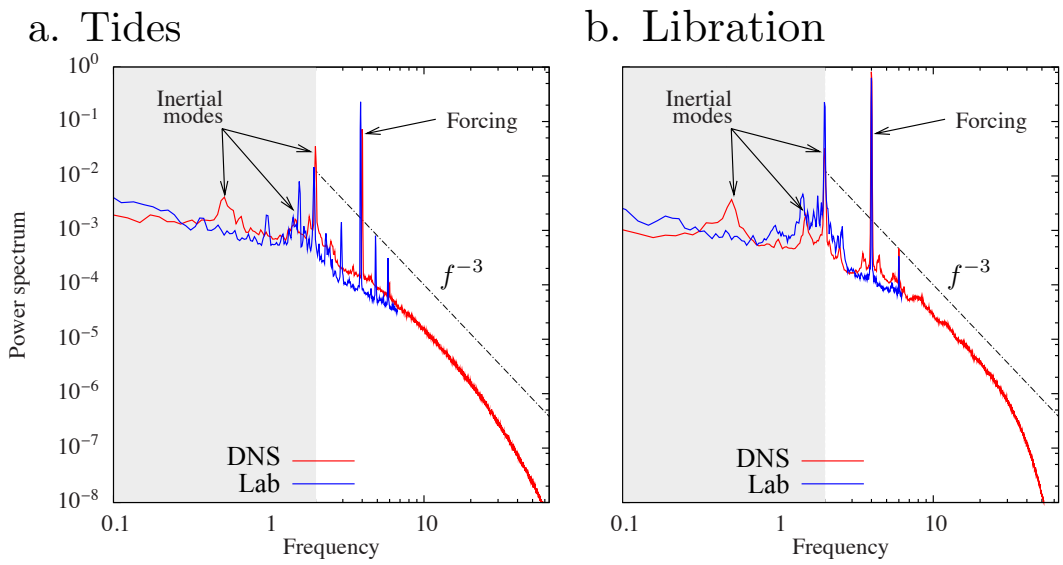

Figure 5.8: **a)** The time-averaged power-spectrum of the saturated turbulent flow in the current tidal studies where $f_{tide} = 4$ and $\beta = 0.09$. The laboratory case, $L8$, where $E = 1.5 \times 10^{-5}$ is shown in blue. The numerical case, $N4$, where $E = 5 \times 10^{-5}$ is shown in red. **b)** The time-averaged power-spectrum of the saturated turbulent flow in the libration studies where $\epsilon_{lib} = 0.8$ and $f_{lib} = 4$. The laboratory case V from Grannan et al. (2014) where $E = 2.7 \times 10^{-5}$ is shown in blue. The DNS case $A6$ from Favier et al. (2015) where $E = 10^{-4}$ is shown in red. The dashed line has an f^{-3} slope.

frequencies the signal to noise ratio is unity in the experimental data and only the numerical spectra fills the high frequency tail.

For both tides and libration the majority of the energy is contained in the forcing and excited inertial modes. The power in the higher frequency spectra more closely follows an f^{-3} scaling indicative of scalings for rotating turbulence wherein the presence of the Coriolis force reduces the forward energy cascade. The same scalings were also found for the wavenumbers in the spatial spectra of local models of tidal forcing and simulations of libration in ellipsoids [i.e., Barker and Lithwick (2013); Favier et al. (2015); Barker et al. (2016)]

5.6 Conclusion

We have combined laboratory experiments with numerical simulations to show, for the first time, that tides can mechanically drive bulk filling turbulence in an interior fluid region via elliptical instability (see Figure 5.3.a,b). We find strong agreement with the theoretical

prediction for the growth rate and the subsequent instability whose forcing and inertial mode frequencies satisfy the resonance conditions for the TDEI (see Figure 5.4). The transition to turbulence is characterized first by the growth of primary inertial modes, then the excitation of additional secondary inertial modes, and finally saturated bulk turbulent flow (see Figure 5.6 and Figure 5.7). Furthermore, our tidal results have both qualitative and quantitative similarities to librationally-driven flows (see Figure 5.3.c,d and Figure 5.8).

Tidal deformation of an elastically deformed ellipsoid and longitudinal libration of an ellipsoid with a rigid boundary represent two end-member cases for the geophysically relevant periodic mechanical forcings that many planetary bodies experience. Our tidal case better describes a flexible icy shell, for instance, in a non-synchronous orbit, where the orbital and spin rate of the body are unequal and the elastic boundary responds quickly to tidal distortions. Our libration case is more relevant for planetary bodies whose shapes have some degree of intrinsic ellipsoidal distortion [e.g., Vesta, Ermakov et al. (2014)], and/or are in so-called synchronous orbits where the time-averaged tidal forcing generates the ellipsoidal deformation.

Although tidal and librational forcing mechanisms are quite different, their mathematical formulation can be generalized in the same way as shown in Section 5.2 and Tables 5.1 and 5.2. The strong agreement found between the transition to, and characteristics of, the bulk turbulence driven by tides and libration hints at a generic response of the fluid interior to elliptical instability as illustrated in Figures 5.3 and 5.8, showing side-view visualizations and power spectra, respectively. Furthermore, the small-scale turbulence observed is more easily excited as the Ekman number is decreased [e.g., Lacaze et al. (2004); Le Bars et al. (2010)] and may be similar to the small-scale turbulence that might be generated in planetary fluid interiors where $E \ll 1$.

We find that the saturated turbulent velocity induced by TDEI scales linearly with $U_{TDEI} \sim \beta$. In comparison, a bulk azimuthal zonal flow is shown to scale with β^2. In planetary settings where $\beta < 10^{-4}$ [e.g., Cébron et al. (2012a)], the turbulent velocity scaling is therefore much larger than that of the zonal flow and may be of critical importance for planetary processes like tidal dissipation in subsurface oceans and magnetic field generation

in liquid metal cores.

To investigate the generation of turbulence in planetary bodies based on the velocity scaling in (5.20), we define a Reynolds number that describes the strength of turbulence in a flow, $Re = UR/\nu$, where U is the dimensional turbulent velocity, R is the outer radius of the fluid layer, and ν is the kinematic viscosity. Using (5.20) a dimensional velocity, $U \sim U_{TDEI}\overline{\Omega}_{spin}R$, is formed. The Reynolds number can then be rewritten in terms of the mechanical forcing parameters such that:

$$Re = \frac{\beta}{E}. \tag{5.23}$$

For elliptical instability to occur, it is required that $\sigma > 0$ in (5.15) and thus

$$\frac{\sigma_{inv}}{\sqrt{E}} \sim \frac{\epsilon_{tide,lib}\beta}{\sqrt{E}} \geq 1 \tag{5.24}$$

This condition for elliptical instability in (5.24) can be rewritten in terms of the Reynolds number in (5.23) forming a critical Reynolds number, Re_{cr}:

$$Re_{cr} = \frac{1}{\epsilon_{tide,lib}\sqrt{E}}. \tag{5.25}$$

Thus the condition for the onset of elliptical instability in (5.24) can be redefined as $Re/Re_{cr} > 1$. For the subsurface ocean on Europa, the parameters $\epsilon = 2 \times 10^{-4}$, $\beta = 9.7 \times 10^{-4}$, and $E = 2 \times 10^{-14}$ are taken from Cébron et al. (2012a). Using the planetary values for Europa, $Re_{cr} \sim 4 \times 10^{10}$ while $Re \sim 5 \times 10^{10}$ indicating that the body is marginally unstable and mechanical forcing may be capable of generating turbulent flow that could play an important geophysical role.

New observations of Enceladus have shown the presence of a large libration in addition to a global subsurface ocean [i.e, Cedak et al. (2016); Thomas et al. (2016)]. For Enceladus, $\epsilon_{lib} = 2 \times 10^{-3}$, $\beta = 9 \times 10^{-3}$ following the formulation used in Cébron et al. (2012a), and $E = 3 \times 10^{-13}$ revealing that $Re_{cr} = 9 \times 10^{8}$ and $Re = 3 \times 10^{10}$ suggesting that the mechanical response of the fluid may drive significant flows in a subsurface ocean.

Currently, most models for tidal dissipation only consider visco-elastic dissipation in a given body's solid layers, such as icy shells. These models ignore the effects of dissipation within lower viscosity fluid regions [e.g., Williams and Boggs (2015)]. Recent models have now begun to include dissipation due to direct tidal resonances in subsurface oceans on icy bodies[e.g., Tyler (2008, 2014); Chen et al. (2014); Matsuyama (2014); Kamata et al. (2015)]. In the future we will extend our models to estimate how tidal and librational elliptical instabilities can drive further dissipation in low viscosity planetary fluid layers [c.f., Ibragimov (2007) for Earth's oceans].

In addition, advance laboratory experiments currently under construction and high resolution numerical simulations using full ellipsoids and local cartesian geometries will focus on elliptical instability with the inclusion of inner cores, fluid stratification, and multiple forcing frequencies at even more extreme ranges of forcing parameters. These studies will aid in investigating whether the scaling for the velocity, like that proposed in (5.20), holds, changes, or saturates at some critical value of the parameters used. Recent precession and tidal studies at more extreme parameters [i.e., Barker and Lithwick (2013, 2014); Lin et al. (2015)] have shown the formation of large scale structures similar to those being investigated in convection [i.e., Julien et al. (2012b); Stellmach et al. (2014); Favier et al. (2014b); Guervilly et al. (2014); Aurnou et al. (2015); Guervilly et al. (2015); Plumley et al. (2016)]. Furthermore, precession, nutation, tides, libration, and even small body impacts, do not work in isolation but are experienced in varying degrees by all bodies. For instance, the combined effect of tidal and precessional forcing, as seen in Morize et al. (2010), permits rich dynamics. Thus, there may be many ways for mechanical forcing to perturb the fluid motions in planetary interiors.

5.7 Appendix A: Boundary Condition in Tide Simulations

In the orbital frame, the elliptical distortion is fixed and the boundary maintains a constant horizontal velocity tangent to the ellipsoidal surface. At any given height $-c < z < c$, the

horizontal shape of the container is given by

$$\frac{x^2}{a'^2} + \frac{y^2}{b'^2} = 1, \tag{5.26}$$

with $a' = a\sqrt{1 - z^2/c^2}$ and $b' = b\sqrt{1 - z^2/c^2}$. This curve can be parametrized by

$$\mathbf{X}(s) = \begin{pmatrix} x = a' \cos s \\ y = b' \sin s \\ z \end{pmatrix}, \quad \text{with} \quad s \in [0 - 2\pi] \tag{5.27}$$

with a normalized tangent vector given by

$$\begin{aligned} \boldsymbol{\tau} = \frac{\mathbf{X}_s}{|\mathbf{X}_s|} &= \frac{1}{\sqrt{a'^2 \sin^2 s + b'^2 \cos^2 s}} \begin{pmatrix} -a' \cos s \\ b' \sin s \\ 0 \end{pmatrix} \\ &= \frac{1}{\sqrt{a^2 y^2/b^2 + b^2 x^2/a^2}} \begin{pmatrix} -ay/b \\ bx/a \\ 0 \end{pmatrix}. \end{aligned} \tag{5.28}$$

The boundary condition for the velocity on the elliptical boundary is finally

$$\mathbf{u}_{b.c.} = (1 - \gamma)\sqrt{\frac{a'^2 + b'^2}{2}}\boldsymbol{\tau}. \tag{5.29}$$

5.8 Appendix B: Parameters from laboratory experimental and numerical studies

Case	β	TDEI	$\lvert\overline{U_\phi}\rvert_{max}$
$L1$	0.01	No	0.0046
$L2$	0.03	Yes	0.0133
$L3$	0.04	Yes	0.0263
$L4$	0.05	Yes	0.0269
$L5$	0.06	Yes	0.0795
$L6$	0.07	Yes	0.0597
$L7$	0.08	Yes	0.0808
$L8$	0.09	Yes	0.1079

Table 5.3: Tidal laboratory experimental cases signified by $(L-)$. For all cases, the Ekman number, $E = \nu/(\overline{\Omega}_{spin}R^2) = 1.5 \times 10^{-5}$ and the ratio of orbital rate the spin rate, $\gamma_{tide} = -1$, are fixed. The equatorial ellipticity is $\beta = (a^2 - b^2)/(a^2 + b^2)$. Case $L1$ is TDEI stable (No) and all other cases are TDEI unstable (Yes). $\lvert\langle\overline{U}_\phi\rangle\rvert_{max}$ is the maximum absolute value for the time and spatially averaged zonal flow defined in (5.21) and plotted in Figure 5.5.

Case	E	N	β	TDEI	$\lvert\langle\overline{U_\phi}\rangle\rvert_{max}$
$N1$	5.0×10^{-5}	17	0.01	No	6.5e-5
$N2$	5.0×10^{-5}	17	0.03	Yes	0.0073
$N3$	5.0×10^{-5}	17	0.04	Yes	0.0202
$N4$	5.0×10^{-5}	17	0.09	Yes	0.0791
$N5$	5.0×10^{-5}	17	0.16	Yes	0.2290
$N6$	2.0×10^{-4}	13	0.16	Yes	0.1094
$N7$	5.0×10^{-4}	9	0.16	Yes	0.0101

Table 5.4: Tidal DNS cases signified by $(N-)$. For all cases, the number of elements, $\mathcal{E} = 3200$, and the ratio of orbital rate to the spin rate, $\gamma_{tide} = -1$, are fixed. N is the order of the Legendre polynomials used in the simulations, $\beta = (a^2 - b^2)/(a^2 + b^2)$, and $E = \nu/(\overline{\Omega}_{spin}R^2)$ is the Ekman number. Case $N1$ is TDEI stable (No) and all other cases are TDEI unstable (Yes). $\lvert\langle\overline{U}_\phi\rangle\rvert_{max}$ is the absolute maximum value for the time and spatially averaged zonal flow defined in (5.21) and plotted in Figure 5.5.

CHAPTER 6

Libration Driven Elliptical Instability Experiments in Ellipsoidal Shells

In this work, I modified the libration apparatus in Chapter 2 by designing and building an adapter that rigidly supports an inner core, and designing and building an adapter to mount a wireless camera into the librating frame. I made the first visualizations of the presence of turbulence in the ellipsoidal shell for the smallest and largest inner cores at two different Ekman numbers. I mentored a visiting student, Daphné Lemasquerier, on how to the operate the experiment and acquire the data using the cameras and light intensity sensor. I instructed her on using the particle image velocimetry software and provided Matlab scripts used for pre-processing the movies. She gathered the majority of the data. I assisted in the interpretation of the results that showed the existence of the LDEI could be extended to the more geophysically relevant ellipsoidal sheIl geometry. While the onset of turbulence through LDEI is similar to the ellipsoidal geometries investigated in Chapters 3 and 4, the shell geometry promotes spatial heterogeneities in the flow response inside and outside the tangent cylinder that may promote unique complexities in planetary interiors. I contributed to the writing of the final document.

6.1 Introduction

6.1.1 Context

Planets and moons spin around their rotation axis at a given angular velocity. However, they are subjected to several types of mechanical forcings that periodically perturb this

rotation, such as precession and libration. This study focuses on longitudinal libration, which physically corresponds to an oscillation of the axial rotation rate of a body that results from gravitational interactions with an orbital partner.

The effects of these mechanical forcings on the dynamics of internal fluids are of major interest for planetary bodies that have a liquid metal core (e.g. Mercury, the Moon, Io, Ganymede), and for bodies that have subsurface oceans (e.g. Europa, Callisto, Ganymede, Enceladus, Titan). In these bodies, internal flows are linked to the generation of magnetic field, planetary heat fluxes, and energy dissipation. A better understanding of these flows is thus important to consider relevant hydrodynamical effects in modelings. Furthermore, since it has been proposed that life may be harbored within these subsurface oceans, their internal structure and dynamics are of broad interest to the planetary science community and beyond. The motivation here is thus to determine whether mechanical forcing can drive strong global-scale flows by injecting energy into interior fluid layers.

One way to perform this exchange of energy is through a viscous coupling between the solid and liquid layers. That is why the first studies of the fluid dynamical effects of libration focused on spherical geometry (full sphere and spherical shell). In such geometries, longitudinal libration excites inertial waves, which find their origin in the restoring effect of the Coriolis force. These waves can then combine to form inertial modes (Aldridge and Toomre, 1969; Noir et al., 2009), which are the eigenmodes of a rapidly rotating fluid cavity (Greenspan, 1969). However no resonant response is expected in the limit of small Ekman number and forcing amplitude (Zhang et al., 2013).

When longitudinal libration affects an elliptically deformed body (e.g. Cébron et al., 2012b; Noir et al., 2012; Grannan et al., 2014; Favier et al., 2015), a topographic torque is generated between the solid outer boundary (e.g. the mantle) and the interior fluid layer (e.g. the liquid core). This mechanical forcing can excite a parametric fluid instability involving two inertial modes of the rotating flow plus the elliptically deformed basic flow in response to the harmonic forcing (Le Bars et al., 2015). This instability is called the libration-driven elliptical instability (LDEI).

6.1.2 Motivations

However, it is currently unclear whether the LDEI investigated in the full ellipsoidal cavity can be extended to the more geophysically-relevant shell geometry. While the solutions for inertial modes have been calculated for a full cylinder and cylindrical shells Herreman et al. (2009), as well as in spheroidal (Zhang et al., 2004) and ellipsoidal (Vantieghem, 2014) cavities, the complete spectrum of eigenfrequencies is unknown for spherical or ellipsoidal shells. In such a configuration, and for very weak libration forcing, the only known regular inviscid solutions are purely toroidal modes because of the new constraints imposed by the inner boundary (Rieutord et al., 2001). Inertial modes are instead confined along singular path of characteristics and form so-called attractors. When adding viscosity but remaining in a regime where the Coriolis force largely dominates the viscous force (typically Ekman number $\sim 10^{-8}$), the singularities take the form of thin shear layers localized around the inviscid attractors (Rieutord and Valdettaro, 2010). This suggests that LDEI might be significantly modified in ellipsoidal shells since inertial modes are not expected to robustly and globally develop in such geometries. Following previous studies of the elliptical instability in shell geometries (Seyed-Mahmoud et al., 2000, 2004; Lacaze et al., 2005; Cébron et al., 2010b), the goal of this investigation is to experimentally and numerically demonstrate that inertial mode resonances do indeed develop in librating ellipsoidal shells, and thus that LDEI can exist in the subsurface oceans and liquid metal cores of librating bodies.

6.2 Theoretical Formalism

6.2.1 Model and Equations

We consider the flow $\mathbf{u}$ of an incompressible ($\nabla\cdot\mathbf{u}=0$) fluid of uniform density and kinematic viscosity ν. The fluid is enclosed between a rigid ellipsoidal outer container, whose surface, in a reference frame fixed to the surface, is defined in Cartesian coordinates by

$$\frac{x^2}{a^2}+\frac{y^2}{b^2}+\frac{z^2}{c^2}=1, \tag{6.1}$$

where a, b, and c are the long equatorial axis, the short equatorial axis and the polar axis, respectively. We define the mean external radius as $R = \sqrt{(a^2+b^2+c^2)/3}$ and the equatorial ellipticity as

$$\beta = \frac{a^2-b^2}{a^2+b^2} \ . \tag{6.2}$$

The aspect ratio of the shell is $\chi = r_i/R$ where r_i is the radius of the spherical inner core. The container (outer ellipsoid and inner core) is subjected to longitudinal libration, i.e. rotates around the vertical axis $\widehat{\mathbf{z}}$ with a time-dependent spin rate given by $\Omega_{\rm spin}(t) = \Omega_0 + \Delta\phi\ \omega_{\rm lib}\sin(\omega_{\rm lib}t)$, where Ω_0 is the mean spin rate, $\Delta\phi$ is the libration amplitude and $\omega_{\rm lib}$ is the angular libration frequency.

We work in the body frame attached with the walls of the librating container (librating frame). The inner and outer boundaries are fixed in that frame. We choose Ω_0^{-1} as the time scale and the shell thickness $R(1-\chi)$ as the length scale. The dimensionless spin rate is

$$\Omega(t) = 1 + \epsilon\sin(ft), \tag{6.3}$$

with $\epsilon = f\ \Delta\phi$ the dimensionless libration amplitude and $f = \omega_{\rm lib}/\Omega_0$ the dimensionless libration frequency. In the librating frame the momentum and continuity equations for the velocity field $\mathbf{u}$ are

$$\frac{\partial \mathbf{u}}{\partial t} + \mathbf{u}\cdot\nabla\mathbf{u} + 2\boldsymbol{\Omega}\times\mathbf{u} = -\nabla\Pi + E_\chi\nabla^2 u - \underbrace{\frac{\mathrm{d}\boldsymbol{\Omega}}{\mathrm{d}t}\times\mathbf{r}}_{\text{Poincaré}} \tag{6.4}$$

$$\nabla\cdot\mathbf{u} = 0, \tag{6.5}$$

with $E_\chi = \nu/[\Omega_0 R^2(1-\chi)^2]$ the Ekman number (dimensionless viscosity), Π the reduced pressure taking into account the centrifugal acceleration, and $\mathbf{r}$ the dimensionless position vector. In equation (6.4) the last term on the right hand side is the Poincaré force generated by the non-uniform rotation of the librating frame. Finally the velocity field satisfies the no-slip boundary condition $\mathbf{u} = \mathbf{0}$ at both the inner spherical and outer ellipsoidal surfaces.

6.2.2 Basic flow

We consider first the equatorial plane ($z = 0$) of our system to determine the two-dimensional base flow $\mathbf{U}$ bounded by an external elliptical boundary and an inner circular boundary. We work in cylindrical coordinates (s, ϕ, z) in the librating frame. The flow is described by the stream function ψ such that $\mathbf{U} = \nabla \times [-\epsilon \sin(ft)\psi\, \widehat{\mathbf{z}}]$. In the inviscid limit $E_\chi = 0$, the flow satisfies the non-penetration conditions $u_s = 0$ at the inner and outer boundaries. Assuming a small equatorial ellipticity $\beta \ll 1$, we expand the stream function as $\psi = \psi_0 + \beta\psi_1$ where $\psi_0 = (s^2 - 1)/2$ is the stream function of the solid body rotation and ψ_1 is the first order elliptical correction. With the ansatz $\psi_1 = F(s)\cos(2\phi)/2$, the inviscid vorticity equation reduces to the Laplace equation $\nabla^2 F = 0$, yielding

$$\psi_1 = \left(\frac{A_1}{s^2} + B_1 s^2\right)\frac{\beta}{2}\cos(2\phi) \tag{6.6}$$

where $A_1 = -\chi^4/(1-\chi^4)$ and $B_1 = 1/(1-\chi^4)$ are fixed by the boundary conditions. The complete stream function is thus

$$\psi = \frac{s^2-1}{2} + \left(\frac{A_1}{s^2} + B_1 s^2\right)\frac{\beta}{2}\cos(2\phi) \tag{6.7}$$

and the cylindrical flow components are reduced to

$$U_s = \epsilon \sin(ft)\left(\frac{A_1}{s^3} + B_1 s\right)\beta \sin(2\phi)\ , \tag{6.8}$$

$$U_\phi = \epsilon \sin(ft)\left[s + \left(-\frac{A_1}{s^3} + B_1 s\right)\beta\cos(2\phi)\right]\ . \tag{6.9}$$

In the librating frame, each fluid parcel thus oscillates back and forth along a part of an elliptical streamline whose flattening depends on the distance from the inner core boundary.

In our experimental setup the basic flow $\mathbf{U}$ is *a priori* three-dimensional. However for $z \in [-\chi, \chi]$, the base flow is enclosed between an ellipsoidal outer boundary and a spherical inner core. We therefore neglect the vertical component and approximate the base flow $\mathbf{U}$ by the horizontal components (6.8) and (6.9), replacing χ by $\sqrt{\chi^2 - z^2}$ to calculate A_1 and B_1.

For $|z| > \chi$, the base flow is only enclosed within an ellipsoidal boundary and the horizontal base flow reduces to (6.8) and (6.9) with $A_1 = 0$ and $B_1 = 1$.

6.2.3 Inertial Waves

A rotating fluid in an unbounded medium supports oscillatory motions called inertial waves. The latter are solutions of (Greenspan, 1969)

$$\frac{\partial \mathbf{u}}{\partial t} + 2\widehat{\mathbf{z}} \times \mathbf{u} = -\nabla \Pi \ , \tag{6.10}$$

$$\nabla \cdot \mathbf{u} = 0, \tag{6.11}$$

which can be rearranged to give a single equation for the pressure field (the Poincaré equation). Equation (6.10) admits plane wave solutions $\mathbf{u} \propto e^{\mathrm{i}(\mathbf{k}\cdot r + \omega t)}$, where $\mathbf{k}$ is the dimensionless wave vector and ω is the dimensionless frequency. These inertial waves satisfy the dispersion relation

$$\omega = \pm 2 \cos\theta \ , \tag{6.12}$$

where θ is the angle between $\mathbf{k}$ and the axis of rotation $\widehat{\mathbf{z}}$. The dispersion relation in (6.12) shows that $|\omega| \leq 2$ and that inertial waves are dispersive and anisotropic. For a finite fluid volume, inertial waves reflect on solid walls, keeping θ constant according to (6.12), and can generate global inertial modes through constructive interference.

Experimental (Aldridge and Toomre, 1969; Noir et al., 2009) and numerical (Rieutord, 1991; Tilgner, 1999; Calkins et al., 2010) studies show that longitudinal libration can excite inertial modes, although a direct resonance mechanism is not predicted by theoretical studies (Zhang et al., 2011, 2013). In viscous spherical shells, internal shear layers, i.e. superposition of inertial waves (Kerswell, 1995) are spawned from the so-called critical latitude where the energy of incoming inertial waves is reflected along the boundary (Phillips, 1963). Shear layers are also associated with the breakdown of the Ekman boundary layer (Greenspan, 1969). For a given forcing frequency f, the critical latitude α_c is determined by $f = 2 \sin \alpha_c$.

Since inertial modes are the starting point for the stability analysis of libration, preces-

sion or tidally-driven flows, their investigation is of interest. In Figure 6.1 we show direct excitations of inertial waves using Kalliroscope visualizations for forcing frequencies $f \leq 2$. The shear layers are qualitatively observed at critical colatitudes in good agreement with the theoretical predictions. However, the precise study of direct resonance of inertial waves in ellipsoidal shells is beyond the scope of this study.

6.2.4 Elliptical Instability

The libration-driven elliptical instability (LDEI) is a linear instability mechanism that arises from the resonant interaction of triads of waves, namely two inertial waves plus the elliptical deformation of the fluid streamlines by the oscillating boundaries (Cébron et al., 2012a; Vidal et al., 2017). Expanding velocity and pressure perturbations around the basic state as a linear combination of inertial modes, one can show that the LDEI grows in time if the following resonance conditions are satisfied (Grannan et al., 2014):

$$|m_1 - m_2| = m_{lib} = 2, \tag{6.13}$$

$$|\omega_1 - \omega_2| = f, \tag{6.14}$$

where m_i is the azimuthal wavenumber and ω_i is the eigenfrequency of the ith inertial mode of the triad. The azimuthal wavenumber $m_{lib} = 2$ of the base flow $\mathbf{U}$ is a direct consequence of the fact that the outer surface of the container is ellipsoidal. Because of the dispersion relation (6.12), $|\omega_i| \leq 2$. In the asymptotic limit of $\beta, \epsilon \to 0$ (*i.e.* weak ellipticity and weak libration amplitude, relevant for planets and moons), the elliptical instability exists only if $|f| < 4$, whereas finite values of β and ϵ allow instabilities when $|f| < 4 + \epsilon\beta$ (see Grannan et al., 2014, for details).

In this study, we realize a survey with a fixed frequency $f = 4$ for several reasons. First, in this frequency regime, no inertial waves are directly excited by the forcing. It allows us to focus only on the LDEI mechanism, *i.e.* on an indirect excitation of inertial modes. Secondly, this case is the one where the determination of the modes and frequency coupling is the simplest. Inertial modes with eigenfrequencies $f_{1,2} \simeq f/2 = 2$ meet the resonance

conditions in (6.14), and are particularly easy to identify with a side-view visualization.

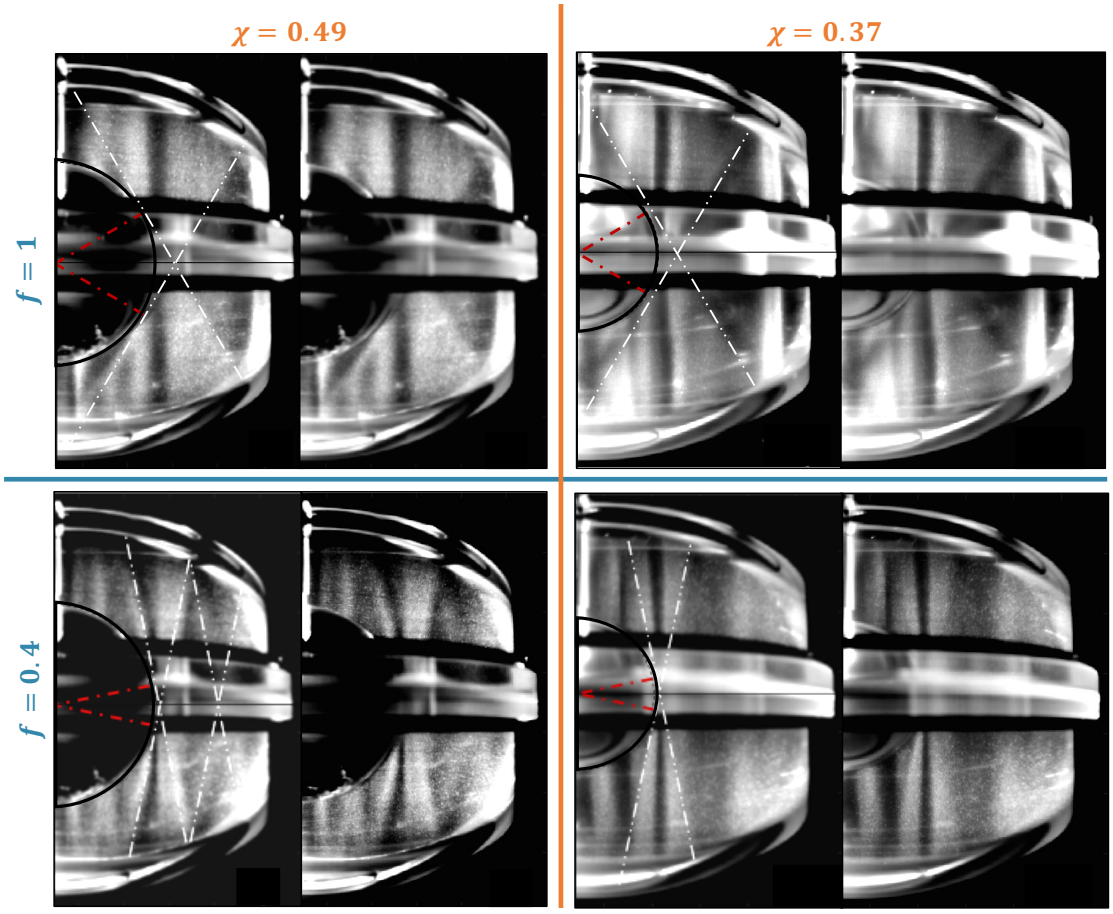

Figure 6.1: Kalliroscope visualizations of the shear layers formed by the direct excitation of inertial waves for two different forcing frequencies ($f = 1$ and 0.4) and two different core sizes ($\chi = 0.49$ and 0.37). Each image is obtained by stacking instantaneous snapshots extracted at $t = n\ T_{lib} + T_{lib}/2$, where T_{lib} is the libration period. From left to right and top to bottom, the stacking is performed over 50, 50, 45 and 41 libration periods. Two images are given for each parameter set: a raw image on the right, and the same image on the left where we have superimposed dashed white lines representing the theoretical direction of the shear layers ($\theta = \arccos(f/2)$) and dashed red lines pointing towards the critical latitude ($\alpha_c = \arcsin(f/2)$).

Indeed, $\mathbf{k}$ is, in this case, parallel to the rotation axis, implying that the group velocity of the excited waves is horizontal. These were identified as the $\Lambda_{8,\pm1,7}$ modes in the absence of inner core (Grannan et al., 2014; Favier et al., 2015) using the description of inertial modes in a rotating spheroid given by Kerswell (1994). Since the radial component of this mode is not zero, by definition, it is not a purely toroidal mode. It is thus also a way to verify if modes having a poloidal component can be excited in an ellipsoidal shell. Additional cases

have also been done with the forcing frequency $f = 2.4$ to show that the spin-over mode (solid-body rotation inclined with the rotation axis) is still excited.

6.2.5 Local Stability Analysis

Cébron et al. (2012a, 2014) performed the local stability analysis of libration-driven basic flows valid in full ellipsoids. The local stability method probes the stability of the path-lines of the basic flow, considering inviscid plane-wave perturbations of small wavelengths (Le Dizes, 2000). The local inviscid growth rate σ_{inv} of LDEI is at first order in $\epsilon\beta$ (Cébron et al., 2012a)

$$\sigma_{inv} = \frac{16 + f^2}{64}\epsilon\beta \ . \tag{6.15}$$

Using the same approach, the inviscid growth rate of LDEI upon the libration-driven base flow in (6.8) and (6.9) is

$$\sigma'_{inv} = \frac{(16 + f^2)|3A_1 + B_1 s^4|}{64 s^4}\epsilon\beta \ . \tag{6.16}$$

The growth rate for the full ellipsoid in (6.15) is recovered from (6.16) when $A_1 = 0$ and $B_1 = 1$. Note that because the streamline deformation is changing with s and z, the growth rate (6.16) is spatially varying. However, for $\chi \in [0, 0.74]$, the spatial mean (along s) of σ'_{inv} is always smaller than σ_{inv}. The highest growth rate, given by (6.15), is the one used in this study. This choice is later supported by the fact that the instability is seen to grow primarily close to the poles where $A_1 = 0$ and $B_1 = 1$.

To include dissipative terms due to the no-slip boundary conditions, Cébron et al. (2012a) assumed that dissipation mainly occurs in the Ekman boundary layer of thickness $E_\chi^{1/2}$. The viscously damped growth rate of LDEI is then

$$\sigma = \sigma_{inv} \ - \ \alpha \ \Psi(\chi)\sqrt{E_\chi}, \tag{6.17}$$

where α is a constant of order unity and Ψ a function taking into account the dependence of the damping with the radius ratio of the shell χ. Hollerbach and Kerswell (1995) show that the tilt-over mode, corresponding to the basic flow of a precessing shell, is damped viscously

following $\Psi = (1-\chi)(1+\chi^4)/(1-\chi^5)$. This tilt-over mode is similar to the so-called spin-over mode of the TDEI (tidally-driven elliptical instability). No generic formula exists to quantify Ψ for other modes of the elliptical instability excited by tides or libration.

6.3 Methods

6.3.1 Experimental Setup

6.3.1.1 Description of the experiment

The container used is a polished acrylic cavity made from two non-axisymmetric hemispheres. The fluid cavity dimensions are $a = 12.7$ cm and $b = c = 8.9$ cm, which gives an equatorial ellipticity of $\beta = 0.34$. A solid acrylic inner core is added inside the ellipsoidal cavity using a metallic rod suspended from the top of the acrylic container. The radius of the inner cores used are $r_i = [2.51, 3.82, 5.07, 6.12, 7.62]$ cm corresponding to $\chi = [0.24, 0.37, 0.49, 0.59, 0.74]$.

This container is fixed on the same device as the one used previously by Noir et al. (2009, 2010, 2012) and Grannan et al. (2014). Two motors are used to replicate a librational forcing. The first one rotates a 1m-diameter turntable at a constant rotation rate Ω_0 varying from 1 to 60 RPM (0.017 to 1 Hz). The second one, which is mounted on this turntable, is directly coupled to the acrylic cavity and superimposes a sinusoidal oscillation $\Delta\phi\ \omega_{lib} \sin(\omega_{lib} t)$ (see Figure 6.2). In this study, the container oscillations are characterized by an amplitude $2\Delta\phi \in [0°, 65°]$ and a frequency $\omega_{lib}/2\pi \in [0, 3.84\ Hz]$. Top-facing and side-facing cameras, shown in Figure 6.2, are used to perform visualizations described in section 6.3.2.

6.3.1.2 Cases realized

Figure 6.3 shows the Ekman number as a function of the background rotation rate Ω_0, using colored curves for the six different values of χ. The upper x-axis shows the dimensional frequency of libration for a fixed non-dimensional frequency $f = 4$. The horizontal dot-dash lines show the six Ekman numbers used in the experiments and the black dots show

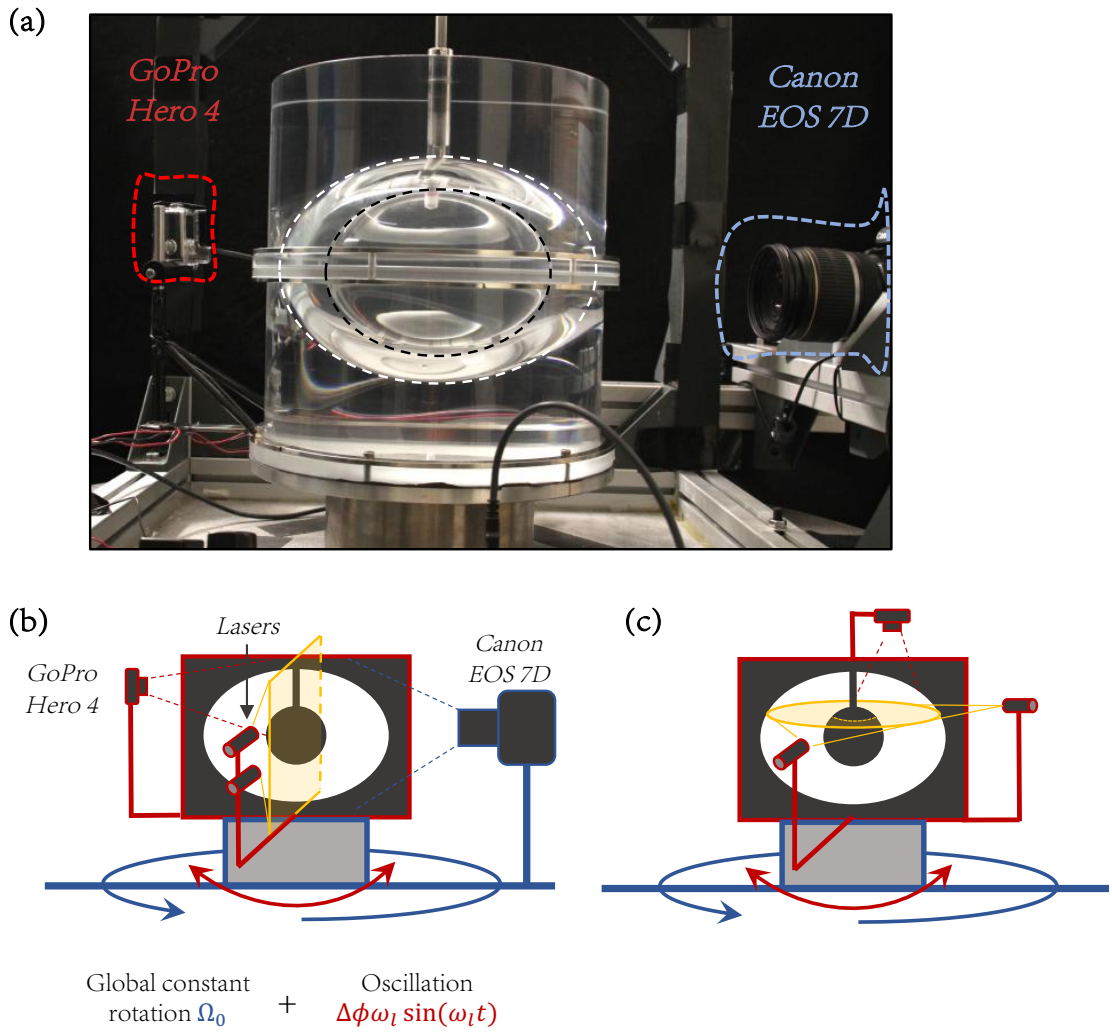

Figure 6.2: **(a)** Side-view image and **(b,c)** schematic representations of the laboratory experiment used to perform visualizations on vertical and horizontal planes. The inner core is spherical, even if it appears ellipsoidal in **(a)** due to optical distortions.

the intersection of these fixed Ekman values with the solid curves. Each experiment is conducted the same way. A constant rotation is applied for several minutes until the fluid reaches solid body rotation. The two cameras start recording movies simultaneously and the oscillation of the acrylic container is then activated. For each set of parameters (E_χ, χ) (black dots in figure 6.3), $\Delta\phi$ is adjusted to determine an approximate amplitude threshold for the instability. To determine whether a case is stable or unstable, we wait for five predicted growth times using (6.17) with $\Psi \approx (1-\chi)$ and visually check whether a turbulent flow develops or not. For some unstable cases, we record longer movies ($\sim$ 10 min) to be able

to perform a signal analysis on both the growing and the fully-turbulent phases. Table 6.1 recapitulates the experimental parameters, definitions, and ranges explored. A complete table of all the cases realized is available in the Supplementary Information (Table S1).

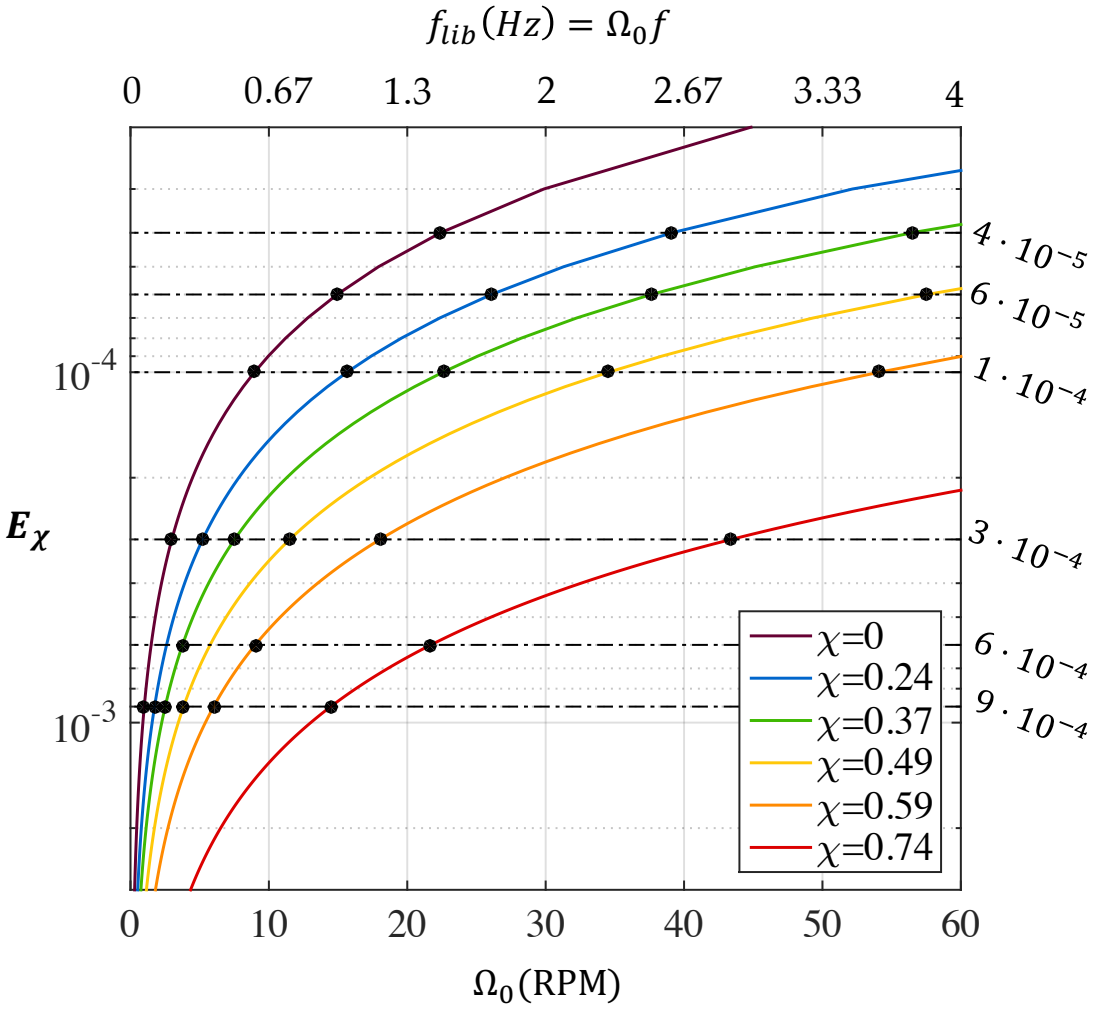

Figure 6.3: Evolution of the Ekman number with the rotation rate of the turntable for various shell ratios. The black dots represent the cases realized for a dimensionless libration frequency $f = 4$.

6.3.2 Flow Analysis Methods

6.3.2.1 Kalliroscope and PIV

Direct side-view visualizations of the flow are performed by seeding the water with Kalliroscope particles, and illuminating the tank with a meridional laser plane. These particles are

Parameter	Definition	Range of values
a	Long equatorial axis	127 mm
b	Short equatorial axis	89 mm
c	Rotational axis	89 mm
β	Ellipticity $\frac{a^2-b^2}{a^2+b^2}$	0.34
r_i	Inner core radius	[0, 25.1, 38.2, 50.7, 61.2, 76.2] mm
R	Mean radius of the ellipsoid $\sqrt{\frac{a^2+b^2+c^2}{3}}$	103.2 mm
χ	Radius ratio of the shell r_i/R	[0, 0.243, 0.370, 0.491, 0.593, 0.738]
$\Omega_0/2\pi$	Mean fluid rotation rate	0.017-1 Hz
$\omega_{lib}/2\pi$	Libration frequency	0.067-4 Hz
$\Delta\phi$	Angular displacement	0.05-1 rad
ν	Kinematic viscosity	10^{-6} m^2/s
f	Dimensionless libration frequency ω_{lib}/Ω_0	4, 2.4 and $f \leq 2$
E_χ	Shell Ekman number $\frac{\nu}{\Omega_0 R^2(1-\chi)^2}$	$4 \cdot 10^{-5}$ - $9 \cdot 10^{-4}$
E	Ekman number $\frac{\nu}{\Omega_0 R^2}$	$1.6 \cdot 10^{-5}$ - $9 \cdot 10^{-4}$

Table 6.1: Laboratory experimental librational forcing parameters.

thin plates that reflect light preferentially along the direction of their short-axis and orient themselves with the shear of the flow. Their collective reflectance thus gives a visual indication of their orientation, and thereby, of the flow behavior (Hecht et al., 2010). The two lasers used to create the light sheet are attached to the librating frame. Two cameras are used to acquire 1920 x 1280 resolution movies of the flow at 30 frames per second. A GoPro Hero4 Silver camera is fixed in the librating frame and acquires movies in the narrow mode to avoid optical distortion. The second camera is a Canon EOS 7D digital camera fixed in the rotating frame. The GoPro angle of view focuses on one quadrant of the cavity, whereas the Canon EOS 7D allows to visualize the whole shell.

To evaluate the information obtained from Kalliroscope visualizations, a selected case is chosen and analyzed using both Kalliroscope particles and Particle Image Velocimetry (PIV) in a vertical plane and in a horizontal plane located at approximately 4.6 cm above the equatorial plane (0.51 c). PIV is performed by seeding the water with 100 μm diameter Optimage^{TM} particles. Movies are acquired with the GoPro camera attached to the librating frame in a top-view or side-view position as shown by Figure 6.2.b and Figure 6.2.c, respectively. Note that, as for Kalliroscope visualizations, the GoPro camera focuses on a given quadrant of both the vertical and the horizontal planes. Frames are then extracted,

converted to black and white images, and their contrast is adjusted for an optimal treatment. Computation of the instantaneous velocity fields is performed using the open source software DPIVSoft2010 (Meunier and Lewecke, 2003). The spatial resolution of the obtained velocity fields is approximatively 2.5 mm and 2 mm for the horizontal and vertical planes respectively. A comparison between the results given by PIV and Kalliroscope visualizations is conducted in Section 6.3.2.3.

6.3.2.2 Analysis Methods

To verify if the bulk turbulence appearing in our system is generated by the LDEI, we choose to perform a Fourier analysis on the direct side-view visualizations. The movie analysis is performed using GoPro movies in the librating frame and MATLAB. First, a window of typically 300 $\times$ 300 pixels is chosen in the movie. This wide window is then typically subdivided into 36 sub-windows of 50 $\times$ 50 pixels for which the mean intensity is calculated for each frame. This method partially removes the noise that is present when considering the signal from a single pixel. A Fast Fourier Transform is then performed on these 36 signals, either over a sliding average of typically 90 libration periods to see temporal changes, or over larger parts of the signal to have a better frequency resolution and conduct a global analysis. We use a Hanning window to avoid spectral leakage. Finally, all these 36 spectra are stacked, once again to reduce the noise.

A similar approach is used to analyze and compare PIV with light intensity results. For each box of the PIV located inside the same window as the one defined for the Kalliroscope movies, a Fast Fourier Transform is performed on both the horizontal and vertical components of the velocity. The spectra corresponding to each box are then stacked.

6.3.2.3 Kalliroscope-PIV comparison

One of the objectives of our study is to develop a method that allows for quick and easy identification the presence of the elliptical instability. Thus, the PIV method is used to verify the results of the light intensity analysis. Figure 6.13 in the Appendix shows the results of

the spectral analysis performed on both PIV and light measurements, in both vertical and horizontal planes. A direct comparison between the predominant frequency peaks shows that the analysis of the Kalliroscope visualizations can capture, qualitatively, the spectral content provided by the PIV results. Therefore, this analysis is sufficient to characterize the frequency signature of the LDEI. In the subsequent analysis, all temporal spectra are thus obtained using Kalliroscope visualizations.

6.3.3 Numerical simulations

To complement experimental measurements, we also perform Direct Numerical Simulations (DNS) in the librating frame, where both the spherical inner and ellipsoidal outer boundaries satisfy a no-slip velocity condition. We solve the equations of motion in (6.4) and (6.5) using the spectral element solver Nek5000 developed and supported by Paul Fischer and collaborators (Fischer et al. (2007, 2008)). This method has already been used to study longitudinal libration and tides in ellipsoidal container (Favier et al. (2015); Barker (2016); Grannan et al. (2017)). Spectral element methods have excellent convergence properties, required to simulate turbulent flows, while being able to consider complex geometries. The mesh is an unstructured array of $\mathcal{E}$ deformed hexahedral elements. Inside each element, the spectral element mesh is structured, with the variables expressed as sums of N-th order Lagrange polynomials on tensor-products of Gauss-Lobatto-Legendre (GLL) quadrature points. In this paper, all the simulations are performed using a third order explicit extrapolation scheme for the nonlinear convective terms and the linear inertial forces, and a third-order implicit Backward Difference scheme for the linear diffusive term. Convergence was checked by increasing the order of the polynomial decomposition within each element.

We first perform a simulation to qualitatively confirm and compare with the experimental results. The geometry is identical to the experiment with $\beta = 0.34$. We focus on a case with $\chi = 0.491$, $f = 4$ and $\epsilon = 0.35$. For this relatively weak librational forcing, we are able to reach the same Ekman number as in the experiment, $E_\chi = 10^{-4}$ (or equivalently $E = E_\chi(1-\chi)^2 = 2.6\times10^{-5}$). For this simulation, the mesh is composed of $\mathcal{E} = 18432$ hexahedral

elements with a polynomial decomposition of order $N = 10$. For the spectral analysis discussed in section 6.4.2.1, we store the velocity components at 200 random positions within the ellipsoid, both inside and outside the tangent cylinder. The velocity is interpolated from the grid to the probe position with spectral accuracy.

Additionally, we run several simulations to study the instability close to threshold. The objective is to confirm the experimental results discussed in section 6.4.3. To do so, we choose the following set of parameters: $\chi = 0.37$, $f = 4$ and we vary both the Ekman number and the libration amplitude ϵ in order to determine empirically the instability threshold. We start the simulations with a low amplitude random initial condition and we wait for the perturbations to vary exponentially with time. For these simulations, the mesh is composed of $\mathcal{E} = 3840$ elements with a polynomial decomposition of order $N = 11$.

6.4 Results

6.4.1 Basic flow

The theoretical basic flow (6.8)-(6.9) is compared to the experimental basic flow measured using PIV analysis. Figure 6.4(a) compares the amplitude of the theoretical basic flow with the experimentally measured basic flow while the vector plots of the theoretical and experimental base flows are shown in Figure 6.4(b). Note that in the relative error panel, the large errors located at the right of the core are due to a reflection creating a large bright patch which prevents the computation of the particle displacements. The general trend of the velocity amplitude along s, indicated by the black arrow in Figure 6.4(b) is found to be in good agreement in Figure 6.4(c). Large discrepancies occur at the viscous layers close to the inner and outer rigid boundaries, which are not accounted for in the theoretical base flow. The fact that the experimental velocity amplitude is slightly lower than the one theoretically-predicted may also be due to the viscous corrections that drive weak zonal flows in the bulk.

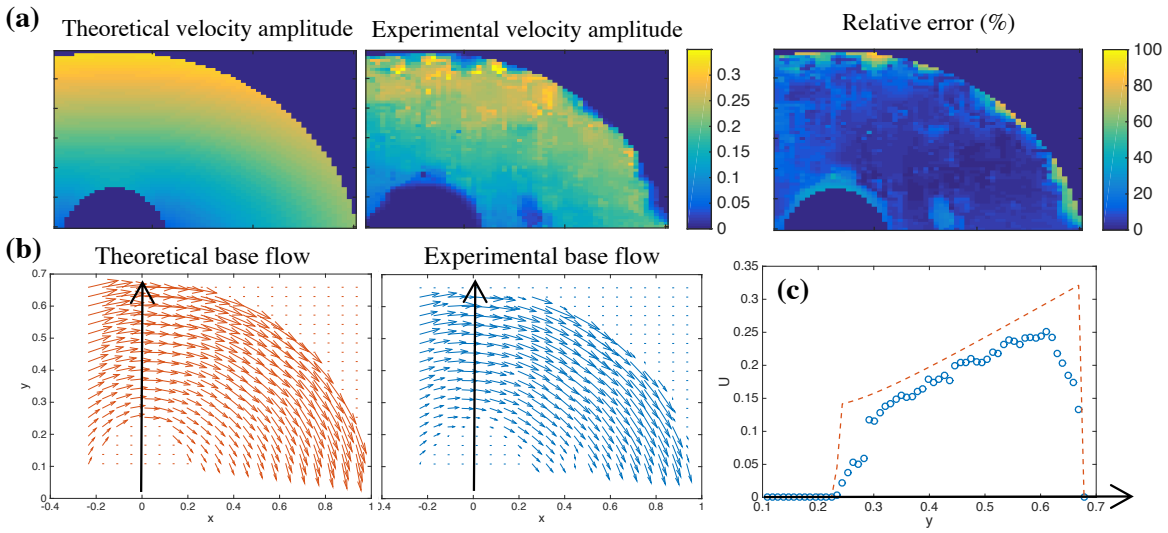

Figure 6.4: Comparison between the theoretical base flow in (6.8) and (6.9) and the PIV measurements. **(a)** Velocity amplitude. **(b)** Velocity field. **(c)** Evolution of the velocity amplitude in the y direction for x=0.

6.4.2 Flow Visualizations and Fourier Analysis

6.4.2.1 Mode coupling and spatial heterogeneity

For all the unstable cases, the flow visualizations show a strong similarity between the full ellipsoid case and the shell case, as illustrated by the snapshots and the spectra in Figures 6.5 and 6.6. Note that snapshots for other core sizes are provided in the appendix (Figure 6.14). Additionally, a video demonstration showing the early stages of the instability with and without an inner core as well as the corresponding numerical simulation is given in Lemasquerier et al. (2016).

We focus on the unstable cases with $f = 4$ shown in Figure 6.5. In Figure 6.5(a), the growth of the instability is shown in three snapshots over approximately 400 librational periods. The red and blue windows on the far right image in Figure 6.5(a) demarcate the areas where the light intensity fluctuations are analyzed outside and inside the tangent cylinder respectively, and shown in Figure 6.5(b). The resulting frequency spectrograms from outside and inside the tangent cylinder are shown in Figure 6.5(c). Advancing through time from left to right in Figure 6.5, after the libration is activated, a tangent cylinder forms

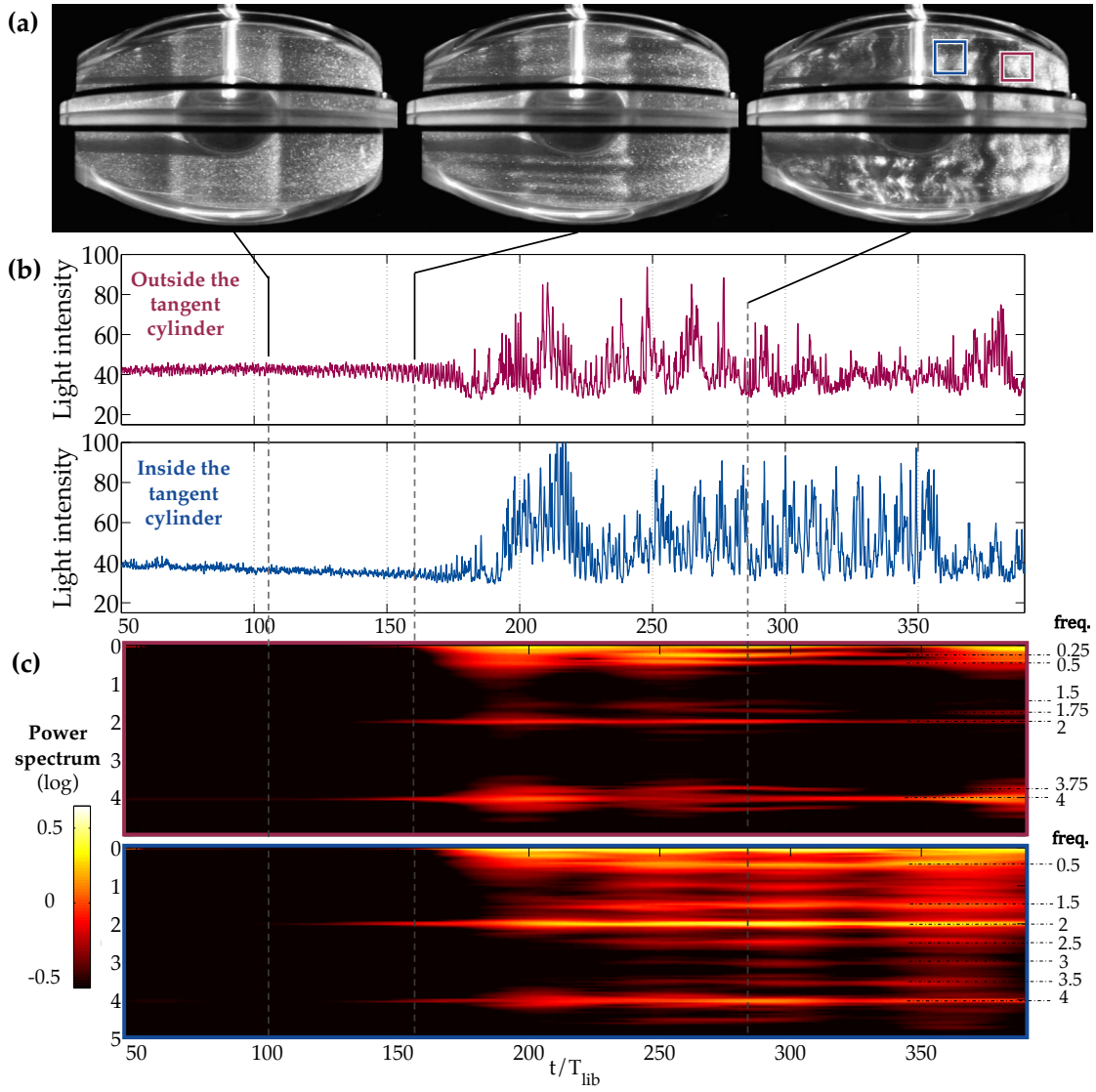

Figure 6.5: Light intensity analysis results for the case $\chi = 0.37$, $E_\chi = 6 \times 10^{-5}$, $\Delta\phi = 5°$ and $f = 4$ ($\epsilon = 0.35$). **(a)** Snapshots extracted at different times from the movie recorded by the Canon camera. **(b)** Light intensity signal extracted from one of the submatrices of the wide windows drawn on the last snapshot. **(c)** Successive power spectra performed over a sliding window of 90 T_{lib} to illustrate the temporal variations of the frequency content of the signal.

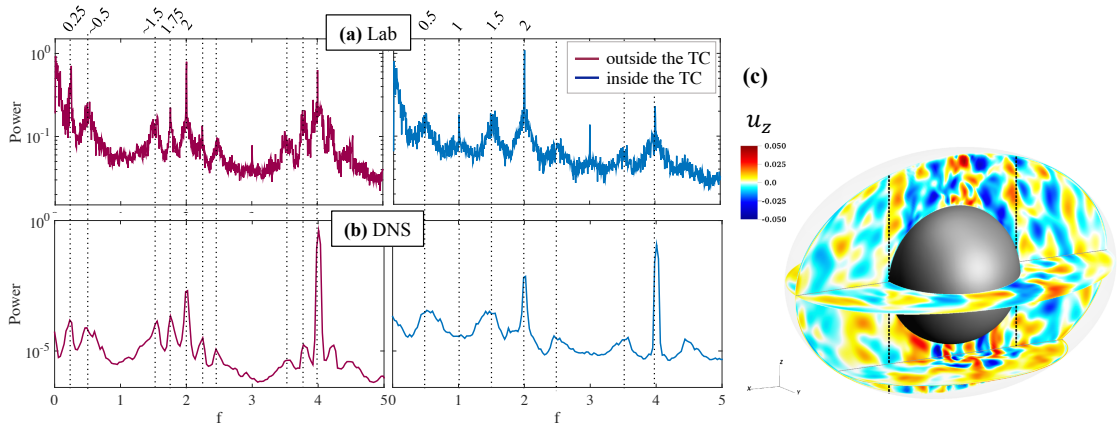

Figure 6.6: Analysis of the case with $E_\chi = 10^{-4}$, $\chi = 0.49$, $\Delta\phi = 5°$ and $f = 4$ ($\epsilon = 0.35$). **(a) Laboratory:** power spectra of the light intensity extracted from $t = 200$ to 1400 T_{lib} on a vertical plane, both inside and outside the tangent cylinder (TC). **(b) Numerics:** power spectra from numerical velocity signals both inside and outside the tangent cylinder. The vertical dotted lines correspond to the frequencies of the main peaks. **(c)** Vertical component of the velocity during the saturated phase shown on three slices across the ellipsoidal shell (see also Figure 6.7 for the early stages of the instability and a comparison with the experiment). The vertical dashed lines correspond to the intersection between the tangent cylinder and the meridional plane.

around the inner core and the light intensity signal is dominated by oscillations at the forcing frequency $f = 4$ corresponding to the base flow. The tangent cylinder is a particular shear layer corresponding to a frequency $f = 0$ for which the cone defined by the wave packet takes the form of a cylinder ($\theta = \pi/2$) reminiscent of a Taylor column (Messio et al., 2008). Then, we see the development of the pancake-like shearing structures similar to those observed by Grannan et al. (2014) and Favier et al. (2015). Its similarity with the inertial modes found in the full ellipsoid case is confirmed by the appearance of an $\omega = 2$ peak as seen in the frequency spectrograms in Figure 6.5(c) between $\sim 100 - 150$ T_{lib}. This frequency meets the first resonance condition $|\omega_1 - \omega_2| = 4$. Finally, when the instability saturates, a wave-breaking event occurs and three-dimensional motions develop. After this breaking, the observed state of bulk turbulence is similar to the intermittent turbulence found by Grannan et al. (2014); Favier et al. (2015) with columnar structures that are sheared by the $\omega = 2$ modes as seen on the last snapshot of Figure 6.5(a). When the quasi-steady state is reached, the $\omega = 2$ peak remains, but additional frequencies ≤ 2 appear as seen in Figure 6.5(c) around 200 T_{lib}. These secondary peaks, namely the couples [1,1], [0.5,1.5], [0.25, 1.75] match

a resonance condition we can write as $|\ \omega_1\ -\ \omega_2\ |\ =\ 2$. They could thus be the result of a secondary resonance with the primary inertial modes at $\omega \sim 2$. Such a secondary resonance has already been observed in full ellipsoids (Grannan et al., 2014; Favier et al., 2015).

This general behavior is common to every unstable cases considered here. The more supercritical the insability is, the less efficient the re-laminarization. However, a spatial discrimination seems to appear and becomes more obvious as the shell gets thinner. We observe that the $\omega = 2$ layered structures appear above and under the inner core and extent horizontally until they reach the outer boundary. For large inner cores, the wave-breaking event always occurs primarily at the poles inside the tangent cylinder resulting in strong turbulence whereas it does not occur as strongly in the equatorial regions outside the tangent cylinder. However, the instability still seems to grow everywhere in the bulk as seen in the second panel of Figure 6.5(a).

To confirm these flow differences, we performed a Fourier analysis on two different windows in the shell as represented on the last snapshot of Figure 6.5(a). Performing a spectral analysis during the turbulent phase at these two different locations directly shows differences in terms of frequency content, as seen experimentally and numerically in Figure 6.6 for a shell of radius ratio $\chi = 0.49$. The major difference, visible in both Kalliroscope or PIV results (Figures 6.6 and 6.13), relates to the frequencies previously identified as secondary inertial modes. Spectra computed outside of the tangent cylinder show the two couples $|\omega_{1,2}| \approx$[0.25,1.75] and [0.5, 1.5], the first one being predominant. On the contrary, inside of the tangent cylinder, the couple $\sim$[0.25,1.75] seems, if not absent, far dominated by the couple [0.5, 1.5]. This difference is observed on all our unstable cases, except for the smallest inner core ($\chi = 0.24$).

Let us mention here that despite the peaks that we attribute to LDEI, the spectra shows other important peaks. Namely, the presence of a peak at $\omega = 0.25$ is almost systematically associated with peaks at $\omega = 2 \pm 0.25$ and 4 ± 0.25, and the same coupling is observed for the peak at $\omega = 0.5$. This may be due to non-linear interactions (non-resonant) between the secondary inertial modes and the base flow or the primary inertial mode.

The same analysis is conducted in the Appendix for $f = 2.4$ (spin-over mode, see appendix 6.6.3). It shows the persistence of the LDEI at this particular forcing frequency.

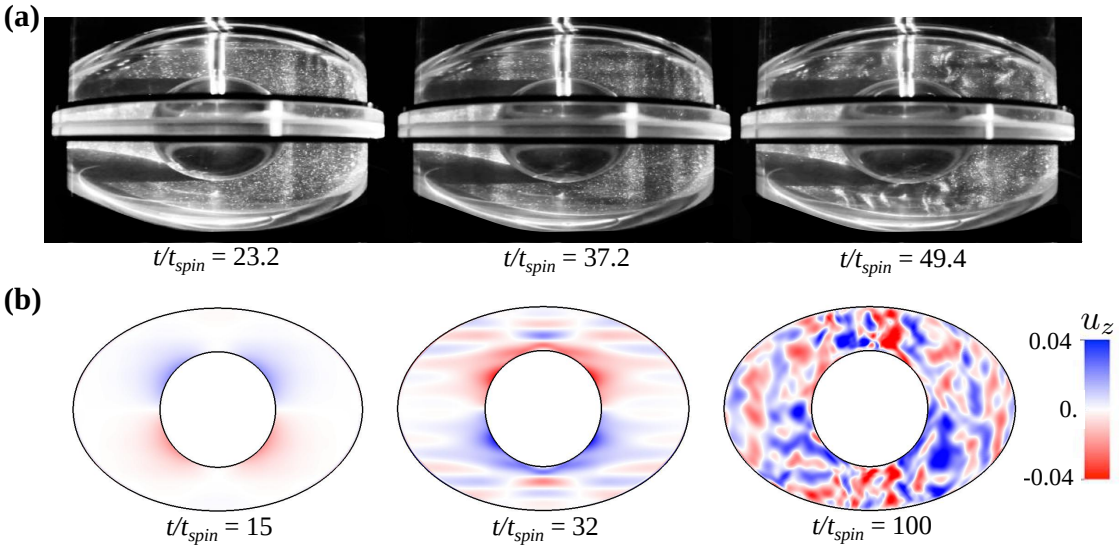

Figure 6.7: Comparison of the onset of LDEI for laboratory experimental and numerical simulations through meridional side-view visualizations at $E_\chi = 10^{-4}$, $f = 4$, $\epsilon = 0.35$, and $\chi = 0.49$. **(a)** Experiments: Kalliroscope visualizations made in the rotating frame. **(b)** Numerical simulations: the vertical velocity is shown through snapshots made in the librating frame.

We confirm these results with a DNS for the particular case $\chi = 0.49$, $\epsilon = 0.35$ and $E_\chi = 10^{-4}$. First, Figure 6.7 shows a qualitative comparison of the onset of LDEI visualized experimentally and numerically in a meridional plane. Then, the results on inertial modes couplings are confirmed by an analysis on the numerical simulation. Velocity signals are extracted at 100 random locations during the saturated phase, both inside and outside the tangent cylinder. Figure 6.6(b) shows the corresponding power spectra, averaged over all three velocity components and over all probes, where the forcing frequency at $\omega = 4$ and primary resonating inertial modes at $\omega = 2$ are the dominant contributions in both regions. Outside the tangent cylinder, the two dominant frequency couples are $|\omega_{1,2}| \approx [0.25, 1.75]$ and $|\omega_{1,2}| \approx [0.5, 1.5]$, as observed in the experimental Kalliroscope data. Inside the tangent cylinder however, the only resonant frequencies are $|\omega_{1,2}| \approx [0.5, 1.5]$. Note that the kinetic energy is typically larger inside the tangent cylinder than outside, which is confirmed by the visualization of the vertical velocity shown in Figure 6.6(c). Intense overturning structures

are observed above and below the inner core whereas a relatively smooth wave field is observed outside the tangent cylinder. Another interpretation is related to the heterogeneity in the effective ellipticity of the streamlines. Above and below the inner core (*i.e.* for $|z| > \chi$), the base flow is only weakly affected by the presence of the inner core so that the ellipticity is approximately uniform and equal to β. When $|z| \leq \chi$ however, the ellipticity of the streamlines is decreasing as they get closer to the inner core (see the base flow properties in section 6.2.2), leading to smaller growth rates (see (6.16)) and presumably less intense flows at saturation. To conclude, our results show that the presence of the inner core leads to significant spatial heterogeneities, both in terms of resonant frequencies but also in terms of fluid motion amplitudes.

6.4.2.2 Influence of the radius ratio of the shell and of the Ekman number

Figure 6.8 represents spectra realized over the turbulent phase of laboratory cases involving different inner core radii. When there is no core inside the ellipsoidal cavity, the temporal spectra are less rich and only the forcing frequency $f = 4$ and the primary inertial modes $|\omega_{1,2}| = 2$ are clearly present. The spectra are richer when a core is added, with typical frequencies around $\omega \sim 0.25, 0.5, 1.5$ and 1.75 as previously discussed. More interestingly, these $\omega < 2$ peaks do not correspond to the exact same frequencies when comparing different χ values. For instance, the $\omega \sim 0.25$ peak is broad, spanning from $\omega_1 = 0.16$ to 0.3, together with its companion of frequency $\omega_2 = 2 - \omega_1$. This is reminiscent of the behavior of forced inertial modes in the spherical shell observed by Ogilvie (2009), where the dissipation at a given frequency strongly depends on the shell aspect ratio. The question remains open whether this change is due to variation in the inviscid eigenfrequency of the resonant mode or due to changes in its viscous damping.

Figure 6.9 compares the frequency content of two cases for which the Ekman number is significantly different. Visually, the two cases become turbulent, beginning at the poles. The $|\omega| = 2$ inertial modes always remain even during the turbulent phase. The low-Ekman case, which is less viscously dominated shows additional peaks compared to the high-Ekman

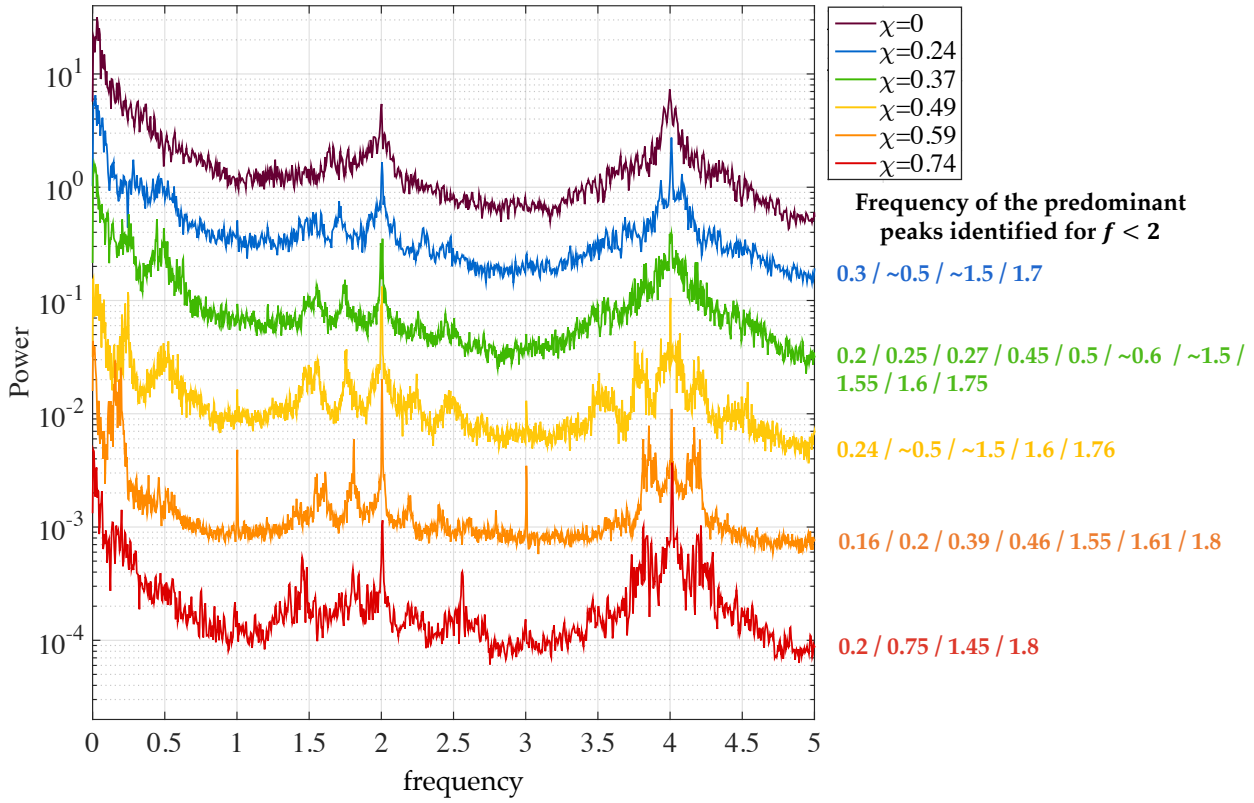

Figure 6.8: Power spectra of "side" signals performed over the turbulent phase of cases with different inner core radius: $[\chi = \mathbf{0},\ E_\chi = 4 \times 10^{-5},\ \epsilon = 0.28]$, $[\chi = \mathbf{0.24},\ E_\chi = 1 \times 10^{-4},\ \epsilon = 0.35]$, $[\chi = \mathbf{0.37},\ E_\chi = 4 \times 10^{-5},\ \epsilon = 0.28]$, $[\chi = \mathbf{0.49},\ E_\chi = 1 \times 10^{-4},\ \epsilon = 0.35]$, $[\chi = \mathbf{0.59},\ E_\chi = 4 \times 10^{-5},\ \epsilon = 0.28]$ and $[\chi = \mathbf{0.74},\ E_\chi = 6 \times 10^{-4},\ \epsilon = 0.70]$. The power spectra are arbitrarily shifted vertically for clarity.

case. This observation is compatible with the results of Le Reun et al. (2017), showing that an inertial wave turbulence regime - i.e. a turbulence made of the superimposition of many low-amplitude inertial waves excited by successive triadic resonances - is expected in the limit of small Ekman number.

6.4.3 Instability Threshold

Results of the libration amplitude threshold for each case are plotted in Figure 6.10(a). Neglecting bulk dissipation, the threshold of instability is defined as the condition for which $\sigma_{inv} > K\sqrt{E_\chi}$. Since f and β are constant, formula (6.17) shows that, in our case, the libration amplitude at the threshold $\Delta\phi_{thres}$ is a function of $E_\chi^{1/2}$ only (for a given χ).

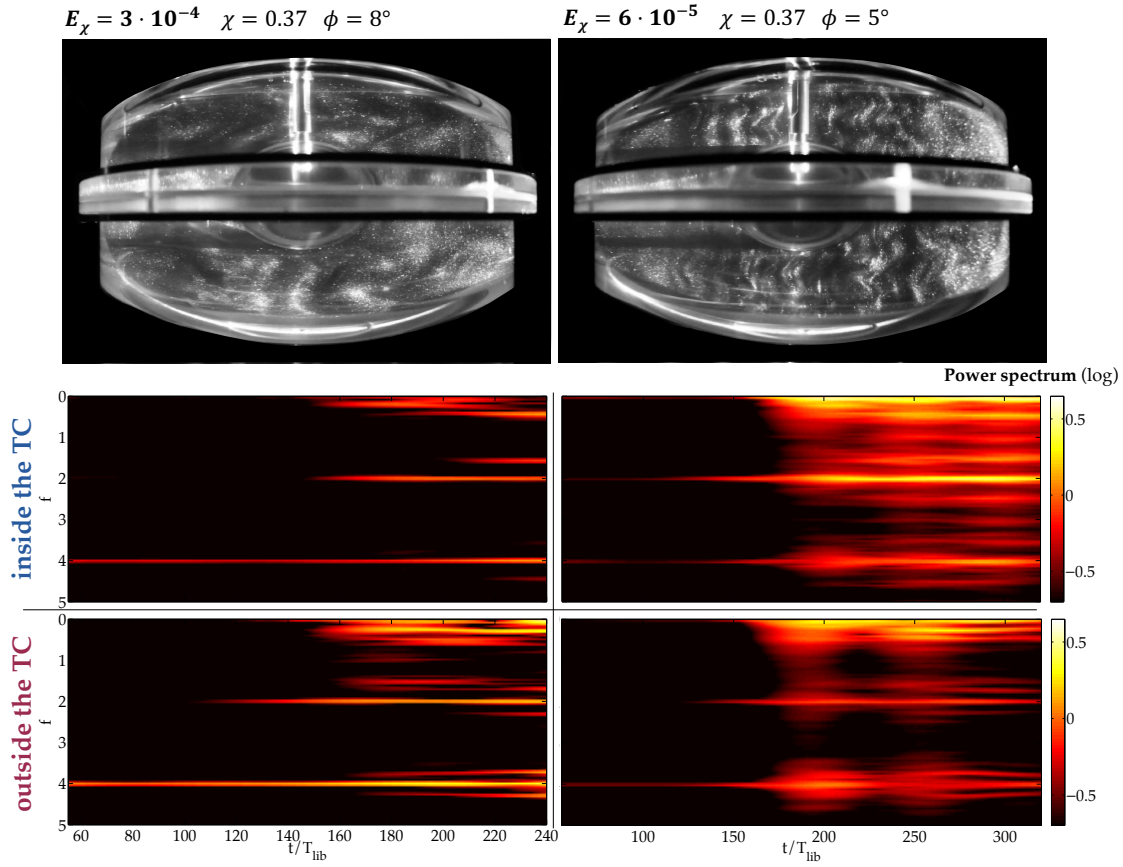

Figure 6.9: Successive power spectra performed over a sliding window of 90 T_{lib}, both inside and outside the tangent cylinder (TC). The two cases correspond to the same shell and forcing parameters but at two different Ekman numbers ($\Omega_0 = 37.6$ RPM on the right-hand panel, and 7.5 RPM on the left).

Figure 6.10 (a) shows that for all our cores, and even in the case of a full ellipsoid ($\chi = 0$), this scaling is not verified. The critical libration amplitude instead varies as $\sim [E_\chi^{0.63} - E_\chi^{0.72}]$, with slight variations depending on the core considered. The numerical results represented on the same figure confirm this for the particular case $\chi = 0.37$. Note that the numerical simulations predict a slightly lower critical libration amplitude compared to the experimental observations. This might be due to the presence of the shaft holding the inner sphere and interfering with large-scale inertial modes while also adding extra dissipation into the system.

Assuming a mean scaling of $E_\chi^{0.65}$, we deduce the corresponding dissipating factor is from formula (6.17)

$$\alpha\Psi(\chi) = \frac{16 + f^2}{64}\epsilon_{thres}\beta E_\chi^{-0.65}. \tag{6.18}$$

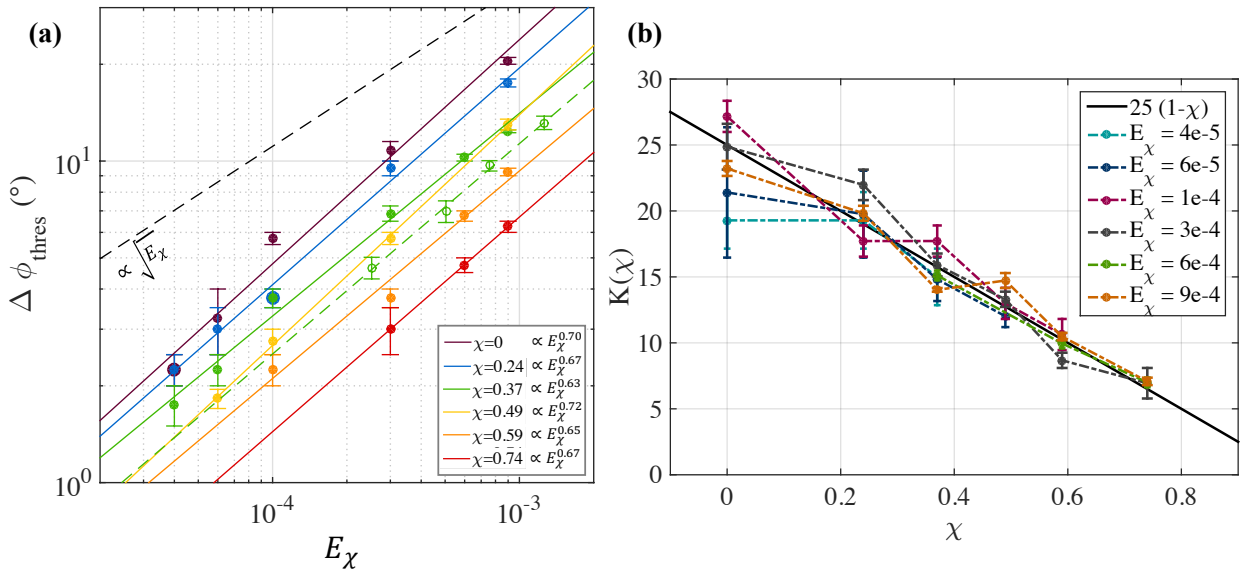

Figure 6.10: **(a)** Libration amplitudes at the threshold determined experimentally (full lines) and numerically (dashed green line) **(b)** Dissipation factors K determined using the $\Delta\phi_{thres}$ values from (a) and (6.18). The black line shows the main dependence with the radius ratio.

The result is represented as a function of χ in Figure 6.10(b). The dependence with the radius ratio of the shell seems to follow $(1-\chi)$ with a slope $\alpha \sim 25$. Nevertheless, we do not claim here that this new estimate for the threshold is universally valid: we rather think that it is valid only for the range of Ekman number explored in this study, corresponding to a transition between the regime at large Ekman number dominated by bulk dissipation (threshold scaling as E_χ^{-1}) and the regime at low Ekman number dominated by boundary dissipation (threshold scaling as $E_\chi^{-1/2}$). This will be further discussed below in section 6.5.2.

6.5 Discussion and perspectives

In this study, we first qualitatively show that longitudinal libration can directly excite inertial waves in an ellipsoidally deformed shell. Then, we used direct Kalliroscope visualizations of the flow as well as PIV to confirm the existence of the libration-driven elliptical instability (LDEI) in a deformed shell geometry when the libration frequency is 4 and 2.4 times the rotation rate. The presence of an inner core does not strongly modify the structure of the unstable mode compared to the full ellipsoid case, at least for those two forcing frequencies.

We recover the participation of inertial modes at frequencies $\pm f/2$ and Fourier analysis suggests that we might also be able to see secondary inertial modes excited by the primary inertial modes, whose frequencies only slightly depend on the radius ratio of the shell.

However, in all our cases, the turbulence that develops in the bulk is never homogeneously distributed. Outside the tangent cylinder, a quick re-laminarization occurs after the growth of the instability, but no LDEI cycle is clearly visible. Instead, the flow is dominated by geostrophic shear layers on which the inertial modes are superimposed. Besides, we notice that the growth of the instability always occurs first at the poles. The fact that the spectral content is different from the rest of the bulk suggests that the resonating inertial modes do not extend uniformly in the whole shell and may be locally stronger in the polar regions. The elliptical instability may thus induce significant spatial differences of the flow in the bulk interior, especially for a large inner core (see Figure 6.14 in Appendix). These different behaviors inside and outside the tangent cylinder are reminiscent of the two regimes of non-linear saturation described by Le Reun et al. (2017). In this study, the authors perform local numerical simulations of highly turbulent flows driven by elliptical instability, considering only a small parcel of the ellipsoidal core. They adjust the amplitude of the boundary dissipation through Ekman friction, depending on the aspect ratio of the excited geostrophic structures. For large aspect ratios corresponding in our case to the region outside the tangent cylinder, boundary dissipation is relatively small, and the non-linear saturation of the elliptical instability gives rise to large scale geostrophic structures concentrating most of the kinetic energy through an inverse cascade mechanism (see e.g. Barker and Lithwick (2013)). On the contrary, for small aspect ratio corresponding in our case to the region inside the tangent cylinder, the non-linear saturation of the elliptical instability gives rise to small-scale bulk filling turbulence following successive triadic resonances of inertial waves: a so-called inertial wave turbulence might be expected asymptotically at low Ekman numbers.

6.5.1 Inertial modes of a shell

The theoretical results concerning inertial modes in a spherical shell derived by Rieutord et al. (2001); Rieutord and Valdettaro (2010) are obtained under the assumption of a very weak forcing ($\epsilon \ll 1$) whereas it is not the case in our experiments ($\epsilon \in [0.1, 2]$). While we do observe localized shear layers generated at the inner boundary (see Figure 6.1), the instability discussed in this paper shares many similarities with the case of a full ellipsoidal container, where resonances between regular global inertial modes are responsible for the instability (Favier et al., 2015). In addition the experiments and numerical simulations are currently limited to much higher values of the Ekman number than those used in theoretical studies. Thus, the relative importance between localized shear layers and global inertial modes remains to be clarified, especially when both the forcing and the Ekman number are decreased. The fact that only localized polar areas seem to resonate (see the heterogeneous nature of the resulting turbulent flow in Figure 6.6(c) for example) may suggest that regular inertial modes can exist locally and that the elliptical instability can locally develop independently of the global geometry. This is reminiscent of high-frequencies equatorially-trapped inertial waves (Zhang, 1993) which are not affected by the presence of an inner core, although the possible link between these two problems remains to be explored. Further studies are therefore needed to assess the relevance of extending the present results to planetary conditions where the Ekman number is vanishing and the forcing is very small.

6.5.2 Apparent discrepancy between observed viscous damping and theory

In our experimental and numerical results shown in Figure 6.10 (a) we do not recover the expected scaling law in $E^{1/2}$ for the Ekman numbers we consider in this study ($E_\chi = 10^{-5} - 10^{-3}$). Instead, we predict for a libration frequency $f = 4$ that the linear viscous growth rate is

$$\sigma \approx \frac{16 + f^2}{64}\epsilon\beta - \alpha(1-\chi)E_\chi^{0.65}, \tag{6.19}$$

with $\alpha \sim 25$. The origin of this scaling in $E^{0.65}$ needs to be addressed. Since it is also observed in the full ellipsoid ($\chi = 0$), the underlying mechanism is not specific to the shell

geometry. Moreover, it is in apparent disagreement with previous studies of the viscous damping of the spin-over mode in full ellipsoids (Lacaze et al., 2004; Cébron et al., 2010a). Focusing on the full ellipsoid case below (where the inertial modes problem is well-posed), we provide a theoretical argument that the scaling in $E^{0.65}$ is possible but only for large Ekman numbers.

Since the inertial modes form a complete basis in full ellipsoids (Backus and Rieutord, 2016), we can expand the velocity perturbation $\mathbf{u}(\mathbf{r},t)$ solution of the momentum equation (6.4) onto inertial modes. Using the boundary layer theory, we can determine the leading order viscous effect on each inertial mode from the inviscid solutions. Following Greenspan (1969), we expand the perturbation solution of the initial-value problem as

$$\mathbf{u}(\mathbf{r},t) = \sum_i \alpha_i(t)\mathbf{Q}_i(\mathbf{r})\exp([\mathrm{i}\omega_i + \tau_i]t), \tag{6.20}$$

where $(\mathbf{Q}_i(\mathbf{r}),\omega_i)$ are eigenvector-eigenfrequency solutions of the inertial mode problem (6.10)-(6.11), $\alpha_i(t)$ the modal coefficients and τ_i the viscous corrections of the inviscid eigenfrequencies ω_i. Greenspan (1969) introduces the theory up to order $E^{1/2}$, considering only dissipation in the Ekman boundary layer and neglecting bulk dissipation which appears at the next order E. One can support this truncation with the fact that inviscid inertial modes satisfy the intriguing property (Zhang et al., 2004; Vantieghem, 2014)

$$E\int_{\mathcal{V}} \mathbf{Q_i}^* \cdot \nabla^2 \mathbf{Q_i}\,\mathrm{d}\mathcal{V} = 0, \tag{6.21}$$

with * indicating the complex conjugate. This volume integral is often associated with the viscous dissipation of inertial modes. However, as explained by Liao and Zhang (2008), property (6.21) is not physically realistic and is due to the unrealistic inviscid boundary conditions. Thus we take into account viscous dissipation up to order E to be accurate in the asymptotic expansion, extending the theory of Liao and Zhang (2008) from spheres to triaxial ellipsoids. We expand the viscous correction τ_i as

$$\tau_i = E^{1/2}s_i + E\lambda_i, \tag{6.22}$$

where s_i is the viscous correction due to the surface Ekman layer, introduced by equation (2.9.12) of Greenspan (1969), and $\lambda_i < 0$ is the leading order volume viscous damping. The former is a complex number whose real part $\Re_e(s_i) < 0$ is the viscous decay rate of the mode and the imaginary part $\Im_m(s_i)$ is the viscous shift in frequency of the mode. Finally the volume damping $\lambda_i < 0$ is proportional to the vorticity of the inviscid mode.

We have computed the first 1480 inviscid inertial modes of our ellipsoidal configuration as described by Vidal et al. (2016, 2017). Then, in figure 6.11, we show the absolute value of the viscous damping as a function of the Ekman number. Only the spin-over mode (dashed back line) and modes of absolutes frequencies $|\omega_i| > 1.8$ (blue shading) are represented, the latter being the most excited modes for the libration frequency $f = 4$. For all the modes, two limiting cases are observed: a viscous damping scaling as E for large Ekman number and as $E^{1/2}$ for low Ekman numbers. Between these two limits there is a transition zone where surface dissipation and bulk dissipation are of the same order of magnitude. For a given inertial mode, the Ekman number of transition depends on the spatial complexity of the flow. Results for the spin-over mode shows that the damping in $E^{1/2}$ overcomes the damping in E when $E \leq 3.10^{-2}$ (vertical dashed line). It is in agreement with previous studies (Lacaze et al., 2004; Cébron et al., 2010a), which considered the spin-over mode at Ekman numbers $E \leq 10^{-3}$. However, the scaling observed in the present study ($E^{0.65}$, red solid line) lies in the transition zone where the two dampings play a role (depending on the excited mode). The $E^{0.65}$ scaling is due to a competition between surface dissipation and bulk dissipation. Finally, we observe in practice that the lowest Ekman number of transition depends on the number of considered modes. However, from Figure 6.11 we expect that the $E^{1/2}$ scaling may be observable for Ekman numbers $E \ll 10^{-7}$.

6.5.3 Extrapolation to planetary interiors conditions

Apart from the question of the existence and the form of inertial modes in a given geometry, local stability analysis can be used to evaluate the presence of the elliptical instability in terrestrial bodies. In terms of stability analysis, in the regimes experimentally and numeri-

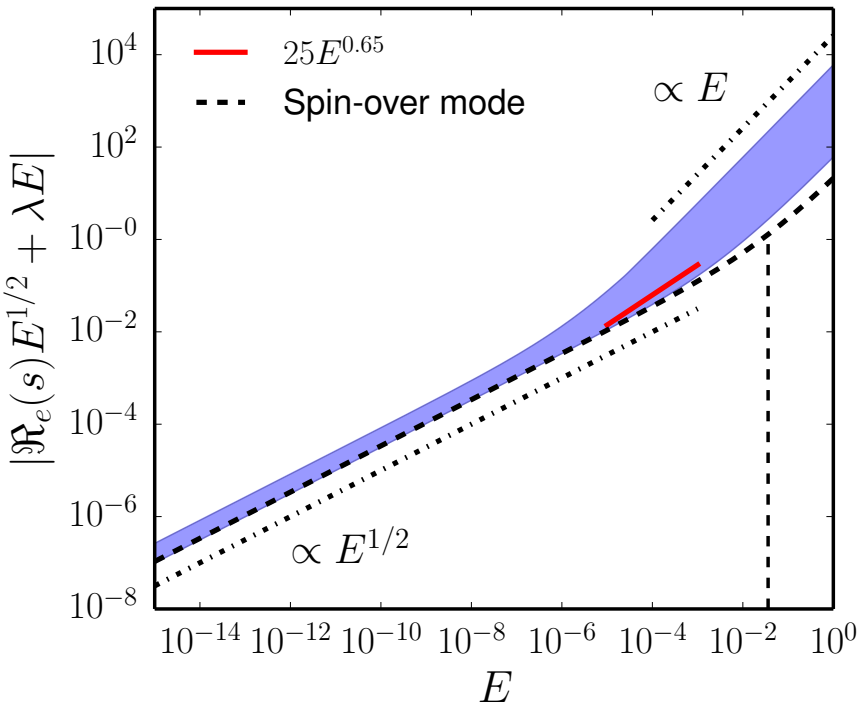

Figure 6.11: Viscous damping of inertial modes as a function of the Ekman number E for the first 1480 inertial modes of our full ellipsoid. The viscous damping is a combination of the surface Ekman layer damping $\Re_e(s)E^{1/2}$ and the bulk viscous damping λE. We only show the spin-over mode (dashed back thick line) and the first 140 modes of frequencies $|\omega_i| > 1.8$ (blue shading), which are the most excited modes for $f = 4$. The vertical dashed line shows the Ekman number for which volume and surface dampings of the spin-over mode are equal. Slopes of asymptotic behaviors associated with surface and volume dampings are also shown. The surface damping only dominates when $E \ll 10^{-7}$.

cally explored in this study the usual scaling $\sqrt{E}$ is not verified because of bulk dissipation. However, it holds when extrapolating to planetary conditions. Thus, for $f = 4$, and in the range of parameters of this study, the growth rate σ is

$$\sigma \approx \frac{16 + f^2}{64}\epsilon\beta - \alpha(1-\chi)E_\chi^{0.65} \tag{6.23}$$

with $\alpha \sim 25$, whereas for $E \ll 10^{-7}$,

$$\sigma \approx \frac{16 + f^2}{64}\epsilon\beta - \alpha\sqrt{E} \tag{6.24}$$

with $\alpha \sim 3$. The criterion of instability $\sigma > 0$ is plotted as a function of E on Figure 6.12.

Knowing the parameters involved in these equations for a given interior layer of a body thus allows to estimate whether it is theoretically unstable or not (criterion $\sigma > 0$). We apply this criterion to the four Galilean moons (Io, Europa, Ganymede and Callisto), two moons of Saturn (Titan and Enceladus) and three Super-Earths expected to be telluric (55 CnC e, CoRoT-7b and GJ 1214b). All the bodies considered here are in synchronous rotation, their mean rotation period being equal to their orbital period (librations of dimensionless frequency $f = 1$).

The maximum amplitude of libration is theoretically equal to the amplitude of the variations of the orbital velocity, *i.e.* $2e$, where e is the orbital eccentricity. However, this is an optimal case which implies that the spin rate of the body is so slow or the body is so elastic that it has the time to completely adapt to the gravitational constraints. This maximal libration is called the *optical libration*. However, because of the rigidity of the outer boundary of the shell and of the spin rate, the amplitude of the differential rotation ϵ between the fluid and the librating static bulge is smaller than $2e$.

Finally, because the equatorial ellipticity β of the considered fluid layer is generally unknown, Cébron et al. (2012a) estimate it by assuming an hydrostatic equilibrium shape, which gives

$$\beta = \frac{3}{2}\left(1 + k_2\right)\frac{M}{m}\frac{R^3}{D^3} \tag{6.25}$$

where m and R are respectively the mass and the mean radius of the considered body with a potential Love number k_2, D the distance between the body and its attractor of mass M. Table 6.2 gives the values used to calculate $\epsilon\beta$ for each body. Figure 6.12 represents the position of these bodies compared to the theoretical threshold extrapolated from our results when assuming an $E^{0.5}$ scaling for $E \ll 10^{-7}$.

This scaling shows that Enceladus ocean is expected to be unstable with a good level of confidence. Besides, since $\chi = 0.78$ (calculated from Cedak et al. (2016)), we expect strong spatial heterogeneities for the LDEI between the poles and the equator, as seen when varying the size of the inner cores used in our experiments. This might help to explain the variations of Enceladus ice shell thickness, which is modeled by Cedak et al. (2016) to be 18-22 km

thick in average, but reduced at the poles (up to 5 km at the South Pole).

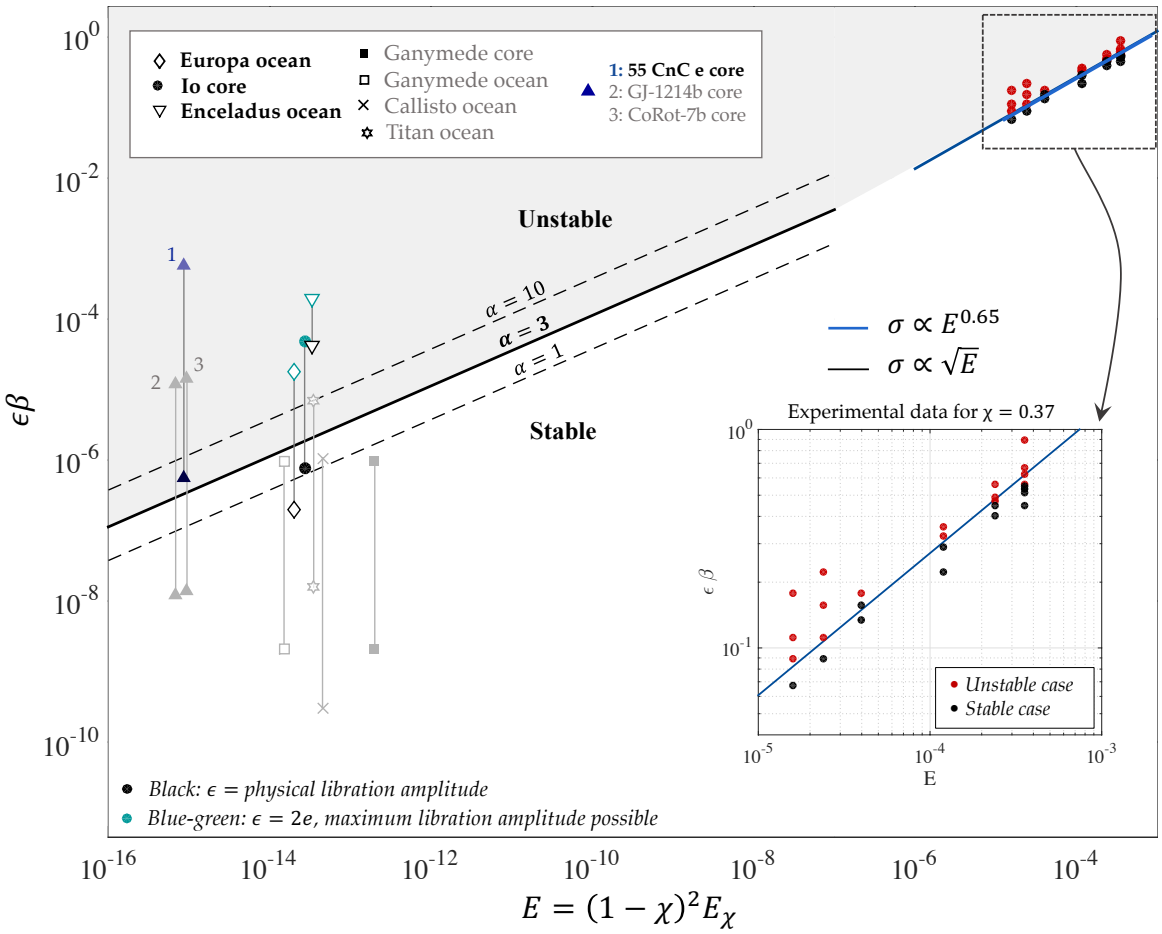

Figure 6.12: LDEI stability diagram. For each body, the vertical line represents the range from a libration amplitude equals to the physical libration up to the optimal libration amplitude $2e$. The bodies for which LDEI is likely absent are plotted in light gray. The oblique lines represent the criterion $\sigma > 0$, using equation (6.23) for $E \gg 10^{-7}$ and equation (6.24) for $E \ll 10^{-7}$. The $E^{0.5}$ scaling is justified by the hypothesis that the dissipation occurs mainly in the Ekman boundary layer. In our experimental survey (up-right corner), the $E^{0.65}$ scaling is due to a transition towards a regime for which bulk dissipation becomes more important. Note that for the regimes explored experimentally, the value of $\epsilon\beta$ at the threshold depends on χ (see Eq.(6.23)). That is why it is only represented for $\chi = 0.37$. The dashed lines represent two extreme values for $\epsilon\beta$ at the threshold, using $\alpha = [1, 10]$. The gray space is the unstable region.

Then, an elliptical instability is possible but uncertain for other fluid layers like Io core and Europa ocean since they are near the threshold when considering their physical libration amplitude. However, the libration amplitude of the icy shell of Europa is taken from Van Hoolst et al. (2008) but has not been measured yet with accuracy. That is why for Europa's

ocean, the whole range of values has to be considered, and it has a non-negligible chance to be unstable. It is improbable that the core of Ganymede and the subsurface oceans of Callisto and Ganymede are unstable, considering their proximity with the threshold. The same uncertainty is observed for the subsurface ocean of Titan, which is nevertheless more likely unstable. Finally, the (supposed) liquid cores of the three exoplanets considered are likely unstable because of their close orbit around their stars. The physical libration amplitude is here arbitrary taken as 3 orders of magnitude lower than the optical libration.

6.5.4 Perspectives and open questions

Our study focuses on the particular case for which the librating forcing ($f = 4$) indirectly excites inertial waves propagating quasi-horizontally. However, a look at 12 different forcing frequencies shows that this also excites $f \leq 2$ inertial waves, observed via the formation of oblique shear layers in the flow (Figure 6.1). Besides, we observe that an instability develops at the poles where the characteristics converge and that differential rotations are generated in the bulk (geostrophic shear layers). It may thus be of interest to conduct quantitative studies in this regime to estimate, for instance, dissipation rate, to verify the width of the shear layers and its scaling with Ekman, to measure the amplitude of the flow and to qualify the associated non-linearities such as the generation of zonal flows (Favier et al., 2014a).

It is now of primary importance to determine whether the elliptical instability persists for other forcing frequencies. Theoretically, all forcing frequencies between 0 and 4 should give rise to LDEI, in the limit of small Ekman. For now, we have simply verified that it was the case for $f = 4$ and $f = 2.4$ (Figures 6.5 and 6.15), and our analysis suggests the same conclusion for $f = 1.6$ for which we identify at least a coupling between inertial modes of frequencies $\omega_{1,2} = [0.35, 1.25]$ (not shown). Quantitative studies are also needed for a fine characterization of the non-linear turbulence following the growth of the instability and to verify and interpret the flow spatial differences observed in the bulk (e.g. Le Reun et al., 2017).

Finally, we show that the elliptical instability occurs in ellipsoidal shells. The associated

instability criterion has been described in this study in the case of longitudinal libration. Further studies are needed to define the instability criteria of latitudinal libration (e.g. Vantieghem et al. (2015) in the case of a full ellipsoid) as well as tidally-driven elliptical instability in ellipsoidal shells (Lacaze et al., 2005; Grannan et al., 2017), which may be less restrictive. Moreover, it has been recently observed that the orbital eccentricity favors elliptical instabilities (Vidal et al., 2017).

More generally, if they exist, the importance of these mechanically driven turbulent motions needs to be addressed. They may be of geophysical relevance for the following:

- **Energy dissipation**. The dissipation induced by direct and indirect tidal or librational resonances of fluid layers may play a role in the rotational or orbital dynamics of the considered planetary system (Le Bars et al., 2015). The relative importance of direct forcing compared to the elliptical instability also needs to be investigated.

- **Ocean Stratification**. Turbulent mixing may indeed lead us to question the stratification of subsurface oceans and the possibility for hosting life there.

- **Core Stratification**. It has been proposed that the supposed stratified layer at the top of Earth's core is the result of the Moon-forming impact (Landeau et al., 2016). However, after impacts, the strong perturbations of rotation may be able to mechanically mix out chemical stratification. The relative importance of such a mechanical mixing compared to a possible convective mixing (see e.g. Levy and Fernando (2002)) also needs to be determined.

- **Dynamo Action**. This type of instability may provide an important piece that explains how dynamos are sustained when the thermo-solutal convection models are insufficient. See for instance Wu and Roberts (2013) for dynamo driven by longitudinal libration, Le Bars et al. (2011) and Dwyer et al. (2011) for the past dynamo of the Moon and Arkani-Hamed et al. (2008) for Mars.

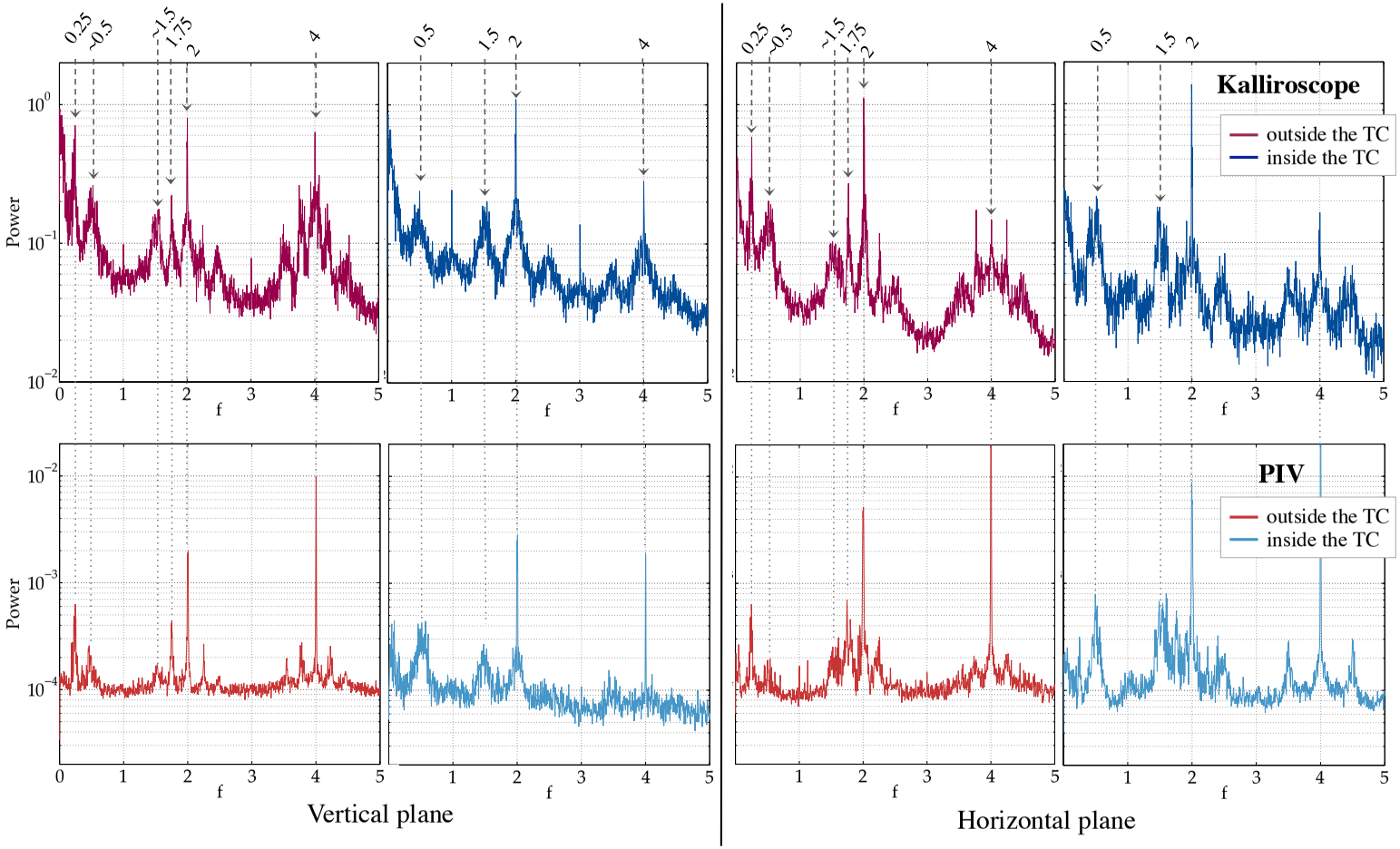

Figure 6.13: Power spectra of the light intensity and velocity signals from $t = 200$ to 1400 T_{lib}, both inside and outside the tangent cylinder (TC). The case parameters are $E_\chi = 1 \times 10^{-4}$, $\chi = 0.49$, $\Delta\phi = 5°$ and $f = 4$ ($\epsilon = 0.35$). The first row represents light intensity results, and the second row PIV results.

6.6 Appendix

6.6.1 Additional side-view visualizations for $f = 4$

6.6.2 Validation of Kalliroscope results by PIV analysis

PIV method is used here to verify the information content of light intensity analysis. Figure 6.13 shows the result of the spectral analysis performed on PIV and light measurements, both in vertical and horizontal planes. The FFT was applied on the signal from the moment when the flow becomes turbulent until the end of the acquisition. The interpretation of the observed peaks is conducted in section 6.4.2.1.

The main difference concerns the relative peak sizes, the PIV data being far dominated by the base flow whereas it is not the case for the light intensity signal. This is not surprising since the base flow is a coherent flow which does not generate any strong velocity gradient nor shearing zone. Thus, it does not create important light contrast in a flow seeded by Kalliroscope particles. Also, the base flow is at rather high frequency, and is intrinsically less obvious from Kalliroscope particles that need time to align with a given shear. The only source of this signal is thus due to the periodic reorientation of the Kalliroscope particles which generates slight light intensity variations. On the contrary, in terms of velocity amplitude, the base flow is very strong and predominates the velocity signal, particularly on a horizontal plane. We conclude from this that one has to be very careful on the relative peak intensity seen in spectra extracted from a light intensity analysis because it depends on the geometry of the flow considered. The Kalliroscope data also shows a strong component at zero frequency, due to the ambient light intensity even in the absence of motion (see e.g. Figure 6.5). That being said, Figure 6.13 shows that the relative amplitudes of the peaks are qualitatively similar for both methods.

The last main difference is that light intensity signals show an artifactual $\omega = 1$ frequency (and its harmonic at $\omega = 3$), which corresponds to the rotation rate Ω_0. This is probably the consequence of light variations due to the non-uniformity of the environment surrounding the experimental setup, or to an external source of light in the experimental room.

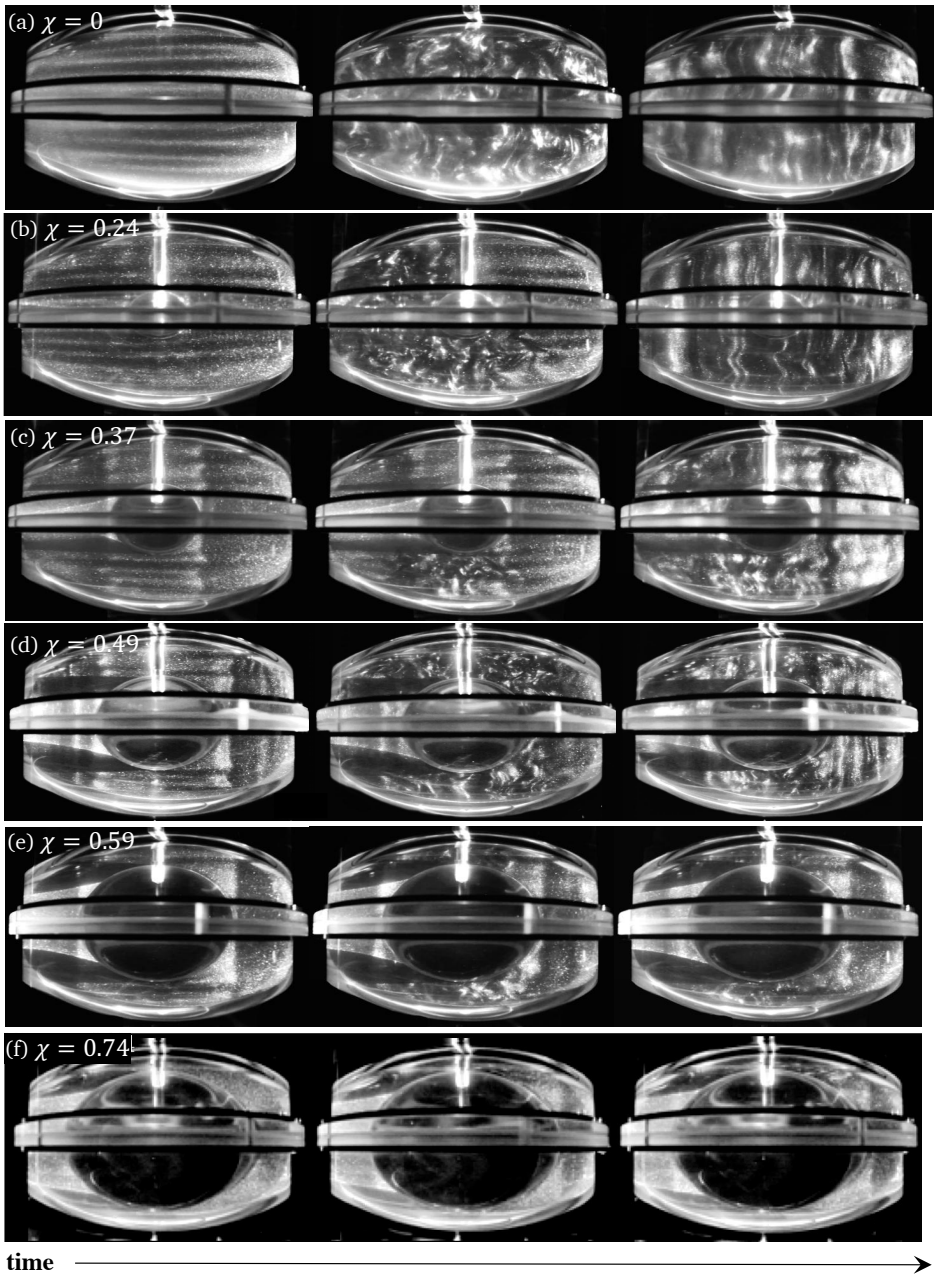

Figure 6.14: Typical flows observed in unstable cases. For each χ, the three snapshots are in the chronological order. The first snapshot shows the development of the $f_{1,2} = 2$ inertial modes. The second snapshot shows moments where strong turbulence is observed. This state can be very short since the relaminarization occurs quickly, that is why the turbulence is shown at moments when it is not yet uniform in the whole shell. The last snapshot illustrates the saturation state, with dominant columnar sheared flow outside the tangent cylinder and turbulence inside. These frames are extracted from the Canon EOS 7D movies. **(a)** $E_\chi = 6 \times 10^{-5},\ \Delta\phi = 10°$ **(b)** $E_\chi = 6 \times 10^{-5},\ \Delta\phi = 5°$ **(c)** $E_\chi = 6 \times 10^{-5},\ \Delta\phi = 5°$ **(d)** $E_\chi = 1 \times 10^{-4},\ \Delta\phi = 7.5°$ **(e)** $E_\chi = 3 \times 10^{-4},\ \Delta\phi = 12.5°$ **(f)** $E_\chi = 9 \times 10^{-4},\ \Delta\phi = 10°$.

6.6.3 Excitation of the Spin-over Mode ($f = 2.4$)

No survey has been realized for a libration forcing $f = 2.4$. However, we show here the persistence of the LDEI at this forcing frequency. Figure 6.15 shows the light intensity analysis results for a typical unstable case. When the periodic forcing is activated, the tangent cylinder appears as well as inertial shear layer, as can be seen on the first snapshot of Figure 6.15(a). Figure 6.15(c) shows that in terms of frequency, inertial modes of frequency $\omega/2 = \pm 1.2$ are indirectly excited. Such a frequency would give shear layers emitted from a critical latitude $\theta_c \approx 37°$ with an angle $\alpha_H \approx 53°$ from the horizontal, which is in good agreement with the geometry of the observed shear layers. Visually, the first instability develops at the two poles. This instability spreads slowly and the sides also becomes unstable (second snapshot of Figure 6.15(a)) before the classical "S" shape of the spin-over mode becomes clearly recognizable (third snapshot) and the whole fluid becomes unstable. As observed in the full ellipsoid case by Grannan et al. (2014), the triadic resonance at $f = 2.4$ involves a coupling of spin-over modes, which are characterized by a solid body rotation around an axis perpendicular to the rotation axis (Lacaze et al., 2005). The frequency content is surprisingly clear in this case, and we identify with good confidence the excitation of (probable) modes of frequencies $\omega = f/2 = 1.2$, followed by the secondary couples of peaks $|\omega| = [0.3, 0.9]$, $|\omega| = [0.33, 0.87]$, $|\omega| = [0.58, 0.62]$. Figure 6.15(c) shows that the spatial difference is now more subtle. The same peaks are present in both spectra, but on the side of the core, the two couples $|\omega| = [0.33, 0.87]$ and $|\omega| = [0.58, 0.62]$ are attenuated in comparison to the others.

Another case at $f = 2.4$ has been realized, with a larger core ($\chi = 0.49$) and farther from the threshold of the instability. The same succession of phases is observed, but the flow becomes more turbulent compared to the previous case. The associated spectra are then less clean, still dominated by the $\omega = 1.2$ frequency, but with less evident secondary resonances, the only one identified with certainty being the couple $\omega = [0.42, 0.78]$, which was not present in the first case described. This result supports the previously mentioned idea that the excited modes change according to the radius ratio of the shell.

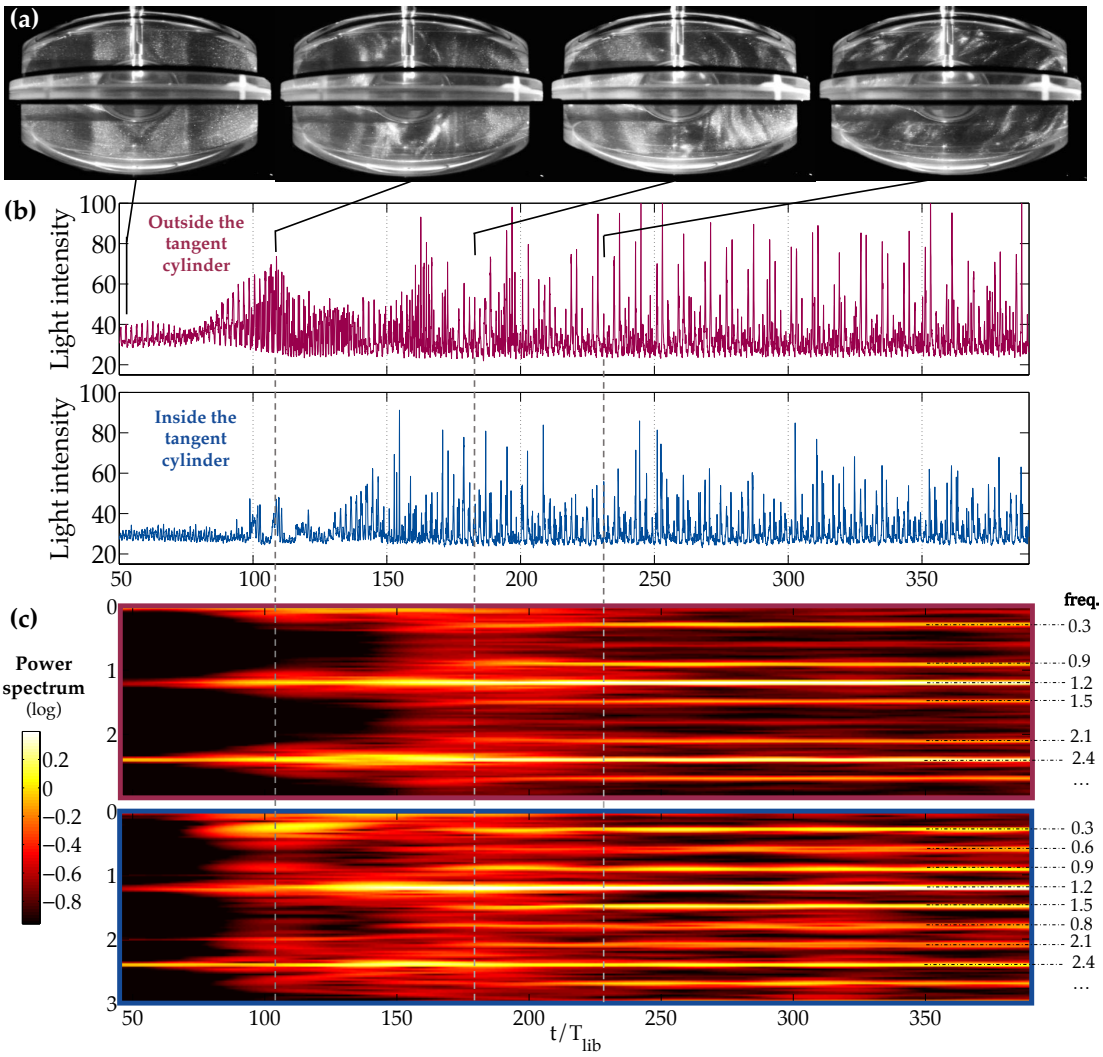

Figure 6.15: Light intensity analysis results for the case $\chi = 0.37$, $E_\chi = 1 \times 10^{-4}$, $\Delta\phi = 15°$ and $f = 2.4$ ($\epsilon = 0.63$). **(a)** Snapshots extracted at different times from the movie recorded by the Canon camera. **(b)** Light intensity signal extracted from one of the submatrices. **(c)** Successive power spectra performed over a sliding window of 90 T_{lib} to illustrate the temporal variations of the frequency content of the signal.

6.7 Physical characteristics used for the stability analysis

	Io[a]	Europa[a]	Ganymede[a]	Callisto[a]	Titan[a]	Enceladus	CoRoT-7b[a]	GJ 1214b[a]	55 CnC e[a]
T_{orb} (d)	1.77	3.55	7.16	16.69	15.95	1.37[b]	0.854	1.58	0.7365
$2e$ (10^3)	8.2	18.8	2.6	14.8	57.6	9.4[c]	2	2	114
ϵ (10^4)	1.3[a]	2[a]	0.056	0.042	1.3	2.1[c]	0.02	0.02	1.14
R (km)	1822	1561	2631	2410	2576	252.1[c]	10703	17062	10385
	core		core				(possible) core	(possible) core	(possible) core
R_{out}/R	0.52		0.27				1/3	1/3	1/3
β (10^4)	60		3.7				70	60	50
χ	0		0				0	0	0
E (10^{14})	2.7		20				0.094	0.068	0.086
		ocean	ocean	ocean	ocean	ocean			
R_{out}/R		0.99	0.96	0.94	0.97	0.94[c]			
β (10^4)		9.7	3.7	0.72	1.2	205[c,d]			
χ		0.94	0.94	0.93	0.92	0.78[c,d]			
E (10^{14})		2	1.5	4.5	3.5	3.4[c,d,e]			

[a] Cébron et al. (2012a) and references therein
[b] McKinnon (2015)
[c] Thomas et al. (2016)
[d] calculated from Cedak et al. (2016)
[e] kinematic viscosity ν taken as $\sim 10^{-6}$ m^2/s

Table 6.2: Physical characteristics used for the stability analysis. Except for Enceladus, all these values are taken from Cébron et al. (2012a) and references therein. The physical libration amplitude of the Super-Earths is assumed to be 10^{-3} times the optical libration amplitude $2e$.

CHAPTER 7

The Rotating Magnetoconvection Device

In this chapter, I provide more detail about how the plumbing, wiring, and gallium cleaning system is laid out and detailed steps for for understanding, operating, and maintaining the rotating magnetoconvection device, RoMag. This device serves as a reduced model for understanding rotating and non-rotating convection in water and rotating and non-rotating magnetoconvection in the liquid metal gallium. This chapter is a supplement to Chapter 2 of E. King. *An Investigation of Planetary Convection: The Role of Boundary Layers*. PhD thesis, University of California-Los Angeles, 2009.

A quick glimpse of the RoMag device in motion is provided through several Youtube films. Web addresses, below, are clickable on the electronic version.

- https://www.youtube.com/watch?v=G1qwMHkboDY
- https://www.youtube.com/watch?v=PFzpei8Qgxw

7.1 Rooftop Chiller

The rooftop chiller, shown in Figure 7.2, is an air cooled General Air recirculating water chiller. It has been installed on the roof, directly above the laboratory and is plumbed to cool three thermal loads. These loads are: the lab chiller, the magnet power supply, and the magnet itself. The rooftop chiller's internal pump is capable of delivering cool water at the necessary 3 gallons per minute (GPM) to each load. The returning, warmer water is cooled by a compressor, releasing the heat from the three thermal loads into the atmosphere. The roof top chiller is controlled manually on it's front panel and requires little maintenance as

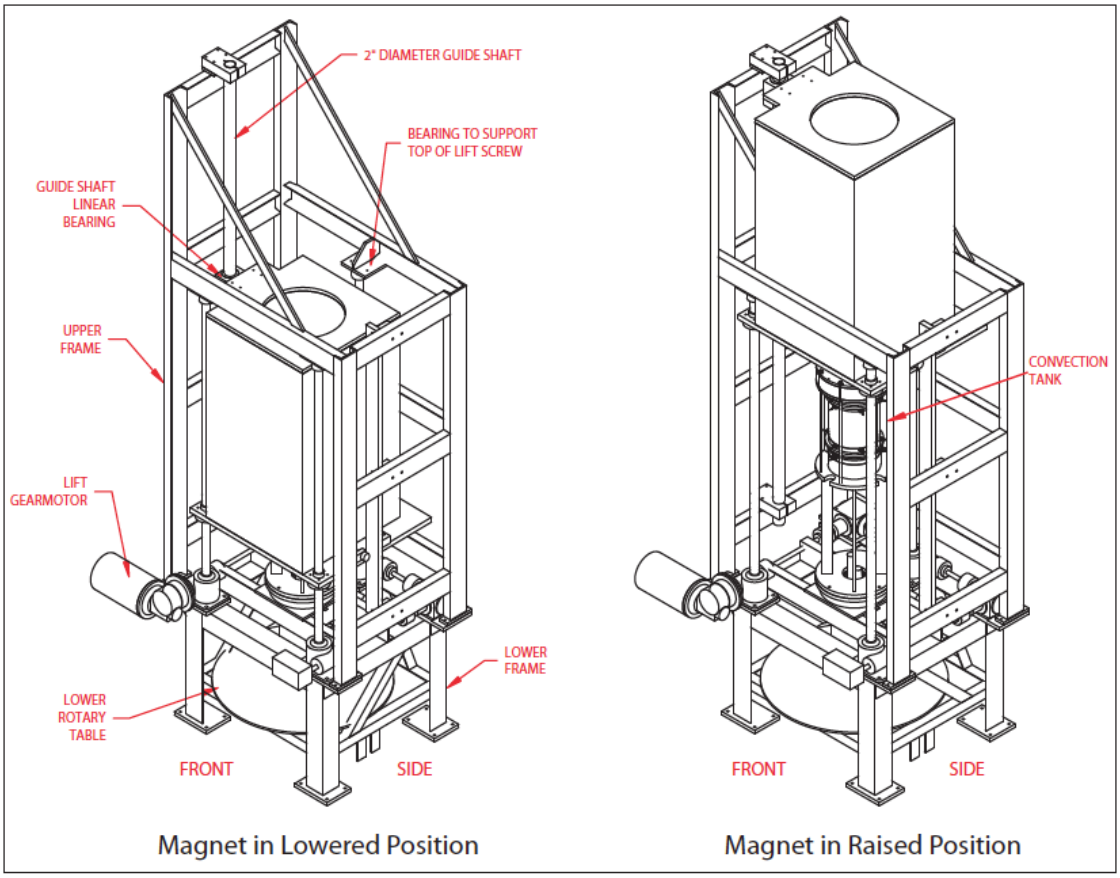

Figure 7.1: The full RoMag experimental apparatus. Image modified from King (2009).

the cooling system is closed and reservoir is auto-filled using the building's water supply.

The laboratory chiller, shown in Figure 7.3, is a Thermo NESLAB HX300 precision chiller, referred to hereafter as the lab chiller. This lab chiller is capable of extracting ∼10kW of heat from the the experimental device. This chiller is water-cooled from the rooftop chiller and has a thermostated temperature set range from 5-35^{o}C with an accuracy of ±0.1^{o}C. This chiller contains a 15 gallon water storage reservoir that is circulated by a CP-75 centrifugal pump with a flow rate at the outlet up to ∼15 gallons per minute.

- Note that the laboratory chiller contains an auto refill valve that is capable of delivering water from a storage tank to the chiller when the reservoir is low. However this function does not currently work.

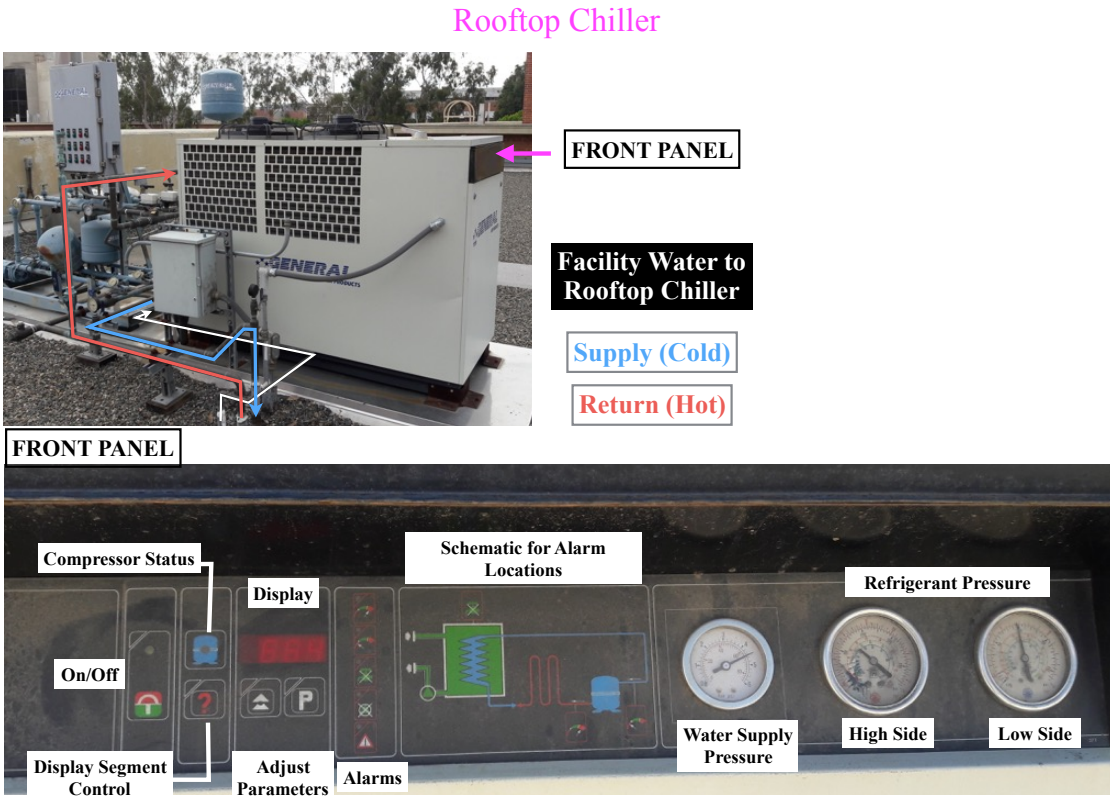

Figure 7.2: The rooftop chiller located on the roof above the lab and it's front panel. Image contributed by Ashna Aggarwal.

7.2 The Heat Pad and Power Supply

The heater is a silicone rubber heater manufactured by OEM. The heaters resistive elements are non-inductively wound, i.e. arranged such that they induce negligible magnetic field. This is important in maintaining a uniform magnetic field within the convection tank. The heater has an electrical resistance of $\sim 18\Omega$. A direct current is passed through the heater by way of an Argantix XDS 300-17 power supply, whose front panel is shown in Figure 7.4. This power supply is capable of delivering up to 300 V at 17A, or up to 5100 W of power. With the power supply, we control the voltage output. The heater's power supply, which is powered by three-phase 208 VAC facility power, is in the stationary lab frame. The heat pad, however, is in the rotating experimental frame.

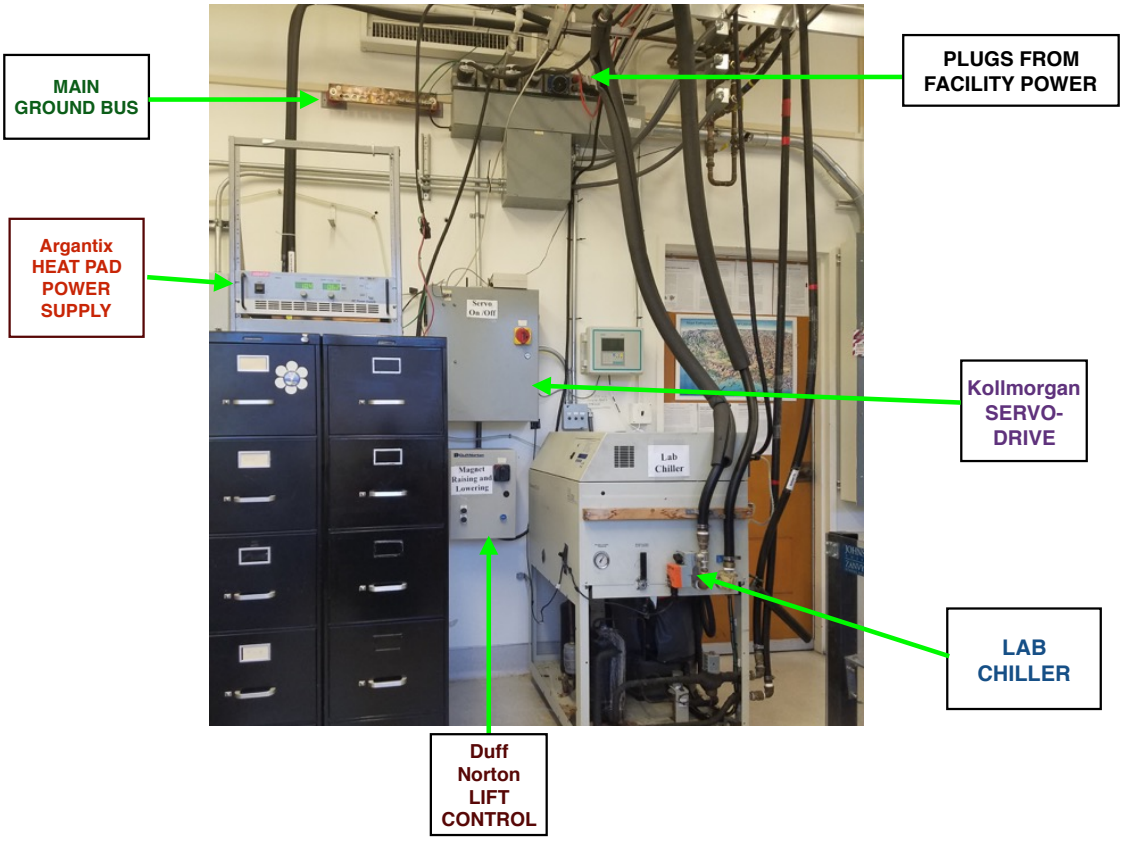

Figure 7.3: Layout of major components located along the north wall. These are: the electrical plugs and grounding bus, the Agrantix heat pad power supply, Walker Scientific magnet power supply, Duff-Norton magnet lift drive and Kollmorgen servo drive , and the lab chiller. The rooftop chiller, not shown, is located directly above the lab chiller on the roof.

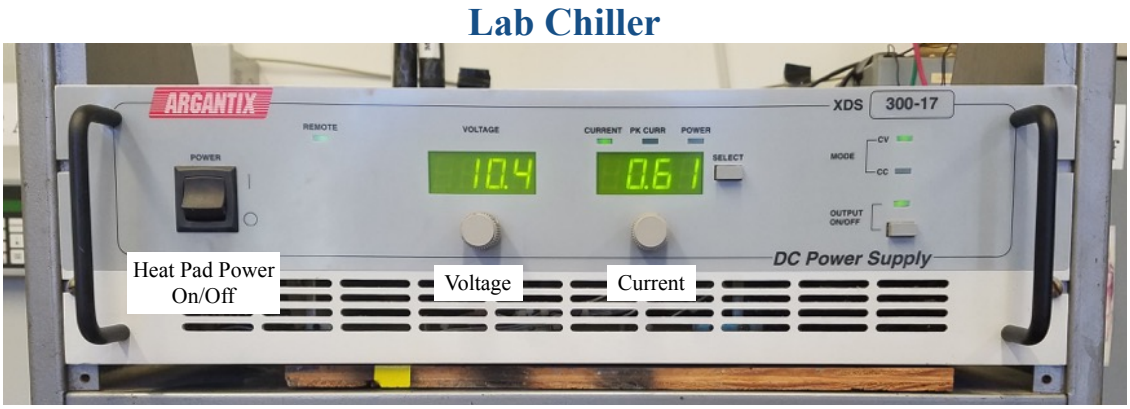

Figure 7.4: The front panel of the Argantix heat pad power supply. The on/off switch is the most commonly used and the displays for the voltage and current are checked constantly but not controlled by the knobs on the front panel

7.3 The Heat Exchanger

The heat exchanger is a cylinder of aluminum with a diameter of 13 inches that is machined with a double spiral in order for the cooled water to pass through and efficiently remove the heat input by the heatpad from the convection tank while maintaining a strong degree of isothermality in the boundary. The amount of heat extracted from the cooling block is given by,

$$P_{\text{cool}} = \rho C_p \Delta T_{\text{cool}} \Phi_{\text{H}_2\text{O}}, \tag{7.1}$$

where ρ and C_p are the density and specific heat of the water flowing through the heat exchange at a volume flow rate, $\Phi_{\text{H}_2\text{O}}$. As the water extracts heat, its temperature is raised by ΔT_{cool}. The heat exchanger has top and bottom aluminum lids

- Note: the heat exchanger requires two of the following oring: Dash No. 277 and McMaster #:9452K376.
- Note: the flow rate of the water through the heat exchanger is not currently measured.

7.4 Wiring System

In order to understand the layout of the wiring and plumbing system, I describe how the major components are wired together in the laboratory frame and the rotating frame.

7.4.1 Laboratory Frame Wiring

The wiring layout in the laboratory frame, shown in Figure 7.5, consists of the connections between the major components starting at the Main Lab Fuse Box where all the circuit breakers are located and ending at the Slip Ring where the signal are passed to the rotating frame. In broad terms, the RoMag device is situated in the center of the lab while the major components to be discussed are located along the North Wall. The majority of the wiring that connects the major components are located in conduits on the North Wall and distributed along the west side and south side of the RoMag device using wire guides suspended from

the ceiling.

The Main Lab Fuse Box contains all the circuit breakers for the Romag components in the laboratory and rotating frame as shown in Figure 7.6. The breakers are indicated in several ways. The breakers specifically used for RoMag are color coded with green tape. Paper labels are also affixed to the front of the breaker, and listing of the breakers functions are located on the inside of the panel door. The power for nearly all the components is 208VAC 3 phase power except for the rotating frame power, indicated in bright orange in Figures 7.5 and 7.6 is the standard 120VAC single phase power. In general the 208VAC 3 phase power consists of a bundle (cable) of four lines: one grounding line (usually green colored) and three AC power lines each out of phase by 120 degrees. For the standard single phase 120VAC power line, the bundle of cables contains a grounding line (usually green colored), a neutral line (usually white colored), and a hot power line (usually black colored).

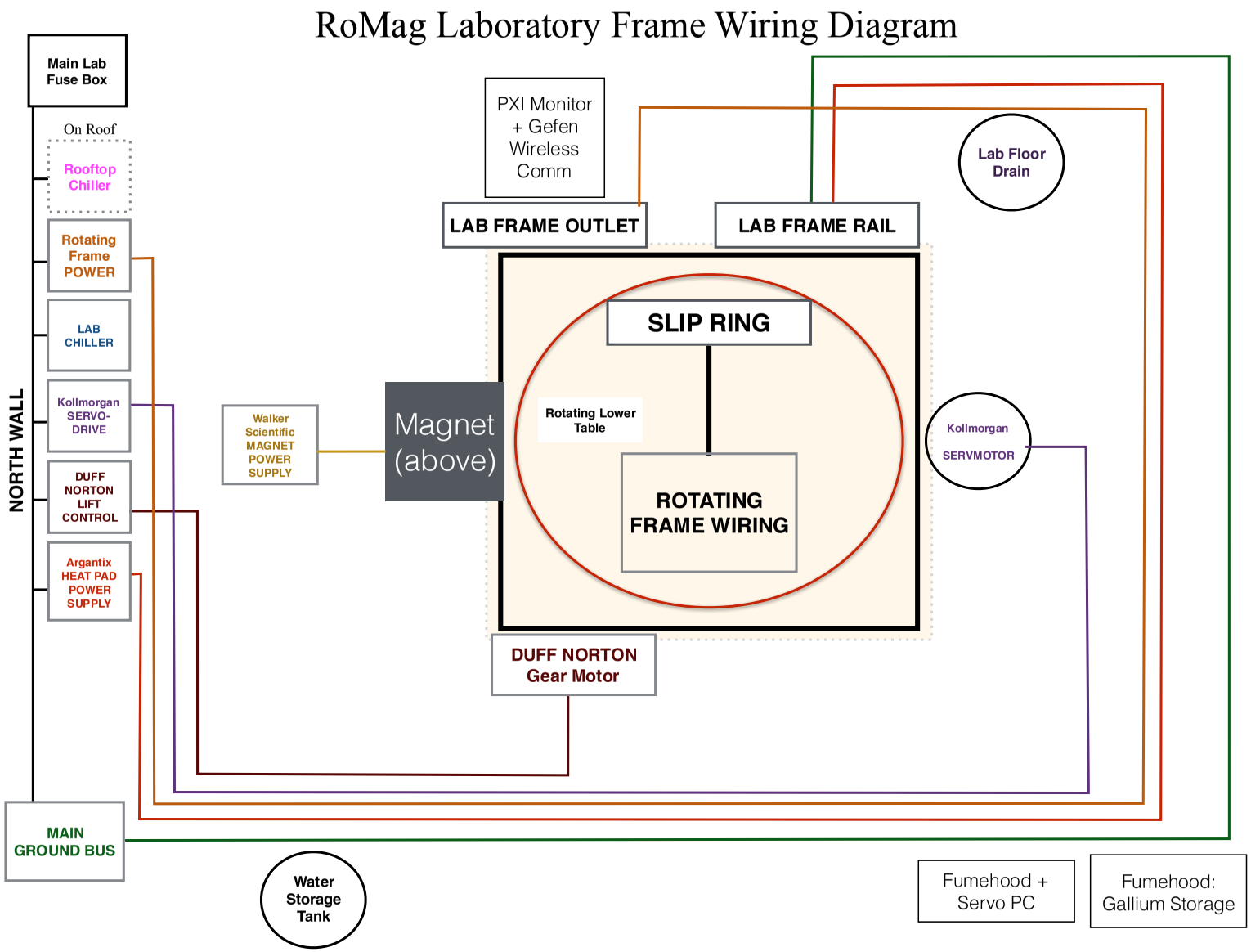

Figure 7.5: Layout of major components in the laboratory frame wiring system of RoMag. The schematic for the rotating frame wiring diagram is shown in Figure 7.9. Image contributed by Ashna Aggarwal.

- Note: that when performing any maintenance or making wiring adjustments, it is necessary to turn off power both on the device where possible and at the Main Lab Fuse Box.

The layout of the major plugs attached to the North Wall are shown in Figure 7.7. Moving

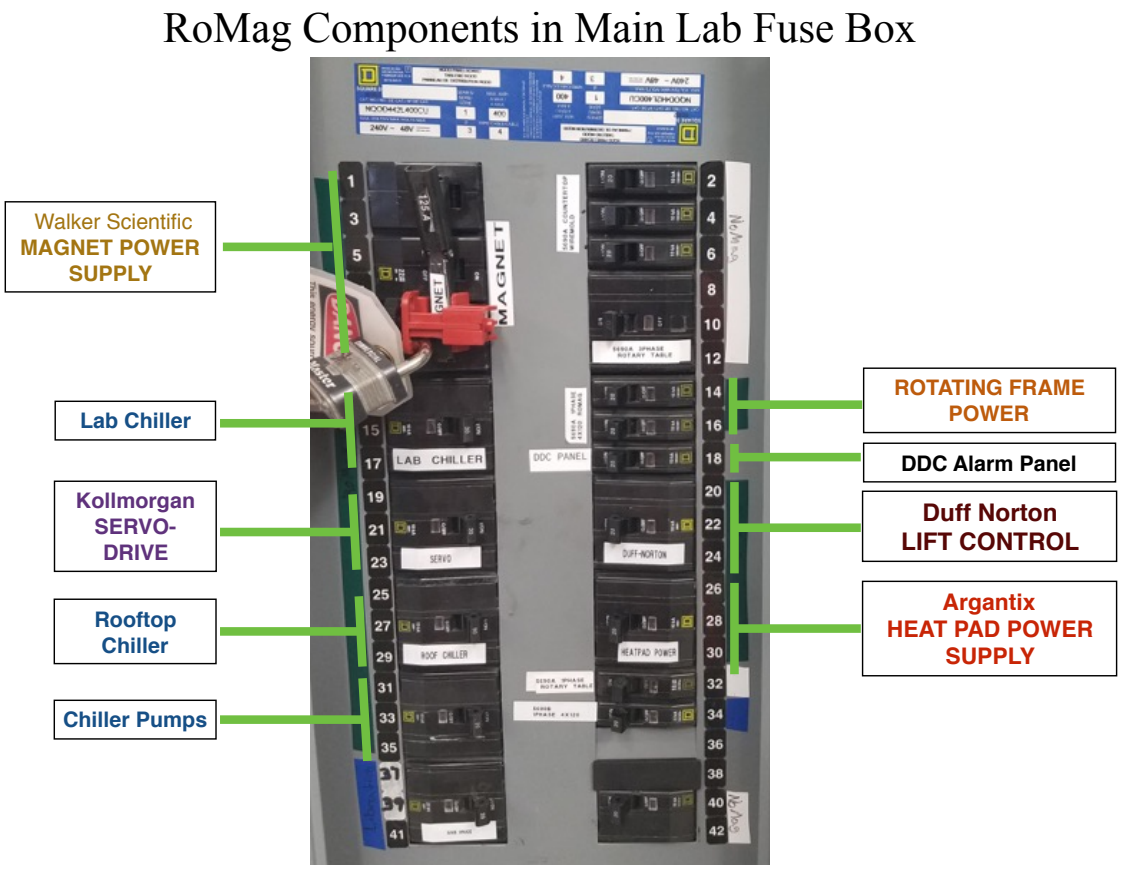

Figure 7.6: Positions of the circuit breakers in the main lab fuse box that must be on for operation of RoMag to occur.

from left to right, these plugs are to the Duff Norton magnet lift, Argantix plug for the heat pad power supply, Servo plug for the Kollmorgen Servo drive, the Thermo Neslab plug for the laboratory chiller, magnet power supply (not plugged in), and set of normal 120VAC plugs providing standard power for the devices in the rotating frame.

The position of the major components positioned in the laboratory frame are shown in Figure 7.3 facing the North Wall. At the top of the image are set of electrical plugs shown in Figure 7.7. Although not shown, the rooftop chiller is located directly above the laboratory

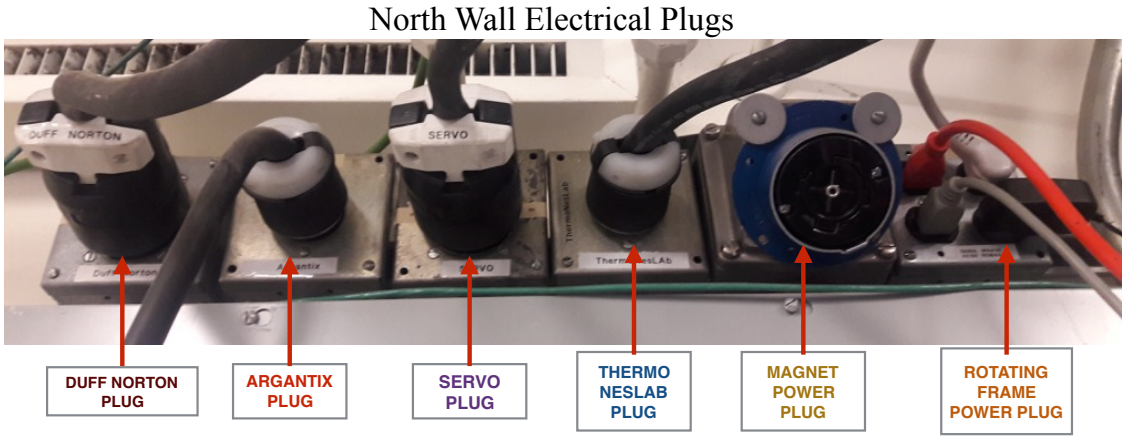

Figure 7.7: The electrical plugs located on the North wall that power the major RoMag devices. Image contributed by Ashna Aggarwal.

chiller on the roof. Also shown on the top left of Figure 7.3 is the main ground bus labeled in green. The Servo-Drive Box where the Kollmorgen servo-drive is kept, also houses an Omega system used to send signals that control the output of the heatpad and lab chiller.

All major wires connected to the wall or major componets on the North Wall are carried via wire support guides suspended from the ceiling. These wires are terminated on the east side of the RoMag device and attach directly to the Lab Frame Rail shown in Figure 7.8 that is used to cleanly separate the power and signal lines in order to pass them into the rotating frame.

To the left of the Lab Frame Rail is a ground bus. Moving from left to right, the ground wires are: a large 6 gauge ground wiring that connects this ground bus to back to the main ground bus located on the North Wall, the ground cable for the heatpad, the ground cable for the 120VAC rotating frame power, the ground cable for the ethernet over power system, and the cable connecting the ground bus to the Lab Frame Rail. There are six major components to the Lab Frame Rail and they are:

1. A terminal with a built-in fuse for the six gauge ground cable.

2. A terminal for the two neutral legs from the Rotating Frame Power cable and from the Ethernet over power cable.

3. A terminal with a built-in fuse for voltage from the heatpad power supply.

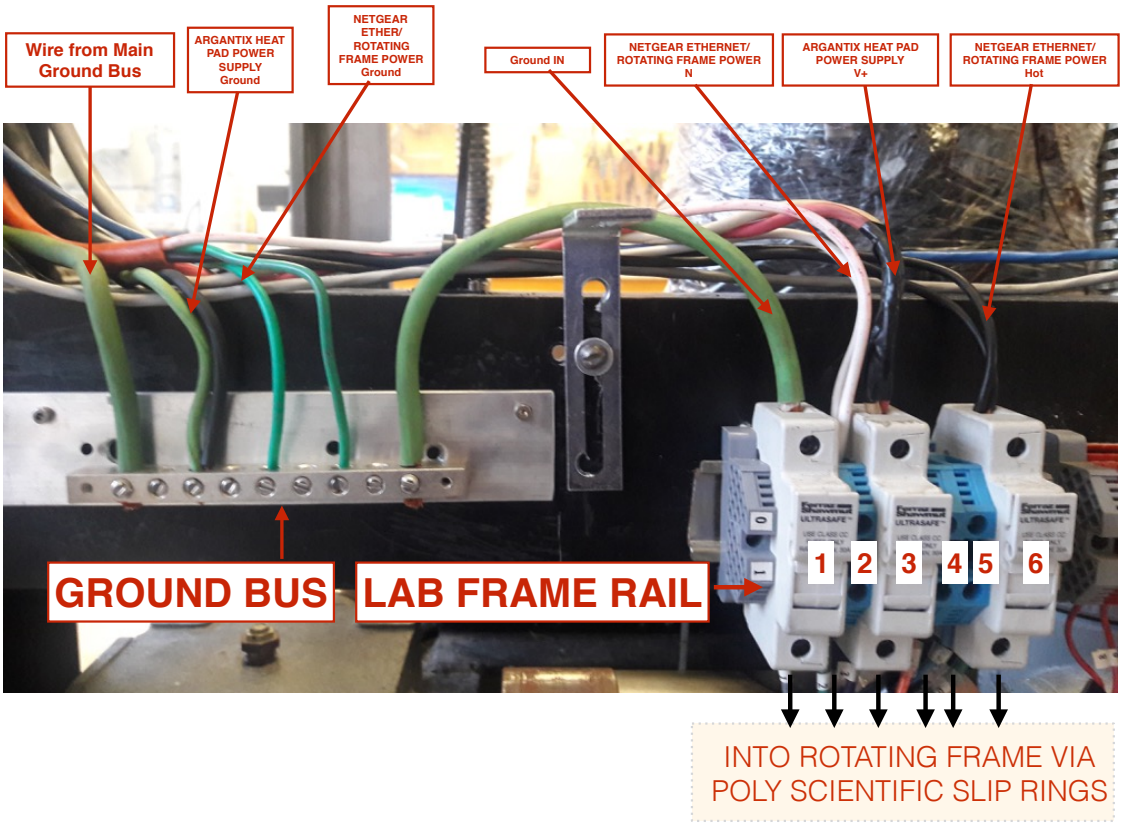

Figure 7.8: The Lab Frame Rail located on the east side of the RoMag device from the layout in Figure 7.5. This rail passes AC Power, DC power , and ethernet signals into the slip ring and thus into the rotating frame wiring system. Image contributed by Ashna Aggarwal.

4. Empty terminal

5. Empty terminal

6. A terminal with a built-in fuse for the hot legs from the Rotating Frame Power cable and from the Ethernet over power cable.

On the underside of the Lab Frame Rail, six heavy gauge wires are directed into the slip ring to pass the high current signals into the rotating frame.

- Note that the first terminal in the Lab Frame Rail is necessary for holding the large gauge ground cable. However, it should not be fused as it would prohibit the flow of excessive currents to the ground thus preventing the main role of the grounding cable. This terminal should be replaced with a fuseless one in the future.

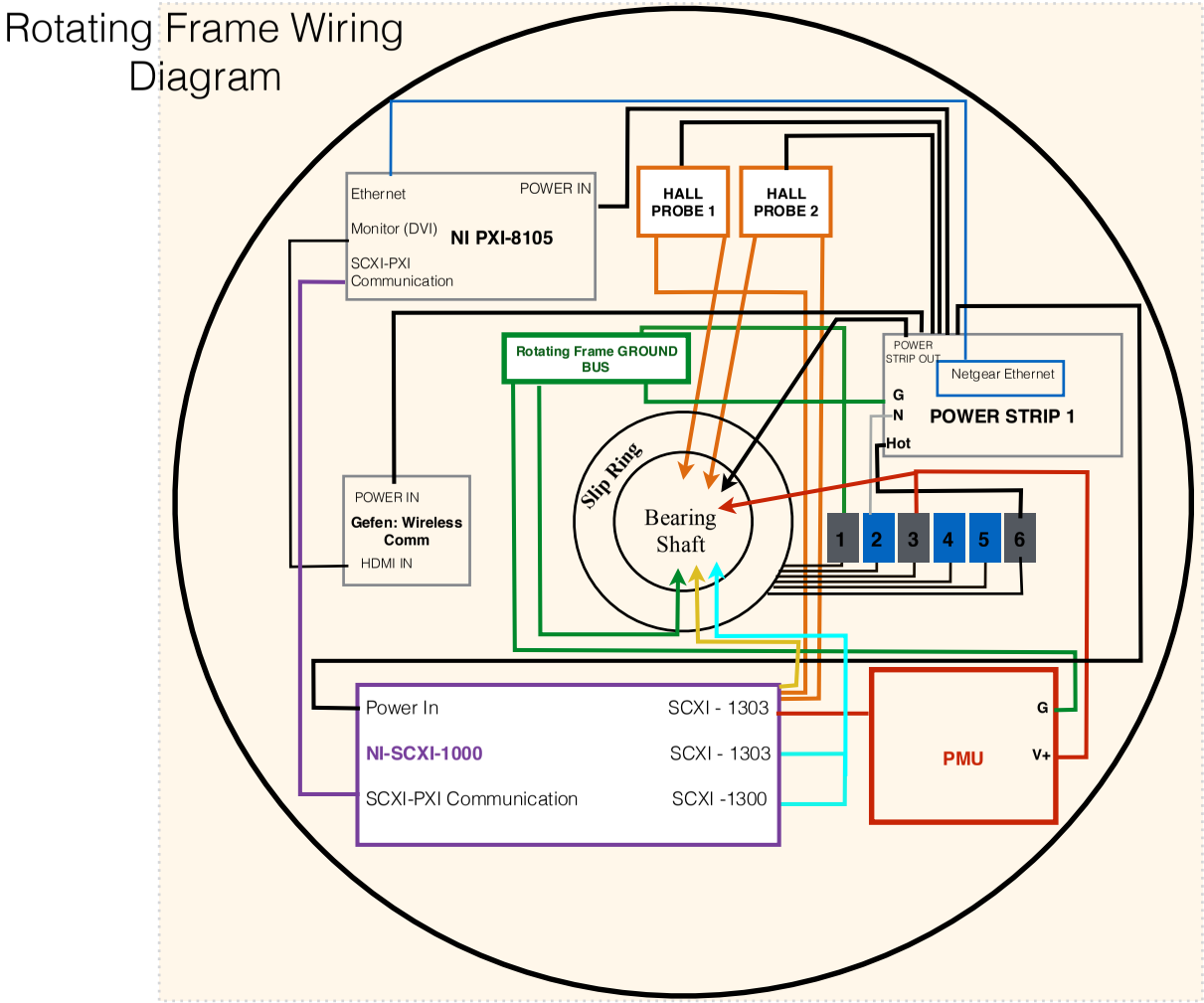

Figure 7.9: Layout of major components on the lower table of the rotating frame. The arrows indicate that wires are passing from the lower table through bearing shaft shown again in Figure 7.12. Image contributed by Ashna Aggarwal.

7.4.2 Slip-Ring

All signals and power must be passed through electrical slip-rings into the rotating frame. The slip-rings are manufactured by Poly-Scientific (of Northrup Grumman), model AC6098-24. The slip rings have a 0.2m outer diameter, and a 0.1m diameter hollow inner bore. This allows the slip-rings to be situated outside the rotating shaft, between the lower rotating table and the main bearing. The solid state slip-rings can maintain connection at up to 250 RPM. They consist of six power rings that can each carry up to 50 A, and 54 additional signal rings that carry no more than 10 A, and are meant for low-voltage sensor signals.

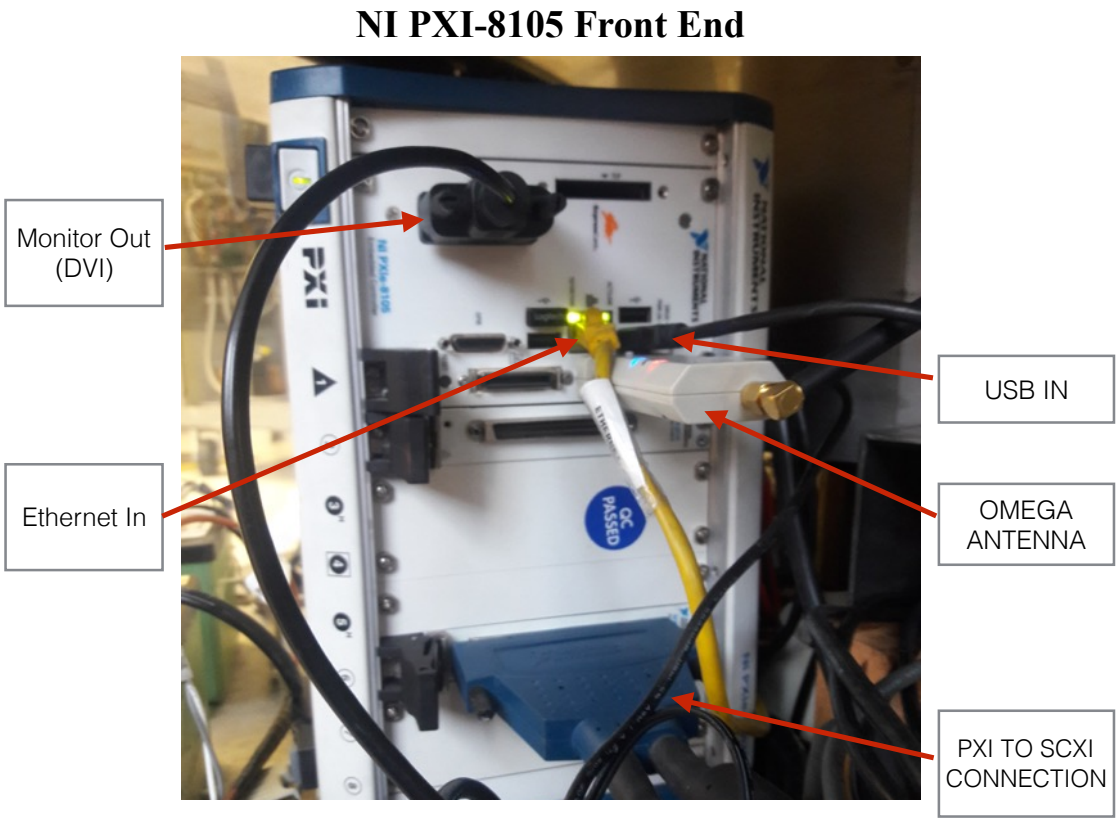

Figure 7.10: Front panel of the RoMag PXI acquisition computer where the ethernet cable, Omega antenna, and the PXI to SCXI cables are plugged in. Image contributed by Ashna Aggarwal.

7.4.3 Rotating Frame Wiring

The layout for the components and wiring on the lower table in the rotating frame are shown in Figure 7.9. All signals and power that is transmitted through the slip-ring arrive at the Rotating Frame Rail. This rail is a mirror image of the Lab Frame Rail shown in Figure 7.8. The major components found on the lower table in the rotating frame are:

- a power strip from which all the following components are plugged in.
- a ground bus identical to the ground bus located next to the Lab Frame Rail.
- the National Instruments (NI) PXI-8105 computer shown in Figure 7.10. This computer is center of data acquisition and control for the RoMag experiment
- the NI SCXI-1000 data acquisition center shown in Figure 7.11 where the terminals for most of the data probes are gathered.
- two signal conditioners for the two Hall probes capable of measuring the strength of the magnetic fields.
- a Gefen Wireless Communication device for transmitting video signals from the PXI to the laboratory frame monitor
- a Netgear XEB1004 powerline ethernet adaptor used primarily for connecting the PXI to the internet.
- a power management unit (PMU), shown in Figure 7.13, used to measure the power being sent to the heatpad.

7.4.3.1 Data Acquisition Components and Layout

In the rotating frame, the data acquisition system, shown in Figure 7.12, consists of the PXI, which takes in the signals gathered by the SCXI. The signals being sent to the SCXI come from the thermal, voltage, and magnetic field data.

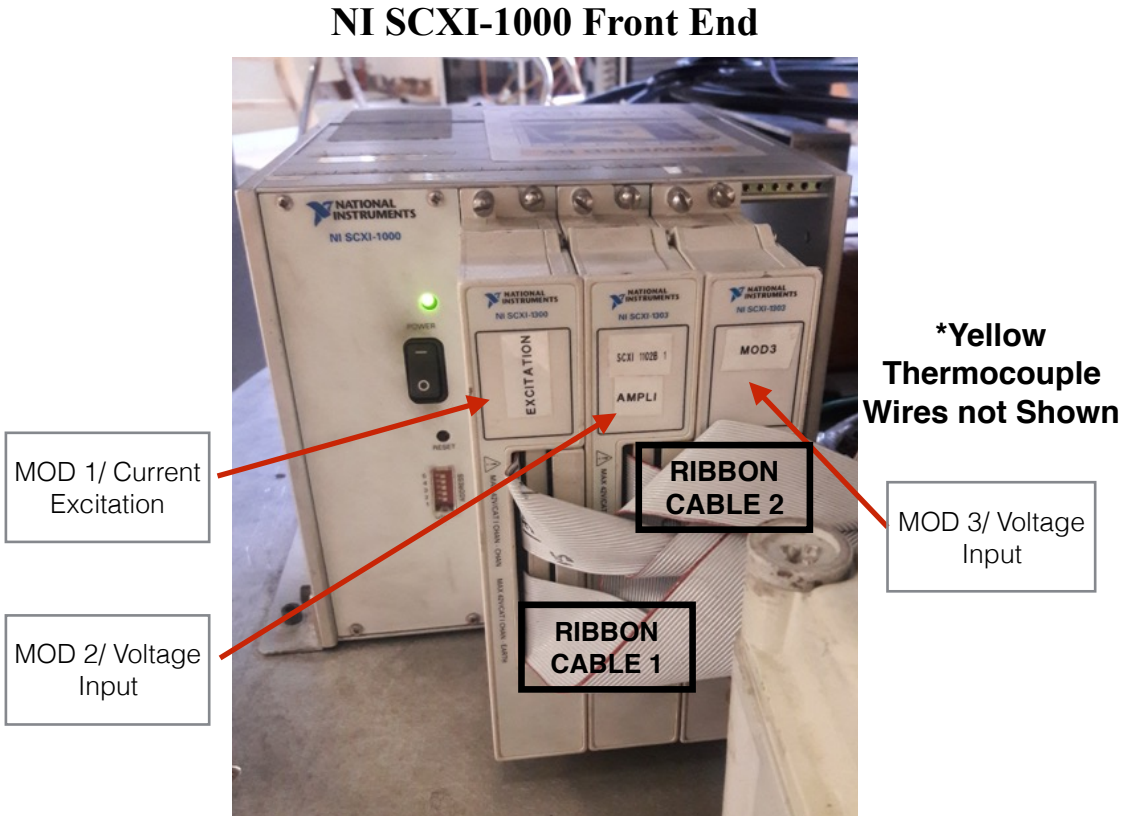

Figure 7.11: The front face of the SCXI box where all data signals are gathered using three pairs of modules and terminal blocks. Image contributed by Ashna Aggarwal.

The front end of the PXI in Figure 7.10 shows an Omega Antenna on the right that sends signals to an identical Omega Antenna found on the Servo-drive Box. The Omega system is then used to change the power to the heat pad and the lab chiller set temperature. The large blue plug on the lower part of the PXI connects the PXI to the SCXI.

The SCXI, whose front panel is shown in Figure 7.11, contains three input modules connected to three terminal blocks used for securing wire of all data probes. The three input modules are

- SCXI-1581 current excitation module attached to a SCXI-1300 terminal block. This module, referred to as MOD1, provides a fixed excitation current of 100μA to up to 32 thermistors.

- SCXI-1102B voltage input module attached to a SCXI-1303 terminal block. This module, referred to as MOD2, measures the resulting voltage in up to 32 thermistors

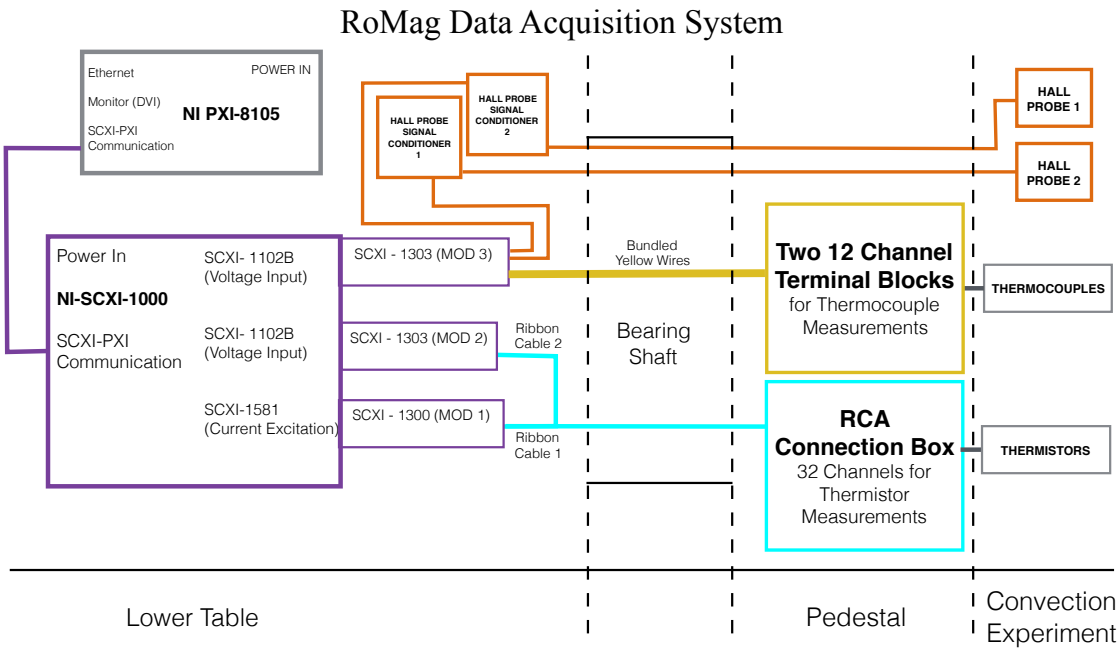

Figure 7.12: The data acquisition system consists of the thermistors, thermocouples, and Hall Probe signal conditioners connected to the SCXI. The SCXI is connected to the PXI computer. Image contributed by Ashna Aggarwal.

whose resistance changes with temperature.

- SCXI-1102B voltage input module attached to a SCXI-1303 terminal block. This module, referred to as MOD3, measures the resulting voltage in up to 32 channels.

Ribbon cables are used to connect MOD1 and MOD2 and then past through the bearing shaft up to the pedestal that supports the convection experiment. On the pedestal is a 32 port RCA connection box to which thermistors used in the experiment can be plugged. In MOD3, screw in terminals are used to connect up to 32 individual wires. Table 7.1 provides a schematic showing where the different probes are terminated. There are twenty thermocouple (TC) probes, two Hall probes, three wired terminals that are currently unused, and two voltages from the PMU.

- Note that it is difficult to pass wires through the bearing shaft. Thus, although not included, a set of additional wires have been added. These include five BNC cables that may be used for the Doppler probes that can be used to measure velocity signals, three pairs of wires that may be used for miscellaneous purposes, and a pair of additional

Channel	Probe	Channel	Probe	Channel	Probe	Channel	Probe
0	-	8	TC	16	Misc.	24	TC
1	TC	9	TC	17	Misc.	25	TC
2	TC	10	TC	18	Misc.	26	TC
3	TC	11	PMU-VoltDiv	19	Hall Probe	27	TC
4	TC	12	-	20	Hall Probe	28	TC
5	TC	13	-	21	TC	29	TC
6	TC	14	-	22	TC	30	TC
7	TC	15	-	23	TC	31	PMU-Shunt

Table 7.1: The SCXI Module 3 contains 32 channels that are currently assigned to acquire 20 K-type thermocouple (TC) signals, two hall probe measurements, signals from the voltage divider and the shunt on the PMU, and three Misc. terminals that contain wires that are unused. The remaining terminals are both unwired and unused.

ribbon cables that may be used if the thermocouples are ever replaced.

Figure 7.12 shows the passage of ribbon cables for the thermistors, a bundle of individual thermocouple wires, and the hall probes passing from the bearing shaft that connects the lower table up to pedestal and convection experiment.

7.4.3.2 Power Managment Unit (PMU)

The power managment unit (PMU) is the device, shown schematically in Figure 7.13, for measuring the power being applied to the heat pad. Because the PXI and SCXI can only measure small voltages, it necessary to reduce the voltage going to the heat pad to a readable level, and it is necessary to use a shunt resistor with a small but well-known resistance so as to measure a small voltage drop across the shunt resistor and compute the resulting current going through the shunt resistor and thus the heat pad. The measurements of the resistors in the voltage divider are $R_1 = 300\text{k}\Omega$, $R_2 = 10\text{k}\Omega$. The current shunt is rated for a 50mV drop at 15A and thus its resistance is small known quantity $R_{\text{shunt}} = 0.0033\Omega$. With the PMU circuit, the voltage is given by

$$V_{\text{heatpad}} = \frac{R_1 + R_2}{R_1} V_{\text{Ch. 11}} = 31 V_{\text{Ch. 11}}, \tag{7.2}$$

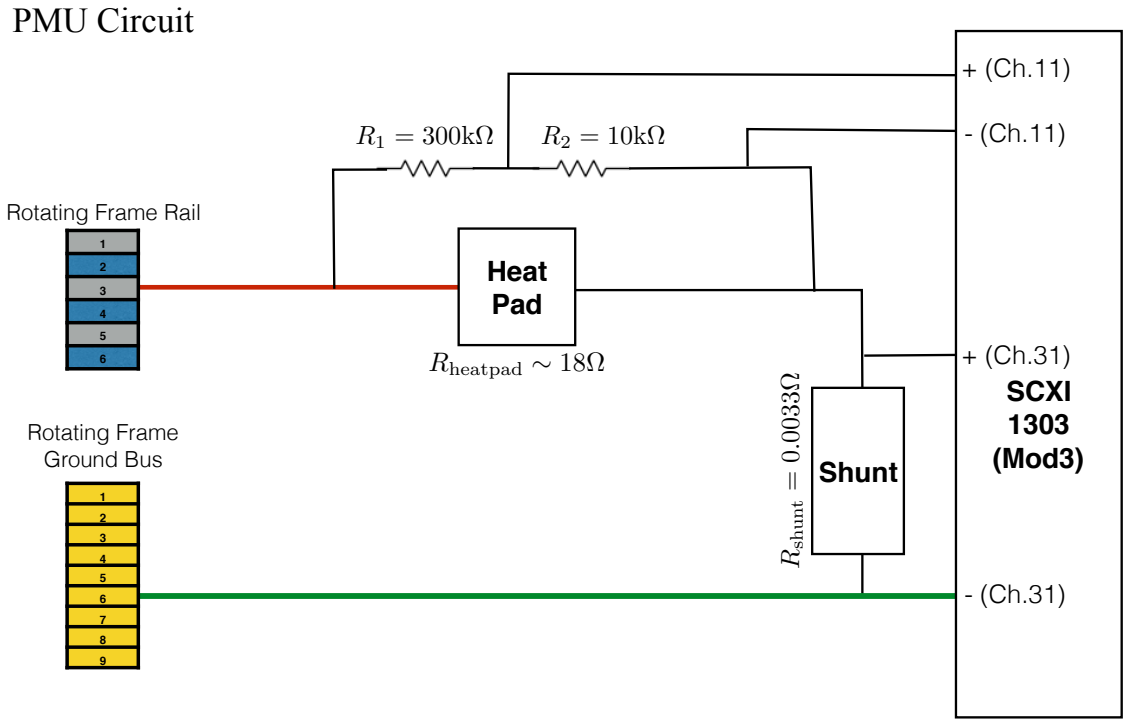

Figure 7.13: The wiring diagram for the power management unit. Image contributed by Ashna Aggarwal.

and the current through the heatpad is given by

$$I_{\text{heatpad}} = \frac{V_{\text{Ch. 31}}}{R_{\text{shunt}}} = 300 V_{\text{Ch. 31}}. \tag{7.3}$$

- Based on a previous calibration, the multiplicative coefficient for the shunt voltage that is used in post-processing is 297 not 300.

The total power input to the heatpad is thus $P_{\text{heatpad}} = I_{\text{heatpad}} V_{\text{heatpad}}$. The power may also be calculated using only the voltage such that $P_{\text{heatpad}} = V^2_{\text{heatpad}}/R_{\text{heatpad}}$. However, this calculation assume the heatpad resistance is fixed. The resistance may, in fact, have some temperature dependence especially at high wattages and thus may be inaccurate at high temperatures.

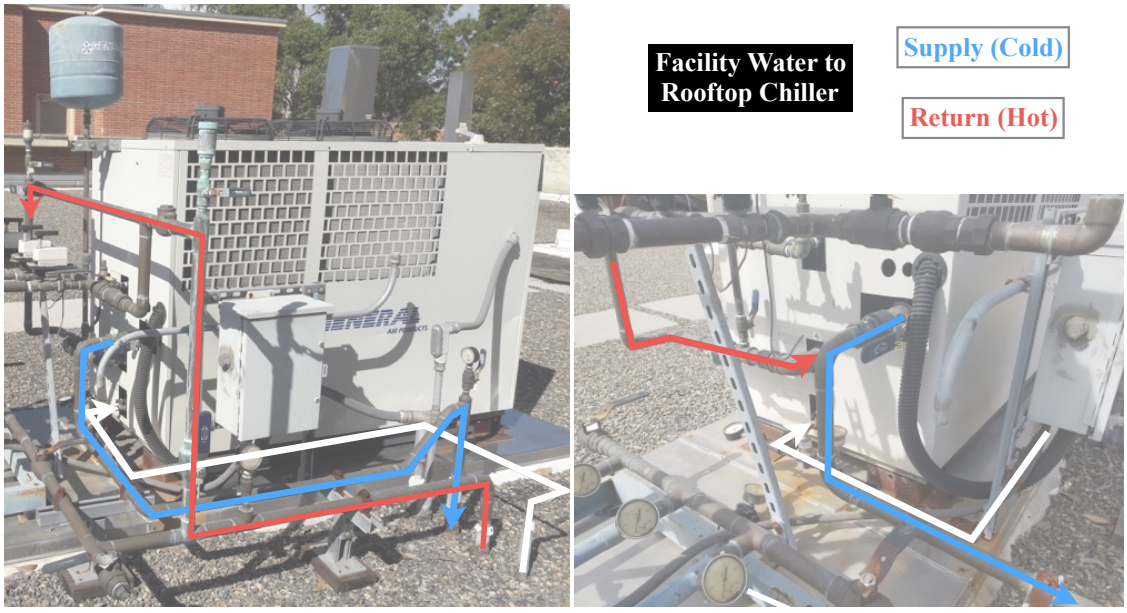

Figure 7.14: Two different views of the rooftop chiller showing hard lines associated with the facility water (white lines) that automatically refills the chillers' reservoir, the supply water lines distributing cool water (blue lines) and the return lines bringing back warm water (red lines). Image contributed by Ashna Aggarwal.

7.5 Plumbing System

The plumbing system is necessary for transporting cooled water in order to remove heat from the three thermal loads in the RoMag system: the power injected by the heat pad into the convection tank, the high currents generating heat in the magnet's power supply, and the high currents generating heat in the coils of the magnet itself.

The beginning and end of the plumbing system is the rooftop chiller where heat from all three thermal loads is eventually released to the atmosphere. Figure 7.14 shows several views of the hard plumbing lines going to and from the rooftop chiller. A facility water supply line, shown in white, automatically refills the rooftop chiller's reservoir. The supply and return lines, shown in blue and red, respectively, distributes the cold water to the thermal loads and returns the warm water. Supply, return, and facility water lines are passed through through the ceiling and split at the plumbing manifold shown in Figure 7.15. At the plumbing manifold, the supply and return lines for each of the thermal loads can be shut off using the ball valves at all inlets and outlets.

The plumbing manifold is shown in the context of the schematic for the entire plumbing system in the laboratory frame as shown in Figure 7.16. A system of ball valves denoted by black squares allow for different segments of the plumbing to be isolated.

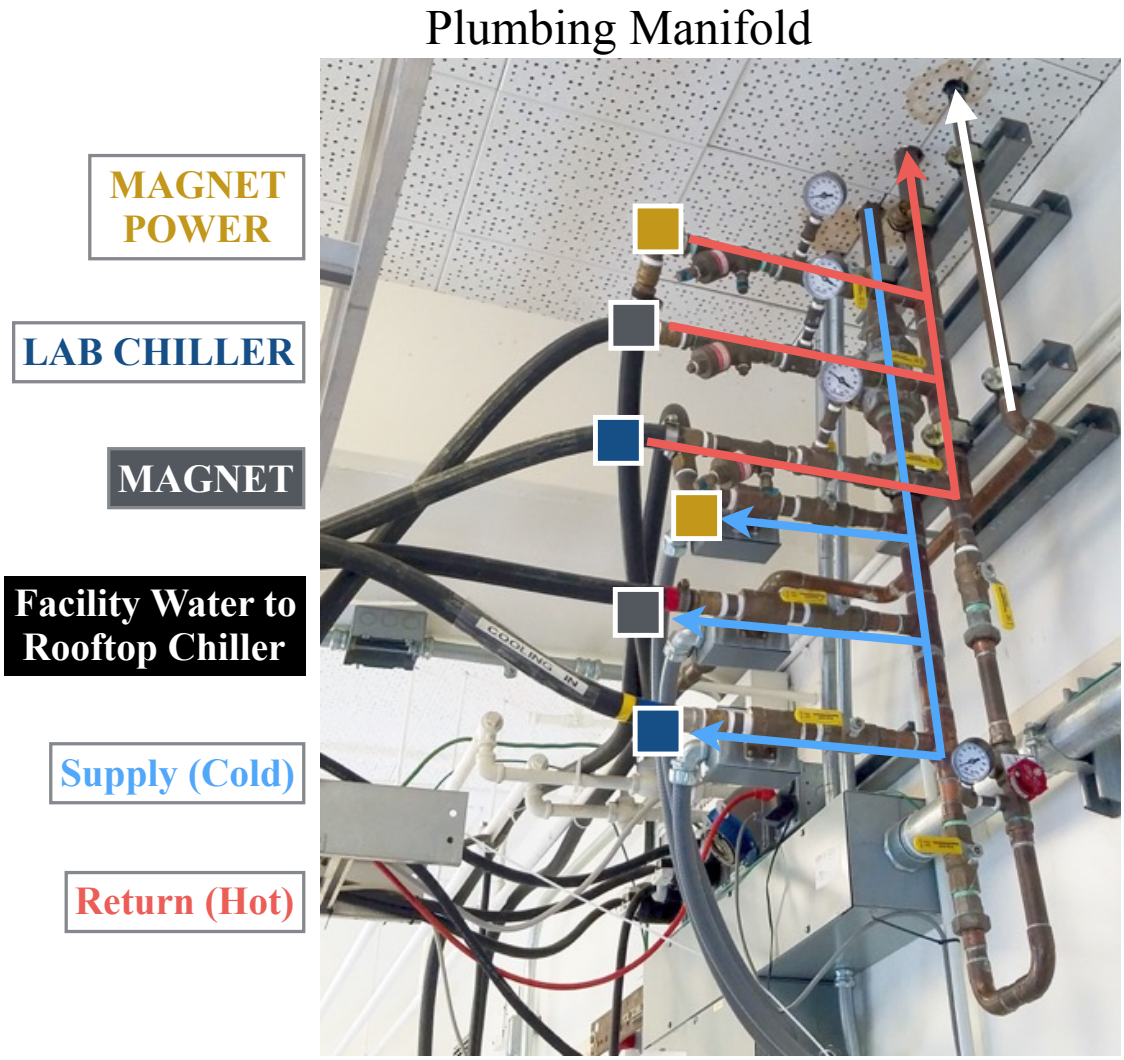

Figure 7.15: The plumbing manifold located above the lab chiller is the distribution point for the hoses going to the the three thermal loads.

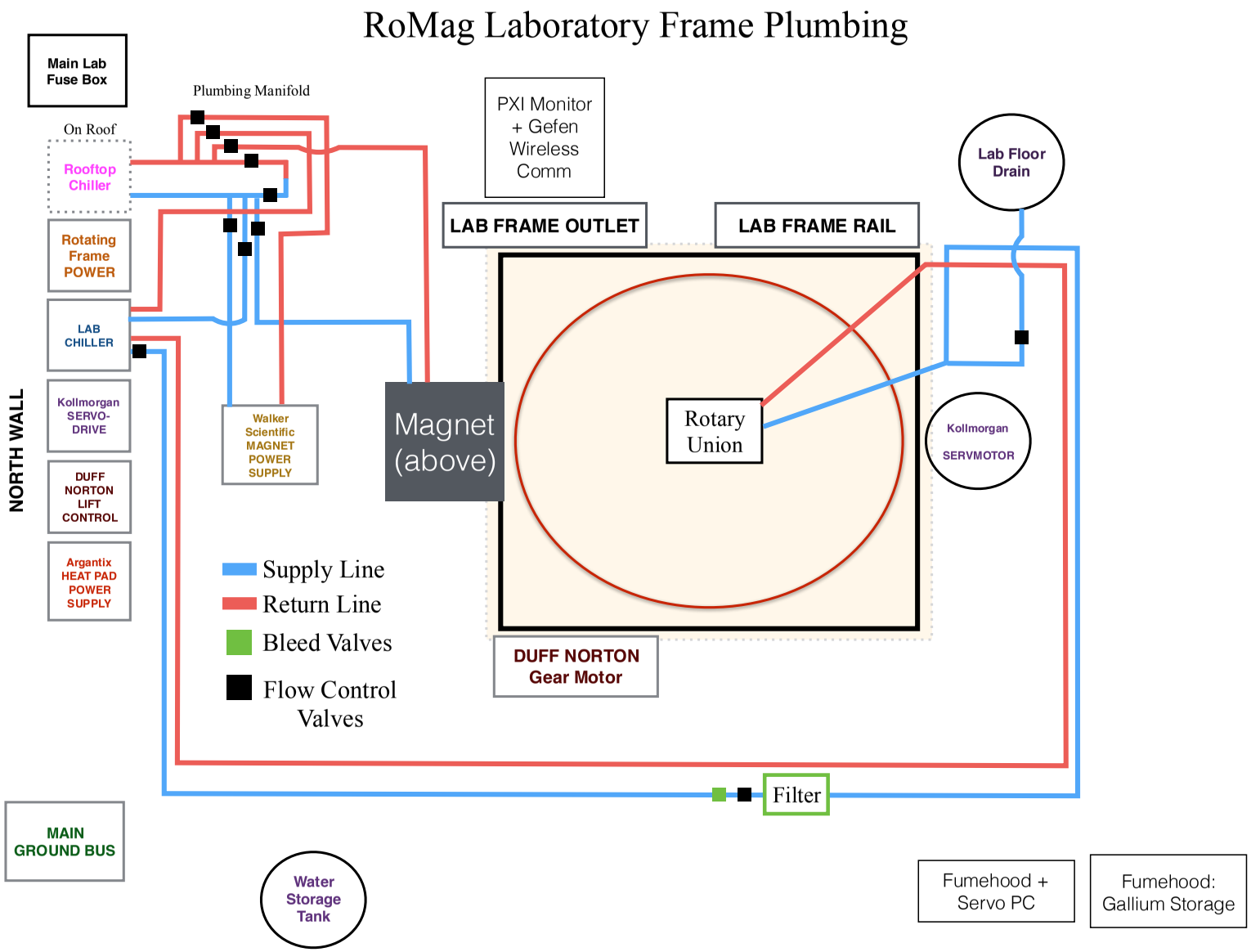

Figure 7.16: Layout of the major plumbing component and the lines that connect them. The plumbing system in the rotating frame (pink shaded region) is shown in Figure 7.17. Image contributed by Ashna Aggarwal.

7.5.1 Rotary Union

As in the case of the heater power supply, here we have to deliver chilled water from a source in the lab frame to the cooling block, which resides in the rotating frame. In order to accomplish this, we utilize a fluid rotary union. We use a two-channel rotary union manufactured by Rotary Systems.

The rotating frame plumbing emanates from two hard lines coming out of the rotary union. The hard lines pass through the same bearing shaft, shown in Figure 7.9 and Figure 7.12, where the ribbon cables and thermocouple wire also. After passing through the bearing shaft, soft rubber tubing connects the hard lines to the heat exchanger. Bleed valves are located above the heat exchanger in order to let any air in the lines escape.

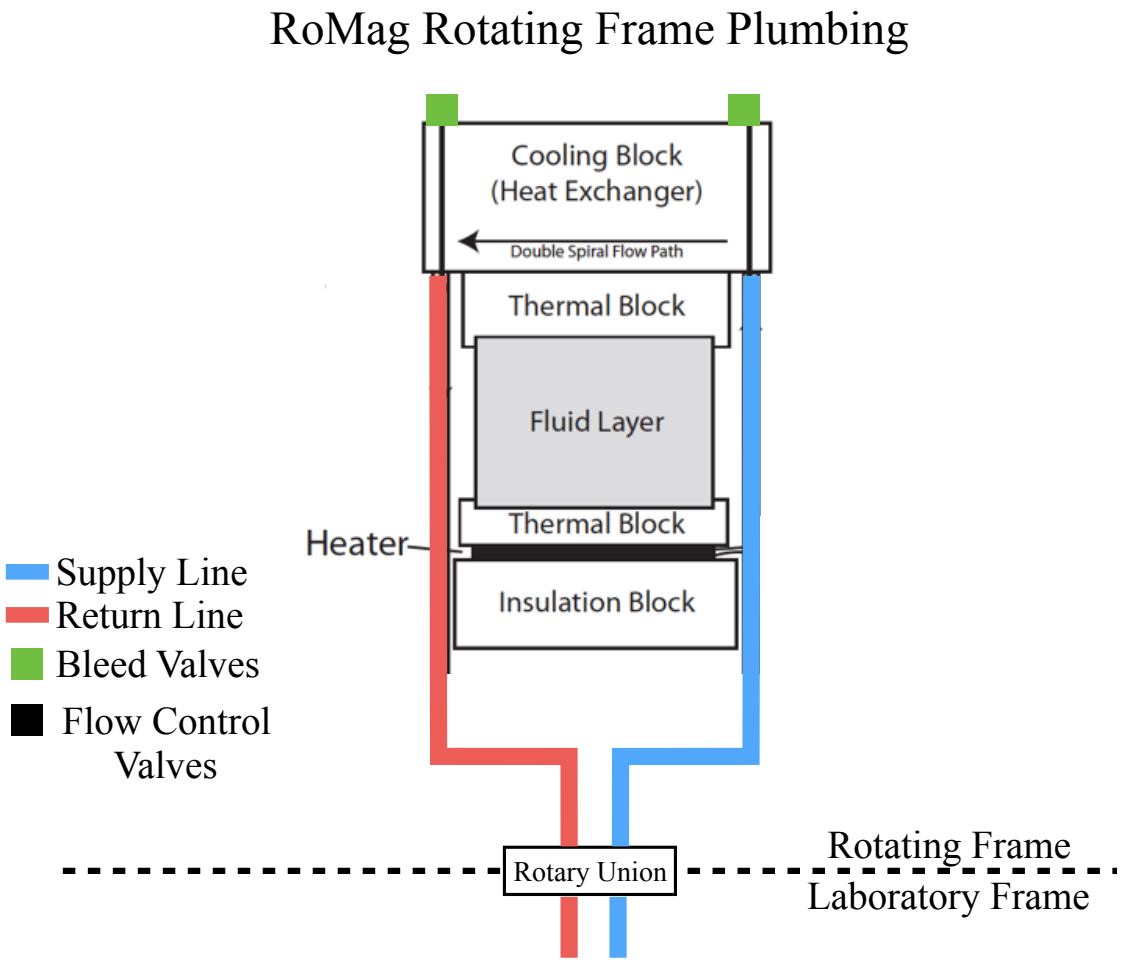

Figure 7.17: Layout of the plumbing components in the rotating frame not shown to scale. Bleed valves are located on top of the heat exchanger. Image is modified from King (2009).

7.5.2 Filling and Draining the Laboratory Chiller

The lab chiller is filled by removing panel found on top of the lab chiller as shown in Figure 7.18. The lab chiller reservoir can be filled using hose connected to the water storage tank placed along the West wall as shown in Figure 7.16 or simply by using a bottle that is filled from a lab sink. The lab chiller reservoir should be filled to about one centimeter below the top of the reservoir.

- Note: There is an autorefill feature on the lab chiller that does not function. However, if the water level drops below a given limit, a clicking is audible that is associated with the autorefill system. The water level should be checked every day.

The lab chiller is drained by placing a bucket under the spigot located at the back of the lab chiller as shown in Figure 7.19. Alternatively, a hose can be connected from the spigot the lab floor drain as shown in Figure 7.16.

7.5.3 Filling and Draining the Heat Exchanger

The following are steps necessary for filling the heat exchanger and associated plumbing lines.

1. Check that ball valves are open except for the lab chiller flow rate valve, shown in Figure 7.18, and the drain valve, shown in Figure 7.20 which should be closed.
2. Check that the hose connected to the heat exchanger have also been secured.
3. Check that all the bleed valves shown in Figure 7.16 and Figure 7.17 are also closed.
4. Place a flexible line from the drain ball valve on the heat exchanger at the bottom of the RoMag device to the lab drain as shown in Figure 7.20.
5. Turn on the rooftop chiller and lab chiller.
6. Open the lab chiller flow valve slightly so that a small amount of water is flowing and check that: by feeling that the heat exchanger supply/return lines are vibrating to

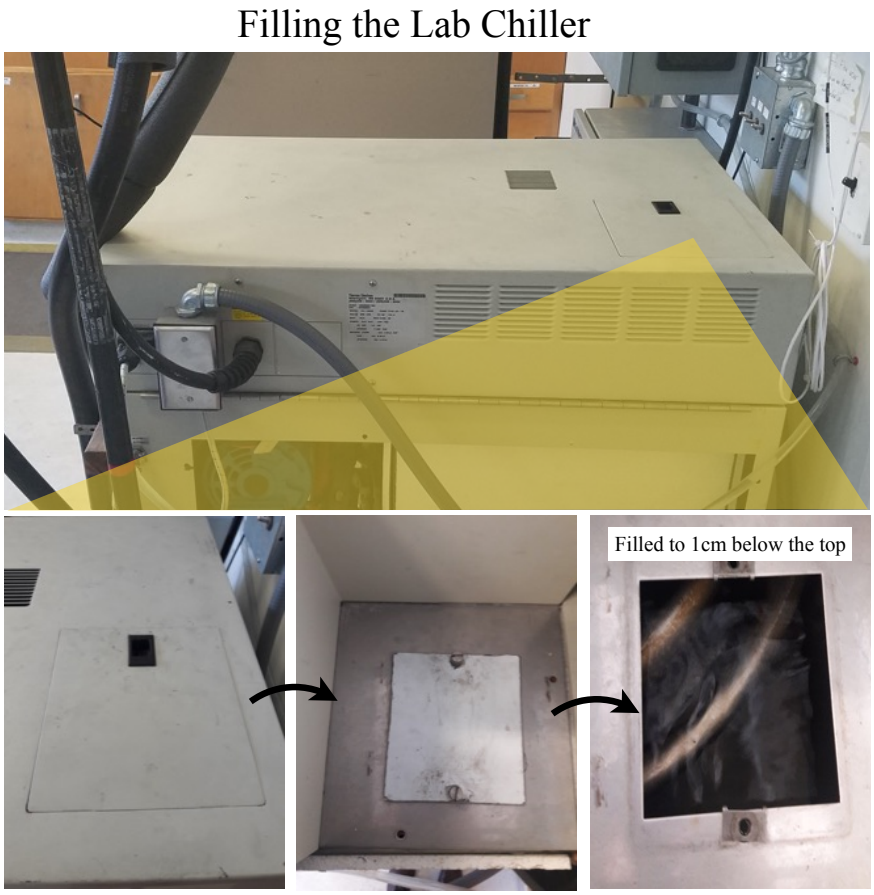

Figure 7.18: The lab chiller is filled by removing the two panels at the top of the lab chiller.

indicate the flow of water, bubbles can be seen moving through the filter, one may here bubbles passing through the lines back into the lab chiller, and that there are no leaks.

- Note: If there is a leak then shut off flow at the lab chiller and open the drain valve to drain the lines.
- Note: Ball valves are generally poor at flow control. The shaded area by the flow rate valve in Figure 7.19 indicates the narrow range where the valve actually controls the flow. The flow rate for a ball valve open at 50% is generally the same as a ball valve open at 100%.

7. Open bleeder valves on the heat exchanger and at the filter one at a time. The bleeder valves may bubble as air and water are released.

8. Move the lab chiller flow rate valve to the fully on position.

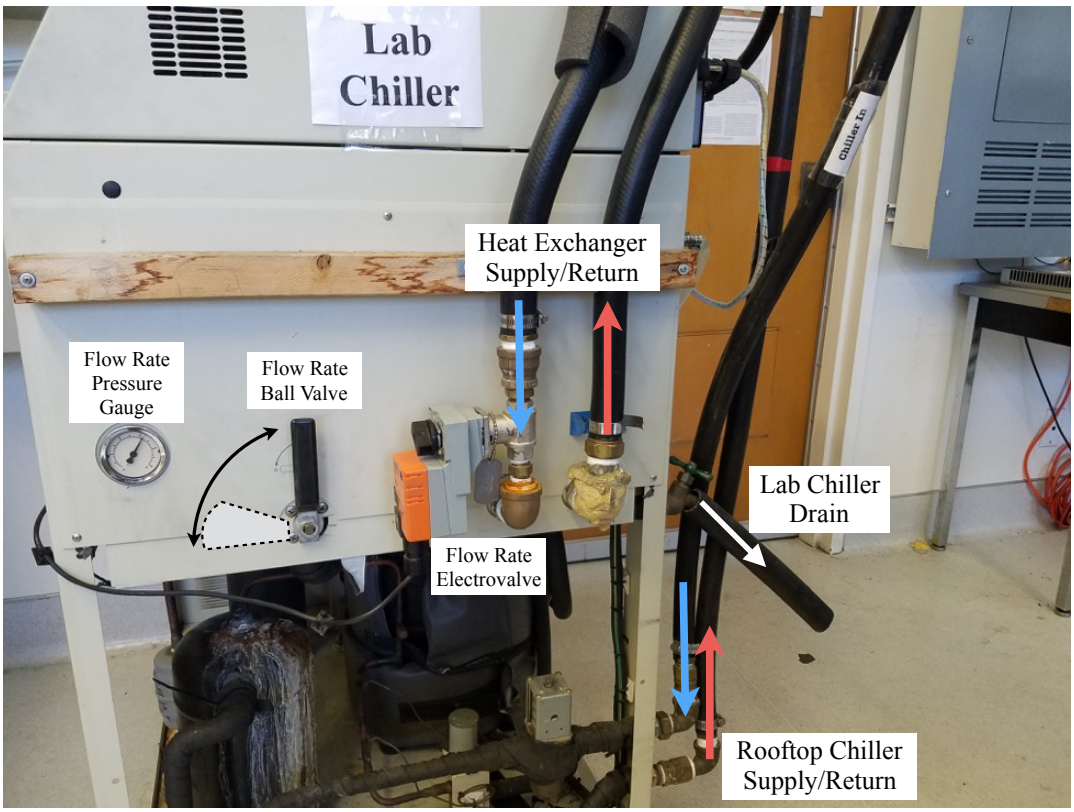

Figure 7.19: The full RoMag experimental apparatus.

During the normal operation of the experiment, the flow valve is fully open and the flexible hose going to the lab drain can be removed to allow for moving safely around the lab. To drain the heat exchanger, re-place the hose to the lab drain as shown in Figure 7.20 and close the flow rate valve at the lab chiller. Note that by opening the drain valve, only the supply side of the plumbing system is drained. The draining process can be sped up by opening up the bleeder valves on top of the heat exchanger.

7.6 Description of the Convective Volume.

This section provides an update to the fluid properties used for gallium and description of the major modifications made to the expansion tank and internal thermistor holders. This section concludes by describing the steps for assembling the convective volume from the heatpad at the bottom to the heat exchanger and expansion tank at the top.

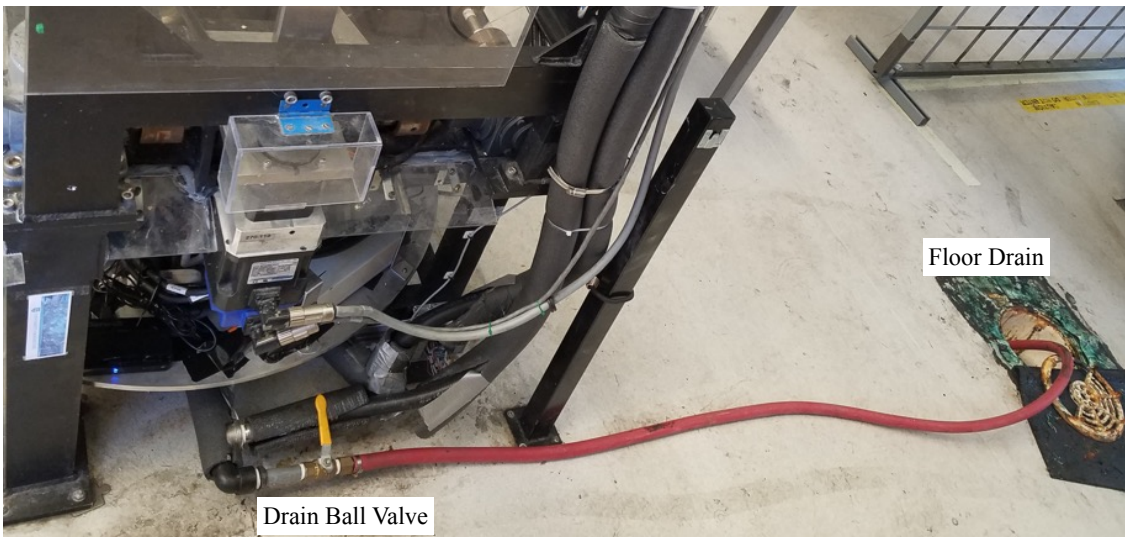

Figure 7.20: A flexible connects the drain ball valve at the bottom of the RoMag device to the lab drain.

7.6.0.1 Fluid Properties of Gallium

The properties for gallium have been updated following the experimental studies of convection in gallium performed in King and Aurnou (2013, 2015); Bertin et al. (2017). The necessary material properties that describe the thermal expansivity, α_T, the density, ρ, the specific heat, C_p, thermal conductivity, k, thermal diffusivity, κ, and dynamic viscosity, μ are given respectively as:

$$\alpha_T[\mathrm{K}^{-1}] = 1.25 \times 10^{-4}, \tag{7.4}$$

$$\rho[\mathrm{kgm}^{-3}] = \rho_{mp}\left(1 - \alpha_T(T - T_{mp})\right), \tag{7.5}$$

$$C_p[\mathrm{Jkg}^{-1}\mathrm{K}^{-1}] = 397.6, \tag{7.6}$$

$$k[\mathrm{Wm}^{-1}\mathrm{K}^{-1}] = 31.3, \tag{7.7}$$

$$\kappa[\mathrm{m}^2\mathrm{s}^{-1}] = \frac{k}{\rho C_p}, \tag{7.8}$$

$$\mu[\mathrm{kgm}^{-1}\mathrm{s}^{-1}] = \nu\rho = \mu_o exp\left(\frac{E_a}{RT_{ab}}\right). \tag{7.9}$$

In (7.5) the density of the gallium at the melting point, ρ_{mp} $[\mathrm{kgm}^{-3}] = 6.09 \times 10^3$, and the melting point temperature is T_{mp} $[^o\mathrm{C}] = 29.8$. The reference dynamic viscosity in (7.9) is

μ_o [Pa s] $= 4.359 \times 10^{-4}$ and E_a [Jmol^{-1}] $= 4000$ are held as constant. The gas constant is given by R [JK^{-1}mol^{-1}] $= 8.3144$ and T_{ab} [K] is the absolute temperature of the gallium in Kelvin.

7.6.0.2 The Expansion Tank

The expansion tank is a stainless steel tank that I have constructed that is attached to the top thermal block of the convecting volume by stainless steel tubing. The purpose of the tank is to allow the gallium to expand and contract thermally so the convecting volume remains full but does not develop excessive pressures as a result of the thermal expansion. The major advantage of this redesigned expansion tank is that it can be deconstructed and cleaned after experiments have been concluded. The top and bottom end caps are each secured with three screws. There are six holes drilled into the outer edge of the each end cap. Three of the holes are through holes that the bolts go through to secure the end cap to the cylindrical container. The three remaining holes are threaded and used with the same screws to push the end caps out without damaging the edges. Th top and bottom end caps both contain central holes threaded for 1/4" pipe fittings. The top end cap also has an additional hole to support internal thermistor holders for monitoring the temperature of the gallium inside the expansion tank.

- The o-rings placed in the expansion tank end caps is Dash No. 139, McMaster #: 9452K145

7.6.0.3 Internal Thermistor Holders

I have re-designed the internal thermistor holders, shown in Figure 7.21. the previously used internal thermistor holders had two separate thicknesses and did not have a long shaft, shown in Figure 7.21.a that sits flush with the copper blocks fluid surface shown in Figure 7.21.c. By standardizing the size of the thermistor holders, the three screws that secure the holder, shown in Figure 7.21.b, to the thermal block are all the same size. Having the thermistor holders sit flush with the copper-fluid interface helps to reduce the potential that bubbles

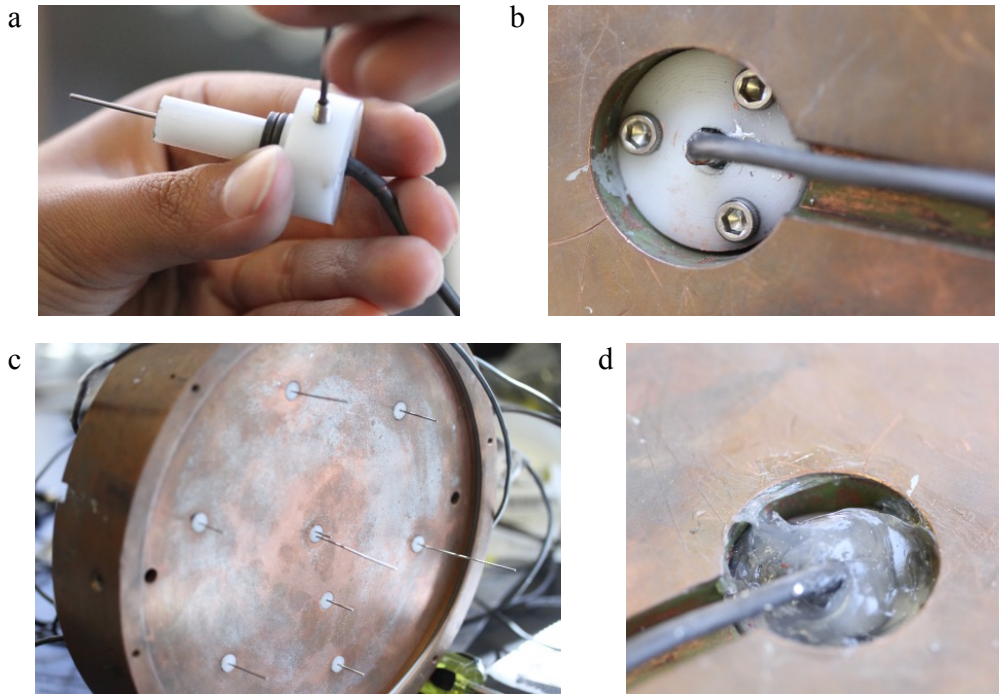

Figure 7.21: **(a)** The internal thermistor holders are made of created from Delrin material. **(b)** These holders are secured to the top thermal block with three screws. **(c)** The top thermal block can support up to eight thermistor holders. Note that the holder in the center can hold two thermistors. **(d)** Silicone (shown), plumber's putty, or a combination of the two are used as redundancies to prevent leaks in the thermistor holders.

are trapped during the filling process and affect the heat transfer during experiments. The steps for putting the internal thermistor holders into the top thermal block are as follows:

1. A very small ring is placed around the internal thermistor and is compressed when the internal thermistor is inserted into the thermistor holder. Oring Dash No. 101 McMaster #:9452K111

2. The internal thermistor is inserted into the thermistor holder such that oring around the thermistor is compressed held in place with a set screw as shown in Figure 7.21.a

3. Two orings are placed around the thermistor holder shaft of the thermistor holder as shown in Figure 7.21.a. The round oring goes on first and the x shaped oring goes on second. Round oring: Dash No. 903, McMaster #:9751K113, x oring: Dash No. 010, McMaster #:90025K133

4. This assembly is inserted into the thermal block and secured using three screws as shown in Figure 7.21.b. The screws are tightened until the thermistor holder is flush with the copper-fluid interface as shown in Figure 7.21.c.

5. To further prevent the possibility of leaks, silicone (shown), plumbers putty, or a combination of the two are used to further seal the thermistor holders as shown in Figure 7.21.d.

7.7 Gallium Cleaning System

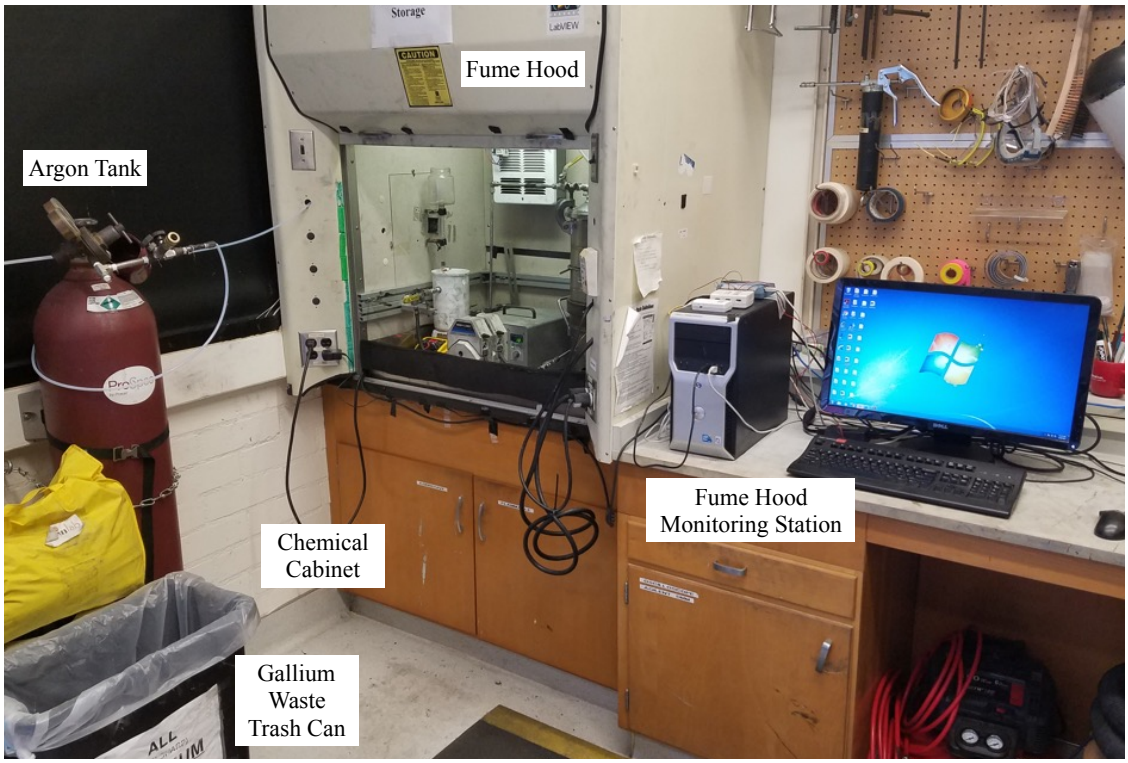

Figure 7.22: The fumehood on the left contains the gallium cleaning and storage components. The fumehood monitoring computer is located to the right. The compressed argon is used during maintenance and gallium storage and all waste contaminated with gallium is placed in the trash can.

The gallium cleaning system, shown in Figure 7.22, is designed to povide a safe and efficient means for circulating gallium and removing gallium-oxide that is generated when gallium is in contact with the air and leads to impurities in the gallium that can change its

fundamental properties.

- NOTE: While gallium is non-toxic, the use of personal protective equipment (PPE) which includes a face mask, safety glasses, latex gloves, and lab coat is encouraged during all activities associated with working on the cleaning system.

The major components of the system are the fumehood where the major components of the gallium cleaning and storage system are kept, the computer used to monitor temperatures in the fume hood, a cylinder of compressed argon, the cabinet of chemicals located underneath the fume hood where the hydrochloric acid (HCl) is kept, and a trash can where gallium contaminated materials are discarded.

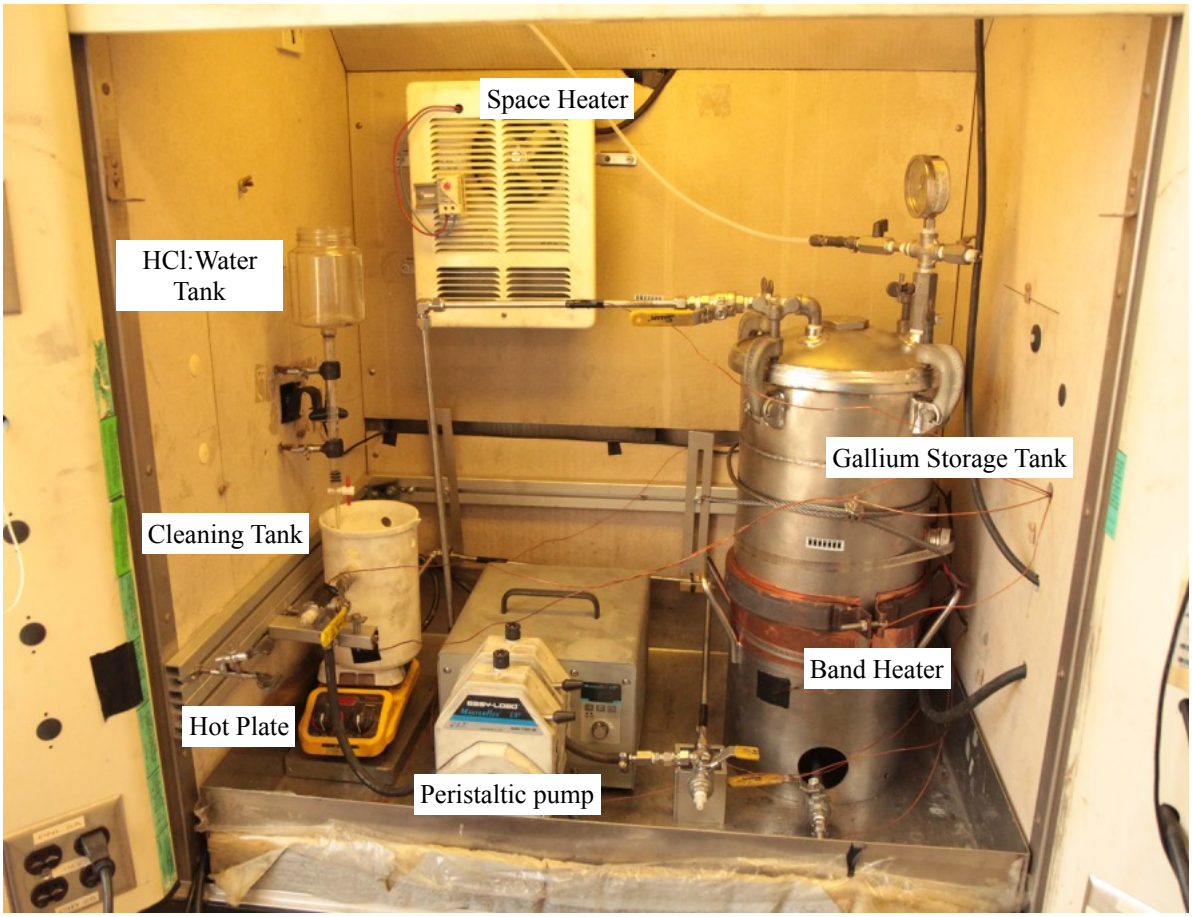

Figure 7.23: The major components of the fume hood are the main gallium storage tank with its band heater, peristaltic pump, cleaning and HCl-water storage tanks, hot plate, and space heater.

The fume hood is a confined semi-sealed compartment where the gallium is stored and

cleaned. The major components of the fume hood are shown in Figure 7.23. These are:

- Binks stainless steel storage tank that is capable of holding approximately 20 liters of gallium.
- Band heater used to heat the main storage tank
- Masterflex I/P Easyload Peristaltic Pump (model #:77601-00) used for transferring the gallium between separate tanks.
- Tank used for holding a water-HCl mixture that is used in the cleaning of the gallium.
- Cleaning tank where the gallium and water-HCl mixture is combined and stirred by the hot plate.
- A hot plate with magnetic stirrer used for stirring the gallium in the cleaning tank.
- Space heater used to keep the entire fume hood warm and maintain the gallium in its liquid phase during cleaning.

In the following set of steps, I discuss the process for cleaning the gallium and for maintaining the cleaning system. The sequence of steps begins by assuming that the fume hood is at room temperature and has been for a long time. The plumbing system used for circulating the gallium must also be assembled as shown schematically in Figure 7.24. The material that is constantly in contact with the gallium is exclusively stainless steel or laboratory grade white polyethylene containers that resists corrosion with gallium. Upon assembling the plumbing system, all the ball valves, shown in yellow in Figure 7.24, should be closed.

The band heater and the space heater should be plugged into 208 VAC single phase outlets located on the right side of the fume hood outer shroud.

- NOTE: While the user should be able to feel the heat coming from the band heater and the space heater when they are on, one should be able to see the fan on the space heater spinning. If it is not the fan may need knocked in order to get it started.

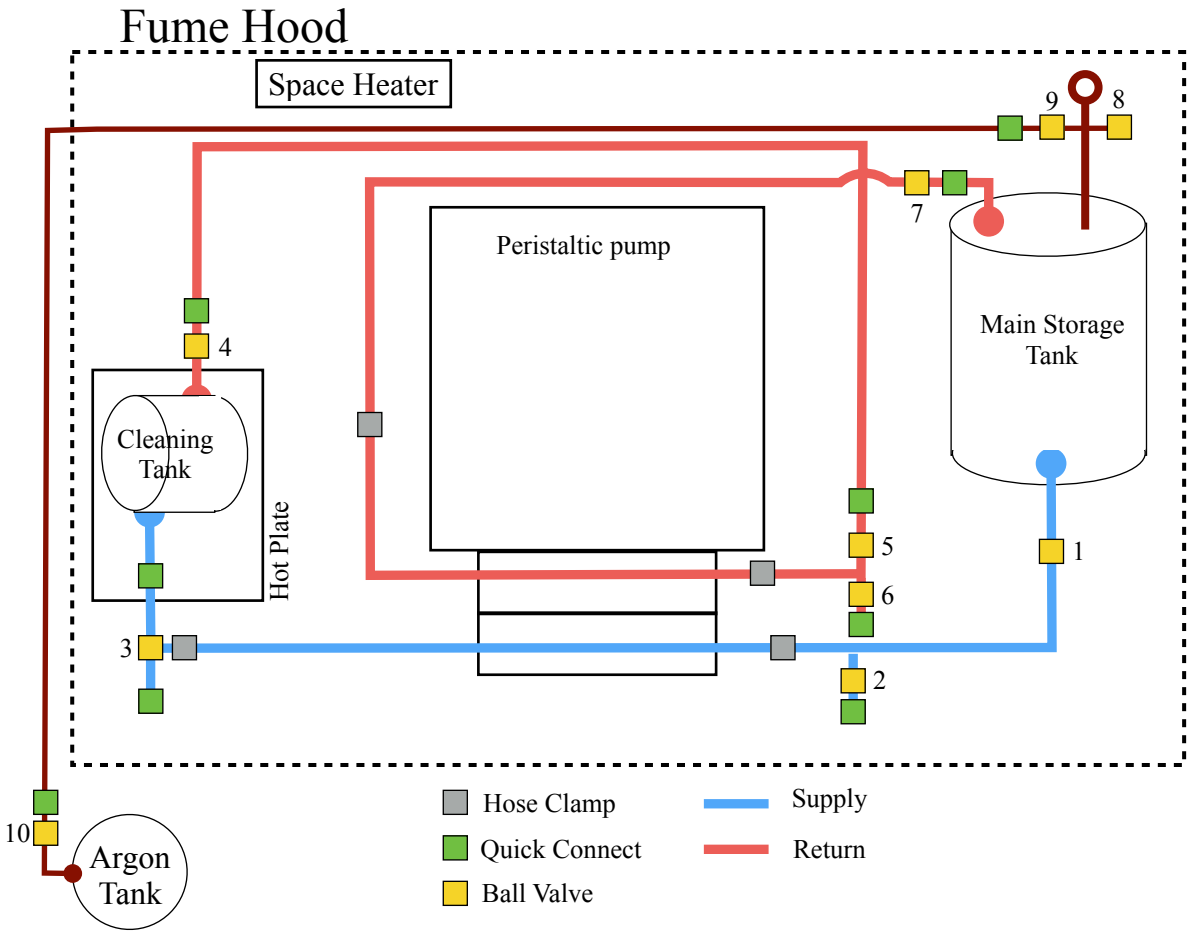

Figure 7.24: A schematic of the fume hood plumbing system. The supply line (blue) starts at the bottom of the main storage tank and arrives at the top of the cleaning tank. The return (red) begins at the bottom of the cleaning tank and arrives at the top of the main storage tank. The hose clamps (gray) connected the stainless steel tubing to the rubber tubing that is used in the peristaltic pump. The ball valves (yellow) allow the user isolate sections of tubing and the quick-connects (green) allow section of plumbing to be modular.

The band heater has a thermostat attached to the storage tank just above the band heater that activates at 105^{o}F or 41^{o}C. The space heater has a thermostat connected to its front face and is set at 80^{o}C. Over the course of a cleaning campaign, temperatures in the fume hood equilibrate at around 45^{o}C so the space heater rarely shuts off. The fume hood should stay closed and above 30^{o}C for a day in order to make sure all the gallium has melted.

Once the gallium has melted, the cleaning process can begin by plugging the hot plate and peristaltic pump into the standard 120VAC outlet located on the left side of the fume hood outer shroud. The hot plate is turned on by setting the temperature to 45^{o}C and the

stirrer speed to 12. The peristaltic pump is turned on by flipping the power switch located on the back of the pump. If the pump and hot plate are on and functioning, their respective displays will be lit. The cleaning process is performed using the following steps that make

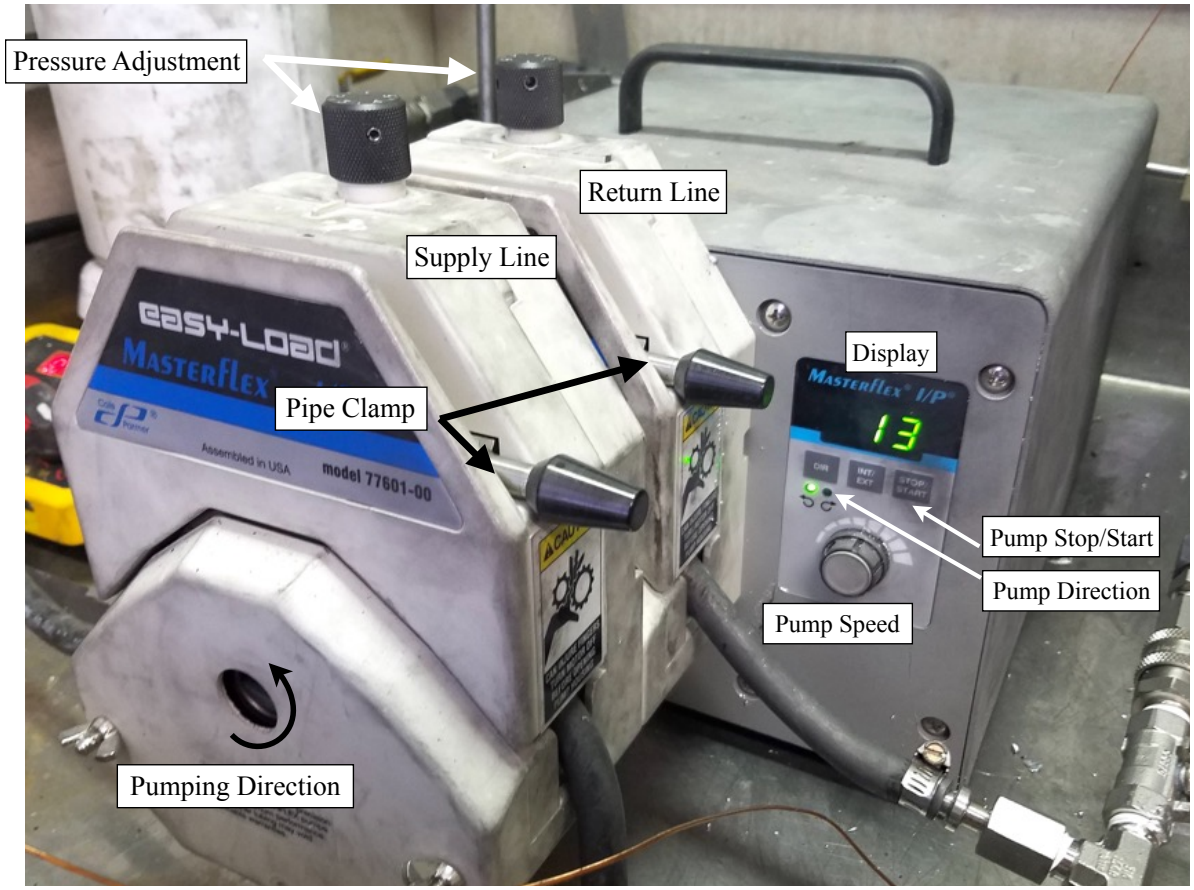

Figure 7.25: The major components at the front of the peristaltic pump. The pump power switch is located on the back of the pump. The pump always rotates in the counter-clockwise direction and the speed and pressure adjustments control the flow of gallium.

use of the numbered ball valves in Figure 7.24.

1. The front panel of the pump is shown in Figure 7.25. The rubber supply line hose should be secured by tightening the supply side pipe clamp.

2. Ball valve 1 needs to be opened and valve 3 needs to be in the vertical position so that gallium will be directed into the cleaning tank.

3. The pump speed should be set to ~ 13 and by pressing the start button, as shown in Figure 7.25, gallium should begin flowing into the cleaning tank.

4. By the time the cleaning tank is half-filled to the point where the supply side inlet is submerged in the gallium, the user can stop the pump and prepare the return side plumbing. To do so, the quick connect at valve 7 is released and a separate tank is set up as shown in Figure 7.26. Although the final leg of the gallium return line is ordinarily vertical, as indicated by a solid line, in order to prime the return lines, this leg is placed horizontal as indicated by the dashed line.

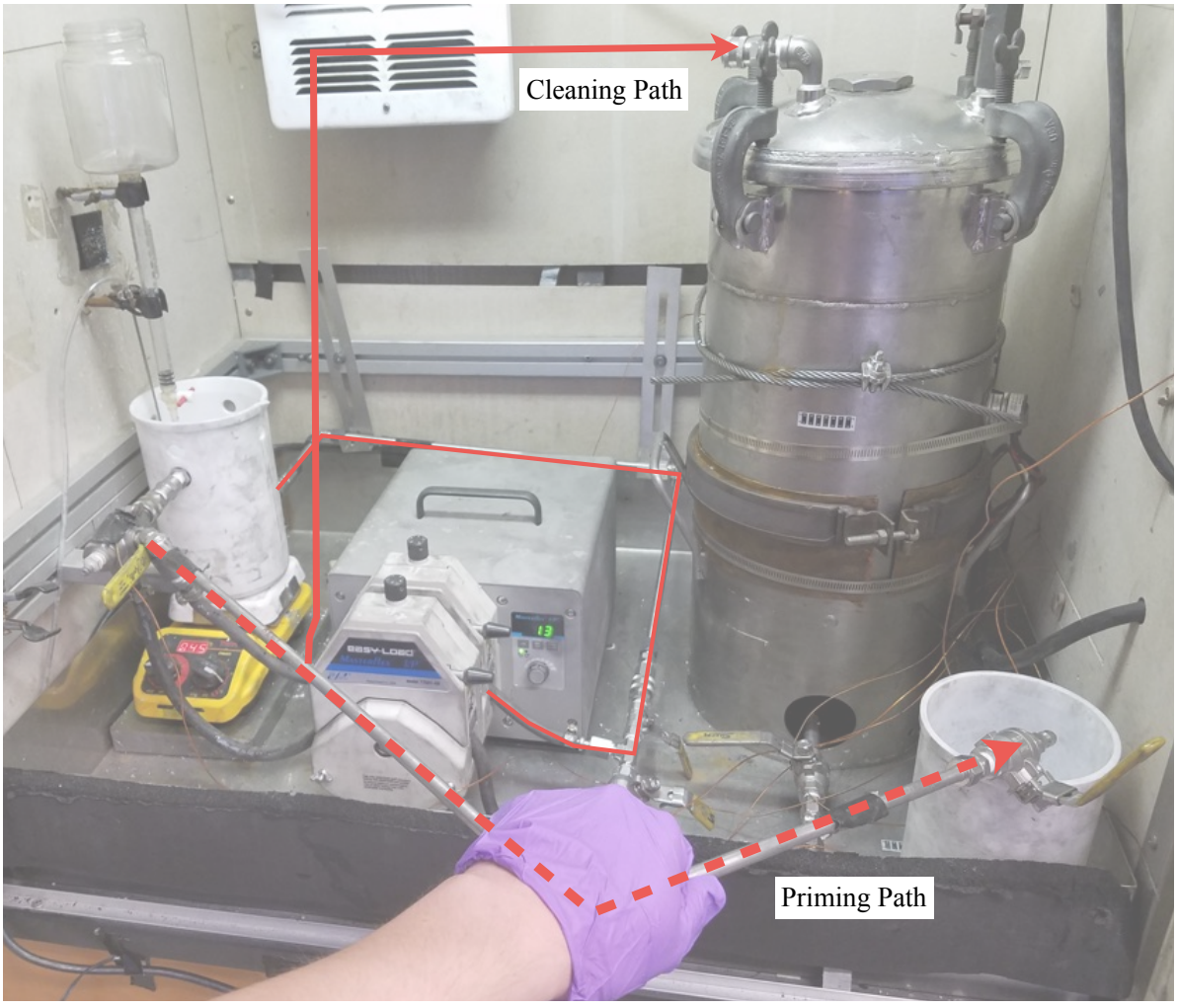

Figure 7.26: In order to prime the gallium return line, the ordinarily vertical return pipe (solid line) is place horizontal (dashed line) in order to fill the line with gallium before reinstalling.

5. The return side rubber hose is secured and clamped on the return side of the pump. Ball valves 4 and 5 in Figure 7.24 can now be opened and the pump can be restarted

with valve 7 initially closed in order for pressure to build up. After 10-20 seconds, valve 7 can be opened. Allow the gallium to flow and fill the spare tank for approximately 5-10 seconds or until satisfied that the flow is steady. Close valve 7, stop the pump, and replace the tubing to its original position has shown by the solid line in Figure 7.26. Re-open valve 7.

6. A solution of hydrochloric acid and water is made. The ratio of HCl to water is 1:10 and typically 10 ml of HCl. This solution is poured into the storage tank, shown in Figure 7.27, and the drip valve is used to allow a thin layer (0.5 cm) of the solution to completely cover the gallium and then shut off.

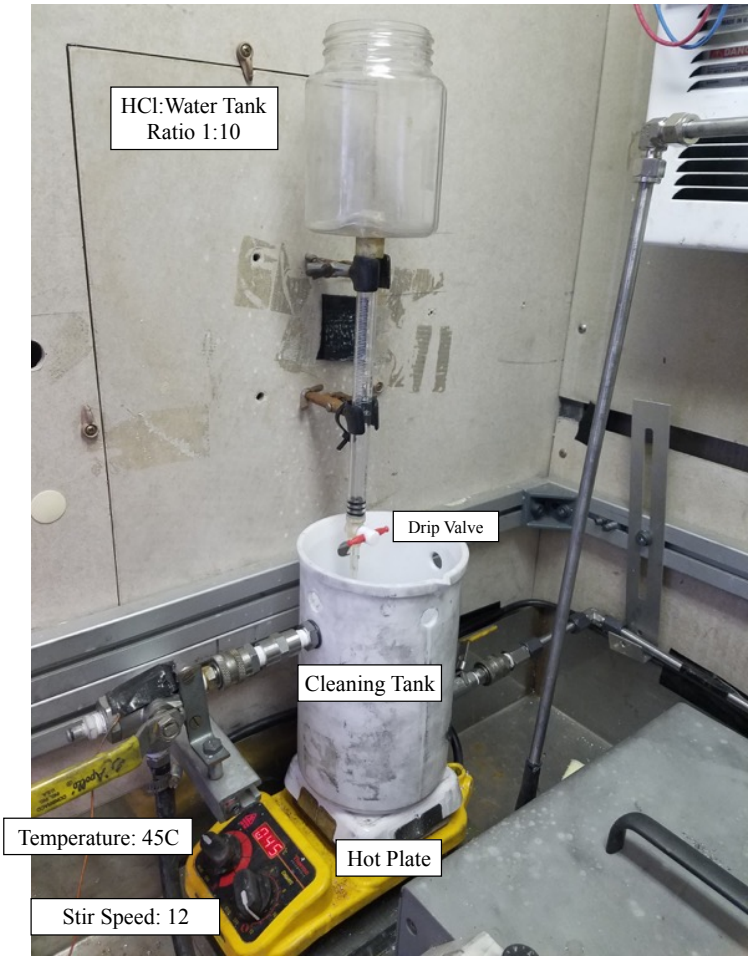

Figure 7.27: A HCl-water solution of concentration is poured onto the liquid gallium forming a thin layer in the cleaning tank. The temperature of the hotplate is set at 45^{o}C and the stir speed is 12.

7. Check that valves 1, 3, 4, 5, 7, and 8 are open. Turn on the pump.

8. The level of the gallium needs to be checked by eye. To adjust the flow rate, the pressure adjustment knobs, shown in Figure 7.25, need to be turned. The knobs are printed with numbers 1-5 indicating a range from weak to strong pressure, with default values set midway at 3. If the level of gallium in the fume hood drops one can increase (decrease) the supply (return) pressure. Typically, with the added pressure head of the gallium in the storage tank, the supply pressure adjustment is usually set more weakly. The user needs to check the level of the gallium every few minutes until the level of the gallium becomes roughly constant. This can be difficult to achieve so the level should be checked every 5-10 minutes until the settings are perfected.

After this final step is completed, the gallium is in the cleaning phase. The phase is typically run for several hours with the user periodically checking (every 10 minutes or as necessary) that the supply tube in the cleaning tank is submerged, that the thin layer of HCl-water solution is maintained over the gallium.

In order to store the gallium, it must be transferred to main storage tank and the plumbing lines must be cleared and flushed with argon. This process is outlined in the following steps.

1. At the end of cleaning phase allow the HCl solution on the gallium to dissolve or evaporate as the solution should not be placed in the storage tank with the gallium.

2. The supply side pump is released and valve is 1 is closed. With the pump on, the return side will continue to drain the cleaning tank until the level of the gallium drops below that level of the outlet.

3. The quick connect for the argon gas line is disconnected at valve 9 and placed at valve 2 and argon is flushed through this line the gallium is cleared from the tubing into the cleaning tank. Close valve 2 and the argon supply and disconnect the argon supply.

4. Connect the argon supply to the quick connect at valve 6. Open the return side pump clamp and close valve 5 with valve 7 open. Open the argon supply at valve 10 and

valve 6 to clear the leg of the return line going to the storage tank. The user may hear the gallium bubbling in the storage tank.

5. Flush the remaining legs of the return line by opening valve 4 and 5. The user may see the gallium in the cleaning tank bubbling. After flushing has occurred for 2 minutes all valves can be closed to trap the argon in the lines.

6. The cleaning tank is then disconnected from the system to pour the remaining gallium into the storage tank. The cleaning tank can then be cleaned in a bucket with warm water. After cleaning is done the tank can be reconnected and the valves can be closed.

7. As a final step, the argon supply is returned to the quick connect at valve 9 so that the main storage tank can be flushed with argon. By closing valve 8 and releasing argon into the storage tank the pressure inside the vessel can be raised to 5 PSI and then slowly released via valve 8. This is done 3-5 times and at the end all valves are closed.

7.8 RoMag Acquisition System

The signals from all the probes are acquired through the PXI and displayed and analyzed using the interface program, Labview 2013. All the necessary Labview programs are found on the PXI in files on the desktop. The monitoring program is found on the desktop at the following location:

- RoMag Data Acquisition Program:
  C:Desktop/Romag_Controls_Acquisition/Romag_Monitoring.vi

To open the program click on it's icon and wait for it to load all necessary dependencies. The monitoring program will load and appear as shown in Figure 7.28. To run the program:

1. Click on the white arrow in the top left corner (arrow turns black as shown in Figure 7.28 when running).

Figure 7.28: User interface for the main RoMag monitoring program used to display all the thermal and voltage signals used investigate convective flows.

2. A dialog window appears where the user can name the file and location to which all the data will be saved. NOTE: a timestamp is automatically appended to the file name.

3. If the user does not wish to save a file then hit cancel.

4. Another dialog box appears where the user specifies the sampling frequency and whether the data is to be saved.

5. The monitoring program, shown in Figure 7.28, should now be running with updates occurring to the values and graphs displayed .

7.8.1 Labview Monitoring System: Front Panel

The monitoring/acquisition program is used to display thermal signals coming from the thermistors and thermocouples, measurements of the magnetic field coming from the hall probes, and voltages from measurements of the heatpad. In addition, this program also analyzes these signals and generates relevant dimensional and non-dimensional estimates of the fluid and flow properties.

The front panel, shown in Figure 7.28, contains the time-series visualization of different flow metrics as well as the output of the dimensional and non-dimensional parameters. The monitoring program's front panel can be separated into three distinct parts. The left side provides of Figure 7.28 contains the "Essentials": a quick summary of the dimensional properties of the current experiment. It contains the elapsed time that the monitoring program has been running, the power generated by the heatpad, temperature measurements of the top and bottom lid, the mean fluid, and the room temperature.

On the top left of the monitoring program are "Set Parameters" controlled directly by the user. These include the height of the tank, rotation rate, strength of the magnetic field, and the name of the file where all the data is saved. In the top middle and top right panels of Figure 7.28 the user can also control the interval that monitoring and alarm emails are sent and the recipients to whom the emails are sent. The monitoring emails contain general information (power, top and bottom lid temperatures, and the expansion tank temperatures)

sent every 30 minutes by default. The alarm emails are sent every two minutes, by default, if the power and/or temperatures are outside a specified range.

The tabbed section that composes the central and largest part of the monitoring program contain information and graphs for: Temperature, Power, Rotation, B-field, Dimensional Estimates, and Non-Dimensional Estimates. These graphs are useful for seeing trends and waves in the flow and provide a means for determining whether the experimental case is equilibrated to the point that the signals do not show any visible trends over several thermal diffusion time scales.

The Temperature tab contains:

- Graph of the six thermistors in the top lid along with the spatially-averaged top lid temperature.
- Graph of the six thermistors in the bottom lid along with the spatially-averaged bottom lid temperature.
- Graph of up to nine internal thermistors in the interior of the fluid.
- Graph of an array of sidewall thermocouples.
- Graph of the temperature drop across a layer of insulation. Such a temperature drop can be used to make estimates of the sidewall heat losses.
- Graph showing the temperatures used to monitor the expansion tank and tubing.
- Graph showing room temperature changes.
- On the right are schematics showing where the thermal probes described above are located in the convection experiment.

The Power tab contains:

- Graphs of the power through the heatpad calculated using $P = IV$ generated from the PMU and $P = V^2/R$ which assumes that the measured heatpad resistance is fixed.

These values are generally quite similar except at large wattage where the temperature dependent properties of the heatpad resistance starts to play a role.

- The instantaneous measurements of the the voltage divider and shunt measurements from the PMU and the the resulting calculated current and voltage of the heatpad.

The Rotation tab is currently unused as the rotation rate is not actively measured. The B-field tab contains:

- Graphs of the two Hall probes
- instantaneous signals of the raw voltages from the Hall probes. Theses values are not currently calibrated.

The Dimensional Estimates tab contains:

- Instantaneous values of the fluid properties ($\rho,\ C_p,\ \alpha_T,\ \nu,\ \kappa,\ k,\ \eta$) described in Section 7.6.0.1
- Instantaneous values of timescales including thermal diffusion time, $\tau_\kappa = H^2/\kappa$, the viscous diffusion time, $\tau_\nu = H^2/\nu$, the magnetic diffusion time, $\tau_\eta = H^2/\eta$, the rotational timescale, $\tau_\Omega = 1/\Omega$, free fall timescale, $\tau_{ff} = H/U_{ff}$, where $U_{ff} = \sqrt{\alpha g \Delta T H}$, and the Alfvén time, $\tau_A = H/U_A$, where $U_A = B/\sqrt{\mu_o \rho}$.

The Non-Dimensional tab contains

- Graphs showing the temporal variations in the Nusselt and Rayleigh numbers.
- Instantaneous values of the, Nusselt, Prandtl, Rayleigh, Interaction, convective Interaction, convective Reynolds, convective Rossby, Chandrasekhar, magnetic Prandtl, etc.
- Instantaneous values for the supercriticality of the flows, Ra/Ra_c, based on the estimates of the critical Rayleigh numbers for steady rotating convection, oscillatory rotating convection, wall-mode rotating convection, and for the magnetic field.

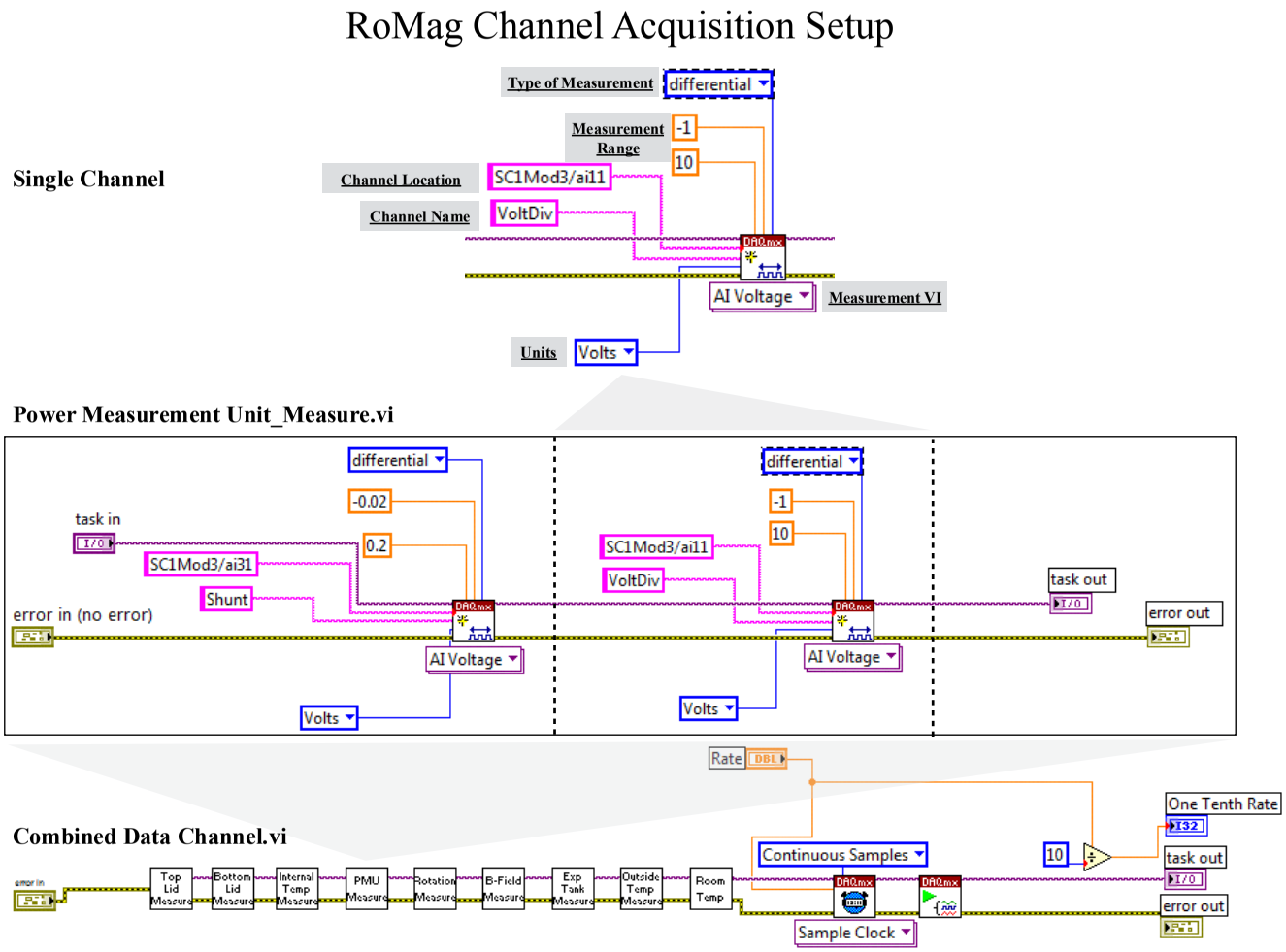

Figure 7.29: Flow chart showing the "wiring" of a single acquistion channel as displayed in Labview code. The information needed for each channel include the physical address of the signal to read, the type of measurement to be performed, the range of values accepted, and the units of the measurement. Each channel is connected to other channels forming a chain. For instance, as shown, the two signals associated with the heatpad form one chain. These chains are ogranized in separate subVI's that are also chained together in the Combined Data Channel.vi program and called by the main monitoring program.

7.8.2 Labview Monitoring System: Back Panel

The back panel of the monitoring program contains a view of the underlying code and the calls to the various sub-programs used to perform various tasks.

7.8.2.1 Gathering Channel Information

Figure 7.29 provides a flow chart of how signals are acquired in the monitoring program. A single channel is acquired by using a built-in data aquisition (DAQ) program where the user decides, the specific type of measurement to make, the physical address of the numbered module and terminal where the signal is to be read, the range for the values to be read, and the units of the measurement. Although a standard analog voltage measurement is shown at the top of Figure 7.29,the DAQ program used to measure temperatures from thermistors and thermocouples are quite similar. At the next level, the different channels are wired together to form longer chains as shown in the middle of Figure 7.29. In principal, these chains can be as long as is necessary but they are separated for organizational purposes into the signals associated with the top lid temperatures, bottom lid temperatures, etc. All channel acquisition is performed in sub-program Combined Data Channel.vi.

7.8.2.2 Displaying Data

One of primary function of the RoMag monitoring program is to display signals using graphs. An excerpt of the typical code used to perform this function is shown in Figure 7.30. This code contains several parts:

- The blue signal lines on the left of Figure 7.30 contain all the the available signals gathered as shown ar the bottom of Figure 7.29.
- The signals of interest are selected from the full list using a built-in Labview program.
- These signals are then displayed using a built-in waveform chart.
- Instantaneous mean quantities may also be determined and displayed at other locations

on the front panel like the “Essentials” section.

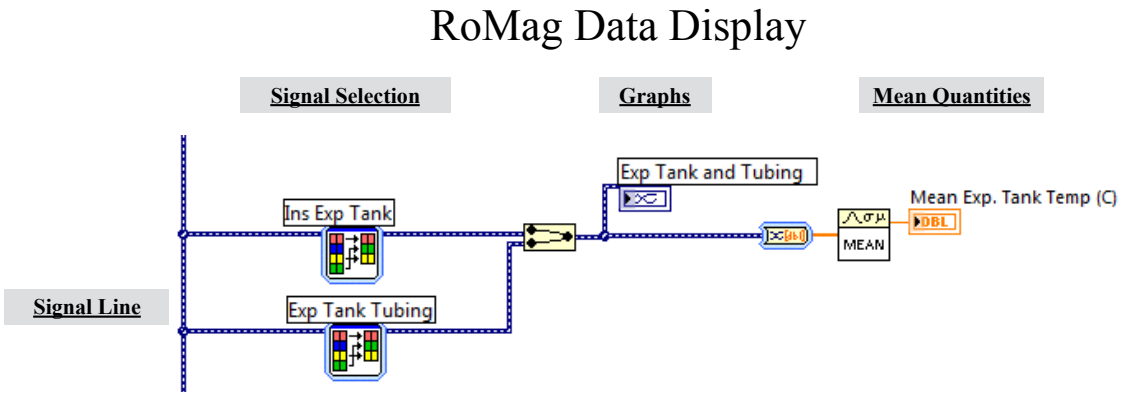

Figure 7.30: Example of the Labview code used to select the data from the signal lines, in blue, to be graphed and instantaneously averaged.

7.8.2.3 Labview Sub-Programs

Table 7.2 provides a list of the primary Labview sub-programs that are utilized by the main monitoring program, the program that calls them, and a short description of the function that the program performs.

7.9 RoMag Controls Program

The major components on RoMag that are varied during normal operation are controlled in three ways.

- The heatpad output and lab chiller set temperature are controlled using the Labview Program on the PXI : `C:Desktop/Romag_Controls_Acquisition/Romag_Controls.vi`.
- The rotational control is carried out using a separate computer also used for monitoring the fumehood.
- The magnet lifting system, magnetic field strength, and heat exchanger flow rate are controlled manually.

Filename	Calling File	Program description
Combined Data Channel.vi	RoMag Monitoring.vi	Contains all SubVIs used to gather data probe information.
Top_Lid_Measure.vi	Combined Data Channel.vi	Gather all channels for measuring the temperatures in the top thermal lid.
Bottom_Lid_Measure.vi	Combined Data Channel.vi	Gather all channels for measuring the temperatures in the bottom thermal lid.
InternalTemp_Measure.vi	Combined Data Channel.vi	Gather all channels for measuring the temperatures inside the convection tank.
Power Measurement Unit_Measure.vi	Combined Data Channel.vi	Gather the two channels for measuring the voltages from the PMU as discussed in Section 7.4.3.2.
Rotation_Measure.vi	Combined Data Channel.vi	Gather signals for measuring rotation. (Currently unused).
MagneticField_Measure.vi	Combined Data Channel.vi	Gather signals from two Hall probes used to measure the strength of the magnetic field.
ExpTank_Measure.vi	Combined Data Channel.vi	Gather temperature signals from Expansion Tank and tubing.
OutsideTemp_Measure.vi	Combined Data Channel.vi	Gather temperature signals from probes around the sidewall.
RoomTemp_Measure.vi	Combined Data Channel.vi	Gather room temperature signals from probes.
RomagMonitor_UserPrompt.vi	RoMag Monitoring.vi	Request user to save data and specify the frequency of data acquisition.
PMU Measurement.vi	RoMag Monitoring.vi	Calculates the power in the heatpad following the equations in Section 7.4.3.2.
Temperature Dependent Fluid Properties.vi	RoMag Monitoring.vi	Calculates fluid properties of the flow given the temperature.
Dimensional_ Calculations_ EH_0516.vi	RoMag Monitoring.vi	Calculates dimensional timescales and velocities of the flow given the temperature and container geometry
Dimensionless_ Calculations_ EH_0516.vi	RoMag Monitoring.vi	Calculates non-dimensional properties of the flow given the temperature, rotation, magnetic field strength, and container geometry
Primary_Monitor_Message.vi	RoMag Monitoring.vi	Sends regular emails containing temperature and power present in the experimental device.
Temperature Alarms SubVI.vi	RoMag Monitoring.vi	Warns user if temperatures and power are outside a prescribed range.
TempAlarm_EmailSend.vi	Temperature Alarms SubVI.vi	Determines if value is outside prescribed range and sends an email alerting the user.

Table 7.2: List of programs and sub-programs found in the main RoMag monitoring program.

7.9.1 Heat Pad and Lab Chiller Control

Before controlling the heat pad and lab chiller it is necessary that they be switched on. The front panel of the lab chiller is shown in Figure 7.31 with an inset of the wall power

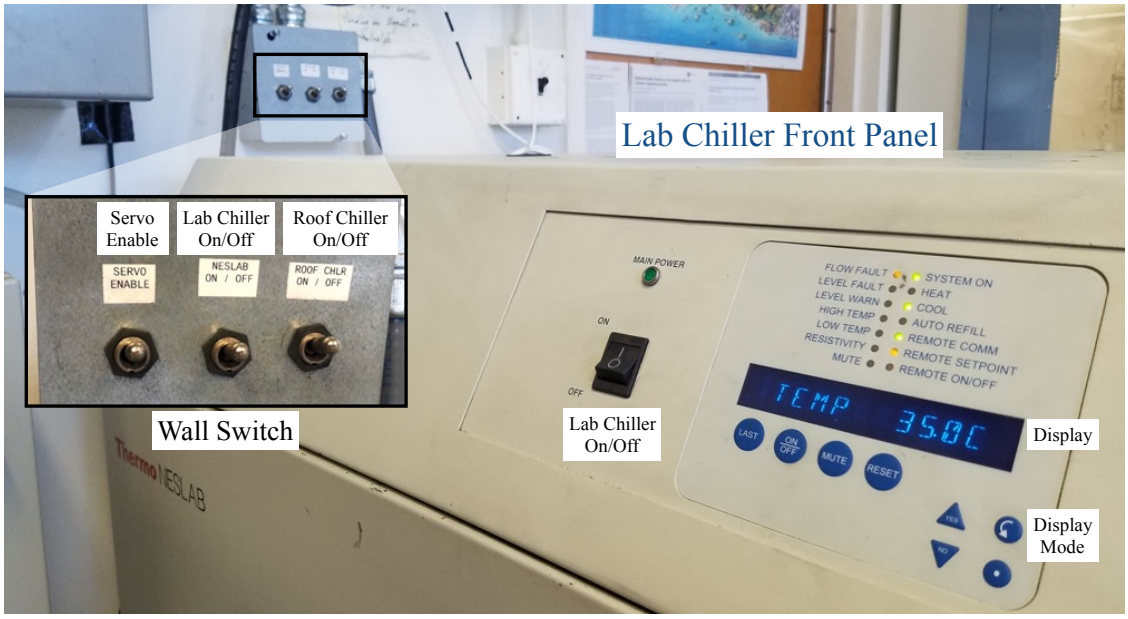

Figure 7.31: The front panel of the lab chiller. Inset is a separate set of switches for enabling the servo drive, and powering the rooftop and lab chillers. Image contributed by Ashna Aggarwal.

switches. The on/off switches for the rooftop chiller and lab chiller must be on at the wall switch and the on.off switch on the lab chiller's front panel must also be on. Changing the heat pad power and lab chiller set temperature is done using the Labview program `Romag_Controls.vi` whose front panel is shown in Figure 7.32.

1. The user inputs the desired power (0-5100W) and lab chiller set temperature (5-35^{o}C), indicated by row 1 in Figure 7.32.

2. The program is run by clicking on the white arrow in the top left corner of the program.

In the underlying code found on the back panel, the desired wattage and set temperature are first converted to a voltage. The Argantix power supply is configured to receive 0-10 volts and the conversion from the desired wattage to voltage is given by

$$V_{\text{Argantix}} \sim 0.1\sqrt{\text{Wattage}}. \tag{7.10}$$

For example the voltage required for 1000W is $V_{\text{Argantix}} \sim 1$V. The exact formula may require re-calibration if the heat pad resistance changes. The conversion from temperature to the

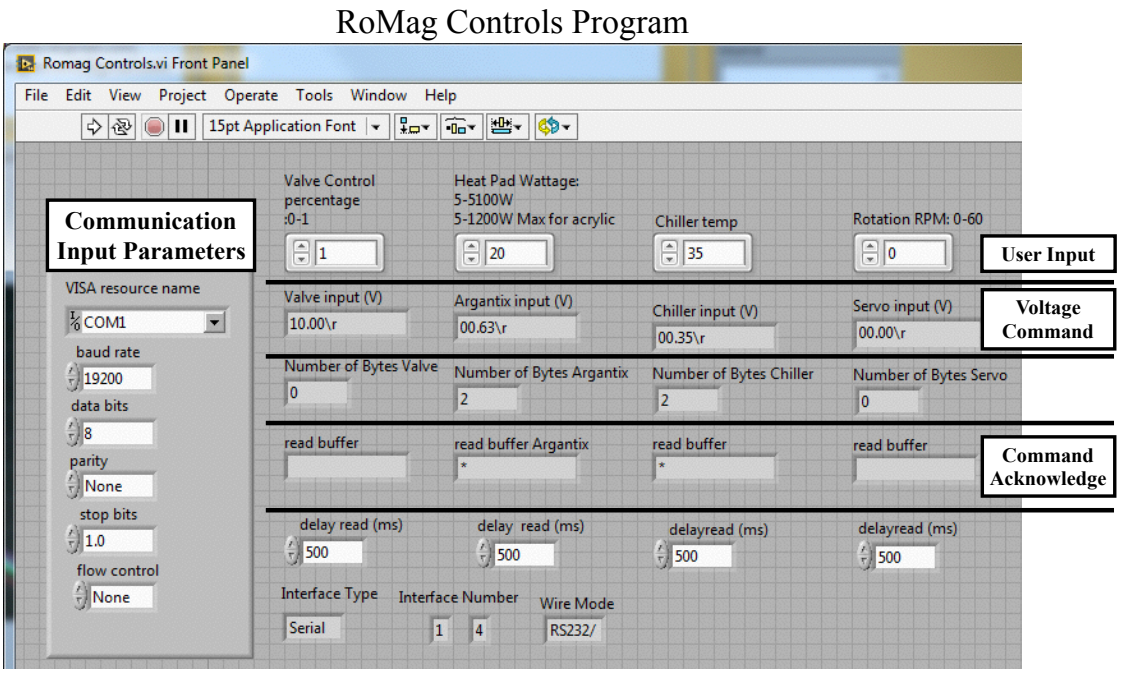

Figure 7.32: The Labview program used to control the heatpad and lab chiller set temperature. The user inputs values in the first row and runs the program by pressing the white arrow in the top left of the screen.

voltage used for controlling the lab chiller set temperature is given by

$$V_{\text{Lab Chiller}} = \frac{\text{Set Temp.}}{100}. \tag{7.11}$$

The voltages, V_{Argantix} and $V_{\text{Lab Chiller}}$ are then converted to a 4 digit and carriage return syntax, 00.00\r and shown in row 2 of Figure 7.32. This syntax is associated with standard VISA protocol commands used to control experiments and is appended to a longer string that also includes address information for communicating with pre-assigned Omega modules located in the Servo-Drive box that output the desired voltage. For instance, if the set temperature is 15^{o}C and then a portion of the string with the voltage value that is sent is given by 00.15\r. Once received, the command is acknowledged and an asterisk (*) is returned (shown in row 4 of Figure 7.32).

- NOTE: In some instances, it is necessary that the maximum requested wattage be lower than the 5100W max that is capable of the power supply. For instance, stainless steel cylinders are appropriate for use at all wattages while acrylic cylinders will lose

structural integrity if the the temperature of the container is $\sim 100^{o}$C.

Figure 7.33: The servo drive front panel with the main power switch located on the right side. An RS232 plug is also located on the top left of the front panel and shown inset. The RS232 cable runs from the fumehood computer where the rotation is controlled to the servo drive box where the servo drive is kept.

For completeness, the program is also configured for controlling the rotation rate (0-60RPM input) and the flow rate to the heat exchanger (0-100% input). The servo-drive is configured to receive voltages from 0-10V such that the conversion is

$$V_{\text{Servo}} = \frac{\text{RPM}}{6}. \tag{7.12}$$

The electrovalve shown in Figure 7.19 is configured to receive voltages from 2-10V such that the conversion is

$$V_{\text{Valve}} = 8\frac{\text{Percentage}}{100} + 2. \tag{7.13}$$

However, the Omega modules for the servo and electrovalve are not currently operational.

7.9.2 Rotational Control

The control of rotation is done using the Servostar Motionlink software located on the Fumehood computer. The first assumption is that the circuit breaker controlling the servo in Figure 7.6 is on and that the Servo Box, shown in Figure 7.33, is also switched on. The Fumehood computer is connected to the servo drive via a standard RS232 cable.

- Note: Communication to the servo with a standard 9pin RS232 connector only requires 3 lines: Data in, Data out, and Ground which corresponds to pin 2, pin 3, and pin 5 respectively on a standard RS232 connector. However the Data in/out is flipped for the servo so going from the computer to the servo, jumper wires, shown in the inset image of Figure 7.33, must connect pin 2 from the computer to pin 3 on the servo, pin 3 on the computer to pin 2 on the servo, and pin 5 on the computer to pin 5 on the servo. If not wired correctly then the servo will not be recognized by the communication software.

1. Click on the Servostar Motionlink shortcut located on the desktop as shown in Figure 7.34.1
2. Click YES on the Controller detection panel in Figure 7.34.2
3. In the Start MOTIONLINK window, initiate communication with the servodrive by clicking on the COM SETUP in Figure 7.34.3
4. Set up the parameters for communicating with servodrive by moving to the RS-232 tab in Figure 7.34.4. Communicate with the COM1 port using a 9600 Baud Rate. Click the SCAN button which will detect the servo-drive.
5. Enable the Servo on the main switch as shown in the left on Figure 7.31. After doing so the RoMag device is locked in position and will not turn by hand.
6. Click OK to move back to the screen shown in Figure 7.34.3 and click START.

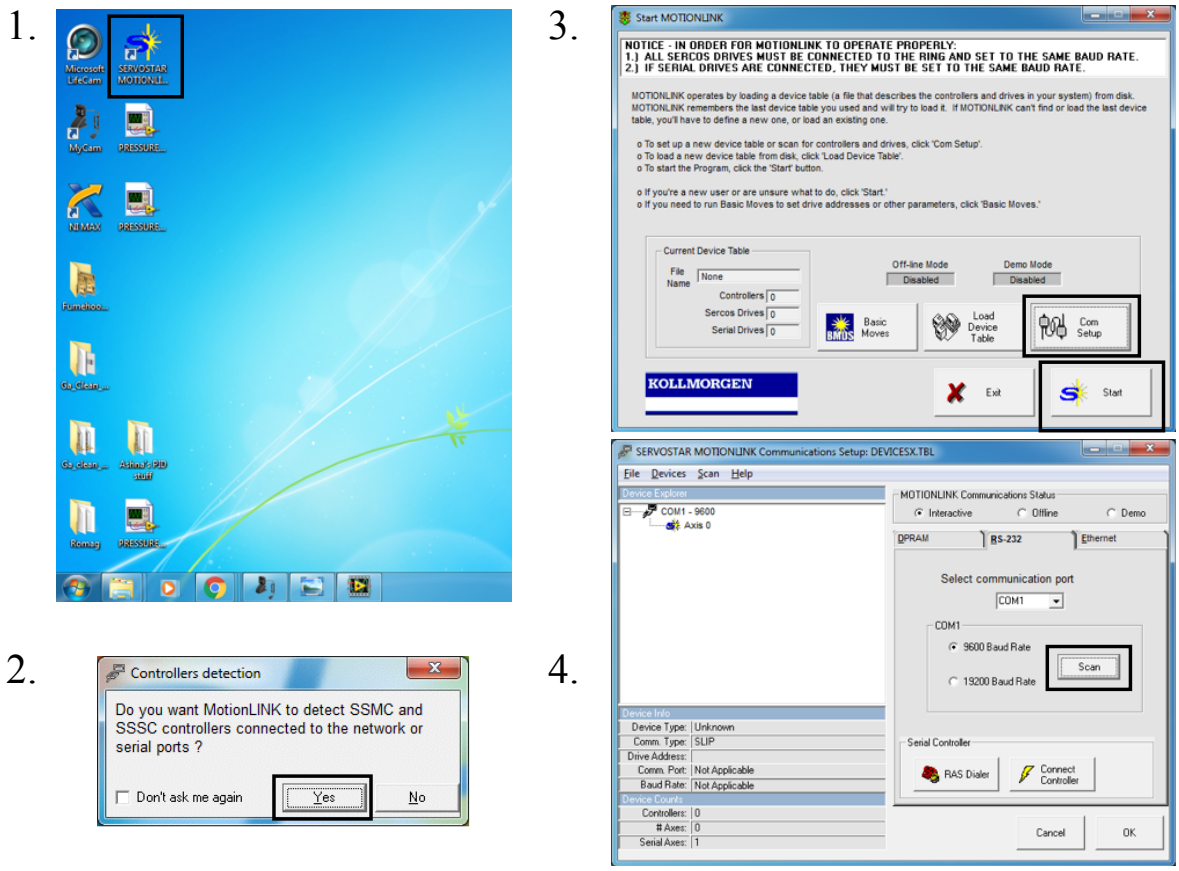

Figure 7.34: Screenshots showing the major steps for setting up the communication from the servo control program, Servostar Motionlink, to the servo drive. The icons or buttons that need clicked are outlined with black boxes.

Having set up the communication and detection parameters of the servodrive it is now possible to control the rotation rate as outlined in the following steps and in Figure 7.35.

1. The control panel can be reached by clicking on the Command Generator in Figure 7.35.1. The status of the servo at the top of the panel should be white. If it is red then the wall switch located above the lab chiller as shown in Figure 7.31 should be switched into the Enabled positon. NOTE: that when enabled, the RoMag device is locked into position and will not rotate hand.

2. Input the desired motor speed as shown in Figure 7.35.2 Note that the speed of the motor is 1/40th the speed of the Romag device using a gear reduction system (i.e., An input of 800 RPM corresponds to 20 RPM on the RoMag device. Initiate or modify

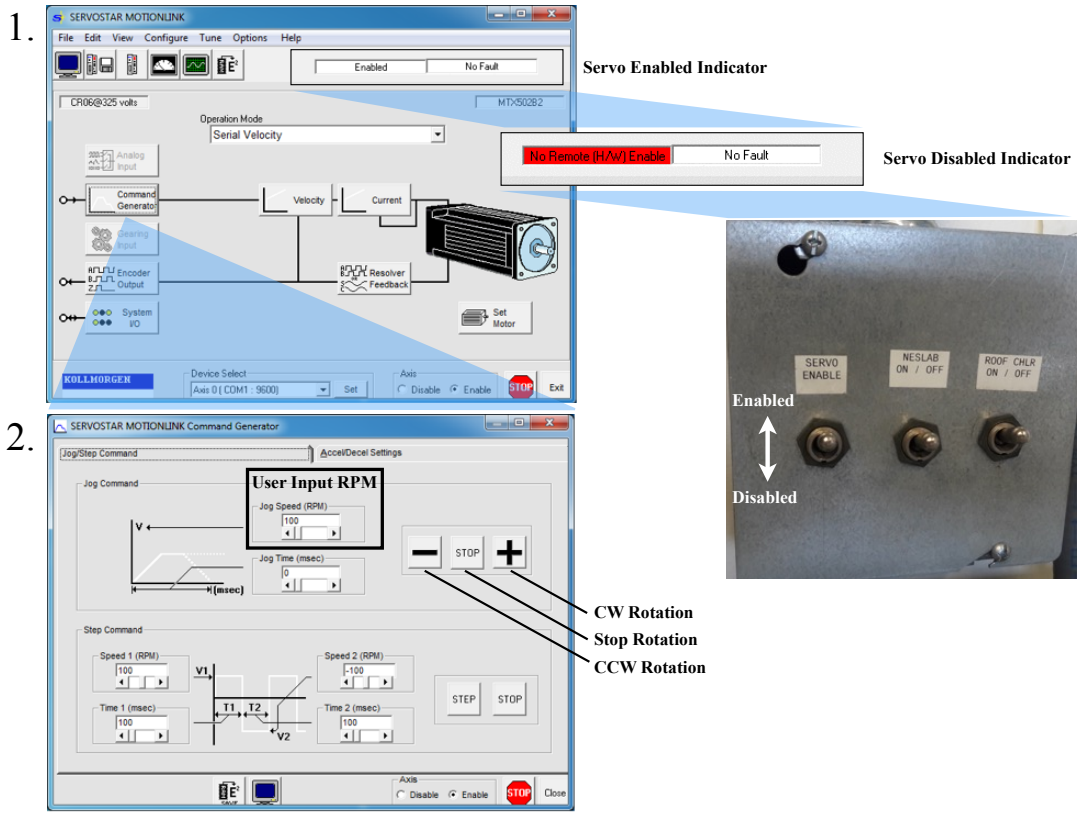

Figure 7.35: Panels from the Servostar Motionlink program used to adjust the rotation rate of the RoMag device. The wall switch is located above the lab chiller in Figure 7.31. Image contributed by Ashna Aggarwal.

the counter-clockwise (clockwise) rotation by pressing the "−" ("+"). Press STOP to stop rotation.

The true rotation rate of the RoMag device has been calibrated such that

$$\Omega_{RPM}^{real} = 1.0206 \frac{\Omega_{RPM}^{requested}}{40} + 0.0011, \tag{7.14}$$

where $\Omega_{RPM}^{requested}$ is the rotation, in RPM, of the RoMag device as input by the user.

7.9.3 Raising and Lowering the Magnet

Before performing the below steps for raising and lowering the magnet, it may be necessary to redistribute any build-up of grease to the threads in order to provide adequate lubrication

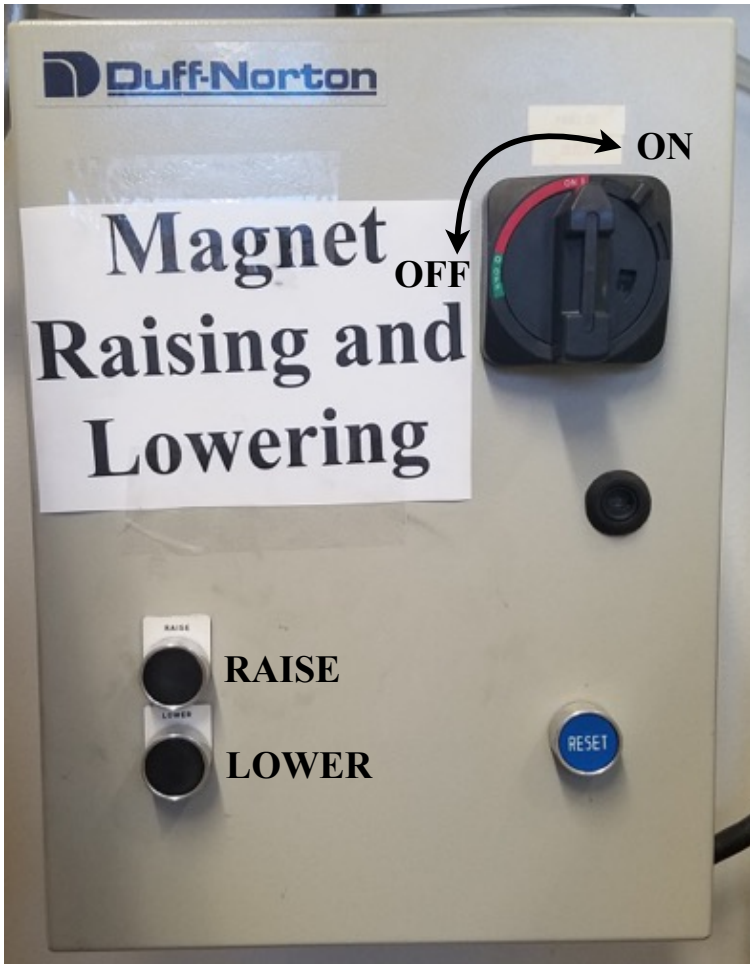

Figure 7.36: Front panel of the Duff-Norton control box used to raise and lower the magnet using the raising and lowering buttons.

during movement. Also make sure that the RoMag convection tank is level and that the threaded rods used to hold the convection tank together are centered so that the magnet is not scratched or gouged during the raising and lowering process.

1. Locate the lab's fuse box and move the circuit breaker labeled "Duff-Norton." Move to the "ON" position.

2. Move to the Duff-Norton box, and rotate the large knob to give power to the Duff-Norton system.

3. Press the button labeled "Raise" or "Lower". Make certain that all the acme threads are rotating. As the magnet is moving downwards, inspect the experimental com-

ponents on the convection tanks (wires, pipes, etc.) and ensure that they are not obstructing the magnet's path. Light contact of the magnet with insulation or plastic wrap is acceptable.

4. The magnet has an upper and lower limit and will stop automatically when these positions are reached.

5. When experimentation is complete, push the "Raise" button to lift the magnet to its original position. It will automatically stop at the top.

CHAPTER 8

Laboratory-numerical models of rapidly rotating convection in planetary cores

Modified from: J. S. Cheng, S. Stellmach, A. Ribeiro, A. Grannan, E. M. King, J. M. Aurnou. *Geophys. J. Int.* (2015) **201**, 1-17

In this work, I developed a thermal loss model used to determine the amount of heat lost through the sidewalls of rotating and non-rotating laboratory convection experiments. By better accounting for sidewall heat losses, we were able to better constrain the amount of heat transferred through the fluid layer and hence determine the Nusselt number more accurately determined. Our results showed that the heat transfer scaling in rotating convection continues to increase with decreasing Ekman numbers. This effectively invalidates the essential arguments of King et al. (2012) and lead to the papers by Stellmach et al. (2014) and Julien et al. (2016) which both invoked Ekman pumping to explain the high scaling exponents first identified here.

8.1 Introduction

In the investigation of planetary core physics, the current methodological paradigm depends primarily upon numerical dynamo models. These models strive to simulate the global scale processes occurring in planetary interiors by solving the governing equations of magnetohydrodynamic flow in a rotating spherical shell of electrically-conductive fluid [e.g., Kagayama and Sato (1995); Glatzmeier and Roberts (1996); Christensen and Aubert (2006)]. The strength of these models is that they are capable of reproducing some major features of the geomagnetic field, including the dipolar morphology, flux patches at high latitudes, and

polarity reversals [e.g., Christensen (2010); Olson et al. (2011)]

However, these models are limited because they require overly strong viscous diffusive effects. Over ten orders of magnitude larger than estimates for Earth's core, the viscous diffusion in current numerical dynamo models ultimately removes all but the largest scale motions in the system [e.g. Soderlund et al. (2012)]. Small-scale turbulence and turbulent fluxes between large- and small-scale processes cannot exist in these models [cf. Braginsky and Meytlis (1990)]. As such, the models are effectively laminar [e.g., Glatzmaier (2002)]. However, turbulent fluid systems, such as exist in planetary cores, are inherently multi-scale: a wide range of flow scales are expected to be active and interrelated [e.g., Nataf and Schaeffer (2015)]. For example, convective energy is likely injected at very small scales into the core fluid, whereas magnetic fields are likely generated by larger-scale flows. In the long term, in order to make accurate predictions of global scale observables, we must understand the path by which small-scale convective energy is transferred to the large-scale flows that effectively induce magnetic fields. To investigate the behavior of rapidly-rotating convection toward the limit of core-style turbulence, we have used laboratory simulations of rapidly rotating convection and high-resolution numerical models in a complementary fashion. Here we present the results of the combined approaches, which have allowed us to access the axialized flows that exist near the onset of convection, as well as the three-dimensional (3D) turbulent flows that develop with stronger forcing. Together our combined laboratory-numerical approach provides a broad view of the regimes that likely describe core-style rotating convective motions. We do not include the effects of magnetic fields on convection [cf. Aurnou and Olson (2001); Cioni et al. (2000); Stellmach and Hansen (2004); Gillet et al. (2007); Hori et al. (2010); King and Aurnou (2015); Ribeiro et al. (2015)]. In addition, we use simplified geometries. Right cylinders are used in the laboratory experiments and Cartesian domains are used in the numerical simulations, both of which remove the effects of spherical shell curvature. In these reduced geometries, we are able to reach more extreme parameter values than are accessible in current global-scale dynamo models.

Our study then differs from the geophysical problem of rotating magnetoconvection in a spherical shell. However, understanding the reduced problem serves as an essential prereq-

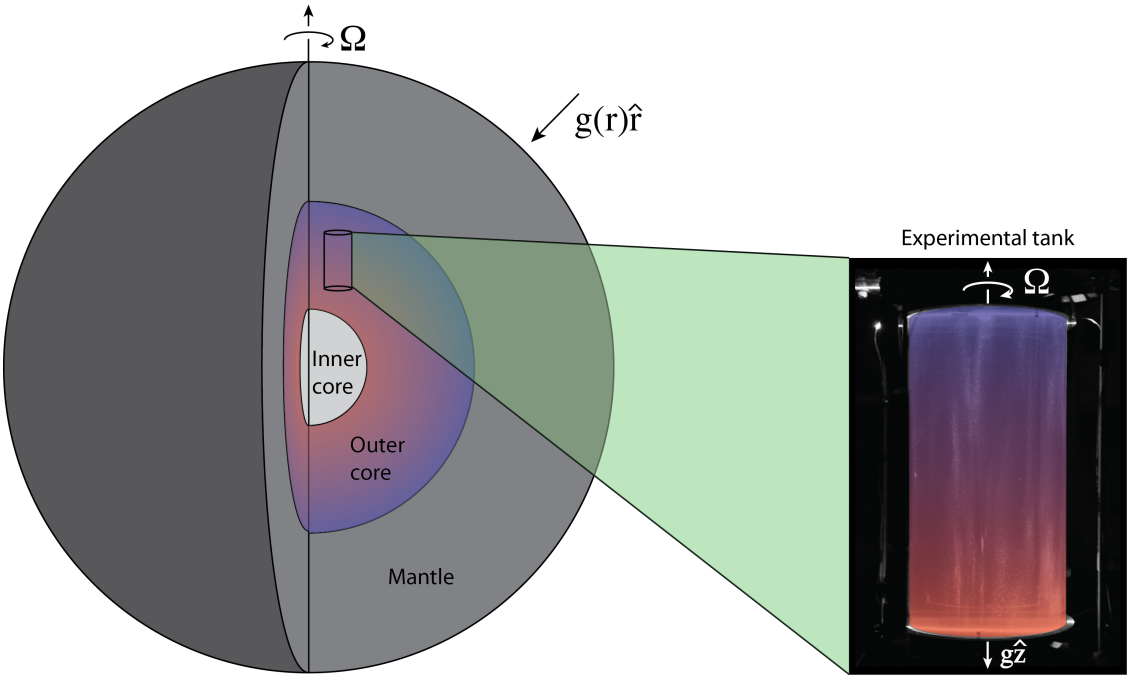

Figure 8.1: Image showing the conceptual relationship between a parcel of core fluid and our laboratory rotating convection experiments. Gravitational acceleration is represented by g and the angular rotation vector is represented by Ω. In addition, the adverse density gradient is qualitatively represented by the background color scheme. Violet represents higher density fluid while pink represents lower density fluid.

uisite to understanding planetary convection. In addition, our systematic approach provides the opportunity to contextualize core fluid dynamics, using the predictions derived in the well-established body of convection physics literature [e.g., Malkus (1954); Kraichnan (1962); Julien et al. (1996); Grossmann and Lohse (2000); Sprague et al. (2006); Ahlers et al. (2009); Grooms and Whitehead (2015)]

In the next section of this paper, we introduce the nondimensional parameters necessary to discuss the theoretically-predicted behaviors of (non-rotating) Rayleigh-Bénard convection and rotating convection. These simplified systems articulate the underlying physical processes that are the basis of all convectively-driven dynamo models. In section 8.3, we present our laboratory and numerical set-ups, with which we make detailed measurements

of the convective heat transfer across a fluid layer and qualitative measurements of the associated flow patterns. Our results are provided in section 8.4. In section 8.5, we discuss the regime transitions that exist in our heat transfer data, which provide important insight about rotating convection systems: we find that axially-invariant rotating convection columns exist only over a very limited range of parameter space. In section 8.6, we consider the extrapolation of our results to planetary core settings. Finally, in section 9.5, we discuss how our findings better tie next-generation dynamo modeling results to established theories of turbulent convection.

8.2 System Parameters and Scaling Behaviors

8.2.1 Rayleigh-Bénard Convection (RBC)

In order to investigate rotating convection systems, we first consider the analogous non-rotating system. This non-rotating style of convection, known as Rayleigh-Bénard convection (RBC), describes the thermally-induced overturning of fluid in a plane layer geometry. Non-rotating convection is relevant to planetary systems because it represents the limiting behavior when convection overcomes rotational effects. We find that convective heat transfer in RBC systems provides upper bounding values on those that will be observed in rotating convection systems.

The effective strength of the thermal buoyancy force in RBC systems is denoted by the Rayleigh number. This nondimensional number represents the ratio between thermally-induced buoyancy and the viscous and thermal diffusive effects:

$$Ra = \frac{\text{Buoyancy}}{\text{Diffusion}} = \frac{\gamma g \Delta T L^3}{\nu \kappa}, \tag{8.1}$$

where γ is the thermal expansivity, g is gravitational acceleration, ΔT is the temperature difference between the top and bottom horizontal boundaries of the fluid layer, L is the distance between these boundaries, ν is the viscous diffusivity, and κ is the thermal diffusivity. At a sufficiently high value of Ra, denoted as the critical Rayleigh number Ra_C, buoyancy

effects overcome diffusion and the fluid layer becomes unstable to convective fluid motions. For an infinite plane layer with rigid, non-slip boundaries, the critical Rayleigh number in RBC has a constant value of $Ra_C = 1708$ [e.g., Pellew and Southwell (1940)].

The other parameter describing RBC systems is the thermal Prandtl number, Pr. This number is the ratio of the thermal and viscous diffusion time scales in the system,

$$Pr = \frac{\nu}{\kappa}\,, \tag{8.2}$$

and, thus, describes the thermophysical properties of the working fluid. For instance, in water, the working fluid used in our laboratory experiments, Pr has a value of $\simeq 7$. Present-day dynamo studies typically use a Prandtl number of $\simeq 1$ [e.g. Olson et al. (2011); Soderlund et al. (2013)]. In contrast, it is estimated that the $Pr \sim 10^{-2}$ in the liquid metal that makes up Earth's outer core [e.g., Pozzo et al. (2012); de Koker et al. (2012)].

For any given set of Ra and Pr input parameters in an RBC system, the nondimensional heat transfer is expressed in terms of the Nusselt number, Nu. The Nusselt number is the ratio of the total heat flux through the system normalized by the conductive heat flux in the absence of convection:

$$Nu = \frac{\text{Total heat flux}}{\text{conductive heat flux}} = \frac{qL}{k\Delta T}\,. \tag{8.3}$$

where q is the total heat flux and k is the working fluid's thermal conductivity. Because the total (superadiabatic) heat flux is the sum of convective and conductive components, the Nusselt number will have a fixed value of unity in the absence of convective motions, and will reach higher values as the convective heat flux increases in strength. (Unlike in planets, the adiabatic heat flux is zero in our experiments.) In our laboratory-numerical RBC experiments, the Nusselt number ranges from values of unity to just over 10^3, demonstrating that we can study the full range of behaviors that exist between the onset of convection and fully-developed, convection-dominated heat transfer.

The Nusselt number provides a globally-integrated description of the vigor of convective motions. As such, trends in the Nusselt number reveal fundamental behaviors of the un-

derlying convection system [e.g. Spiegel (1971); Glazier et al. (1999)]. In the literature on convective turbulence, heat transfer in RBC systems follows several well known scaling laws of the form $Nu \sim Ra^{\alpha} Pr^{\chi}$ [e.g., Ahlers et al. (2009)]. However, since we use a fixed Prandtl number in our experiments, we will consider RBC scalings of the simpler form

$$Nu = c_1 Ra^{\alpha} , \tag{8.4}$$

where c_1 is the prefactor and α is the scaling exponent. Such scalings have been predicted theoretically and confirmed experimentally over wide ranges of parameter space [e.g., Rossby (1969); Castaing et al. (1989); Glazier et al. (1999); Funfschilling et al. (2005)].

There are two well-known $Nu \sim Ra^{\alpha}$ scaling regimes of RBC heat transfer that are accessible with our experiments. One classical prediction, first theorized by Malkus (1954), is the $\alpha = 1/3$ relation. Malkus' arguments apply to systems containing vigorous convective mixing, where the bulk fluid becomes isothermal and the time-averaged temperature gradients are localized to thin thermal boundary layers adjacent to the top and bottom of the fluid layer. Conductive heat transport dominates in these quasi-static boundary layers. The $\alpha = 1/3$ law arises under conditions in which the opposing boundary layers do not interact, and the fluid layer height therefore does not enter into the heat transfer scaling. This depth-independent heat transfer then leads to the following scaling law:

$$Nu \sim (Ra/Ra_C)^{1/3} \tag{8.5}$$

This scaling law has been verified in a number of experiments carried out at $Ra \gtrsim 10^{10}$ [e.g., Ahlers et al. (2009)]. It is often argued that the $\alpha = 1/3$ law is appropriate for geophysical systems in which the boundary layers act in relative isolation, such as when they are much thinner than the total thickness of the fluid layer [e.g., Castaing et al. (1989)].

In RBC laboratory and numerical experiments at moderate buoyancy forcings ($Ra \lesssim 10^{10}$), characteristic of values used in current-day dynamo models, the $\alpha = 1/3$ law is not typically observed. Instead, experiments in this moderate Ra range find that the RBC

heat transfer follows a law closer to $Nu \sim Ra^{2/7}$ [e.g., Chillá et al. (1993); Glazier et al. (1999); Ahlers and Xu (2001)]. In most $Ra \gtrsim 10^5$ laboratory and numerical experiments, a container scale overturning circulation occurs in the bulk fluid, providing a shear flow across the boundaries. The presence of this circulation implies communication between the boundary layers and that the depth of the fluid layer is a critical characteristic of the system. By including the effects of a shear flow across the thermal boundary layers, Shraiman and Siggia (1990) argue that an $\alpha = 2/7$ heat transfer scaling develops.

At extremely high Ra, which presently exceed laboratory and numerical experimental capabilities, an $\alpha = 1/2$ scaling law has been hypothesized [e.g., Kraichnan (1962); Spiegel (1971)]. In this regime, the thermal boundary layers become fully turbulent. In the absence of quasi-static boundary layers, the heat flux will be controlled solely by turbulent flows occurring within the fluid bulk and the microscopic, molecular properties of the fluid may cease to play a role. This RBC heat transfer regime is represented by the scaling law

$$Nu \sim (RaPr)^{1/2} \,. \tag{8.6}$$

Although this scaling has yet to be observed experimentally (e.g., Roche (2010)), it may ultimately apply to buoyancy-dominated planetary and astrophysical convection systems. In our present laboratory and numerical experiments, we are able to access the $\alpha \simeq 2/7$ and $1/3$ regimes.

8.2.2 Rotating Convection

With the inclusion of rotation in a given system, new modes of convection can develop, associated with alternate regimes of convective heat transfer. A new nondimensional parameter, the Ekman number E, is required to characterize the effect of the system's rotation. This parameter is defined by the ratio between the system-scale viscous force and the Coriolis force:

$$E = \frac{\text{Viscosity}}{\text{Coriolis}} = \frac{\nu}{2\Omega L^2} \tag{8.7}$$

where Ω is the system's angular rotation rate. In many geophysical settings, the Ekman number is extremely small, implying that rotational effects massively overwhelm global-scale viscous forces. For instance, the Ekman number is estimated to be of order 10^{-15} in Earth's core [e.g., Schubert and Soderlund (2011)]. At such low values, the system-scale flows are expected to be essentially unaffected by fluid viscosity [e.g. Roberts and King (2013)].

The effect of rotation is strongly constraining and has the effect of suppressing the onset of convection [e.g., Nakagawa and Frenzen (1955)]. The critical Rayleigh number in a rotating convection system is no longer a constant for a given geometry. Instead, Ra_C grows with the system's rotation rate:

$$Ra_C = c_2 E^{-4/3}\,, \tag{8.8}$$

where c_2 is 8.696 for the onset of steady rotating convection as $E \to 0$ (Chandrasekhar (1961)). At the onset of rotating convection, fluid motions occur in the form of long, thin columns that are aligned with the rotation axis [e.g., Grooms et al. (2010); King and Aurnou (2012)]. The narrow horizontal width of these columns, ℓ, results in viscous forces that locally relax the rotational constraint on fluid flow. The width of the columns at the onset of convection scales as:

$$\ell = c_3 E^{1/3} L\,, \tag{8.9}$$

where $c_3 = 4.8$ as $E \to 0$ [e.g., Julien and Knobloch (1998)]. This $E^{1/3}$ scaling result appears to hold well past onset and thus likely characterizes flow scales in a broad array of rapidly rotating convection settings [e.g., Zhang and Schubert (2000); Stellmach and Hansen (2004); King and Buffett (2013)].

In spheres and spherical shells (with inner radius less than 3/4 of the outer shell radius), most of the fluid volume exists outside of the tangent cylinder. These lower latitude convection columns are generated by thermal Rossby waves and are not fully equivalent to our Cartesian cases, which better simulate convection at higher latitudes within the tangent cylinder [e.g., Busse and Cuong (1977); Sreenivasan and Jones (2006a); Takehiro (2008); Calkins et al. (2013)]. Because the vorticity changes sign across the mid-layer only in high latitude columns, they have differing topologies (Chandrasekhar (1961)), differing heat trans-

fer behaviors (e.g. Aurnou (2007)) and their vortex-vortex interactions are likely different. However, they have some important similarities. In particular, they represent strongly axialized vortices that have $\ell = O(E^{1/3})$ length scales [e.g., Zhang and Schubert (2000); King and Buffett (2013)].

The vast majority of planetary dynamo models are carried out in the vicinity of $E \sim 10^{-4}$ (e.g., King and Buffett (2013)) where these axial columns, forming near the onset of convection, are the dominant flow structures. The columns in these models typically have widths that are large, in fact, close to the scale of the system, $\ell/L \sim E^{1/3} \simeq 0.1$, and have been argued to be an essential feature of Earth-like models (e.g. Christensen and Aubert (2006); Christensen (2010)). The highly coherent axial flow structures are responsible for generating dipolar magnetic fields that are well-aligned with the rotation axis. In fact, typical $E \sim 10^{-4}$ models cannot generate Earth-like magnetic fields without the presence of axially coherent columns (e.g. Sreenivasan and Jones (2006b); Christensen (2010); Miyagoshi et al. (2010); Soderlund et al. (2012, 2013)).

Even though dynamo models depend on columns as an essential building block, the width of those that exist in present-day models fundamentally differ from the columns that are presumed to exist in the core. For instance, in Earth's core, columns are not predicted to be the system-scale in width, but instead are likely to be extremely narrow with $\ell/L \sim E^{1/3} \simeq 10^{-5}$. This corresponds to core columns of order 1000 km high by 10 m wide. It is unlikely that such structures can induce magnetic fields or remain stable under turbulent core conditions (e.g. Glatzmaier (2002)). Thus, lower E realizations of rotating convection are necessary to determine the stability range of columnar-style rotating convective flows as core-like parameters are approached. Furthermore, accurate models of global heat transfer (eventually, in spherical shell geometries) are also required in the regime in which coherent rotating convection columns exist. By comparing the heat flux estimates from a given planetary core, it should then be possible to infer whether coherent columns will stably exist in a given geophysical system (e.g., King and Aurnou (2012); Soderlund et al. (2014)).

King et al. (2012) argue that boundary layer physics controls rotating convective heat transfer in water. By assuming that the Malkus (1954) marginal boundary layer arguments

hold in a rapidly rotating system, they develop theoretical arguments predicting that rotating convective heat transfer scales steeply:

$$Nu = (Ra/Ra_C)^3 \,. \tag{8.10}$$

This steep, cubic scaling (8.10) is argued to hold from near the onset of convection until the Ra value at which the thermal boundary layer becomes nested within the mechanical Ekman layer:

$$Ra_T \sim E^{-3/2} \,. \tag{8.11}$$

Furthermore, it is hypothesized that the columns will lose their axial coherency in the vicinity of $Ra/Ra_T \sim 1$. The $Pr \simeq 7$, $E \simeq 10^{-7}$ numerical experiments carried out in this study reach lower values of Ra/Ra_T than any previous studies and, thus, are the first to clearly test the King et al. (2012) predictions.

8.3 Methods

Our investigation involves both laboratory experiments and numerical simulations of convection in non-rotating and rotating systems.

8.3.1 Laboratory Experiments

We perform Rayleigh-Bénard convection (RBC) and rotating convection experiments in an axially-aligned cylindrical container with water as the working fluid. The top and bottom of the container are made of aluminum, which provides nearly isothermal boundary conditions in all our laboratory experiments. We maintain a Biot number $Bi \leq 0.1$, implying that thermal gradients in the boundaries are negligible compared to those in the fluid. The cylindrical sidewall is made of Reynolds Polymer acrylic, which has a low thermal conductivity of $k = 0.19$ $\mathrm{Wm^{-1}K^{-1}}$ and is optically clear. The sidewall has a thickness of 0.635 cm and an inner diameter of 19 cm. We are able to vary the height of the container, here using 40, 80 or 160 cm tall sidewalls (Figure 8.2). A brushless servomotor rotates the device at rates

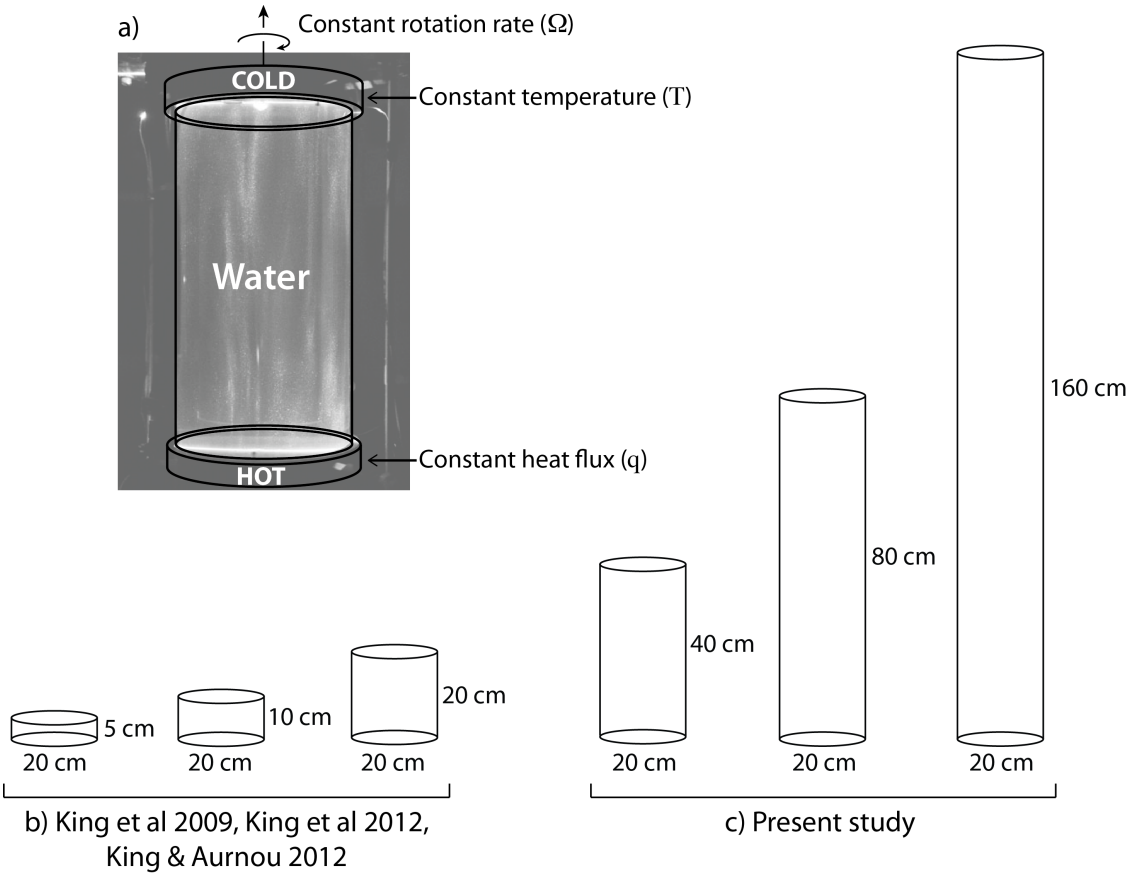

Figure 8.2: Experimental set-up. a) A schematized image of the 40 cm high by 20 cm wide tank. An electrical heater provides a constant heat flux q to the base of the experiment. A water-cooled heat exchanger maintains a fixed temperature at the top of the system. A servomotor rotates the tank about a vertical axis at up to 60 revolutions per minute (rpm). All laboratory experiments have a fixed diameter of 20 cm. However, the heights of the tanks can be varied. b) Preceding laboratory studies have employed 5, 10, and 20 cm high tanks (King et al. (2009, 2012); King and Aurnou (2012, 2013)). c) In the present study, laboratory experiments are carried out in 40, 80, and 160 cm high tanks in order to reach more extreme ranges of parameter space. For example, in a 160 cm high tank of water it is possible to attain $E \gtrsim 3 \times 10^{-8}$ and $Ra \lesssim 10^{13}$.

between 0 and 60 revolutions per minute (rpm).

The fluid layer is heated from below by a non-inductively wound, electrical resistance element that applies between 10 and 600 W of power. Following Rossby (1969), the experiment is cooled from above via a double-spiral wound heat exchanger maintained at a constant temperature by a precision thermal bath. Temperature measurements are made by 12 temperature sensors located within 2 mm of the top and bottom boundaries of the fluid layer, providing accurate measurement of the vertical temperature difference across the fluid layer, ΔT. The minimum ΔT that can be measured is approximately 0.25 K, which sets the minimum Ra that we can access with any given tank. The combination of applied heating power and resultant temperature drop measured across the fluid layer allows us to calculate the Nusselt and Rayleigh numbers for each experimental case.

These geometrically narrow tanks require careful treatment of potential thermal losses through the sidewalls. To minimize these losses, the temperature of the room is set as closely as possible to the mean temperature of the working fluid. Furthermore, the device is wrapped in a 10 cm thick layer of Insulfrax insulation. The room and mean fluid temperatures are continually measured, allowing us to estimate horizontal conductive, convective and radiative heat losses from the device. For all cases above 30 W of input heating power, sidewall heat losses account for less than 5% of the total.

In every Nu-Ra case, the experiment is allowed to equilibrate until the mean temperature on each thermal sensor does not change by more than $\sim 1\%$ over the course of two hours. This process usually takes approximately 8-12 hours. We then collect data for 2-3 hours per case at a data rate of 10 samples per second.

A suite of experiments that omit the sidewall insulation has also been made in order to make qualitative optical characterizations of the flow fields in our experiments. Without sidewall insulation, it is possible to pass a vertical laser light sheet through the optically clear sidewalls. By seeding the working fluid with reflective Kalliroscope flakes, we are able to visualize the pattern of differential shear within the fluid. These patterns are recorded with the use of a digital camera situated in the laboratory frame.

8.3.2 Thermal losses model

Not all of the applied heat flux in our experiments is transferred vertically through the fluid layer. Even with a 10 cm thick layer of insulation, some of the heating power escapes through the sidewalls of the tank. Our data presented in Figures 8.4 and 8.5 are corrected for thermal losses using a theoretical model outlined here.

This model assumes conductive, convective and radiative forms of heat loss following Fourier's law, $q = -k\nabla T$ where k is the thermal conductivity. There are two layers of solid material, the tank sidewall and the insulation. Thus, the conductive components are placed in series with each other while the convective and radiative components are in parallel with the outer layer. This gives an overall form of:

$$Q_{loss} = \frac{T_{fluid} - T_{room}}{x_{cond,acrylic} + x_{cond,insul} + x_{conv+rad}}\,, \tag{8.12}$$

where $x_{cond,acrylic}$, $x_{cond,insul}$, x_{conv} represent the non-ΔT component for conduction through acrylic, conduction through insulation, and convection and radiation together.

Each layer has an individual k value and the total conductive heat loss over a single layer is given by:

$$\frac{T_{fluid} - T_{room}}{\frac{ln(r_2/r_1)}{2\pi lk}}\,. \tag{8.13}$$

where r_2 is the radius of the outer layer, r_1 is the radius of the inner layer, and l is the thickness of the layer.

The convective heat loss from the outside of the insulation is given by:

$$Nu_{air}k_{air}A/l\,(T_{mid} - T_{room})\,, \tag{8.14}$$

where T_{mid} is the temperature at the interface of the acrylic and insulation and A is the total surface area in contact with the air. The Nusselt number estimate for the air, Nu_{air}, is different for nonrotating and rotating cases. We use a nonrotating estimate from Churchill and Chu (1975) and a rotating estimate from Kendoush (1996).

The radiative component is given by:

$$Q_{loss,rad} = \sigma \epsilon A \left(T_{mid}^4 - T_{room}^4 \right) \tag{8.15}$$

We can combine this with the convective and conductive components to write:

$$Q_{loss} = \frac{T_{fluid} - T_{room}}{\frac{ln(r_2/r_1)}{2\pi l k_{insul}} + \frac{ln(r_2/r_1)}{2\pi l k_{acrylic}} + \frac{1}{Nu_{air} k_{air} A/l + \sigma \epsilon A (T_{mid}+T_{room})(T_{mid}^2+T_{room}^2)}} \,. \tag{8.16}$$

This heat loss estimate manifests as a correction to the Nusselt number in the data:

$$Nu_{corrected} = \frac{(q_{raw} - q_{loss})\, L}{k \Delta T} \,, \tag{8.17}$$

where q_{raw} is the uncorrected heat flux per unit area of heating and q_{loss} is Q_{loss} per unit area of heating.

Applying our heat losses model to our data shows that the losses are more significant at lower heat fluxes and less significant at higher heat fluxes. For example, in the nonrotating 160 cm tank case with 10 W of applied heat flux, about 14% of the power is lost through the sidewalls. In contrast, in the same tank with 300 W of applied heat flux, only 4% of applied power is lost through the sidewalls. Taking the data as a whole, the effect of sidewall heat loss on our *Nu*-*Ra* scaling results is minimal: for Rayleigh-Bénard convection, the difference in best-fit slopes between the raw data and data corrected for losses is less than 2%.

8.3.3 Numerical Simulations

While laboratory experiments enable us to characterize rapidly rotating turbulent convection at high Rayleigh and low Ekman numbers ($5 \lesssim Ra/Ra_C \lesssim 60$ at $E = 10^{-7}$), our laboratory system cannot reach low enough Ra values to investigate the physics between Ra_C and Ra_T for $E \lesssim 3 \times 10^{-4}$. Numerical simulations, in contrast, allow us to study the behavior of rotating convection at the low Ra values inaccessible in the laboratory. The combination of laboratory and numerical methods provides a complementary characterization of rotating

convection physics, accessing the full range from weakly supercritical to fully turbulent flows.

The numerical models solve the Boussinesq momentum, energy, and mass conservation equations in a rotating, Cartesian fluid layer. The top and bottom fluid layer boundaries are isothermal, rigid and non-slip. The solutions are periodic in the horizontal directions. Chebyshev polynomials are employed in the vertical direction and Fourier expansions in the horizontal directions. The vertical resolution is set in order to maintain at least ten grid points within the Ekman boundary layer. The code has been validated in prior studies by Stellmach and Hansen (2008) and King et al. (2012).

8.4 Results

Here, we briefly summarize our essential findings. First, we find in RBC experiments that a Nu-Ra scaling of $\alpha = 0.284$ describes the heat transfer for $Ra \lesssim 10^{10}$ and a scaling of $\alpha = 0.322$ develops at roughly $Ra \gtrsim 10^{10}$, corresponding closely to the predicted 1/3 law. In rotating convection experiments, we find a steep heat transfer scaling law in the region where coherent convection columns exist. By comparing laboratory visualizations and heat transfer measurements, we show that this steep heat transfer scaling manifests when convection occurs in the form of axially-invariant columns; when the columns become unstable to three-dimensional motions, the heat transfer becomes less efficient, trending back toward the nonrotating scaling. These results indicate that rotating convection columns, which form the conceptual underpinning for current Earth-like planetary dynamo models, exist only over a limited range of parameter space.

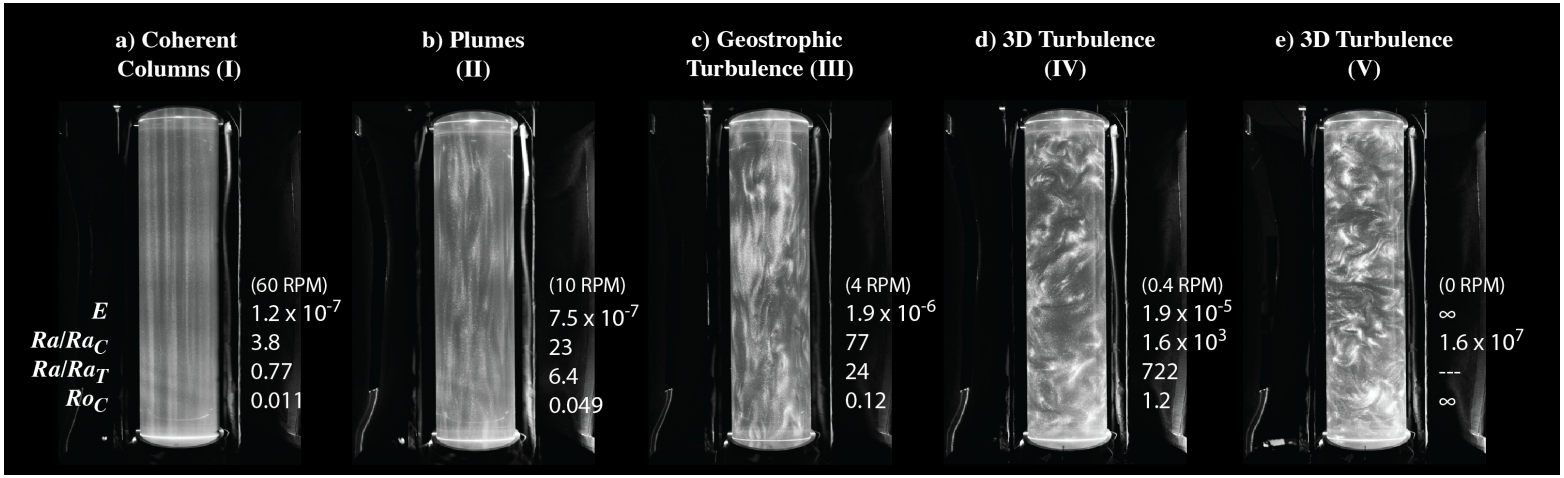

Figure 8.3: Laboratory visualizations of rotating convection in water at fixed heat flux. Panels a) through e) correspond to Ekman number values of $E = 1.2 \times 10^{-7}$, 7.5×10^{-7}, 1.9×10^{-6}, 1.9×10^{-5} and ∞, respectively. All cases are carried out in an 80 cm high by 20 cm wide tank and at fixed flux Rayleigh number $Ra_{F_0} = 4.0 \times 10^{12}$. Dimensionally, the rotation rates translate to 60, 10, 4, 0.4, and 0 revolutions per minute (rpm) and a constant heating power of 10 W. At $E = 1.2 \times 10^{-7}$, the flow is comprised of coherent, axialized convection columns. As E increases, the flow transitions to wavy plumes, then geostrophic turbulence, then homogenous turbulence (cf. Julien et al. (2012b) Figure 1). The *Nu-Ra-E* data from these visualization cases are demarcated by black-bordered yellow stars in heat transfer plots (Figures 8.4, 8.5 and 8.7), allowing us to qualitatively relate changes in flow morphology to changes in convective heat transfer regime. Movies corresponding to these cases can be found online at *www.youtube.com/watch?v=p01r6l71ELA*.

8.4.1 Laboratory Flow Visualizations

Figure 8.3 shows Kalliroscope images of shear patterns in an 80 cm high tank of convecting water for a fixed heating power of 10 W, corresponding to a fixed flux-based Rayleigh number

$$Ra_F = RaNu = \frac{\gamma g L^4 q}{\rho C_p \kappa^2 \nu} = 4.0 \times 10^{12}\,. \tag{8.18}$$

In each experiment we test a different rate of rotation, ranging from 60 rpm down to 0 rpm. As the rotation rate is decreased, we see the organizing effect of Coriolis force weaken and give way to small-scale turbulence in the bulk fluid. The image in Figure 8.3a, displaying a snapshot of the cylinder rotating at 60 rpm, shows the columnar convective regime. The strongly coherent columns extend between the bottom to the top boundary with almost no variation along the axial direction. Figure 8.3b shows the flow field in a case rotating at 10 rpm ($E = 7.5 \times 10^{-7}$). With this decrease in rotation rate, the columns become wavy and begin to lose their axial invariance. Figure 8.3c shows the development of 3D, anisotropic flows. Figure 8.3d and e show 3D turbulence that appears to be isotropic in nature and is likely unaffected by rotation.

In addition, in Figure 8.3, we estimate the strength of buoyancy effects for each of the five cases, but normalized in different ways. The first row gives the Rayleigh number normalized by the value at which bulk convection onsets, Ra/Ra_C (following (8.8)). The second row gives the Rayleigh number normalized by the boundary layer transition value, Ra_T, predicted in King et al. (2012). The third row gives the system-scale buoyancy force normalized by the Coriolis force, called the convective Rossby number Ro_c. The convective Rossby number can be written as:

$$Ro_c = \frac{\text{Buoyancy}}{\text{Coriolis}} = \left(\frac{RaE^2}{Pr}\right)^{1/2} \tag{8.19}$$

where the buoyancy and inertial terms have been set equal, and the inertial term can then be written in terms of the convective free-fall velocity, $U_f \sim \sqrt{\gamma g \Delta T L}$. The convective Rossby number is related to the modified Rayleigh number Ra^* defined in Christensen (2002) by $Ro_C = Ra^{*2}$.

We argue that the case visualized in Figure 8.3c corresponds to the geostrophic turbulence regime, where flows exhibit small-scale 3D structure at convective Rossby number $Ro_c \ll 1$ (cf. Sprague et al. (2006); Julien et al. (2012b)). The flows in Figure 8.3a, b and c, then, are in good agreement with the convective Taylor column, plume, and geostrophic turbulence regimes, respectively, found in asymptotically-reduced rotating convection models of Julien et al. (2012b) and in direct numerical simulations conducted by Stellmach et al. (2014).

8.4.2 Rayleigh-Bénard Convection

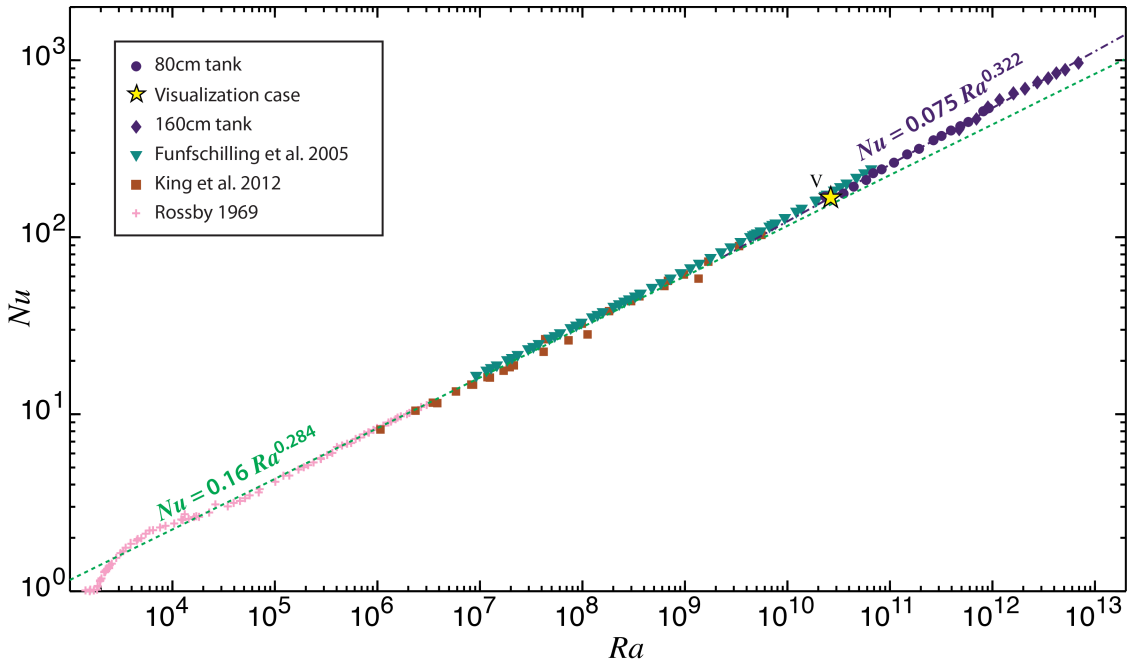

Figure 8.4: Laboratory Rayleigh-Bénard convection (RBC) heat transfer data alongside earlier data from Rossby (1969); Funfschilling et al. (2005), and King et al. (2012). The black-bordered yellow star denotes case V shown in Figure 8.3, made at $Ra_F = NuRa = 4 \times 10^{12}$. For our present experiments ($4 \lesssim Pr \lesssim 7$) in 80 and 160 cm tall tanks, the best-fit heat transfer trend is $Nu = (0.075 \pm 0.005)Ra^{0.322\pm0.003}$, in approximate agreement with the theoretically predicted $Nu \sim Ra^{1/3}$ law of Malkus (1954). At lower Rayleigh number experiments ($4 \lesssim Pr \lesssim 10$) the best-fit trend is $Nu = (0.162 \pm 0.006)Ra^{0.284\pm0.002}$, in agreement with the $Nu \sim Ra^{2/7}$ law theorized in Shraiman and Siggia (1990) and observed in other laboratory experiments (e.g. Wu and Libchaber (1992); Chillá et al. (1993); Liu and Ecke (1997); Glazier et al. (1999)).

Figure 8.4 shows Rayleigh-Bénard convective heat transfer data. The effective buoyancy force, Ra, is plotted on the x-axis; the resulting convective heat transfer, Nu, is plotted on

the y-axis. Data from our 80 cm and 160 cm tall tank experiments are shown as purple-filled circles and diamonds, respectively, and are shown in comparison with data sets from previous RBC studies of Rossby (1969), Funfschilling et al. (2005), and King et al. (2012). The dashed green line

$$Nu = (0.162 \pm 0.006) Ra^{0.284 \ \pm \ 0.002} \tag{8.20}$$

is the best-fit to the Rossby (1969) and King et al. (2012) data in the range $10^5 < Ra < 10^{10}$. This scaling exponent of $\alpha = 0.284$ is in good agreement with a 2/7 law.

Beyond $Ra = 10^{10}$, the data from the 80 cm and 160 cm tanks and Funfschilling et al. (2005) rise more sharply than the $\alpha \simeq 2/7$ green-dashed line. Instead, our 80 cm and 160 cm tank data then give a best-fit scaling law of

$$Nu = (0.075 \pm 0.005) Ra^{0.322 \ \pm \ 0.003}, \tag{8.21}$$

which is statistically well outside the range of the 2/7 law, and in better agreement with Malkus (1954) $\alpha = 1/3$ law. This scaling is robust over several decades, from $Ra \sim 10^{10}$ to 10^{13}. Thus, we argue that the $\alpha = 1/3$ law is affirmed in our laboratory RBC experiments.

8.4.3 Rotating Convection

Figure 8.5 shows rotating convection heat transfer data from our current laboratory and numerical experiments as well as the laboratory data from Rossby (1969) and the laboratory-numerical data from King et al. (2012). The color coding denotes the Ekman number used in each experiment. Filled-in symbols indicate laboratory experiments, and open symbols indicate numerical simulations. The data show that, at each given rotation rate, convection onsets at different Rayleigh numbers, in good agreement with the prediction for the onset of convection in a rotating fluid layer (8.8). Once convection onsets, Nu increases more steeply with Ra than in non-rotating convection experiments (we refer to this steeper slope as β). However, at high enough Ra, the rotating heat transfer data conforms to the non-rotating 2/7 scaling trend.

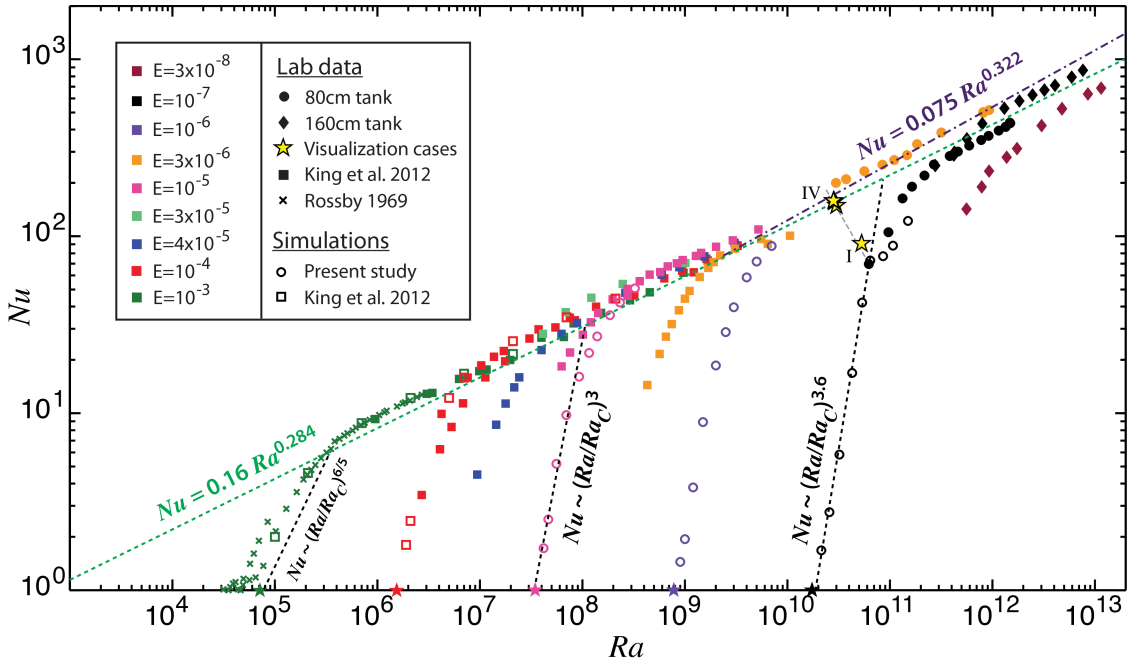

Figure 8.5: Laboratory ($Pr \simeq 7$) and numerical ($Pr = 7$) rotating convection heat transfer data from the present study, Rossby (1969) and King et al. (2012). The black-bordered yellow stars denote cases I-IV shown in Figure 8.3, made at fixed $Ra_F = NuRa = 4 \times 10^{12}$. This Ra_F value is denoted by the grey dashed line behind the stars. Critical Rayleigh number values from Table 8.5 are plotted as colored stars along the x-axis. The best-fit heat transfer trend of $Nu \simeq (Ra/Ra_C)^{3.6}$ is plotted for $E \sim 10^{-7}$. For comparison, $Nu = (Ra/Ra_C)^3$ (King et al. (2012)) is plotted for $E \sim 10^{-5}$ and $Nu = (Ra/Ra_C)^{6/5}$ (King et al. (2009, 2010)) for $E \sim 10^{-3}$. Note that with each study at lower E, the scaling exponent becomes larger. This implies that the behavior of rotating convection is not yet asymptotic in the presently accessible range of Nu-Ra-E space.

Thus, RBC scalings provide the effective upper bounds for heat transfer in rotating convection systems. The RBC heat transfer data acts as a ceiling, which the rotating heat transfer data either meets or falls beneath. There is a slight overshoot of rotating heat transfer beyond the RBC scalings for $Ra \gtrsim Ra_T$ (cf. Niiler and Bisshop (1965); Julien et al. (1996); Kunnen et al. (2008)). However, this effect is strong only at relatively high E. In fact, our data shows that the overshoot becomes small for $E \lesssim 10^{-5}$. The slope of the steep scaling regime changes as a function of E. At the highest E values ($E \simeq 10^{-3}$), the data conform to a $\beta \simeq 6/5$ law (Christensen (2002); Aurnou (2007); Schmitz and Tilgner (2009); King et al. (2009, 2010). At lower E values in the vicinity of 10^{-5}, the data fit a steeper, roughly cubic scaling law in agreement with King et al. (2012). However, for even more

Table 8.1: Critical Rayleigh number estimates for no-slip boundaries, following Chandrasekhar (1961), § 27 (b).

E	Ra_C
10^{-3}	7.159×10^4
10^{-4}	1.544×10^6
10^{-5}	3.482×10^7
10^{-6}	7.825×10^8
10^{-7}	1.741×10^{10}

rapidly rotating cases, with data lying in the range $10^{10} \lesssim Ra \lesssim 10^{11}$, the best-fit trend to the predominantly numerical $E = 10^{-7}$ data is:

$$Nu = (0.71 \pm 0.09)(Ra/Ra_C)^{3.56 \ \pm \ 0.08}. \tag{8.22}$$

Here, Ra_C is estimated following Chandrasekhar (1961) (see Table 8.1). This $\beta \simeq 3.6$ trend is significantly steeper than any previous rotating convection experiments, exceeding even the cubic heat transfer scaling of King et al. (2012). Although we have carried out a limited number of numerical simulations in this low E, steep scaling regime, the best-fit trend is statistically distinct from a cubic law. Julien et al. (2012a) argue that the $\beta = 3$ law is among a family of plausible solutions for rapidly-rotating convection, found to contain marginally unstable thermal boundary layers. However, our $\beta = 3.6$ result implies that the marginal rotating boundary layer mechanism put forth in King et al. (2012) does not control the convective heat transfer at very low E. Clearly, though, the robustness of this $\beta \simeq 3.6$ trend must be confirmed with more $Ra \ll Ra_T$ data (see data Tables 8.4 and 8.5 in the Appendix). Figure 8.6 shows the best-fit values for β as a function of the inverse Ekman number. Data points below $Nu = 1.3$ are not considered in these fits, as they correspond to a shallower Nu-Ra near onset (e.g. Julien et al. (2012a)). For the steep scaling regime, we find that β monotonically increases with decreasing E, with a roughly linear trend between $log(E)$ and β. This suggests that in the presence of no-slip boundaries the heat transfer scaling will continue to steepen as E is further decreased towards geophysically realistic values (cf. Grooms and Whitehead (2015)). Our heat transfer measurements show that no clear asymptotic behavior has been found in the rapidly rotating, steep scaling regime.

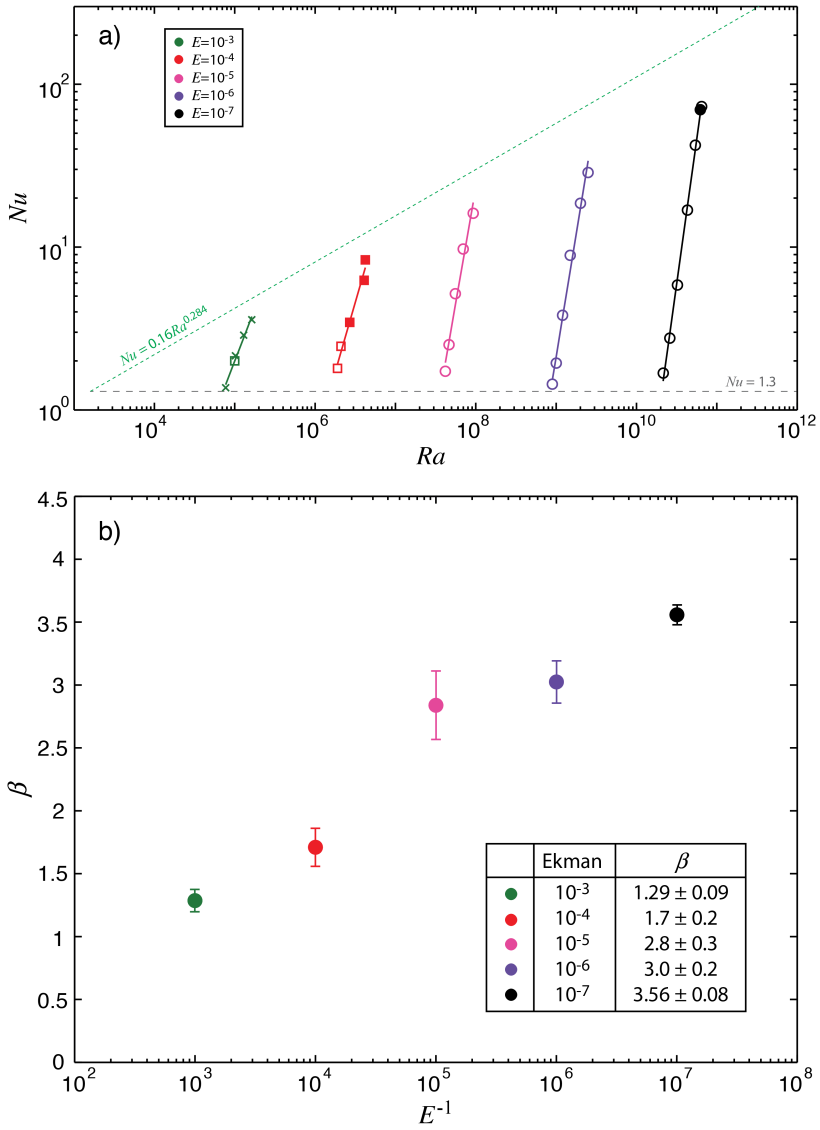

Figure 8.6: Heat transfer scaling exponents as a function of Ekman number. a) Solid lines show the best-fit $Nu \sim Ra^{\beta}$ trends to combined laboratory and numerical datasets at $E = 10^{-3}$, 10^{-4}, 10^{-5}, 10^{-6} and 10^{-7} in the steep heat transfer scaling regime. Data points used in the fits are selected to lie above $Nu = 1.3$, represented by the grey dashed line, and below the RBC trend of $Nu = 0.16Ra^{0.284}$, represented by the green dashed line. Symbols are as defined in Figure 8.5. b) Plot of β versus inverse E from the fits shown in panel a). No clear asymptotic scaling behavior has been found in our experiments: the values of β continually increases as a function of E^{-1} (cf. Julien et al. (2012a); Grooms and Whitehead (2015)).

In rotating convection experiments, we find a shallow RBC-style heat transfer scaling (independent of E) with $\alpha \simeq 2/7$ at our highest Ra values (cf. Liu and Ecke (1997)). In contrast, we find an $\alpha \simeq 1/3$ scaling in the RBC experiments for $Ra \gtrsim 10^{10}$. We postulate that this high Ra rotating 2/7 scaling is a byproduct of finite centrifugation effects in our present laboratory set-up. In our 80 cm tank experiments, the Froude number, which is the ratio of centrifugal force and laboratory gravity, $Fr = \Omega^2 r/g$, is approximately 0.4 in the $E \simeq 10^{-7}$ experiments. The strong centrifugal buoyancy in these cases likely drives a mean meridional circulation across the tank boundaries (e.g. Marques et al. (2007)) which we argue modifies the heat transfer to a 2/7 scaling, in accordance with the arguments of Shraiman and Siggia (1990). To test this hypothesis, we doubled the height of the tank (160 cm) while fixing the Ekman number ($E \simeq 10^{-7}$), which decreases the strength of centrifugation by a factor of 16. This yields a Froude number of 0.025. In Figure 8.5, we show that the highest Ra data in the 160 cm tank have higher Nu values that appear to be trending toward a 1/3 law. The effects of centrifugation will be studied in detail in a following suite of experiments.

In our rotating convection experiments, the RBC scaling—in particular, the 2/7 law—is observed to form the upper bound for heat transfer. Thus, the RBC and rotating convection (RC) scaling behaviors are deeply connected; knowledge of the RBC scalings is pertinent to our understanding of both systems. We hypothesize then that rotating convection and dynamo studies, carried out at sufficiently extreme parameter values, will also be able to access theoretically-predicted regimes of behavior (e.g. Soderlund et al. (2012). In particular, asymptotically-reduced rotating convection models by Julien et al. (2012b) predict distinct heat transfer scalings corresponding to each of the regimes visualized in Figure 8.3b-d. In our $E \geq 3 \times 10^{-8}$ data, we can unambiguously detect a steep and a shallow Nu-Ra scaling, but even lower values of E are required to differentiate the independent scalings for intermediate regimes (cf. Ecke and Niemela (2014)).

8.5 Comparing Regime Transition Hypotheses

Our rotating convective heat transfer data shows a clear transition from a steep scaling regime near the onset of convection to a shallower heat transfer scaling at strongly supercritical Rayleigh numbers. The data appears to deviate away from the steep scaling law near to where rotating convection columns lose their strong axial coherence. This is relevant to our understanding of present-day ($E \sim 10^{-4}$) planetary dynamo models because Earth-like dipolar dynamo action has been shown to fail in the vicinity of the heat transfer transition in these models (King et al. (2012)), where rotating convection columns also lose their axial coherency (Soderlund et al. (2012)). Thus, we hypothesize that the heat transfer transition in our extreme rotating convection data will provide a proxy for behavioral transitions in more extreme dynamo models.

The transition Rayleigh number, Ra_T, is defined empirically here to be the intersection between the steep heat transfer scaling $Nu = (Ra/Ra_C)^{\beta}$, and the shallow, RBC-style scaling $Nu = c_1 Ra^{\alpha}$. Setting these heat transfer trends equal and using (8.8) yields:

$$Ra_T = c_1^{1/(\beta-\alpha)} Ra_C^{\beta/(\beta-\alpha)} = c_1^{1/(\beta-\alpha)} c_2^{\beta/(\beta-\alpha)} E^{4\beta/3(\alpha-\beta)} . \tag{8.23}$$

The supercriticality at which this transition occurs can then be written as:

$$\frac{Ra_T}{Ra_C} = c_1^{1/(\beta-\alpha)} c_2^{\alpha/(\beta-\alpha)} E^{4\alpha/3(\alpha-\beta)} . \tag{8.24}$$

By applying (8.23) to the best-fit scaling laws (8.21) and (8.22), we find:

$$Ra_T = (5.4 \pm 0.1) E^{-1.466 \ \pm \ 0.005} . \tag{8.25}$$

The steep heat transfer scaling exponent $\beta = 3.6$ differs from a cubic law by about 16%. However, the exponent in Ra_T differs from (8.11) by only about 2%. This small 2% difference

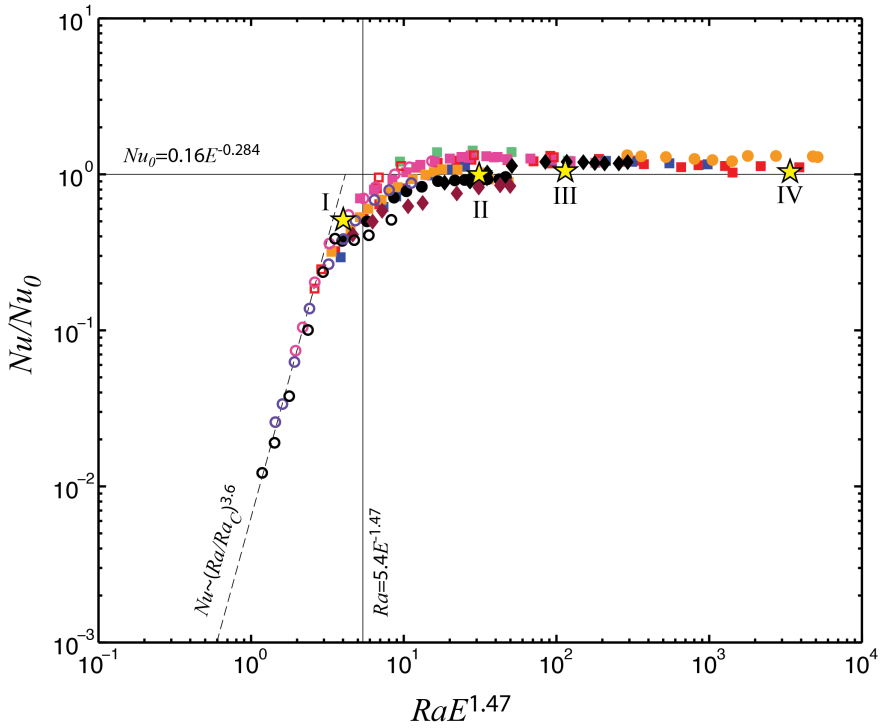

Figure 8.7: Test of the heat transfer transition argument based on our most extreme data. Data are from laboratory ($Pr \simeq 7$) and numerical ($Pr = 7$) rotating convection experiments with $E \leq 10^{-4}$. Symbols are as defined in Figure 8.5. The y-axis is the nondimensional heat transfer normalized by the nonrotating scaling Nu/Nu_0, where $Nu_0 = 0.16Ra^{0.284}$ (8.20). The x-axis is the Rayleigh number normalized by the transition value Ra_T. This transition is empirically defined here as the intersection between the nonrotating heat transfer trend, $Nu = 0.075Ra^{0.32}$, and the rapidly rotating trend, $Nu = 0.71\,(Ra/Ra_C)^{3.6}$, and occurs at $Ra_T = 5.4E^{-1.47}$ (8.25). The data from Figure 8.3 have been included as black-bordered yellow stars in the collapse. These demonstrate that only the 60 rpm case (I) with coherent axial columns is found to plot within the steep heat transfer scaling regime.

arises because of the limited range between Ra_C and Ra_T:

$$\frac{Ra_T}{Ra_C} = 144E^{-0.14} \sim E^{-1/7} \tag{8.26}$$

at $E = 10^{-7}$. At presently accessible Ekman numbers, the $\beta = 3.6$ slope and the cubic slope correspond to very similar intersections with the RBC trend. The weak $E^{-1/7}$ dependence in (8.26) also implies that the steep scaling regime occupies a limited range of parameter space even when extrapolated to planetary conditions. In Figure 8.7, we collapse the laboratory-numerical data from the present study and King et al. (2012) using the best-fit scaling for

the majority of the nonrotating data, (8.20), to compensate the Nusselt number data on the y-axis and using our best-fit transition scaling (8.25) to compensate the Rayleigh number on the x-axis. The mean Prandtl number in laboratory cases is 6.8 and the numerical cases employ a Prandtl number of 7. The black-bordered yellow stars correspond to the visualization cases shown in Figure 8.3. The locations of the black-bordered yellow stars demonstrate that columnar flows are associated solely with the steep heat transfer scaling: only the $E = 1.2 \times 10^{-7}$ visualization case (I) has a Rayleigh number value that is less than Ra_T. This shows, in our $Pr \simeq 7$ experiments, that the efficiency of heat transfer greatly lessens and transitions over to the RBC scaling trend once convection columns lose their axial coherency.

In Figure 8.8, we test the ability of a number of mechanistic (non-empirical) rotating convection transition hypotheses available in the literature to collapse our heat transfer data. In panel 8.8a, the x-axis is normalized by the convective Rossby number (8.19). It has been argued that the convection regime dominated by rotation extends from the onset of rotating convection at Ra_C near to where the convective Rossby number is of order unity, $Ro_c \lesssim 1$ (e.g. Gilman (1977); Aurnou (2007); Zhong and Ahlers (2010); Gastine et al. (2013); Stevens et al. (2013); Gastine et al. (2014)). This predicts that the steep heat transfer scaling regime will extend over the range $Ra_C \lesssim Ra \lesssim E^{-2}Pr$. This Rayleigh number range has a width of $\sim E^{-2/3}Pr$. However, Figure 8.8a shows that the Ro_c normalization greatly spreads our heat transfer data and, therefore, does not correctly define the transition. Our results from Figure 8.7 instead imply that the steep scaling regime – where we find that columns are stable – is a factor of $\sim E^{3/5}$ narrower than the $Ro_c \sim 1$ prediction.

It should be noted, however, that $Ro_c \sim 1$ does provide an adequate transition prediction for zonal flow behavior in rotating spherical shells because these flows occur on the system's global scale (e.g. Aurnou (2007); Gastine et al. (2013, 2014)). However, in our rotating convection experiments, in which convective heat transfer is controlled by distinctly smaller scale motions, the data are not well-collapsed by this system-scale parameter. Figure 8.8b shows a test of the *local* convective Rossby number, Ro_ℓ. This parameter has been proposed in a number of previous dynamo studies (e.g. Sreenivasan and Jones (2006b); Christensen

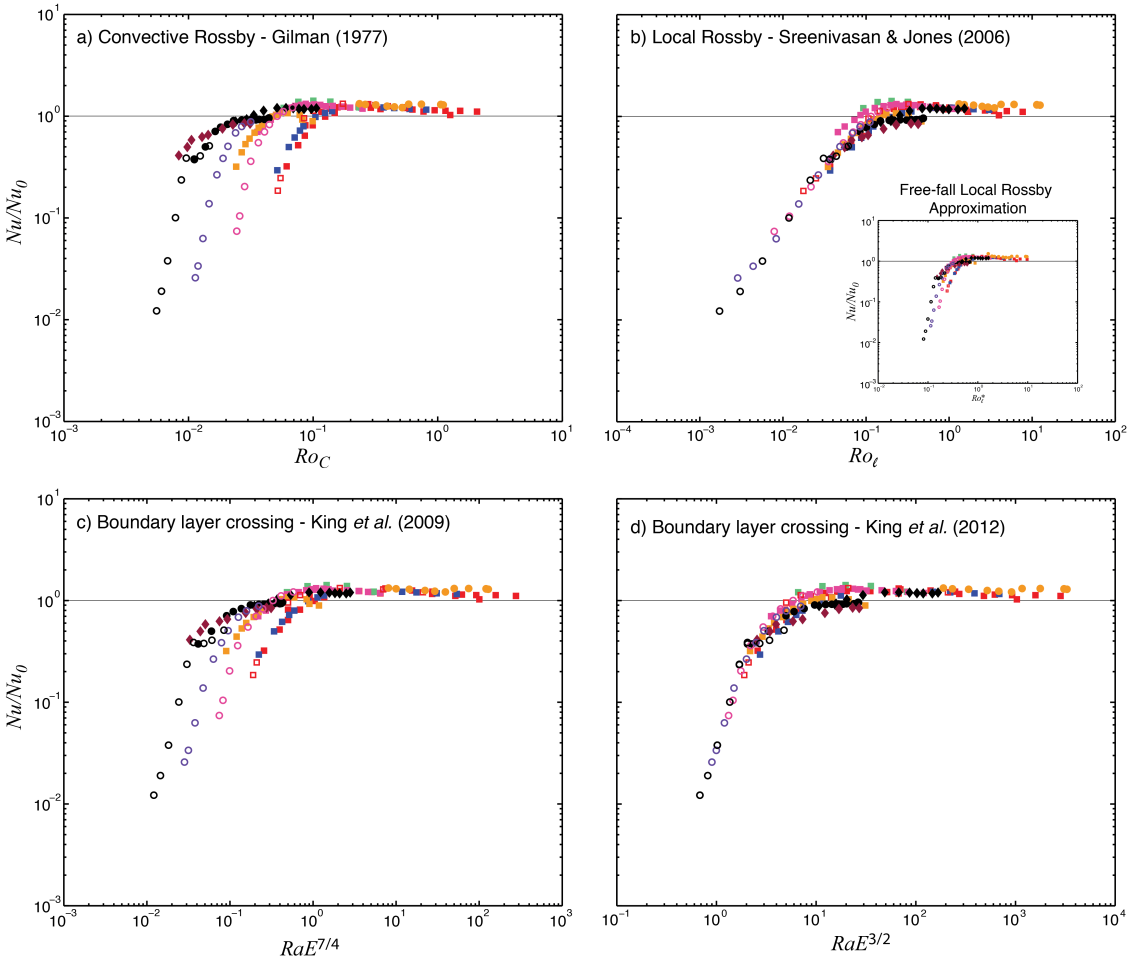

Figure 8.8: Tests of various heat transfer transition arguments. Data are from laboratory ($Pr \simeq 7$) and numerical ($Pr = 7$) rotating convection experiments with $E \leq 10^{-4}$. Symbols are as defined in Figure 8.5. The nondimensional heat transfer, normalized by the weakly rotating trend $Nu_0 = 0.16Ra^{0.284}$, is plotted against several proposed transition parameters. a) Convective Rossby transition, $Ro_C = (RaE^2/Pr)^{1/2}$. b) Local Rossby transition (e.g. Sreenivasan and Jones (2006b)) estimated using heat transfer parameters, $\widetilde{Ro_\ell} = c_3^{-1}\widetilde{Re}E^{2/3}$ based upon the velocity scaling from King et al. (2013) (see text for details). The inset figure tests a different estimate for local Rossby, $Ro_\ell^* = (\gamma g \Delta T)/(\Omega L^{1/2})$, where the free-fall velocity scaling is assumed. c) Boundary layer crossing transition proposed by King et al. (2009), $RaE^{7/4}$. d) Boundary layer crossing transition proposed by King et al. (2012).

and Aubert (2006)) to control the transition between dipolar and multipolar magnetic field generation, with a critical value of $Ro_\ell \simeq 0.1$. Here we write Ro_ℓ as

$$Ro_\ell = \frac{U}{2\Omega\ell} = \frac{UL}{\nu}\frac{\nu}{2\Omega L^2}\frac{L}{\ell} = ReE\frac{L}{\ell} \tag{8.27}$$

where the Reynolds number, Re, is defined as:

$$Re = \frac{\text{Inertia}}{\text{Viscosity}} = \frac{UL}{\nu} \tag{8.28}$$

We cannot directly measure velocities in our laboratory experiments. In order, then, to express the local Rossby number in terms of our heat transfer data, we must make two assumptions. First, we replace L/ℓ with $(c_3 E^{1/3})^{-1}$ using (8.9), an approximation relevant to present-day dynamo studies following the arguments of King and Buffett (2013). Second, we give an approximate value of the Reynolds number, $\widetilde{Re}$, using the visco-Archimedean-Coriolis (VAC) second-order balance arguments in King et al. (2013):

$$\widetilde{Re} = \frac{c_3(Nu-1)^{1/2}Ra^{1/2}E^{1/3}}{Pr}\,. \tag{8.29}$$

Substituting $\widetilde{Re}$ into (8.27), gives

$$\widetilde{Ro_\ell} = c_3^{-1}\widetilde{Re}E^{2/3}\,. \tag{8.30}$$

We find that the Ro_ℓ parametrization adequately collapses our $Pr \simeq 7$ heat transfer data.

The inset in Figure 8.8b tests another estimate for the local Rossby number, $Ro_\ell^* = (\gamma g \Delta T)/(\Omega L^{1/2})$, based on the free-fall velocity U_f. This estimate does not collapse the data as well as the Ro_ℓ estimate derived from the VAC balance arguments presented in (8.29) and (8.30).

In Figure 8.8c, we test the transition arguments of King et al. (2009), which rely on the empirical $Nu \sim (Ra/Ra_C)^{6/5}$ steep scaling regime and the $Nu \sim Ra^{2/7}$ shallow scaling regime. The resulting transition scaling, $Ra_T \sim E^{-7/4}$, does not strongly collapse our present,

lower E heat transfer data. However, the essential concept posited in King et al. (2009) –that boundary layer processes underly the heat transfer transition – are not refuted (Niemela and Sreenivasan (2006); Cébron et al. (2010b); Julien et al. (2012a)).

Figures 8.8d tests the $Ra_T \sim E^{-3/2}$ transition argument from King et al. (2012). This transition parametrization collapses the data comparably well to that of Figure 8.7. This agreement is expected since the present best-fit transition scaling and King *et al.*'s transition scaling differ only by a factor of $\sim E^{1/50}$.

In sum, there is great variance in the mechanistic arguments which seek to parameterize the behavioral regimes of rotating convective heat transfer, implying that our understanding of this system is still far from complete. Thus, further data sets that extend well below $E = 10^{-7}$ are needed to determine an unambiguous, asymptotically robust, mechanistic transition argument that may be extrapolated to planetary conditions with confidence.

8.6 Extrapolation to Planetary Core Settings

Our mixed heat transfer-visualization data, shown in Figure 8.7, forms the basis of our assumption that axially-coherent columns exist in rotating convection over the range $Ra_C < Ra < Ra_T$. Figure 8.9 graphically represents this by plotting Ra_T/Ra_C as a function of inverse E for various transition scalings. Table 8.2 lists values of Ra_T and Ra_T/Ra_C extrapolated to $E = 10^{-15}$. The classical transition estimate of $Ro_c \sim 1$ suggests that convection columns will be stable over 8 orders of magnitude in Ra. However, this scaling fails to meaningfully collapse the available data, as shown in Figure 8.8. Our present results and other recent studies all estimate significantly smaller $Ra_C < Ra < Ra_T$ ranges under which columns will be stable in the core. The Ra_T/Ra_C estimates in Table 8.2 show that, irrespective of the convection column breakdown mechanism, it is likely that traditional columns are unstable in core-like environments. Figure 8.10 displays, in the lower left-hand corner, all the rotating convection data from Figure 8.5. On the right side of the figure, we extrapolate our most extreme, steep heat transfer scaling, $\beta = 3.6$, from $E = 10^{-7}$ to the typical estimate for the Ekman number in the Earth's core, $E = 10^{-15}$. Here, we do not consider magnetic

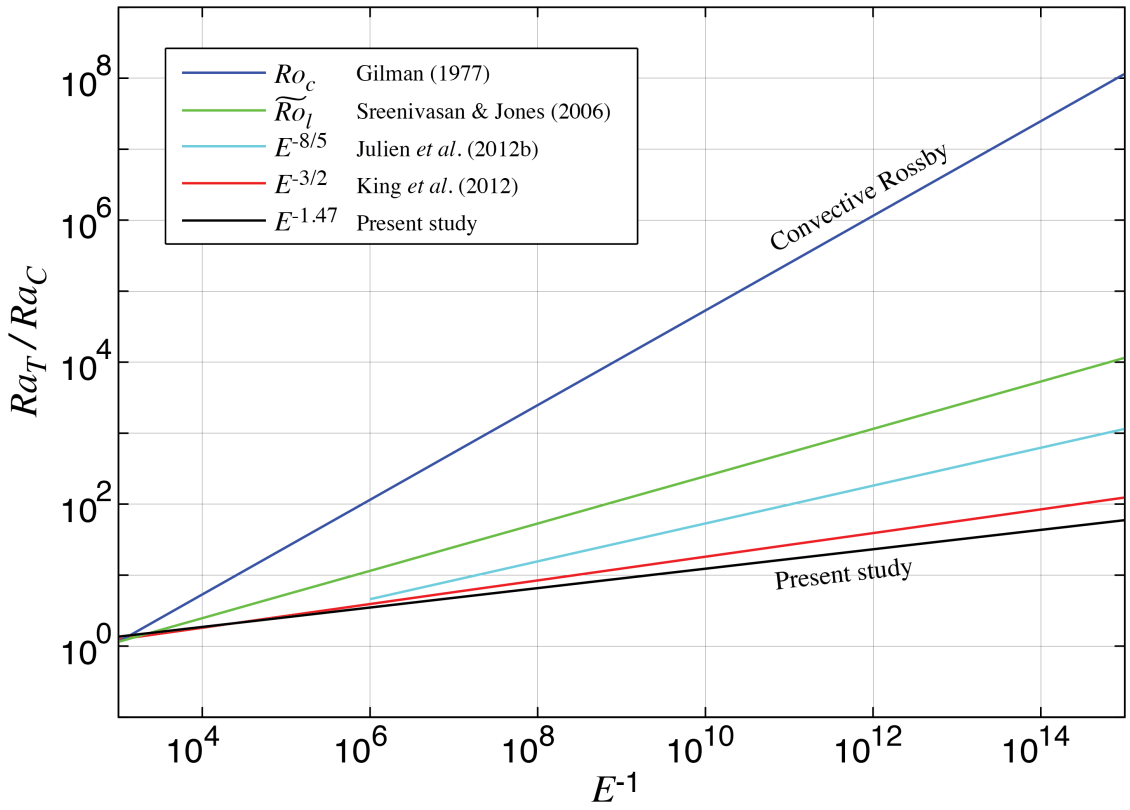

Figure 8.9: Estimated values of Ra_T/Ra_C for E ranging from 10^{-3} to 10^{-15}. These values approximate the range, $Ra_C < Ra < Ra_T$, over which different models predict the existence of axially coherent convection columns. For $E \gtrsim 10^{-6}$, the King et al. (2012) transition of $Ra_T \sim E^{-3/2}$ is nearly indistinguishable from the present fit of $Ra_T \sim E^{-1.47}$. The light blue curve is terminated above $E = 10^{-6}$ because the asymptotic model from Julien et al. (2012a) is valid in the limit of low E. In calculating the $Ro_c \sim 1$ and $\widetilde{Ro}_\ell \sim 1$ curves, we assume $Pr = 10^{-1}$ (see Table 8.3).

Table 8.2: Estimates under Earth-like conditions ($E = 10^{-15}$; $Pr = 10^{-1}$) for the transition Rayleigh number (Ra_T) at which columns become unstable as well as the predicted range of column stability (Ra_T/Ra_C).

Transition Argument	Reference	Ra_T	Ra_T/Ra_C
$Ro_c \sim 1$	Gilman (1977)	$\sim 10^{29}$	$\sim 10^8$
$\widetilde{Ro}_\ell \sim 1$	Sreenivasan and Jones (2006b)	$\sim 10^{25}$	$\sim 10^4$
$RaE^{8/5} \sim 1$	Julien et al. (2012a)	$\sim 10^{24}$	$\simeq 1100$
$RaE^{3/2} \sim 1$	King et al. (2012)	$\sim 10^{23}$	$\simeq 120$
$RaE^{1.47} \sim 1$	Present study	$\sim 10^{23}$	$\simeq 60$

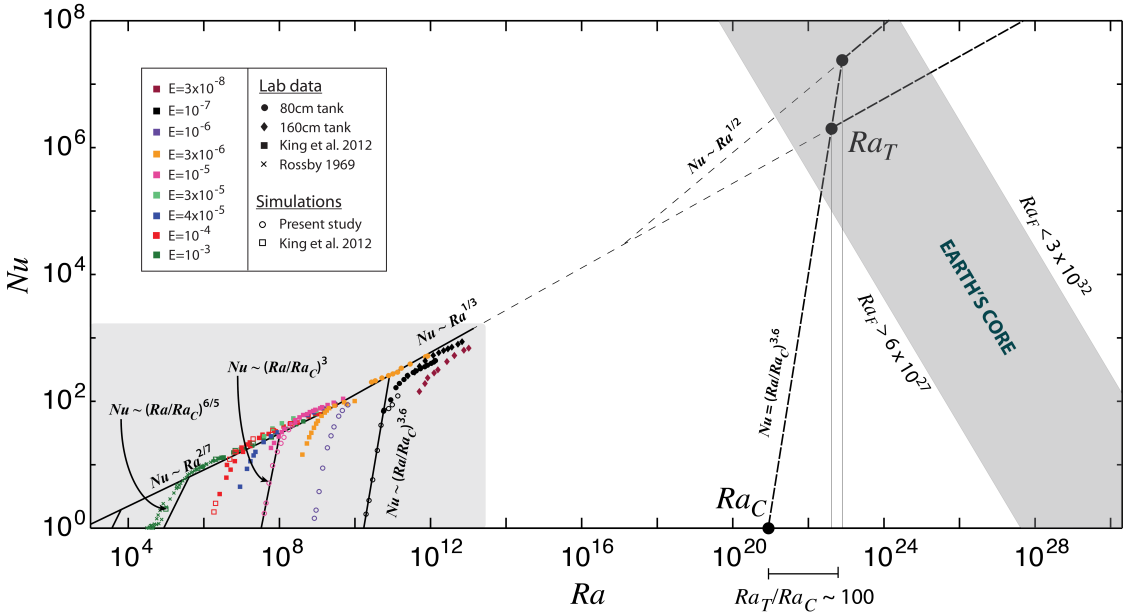

Figure 8.10: Comparison between laboratory-numerical heat transfer data (predominantly at $Pr \simeq 7$) and estimated ranges of heat transfer parameters in Earth's core ($Pr \simeq 10^{-1}$ to 10^{-2}). In the lower left hand corner of this figure, we plot all our Nu-Ra data as well as the best-fit trends discussed in Figures 8.4 and 8.5. Here, we show the $Nu \sim Ra^{1/3}$ and $Nu \sim Ra^{1/2}$ scalings for $Ra \gtrsim 10^{13}$ since centrifugal effects are not relevant in the core. The range of accessible Nu-Ra space for convection in Earth's core is denoted by the diagonal grey stripe on the figure's right side. The bounds on this diagonal stripe are defined by the maximum and minimum possible values of the superadiabatic flux Rayleigh number in Earth's core, $6 \times 10^{27} \lesssim Ra_F \lesssim 3 \times 10^{32}$ (see text for details). Extrapolating our lowest available Ekman number results to core conditions, we find that our heat transfer scalings (thick dashed lines) intersect core Nu-Ra estimates predominantly in the vicinity of and beyond the transition Rayleigh number, Ra_T. Since columnar convection breaks down near Ra_T, we hypothesize that local-scale columnar convection structures are not likely to exist in Earth's core.

field effects, geometrical effects and differences in fluid Pr values. We also extrapolate our best-fit RBC scaling law, $Nu = 0.075Ra^{0.322}$, to represent an upper bound for the rapidly rotating regime at planetary conditions. Another RBC scaling that may apply at such extreme Nu-Ra values is the $Nu = c_4 Ra^{1/2}$ law (Kraichnan (1962)), where c_4 is an undetermined prefactor. Here we suppose that the 1/2 law branches off from the 1/3 law at $Ra \gtrsim 10^{17}$ (cf. Niemela et al. (2000)), giving $c_4 = 1.1 \times 10^{-4}$. From (8.24), columnar convection is estimated to be stable for $Ra_{T_1} \lesssim 60 Ra_C$ using the $\alpha = 1/3$ RBC law and $Ra_{T_2} \lesssim 150 Ra_C$ using the $\alpha = 1/2$ RBC law.

Figure 8.10 shows both of these transition estimates in the context of Nu-Ra approximations for the Earth's core. The values of Ra_T/Ra_C presented here may represent an upper bound on the extent of the columnar regime. First, the slope of the rapidly rotating regime continues to steepen with decreasing Ekman number for our available data (see Figure 8.6). If this trend continues, then the columnar regime is stable for an even smaller region than indicated on Figure 8.10. Second, the $E \to 0$ models of Julien et al. (2012a,b) show that columnar convection can break down into geostrophic turbulence well before the intersection of the steep scaling trend with the RBC trend, further implying a limited range of stability for columns.

Although experimental studies utilize Ra and Nu to characterize rotating convection systems, these quantities are nearly impossible to accurately determine in Earth's core. Typical estimates of the core Rayleigh number range between $10^{20} \lesssim Ra \lesssim 10^{30}$ (e.g. Gubbins (2001); Kono and Roberts (2002); Aurnou et al. (2003); Schubert and Soderlund (2011); Roberts and King (2013)). However, some estimates are as low as 10^{15} (Roberts and Aurnou (2012)) while others are as high as 10^{38} (Gubbins (2001)). The (superadiabatic) Nusselt number in the core is also very poorly constrained. In contrast, the flux Rayleigh number,

$$Ra_F = RaNu = \frac{\gamma g L^4 q_{sa}}{k\kappa\nu}\,, \tag{8.31}$$

can be directly estimated in Earth's core, because it depends only on physical and chemical properties and the superadiabatic heat flux from the core, q_{sa}. These values can, in turn, be estimated based on observable quantities. A broad range of upper and lower bound estimates for each of these quantities are given in Table 8.3.

Table 8.3: Core property estimates used in calculating the bounding flux Rayleigh number values shown in Figure 8.10.

Symbol	Parameter	Lower bound	Upper bound	Sources (lower bound; upper bound)
γ	thermal expansivity [K^{-1}]	10^{-5}	1.8×10^{-5}	Buffett (2000); Stacy and Davis (2008)
g	gravitational acceleration [ms^{-2}]	5	11	g at ICB; g at CMB (Dziewonski and Anderson (1981))
L	layer thickness [m]	2.3×10^{6}	3.5×10^{6}	thickness of outer core; diameter of outer core (Dziewonski and Anderson (1981))
ν	viscosity [m^2s^{-1}]	10^{-7}	10^{-6}	Buffett (2000); Roberts and King (2013)
k	thermal conductivity [$Wm^{-1}K^{-1}$]	30	100	Stacy and Davis (2008); Pozzo et al. (2012)
ρ	density [kg m^{-3}]	9×10^{3}	1.2×10^{4}	ρ at CMB; ρ at ICB (Stacy and Davis (2008))
C_p	specific heat [$JK^{-1}kg^{-1}$]	790	815	C_p at CMB; C_p at ICB (Stacy and Davis (2008))
κ	thermal diffusivity [m^2s^{-1}]	3×10^{-6}	10^{-5}	estimated using above values of k, ρ and C_p
q_{sa}	superadiabatic heat flux [Wm^{-2}]	6.5×10^{-3}	6.5×10^{-2}	1–10 TW of total heating power (Buffett (2000))

The associated range of Ra_F is far more tightly constrained than estimates of Ra in Earth's core: $6 \times 10^{27} \lesssim Ra_F \lesssim 3 \times 10^{32}$. This Ra_F range is shown as the diagonal grey stripe on the figure's right side in Figure 8.10. Using only the recent thermal conductivity estimate from Pozzo et al. (2012) would yield a slightly lower upper bounding value for Ra_F of 2×10^{31}. The dashed line connecting $Ra_C \simeq 10^{21}$ to $Ra_{T_1} \simeq 6 \times 10^{22}$ and $Ra_{T_2} \simeq 1.5 \times 10^{23}$ is the extrapolation of our laboratory-numerical findings to Earth's core parameters. We find that our heat transfer extrapolations predominantly intersect core Ra_F estimates such that $Ra \gtrsim Ra_T$, suggesting that rotating convective flows in the core will not be columnar and are instead likely to be comprised of more complex motions.

8.7 Discussion

The results of our suite of laboratory-numerical Rayleigh-Bénard and rotating convection experiments show the overarching behaviors of Boussinesq convection in right cylindrical tanks (laboratory) and in doubly-periodic Cartesian domains (numerical).

We find that Rayleigh-Bénard convection physics is essential to our understanding of rotating convection systems. At low Ekman numbers, as are relevant to planets and stars, the RBC trend provides the upper bound for heat transfer in our rotating convection experiments. In addition, at high Ra, our results show that the RBC heat transfer follows predictions from turbulent convection theory (e.g. Malkus (1954); Ahlers et al. (2009)) providing an important tie between RBC and the behavioral regimes of rotating convection and convection-driven dynamo systems.

Our experiments show that rotating convection columns carry heat with great efficiency. In particular, our $Pr \simeq 7$, $E \simeq 10^{-7}$ data provides a heat transfer scaling exponent of $\beta \simeq 3.6$, which exceeds even the cubic predictions of King et al. (2012). Furthermore, Figure 8.6 yields an ever-steepening β value as Ekman is decreased, suggesting that the convection physics of rapidly rotating systems has not yet been fully described. An open question remains whether, and to what extent, the scaling exponent in the steep scaling regime will continue to steepen with decreasing E (cf. Grooms and Whitehead (2015); Stellmach et al.

(2014)).

The question also remains how the change in heat transfer scalings and the breakdown in coherent columns are mechanistically connected. For instance, do boundary layer nesting phenomena break the columns or vice versa? Further, does the steep heat transfer scaling break down due to the boundary layer physics (e.g. King et al. (2012)) or due to changes in the interior flow patterns (e.g. Julien et al. (2012a))?

Our present study only considers the hydrodynamic behavior of core-style convection. Theoretical studies predict that the presence of magnetic fields will destabilize columnar convective flows (Chandrasekhar (1961); Eltayeb and Roberts (1970); Roberts and King (2013)). In that case, our present hydrodynamic results may provide an upper bound on the stability range of local-scale columns. However, it still remains to be directly determined how strong magnetic fields affect the heat transfer and stability of high Ra flows in low E, low Pr core settings (cf. Aurnou and Olson (2001); Jones et al. (2003); Gillet et al. (2007)).

In spherical shell geometries, low latitude convection columns (outside the tangent cylinder) substantively differ from columnar flows at high latitudes (as simulated in our cylindrical and Cartesian experiments) (e.g. Busse and Cuong (1977); Calkins et al. (2013)). While specific heat transfer scalings will likely differ at lower latitudes, we predict the same fundamental physical behaviors as found here: a regime of steep convective heat transfer affiliated with the existence of coherent, axial columns that merges with the RBC heat transfer trend at high Ra, where rotating fluid motions lose their axial coherency. The specific differences between high and low latitude rotating convection behaviors provide an open topic for future research.

Our combination of laboratory-numerical and theoretical models affords a novel view of rapidly-rotating (non-magnetic) convection as planetary conditions are approached. As the Ekman number is decreased through larger-scale laboratory experiments and better-resolved computations, the parameter space in which coherent convection columns exist is found to dwindle. Because columns exist only in a limited range of Ra before they break down, coherent columns as found in present-day models may not be stable at core conditions.

We hypothesize, then, that large-scale flow structures in planetary cores, such as system-scale columns, are not a *direct* result of rotating convection. Instead, we hypothesize that convection occurs in the form of 3D geostrophic turbulence on smaller scales, whose energy then cascades upwards to larger-scale quasi-2D flows (e.g. Mininni and Pouquet (2010); Käpylä et al. (2011); Chan and Mayr (2013); Favier et al. (2014b); Guervilly et al. (2014); Nataf and Schaeffer (2015); Rubio et al. (2014); Stellmach et al. (2014)), which are capable of efficiently generating observable magnetic fields. Ultimately, our findings suggest the need to revise current planetary dynamo models to include the effects of multi-scale rotating convection dynamics and to determine how such flows produce planetary dynamo action.

8.8 Data

Table 8.4: Laboratory convection data. Here, $\overline{\tau}$ denotes the averaging time in thermal diffusion time scale units L^2/κ. Note that $\tau \ll 1$ in all our experiments. However, the time series data have reached a statistical steady state prior to the start of data acquisition in all the cases. Before acquisition, each case is allowed to equilibrate for approximately 12 hours until the variation in mean temperature is less than 1%. Data is then acquired for at least 2 hours per case (see Section 8.3.1).

height (m)	rpm	Power (W)	Mean T (^oC)	ΔT (^oC)	Pr	E	Ra	Nu	$\bar{\tau}$
0.798	0	9.58	23.31	2.88	6.338	∞	2.626×10^{10}	166.85	2.25×10^{-3}
0.798	0	9.83	23.12	2.60	6.370	∞	2.341×10^{10}	166.89	1.31×10^{-3}
0.798	0	14.87	23.52	3.82	6.301	∞	3.529×10^{10}	176.49	2.29×10^{-3}
0.798	0	19.72	24.39	4.56	6.159	∞	4.430×10^{10}	193.42	8.72×10^{-4}
0.798	0	30.05	23.14	6.49	6.365	∞	5.851×10^{10}	210.89	1.44×10^{-3}
0.798	0	39.18	22.81	7.76	6.422	∞	6.847×10^{10}	230.07	1.51×10^{-3}
0.798	0	49.42	22.87	9.32	6.412	∞	8.260×10^{10}	242.17	1.66×10^{-3}
0.798	0	69.10	23.60	11.75	6.288	∞	1.090×10^{11}	264.23	1.70×10^{-3}
0.798	0	98.52	24.57	14.90	6.129	∞	1.464×10^{11}	294.33	2.07×10^{-3}
0.798	0	149.26	23.15	21.17	6.365	∞	1.908×10^{11}	316.30	1.04×10^{-3}
0.798	0	197.37	26.12	24.60	5.889	∞	2.639×10^{11}	353.37	1.54×10^{-3}
0.798	0	244.96	26.30	29.11	5.861	∞	3.155×10^{11}	374.03	1.71×10^{-3}
0.798	0	294.56	28.60	31.94	5.531	∞	3.905×10^{11}	401.58	1.20×10^{-3}
0.798	0	341.22	31.01	35.02	5.214	∞	4.807×10^{11}	424.39	1.64×10^{-3}
0.798	0	394.31	33.40	37.72	4.926	∞	5.757×10^{11}	448.27	1.17×10^{-3}
0.798	0	495.68	39.41	41.57	4.299	∞	8.047×10^{11}	503.15	1.77×10^{-3}
0.798	0	495.56	39.42	41.58	4.298	∞	8.053×10^{11}	503.19	1.61×10^{-3}
0.798	0	543.07	41.51	43.61	4.108	∞	9.100×10^{11}	520.14	1.87×10^{-3}
0.798	2	14.70	23.47	3.24	6.311	3.43×10^{-6}	2.976×10^{10}	200.34	1.91×10^{-3}
0.798	2	19.76	23.92	3.95	6.235	3.39×10^{-6}	3.739×10^{10}	210.25	1.74×10^{-3}
0.798	2	29.41	25.01	5.58	6.060	3.31×10^{-6}	5.628×10^{10}	233.18	1.58×10^{-3}
0.798	2	49.60	24.13	8.78	6.201	3.37×10^{-6}	8.405×10^{10}	253.79	1.52×10^{-3}
0.798	2	68.94	24.01	11.52	6.221	3.38×10^{-6}	1.095×10^{11}	269.80	1.43×10^{-3}
0.798	2	99.61	23.81	15.54	6.254	3.40×10^{-6}	1.459×10^{11}	287.72	1.74×10^{-3}
0.798	2	149.13	23.34	20.07	6.332	3.44×10^{-6}	1.831×10^{11}	331.53	1.41×10^{-3}
0.798	2	248.44	26.96	28.07	5.764	3.16×10^{-6}	3.152×10^{11}	386.23	1.89×10^{-3}
0.798	2	493.03	39.39	41.63	4.301	2.44×10^{-6}	8.053×10^{11}	499.11	1.88×10^{-3}

height (m)	rpm	Power (W)	Mean T (^oC)	ΔT (^oC)	Pr	E	Ra	Nu	$\bar{\tau}$
0.798	2	543.30	41.59	43.86	4.101	2.34×10^{-6}	9.178×10^{11}	516.85	1.90×10^{-3}
0.798	2	495.68	39.41	41.57	4.299	2.44×10^{-6}	8.047×10^{11}	503.15	1.87×10^{-3}
0.798	60	9.80	24.95	6.19	6.069	1.10×10^{-7}	6.215×10^{10}	69.62	1.41×10^{-3}
0.798	60	20.09	26.77	8.66	5.792	1.06×10^{-7}	9.629×10^{10}	105.48	1.92×10^{-3}
0.798	60	49.76	24.16	13.79	6.197	1.12×10^{-7}	1.322×10^{11}	163.69	1.30×10^{-3}
0.798	60	69.74	24.78	16.41	6.096	1.11×10^{-7}	1.633×10^{11}	190.77	1.93×10^{-3}
0.798	60	98.31	26.25	19.95	5.868	1.07×10^{-7}	2.157×10^{11}	220.40	1.93×10^{-3}
0.798	60	147.93	25.27	26.04	6.018	1.10×10^{-7}	2.666×10^{11}	254.53	1.79×10^{-3}
0.798	60	201.56	28.36	31.47	5.565	1.02×10^{-7}	3.801×10^{11}	284.21	1.79×10^{-3}
0.798	60	244.13	29.41	35.80	5.421	9.99×10^{-8}	4.556×10^{11}	301.29	1.79×10^{-3}
0.798	60	297.83	32.56	39.86	5.024	9.34×10^{-8}	5.868×10^{11}	325.33	1.80×10^{-3}
0.798	60	491.88	42.77	52.19	4.000	7.64×10^{-8}	1.137×10^{12}	395.55	1.80×10^{-3}
0.798	60	347.30	38.06	41.70	4.429	8.36×10^{-8}	7.677×10^{11}	350.05	1.80×10^{-3}
0.798	60	394.65	40.79	44.51	4.172	7.93×10^{-8}	9.056×10^{11}	369.48	1.79×10^{-3}
0.798	60	544.15	46.43	53.95	3.708	7.14×10^{-8}	1.326×10^{12}	416.00	1.77×10^{-3}
0.798	60	544.12	46.47	54.07	3.705	7.13×10^{-8}	1.330×10^{12}	414.93	1.58×10^{-3}
0.798	60	597.12	48.42	55.80	3.563	6.89×10^{-8}	1.459×10^{12}	438.69	1.61×10^{-3}
0.798	60	597.11	48.52	56.16	3.556	6.88×10^{-8}	1.473×10^{12}	435.82	1.63×10^{-3}
1.595	0	29.56	24.71	5.92	6.107	∞	4.689×10^{11}	406.83	4.54×10^{-4}
1.595	0	49.74	23.88	9.18	6.241	∞	6.913×10^{11}	466.58	3.20×10^{-4}
1.595	0	70.12	23.80	11.91	6.255	∞	8.930×10^{11}	544.63	4.52×10^{-4}
1.595	0	98.01	23.56	15.68	6.295	∞	1.158×10^{12}	598.38	4.52×10^{-4}
1.595	0	98.12	23.53	15.68	6.301	∞	1.155×10^{12}	597.24	4.51×10^{-4}
1.595	0	149.08	23.66	21.25	6.278	∞	1.579×10^{12}	654.58	4.52×10^{-4}
1.595	0	149.18	23.66	21.31	6.279	∞	1.583×10^{12}	647.18	4.51×10^{-4}
1.595	0	198.79	24.53	26.16	6.136	∞	2.048×10^{12}	693.79	4.54×10^{-4}
1.595	0	198.82	24.37	26.36	6.163	∞	2.044×10^{12}	689.03	4.52×10^{-4}
1.595	0	248.39	27.33	29.61	5.710	∞	2.708×10^{12}	753.64	4.57×10^{-4}
1.595	0	247.77	27.24	29.54	5.723	∞	2.689×10^{12}	747.77	4.55×10^{-4}
1.595	0	299.24	30.14	32.77	5.326	∞	3.448×10^{12}	794.43	4.61×10^{-4}
1.595	0	299.26	29.97	32.91	5.347	∞	3.435×10^{12}	790.69	4.60×10^{-4}
1.595	0	299.30	29.91	32.91	5.355	∞	3.425×10^{12}	790.40	4.59×10^{-4}
1.595	0	346.29	32.48	35.27	5.034	∞	4.130×10^{12}	848.01	4.65×10^{-4}
1.595	0	346.28	32.47	35.23	5.035	∞	4.125×10^{12}	847.02	4.64×10^{-4}
1.595	0	397.08	35.17	38.35	4.727	∞	5.033×10^{12}	884.01	4.69×10^{-4}
1.595	0	396.82	35.17	38.28	4.728	∞	5.023×10^{12}	885.88	4.26×10^{-4}
1.595	0	495.21	39.79	43.07	4.264	∞	6.749×10^{12}	969.87	4.73×10^{-4}
1.595	0	495.15	39.87	43.20	4.256	∞	6.789×10^{12}	965.78	3.83×10^{-4}
1.595	15	9.98	23.27	3.79	6.344	1.15×10^{-7}	2.750×10^{11}	250.91	2.92×10^{-4}
1.595	15	19.61	24.30	5.46	6.174	1.12×10^{-7}	4.215×10^{11}	298.44	4.53×10^{-4}
1.595	15	19.62	24.28	5.43	6.177	1.12×10^{-7}	4.188×10^{11}	288.29	4.54×10^{-4}
1.595	15	19.62	24.23	5.34	6.185	1.12×10^{-7}	4.107×10^{11}	290.43	4.53×10^{-4}
1.595	15	19.64	24.25	5.37	6.182	1.12×10^{-7}	4.134×10^{11}	289.31	1.67×10^{-4}
1.595	15	29.87	25.20	6.86	6.031	1.10×10^{-7}	5.578×10^{11}	355.63	4.55×10^{-4}
1.595	15	50.04	24.39	10.15	6.159	1.12×10^{-7}	7.879×10^{11}	433.43	4.51×10^{-4}
1.595	15	98.90	24.04	16.96	6.216	1.13×10^{-7}	1.290×10^{12}	529.05	4.51×10^{-4}
1.595	15	150.02	24.46	23.17	6.148	1.12×10^{-7}	1.806×10^{12}	581.76	4.54×10^{-4}
1.595	15	199.44	25.78	28.82	5.940	1.08×10^{-7}	2.424×10^{12}	628.86	4.55×10^{-4}
1.595	15	249.44	28.55	32.39	5.538	1.02×10^{-7}	3.154×10^{12}	669.95	4.59×10^{-4}
1.595	15	249.22	28.59	32.41	5.533	1.02×10^{-7}	3.162×10^{12}	671.16	4.57×10^{-4}
1.595	15	296.54	31.46	35.83	5.157	9.57×10^{-8}	4.009×10^{12}	713.01	4.63×10^{-4}
1.595	15	393.91	36.72	41.65	4.564	8.59×10^{-8}	5.816×10^{12}	792.88	4.68×10^{-4}
1.595	15	481.66	40.87	45.97	4.165	7.93×10^{-8}	7.489×10^{12}	868.14	4.73×10^{-4}
1.595	60	9.88	24.89	6.94	6.079	2.77×10^{-8}	5.545×10^{11}	142.27	4.56×10^{-4}
1.595	60	20.54	26.13	9.09	5.888	2.69×10^{-8}	7.792×10^{11}	189.83	2.37×10^{-4}
1.595	60	29.55	26.82	10.33	5.784	2.65×10^{-8}	9.201×10^{11}	233.33	4.41×10^{-4}
1.595	60	49.54	26.87	15.27	5.777	2.65×10^{-8}	1.362×10^{12}	279.36	1.66×10^{-4}
1.595	60	68.79	27.18	18.93	5.732	2.63×10^{-8}	1.717×10^{12}	312.75	2.27×10^{-4}
1.595	60	148.93	28.27	31.03	5.577	2.56×10^{-8}	2.979×10^{12}	421.33	1.92×10^{-4}
1.595	60	248.21	32.28	40.44	5.058	2.35×10^{-8}	4.695×10^{12}	526.35	2.32×10^{-4}
1.595	60	247.53	32.32	40.44	5.053	2.35×10^{-8}	4.703×10^{12}	523.84	2.32×10^{-4}
1.595	60	395.75	41.11	51.11	4.143	1.97×10^{-8}	8.398×10^{12}	636.53	2.38×10^{-4}
1.595	60	488.78	46.37	57.66	3.713	1.79×10^{-8}	1.129×10^{13}	686.70	2.41×10^{-4}

Table 8.5: Numerical rotating convection data. Here, $\overline{\tau}$ denotes the time over which the diagnostics have been averaged in thermal diffusion time scale units L^2/κ. Even though millions of time steps were performed, $\tau < 1$ in all our simulations, such that the quoted temporal averages may not be fully accurate (see e.g. Julien et al 2012a for a discussion of the broad range of time scales involved in rapidly rotating convection). In general however, the averaging times are comparable to or even exceed those used in the laboratory experiments (Table 8.4).

Pr	E	Ra	Nu	$\bar{\tau}$
7	1.00×10^{-5}	4.18×10^{7}	1.73	1.05
7	1.00×10^{-5}	4.64×10^{7}	2.51	5.31×10^{-1}
7	1.00×10^{-5}	5.57×10^{7}	5.17	3.42×10^{-1}
7	1.00×10^{-5}	6.96×10^{7}	9.75	1.85×10^{-1}
7	1.00×10^{-5}	9.28×10^{7}	16.1	1.06×10^{-1}
7	1.00×10^{-5}	1.16×10^{8}	21.9	7.69×10^{-2}
7	1.00×10^{-5}	1.39×10^{8}	27.1	6.17×10^{-2}
7	1.00×10^{-5}	1.86×10^{8}	35.7	4.56×10^{-2}
7	1.00×10^{-5}	2.32×10^{8}	42.2	3.66×10^{-2}
7	1.00×10^{-5}	3.25×10^{8}	50.7	2.82×10^{-2}
7	1.00×10^{-6}	9.00×10^{8}	1.44	1.79×10^{-1}
7	1.00×10^{-6}	1.00×10^{9}	1.94	4.30×10^{-1}
7	1.00×10^{-6}	1.20×10^{9}	3.81	1.15×10^{-1}
7	1.00×10^{-6}	1.50×10^{9}	8.90	8.73×10^{-2}
7	1.00×10^{-6}	2.00×10^{9}	18.6	4.07×10^{-2}
7	1.00×10^{-6}	2.50×10^{9}	28.7	2.39×10^{-2}
7	1.00×10^{-6}	3.00×10^{9}	39.7	1.92×10^{-2}
7	1.00×10^{-6}	4.00×10^{9}	58.5	1.28×10^{-2}
7	1.00×10^{-6}	5.00×10^{9}	71.9	1.00×10^{-2}
7	1.00×10^{-6}	7.00×10^{9}	88.0	7.30×10^{-3}
7	1.00×10^{-7}	2.15×10^{10}	16.8	7.09×10^{-2}
7	1.00×10^{-7}	2.59×10^{10}	27.6	6.90×10^{-2}
7	1.00×10^{-7}	3.23×10^{10}	58.4	3.64×10^{-2}
7	1.00×10^{-7}	4.31×10^{10}	16.9	1.06×10^{-2}
7	1.00×10^{-7}	5.39×10^{10}	42.2	1.05×10^{-2}
7	1.00×10^{-7}	6.46×10^{10}	72.9	4.95×10^{-3}
7	1.00×10^{-7}	8.62×10^{10}	77.1	2.79×10^{-3}
7	1.00×10^{-7}	1.08×10^{11}	88.4	1.24×10^{-3}
7	1.00×10^{-7}	1.51×10^{11}	122.0	9.65×10^{-4}

CHAPTER 9

Rotating thermal convection in liquid gallium: Multi-modal flow absent steady columns

In this work, I made several modifications to the experiment. First, I redesigned and built the internal thermistor holders in order to prevent the leakage of gallium throughout the duration of the experimental campaign. I also redesigned and built the external reservoir that allows the gallium to expand and contract with temperature changes and can be cleaned at the end of the experimental campaign in order to avoid contamination of gallium through the build-up of oxide residue. I first set up and performed the experiments and then analyzed a portion of the laboratory experiments. Then, I instructed a visiting student, Vincent Bertin, on running the experiment and the steps required for analyzing a majority of the data. We show that, in rotating convection of liquid metals, the quasi-steady columns that exist in high Prandtl number dynamo simulations do not exist in the low Prandtl liquid metals. Further, we show that the onset values for rotating convection in liquid metals is roughly two orders of magnitude lower than the onset for high Prandtl fluids. Lastly, we find the coexistence of wall-modes with the oscillatory convection in the bulk. These all suggest that core convection in metals can greatly differ from the what is presently simulated in most quasi-laminar, high Prandtl, present day dynamo models. I also contributed to the writing of the final document.

9.1 Introduction

Palaeomagnetic data have shown that the Earth's magnetic field has existed for more than 3 billion years (e.g., Tarduno et al., 2015). Thermocompositional convection is the primary

driver of the dynamo generation processes that occur in Earth's liquid metal core (Buffett et al., 1996; Roberts and King, 2013). Prior to the nucleation of the solid inner core, most evolution models find that thermally-buoyancy anomalies drove core convection, whereas compositionally-fueled core flow has dominated since the formation of the inner core (e.g., Davies et al., 2015, cf. O'Rourke and Stevenson (2016)). In order to accurately models dynamo action driven by present day thermo-compositional core convection as well as by thermal convection prior to inner core nucleation, it is essential to understand the underlying convection dynamics. However, the detailed dynamics of convective flows in planetary core-like liquid metals still remain largely unknown (e.g. Guervilly and Cardin, 2017).

In order to address this deficit, this laboratory experimental study focuses on thermally-driven, rotating convection in the liquid metal gallium. The characterization of the thermally-driven flows provide an essential step in order to fully understand the thermocompositionally-driven, turbulent rotating magnetoconvection which fuels the dynamo in Earth's outer core. Such convective flows underly thermally-driven, quasi-geostrophic dynamo action (e.g., Calkins et al., 2015; Nataf and Schaeffer, 2015), as likely occurs in a number of solar system planetary dynamos and the majority of present day numerical dynamo models (e.g., Soderlund et al., 2015; Aurnou and King, 2017). Furthermore, it is necessary that we quantify the behaviors of thermally-driven rotating convection in liquid metals in order to understand the changes that occur to the flow field in the largely unexplored magnetostrophic regime (e.g., Roberts and King, 2013; King and Aurnou, 2015; Yadav et al., 2016).

The paper is organized as follows. In the following introductory section 9.2, we present the dimensionless parameters that characterize the rotating Rayleigh Bénard convection system as well as the basic scaling results for the threshold of the convective instability. In section 9.3, we present our laboratory set-up and the material properties of liquid gallium. The laboratory experimental results are given in section 9.4. Finally, in section 9.5, comparisons are made between the novel liquid metal rotating convective flows found here with non-metallic rotating convective flows and extrapolate our results to extreme planetary core settings.

9.2 Parameter Definitions and Scaling Predictions

9.2.1 Nondimensional parameters

In thermal convection systems, the molecular properties of the fluid are non-dimensionally characterized by the thermal Prandtl number:

$$Pr = \nu/\kappa\,. \tag{9.1}$$

This is the ratio of the thermal diffusion time $\tau_\kappa = H^2/\kappa$ and the viscous diffusion time $\tau_\nu = H^2/\nu$, where H is the fluid layer depth, κ is the thermal diffusivity and ν is the kinematic viscosity. In thermally conductive metals, κ typically exceeds ν. The Prandtl number is 0.025 in liquid gallium and, similarly, estimates give $Pr \sim 0.1$ to 0.01 in planetary core fluids (e.g., Davies et al., 2015). However, if we consider only compositional buoyancy, then the compositional Prandtl number in planetary core fluids is estimated to be of order 10^2 to 10^3 (e.g., Calkins et al., 2012b; Manglik et al., 2010). In the majority of current-day dynamo models, the Prandtl number is taken to have a value of unity (e.g., see Table 1 in Aurnou and King, 2017). This value is computationally the least demanding to simulate. Further, the Prandtl hypothesis claims that strong turbulence will render all the Prandtl numbers to have effective values near unity (Roberts and Aurnou, 2012). Little evidence exists, though, in clear support of this claim in convection systems (e.g., Emran and Schumacher, 2015).

The cylindrical geometry of the experimental device is described by the aspect ratio

$$\Gamma = D/H, \tag{9.2}$$

which is the ratio of the working fluid's diameter D to its height H. In the present study, this value is fixed at $\Gamma = 1.94$.

The thermal buoyancy forcing is charaterized by the Rayleigh number:

$$Ra = \frac{\tau_\kappa\,\tau_\nu}{\tau_{ff}^2} = \frac{\alpha g\,\Delta T H^3}{\nu\,\kappa}\,, \tag{9.3}$$

which is the ratio of the thermo-viscous diffusion times and the square of the buoyant free-fall time across the layer, $\tau_{ff} = H/U_{ff} = \sqrt{H/(\alpha g\,\Delta T)}$. Here, α is the thermal expansivity, g is the gravitational acceleration, ΔT is the (superadiabatic) temperature difference across the fluid layer, and $U_{ff} = \sqrt{\alpha g \Delta T H}$ is the free-fall velocity. The value of the Rayleigh number in Earth's core is very poorly constrained, likely ranging between 10^{20} to 10^{30} (e.g., Gubbins, 2001; Cheng et al., 2015; Aurnou et al., 2003; Roberts and King, 2013). In the experiments carried out here, Ra varies over approximately two orders of magnitude, $2 \times 10^5 \lesssim Ra \lesssim 2 \times 10^7$.

In rotating systems, the (inverse) strength of rotational effects are typically characterized via the Ekman number E, which is the ratio of the characteristic rotation time scale $\tau_\Omega = 1/(2\Omega)$ and the viscous diffusion time τ_ν:

$$E = \frac{\tau_\Omega}{\tau_\nu} = \frac{\nu}{2\Omega H^2}\,, \tag{9.4}$$

where $\Omega = 2\pi/T_\Omega$ is the angular rotation rate, $f_\Omega = 1/T_\Omega = \nu/(4\pi E H^2)$ is the angular rotation frequency, and T_Ω is the system's rotation period. In Earth's core, $E \simeq 10^{-15}$, whereas $E \gtrsim 10^{-7}$ in present day direct numerical simulations of core processes (e.g., Stellmach et al., 2014; Cheng et al., 2015; Aubert et al., 2017; Schaeffer et al., 2017). The laboratory experiments are performed at four different rotations rates corresponding to approximate Ekman number values of $E = 5 \times 10^{-5}$, 2×10^{-5}, 1×10^{-5}, and 5×10^{-6}. (See Table 9.6.3 in the Appendix for precise E values.)

The convective Rossby number, Ro_C, is used to characterized the strengh of the Coriolis force relative to the buoyancy forcing (e.g., Julien et al., 1996). This number is the ratio between the typical rotation time and the free fall time:

$$Ro_C = \frac{\tau_\Omega}{\tau_{ff}} = \sqrt{\frac{\alpha g \Delta T}{4\Omega^2\, H}} = \sqrt{\frac{Ra\, E^2}{Pr}}\,. \tag{9.5}$$

The convective Rossby number can also be interpretated, in the free-fall limit, as the ratio of the inertial force ($|\vec{u}\cdot\vec{\nabla}|\vec{u}\,| \simeq U_{ff}^2/H \sim \alpha\, g\, \Delta T$) and the Coriolis force ($|2\,\vec{\Omega}\times\vec{u}| \simeq 2\,\Omega\, U_{ff}$).

The low Pr values in liquid metals act to increase Ro_C, showing that inertial effects are amplified in low Pr flows. It is often argued that substantive changes in the large-scale structure of rotating convective flow will occur in the vicinity of $Ro_C \sim 1$ (Gilman, 1977; King and Aurnou, 2013; Stevens et al., 2013; Zhong et al., 2009; Gastine et al., 2013, 2014; Soderlund et al., 2013, 2014; Horn and Shishkina, 2015; Featherstone and Miesch, 2015; Mabuchi et al., 2015).

When the convective flow structures are smaller than the system scale H, it can be argued that a locally-defined version of the convective Rossby number will better describe dynamical changes in local flow behaviors (Christensen and Aubert, 2006; Sprague et al., 2006; Julien et al., 2012b; Cheng et al., 2015). This parameter is defined as

$$Ro_\ell = \sqrt{\frac{\alpha g \, \Delta T}{4 \, \Omega^2 \, \mathcal{L}}} = \sqrt{\frac{Ra \, E^2}{Pr \, \ell}} \tag{9.6}$$

where $\mathcal{L}$ is the local horizontal scale of flow structures and $\ell = \mathcal{L}/H$ is its non-dimensional value. (Alternatively, ℓ can be thought of as the aspect ratio of the flow structures.) This local Rossby number will be defined more precisely later in the text, where it is used in Figure 9.8b.

9.2.2 Theoretical Scaling Predictions

In planar, non-rotating, non-magnetic systems, Rayleigh-Bénard convection (RBC) first develops, or onsets, via steady flow at a fixed critical value of Rayleigh number of order 10^3 where buoyancy first overcomes diffusive losses (Chandrasekhar, 1961). Since inertial effects are enhanced in low Pr fluids, RBC flows in low Pr fluids tend to attain free-fall scaling relatively soon after convective onset (e.g., Tsuji et al., 2005). Such flows often manifest in the form of system-scale turbulent overturning rolls, called large-scale circulations (LSCs).

9.2.2.1 Steady Convection

In rotating convection systems, thermal buoyancy primarily has to overcome the constraining effects of rotation (e.g., Zhang and Schubert, 2000). Theoretical analyses in a horizontally infinite plane layer (∞) subject to isothermal boundaries yield that steady (S) rotating convection onsets in the small E limit when the Rayleigh number exceeds the critical value

$$Ra_S^\infty = \frac{3\pi^4}{(2\pi^4)^{2/3}} E^{-4/3} \simeq 8.7\ E^{-4/3}\,, \tag{9.7}$$

and occurs in the form of axially elongated structures with non-dimensional horizontal flow scales

$$\ell_S^\infty = \frac{\pi}{(\frac{1}{2}\pi^2)^{1/6}}\, E^{1/3} \simeq 2.4\, E^{1/3} \tag{9.8}$$

(e.g., Chandrasekhar, 1961; Julien and Knobloch, 1998; Clune and Knobloch, 1993).

9.2.2.2 Oscillatory Convection

In rapidly rotating systems with $Pr < 0.68$, convection firsts occurs in the form of thermally driven inertial oscillations (e.g., Chandrasekhar, 1961; Julien et al., 1999; Zhang and Liao, 2009). In contrast to steady rotating convection, which is controlled by E, this oscillatory mode is controlled by the value of the thermal Ekman number E/Pr (Julien et al., 1999; Gillet et al., 2007). Oscillatory (O) convection is predicted to onset in a horizontally infinite plane (∞) at

$$Ra_O^\infty \simeq 6\frac{(\frac{1}{2}\pi^2)^{2/3}}{(1+Pr)^{1/3}} \left(\frac{E}{Pr}\right)^{-4/3} \simeq 17.4 \left(\frac{E}{Pr}\right)^{-4/3}\,, \tag{9.9}$$

with a larger horizontal length scale than that of steady convection

$$\ell_O^\infty \simeq (1+Pr)^{1/3}\, \frac{\pi}{(\frac{1}{2}\pi^2)^{1/6}} \left(\frac{E}{Pr}\right)^{1/3} \simeq 2.4 \left(\frac{E}{Pr}\right)^{1/3}. \tag{9.10}$$

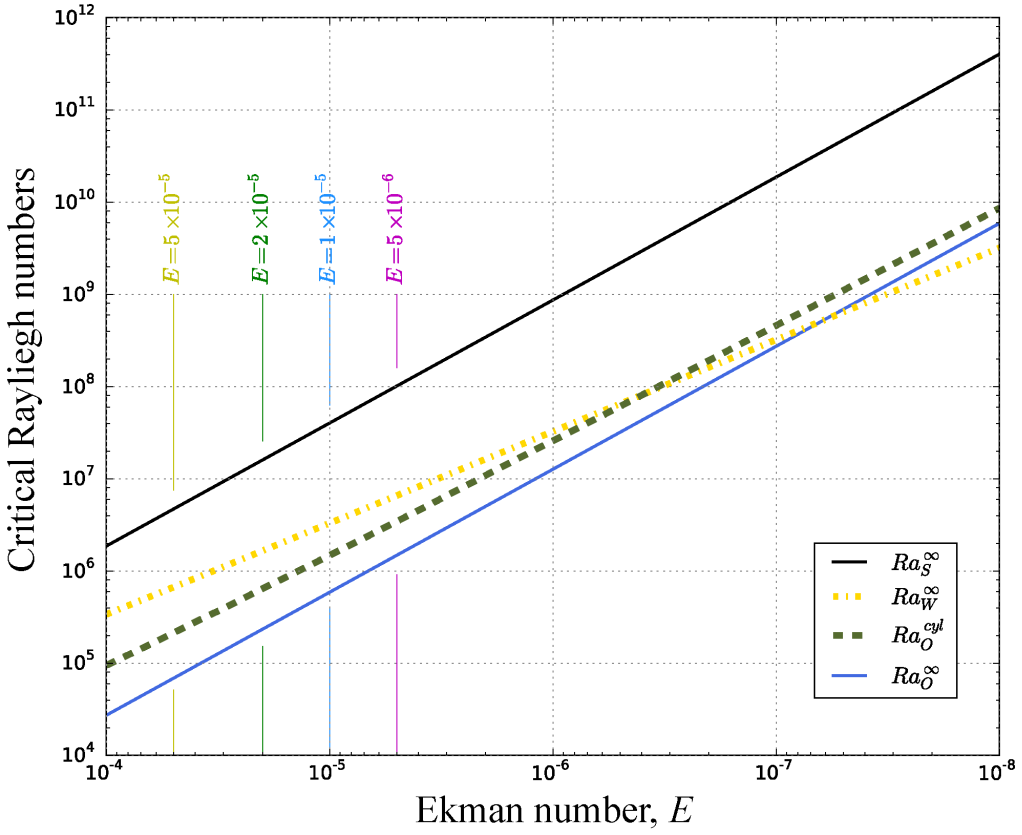

Figure 9.1: Rayleigh numbers at convective onset plotted as a function of the Ekman number for parameters of our laboratory experiments, aspect ratio $\Gamma = 1.94$ and Prandtl number $Pr \simeq 0.025$. The solid blue and black lines, respectively, denote the plane layer theoretical estimates for the oscillatory convection Ra_O^∞ and steady convection Ra_S^∞. The dot-dashed yellow line denotes the onset estimates for the wall modes in a semi-infinite layer Ra_W^∞ and the dot-dashed yellow line marks the exact solutions in a cylinder Ra_O^{cyl}, both taken from (Zhang and Liao, 2009).

The oscillation frequency at the onset of convective motions, normalized by f_Ω, is estimated to be:

$$f_O^\infty \simeq 4\pi \frac{(2-3Pr^2)^{1/2}}{(1+Pr^2)^{1/3}} \left(\frac{1}{2}\pi^2\right)^{1/3} \left(\frac{E}{Pr}\right)^{1/3} \simeq 4.8 \left(\frac{E}{Pr}\right)^{1/3}. \tag{9.11}$$

The right hand expressions in (9.9) - (9.11) hold for $Pr \ll 1$.

Comparing the linear theoretical predictions for steady and oscillatory low Pr convection yields

$$Ra_O^\infty / Ra_S^\infty \simeq 2Pr^{4/3} \quad \text{and} \quad \ell_O^\infty / \ell_S^\infty \simeq Pr^{-1/3}. \tag{9.12}$$

E	Ra_O^∞	f_O^∞	Ra_O^{cyl}	f_O^{cyl}	Ra_W^∞	f_W^∞	Ra_s^∞
5×10^{-5}	6.91×10^4	0.61	2.15×10^5	0.455	6.71×10^5	0.210	4.72×10^6
2×10^{-5}	2.34×10^5	0.45	6.42×10^5	0.366	1.65×10^6	0.0898	1.60×10^7
1×10^{-5}	5.90×10^5	0.35	1.48×10^6	0.281	3.28×10^6	0.0465	4.04×10^7
5×10^{-6}	1.49×10^6	0.28	3.45×10^6	0.232	6.52×10^6	0.0239	1.02×10^8

Table 9.1: Asymptotic estimates of liquid gallium ($Pr \simeq 0.025$) onset parameter values in a horizontally infinite plane layer geometry (∞) subject to isothermal boundary conditions, and in cylindrical geometry (cyl) with no-slip boundaries and aspect ratio $\Gamma = 1.94 = D/H$. Column 1: Experimental Ekman number values. Columns 2 and 3: Rayleigh number and frequency at the onset of oscillatory convection. Columns 4 and 5: Oscillatory bulk onset values in a finite cylinder from Zhang and Liao (2009). Columns 6 and 7: Onset values for sidewall modes in a semi-infinite layer with non-slip vertical wall (Liao et al., 2006). Column 8: Rayleigh number at the onset of steady convection. All frequencies reported here, and throughout this study, are normalized by f_Ω.

The left-hand ratio in (9.12) implies that, at a given E, the value of Ra_O^∞ will be roughly 70 times smaller than Ra_S^∞ in gallium ($Pr \simeq 0.025$). In conjunction with oscillatory convection's lower critical Rayleigh number, the asymptotic predictions for the characteristic horizontal length scale of oscillatory motions in gallium are approximately 3.4 times larger than the corresponding scale for steady rotating convective flows. This likely explains the differences in characteristic flow scale found in the low and high Pr simulations shown in (Calkins et al., 2012b).

Our experiments are carried out, not in an laterally infinite fluid layer, but instead in a finite-volume $\Gamma = 1.94$ cylindrical container. It is expected then that fluid layer geometrical effects have to be taken into account to accurately predict the convective onset parameter values (e.g., Goldstein et al., 1994). To do so, we employ the theoretical results of Zhang and Liao (2009), which predict that low Pr rotating convection cylindrical systems (cyl) first occurs as container-scale oscillatory inertial modes. We use their small E asymptotic analyses to estimate the Rayleigh number, oscillation frequency and modal structure at onset by minimizing equations (4.21) and (4.22) in Zhang and Liao (2009). This critical Rayleigh number is denoted Ra_O^{cyl} and the oscillation frequency, normalized by f_Ω, is denoted f_O^{cyl}.

E	Ra_O^∞/Ra_O^{cyl}	Ra_O^{cyl}	Ra_W^∞/Ra_O^{cyl}	Ra_s^∞/Ra_O^{cyl}
5×10^{-5}	0.321	2.15×10^5	3.12	22.0
2×10^{-5}	0.365	6.42×10^5	2.57	24.9
1×10^{-5}	0.399	1.48×10^6	2.23	27.3
5×10^{-6}	0.432	3.45×10^6	1.90	29.6

Table 9.2: Onset Rayleigh numbers relative to Ra_O^{cyl} from Zhang and Liao (2009).

9.2.2.3 Wall Modes

The existence of vertical boundaries can help release the rotational constraint on the fluid. In this case, so-called 'wall modes' develop in the form of precessing thermal waves that travel around the periphery of the tank (e.g., Zhong et al., 1991; Herrmann and Busse, 1993; Bajaj et al., 2002). Following Liao et al. (2006) and Zhang and Liao (2009), wall modes are predicted to first develop in a semi-infinite channel with a non-slip, thermally-insulating wall at

$$Ra_W^\infty \simeq 31.8E^{-1} + 46.5E^{-2/3} \tag{9.13}$$

with azimuthal wavenumber

$$m_W^\infty = \frac{2\pi H}{2\ell_W^\infty} \simeq \Gamma\left(3.03 - 17.5E^{1/3}\right) , \tag{9.14}$$

where we take $2\ell_W^\infty$ as the wall mode wavelength and note that (9.14) applies at the tank's periphery where the wall modes are localized. Furthermore, (9.14) is formally valid in the limit of low E and, practically, remains a positive quantity only for $E \lesssim 5\times10^{-3}$. Normalizing by f_Ω, the wall modes precess in azimuth around the sidewall of the tank with a retrograde drift frequency of

$$f_W^\infty \simeq 131.8\left(\frac{E}{Pr}\right) - 1464.5\left(\frac{E^{4/3}}{Pr}\right) . \tag{9.15}$$

Figure 9.1 shows the Rayleigh number predictions (9.7), (9.9), (9.13) and the computed values of Ra_O^{cyl}, all plotted as a function of the Ekman number and employing our experimentally fixed values of $\Gamma = 1.94$ and $Pr \simeq 0.025$. The thin vertical colored lines mark the four E values that are investigated here.

The factor of $\sim$70 offset between Ra_S^∞ (solid black line) and Ra_O^∞ (solid blue line) holds for all E values. The computed values of Ra_O^{cyl} (dashed green line) are approximately three times greater than Ra_O^∞ at high E values where boundary dissipation effects are strongest. However, Ra_O^{cyl} trends towards Ra_O^∞ with decreasing E, as expected.

The dot-dashed yellow line in Figure 9.1 denotes the critical Rayleigh number for wall modes, based on (9.13). Due to gallium's low Pr value, oscillatory convective motions develop before wall modes for $E \gtrsim 5 \times 10^{-7}$. Thus, the regime in which wall modes are the onset mode cannot be investigated here since all our experiments are performed at $E > 10^{-6}$.

The theoretical onset parameter predictions are given in Table 9.1 for the four Ekman numbers of our survey. Table 9.2 contains ratios of the critical Rayleigh numbers relative to the Ra_O^{cyl} predictions from Zhang and Liao (2009). In particular, we point out that $Ra_S^\infty/Ra_O^{cyl} \simeq 20$ to 30 in the rightmost column of Table 9.2. In all the laboratory experiments, however, the values of $Ra/Ra_O^{cyl} \lesssim 12$, which implies that none of the behaviors found in our experiments are the result of steady rotating convective flow processes. Thus, the quasi-steady columnar convection modes that dominate models of $Pr \gtrsim 1$ rotating convection (e.g., Grooms et al., 2010; King and Aurnou, 2012; Gastine et al., 2016) and dynamo action (e.g., Jones, 2011; Christensen, 2011; Schaeffer et al., 2017) do not exist in the experimental simulations carried out here.

9.3 Experimental set-up

The laboratory set-up consists of a Rayleigh Bénard convection (RBC) device that is seated on a rotating pedestal, as shown in Figure 9.2. In this study, we use this device to perform 15 non-rotating, RBC cases and more than 60 rotating convection (RC) cases. All the experiments are carried out in a axially aligned cylinder container with a height $H = 10.0$ cm, and an inner diameter $D = 19.4$ cm, such that the aspect ratio is fixed at $\Gamma = 1.94$. The cylindrical sidewall is made of Reynolds R-Cast acrylic, which has a thermal conductivity of $k = 0.2$ W/(m K), which is less than 1% that of gallium. The fluid is heated from below by a non-inductively wound, electrical resistance element. The input power in our experiments

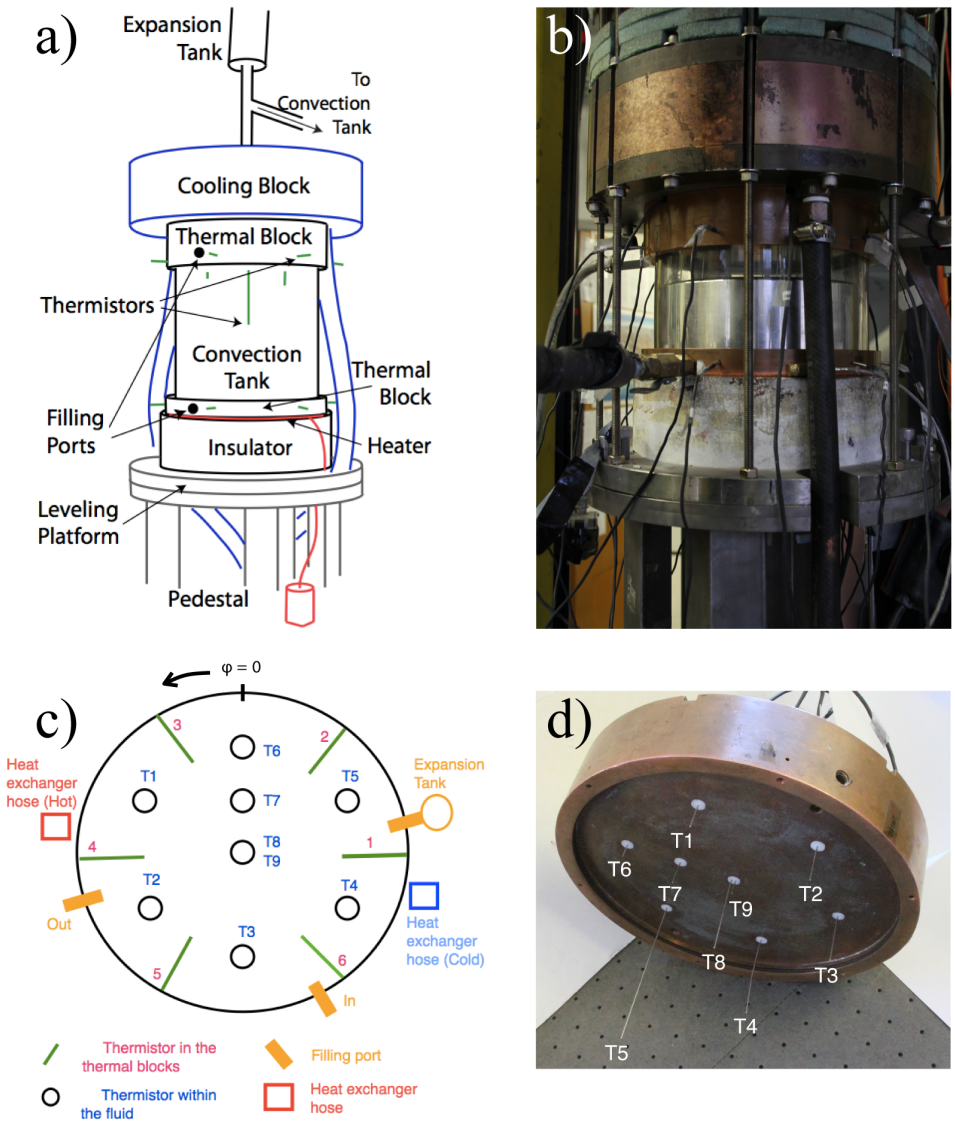

Figure 9.2: **a)** Schematic of the experimental set-up, adapted from King et al. (2012). **b)** Image of the experimental set-up, while the tank is being filled with gallium. For scale, the acrylic sidewall outer diameter is 20.0 cm. **c)** Top view schematic of the positions of the thermistors in and below the top thermal block. **d)** Oblique view of the top thermal block showing internal thermistors T1 through T9.

varies from 10 W to 2 kW. This heater is placed below a copper bottom thermal block of 1.5 cm thickness. Heat is removed from the system by a double-spiral wound heat exchanger maintained at a constant temperature by a Thermo-NESLab HX-300 precision thermal bath. This heat exchanger is placed above a copper top thermal block of 4 cm thickness. The vertical temperature difference across the fluid layer, ΔT, is measured using two arrays of six thermistors located 2 mm above and below the fluid layer, respectively, in the top and bottom thermal block. The temperature drop from the bottom to the top of the tank varies from 1°C to 50°C and the mean fluid temperature varies from 36°C to 55°C. For example, the green lines in Figure 9.2c show the locations of the 6 thermistors that are embedded in the top thermal block. In addition, 9 thermistors are placed inside the fluid layer, as shown in Figure 9.2c and Figure 9.2d. The exact location of these internal thermistors are given in Appendix 9.6.1. Temperatures and heating rate are via a National Instruments data acquisition system that is located in the rotating frame and acquires data typically at 10 samples per second. We assume the system to be equilibrated when the mean temperature, $\overline{T}$, on each thermistor does not change by more than 1% during the previous 30 minutes. We then record equilibrated data for up to 10 hours ($\sim 45\tau_\kappa$). The tank is insulated on all sides by two layers of thermal insulating materials. The outer layer is a ~ 5 cm thick of Insulfrax fiberous insulation and the second layer is a ~ 10 cm thick layer of closed cell foam. K-type thermocouples placed within the two insulation layers enable us to estimate the sidewall heat losses. The motion of the rotating pedestal is controlled by a belt-driven brushless servomotor. The rotation rate varies from 0 to 60 revolution per minutes (rpm). In this study, four rotation rates were investigated: 3.06, 8.17, 16.33 and 32.66 rpm.

For further device details, see the supplementary material in King et al. (2012).

9.3.1 Gallium properties

The density of liquid gallium is taken to vary with temperature as

$$\rho(T) = \rho_{mp}(1 - \alpha(T - T_{mp})) \tag{9.16}$$

where $\rho_{mp} = 6.09 \times 10^3$ kg/m^3 is the density at the melting point and $\alpha = 1.25 \times 10^{-4}$ K^{-1} is the thermal expansion coefficient and $T_{mp} = 29.8°$ C is the melting point. These values are in good agreement with Assael et al. (2012); Spells (1936); Brandes and Brook (1992).

Gallium's specific heat capacity, C_p, is only weakly temperature dependent and these variations are usually smaller than the accuracy of the measurement over the temperature range of our experiments. Thus, we chose a constant value of

$$C_p = 397.6 \text{ J/(kg K)} \tag{9.17}$$

as reported in Brandes and Brook (1992) and used in prior studies with this device (e.g., King and Aurnou, 2015).

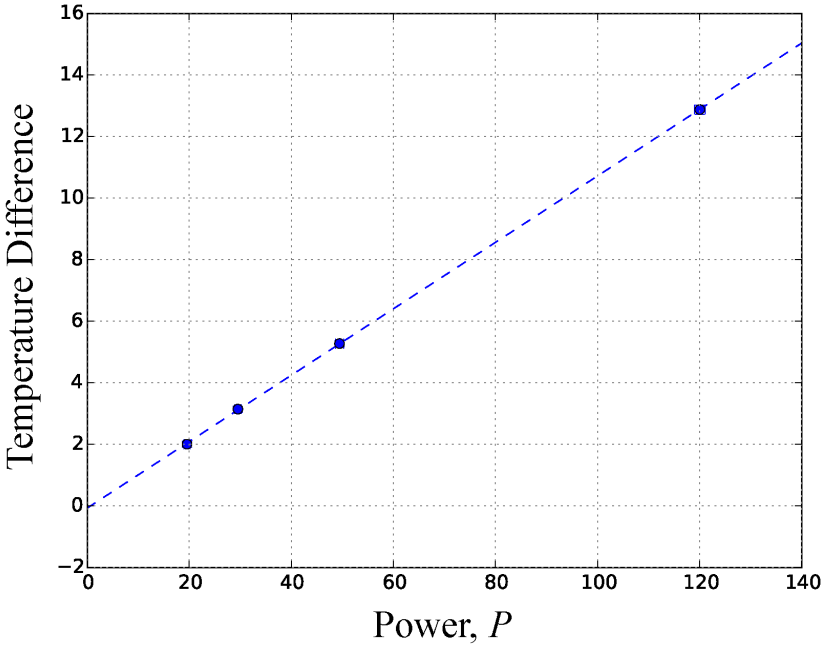

Figure 9.3: Vertical temperature difference, ΔT, measured versus the input power, P, for the four thermal conduction experiments realized. The dashed blue line shows the best linear fit $\Delta T = 0.1079\, P - 0.067$. These data are reported in Appendix 9.6.2.

9.3.1.1 Thermal conductivity measurements

In relatively high rotation rate, low thermal forcing cases, the fluid is convectively stable and the heat tranfered across the gallium conductively. These conduction cases allow us to make *in situ* measurement of the thermal conductivity, k, of the gallium within our set-up. Figure 9.3 shows the temperature difference between the top and the bottom of the tank, ΔT [K], plotted versus the input power, P [W], for the four conduction cases carried out. The dashed line is a linear regression $\Delta T = \beta P + b$. In conjunction with Fourier's law of conduction, the value of the slope, $\beta = 0.1079$ K/W, gives a thermal conductivity value

$$k = H/(\pi R_i^2 \beta) = 31.3 \pm 0.1 \text{ W/(m K)} \tag{9.18}$$

where $R_i = D/2 = 0.097$ m is the inner radius of the acrylic cylinder. The coefficient of determination of this linear fit is $R^2 = 0.9999$. Further, the intercept of the linear regression, $b = -0.067$ K, is close to zero and is small compared to the temperature differences in these conduction cases ($\lesssim 1\%$). This suggests that our thermal conductivity measurement is relatively accurate. In addition, it agrees well with other, independent laboratory estimations (Aurnou and Olson, 2001; King and Aurnou, 2013).

9.3.1.2 Viscosity measurements

The viscosity of liquid gallium is difficult to precisely measure for a number of reasons, including its affinity to oxygen. As soon as liquid gallium comes in contact with the atmosphere, gallium oxides form on its free surface and then populate the bulk fluid. These oxides can affect the measurement of the viscosity. To minimize this phenomenon, our entire experimental system is flushed with argon. Following Brito et al. (2001), we cycle our 99.99% purity liquid gallium through a 5% hydrochloric acid solution before filling the tank (e.g., https://www.youtube.com/watch?v=G1qwMHkboDY).

Even under well-controlled conditions, however, measurements of liquid gallium's dynamic viscosity, $\eta = \rho\nu$, vary by as much 30% between differing studies (Spells, 1936; Grosse,

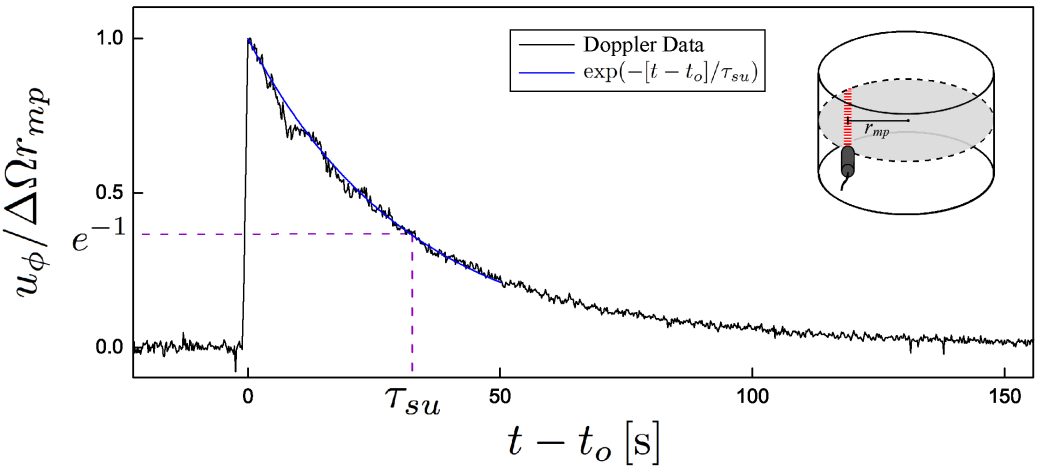

Figure 9.4: Acoustic Doppler velocimetry measurement (black line) of a spin-up experiment carried out at $T = 35.8°$ C. The data shows the temporal evolution of the midplane azimuthal velocity, u_ϕ, normalized by the maximum predicted spin-up velocity, $(\Delta\Omega\, r_{mp})$. Here $\Delta\Omega$ is the impulsive change in rotation rate occurring at time t_o, and r_{mp} is the radial position at the mid-point along the Doppler chord (inset). We denote the spin-up time, τ_{su}, as the point in the time series where the normalized velocity reaches a value of $1/e$ (dashed purple lines). The blue line shows a plot of an exponential fall off with characteristic time scale τ_{su}.

1961; Genrikh et al., 1972; Assael et al., 2012; Xu et al., 2012; Brandes and Brook, 1992; Iida et al., 1975, 2006). To address this issue, we have carried out a suite set of experiments in which we use acoustic Doppler velocimetry to measure linear spin up in our tank of gallium under nearly isothermal conditions (cf. Brito et al., 2004). In these experiments, the tank is spun-up in less than 1 second (fixed 4 rpm/s ramp) from an initial rotation rate Ω_i to $\Omega_i + \Delta\Omega$. Azimuthal velocity, u_ϕ, measurements are made along a mid-plane chord (inset, Figure 9.4). The velocity data are averaged around the mid-point (mp) of the chord, which is located 73 to 77 mm from the ultrasonic transducer and at a radial position $r_{mp} \simeq 0.70 R_i$.

Figure 9.4 shows normalized Doppler velocity measurements, $u_\phi/\Delta\Omega r_{mp}$, versus time shifted relative to t_o, the instant of peak measured velocity. The fluid temperature is $T = 35.8°$ C here and the spin-up goes from 40.0 rpm to 44.0 rpm ($\Delta\Omega/\Omega_i = 0.1$). The fluid responds via an exponential temporal adjustment to the new solid-body rotation rate. This

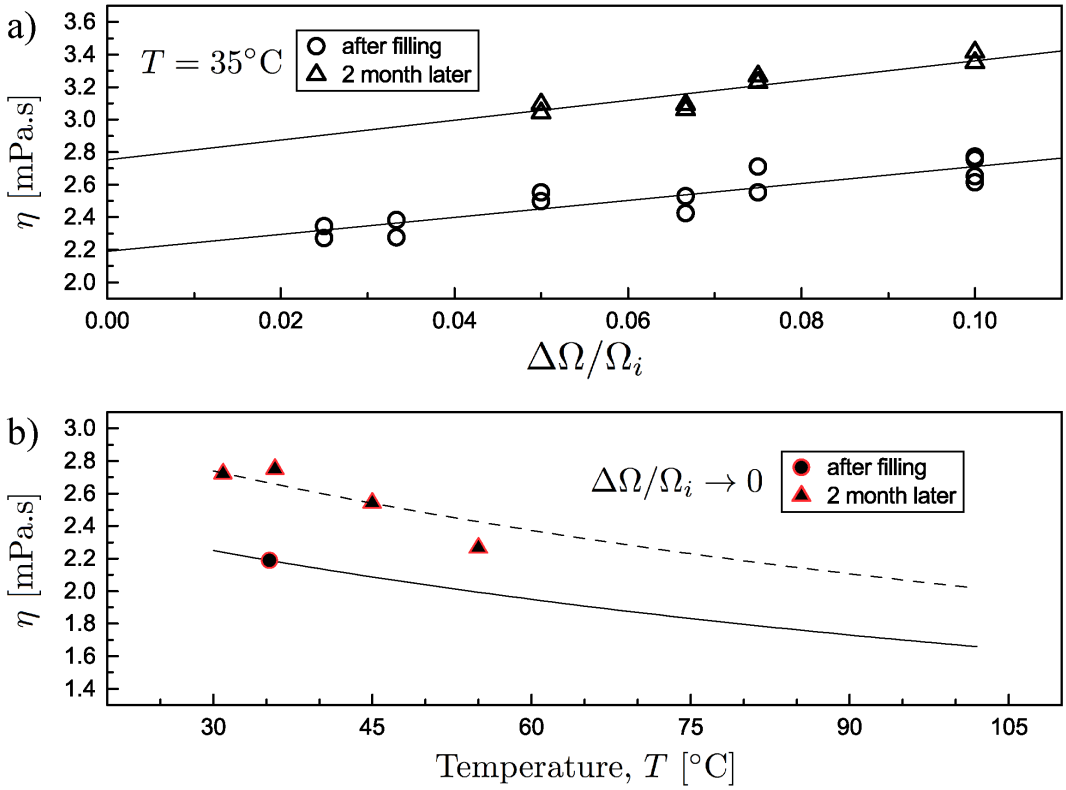

Figure 9.5: *In situ* dynamic viscosity estimates made from spin-up experiments. a) Estimates for fluid at $T \simeq 35°$ C as a function of spin-up amplitude $\Delta\Omega/\Omega_i$. The hollow circles (triangles) denote data acquired roughly 1 week (2 months) after the container was filled with gallium. b) Viscosity extrapolations to zero forcing amplitude at different fluid temperatures.

occurs on the spin-up time scale:

$$\tau_{su} = (8E)^{-1/2}\,\Omega_i^{-1} = H/(2\sqrt{\nu\Omega_i}) \tag{9.19}$$

(Greenspan and Howard, 1963; Greenspan, 1969; Warn-Varnas et al., 1978). We estimate τ_{su} here as the time at which the $u_\phi/\Delta\Omega r_{mp} = \exp(-1)$. From τ_{su}, the dynamic viscosity is found by recasting (9.19) as

$$\eta = \rho H^2/\left(4\Omega_i \tau_{su}^2\right)\,. \tag{9.20}$$

Figure 9.5a shows spin-up measurements of η for fluid at $T \simeq 35°$ C and for a range of Ω_i and $\Delta\Omega/\Omega_i$ values. The hollow circles correspond to spin-up measurements acquired the same week that we filled the tank with cleaned gallium. The hollow triangles correspond to measurements made two months later. The fluid viscosity increases over this 2 month time window. This is caused by the existence of an intermetallic phase that develops on the tank's horizontal boundaries. Although relatively thin ($\lesssim 1$ mm thick), this heterogeneous layer increases the mechanical coupling relative to the initially smooth walls present at the time of the fill. This layer does not, however, change the bulk properties of the fluid; heat transfer measurements were repeatable over the 2 month window for RBC cases made with the same input heating.

For each suite of experiments made at a fixed time, the viscosity estimates in Figure 9.5a increase with increasing spin-up amplitude $\Delta\Omega/\Omega_i$. We account for this by linearly extrapolating the viscosity data to $\Delta\Omega/\Omega_i = 0$ (filled symbols with red outlines). These extrapolated values, which we take to be working viscosity of the fluid, are plotted in Figure 9.5b. Four different temperatures were measured two months after the tank was filled, whereas measurements were only made at near 35° C just after the tank was filled.

We best fit our gallium viscosity data as a function of temperature using the Andrade (1934) formulation,

$$\eta = \eta_0\,\exp(E_a/R\mathcal{T})\,, \tag{9.21}$$

where the activation energy is $E_a = 4000$ J/mol, the gas constant is $R = 8.3144$ J/(mol

K) and $\mathcal{T}$ is the absolute temperature in degrees Kelvin. This functional form was first employed by Grosse (1961) to fit the gallium viscosity data of Spells (1936), and has been used broadly since (Brandes and Brook, 1992; Braunsfurth et al., 1997; King and Aurnou, 2013). We argue here that our '2 month' data is reasonably well fit by (9.21) with a viscosity coefficient of $\eta_o = 0.56$ mPa s (dashed line in Figure 9.5b). However, we believe the $T = 35°$ C data acquired just after filling the tank more accurately characterizes the bulk viscosity of the fluid. This data yields a viscosity coefficient value of $\eta_0 = 0.46$ mPa s (solid line in Figure 9.5b), in adequate agreement with the values of Spells (1936); Iida et al. (1975); Brandes and Brook (1992); King and Aurnou (2013). Thus, we use $\eta_0 = 0.46$ mPa s in (9.21) in all the ensuing viscosity estimates employed in this study.

9.4 Results

9.4.1 Heat Transfer

We first present heat transfer measurements from non-rotating ($E = \infty$) Rayleigh-Bénard convection (RBC) cases. These provide a baseline for comparison with other low Pr RBC studies (e.g., Scheel and Schumacher, 2016). In addition, heat transfer in RBC cases approximates the upper bounding values for RC datasets (Cheng et al., 2015; Gastine et al., 2016).

The temperature drop across the tank varied with the heat power as $\Delta T = 0.602 \pm 0.02\, P^{0.794\pm0.007}$. This power law is in good quantitative agreement with prior RBC data taken with this device by King and Aurnou (2013) using a $\Gamma = 0.97$ stainless steel sidewall tank. The exponents agree to within the uncertainties of the measurements whereas the coefficients differ by roughly 8%. This variation in the coefficient may be due to the different aspect ratios and sidewall materials employed.

The efficiency of heat transfer is expressed nondimensionally in terms of the Nusselt number,

$$Nu = \frac{Q_{tot}}{Q_{cond}} = \frac{P\,H}{k\,\Delta T\,A}\,, \tag{9.22}$$

which is the ratio of the total vertical heat flux $Q_{tot} = P/A$ through the fluid layer of horizontal cross-sectional area $A = \pi R_i^2$, and the conductive flux $Q_{cond} = k\Delta T/H$. This parameter equals unity when thermal conduction is the sole heat transport process and exceeds unity whenever convective motions also take part in fluxing heat across the fluid layer.

Figure 9.6 shows Nu plotted as a function of the buoyancy forcing, Ra. The red-filled circles mark the RBC cases. The best-fit power law to this RBC data gives $Nu = (0.151 \pm 0.02)\, Ra^{0.256\pm0.01}$. The power law exponent value is in good agreement with those reported in the laboratory studies of Rossby (1969) and King and Aurnou (2013), as well as in the high resolution $Pr = 0.021$ numerical simulations of Scheel and Schumacher (2016). However, the coefficient is nearly 20% smaller than the value found in King and Aurnou (2013). In addition to aspect ratio (Bailon-Cuba et al., 2010) and sidewall conductivity differences (e.g., Ahlers, 2000), the coefficient may also be affected by small differences in our material properties parameterizations and in the mean fluid temperature values at a given Ra.

Rotating convective heat transfer data is also displayed in Figure 9.6. Mustard coloured filled symbols mark the $E = 5 \times 10^{-5}$ cases. Green, blue and magneta symbols mark $E = 2 \times 10^{-5}$, $E = 10^{-5}$ and $E = 5 \times 10^{-6}$ cases, respectively, corresponding to respective tank rotation rates of close to 3, 8, 16 and 32 rpm. The onset of convection occurs when Nu increases beyond unity in each E-dataset. As expected from (9.9), the convective onset occurs at successively higher Ra values with decreasing values of the Ekman number. The supercritical data shows a region of relatively weak convective heat transfer in the $E = 2 \times 10^{-5}$, 10^{-5} and 5×10^{-6} datasets. A regime of weak heat transfer scaling also exists in RBC in metals near onset (Chiffaudel et al., 1987; Kek and Müller, 1993). However, in low Pr RBC, the weak heat transfer regimes arises due to a balance between viscous and weak thermal buoyancy forces. In contrast, in our RC data, this weak heat transfer regime arises because the inertially-dominated, oscillatory convection that develops just past onset transfers no net mass across the fluid layer, and, thus, is inefficient at transferring heat.

Figure 9.7 shows the Nusselt number plotted versus the Rayleigh number normalized by its critical value in a cylinder, Ra/Ra_O^{cyl}. The values of Ra_O^{cyl} are given in third column of

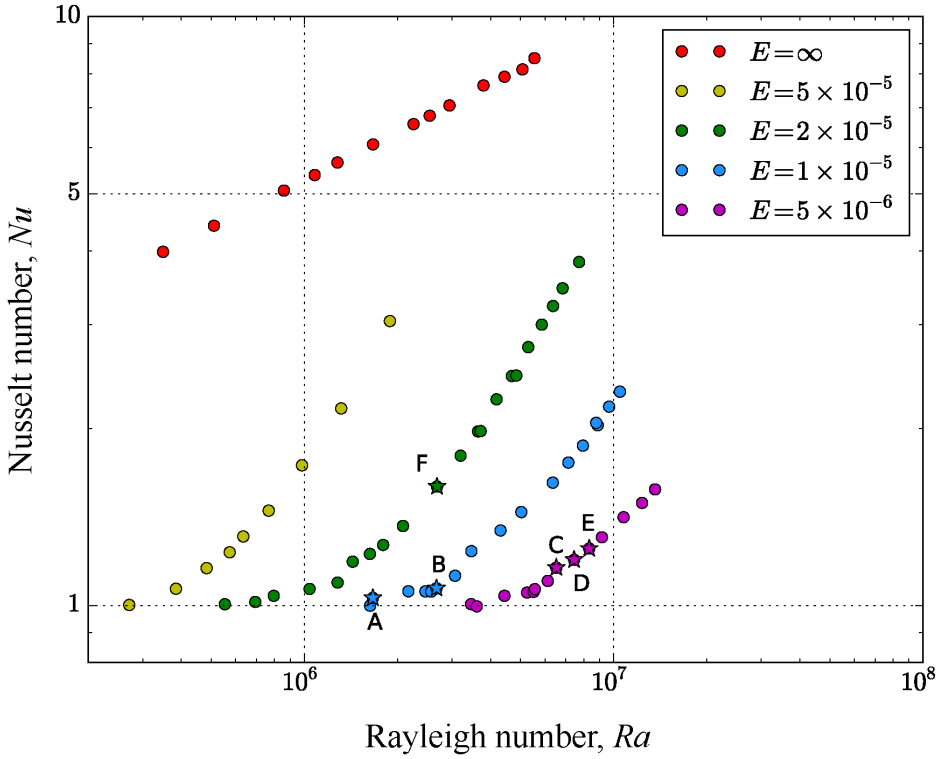

Figure 9.6: The Nusselt number, Nu, plotted versus the Rayleigh number, Ra, for all the rotating (RC) and non-rotating (RBC) cases. The corresponding Ekman number is indicated with the symbol color. The cases denoted A through F (star symbols) are considered in detail in the following sections.

Table 9.2. The Nu-(Ra/Ra_O^{cyl}) data collapse well, which implies that Ra_O^{cyl} as formulated by Zhang and Liao (2009) adequately describes the onset of convection in our laboratory experiments. If Ra_O^{∞} better described the onset of convection, then the Nu data would first depart from unity at values of $Ra/Ra_O^{cyl} \simeq 0.3$ (second column in Table 9.2). The results in Figure 9.7 shows that is not the case (cf. Ribeiro et al., 2015).

The triangles in Figure 9.7 denote cases at or just after the onset of sidewall convection, whereas the rhombi denote cases where the wall modes are the dominant signal in the spectra. The wall modes come to dominate the heat transfer, causing the increased heat transfer scaling at $Ra/Ra_O^{cyl} \gtrsim 2$. In the precessing frame of the wall modes, the wall modes provide a steadily transfer mass vertically across the fluid layer. These mean flows (in the precessing frame) are far more efficient at fluxing heat than the oscillatory bulk motions

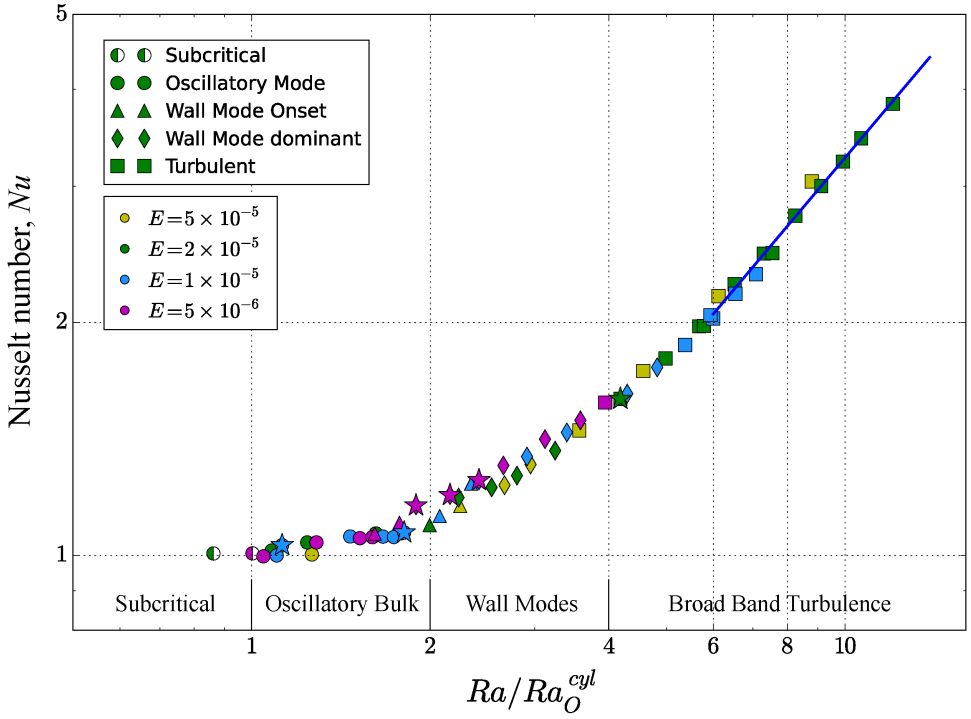

Figure 9.7: Nusselt number plotted versus supercriticality Ra/Ra_O^{cyl} for rotating convection in gallium. Four main regimes are found: subcritical to convection; oscillatory convection in the fluid bulk; wall mode dominated convection; and broad band turbulence. In the turbulent regime, the best fit is $Nu \sim (Ra/Ra_O^{cyl})^{0.9}$ for $Ra/Ra_O^{cyl} \geq 6$, shown as the blue solid line. The star symbols mark cases 'A' through 'F' shown in Figure 9.6 and listed in Appendix 9.6.3.

that develop first in our experiments. The critical Rayleigh number for sidewall convection decreases with decreasing E. This effect can be seen in Figure 9.7 in two ways. First, the triangles move to the right in the figure as E is lowered. Second, the Nu values are 'layered' in the range $2 \lesssim Ra/Ra_O^{cyl} \lesssim 4$ with the magenta $E = 5 \times 10^{-6}$ rhombi on top and the mustard $E = 5 \times 10^{-5}$ rhombi below. The trends of each 'layer' appear to be similar, which suggests that this layering is due to the decreasing value of Ra_W^∞ as a function of decreasing E.

Broad band spectra are measured on our internal thermistors in the range $4 \lesssim Ra/Ra_O^{cyl} \lesssim 12$, as discussed in Section 9.4.2. We interpret these broad band spectral signatures to imply that rotating convective turbulence develops at $Ra/Ra_O^{cyl} \simeq 4$. Turbulent convection develops then in gallium well before steady columnar-style convection even onsets ($Ra_S^\infty/Ra_O^{cyl} \gtrsim 20$;

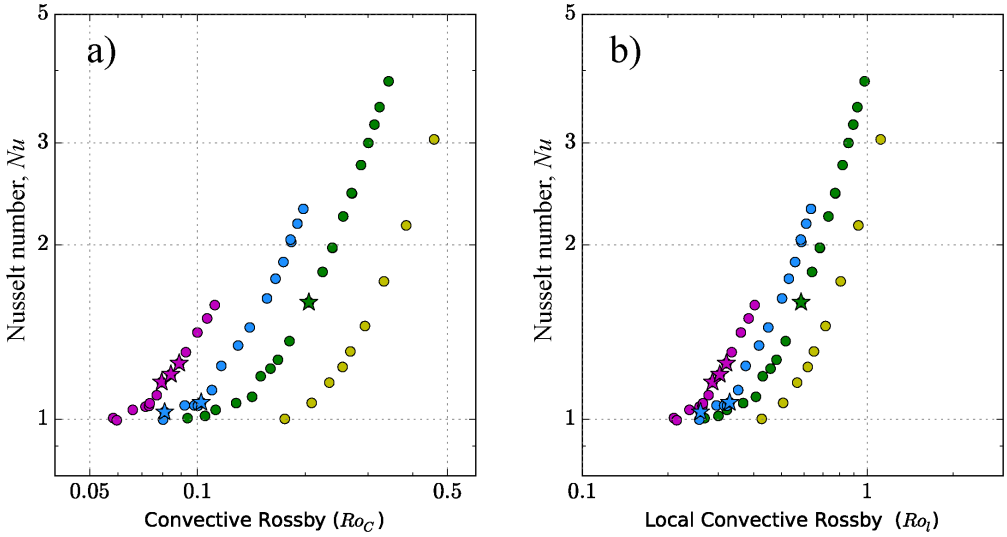

Figure 9.8: Using the same color code as in Figure 9.6, the Nusselt number is plotted versus a) the convective Rossby number, Ro_C, and b) the local convective Rossby number, Ro_ℓ, defined in (9.23). Supercriticality, Ra/Ra_O^{cyl}, collapses the heat transfer data better than either of these dynamical re-scalings.

Table 9.2), in basic agreement with Julien et al. (2012b). This behavior differs sharply from convection in $Pr > 1$ fluids, where quasi-steady rotating convection columns can exist over a significant range of supercriticalities before breaking down into geostrophic turbulence (Julien et al., 2012b; King and Aurnou, 2012; Aurnou et al., 2015; Cheng et al., 2015; Sprague et al., 2006; Horn and Shishkina, 2014; Stellmach et al., 2014; Gastine et al., 2016; Yadav et al., 2016). Thus, the path to turbulence in low Prandtl number fluids differs from that in higher Pr fluids. Further, this raises the question (which is not addressed here) as to whether the regimes of rotating convective turbulence in low Pr fluids differs in nature from those in $Pr \gtrsim 1$ fluids (e.g., Julien et al., 2012b).

The blue solid line in Figure 9.7 shows the best fit power-law, $Nu = 0.40\,(Ra/Ra_O^{cyl})^{0.91}$, to all the data with $Ra/Ra_O^{cyl} \geq 6$. This scaling differs significantly from the $Nu \sim (RaE^{4/3}Pr^{-1/3})^{3/2}$ scaling that was found in $0.3 \leq Pr \leq 1$ fluids (Julien et al., 2012a). This $Ra^{3/2}$ scaling is argued to hold in the limit of low Ro geostrophic turbulence. Our $Ra^{0.9}$ scaling differs from the prediction, but likely for good reasons: i) our data is still close to

onset and does not exhibit any asymptotic behaviors; ii) we are fitting less than a decade of data in terms of supercriticality; iii) and, as shown in Figure 9.8, the global and local convective Rossby numbers are all above 0.1 for the 'broad band' data and thus is unlikely to be in the geostrophic turbulence regime.

Using a tall tank and higher heat fluxes, King and Aurnou (2013) found that rotationally-influenced heat transfer in gallium transitioned to the RBC trend at $Ro_C \sim 1$. Figure 9.8a shows our lower Ra heat transfer data plotted versus Ro_C. Our present data is not well collapsed by Ro_C. Figure 9.8b shows Nu plotted versus a local convective Rossby, where we have chosen (9.10) as the characteristic length scale estimate, yielding

$$Ro_\ell = \sqrt{\frac{\alpha g \Delta T}{4\Omega^2 \ell_O^\infty}} = \sqrt{\frac{RaE^{5/3}}{2.4Pr^{2/3}}} \,. \tag{9.23}$$

This local parameter, which has been proposed in several dynamo studies to control the transition between dipolar and multipolar dynamo action (e.g., Christensen and Aubert, 2006), does not seem to collapse our heat transfer data either. Thus, our relatively low Ra heat transfer data are best collapsed by their supercriticality Ra/Ra_O^{cyl}, whereas the heat transfer behavior of the more strongly supercritical data in King and Aurnou (2013) appears to be better collapsed by the convective Rossby number, Ro_C.

9.4.2 Spectral analysis

Figures 9.9a, c, e, g show respective temperature time series measurements from cases A, B, C and F in Figure 9.6, each plotted for 200 rotational time units. Figures 9.9b, d, f, h show the respective temperature spectra from their equilibrated time series (typically $\gtrsim$ 2 hours in length). The blue lines correspond to data from thermistor T8, which is located at the center of the cylinder. The red lines corresponds to thermistor T4, which is located relatively close to the side wall ($r/R_i = 0.70$) and slightly below the mid-plane ($z/H = 0.43$).

The time series in the left hand column of Figure 9.9 show strongly coherent oscillations for case A and become increasingly broad band in each successive case. The spectra shown in

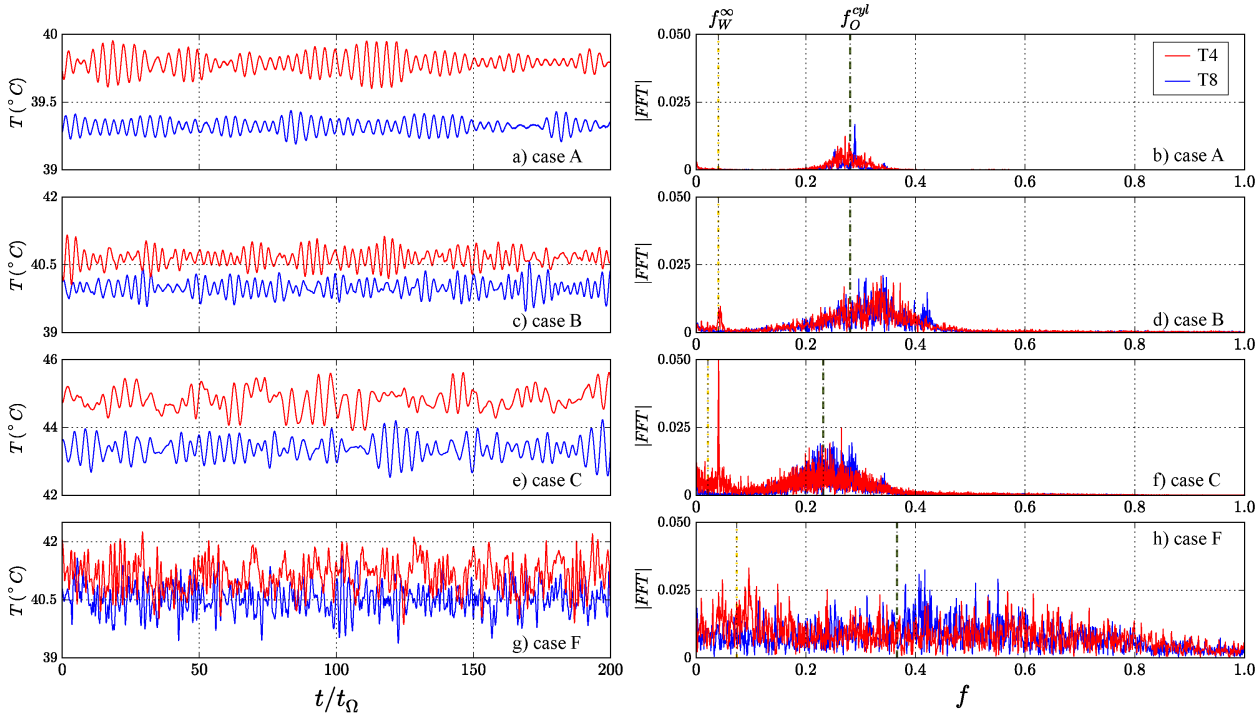

Figure 9.9: **Left Column**: Temperature time series recorded on thermistors T4 (red) and T8 (blue) in cases A, B, C, F for 200 rotation periods of the tank. **Right Column**: The Fourier transform of the temperature signals computed over 290 T_Ω for case A, over 1152 T_Ω for case B, over 3580 T_Ω for case C and over 853 t_Ω for case F. Frequencies are normalized by the rotation frequency f_Ω. The green (yellow) dashed lines corresponds to the onset frequency of the bulk oscillatory mode (wall mode).

the right hand column images are more revealing. In case A, carried out at $Ra/Ra_O^{cyl} \simeq 1.2$, oscillations exist in a finite band around the predicted value f_O^{cyl} on both thermistors. In case B, carried out at $Ra/Ra_O^{cyl} \simeq 1.9$, the width of the frequency band around f_O^{cyl} has expanded. Furthermore, there is also evidence for a wall mode on thermistor T4, located at $0.7R_i$. In case C, carried out at $Ra/Ra_O^{cyl} \simeq 1.95$, the T4 wall mode signal on is now the dominant spectral peak, reaching up to an amplitude value of 0.087. In addition, the wall mode frequency has shifted to $f = 0.0406\, f_\Omega$, which is nearly twice the predicted wall mode frequency $f_W^\infty = 0.0239\, f_\Omega$, suggesting a possible change in wall mode structure. Lastly, in case F at $Ra/Ra_O^{cyl} \simeq 4$, the coherent oscillatory signals are no longer apparent. However, the spectrum of the side thermistor T4 has more power near the theoretical wall mode frequency than the central thermistor T8, which has slightly more power closer to the bulk oscillation frequency. This suggests that the near onset modes may still be intact, but are harder to

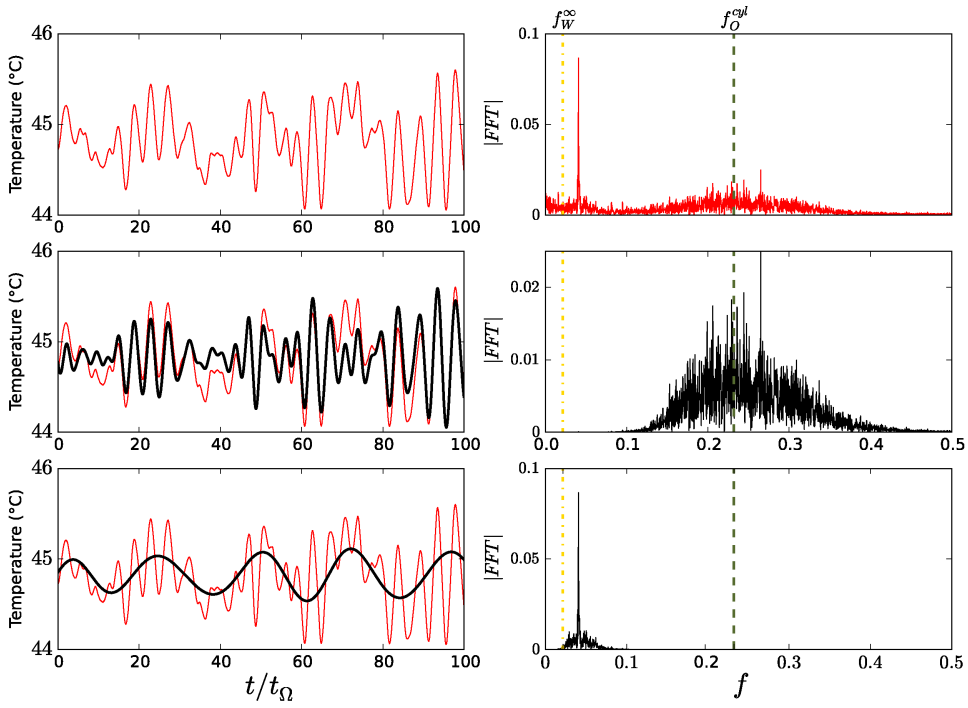

Figure 9.10: Band-pass filtering of the case C, T4 temperature data ($E = 5 \times 10^{-6}$; $Ra/Ra_O^{cyl} = 1.99$). Red lines show raw T4 data; black lines show filtered data. The left hand column shows time series data, whereas the right hand column shows spectra. Top row: raw T4 data. Middle row: band-pass filtering around f_O^{exp}. Bottom row: band-pass filtering around $f_W^{\exp}$.

decipher in the broad band spectra generated on both sensors at these higher Ra/Ra_O^{cyl} values.

Our laboratory data provide the first experimental evidence of multi-modal flow in low Pr rotating convection. To demonstrate this unequivocally, Figure 9.10 shows a more detailed analysis of the case C, T4 temperature data shown in Figures 9.9e,f. The top row shows the raw T4 data, similar to that of Figure 9.9. The middle and bottom rows show the data, respectively, band-pass filtered around f_O^{cyl} and f_W^∞. Red lines represent the raw data, whereas black lines show the band-passed signals. The band-pass operation was accomplished by convolving the T4 signal with a transfer function, $H(f)$, defined as

$$H(f) = \left[1 + i\left(\frac{f}{f_c} - \frac{f_c}{f}\right)^3\right]^{-1} \tag{9.24}$$

with $f_c = 0.25 f_\Omega$ in the middle row and $f_c = 0.041 f_\Omega$ in the lower row. This filter was chosen so that the band-pass region was wide enough to keep the relevant oscillatory modes.

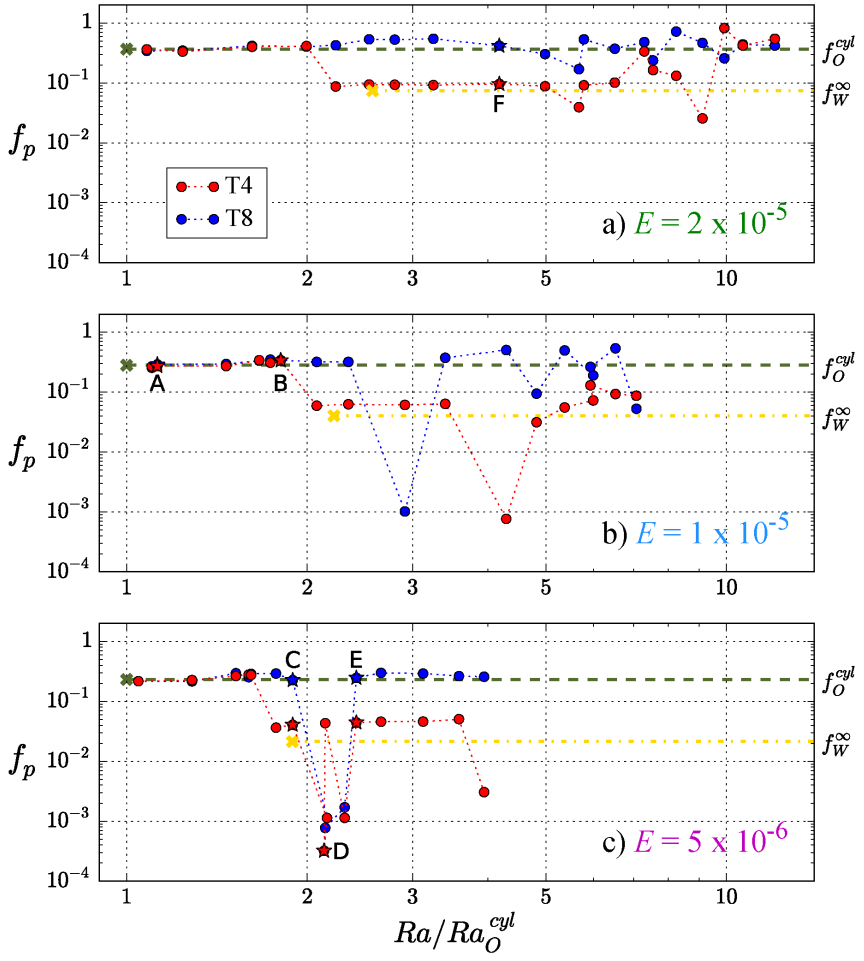

Figure 9.11: Dominant spectral frequency normalized by the rotation frequency, f_p, plotted versus Ra/Ra_O^{cyl}. a) $E = 2 \times 10^{-5}$; b) $E = 1 \times 10^{-5}$ and c) $E = 5 \times 10^{-6}$. The red (blue) symbols correspond to T4 (T8) data. The dashed green and yellow lines denote the onset frequencies f_O^{cyl} and f_W^{∞}, whereas the green and yellow x's mark Ra_O^{cyl} and Ra_W^{∞}, respectively.

The filtered signal around f_O^{exp} shows the same qualitative characteristics as the signal in Figure 9.9a. The time series is oscillatory within a lower frequency envelope, as expected for a finite range of frequencies centered around f_O^{exp}. The filtered signal around f_W^{exp} shows the impact of the wall mode on the temperature field relatively far from the the sidewall. This wall mode signal is recorded on T4 because of the large-amplitude of the thermal oscillations

and due to the high thermal diffusivity of liquid gallium. Here a single coherent thermal oscillation dominates the band-passed signal, implying the existence of one dominant wall mode in this case. Lastly, note in comparing the two filtered time series that the wall mode signal (recorded at $0.7R_i$) is comparable in amplitude to that of the bulk oscillatory signal.

Figure 9.11 shows the frequency of the peak amplitude of the Fourier spectra, f_p, plotted as a function of Ra/Ra_O^{cyl} for each of the convection experiments carried out at a) $E = 2 \times 10^{-5}$; b) $E = 1 \times 10^{-5}$ and c) $E = 5 \times 10^{-6}$. Blue symbols correspond to the spectral peaks on thermistor T8 located at the tank's center. Red symbols correspond to thermistor T4 located at roughly 2/3 radius and near the mid-plane. The dashed green and yellow horizontal lines are the onset frequency predictions for f_O^{cyl} and f_W^{∞}, respectively. Green and yellow x's mark the left-hand endpoints of the horizontal dashed lines. These x's demarcate the estimated values of Ra_O^{cyl} and Ra_W^{∞}. Thus, the green x stays fixed at $Ra/Ra_O^{cyl} = 1$ in all three panels, whereas the yellow x moves to successively lower values with decreasing E (cf. Figure 9.1). All frequencies are normalized by f_Ω (throughout this study).

We interpret Figure 9.11 as showing the dominant processes occurring in a given experimental case. All cases with $Ra \lesssim 0.8Ra_W^{\infty}$ have $f_p \simeq f_O^{cyl}$ on both T4 and T8, indicating that the bulk oscillatory convection is indeed dominant over this range. At values slightly below Ra_W^{∞}, f_p on T4 changes to values relatively close to f_W^{∞}. Note further that this change in T4 f_p does not specify the onset value of wall mode convection. For instance, the T4 spectrum in Figure 9.9d (case B) shows significant power at f_W^{∞}, but the peak amplitude in the spectrum still resides just above f_O^{cyl}.

A non-trivial very low frequency f_p value is found to develop on both the T4 and T8 sensors in several $E = 5 \times 10^{-6}$ cases (e.g., case D). This phenomenon will be considered further in section 9.4.4.

9.4.3 Onset Estimates

Table 9.3 shows experimentally-determined onset parameter estimates for the two main modes observed, the bulk oscillatory mode and the wall mode. The onset values are found

E	Ra_O^{exp}/Ra_O^{cyl}	f_O^{exp}/f_O^{cyl}	Ra_W^{exp}/Ra_W^{∞}	f_W^{exp}/f_W^{∞}
2×10^{-5}	1.08 ± 0.05	0.96 ± 0.03	0.78 ± 0.05	0.98 ± 0.05
1×10^{-5}	1.10 ± 0.03	1.00 ± 0.03	0.81 ± 0.02	1.10 ± 0.05
5×10^{-6}	1.05 ± 0.02	0.94 ± 0.01	0.85 ± 0.01	1.17 ± 0.01

Table 9.3: Ratios of onset parameter values with theoretical predictions. Superscript "*exp*" means experimental measurement, "*cyl*" means theoretical prediction in a cylinder and "∞" means theoretical prediction of the plane layer theory. The data at $E = 5 \times 10^{-5}$ are not presented due to a lack of data sufficiently near onset.

via bifurcations in Nu to values above unity and also via detection and characterization of thermal oscillations on the internal thermistors.

The experimentally-determined Rayleigh numbers for the onset of oscillatory convection in the bulk fluid, Ra_O^{exp}, are 5% to 10% higher than the asymptotic estimates from Zhang and Liao (2009). The frequencies measured at the onset of bulk oscillatory convection are in good agreement with the theoretical predictions. Interestingly, Zhang and Liao (2009) provide some onset values from their linear stability solver. For the case at $E = 5 \times 10^{-5}$, $Pr = 0.025$ and $Gamma = 2$, they find a critical Rayleigh number for oscillatory convection that is about 5% higher than their asymptotic Ra_O^{cyl} predictions. Further, they find nearly exact agreement between the onset frequencies in their linear solutions and their asymptotics. Thus, we argue that our onset values are reasonably accurate. Further, this (circularly) suggests that our determination of fluid viscosity is accurate as well.

The wall modes have onset Ra estimates that are approximately 20% below theoretical predictions in a semi-infinite layer (Liao et al., 2006). The frequencies measured for the wall modes are near to the theoretical values for $E = 2 \times 10^{-5}$ and 1×10^{-5}. In the $E = 5 \times 10^{-6}$ experiments, the measured frequency is roughly 20% greater than expected. These discrepancies in the wall mode onset values could arise for a number of reasons. They could be due to finite geometry effects in our $\Gamma = 1.94$ container, or from imperfect sidewall thermal boundary conditions. Lastly, maybe the active bulk oscillatory convective motions affect the system near the sidewalls, such that the onset properties are altered (Geoff Vasil, private communication).

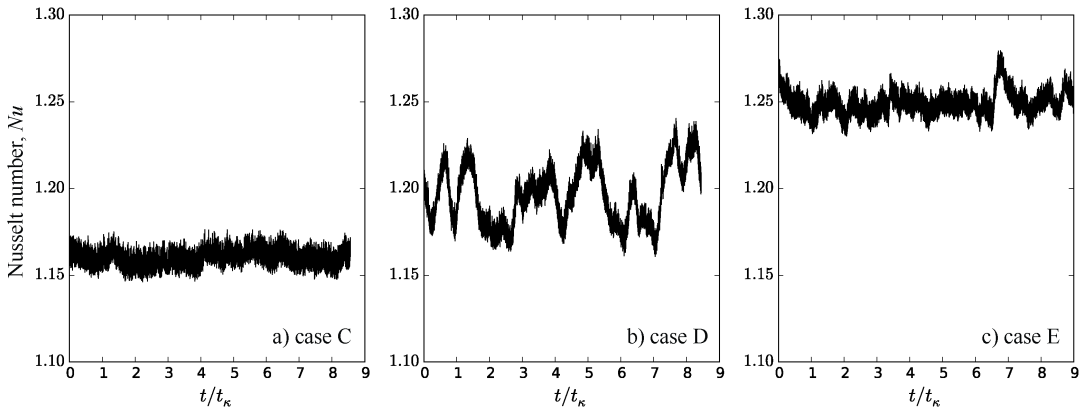

Figure 9.12: Nusselt number plotted versus time in thermal diffusion time scale units. a) case C; b) case D; c) case E.

9.4.4 Bimodal, Low-Frequency Regime

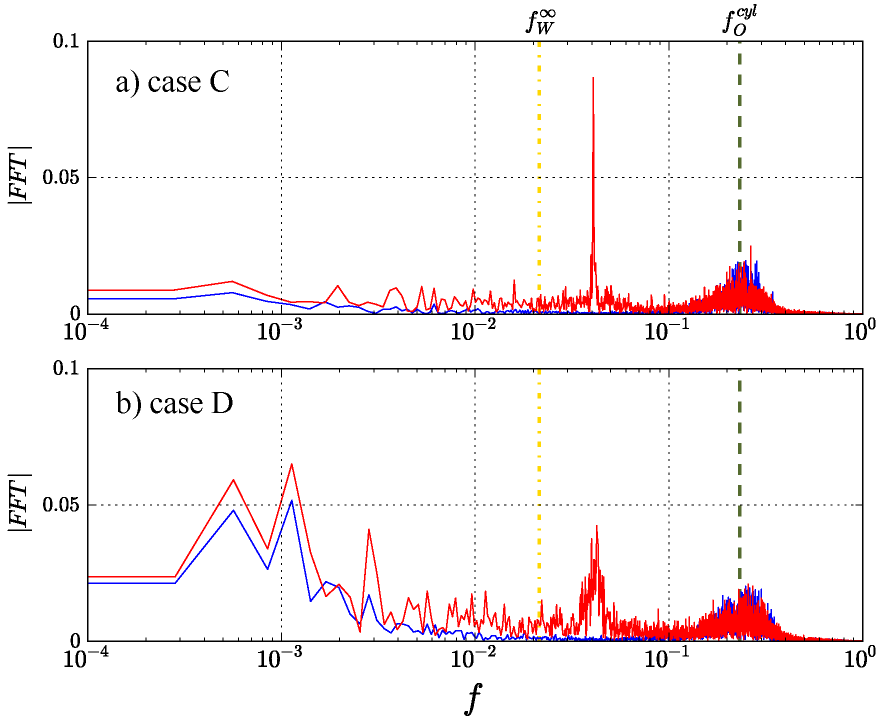

Figure 9.13: Temperature spectra from a) case C ($E = 5.09\ 10^{-6}$ and $Ra/Ra_O^{cyl} = 1.99$) and b) case D ($E = 5.01 \times 10^{-6}$ and $Ra/Ra_O^{cyl} = 2.28$). Frequencies f are normalized by the rotation frequency and are plotted in log-scale. The spectra for case E (not show) are qualitatively similar to those in case 'C'.

The very low $f_p \simeq 10^{-3}$ result for case D in Figure 9.11c implies the existence of a

bimodal or multimodal heat transfer regime and demonstrates the broad range of disparate time scales that can arise in low Pr rotating convection. Figure 9.12 shows Nusselt number time series from a) case C, b) case D and c) case E, each plotted for roughly 9 thermal diffusion time scales, τ_κ. The rotation rate is the same for these three cases, whereas the thermal forcing is increased successively from C through E. The time variations of the Nusselt numbers in cases C and E occur on the fluctuation time scales of the oscillatory convective flows, qualitatively similar to the time series fluctuations in Figure 9.9. In contrast, case D features much longer time scale, large amplitude swings in Nu. Here the characteristic time scale of the Nu fluctuations is close to τ_κ.

Figure 9.13 shows spectra for the T4 and T8 thermistor time series from a) case C and b) case D. The low frequency ranges of the spectra differ significantly. Case D has significant spectral power at $f \sim 10^{-3}$ on both internal thermistors. In addition, the two cases differ in the spectral range of the wall modes. Only a single dominant wall mode peak exists in case C, whereas a broader range of wall mode frequencies are excited in case D. This allows for a number of possible explanations for the low frequency heat transfer variability in case D. One possibility is that multiple wall modes are interfering to give a low frequency beating phenonmenon that manifests in the global heat transfer dynamics. Alternatively, there may be different wall modes that are dominating at different times, each with different convective heat transfer capabilities. In addition, it could be that wall modes and oscillatory modes are interacting and resonating, such that energy is driven to low frequencies, and possible to large scales (cf. Favier et al., 2014b; Plumley et al., 2016). Future experiments will also include a high spatial resolution sidewall sensor array that I have built in order to better map the wall mode dynamics in these cases. Irrespective of the precise explanation, the case D results illustrate the propensity for multi-modal, scale-separated dynamics in low Pr, rotating convection systems.

9.5 Discussion

9.5.1 Experimental Summary

Our experimental results demonstrate that different convective modes can co-habitate within the same fluid domain in low Pr rotating convection, as predicted by Goldstein et al. (1994). Convection first onsets via bulk oscillatory modes, in good agreement with the theoretical analysis of Zhang and Liao (2009) (Table 9.3). Wall modes are identified for the first time in liquid gallium, developing at $Ra \simeq 2Ra_O^{cyl}$ (e.g., Figures 9.9d,f). The wall mode frequencies are in adequate agreement with the linear asymptotic analysis made in Liao et al. (2006). However, it is possible that the wall modes are developing at lower onset Ra values than predicted by plane layer analyses. Experimental case C, shown in detail in Figure 9.10, demonstrates that high frequency inertial oscillatory modes can dominate the fluid bulk, while lower frequency wall modes can simultaneously precess around the container's periphery. Further, a number of cases in Figure 9.11 have low frequency heat transfer variability that occurs not on the inertial time scales, but on thermal diffusion time scales. A broadband, turbulent regime is found at still stronger forcings such that $Ra \gtrsim 4Ra_O^{cyl}$ (Figure 9.9.g,h). However, since the convective Rossby numbers are relatively close to unity in these turbulent cases ($Ro_C \gtrsim 0.1$), it is not likely that our experiments directly sample the low Pr, geostrophic turbulence regime.

9.5.2 Geophysical Considerations

Broadly, we find rather different rotating convective flows in liquid metals in comparison to those that develop in current day models of planetary core dynamics (cf. Christensen, 2011; Jones, 2011). In particular, no regime with steady columnar convection is found to exist in liquid metal. This differs from convective flows in current non-metal-based dynamo models, in which a finite regime of steady columnar convective flows exists and appears to be important for the generation of Earth-like magnetic fields (Sreenivasan, 2010; Christensen, 2011; Soderlund et al., 2012). Our liquid metal rotating thermal convection results imply then

that the quasi-geostrophic induction processes (Calkins et al., 2015) that occur in current dynamo models (e.g., Yadav et al., 2016; Schaeffer et al., 2017) may differ significantly from those occurring in planetary cores especially during epochs when thermal buoyancy is the prime driver of fluid motions.

Similarly, in asymptotically reduced models of low Pr rotating convection, oscillatory convection gives way to geostrophic turbulence without ever forming steady columns (e.g., see the $Ra = Ra_S^{\infty}$, $Pr = 0.0235$ case in Figure 14 of Aurnou et al., 2015). Thus, steady convection columns do not form in laboratory-numerical, low Pr models made at finite E, nor do they form in reduced models made in the asymptotically-reduced, low E, low Ro limit (Julien et al., 2012b). This suggests that steady columnar motions will not be excited by low Pr thermal convection in planetary core settings as well. Our liquid gallium results lead us to hypothesize that, as models become capable of simulating lower, more realistic values of E and Pr, the steady local-scale convection column-based paradigm for planetary dynamo generation will not prove to be robust.

Flows dominated by small-scale (e.g., $\ell_O \sim (E/Pr)^{1/3}$) inertial oscillations have been shown to be capable of generating dynamo action (e.g., Davidson and Ranjan, 2015; Calkins et al., 2016). However, it has been argued that oscillatory modes cannot underly quasi-steady dynamo action in planetary core settings since oscillatory convection tends to drive oscillatory dynamo action (Roberts and King, 2013). Hypothetically, purely oscillatory local-scale convection that is modulated on much larger scales should be capable of generating Earth-like magnetic fields (Calkins et al., 2015). If this proves *not* to be the case, then we must address how oscillatory flows can generate large-scale quasi-steady dynamo action. One answer may be that the inertial nature of low Pr flows will tend to drive upscale, inverse energy cascades, which generate large-scale barotropic axial columns (e.g., Julien et al., 2012b; Favier et al., 2014b; Rubio et al., 2014; Stellmach et al., 2014; Aurnou et al., 2015). Then it would be these larger-scale quasi-steady barotropic structures that support the quasi-steady dynamo field (Guervilly et al., 2015). However, such a multi-scale, low Pr dynamo system has yet to be realized in a global scale, spherical model.

The arguments above assume that thermal driving dominates the convection occurring

in planetary cores. For Earth, this may be a reasonable argument prior to the formation of the solid inner core (cf. O'Rourke and Stevenson, 2016). In contrast, we hypothesize here that it may even be possible for oscillatory convection to dominate the local-scale, thermo-compositional convection occurring in the present-day Earth. Since $Ra_O^\infty \sim 10^{-2} Ra_S^\infty$, it is plausible that thermally-driven oscillatory flows will develop more easily and destabilize compositionally-driven quasi-steady flows, even if the compositional buoyancy forcing exceeds the thermal forcing. Alternatively, the admixture of these two buoyancy sources may directly drive a broad-band quasi-geostrophic convective turbulence. To address these zeroth-order dynamical questions, strongly-nonlinear models of thermo-compositional convection must be developed that use realistic diffusivity values for the dynamically active components.

Lastly, our experimental results demonstrate that wave modes naturally develop adjacent to the container's boundary, even in a fully convective fluid layer. These convective wall modes should be the onset mode at Ekman numbers below about 10^{-7} (see Figure 9.1). These types of modes should be easily excited in planetary core settings (Zhang, 1994; Vidal and Schaeffer, 2015), given that $Ra_W^\infty \sim 10^{-3}\, Ra_O^\infty \sim 10^{-5}\, Ra_S^\infty$. Thus, our findings can provide support for scenarios in which planetary dynamo action is driven by multi-modal turbulent convective flows, whilst the secular variation of the magnetic field is controlled by the dynamics of larger-scale, slow wave modes localized near the core-mantle boundary (e.g., Zhang, 1994; Finlay and Jackson, 2003; Buffett, 2014).

9.6 Appendix

9.6.1 Internal Thermistors

9.6.2 Thermal Conductivity Data

Sensor	r/R_i	ϕ [deg.]	z/H
T1	0.70	60	0.838
T2	0.70	120	0.763
T3	0.70	180	0.673
T4	**0.70**	**240**	**0.431**
T5	0.70	300	0.007
T6	0.70	0	0.903
T7	0.35	0	0.836
T8	**0.01**	**0**	**0.487**
T9	0.01	180	0.902

Table 9.4: Positions of the internal thermistors T1 through T9 (column 1) shown in Figures 9.2c and 9.2d. The radial position of thermistors is shown in column 2, normalized by the inner radius of the container $R_i = D/2 = 9.7$ cm. The azimuthal positions, ϕ, are reported in degrees in column 3 (also see Figure 9.2c). Column 4 gives the thermistors' axial coordinates z measured upwards from the base of the fluid layer and normalized by the height of the fluid layer $H = 10.0$ cm. The rows for T4 and T8 are shown in bold, as their data are compared in detail throughout our study.

ΔT	P	rpm	Ra/Ra_O^{exp}
2.01	19.55	8.17	0.80
3.15	29.52	30.6	0.26
5.28	49.44	30.6	0.43
12.88	120.06	32.7	0.96

Table 9.5: Conduction measurements of the thermal conductivity of liquid gallium. Column 1: temperature difference, ΔT, across the tank in degrees Kelvin. Column 2: power input to the heat pad, P, in Watts. The heat flux is equal to this power divided by the area of the tank (i.e., $(\pi D^2)/4$) with $D = 0.194$ m. Column 3: angular rotation rate reported in revolutions per minute (rpm). Column 4: Ratio of the Rayleigh number and the experimentally-determined Rayleigh number at the onset of convection, Ra_O^{exp}, given in Table 9.3.

9.6.3 Convection Data

Case	rpm	P (W)	ΔT (°C)	$\overline{T}$ (°C)	$10^5\,E$	$10^{-6}\,Ra$	$10^2\,Pr$	Ra/Ra_O^{cyl}	Nu	Regime
	0	49.0	1.32	36.83	∞	0.349	2.76	–	3.99	RBC
	0	78.1	1.93	37.55	∞	0.510	2.75	–	4.42	RBC
	0	151.2	3.22	39.16	∞	0.859	2.72	–	5.07	RBC
	0	201.1	4.03	40.24	∞	1.08	2.71	–	5.38	RBC
	0	249.1	4.75	41.26	∞	1.28	2.70	–	5.65	RBC
	0	349.4	6.21	40.60	∞	1.67	2.71	–	6.07	RBC
	0	498.2	8.18	46.37	∞	2.25	2.64	–	6.57	RBC
	0	601.0	9.55	38.85	∞	2.54	2.73	–	6.79	RBC
	0	696.9	10.64	47.52	∞	2.95	2.62	–	7.07	RBC
	0	995.4	14.05	41.81	∞	3.79	2.69	–	7.64	RBC
	0	1195	16.30	43.59	∞	4.44	2.67	–	7.91	RBC
	0	1388	18.40	46.35	∞	5.07	2.64	–	8.14	RBC
	0	1586	20.12	46.36	∞	5.54	2.64	–	8.50	RBC
	3.06	9.6	1.03	36.15	5.60	0.272	2.77	1.26	1.00	BO
	3.06	14.5	1.46	36.43	5.60	0.384	2.77	1.79	1.07	BO
	3.06	19.7	1.83	36.68	5.59	0.483	2.76	2.25	1.16	OW
	3.06	24.8	2.17	36.92	5.58	0.574	2.76	2.67	1.23	WM
	3.06	29.2	2.4	37.09	5.58	0.635	2.76	2.95	1.31	WM
	3.06	38.9	2.9	37.49	5.57	0.767	2.75	3.57	1.45	T
	3.06	59.4	3.7	38.13	5.55	0.983	2.74	4.57	1.73	T
	3.06	98.8	4.93	39.25	5.52	1.32	2.73	6.12	2.16	T
	3.06	199.2	7.06	39.93	5.50	1.89	2.72	8.79	3.04	T
	8.17	19.6	2.10	36.81	2.10	0.553	2.76	0.86	1.01	Sub
	8.17	24.7	2.63	37.13	2.09	0.694	2.76	1.08	1.01	BO
	8.17	29.0	3.01	37.39	2.09	0.796	2.75	1.24	1.04	BO
	8.17	38.8	3.92	37.96	2.08	1.04	2.74	1.62	1.07	BO
	8.17	48.9	4.82	38.47	2.08	1.28	2.74	1.99	1.09	OW
	8.17	59.2	5.38	38.97	2.07	1.43	2.73	2.23	1.19	WM
	8.17	69.2	6.10	39.44	2.07	1.63	2.72	2.54	1.22	WM
	8.17	78.9	6.72	39.89	2.07	1.80	2.72	2.80	1.27	WM
	8.17	98.6	7.79	39.88	2.07	2.08	2.72	3.25	1.37	WM
F	**8.17**	**147.6**	**10.0**	**40.67**	**2.06**	**2.68**	**2.71**	**4.18**	**1.59**	**T**
	8.17	198.8	11.93	40.35	2.06	3.20	2.71	4.99	1.80	T
	8.17	248.3	13.56	40.87	2.06	3.64	2.71	5.68	1.98	T
	8.17	248.1	13.53	45.54	2.01	3.71	2.65	5.78	1.98	T
	8.17	323.1	15.56	40.89	2.06	4.18	2.71	6.52	2.24	T
	8.17	396.4	17.34	40.86	2.06	4.68	2.71	7.30	2.45	T
	8.17	395.2	17.43	49.38	1.98	4.85	2.60	7.55	2.46	T
	8.17	498.2	19.57	42.33	2.04	5.30	2.69	8.25	2.75	T
	8.17	597.9	21.51	43.70	2.03	5.86	2.67	9.12	3.0	T
	8.17	695.7	23.26	44.95	2.01	6.37	2.65	9.92	3.23	T
	8.17	796.3	24.84	46.08	2.01	6.84	2.64	9.65	3.46	T
	8.17	991.8	27.92	47.44	2.00	7.73	2.62	12.04	3.83	T

Table 9.6: Convection data. Applied heating power is P; vertical temperature difference is ΔT; mean fluid temperature is $\overline{T}$. Ekman number is E; Rayleigh number is Ra; Prandtl number is Pr; supercriticality is Ra/Ra_O^{cyl}; and Nusselt number is Nu. Regimes: subcritical cases are "Sub"; bulk oscillatory convection is "BO"; first detection (onset) of wall modes is denoted "OW"; wall mode cases are "WM"; broad band spectra are interpreted to be turbulent convection "T".

Case	rpm	P (W)	ΔT (°C)	$\overline{T}$ (°C)	$10^5\,E$	$10^{-6}\,Ra$	$10^2\,Pr$	Ra/Ra_O^{cyl}	Nu	Regime
	16.33	56.6	6.11	39.29	1.04	1.63	2.73	1.10	1.00	BO
A	**16.33**	**59.6**	**6.24**	**39.40**	**1.04**	**1.67**	**2.73**	**1.13**	**1.03**	**BO**
	16.33	79.2	8.08	40.60	1.03	2.17	2.71	1.47	1.06	BO
	16.33	89.6	9.15	41.24	1.03	2.46	2.70	1.66	1.06	BO
	16.33	93.6	9.57	40.70	1.03	2.57	2.71	1.74	1.06	BO
B	**16.33**	**99.1**	**9.99**	**40.05**	**1.03**	**2.67**	**2.72**	**1.81**	**1.07**	**OW**
	16.33	119.4	11.47	40.05	1.03	3.07	2.72	2.07	1.12	WM
	16.33	148.4	12.94	40.15	1.03	3.47	2.72	2.34	1.24	WM
	16.33	199.7	16.06	40.44	1.03	4.31	2.71	2.91	1.34	WM
	16.33	249.3	18.66	41.42	1.03	5.03	2.70	3.40	1.44	WM
	16.33	349.3	23.30	44.10	1.01	6.36	2.66	4.30	1.62	WM
	16.33	421.8	26.01	45.47	1.01	7.14	2.65	4.82	1.75	WM
	16.33	498.9	28.79	46.89	1.00	7.96	2.63	5.38	1.87	T
	16.33	597.8	31.86	48.81	0.991	8.88	2.61	6.00	2.02	T
	16.33	597.8	31.56	48.52	0.993	8.78	2.61	5.93	2.04	T
	16.33	695.6	34.47	50.35	0.985	9.67	2.59	6.53	2.18	T
	16.33	796.4	37.22	51.17	0.981	10.5	2.58	7.08	2.31	T
	32.66	120.1	12.88	40.72	0.515	3.46	2.71	1.00	1.01	Sub
	32.66	124.6	13.48	40.10	0.516	3.61	2.72	1.05	1.00	BO
	32.66	159.4	16.56	40.13	0.516	4.44	2.72	1.29	1.04	BO
	32.66	190.3	19.51	41.06	0.514	5.25	2.70	1.52	1.05	BO
	32.66	199.8	20.43	41.64	0.512	5.51	2.70	1.60	1.06	BO
	32.66	203.7	20.61	41.76	0.512	5.56	2.69	1.61	1.07	OW
	32.66	230.1	22.55	43.11	0.509	6.12	2.68	1.77	1.10	WM
C	**32.66**	**258.3**	**24.02**	**43.22**	**0.509**	**6.53**	**2.68**	**1.89**	**1.16**	**WM**
D	**32.66**	**299.7**	**27.03**	**46.32**	**0.501**	**7.45**	**2.64**	**2.16**	**1.20**	**WM**
E	**32.66**	**348.7**	**30.10**	**47.46**	**0.499**	**8.34**	**2.62**	**2.42**	**1.25**	**WM**
	32.66	397.1	32.80	49.46	0.494	9.16	2.60	2.66	1.31	WM
	32.66	498.3	38.05	52.45	0.488	10.8	2.56	3.12	1.41	WM
	32.66	597.5	43.13	55.29	0.482	12.4	2.53	3.58	1.49	WM
	32.66	694.8	47.58	54.98	0.482	13.6	2.53	3.95	1.58	T

Table 9.7: Convection data, continued. Applied heating power is P; vertical temperature difference is ΔT; mean fluid temperature is $\overline{T}$. Ekman number is E; Rayleigh number is Ra; Prandtl number is Pr; supercriticality is Ra/Ra_O^{cyl}; and Nusselt number is Nu. Regimes: subcritical cases are "Sub"; bulk oscillatory convection is "BO"; first detection (onset) of wall modes is denoted "OW"; wall mode cases are "WM"; broad band spectra are interpreted to be turbulent convection "T".

Conclusion

I have conducted laboratory experiments to study the characteristics of mechanical- and convective-forcing as is relevant for understanding the turbulent flows generated in the low viscosity oceans and liquid metal cores of planetary interiors. To carry out such experiments, I have used three unique devices that are capable of modeling the fundamental ingredients needed to understand two types of mechanical forcing: libration and tides in the geophysically relevant ellipsoids and ellipsoidal shells and convection in right cylindrical geometries characterizing high latitude planetary core style convection. Laboratory experiments currently provide the best means for investigating these turbulent flows at extreme parameters that are closer to those expected in planetary settings. Although laboratory experiments offer more extreme parameters, the spatial and temporal resolution of the diagnostics used are generally limited and thus these studies are accompanied by direct numerical simulations capable of resolving the entire flow field albeit at generally lower parameters.

I have presented laboratory experimental results demonstrating that librational forcing of an ellipsoidal container of water can produce intense motions through the mechanism of a libration driven elliptical instability (LDEI). These libration studies are conducted using an ellipsoidal acrylic container filled with water. A particle image velocimetry method is used to measure the 2D velocity field in the equatorial plane over hundreds libration cycles for a fixed Ekman number, $E = 2 \times 10^{-5}$. In doing so, we recover the libration induced base flow and a time averaged zonal flow. Further, we show that LDEI in non-axisymmetric container geometries is capable of driving both intermittent and saturated turbulent motions in the bulk fluid. Additionally, we measure the growth rate and amplitude of the LDEI induced excited flow in a fully ellipsoidal container at more extreme parameters than previously studied.

By combining laboratory experiments with high resolution numerical simulations in identical geometries, the LDEI is observed both numerically and experimentally. As the Ekman number is varied from over nearly an order of magnitude from $E \leq 5.5 \times 10^{-4}$, the elliptical instability is characterized by discrete temporal spectra with signals at the forcing frequency

and at half the forcing frequency. The decrease of the Ekman number and hence a decrease in the strength of the viscous forces allows the excitation of additional triadic resonances finally resulting in the transition to turbulence and a continuous frequency spectra characterized as rotating turbulence.

A combined laboratory experimental and numerical approach was adapted to investigate the response of an fluid to tidal forcing by combining laboratory equatorial velocity measurements with selected high-resolution numerical simulations to show, for the first time, the generation of bulk filling turbulence. The mathematical formulation used for librational forcing is generalized to model tidal effects. The transition to saturated turbulence, analogous to librational forcing, is characterized by an elliptical instability that first excites primary inertial modes of the system, then secondary inertial modes forced by the primary inertial modes, and then bulk filling turbulence. The amplitude of this saturated turbulence scales with the bodys elliptical distortion, $U \sim \beta$, while a time- and radially averaged azimuthal zonal flow scales with β^2. The striking similarities between tidally and librationally driven flow transitions to bulk turbulence and zonal flows suggest a generic fluid response independent of the style of mechanical forcing. Since $\beta \leq 10^{-4}$ in planetary bodies, it is often argued that mechanically driven zonal velocities will be small. In contrast, our linear scaling for mechanically driven bulk turbulence, $U \sim \beta$, suggests geophysically significant velocities that can play a significant role in planetary processes including tidal dissipation and magnetic field generation.

The persistence of the LDEI is confirmed in the more geophysically relevant ellipsoidal shells using a combined laboratory experimental and numerical approach even though the existence of inertial modes in such a geometry was previously uncertain. By using five different spherical inner cores of varying sizes, $\chi = 0 - 0.74$, librational forcing in the ellipsoidal shell supports the direct excitation of inertial modes and LDEI that is spatially inhomogeneous as χ increases. The different responses at high latitudes and low latitudes indicates that in addition to the necessity for understanding the turbulence and resulting dissipation at more extreme parameters, $E \sim \mathcal{O}(10^{-15})$, it may also be necessary to understand the geometric effects for such an instability where $\chi \to 1$ as is the case for subsurface oceans.

For rotating convection in moderate Prandtl number ($Pr \sim 7$) fluids, the $Nu - Ra$ scaling slope increase as the Ekman number decreases. For $E = 10^{-7}$, the heat transfer scaling is given by $Nu \sim (Ra/Ra_{crit})^{3.6}$, which is the steepest slope observed in any rotating convection setting. Such increasingly steep scalings that correspond, structurally, to coherent axialized convective columns that play fundamental roles for the dynamo generation in current numerical models are found in a shrinking parameter space. Once Ra passes a transition value Ra_T, the data follows a shallower slope corresponding to the nonrotating scaling slope, $Nu \sim Ra^{0.322}$. The transition from the columnar regime to the inertial dominated regime depends on rotation such that $Ra_T \sim E^{3/2}$ and estimates for supercriticality in the Earth's core suggest that the convective flows are not comprised of columns but may be more accurately described by a geostrophic turbulence not encompassed by current dynamo models.

While the laboratory experimental results at moderate Pr suggest that for large supercriticality, far from onset, the existence of coherent convective columns is unlikely, the laboratory experimental results for rotating convection of a low Pr liquid metal suggest that such structures are also not likely near the onset of convection. Analysis of thermal signals inside the fluid layer reveal that the convection threshold is first overcome in the form of a container scale inertial oscillatory modes. This oscillatory mode sets in at values of Ra well below the critical Rayleigh numbers where steady rotating columnar convection occurs. At stronger forcing, sidewall-attached modes are generated that coexist with the bulk oscillatory modes.

Since oscillatory convection is significantly easier to excite than the steady convection that takes place in many dynamo models, it may be that thermally-driven oscillatory motions will generate dynamo action in planetary settings, well before steady convective flows are generated. While the simulation of rotating convection and dynamos in liquid metals is not currently computationally feasible, our findings highlight the need for combining theory and simulations with coupled laboratory experiments in order to understand the unique combination of strongly turbulent yet strongly constrained planetary core-style turbulence in liquid metals

The success of the combined laboratory experimental and numerical studies discussed in this dissertation challenges the current understanding of planetary dynamics. The studies of Christensen and Aubert (2006) and Aubert et al. (2017) have suggested that the path that connects the fundamental behaviors of the current dynamo models with the underlying dynamics of planetary dynamos is clear despite the large strength of diffusion and unrealistic material properties used in those current models. The work in this dissertation has shown the existence of new behaviors found in realistic fluids at more extreme parameters that are not represented in the current dynamo models and are likely relevant for understanding planetary dynamos. To better address the asymptotic behaviors of turbulent dynamos constrained by strong rotation and magnetic fields, a new generation of larger experiments and higher resolution numerical simulations that can access more extreme parameters and capture more realistic types of planetary turbulence. For mechanical forcing, a larger libration device is currently being designed in the IRPHE Laboratory in Marseille, France, while the most extreme numerical simulations at $E \sim 10^{-6}$ and $\beta \sim 10^{-2}$ are disentangling the characteristics of wave turbulence generated by elliptical instability [e.g., Le Reun et al. (2017)]. The theoretical framework for this turbulence is currently being investigated by R. Kerswell who helped generalize the theoretical foundation for the elliptical instability [e.g., Kerswell (2002)].

An understanding of mechanically-forced turbulence will also help to foster a new generation of studies assessing the dynamo capabilities of such flows. Mechanically forced dynamos have already been demonstrated through precession in spherical geometries (Tilgner (2005); Lin (2015)) as well as in oblate spheroids (Wu and Roberts (2009)). Tidally-forced dynamos have been studied in spheres (Cébron and Hollerbach (2014)) and in local Cartesian models (Barker and Lithwick (2014)) where the tidal deformation is represented as a body force that imposes a base flow. Librationally-forced dynamos have also been investigated in oblate spheroidal geometries (Wu and Roberts (2013)) with stress-free boundaries. However, the secondary flow generated in the boundary to satisfy the stress-free condition was capable of generating a dynamo when no instability in the bulk was present. More realistic librationally-driven dynamos require a geometry that is ellipsoidal about the axis of rotation. However,

the governing equations are challenging to solve efficiently in such geometries with accurate velocity and magnetic boundary conditions. To this end, my colleague Benjamin Favier is currently working on developing more efficient numerical methods using the spectral element code, Nek5000, whose hydrodynamic results were used in Chapters 4, 5, and 6.

In addition, mechanically-forced dynamo experiments have been, and currently are being, designed and constructed. The first and largest experiment is the three meter outer diameter, $\chi = 0.3$, spherical shell filled with liquid sodium and located at the University of Maryland [e.g., Zimmerman et al. (2014)]. The mechanical forcing is generated through differential rotation of the inner core relative to the outer core that then generates flow through viscous coupling. The lack of dynamo action in the experiment to date emphasizes the inefficiency of viscous coupling to generate bulk turbulence. As such, the experiment is being modified with baffles attached to the inner core in order to provide a stronger topographic coupling and, in turn, more efficiently generate turbulence. A separate precessionally-driven cylindrical experiment using liquid sodium is being designed and constructed in Germany [e.g., Stefani et al. (2014)]. The cylindrical container has a unit aspect ratio with a height of two meters. Proof-of-concept, 1:6 scaled, hydrodynamic experiments have shown that this precessional forcing is indeed capable of generating unstable flow so the full scale experiment holds promise for generating mechanically-forced turbulence capable of sustaining dynamo action [e.g., Herault et al. (2015)].

For studies of rotating thermal convection, new, larger device are currently being designed, built, and run at UCLA, the Netherlands, Italy, and Germany [e.g., Cheng et al. (2017)]. These laboratory experiments can access a wide range of parameters and investigate turbulent flow transitions and asymptotically predicted regimes. These tools will also be able to explore new regimes where the turbulence, likely driven at small scales, cascades to larger scale structures that are an ultimate regime in rapidly rotating yet turbulent systems and can be generated in both mechanically forced and convectively-forced systems [e.g., Mininni and Pouquet (2010); Käpylä et al. (2011); Julien et al. (2012b); Chan and Mayr (2013); Barker and Lithwick (2013); Guervilly et al. (2015); Lin et al. (2015); Le Reun et al. (2017)].

Fluid motions in planetary interiors and the forces acting on them are more complex than the simplified representation provided by the reduced models used in this work. It is well understood that many forces, thermochemical convection or stratification, librational forcing, tidal forcing etc., are acting on the planetary fluid layers simultaneously over a variety of length and time scales. While some might argue that the intraforce interactions can stifle planetary processes like dynamo action, it is also possible that such processes are enhanced by intraforce interactions creating new instabilities and enhancing others. As a simple analog, the interaction of libration and tidal forcing in stratified fluid layers that are ubiquitous in planets is worth investigating as it may generate, not an inertial wave elliptical instability as was discussed in this dissertation, but a gravito-inertial wave elliptical instability. Instead, by showing that the turbulent response of fluids to tides and libration is equivalent (Chapter 5), I hypothesize that multi-frequency librational forcing might act as a proxy for a combined tidal-librational forcing. This forcing can be more easily realized by making minor modifications to the libration experiment described in Chapter 2.

For convective forcing, we are beginning to understand fundamental differences in the convective response of rotationally constrained low Prandtl fluids with moderate Prandtl flows. Additionally, I am also in the process of investigating the zeroth order flow responses and transitions that take place when magnetic forces are applied separately and then together with rotation in order to investigate theories of magnetostrophy in comparison with those of rotating convection and magnetoconvection. Furthermore, it is likely that thermal *and* chemical processes related to the release of light elements from inner core cooling and solidification and from exsolution of material from the mantle may contribute to convection. To date, few studies have investigated thermochemical convection and the effects that it has on flows structures and other dynamics. Qualitative experimental work by Cardin and Olson (1992) found similarities between the flow structures generated by thermal convection and thermochemical convection in moderate Prandtl number fluids. It is then useful to apply the tools used in this dissertation to measure flow velocities and temperatures of such flows and to investigate how thermochemical convection might be studied in low Prandtl number fluids as are more geophysically relevant for modeling core flows but certainly a challenge

experimentally.

Bibliography

G. Ahlers. Effect of sidewall conductance on heat-transport measurements for turbulent Rayleigh-Bénard convection. *Phys. Rev. E*, 63(1):015303, 2000.

G. Ahlers and X. Xu. Prandtl-number dependence of heat transport in turbulent Rayleigh-Bénard convection. *Phys. Rev. Lett.*, 86:3320, 2001.

G. Ahlers, S. Grossmann, and D. Lohse. Heat transfer and large scale dynamics in turbulent Rayleigh-Bénard convection. *Rev. Mod. Phys.*, 81(2):503, 2009.

K. Aldridge. *An Experimental Study of Axisymmetric Inertial Oscillations of a Rotating Spherical Container*. PhD thesis, Massachusetts Institute of Technology, 1967.

K. Aldridge and A. Toomre. Axisymmetric inertial oscillation of a fluide in a rotating spherical container. *J. Fluid Mech.*, 37:307–323, 1969.

J. Anderson, G. Schubert, R. Jacobson, E. Lau, W. Moore, and W. Sjogren. Europa's differentiated internal structure: inferences from four Galileo encounters. *Science*, 281 (5385):2019–2022, 1998.

J. Anderson, R. Jacobson, T. McElrath, W. Moore, G. Schubert, and P. Thomas. Shape, mean radius, gravity field, and interior structure of Callisto. *Icarus*, 153(1):157–161, 2001.

J. D. Anderson, W. L. Sjogren, and G. Schubert. Galileo gravity results and the internal structure of Io. *Science*, 272:709–712, 1996.

E. Andrade. LVIII. A theory of the viscosity of liquids: Part II. *The London, Edinburgh, and Dublin Phil. Mag. J. Sci.*, 17(113):698–732, 1934.

J. Arkani-Hamed, B. Seyed-Mahmoud, K. D. Aldridge, and R. E. Baker. Tidal excitation of elliptical instability in the Martian core: possible mechanism for generating the core dynamo. *J. Geophys. Res. Planets*, 113, 2008.

M. J. Assael, I. J. Armyra, J. Brillo, S. V. Stankus, J. Wu, and W. A. Wakeham. Reference data for the density and viscosity of liquid cadmium, cobalt, gallium, indium, mercury, silicon, thallium, and zinc. *J. Phys. Chem. Ref. Data*, 41(3):033101, 2012.

J. Aubert, T. Gastine, and A. Fournier. Spherical convective dynamos in the rapidly rotating asymptotic regime. *J. Fluid Mech.*, 813:558–593, 2017.

J. M. Aurnou. Planetary core dynamics and convective heat transfer scaling. *Geophys. Astrophys. Fluid Dyn.*, 101:327–345, 2007.

J. M. Aurnou and E. M. King. The cross-over to magnetostrophic convection in planetary dynamo systems. *Proc. R. Soc. A*, 473(2199):20160731, 2017.

J. M. Aurnou and P. L. Olson. Experiments on Rayleigh-Bénard convection, magnetoconvection and rotating magnetoconvection in liquid gallium. *J. Fluid Mech.*, 430:283–307, 2001.

J. M. Aurnou, S. Andreadis, L. Zhu, and P. L. Olson. Experiments on convection in Earth's core tangent cylinder. *Earth and Planetary Science Letters*, 212:119–134, 2003.

J. M. Aurnou, M. A. Calkins, J. S. Cheng, K. Julien, E. M. King, D. Nieves, K. M. Soderlund, and S. Stellmach. Rotating convective turbulence in Earth and planetary cores. *Phys. Earth Planet. Inter.*, 246:52–71, 2015.

G. Backus and M. Rieutord. Completeness of inertial modes of an incompressible non-viscous fluid in a corotating ellipsoid. *J. Fluid Mech.*, Submitted, 2016.

J. Bailon-Cuba, M. S. Emran, and J. Schumacher. Aspect ratio dependence of heat transfer and large-scale flow in turbulent convection. *J. Fluid Mech.*, 655:152–173, 2010.

K. M. S. Bajaj, G. Ahlers, and W. Pesch. Rayleigh-Bénard convection with rotation at small Prandtl numbers. *Phys. Rev. E*, 65(5):056309, 2002.

A. J. Barker. Non-linear tides in a homogeneous rotating planet or star: global simulations of the elliptical instability. *Month. Not. of the Royal Astro. Soc.*, 459(1):939–956, 2016.

A. J. Barker and Y. Lithwick. Non-linear evolution of the tidal elliptical instability in gaseous planets and stars. *Month. Not. of the Royal Astro. Soc.*, 435(4):3614–3626, 2013.

A. J. Barker and Y. Lithwick. Non-linear evolution of the elliptical instability in the presence of weak magnetic fields. *Month. Not. of the Royal Astro. Soc.*, 437:305–315, 2014.

A. J. Barker, H. J. Braviner, and G. I. Ogilvie. Non-linear tides in a homogeneous rotating planet or star: global modes and elliptical instability. *Month. Not. of the Royal Astro. Soc.*, 459(1):924–938, 2016.

V. Bertin, A. M. Grannan, and J. M. Aurnou. Rotating convection in liquid gallium: Oscillations, Wall Modes and Turbulence. *Geophys. J. Int.*, In Prep., 2017.

M. Beuthe, A. Rivoldini, and A. Trinh. Enceladus' and Dione's floating ice shells supported by minimum stress isostasy. *Geophys. Res. Lett.*, 43(19), 2016.

J. Bloxham and A. Jackson. Fluid flow near the surface of Earth's outer core. *Rev. Geophys.*, 29(1):97–120, 1991.

H. Bondi and R. Lyttleton. On the dynamical theory of the rotation of the Earth. II. the effect of precession on the motion of the liquid core. *Proc. Camb. Philos. Soc.*, 49:498–515, 1953.

S. I. Braginsky and V. P. Meytlis. Local turbulence in the Earth's core. *Geophys. Astrophys. Fluid Dyn.*, 55:71–87, 1990.

E. A. Brandes and G. B. Brook. *Smithells Metals Reference Book*, volume 7th Edition. Butterworths/Heinemann, 1992.

M. G. Braunsfurth, A. C. Skeldon, A. Juel, T. Mullin, and D. S. Riley. Free convection in liquid gallium. *J. Fluid Mech.*, 342:295–314, 1997.

D. Brito, H.-C. Nataf, P. Cardin, J. Aubert, and J.-P. Masson. Ultrasonic doppler velocimetry in liquid gallium. *Exp. Fluids*, 31(6):653–663, 2001.

D. Brito, J. M. Aurnou, and P. Cardin. Turbulent viscosity measurements relevant to planetary core-mantle dynamics. *PEPI*, 141(1):3–8, 2004.

B. Buffett. Dynamics of the Earth's core. *Earth's Deep Interior: Mineral Physics and Tomography From the Atomic to the Global Scale*, pages 37–62, 2000.

B. Buffett. Geomagnetic fluctuations reveal stable stratification at the top of the Earth's core. *Nature*, 507(7493):484–487, 2014.

B. Buffett and U. Christensen. Magnetic and viscous coupling at the core-mantle boundary: inferences from observations of Earth's rotation. *Geophys. J. Int.*, 171:145–152, 2007.

B. Buffett, H. E. Huppert, J. R. Lister, and A. W. Woods. On the thermal evolution of the Earth's core. *J. Geophys. Res.*, 101(84):7989–8006, 1996.

F. Busse. Mean zonal flows generated by librations of a rotating spherical cavity. *J. Fluid Mech.*, 650:505–512, 2010.

F. Busse. Zonal flow induced by longitudinal librations of a rotating cylindrical cavity. *Physica D*, 240:208–211, 2011.

F. H. Busse and P. G. Cuong. Convection in rapidly rotating spherical fluid shells. *Geophys. Astrophys. Fluid Dyn.*, 8:17–41, 1977.

M. Calkins, J. Noir, J. Eldredge, and J. Aurnou. Axisymmetric simulations of libration-driven fluid dynamics in a spherical shell geometry. *Phys. Fluids*, 22:1–12, 2010.

M. Calkins, J. Noir, J. Eldredge, and J. M. Aurnou. The effects of boundary topography on convection in Earth's core. *Geophys. J. Int.*, 189:799–814, 2012a.

M. A. Calkins, J. M. Aurnou, J. D. Eldredge, and K. Julien. The influence of fluid properties on the morphology of core turbulence and the geomagnetic field. *Earth Planet. Sci. Lett.*, 359-360:55–60, 2012b.

M. A. Calkins, K. Julien, and P. Marti. Three-dimensional quasigeostrophic convection in the rotating cylindrical annulus with steeply sloping end walls. *J. Fluid Mech.*, 732: 214–244, 2013.

M. A. Calkins, K. Julien, S. M. Tobias, and J. M. Aurnou. A multiscale dynamo model driven by quasi-geostrophic convection. *J. Fluid Mech.*, 780:143–166, 2015.

M. A. Calkins, K. Julien, S. M. Tobias, J. M. Aurnou, and P. Marti. Convection-driven kinematic dynamos at low Rossby and magnetic Prandtl numbers: Single mode solutions. *Phys. Rev. E*, 93:023115, 2016.

C. Cambon, N. N. Mansour, and F. S. Godeferd. Energy transfer in rotating turbulence. *J. Fluid Mech.*, 337:303–332, 1997.

P. Cardin and P. Olson. An experimental approach to thermochemical convection in the Earth's core. *Geophys. Res. Lett.*, 19(20):1995–1998, 1992.

B. Castaing, G. Gunaratne, L. Kadanoff, A. Libchaber, and F. Heslot. Scaling of hard thermal turbulence in Rayleigh-Bénard convection. *J. Fluid Mech.*, 204:1–30, 1989.

D. Cébron and R. Hollerbach. Tidally driven dynamos in a rotating sphere. *Astrophys. J. Let.*, 789(1):L25 (5pp), 2014.

D. Cébron, M. Le Bars, J. Leontini, and P. Le Gal. A systematic numerical study of the tidal instability in a rotating triaxial ellipsoid. *Phys. Earth Planet. Inter.*, 182:119–128, 2010a.

D. Cébron, P. Maubert, and M. Le Bars. Tidal instability in a rotating and differentially heated ellipsoidal shell. *Geophys. J. Int.*, 182(3):1311–1318, 2010b.

D. Cébron, M. Le Bars, C. Moutou, and P. Le Gal. Elliptical instability in terrestrial planets and moons. *Astro. Astrophys.*, 539:A78 (16pp), 2012a.

D. Cébron, M. Le Bars, J. Noir, and J. M. Aurnou. Libration driven elliptical instability. *Phys. Fluids*, 24:061703 (7pp), 2012b.

D. Cébron, S. Vantieghem, and W. Herreman. Libration driven multipolar instabilities. *J. Fluid Mech.*, 739:502–543, 2014.

O. Cedak, G. Tobie, T. Van Hoolst, M. Massé, G. Choblet, A. Lefévre, G. Mitri, R.-M. Baland, M. Behounkova, O. Bourgeois, and A. Trinh. Enceladus' internal ocean and ice shell constrained from Cassini gravity, shape, and libration data. *Geophys. Res. Lett.*, 43 (11):5653–5660, 2016.

K. Chan, X. Liao, and K. Zhang. Simulations of fluid motions in ellipsoidal planetary cores driven by longitudinal libration. *Phys. Earth Planet. Inter.*, 187:139–403, 2011.

K. L. Chan and H. G. Mayr. Numerical simulation of convectively generated vortices: Application to the Jovian planets. *Earth and Planetary Science Letters*, 371-372(0):212–219, 2013.

S. Chandrasekhar. *Hydrodynamic and Hydromagnetic Stability*. Dover Publications, 1961.

S. Chandrasekhar. *Ellipsoidal figures of equilibrium*, volume 9. Yale University Press, 1969.

E. M. A. Chen, F. Nimmo, and G. A. Glatzmaier. Tidal heating in icy satellite oceans. *Icarus*, 229:11–30, 2014.

J. S. Cheng, S. Stellmach, A. Ribeiro, A. Grannan, E. King, and J. M. Aurnou. Laboratory-numerical models of rapidly rotating convection in planetary cores. *Geophys. J. Int.*, 201: 1–17, 2015.

J. S. Cheng, J. M. Aurnou, K. Julien, and R. P. J. Kunnen. On the accessibility of rotating convection regimes in laboratory experimental studies. *ArXiv e-prints*, 2017.

A. Chiffaudel, S. Fauve, and B. Perrin. Viscous and inertial convection at low Prandtl number: Experimental study. *Europhys. Lett.*, 4:555–560, 1987.

F. Chillá, S. Ciliberto, C. Innocenti, and E. Pampaloni. Boundary layer and scaling properties in turbulent thermal convection. *Il Nuovo Cimento D.*, 15:1229–1249, 1993.

U. R. Christensen. Zonal flow driven by stronlgy supercritical convection in rotating spherical shells. *J. Fluid Mech.*, 470:115–133, 2002.

U. R. Christensen. Dynamo scaling laws and applications to the planets. *Space Sci. Rev.*, 152:565–590, 2010.

U. R. Christensen. Geodynamo models: Tools for understanding properties of Earth's magnetic field. *Phys. Earth Planet. Inter.*, 187:157–169, 2011.

U. R. Christensen and J. Aubert. Scaling properties of convection-driven dynamos in rotating spherical shells and applicationsto planetary mangetic fields. *Geophys. J. Int.*, 166:97–114, 2006.

S. Cioni, S. Ciliberto, and J. Sommeria. Strongly turbulent Rayleigh-Bénard convection in mercury: comparison with results at moderate Prandtl number. *J. Fluid Mech.*, 335: 111–140, 1997.

S. Cioni, S. Chaumat, and J. Sommeria. Effect of a vertical magnetic field on turbulent Rayleigh-Bénard convection. *Phys. Rev. E*, 62:R4520–R4523, 2000.

T. Clune and E. Knobloch. Pattern selection in rotating convection with experimental boundary conditions. *Phys. Rev. E*, 47(4):2536, 1993.

R. L. Comstock and B. G. Bills. A solar system survey of forced librations in longitude. *J. Geophys. Res. Planets*, 108:1–13, 2003.

P. A. Davidson and A. Ranjan. Planetary dynamos driven by helical waves ii. *Geophys. J. Int.*, 202:1646–1662, 2015.

C. Davies, M. Pozzo, D. Gubbins, and D. Alfé. Constraints from material properties on the dynamics and evolution of Earth's core. *Nat. Geo.*, 8:678–685, 2015.

N. de Koker, G. Steinle-Neumann, and V. Vlček. Electrical resistivity and thermal conductivity of liquid Fe alloys at high P and T, and heat flux in Earth's core. *Proc. Natl. Acad. Sci.*, 109(11):4070–4073, 2012.

A. Delache, C. Cambon, and F. Godeferd. Scale by scale anisotropy in freely decaying rotating turbulence. *Phys. Fluids*, 26:0252014, 2014.

B. Deleplace and P. Cardin. Viscomagnetic torque at the core mantle boundary. *Geophys. J. Int.*, 167:557–566, 2006.

C. A. Dwyer, D. J. Stevenson, and F. Nimmo. A long-lived lunar dynamo driven by continuous mechanical stirring. *Nature*, 479(7372):212–214, 2011.

A. M. Dziewonski and D. L. Anderson. Preliminary reference Earth model. *Phys. Earth Planet. Inter.*, 25:297–356, 1981.

R. E. Ecke and J. Niemela. Heat transport in the geostrophic regime of rotating Rayleigh-Bénard convection. *J. Fluid Mech.*, 113:114301, 2014.

G. D. Egbert and R. D. Ray. Semi-diurnal and diurnal tidal dissipation from Topex/Poseidon altimetry. *Geophys. Res. Lett.*, 30(17):9 (4pp), 2003.

C. Eloy, P. Le Gal, and S. Le Dizes. Experimental study of the multipolar vortex instability. *Phys. Rev. Lett.*, 85:3400–3403, 2000.

I. A. Eltayeb and P. H. Roberts. On the hydromagnetics of rotating fluids. *Astrophys. J.*, 162:699–701, 1970.

M. S. Emran and J. Schumacher. Large-scale mean patterns in turbulent convection. *J. Fluid Mech.*, 776:96–108, 2015.

A. I. Ermakov, M. T. Zuber, D. E. Smith, C. A. Raymond, G. Balmino, R. R. Fu, and B. A. Ivanov. Constraints on Vesta's interior structure using gravity and shape models from the Dawn mission. *Icarus*, 240:146–160, 2014.

B. Favier, A. J. Barker, C. Baruteau, and G. I. Ogilvie. Non-linear evolution of tidally forced inertial waves in rotating fluid bodies. *Month. Not. of the Royal Astro. Soc.*, 439:845–860, 2014a.

B. Favier, L. J. Silvers, and M. R. E. Proctor. Inverse cascade and symmetry breaking in rapidly rotating Boussinesq convection. *Phys. Fluids*, 9:096605, 2014b.

B. Favier, A. M. Grannan, M. Le Bars, and J. M. Aurnou. Generation and maintenance of bulk turbulence by libration-driven elliptical instability. *Phys. Fluids*, 27(6):066601, 2015.

N. A. Featherstone and M. S. Miesch. Meridional circulation in solar and stellar convection zones. *Astrophys. J.*, 804(67):(22pp), 2015.

C. C. Finlay and A. Jackson. Equatorially dominated magnetic field change at the surface of Earth's core. *Science*, 300(5628):2084–2086, 2003.

C. C. Finlay, A. Jackson, N. Gillet, and N. Olsen. Core surface magnetic field evolution 2000-2010. *Geophys. J. Int.*, 189(2):761–781, 2012.

P. F. Fischer, F. Loth, S. E. Lee, S.-W. Lee, D. S. Smith, and H. S. Bassiouny. Simulation of high-Reynolds number vascular flows. *Comp. Meth. App. Mech. and Eng.*, 196(31): 3049–3060, 2007.

P. F. Fischer, J.-W. Lottes, and S.-G. Kerkemeier. nek5000 Web page, 2008. URL http://nek5000.mcs.anl.gov.

R. R. Fu, B. P. Weiss, D. L. Shuster, J. Gattacceca, T. L. Grove, C. Suavet, E. A. Lima, L. Li, and A. T. Kuan. An ancient core dynamo in asteroid Vesta. *Science*, 338:238–241, 2012.

D. Funfschilling, E. Brown, A. Nikolaenko, and G. Ahlers. Heat transport by turbulent Rayleigh-Bénard convection in cylindrical samples with aspect ratio one and larger. *J. Fluid Mech.*, 536:145–154, 2005.

I. Garrick-Bethell, B. P. Weiss, D. L. Shuster, and J. Buz. Early lunar magnetism. *Science*, 323(5912):356–359, 2009.

T. Gastine, J. Wicht, and J. M. Aurnou. Zonal flow regimes in rotating anelastic spherical shells: an application to giant planets. *Icarus*, 225:156–172, 2013.

T. Gastine, R. K. Yadav, J. Morin, A. Reiners, and J. Wicht. From solar-like to antisolar differential rotation in cool stars. *Month. Not. of the Royal Astro. Soc.*, 438:L76–L80, 2014.

T. Gastine, J. Wicht, and J. Aubert. Scaling regimes in spherical shell rotating convection. *J. Fluid Mech.*, 808:690–732, 2016.

V. N. Genrikh, A. B. Kaplun, and A. N. Solovev. Study of liquid viscosity by means of vibration method. Technical report, DTIC Document, 1972.

N. Gillet, D. Brito, D. Jault, and H. C. Nataf. Experimental and numerical studies of magnetoconvection in a rapidly rotating spherical shell. *J. Fluid Mech.*, 580:123–143, 2007.

P. A. Gilman. Nonlinear dynamics of Boussinesq convection in a deep rotating shell – I. *Geophys. Astrophys. Fluid Dyn.*, 8:93–135, 1977.

G. A. Glatzmaier. Geodynamo simulations – how realistic are they? *Ann. Rev. of Earth and Plan. Sci.*, 30(1):237–257, 2002.

G. Glatzmeier and P. Roberts. Rotation and magnetism of Earth's inner core. *Science*, 274: 1887–1891, 1996.

J. A. Glazier, T. Segawa, A. Naert, and M. Sano. Evidence against 'ultrahard' thermal turbulence at very high Rayleigh numbers. *Nature*, 398:307–310, 1999.

E. Gledzer and V. Ponomarev. Instability of bounded flows with elliptical streamlines. *J. Fluid Mech.*, 240:1–30, 1992.

P. Goldreich and J. Mitchell. Elastic ice shells of synchronous moons: Implications for cracks on europa and non-synchronous rotation of titan. *Icarus*, 209:631–638, 2010.

H. F. Goldstein, E. Knobloch, I. Mercader, and M. Net. Convection in a rotating cylinder. Part 2. Linear theory for low Prandtl numbers. *J. Fluid Mech.*, 262:293–324, 1994.

S. Goto, A. Matsunaga, M. Fujiwara, M. Nishioka, S. Kida, M. Yamato, and S. Tsuda. Turbulence driven by precession in spherical and slightly elongated spheroidal cavities. *Phys. Fluids*, 26(5):055107, 2014.

A. M. Grannan, M. Le Bars, D. Cébron, and J. M. Aurnou. Experimental study of global-scale turbulence in a librating ellipsoid. *Phys. Fluids*, 26:126601, 2014.

A. M. Grannan, B. Favier, M. Le Bars, and J. M. Aurnou. Tidally-forced turbulence in planetary interiors. *Geophys. J. Int.*, 208(3):1690–1703, 2017.

H. P. Greenspan. *The Theory of Rotating Fluids*. Cambridge University Press, 1969.

H. P. Greenspan and L. N. Howard. On a time-dependent motion of a rotating fluid. *J. Fluid Mech.*, 17(3):385–404, 1963.

M. Greff-Lefftz, L. Métivier, and H. Legros. Analytical solutions of Love numbers for a hydrostatic ellipsoidal incompressible homogeneous Earth. *Cel. Mech. Dyn. Astro.*, 93 (1-4):113–146, 2005.

N. Grisouard, C. Staquet, and I. Pairaud. Numerical simulation of a two-dimensional internal wave attractor. *J. Fluid Mech.*, 614:1–14, 2008.

I. Grooms and J. P. Whitehead. Bounds on heat transport in rapidly rotating Rayleigh-Bénard convection. *Nonlinearity*, 28:29–41, 2015.

I. Grooms, K. Julien, J. B. Weiss, and E. Knobloch. Model of convective Taylor columns in rotating Rayleigh-Bénard convection. *Phys. Rev. Lett.*, 104:224501, 2010.

A. V. Grosse. The viscosity of liquid metals and an empirical relationship between their activation energy of viscosity and their melting points. *J. Inorg. Nuc. Chem.*, 23(3-4): 333–339, 1961.

S. Grossmann and D. Lohse. Scaling in thermal convection: a unifying theory. *J. Fluid Mech.*, 407:27–56, 2000.

D. Gubbins. The Rayleigh number for convection in the Earth's core. *Phys. Earth Planet. Inter.*, 128:3–12, 2001.

C. Guervilly and P. Cardin. Subcritical convection of liquid metals in a rotating sphere using a quasi-geostrophic model. *ArXiv*, 2017.

C. Guervilly, D. W. Hughes, and C. A. Jones. Large-scale vortices in rapidly rotating Rayleigh-Bénard convection. *J. Fluid Mech.*, 758:407–435, 2014.

C. Guervilly, D. W. Hughes, and C. A. Jones. Generation of magnetic fields by large-scale vortices in rotating convection. *Phys. Rev. E*, 91:041001, 2015.

J. Hazewinkel, P. Van Breevoort, S. B. Dalziel, and L. R. M. Maas. Observations on the wavenumber spectrum and evolution of an internal wave attractor. *J. Fluid Mech.*, 598: 373–382, 2008.

F. Hecht, P. J. Mucha, and G. Turk. Virtual rheoscopic fluids. *IEEE Transactions on Visualization and Computer Graphics*, 16(16):147–160, 2010.

J. Herault, T. Gundrum, A. Giesecke, and F. Stefani. Subcritical transition to turbulence of a precessing flow in a cylindrical vessel. *Phys. Fluids*, 27:124102, 2015.

W. Herreman. *Instabilité elliptique sous champ magnétique et dynamo d'ondes inertielles.* PhD thesis, Aix-Marseille Université, 2009.

W. Herreman, M. Le Bars, and P. Le Gal. On the effects of an imposed magnetic field on the elliptical instability in rotating spheroids. *Phys. Fluids*, 21(4):046602, 2009.

J. Herrmann and F. H. Busse. Asymptotic theory of wall-attached convection in a rotating fluid layer. *J. Fluid Mech.*, 255:183–194, 1993.

R. Hollerbach and R. R. Kerswell. Oscillatory internal shear layers in rotating and precessing flows. *J. Fluid Mech.*, 298:327–339, 1995.

K. Hori, J. Wicht, and U. R. Christensen. The effect of thermal boundary conditions on dynamos driven by internal heating. *Phys. Earth Planet. Inter.*, 182:85–97, 2010.

S. Horn and O. Shishkina. Rotating non-Oberbeck–Boussinesq Rayleigh–Bénard convection in water. *Phys. Fluids*, 26:055111, 2014.

S. Horn and O. Shishkina. Toroidal and poloidal energy in rotating Rayleigh-Bénard convection. *J. Fluid Mech.*, 762:232–255, 2015.

R. N. Ibragimov. Oscillatory nature and dissipation of of the internal waves energy spectrum in the deep ocean. *Eur. Phys. J. Appl. Phys.*, 40(3):315–334, 2007.

T. Iida, Z. Morita, and S. Takeuchi. Viscosity measurements of pure liquid metals by the capillary method. *J. Japan Inst. Metals*, 39.11:1169–1175, 1975.

T. Iida, R. Guthrie, and N. Tripathi. A model for accurate predictions of self-diffusivities in liquid metals, semimetals, and semiconductors. *Metal. Mat. Trans. B*, 37(4):559–564, 2006.

C. L. Johnson, C. G. Constable, and L. Tauxe. Mapping long-term changes in Earth's magnetic field. *Science*, 300(5628):2044–2045, 2003.

C. L. Johnson, R. J. Phillips, M. E. Purucker, B. J. Anderson, et al. Low-altitude magnetic field measurements by MESSENGER reveal Mercury's ancient crustal field. *Science*, 348 (6237):892–895, 2015.

C. A. Jones. Planetary magnetic fields and fluid dynamos. *Ann. Rev. of Fluid Mech.*, 43(1): 583–614, 2011.

C. A. Jones, A. I. Mussa, and S. J. Worland. Magnetoconvection in a rapidly rotating sphere: the weak-field case. *Phil. Trans. Roy. Soc. London A.*, 459:773–797, 2003.

L. Jouve and G. I. Ogilvie. Direct numerical simulations of an inertial wave attractor in linear and nonlinear regimes. *J. Fluid Mech.*, 745:223–250, 2014.

K. Julien and E. Knobloch. Strongly nonlinear convection cells in a rapidly-rotating fluid layer: the tilted f-plane. *J. Fluid Mech.*, 360:141–178, 1998.

K. Julien, S. Legg, J. C. McWilliams, and J. Werne. Rapidly rotating turbulent Rayleigh-Bénard convection. *J. Fluid Mech.*, 322:243–273, 1996.

K. Julien, E. Knobloch, and J. Werne. Reduced equations for rotationally constrained convection. In S. Banerjee and J. K. Eaton, editors, *Turbulence and Shear Flows - I*, pages 101–106. Begell House, 1999.

K. Julien, E. Knobloch, A. M. Rubio, and G. M. Vasil. Heat transport in low-Rossby-number Rayleigh-Bénard convection. *Phys. Rev. Lett.*, 109:254503, 2012a.

K. Julien, A. M. Rubio, I. Grooms, and E. Knobloch. Statistical and physical balances in low-Rossby-number Rayleigh-Bénard convection. *Geophys. Astrophys. Fluid Dyn.*, 106:4-5: 392–428, 2012b.

K. Julien, J. M. Aurnou, M. A. Calkins, E. Knobloch, P. Marti, S. Stellmach, and G. Vasil. A nonlinear model for rotationally constrained convection with Ekman pumping. *J. Fluid Mech.*, 798:50–87, 2016.

A. Kagayama and T. Sato. Computer simulation of a magnetohydrodynamic dynamo II. *Phys. Plasmas*, 2(5):1421–1431, 1995.

S. Kamata, I. Matsuyama, and F. Nimmo. Tidal resonance in icy satellites with subsurface oceans. *J. Geophys. Res. Planets*, 120(9):1528–1542, 2015.

P. J. Käpylä, M. J. Mantere, and T. Hackman. Starspots due to large-scale vortices in rotating turbulent convection. *Astrophys. J.*, 742:34, 2011.

V. Kek and U. Müller. Low Prandtl number convection in layers heated from below. *Int. J. Heat Mass Transfer*, 36:2795–2804, 1993.

R. R. Kerswell. Elliptical instabilities of stratified, hydromagnetic waves. *Geophys. Astrophys. Fluid Dyn.*, 72:107–144, 1993.

R. R. Kerswell. Tidal excitation of hydromagnetic waves and their damping in the Earth. *J. Fluid Mech.*, 274:219–241, 1994.

R. R. Kerswell. On the internal shear layers spawned by the critical regions in oscillatory Ekman boundary layers. *J. Fluid Mech.*, 298:311–325, 1995.

R. R. Kerswell. Secondary instabilities in rapidly rotating fluids: inertial wave breakdown. *J. Fluid Mech.*, 382:283–306, 1999.

R. R. Kerswell. Elliptical instability. *Ann. Rev. of Fluid Mech.*, 34:83–113, 2002.

R. R. Kerswell and W. V. R. Malkus. Tidal instability as the source for Io's magnetic signature. *Geophys. Res. Lett.*, 25(5):603–606, 1998.

J. K. Kevorkian and J. D. Cole. *Multiple Scale and Singular Perturbation Methods*, volume 114 of *Applied Mathematical Sciences*. Springer New York, 1996.

E. King. *An Investigation of Planetary Convection: The Role of Boundary Layers*. PhD thesis, University of California-Los Angeles, 2009.

E. King and J. M. Aurnou. Thermal evidence for Taylor columns in turbulent rotating Rayleigh-Bénard convection. *Phys. Rev. E 85*, 85:016313, 2012.

E. King and J. M. Aurnou. Turbulent convection in liquid metal with and without rotation. *Proc. Natl. Acad. Sci.*, 110:6688–6693, 2013.

E. King and B. Buffett. Flow speeds and length scales in geodynamo models: The role of viscosity. *Earth and Planetary Science Letters*, 371-372(0):156 – 162, 2013.

E. King, S. Stellmach, J. Noir, U. Hansen, and J. M. Aurnou. Boundary layer control of rotating convection systems. *Nature*, 457(7227):301–304, 2009.

E. King, S. Stellmach, and J. M. Aurnou. Heat transfer by rapidly rotating Rayleigh-Bénard convection. *J. Fluid Mech.*, 691:568–582, 2012.

E. M. King and J. M. Aurnou. Magnetostrophic balance as the optimal state for turbulent magnetoconvection. *Proc. Natl. Acad. Sci.*, 112(4):990–994, 2015.

E. M. King, K. M. Soderlund, U. R. Christensen, J. Wicht, and J. M. Aurnou. Convective heat transfer in planetary dynamo models. *Geochem. Geophys. Geosyst.*, 11, 2010.

E. M. King, S. Stellmach, and B. Buffett. Scaling behaviour in Rayleigh-Bénard convection with and without rotation. *J. Fluid Mech.*, 717:449–471, 2013.

R. Kippenhang, A. Weigert, and A. Weiss. *Stellar structure and evolution*, volume 282. Springer, 1990.

A. N. Kolmogorov. The local structure of turbulence in incompressible viscous fluid for very large Reynolds numbers. In *Dokl. Akad. Nauk SSSR*, volume 30, pages 301–305. JSTOR, 1941.

D. Kong, K. Zhang, and G. Schubert. On the variation of zonal gravity coefficients of a giant planet caused by its deep zonal flows. *Astrophys. J*, 748(143):9 pp, 2012.

M. Kono and P. H. Roberts. Recent geodynamo simulations and observations of the geomagnetic field. *Rev. Geophys.*, 40(4), 2002.

R. H. Kraichnan. Turbulent thermal convection at arbitrary Prandtl number. *Phys. Fluids*, 5:1374–1389, 1962.

R. P. J. Kunnen, H. J. H. Clercx, and B. J. Geurts. Breakdown of large-scale circulation in turbulent rotating convection. *Europhysics Letters*, 84:24001, 2008.

L. Lacaze, P. Le Gal, and S. Le Dizes. Elliptical instability in a rotating spheroid. *J. Fluid Mech.*, 505:1–22, 2004.

L. Lacaze, P. Le Gal, and S. Le Dizes. Elliptical instability of the flow in a rotating shell. *Phys. Earth Planet. Inter.*, 151:194–205, 2005.

M. Landeau, P. Olson, R. Deguen, and B. H. Hirsh. Core merging and stratification following giant impact. *Nat. Geo.*, 9:786–789, 2016.

M. Le Bars, S. Le Dizes, and P. Le Gal. Coriolis effects on the elliptical instability in cylindrical and spherical rotating containers. *J. Fluid Mech.*, 585:323–342, 2007.

M. Le Bars, L. Lacaze, S. Le Dizes, P. Le Gal, and M. Rieutord. Tidal instability in stellar and planetary binary systems. *Phys. Earth Planet. Inter.*, 178:48–55, 2010.

M. Le Bars, M. A. Wieczorek, O. Karatekin, D. Cébron, and M. Laneuville. An impact-driven dynamo for the early Moon. *Nature*, 479:215–218, 2011.

M. Le Bars, D. Cébron, and P. Le Gal. Flows driven by libration, precession, and tides. *Ann. Rev. of Fluid Mech.*, 47:163–194, 2015.

S. Le Dizes. Three-dimensional instability of a multipolar vortex in a rotating flow. *Phys. Fluids*, 12:2762–2774, 2000.

T. Le Reun, B. Favier, A. J. Barker, and M. Le Bars. Inertial wave turbulence driven by elliptical instability. *Phys. Rev. Lett. Submitted*, 2017.

D. Lemasquerier, A. M. Grannan, B. Favier, J. Vidal, D. Cébron, M. Le Bars, and J. M. Aurnou. Ellipsoidal Shell Libration: The Movie, 2016. URL https://www.youtube.com/watch?v=WGe-vLsm9Ho.

M. A. Levy and H. J. S. Fernando. Turbulent thermal convection in a rotating stratified fluid. *J. Fluid Mech.*, 467:19–40, 2002.

X. Liao and K. K. Zhang. On viscous decay factors for spherical inertial modes in rotating planetary fluid cores: comparison between asymptotic and numerical analysis. *Phys. Earth Planet. Int.*, 169(1):211–219, 2008.

X. Liao, K. Zhang, and Y. Chang. On boundary-layer convection in a rotating fluid layer. *J. Fluid Mech.*, 549:375–384, 2006.

Y. Lin. *Experimental and Numerical Study of Precession and Libration Driven Flows in Planetary Cores*. PhD thesis, ETH Zurich, 2015.

Y. Lin, P. Marti, and J. Noir. Shear-driven parametric instability in a precessing sphere. *Phys. Fluids*, 27(4):046601, 2015.

Y. Liu and R. E. Ecke. Heat transport scaling in turbulent Rayleigh-Bénard convection: effects of rotation and Prandtl number. *Phys. Rev. Lett.*, 79:2257–2260, 1997.

J. M. Lopez and F. Marques. Instabilities and inertial waves generated in a librating cylinder. *J. Fluid Mech.*, 687:171–193, 2011.

T. S. Lundgren and N. N. Mansour. Transition to turbulence in an elliptic vortex. *J. Fluid Mech.*, 307:43–62, 1996.

J. Mabuchi, Y. Masada, and A. Kageyama. Differential rotation in magnetized and non-magnetized stars. *Astrophys. J.*, 806(10):(16pp), 2015.

W. V. R. Malkus. The heat transport and spectrum of thermal turbulence. *Proc. Roy. Soc. London A*, 225:196–212, 1954.

W. V. R. Malkus. An experimental study of global instabilities due to the tidal (elliptical) distortion of a rotating elastic cylinder. *Geophys. Astrophys. Fluid Dyn.*, 48(1-3):123–134, 1989.

A. Manglik, J. Wicht, and U. R. Christensen. A dynamo model with double diffusive convection for Mercury's core. *Earth Planet. Sci. Lett.*, 289:619–628, 2010.

J.-L. Margot, S. J. Peale, R. F. Jurgens, M. A. Slade, and I. V. Holin. Large longitude libration of Mercury reveals a molten core. *Science*, 316(5825):710–714, 2007.

F. Marques, I. Mercader, . Batiste, and J. M. Lopez. Centrifugal effects in rotating convection: axisymmetric states and three-dimensional instabilities. *J. Fluid Mech.*, 580:303–318, 2007.

D. M. Mason and R. R. Kerswell. Nonlinear evolution of the elliptical instability: an example of inertial wave breakdown. *J. Fluid Mech.*, 396:73–108, 1999.

I. Matsuyama. Tidal dissipation in the oceans of icy satellites. *Icarus*, 242:11–18, 2014.

W. B. McKinnon. Effect of Enceladus' rapid spin on interpretation of Cassini gravity. In *Lunar and Planetary Science Conference*, volume 46, page 2615, 2015.

L. Messio, C. Morize, M. Rabaud, and F. Moisy. Experimental observation using particle image velocimetry of inertial waves in a rotating fluid. *Exp. in Fluids*, 44:519–528, 2008.

P. Meunier and T. Lewecke. Analysis and treatment of errors due to high velocity gradients in particle image velocimetry. *Exp. in Fluids*, 35:408–421, 2003.

P. D. Mininni and A. Pouquet. Rotating helical turbulence: I. Global evolution and spectral behavior. *Phys. Fluids*, 22:035105, 2010.

P. D. Mininni, D. Rosenberg, and A. Pouquet. Isotropization at small scales of rotating helically driven turbulence. *J. Fluid Mech.*, 699:263–279, 2012.

T. Miyagoshi, A. Kagayama, and T. Sato. Zonal flow formation in the Earth's core. *Nature*, 463:793–796, 2010.

C. Morize, M. Le Bars, P. Le Gal, and A. Tilgner. Experimental determination of zonal winds driven by tides. *Phys. Rev. Lett.*, 104:214501, 2010.

Y. Nakagawa and P. Frenzen. A theoretical and experimental study of cellular convection in rotating fluids. *Tellus*, 7:1–21, 1955.

H.-C. Nataf and N. Schaeffer. Turbulence in the core. *Treatise on Geophysics, 2nd ed., Core Dynamics. Elsevier BV, Amsterdam*, 8:161–181, 2015.

J. J. Niemela and K. R. Sreenivasan. Turbulent convection at high Rayleigh numbers and aspect ratio 4. *J. Fluid Mech.*, 557:411–422, 2006.

J. J. Niemela, L. Skrbek, K. R. Sreenivasan, and R. J. Donelly. Turbulent convection at very high Rayleigh numbers,. *Nature*, 404:837–840, 2000.

P. P. Niiler and F. E. Bisshop. On the influence of Coriolis force on onset of thermal convection. *J. Fluid Mech.*, 22:753–761, 1965.

F. Nimmo. Energetics of asteroid dynamos and the role of compositional convection. *Geophys. Res. Lett.*, 36:L10201, 2009.

J. Noir, F. Hemmerlin, J. Wicht, S. Baca, and J. M. Aurnou. An experimental and numerical study of librationally driven flow in planetary cores and subsurface oceans. *Phys. Earth Planet. Inter.*, 173:141–152, 2009.

J. Noir, M. Calkins, M. Lasbleis, J. Cantwell, and J. M. Aurnou. Experimental study of libration-driven zonal flows in a straight cylinder. *Physics of the Earth and Planetary Interiors*, 182:98–1106, 2010.

J. Noir, D. Cébron, M. Le Bars, A. Sauret, and J. M. Aurnou. Experimental study of libration-driven zonal flows in non-axisymmetric containers. *Phys. Earth Planet. Inter.*, 204-205:1–10, 2012.

G. I. Ogilvie. Tidal dissipation in rotationg fluid bodies: a simplified model. *Month. Not. of the Royal Astro. Soc.*, 396:794–806, 2009.

P. L. Olson. The new core paradox. *Science*, 342(6157):431–432, 2013.

P. L. Olson, G. A. Glatzmaier, and R. S. Coe. Complex polarity reversals in a geodynamo model. *Earth and Planetary Science Letters*, 304:168–179, 2011.

J. G. O'Rourke and D. J. Stevenson. Powering Earth's dynamo with magnesium precipitation from the core. *Nature*, 529(7586):387–389, 2016.

A. Pellew and R. V. Southwell. On maintained convective motions in a fluid heated from below. *Phil. Trans. Roy. Soc. London A.*, 176:312–343, 1940.

O. M. Phillips. Energy transfer in rotating fluids by reflection of inertial waves. *Phys. Fluids*, 6(4):513–520, 1963.

M. Plumley, K. Julien, P. Marti, and S. Stellmach. The effects of Ekman pumping on quasi-geostrophic Rayleigh–Bénard convection. *J. Fluid Mech.*, 803:51–71, 2016.

M. Pozzo, C. Davies, D. Gubbins, and D. Alfé. Thermal and electrical conductivity of iron at Earth's core conditions. *Nature*, 485:355–358, 2012.

A. Ribeiro, G. Fabre, J.-L. Guermond, and J. M. Aurnou. Canonical models of geophysical and astrophysical flows: Turbulent convection experiments in liquid metals. *Metals*, 5: 289–335, 2015.

M. Rieutord. Linear theory of rotating fluids using spherical harmonics part II, time-periodic flows. *Geophys. & Astrophys. Fluid Dyn.*, 59:185–208, 1991.

M. Rieutord. Evolution of rotation in binaries: physical processes. *Stellar Rotation, Proc. IAU Symp.*, 215:394–403, 2003.

M. Rieutord and L. Valdettaro. Inertial waves in a rotating spherical shell. *J. Fluid Mech.*, 341:77–99, 1997.

M. Rieutord and L. Valdettaro. Viscous dissipation by tidally forced inertial modes in a rotating spherical shell. *J. Fluid Mech.*, 643:363–394, 2010.

M. Rieutord, B. Georgeot, and L. Valdettaro. Inertial waves in a rotating spherical shell: attractors and asymptotic spectrum. *J. Fluid Mech.*, 435:103–144, 2001.

P. Roberts and J. M. Aurnou. On the theory of core-mantle coupling. *Geophys. Astrophys. Fluid Dyn.*, 106:157–230, 2012.

P. H. Roberts and E. M. King. On the genesis of the Earth's magnetism. *Rep. Prog. Phys.*, 76(9):096801, 2013.

P. Roche. On triggering of the ultimate regime of convection. *New J. Phys.*, 12:085014, 2010.

H. T. Rossby. A study of Bénard convection with and without rotation. *J. Fluid Mech.*, 36 (2):309–335, 1969.

A. M. Rubio, K. Julien, E. Knobloch, and J. B. Weiss. Upscale energy transfer in three-dimensional rapidly rotating turbulent convection. *Phys. Rev. Lett.*, 112:144501, 2014.

A. Sauret. *Forçage Harmonique D'Écoulements en Rotation: Vents Zonaux, Ondes Inertielles et Instabilités*. PhD thesis, Universite Aix-Marseille, 2012.

A. Sauret and S. Le Dizes. Libration-induced mean flow in a spherical shell. *J. Fluid Mech.*, 718:181–209, 2013.

A. Sauret, D. Cébron, C. Morize, and M. Le Bars. Experimental and numerical study of mean zonal flows generated by librations of a rotating spherical cavity. *J. Fluid Mech.*, 662:260–268, 2010.

A. Sauret, D. Cébron, M. Le Bars, and S. Le Dizes. Fluid flows in a librating cylinder. *Phys. Fluids*, 24:1–23, 2012.

A. Sauret, D. Cébron, and M. Le Bars. Spontaneous generation of inertial waves from boundary turbulence in a librating sphere. *J. Fluid Mech.*, 728:R25, 2013.

A. Sauret, M. Le Bars, and P. Le Gal. Tide-driven shear instability in planetary liquid cores. *Geophys. Res. Lett.*, 41:6078–6083, 2014.

N. Schaeffer and S. Le Dizes. Nonlinear dynamics of the elliptic instability. *J. Fluid Mech.*, 646:471–480, 2010.

N. Schaeffer, D. Jault, H.-C. Nataf, and A. Fournier. Geodynamo simulations with vigorous convection and low viscosity. *Geophys. J. Int.*, Submitted, 2017.

J. D. Scheel and J. Schumacher. Global and local statistics in turbulent convection at low Prandtl numbers. *J. Fluid Mech.*, 802:147–173, 2016.

P. J. Schmid. Nonmodal stability theory. *Ann. Rev. of Fluid Mech.*, 39:129–162, 2007.

P. J. Schmid and D. S. Henningson. *Stability and transition in shear flows*, volume 142. Springer Science & Business Media, 2012.

S. Schmitz and A. Tilgner. Heat transport in rotating convection with-out Ekman layers. *Phys. Rev. Lett.*, 80:015305, 2009.

G. Schubert and K. Soderlund. Planetary magnetic fields: observations and models. *Phys. Earth Planet. Inter.*, 187:92–108, 2011.

G. Schubert, J. Anderson, T. Spohn, and W. Mckinnon. Interior composition, structure and dynamics of the Galilean satellites. *Jupiter: The planet, satellites and magnetosphere*, 1, 2004.

B. Seyed-Mahmoud, G. Henderson, and K. D. Aldridge. A numerical model for elliptical instability of the Earth's fluid outer core. *Phys. Earth Planet. Int.*, 117(1):51–61, 2000.

B. Seyed-Mahmoud, K. D. Aldridge, and G. Henderson. Elliptical instability in rotating spherical fluid shells: application to Earth's fluid core. *Phys. Earth Planet. Int.*, 142: 257–282, 2004.

B. I. Shraiman and E. D. Siggia. Heat transport in high-Rayleigh number convection. *Phys. Rev. A*, 42:3650–3653, 1990.

K. Soderlund, E. King, and J. M. Aurnou. The influence of magnetic fields in planetary dynamo models. *Earth and Planetary Science Letters*, 333:9–20, 2012.

K. M. Soderlund, M. H. Heimpel, E. M. King, and J. M. Aurnou. Turbulent models of ice giant internal dynamics: Dynamos, heat transfer, and zonal flows. *Icarus*, 224(1):97–113, 2013.

K. M. Soderlund, B. E. Schmidt, J. Wicht, and D. D. B. and. Ocean-driven heating of Europa's icy shell at low latitudes. *Nat. Geo.*, 7:16–19, 2014.

K. M. Soderlund, A. Sheyko, E. M. King, and J. M. Aurnou. The competition between Lorentz and Coriolis forces in planetary dynamos. *Prog. Earth and Plan. Sci.*, 2(1):1–10, 2015.

K. E. Spells. The determination of the viscosity of liquid gallium over an extended range of temperature. *Proc. Phys. Soc.*, 48(2):299–311, 1936.

E. A. Spiegel. Convection in stars: I. Basic Boussinesq convection. *Ann. Rev. of Astro. and Astrophys.*, 9:323–352, 1971.

M. Sprague, K. Julien, E. Knobloch, and J. Werne. Numerical simulation of an asymptotically reduced system for rotationally constrained convection. *J. Fluid Mech.*, 551:141–174, 2006.

B. Sreenivasan. Modelling the geodynamo: Progress and challenges. *Curr. Sci.*, 99:1739–1749, 2010.

B. Sreenivasan and C. A. Jones. Azimuthal winds, convection and dynamo action in the polar regions of planetary cores. *Geophys. Astrophys. Fluid Dyn.*, 100:319–339, 2006a.

B. Sreenivasan and C. A. Jones. The role of inertia in the evolution of spherical dynamos. *Geophys. J. Int.*, 164:467–476, 2006b.

F. D. Stacy and P. M. Davis. *Physics of the Earth*. Cambrdige University Press, 4 edition, 2008.

A. Stark, J. Oberst, F. Preusker, S. J. Peale, J.-L. Margot, R. J. Phillips, G. A. Neumann, D. E. Smith, M. T. Zuber, and S. C. Solomon. First MESSENGER orbital observations of Mercury's librations. *Geophys. Res. Lett.*, 42:1–9, 2015.

F. Stefani, T. Albrecht, G. Gerbeth, A. Giesecke, T. Gundrum, J. Herault, C. Nore, and C. Steglich. Towards a precession driven dynamo experiment. *arXiv preprint*, 2014.

S. Stellmach and U. Hansen. Cartesian convection driven dynamos at low Ekman number. *Phys. Rev. E*, 70:0563112, 2004.

S. Stellmach and U. Hansen. An efficient spectral method for the simulation of dynamos in Cartesian geometry and its implementation on massively parallel computers. *Geochem. Geophys. Geosyst.*, 9, 2008.

S. Stellmach, M. Lischper, K. Julien, G. Vasil, J. S. Cheng, A. Ribeiro, E. M. King, and J. M. Aurnou. Approaching the asymptotic regime of rapidly rotating convection: Boundary layers versus interior dynamics. *Phys. Rev. Lett.*, 113:254501, 2014.

R. J. Stevens, H. J. Clercx, and D. Lohse. Heat transport and flow structure in rotating Rayleigh-Bénard convection. *Eur. J. Mech.*, 40:41–49, 2013.

D. J. Stevenson. Planetary magnetic fields. *Earth and Planetary Science Letters*, 208:1–11, 2003.

S. Suess. *Some Effects of Gravitational Tides on a Rotating Fluid*. PhD thesis, University of California, Los Angeles, 1969.

S. Suess. Viscous flow in a deformable rotating container. *J. Fluid Mech.*, 45:189–201, 1971.

S. I. Takehiro. Physical interpretation of spiralling-columnar convection in a rapidly rotating annulus with radial propagation properties of Rossby waves. *J. Fluid Mech.*, 614:67–86, 2008.

J. A. Tarduno, R. D. Cottrell, F. Nimmo, J. Hopkins, J. Voronov, A. Erickson, E. Blackman, E. R. D. Scott, and R. Mckinney. Evidence for a dynamo in the main group pallasite parent body. *Science*, 338:93–95, 2012.

J. A. Tarduno, R. D. Cottrell, W. J. Davis, F. Nimmo, and K. Richard. A Hadean to Paleoarchean geodynamo recorded by single zircon crystals. *Science*, 349:521–524, 2015.

P. C. Thomas, R. Tajeddine, M. S. Tiscareno, J. A. Burns, J. Joseph, T. J. Loredo, P. Helfenstein, and C. Porco. Enceladus' measured physical libration requires a global subsurface ocean. *Icarus*, 264:37–47, 2016.

A. Tilgner. Driven inertial oscillations in spherical shells. *Phys. Rev. E*, 59(2):1789, 1999.

A. Tilgner. Precession driven dynamos. *Phys. Fluids*, 17:034104, 2005.

A. Tilgner. Rotational dynamics of the core. *Treatise on Geophysics*, 8:207–243, 2007.

Y. Tsuji, T. Mizuno, T. Mashiko, and M. Sano. Mean wind in convective turbulence of Mercury. *Phys. Rev. Lett.*, 94:034501, 2005.

R. H. Tyler. Strong ocean tidal flow and heating on moons of the outer planets. *Nature*, 456:770–772, 2008.

R. H. Tyler. Comparative estimates of the heat generated by ocean tides on icy satellites in the outer Solar System. *Icarus*, 243(0):358–385, 2014.

T. Van Hoolst, N. Rambaux, O. Karatekin, V. Dehant, and A. Rivoldini. The librations, shape, and icy shell of Europa. *Icarus*, 195(1):386–399, 2008.

T. Van Hoolst, R.-M. Baland, and A. Trinh. On the librations and tides of large icy satellites. *Icarus*, 226:299–315, 2013.

S. Vantieghem. Inertial modes in a rotating triaxial ellipsoid. *Proc. R. Soc. A*, 470:20140093, 2014.

S. Vantieghem, D. Cébron, and J. Noir. Latitudinal libration driven-flows in triaxial ellipsoids. *J. Fluid Mech.*, 771:193–228, 2015.

J. Verhoogen. Thermal regime of the Earth's core. *Phys. Earth Planet. Inter.*, 7:47–58, 1973.

J. Vidal and N. Schaeffer. Quasi-geostrophic modes in the Earth's fluid core with an outer stably stratified layer. *Geophys. J. Int.*, 202(3):2182–2193, 2015.

J. Vidal, D. Cébron, and N. Schaeffer. Diffusionless hydromagnetic modes in rotating ellipsoids: A road to weakly nonlinear models? *Comptes-Rendus de la 19 e Rencontre du Non-Linéaire Paris 2016*, page 121, 2016.

J. Vidal, D. Cébron, and N. Schaeffer. Inviscid instabilities in rotating ellipsoids on eccentric Kepler orbits. *Submitted to J. Fluid Mech.*, 2017.

C.-Y. Wang. Cylindrical tank of fluid oscillating about a state of steady rotation. *J. Fluid Mech.*, 41:581–592, 1970.

A. Warn-Varnas, W. W. Fowlis, S. Placsek, and S. M. Lee. Numerical solutions and laser-Doppler measurements of spin-up. *J. Fluid Mech.*, 85(04):609–639, 1978.

X. Wei, R. Arlt, and A. Tilgner. A simplified model of collision-driven dynamo action in small bodies. *Phys. Earth Planet. Inter.*, 231:30–38, 2014.

J. G. Williams and D. Boggs. Tides on the moon: Theory and determination of dissipation. *J. Geophys. Res. Planets*, 120(4):689–724, 2015.

C. Wu and P. H. Roberts. On a dynamo driven by topographic precession. *Geophys. Astrophys. Fluid Dyn.*, 13:467–501, 2009.

C. Wu and P. H. Roberts. On a dynamo driven topographically by longitudinal libration. *Geophys. Astrophys. Fluid Dyn.*, 107:20–44, 2013.

X. Z. Wu and A. Libchaber. Scaling relations in thermal turbulence: the aspect-ratio dependence. *Phys. Rev. A*, 45:842–845, 1992.

Q. Xu, N. Oudalov, Q. Guo, H. Jaeger, and E. Brown. Effect of oxidation on the mechanical properties of liquid gallium and eutectic gallium-indium. *Phys. Fluids*, 24:063101, 2012.

R. K. Yadav, T. Gastine, U. R. Christensen, L. D. V. Duarte, and A. Reiners. Effect of shear and magnetic field on the heat-transfer efficiency of effect of shear and magnetic field on the heat-transfer efficiency of convection in rotating spherical shells. *Geophys. J. Int.*, 204 (2):1120–1133, 2016.

C. F. Yoder, A. S. Konopliv, D. N. Yuan, E. M. Standish, and W. M. Folkner. Fluid core size of Mars from detection of the solar tide. *Science*, 300(5617):299–303, 2003.

O. Zeman. A note on the spectra and decay of rotating homogeneous turbulence. *Phys. Fluids*, 6(10):3221–3223, 1994.

K. Zhang. On equatorially trapped boundary inertial waves. *J. Fluid Mech.*, 248:203–217, 1993.

K. Zhang. On coupling between the Poincaré equation and the heat equation. *J. Fluid Mech.*, 268:211–229, 1994.

K. Zhang and X. Liao. The onset of convection in rotating circular cylinders with experimental boundary conditions. *J. Fluid Mech.*, 622:63–73, 2009.

K. Zhang and G. Schubert. Magnetohydrodynamics in rapidly rotating spherical systems. *Ann. Rev. of Fluid Mech.*, 32(1):409–443, 2000.

K. Zhang, X. Liao, and P. Earnshaw. On inertial waves and oscillations in a rapidly rotating spheroid. *J. Fluid Mech.*, 504:1–40, 2004.

K. Zhang, K. Chan, and X. Liao. On fluid motion in librating ellipsoids with moderate equatorial eccentricity. *J. Fluid Mech.*, 673:468–479, 2011.

K. Zhang, K. H. Chan, X. Liao, and J. M. Aurnou. The non-resonant response of fluid in a rapidly rotating sphere undergoing longitudinal libration. *J. Fluid Mech.*, 720:212–235, 2013.

P. Zhang, R. E. Cohn, and K. Haule. Effects of electron correlations on transport properties of iron at Earth's core conditions. *Nature*, 517:605–607, 2015.

F. Zhong, R. E. Ecke, and V. Steinberg. Asymmetric modes and the transition to vortex structures in rotating Rayleigh-Bénard convection. *Phys. Rev. Lett.*, 67(18):2473–2476, 1991.

J. Q. Zhong and G. Ahlers. Heat transport and the large-scale circulation in rotating turbulent Rayleigh-Bénard convection. *J. Fluid Mech.*, 665:300–333, 2010.

J. Q. Zhong, R. J. Stevens, H. J. H. Clercx, R. Verzicco, D. Lohse, and G. Ahlers. Prandtl-, Rayleigh-, and Rossby-number dependence of heat transport in turbulent rotating Rayleigh-Bénard convection. *Phys. Rev. Lett.*, 102(4):044502, 2009.

Y. Zhou. A phenomenological treatment of rotating turbulence. *Phys. Fluids*, 7(8):2092–2094, 1995.

D. S. Zimmerman, S. A. Triana, H.-C. Nataf, and D. Lathrop. A turbulent, high magnetic Reynolds number experimental model of Earth's core. *J. Geophys. Res. Solid Earth*, 119: 4538–4557, 2014.